NUREG/CP-0157
Vol. 2

Proceedings of the U.S. Nuclear Regulatory Commission

Twenty-Fourth Water Reactor Safety Information Meeting

Volume 2

- Reactor Pressure Vessel Embrittlement and Thermal Annealing
- Reactor Vessel Lower Head Integrity
- Evaluation and Projection of Steam Generator Tube Condition and Integrity

Held at
Bethesda Marriott Hotel
Bethesda, Maryland
October 21–23, 1996

U.S. Nuclear Regulatory Commission

Office of Nuclear Regulatory Research

Proceedings prepared by
Brookhaven National Laboratory

AVAILABILITY NOTICE

Availability of Reference Materials Cited in NRC Publications

Most documents cited in NRC publications will be available from one of the following sources:

1. The NRC Public Document Room, 2120 L Street, NW., Lower Level, Washington, DC 20555-0001
2. The Superintendent of Documents, U.S. Government Printing Office, P. O. Box 37082, Washington, DC 20402-9328
3. The National Technical Information Service, Springfield, VA 22161-0002

Although the listing that follows represents the majority of documents cited in NRC publications, it is not intended to be exhaustive.

Referenced documents available for inspection and copying for a fee from the NRC Public Document Room include NRC correspondence and internal NRC memoranda; NRC bulletins, circulars, information notices, inspection and investigation notices; licensee event reports; vendor reports and correspondence; Commission papers; and applicant and licensee documents and correspondence.

The following documents in the NUREG series are available for purchase from the Government Printing Office: formal NRC staff and contractor reports, NRC-sponsored conference proceedings, international agreement reports, grantee reports, and NRC booklets and brochures. Also available are regulatory guides, NRC regulations in the *Code of Federal Regulations*, and *Nuclear Regulatory Commission Issuances*.

Documents available from the National Technical Information Service include NUREG-series reports and technical reports prepared by other Federal agencies and reports prepared by the Atomic Energy Commission, forerunner agency to the Nuclear Regulatory Commission.

Documents available from public and special technical libraries include all open literature items, such as books, journal articles, and transactions. *Federal Register* notices, Federal and State legislation, and congressional reports can usually be obtained from these libraries.

Documents such as theses, dissertations, foreign reports and translations, and non-NRC conference proceedings are available for purchase from the organization sponsoring the publication cited.

Single copies of NRC draft reports are available free, to the extent of supply, upon written request to the Office of Administration, Distribution and Mail Services Section, U.S. Nuclear Regulatory Commission, Washington, DC 20555-0001.

Copies of industry codes and standards used in a substantive manner in the NRC regulatory process are maintained at the NRC Library, Two White Flint North, 11545 Rockville Pike, Rockville, MD 20852-2738, for use by the public. Codes and standards are usually copyrighted and may be purchased from the originating organization or, if they are American National Standards, from the American National Standards Institute, 1430 Broadway, New York, NY 10018-3308.

NUREG/CP-0157
Vol. 2

Proceedings of the U.S. Nuclear Regulatory Commission

Twenty-Fourth Water Reactor Safety Information Meeting

Volume 2

- Reactor Pressure Vessel Embrittlement and Thermal Annealing
- Reactor Vessel Lower Head Integrity
- Evaluation and Projection of Steam Generator Tube Condition and Integrity

Held at
Bethesda Marriott Hotel
Bethesda, Maryland
October 21-23, 1996

Manuscript Completed: January 1997
Date Published: February 1997

Compiled by: Susan Monteleone

C. Bonsby, NRC Project Manager

Office of Nuclear Regulatory Research
U.S. Nuclear Regulatory Commission
Washington, DC 20555-0001

Proceedings prepared by
Brookhaven National Laboratory

NUREG/CP-0157, Vol. 2 has been reproduced from the best available copy.

ABSTRACT

This three-volume report contains papers presented at the Twenty-Fourth Water Reactor Safety Information Meeting held at the Bethesda Marriott Hotel, Bethesda, Maryland, October 21-23, 1996. The papers are printed in the order of their presentation in each session and describe progress and results of programs in nuclear safety research conducted in this country and abroad. Foreign participation in the meeting included papers presented by researchers from Czech Republic, Finland, France, Japan, Norway, Russia and United Kingdom. The titles of the papers and the names of the authors have been updated and may differ from those that appeared in the final program of the meeting.

PROCEEDINGS OF THE
24TH WATER REACTOR SAFETY INFORMATION MEETING

OCTOBER 21-23, 1996

Published in Three Volumes

GENERAL INDEX

Volume 1

- Plenary Sessions
- High Burnup Fuel
- Containment and Structural Aging

Volume 2

- Reactor Pressure Vessel Embrittlement and Thermal Annealing
- Reactor Vessel Lower Head Integrity
- Evaluation and Projection of Steam Generator Tube Condition and Integrity

Volume 3

- PRA and HRA
- Probabilistic Seismic Hazard Assessment and Seismic Siting Criteria

REGISTERED ATTENDEES (NON-NRC)
24TH WATER REACTOR SAFETY INFORMATION MEETING

J. ALMBERGER
VATTENFALL FUEL
STOCKHOLM, S-16287 SWEDEN
46-8-7395444 FAX 46-8-178640
JAN@FUEL.VATTENFALL.SE

A. ALONSO
CONSEJO DE SEGURIDAD NUCLEAR
JUSTO DORADO, 11
MADRID, 28040 SPAIN
341-346-0334 FAX 341-346-0378
AAS@CSN.ES

L. ANDERMO
SWEDISH NUCLEAR POWER INSPECTORATE
KLARABERGSVIADUKTEN 90
STOCKHOLM, 10658 SWEDEN
46-8-6988484 FAX 46-8--6619086
LARSA@SKI.SE

R. ANDERSON
NORTHERN STATES POWER CO.
414 NICOLLET MALL, RSq 8
MINNEAPOLIS, MN 55401 USA
612-337-2050 FAX 612-337-2042

A. ANKRUM
PACIFIC NORTHWEST NATIONAL LABORATORY
PO BOX 999, MSIN: K8-28
RICHLAND, WA 99352 USA
509-372-4095 FAX 509-375-3970
AR_ANKRUM@PNL..GOV

E. ARAIZA
COMISION NACIONAL DE SEGURIDAD NUCLEAR
DR. BARRAGAN 779 COL. NARVARTE
MEXICO CITY, 03020 MEXICO
525 590-8113 FAX 525 590-6103

V. ASMOLOV
RRC KURCHATOV INSTITUTE, NSI
KURCHATOV SQ. 1
MOSCOW, 123182 RUSSIA
7-095-1969320 FAX 7-0951961702
ASMOLOV@OBAE.KIAE.SU

M. AZARM
BROOKHAVEN NATIONAL LABORATORY
BLDG. 130, PO BOX 5000
UPTON, NY 11973-5000 USA
516-344-4922 FAX 516-344-5730
AZARM@BNL.GOV

S. AZUMI
KANSAI ELECTRIC POWER CO., INC.
2001 L STREET, NW, SUITE 801
WASHINGTON, DC 20036 USA
202-658-1138 FAX 202-457-0272

J. BAILEY
ARIZONA PUBLIC SERVICE CO.
P.O. BOX 53999
PHOENIX, AZ 85072-3999 USA

S. BAKHTIARI
ARGONNE NATIONAL LABORATORY
9700 S. CASS AVE.
ARGONNE, IL 60439 USA
630-252-8962 FAX 630-252-3250
SASAN_BAKHTIARI@GMGATE.ANL.GOV

W. BALZ
COMMISSION OF THE EUROPEAN COMMUNITIES
200, RUE DE LA LOI
BRUSSELS, 1049 BELGIUM
32-2-2954164 FAX 32-2-2966883

Y. BANG
KOREA INSTITUTE OF NUCLEAR SAFETY
PO BOX 114 YUSONG
TAEJON, 305-600 KOREA
82-42-868-0140 FAX 82-42-861-2535
K164BYS@KINSWS.KINS.RE.KR

A. BARATTA
PENNSYLVANIA STATE UNIVERSITY, DNE
231 SACKETT BLDG.
UNIVERSITY PARK, PA 16802 USA
814-865-1341 FAX 814-865-8499
AB2@PSUVM.PSU.EDU

R. BARI
BROOKHAVEN NATIONAL LABORATORY
BLDG. 197C, PO BOX 5000
UPTON, NY 11973-5000 USA
516-344-2629 FAX 516-344-5266
BARI1@BNL.GOV

J.P. BERGER
EDF - SEPTEN
12 AV. DU DUTRIEVOZ
VILLEURBANNE, 69628 FRANCE
72-82-7599 FAX 72-82-7690

C. BEYER
BATTELLE PACIFIC NORTHWEST LABORATORY
PO BOX 999
RICHLAND, WA 99352 USA
509-372-4605 FAX 509-372-4439
CE_BEYER@PNL.GOV

D. BHARGAVA
VIRGINIA POWER
5000 DOMINION BLVD.
GLEN ALLEN, VA 23060 USA
804-273-3638 FAX 804-273-2188
DIVAKAR_BHARGAVA@VAPOWER.COM

J. BOCCIO
BROOKHAVEN NATIONAL LABORATORY
BLDG. 130, PO BOX 5000
UPTON, NY 11973-5000 USA
516-344-7690 FAX 516-344-5730
BOCCIO@BNL.GOV

R. BORSUM
FRAMATOME TECHNOLOGIES, INC.
1700 ROCKVILLE PIKE, SUITE 525
ROCKVILLE, MD 20852-1631 USA
301-230-2100 FAX 301-468-6246

G. BROWN
AEA TECHNOLOGY
RISLEY, WARRINGTON
CHESHIRE, ENGLAND UK
01925-254473 FAX 1925254576
GEOFF.BROWN@AEAT.CO.UK

M. BRUMOVSKY
NUCLEAR RESEARCH INSTITUTE REZ
REZ PLE
REZ, 25068 CZECH REPUBLIC
42-2-6857979 FAX 42-2-6857519

W. BRUNSON
FRAMATOME COGEMA FUELS
3315 OLD FOREST RD.
LYNCHBURG, VA 24506-0935 USA
804-832-2687 FAX 804-832-3663
WBRUNSON@FRAMATECH.COM

A. CAMP
SANDIA NATIONAL LABORATORIES
PO BOX 5800
ALBUQUERQUE, NM 87185-0747 USA
505-844-5960 FAX 505-844-3321
ALCAMP@SANDIA.GOV

G. CAPPONI
AGENZIA NAZ. PER LA PROT. DE'L' AMBIENTE
VIA V. BRANCATI, 48
ROMA, 00144 ITALY
39-6-50072198 FAX 39-6-50072044
CAPPG@ANPA.IT

M. CARLSSON
STUDSVIK NUCLEAR AB
NYKOPING, 61182 SWEDEN
46-155-221000 FAX 46-155-263070

W. PAUL CHEN
ENERGY TECHNOLOGY ENGINEERING CENTER
6633 CANOGA AVENUE
CANOGA PARK, CA 91304 USA
818-586-5285 FAX 818-586-5118

J. CHERRY
SANDIA NATIONAL LABORATORIES
PO BOX 5800, MS 0741
ALBUQUERQUE, NM 87185-0741 USA
505-844-0090 FAX 505-844-1648
JCHERR@SANDIA.GOV

F.B. CHEUNG
PENNSYLVANIA STATE UNIVERSITY
304 REBER BLDG.
UNIVERSITY PARK, PA 16802 USA
814-863-4261 FAX 814-863-8682
FXC4@PSU.EDU

D. CHO
KOREA INSTITUTE OF NUCLEAR SAFETY
PO BOX 114 YUSONG
TAEJON, 305-600 KOREA
82 042 868 0229

W. CHOE
TU ELECTRIC NUCLEAR SAFETY ANALYSIS
1601 BRYAN ST., EP 15
DALLAS , TX 75201-3411 USA
214-812-4371 FAX 214-812-8687

Y.J. CHOI
KOREA INSTITUTE OF NUCLEAR SAFETY
PO BOX 114 YUSONG
TAEJON, 305-600 KOREA
82-42-868-0139 FAX 82-42-861-2535
K149CYJ@KINSWS.KINS.RE.KR

T.Y. CHU
SANDIA NATIONAL LABORATORIES
PO BOX 5800, MS 1139
ALBUQUERQUE, NM 87185-1139 USA
505-845-3217 FAX 505-845-3117
TYCHU@SANDIA.GOV

H.M. CHUNG
ARGONNE NATIONAL LABORATORY
9700 SO. CASS AVE.
ARGONNE, IL 60439 USA
630-252-5111 FAX 630-252-3604
HEE_CHUNG@QMGATE.ANL.GOV

R. CLARK
GOLDER ASSOCIATES, INC.
4104 148TH AVE., NE
REDMOND, WA 98052 USA
206-883-0777 FAX 206-882-5474
RCLARK@GOLDER.COM

T. CLONINGER
HOUSTON LIGHTING & POWER COMPANY
P.O. BOX 289
WADSWORTH, TX 77483 USA

J. CONDE
CONSEJO DE SEGURIDAD NUCLEAR
JUSTO DORADO, 11
MADRID, 28040 SPAIN
34-1-3460-253 FAX 34-1-3460-588
JMCL@CSM.ES

R. COPELAND
SIEMENS POWER CO.
2101 HORN RAPIDS ROAD
RICHLAND, WA 99352 USA
509 375-8290

D. COPINGER
OAK RIDGE NATIONAL LABORATORY
PO BOX 2009, BLDG. 9201-3
OAK RIDGE, TN 37831 USA
423-574-3222 FAX 423-574-0382
D9C@ORNL.GOV

C. CORNELL
C. ALLEN CORNELL CO.
110 COQUITO WAY
PORTOLA VALLEY, CA 94028 USA
415-854-8053 FAX 415-854-8075
CORNELL@SURGE.STANFORD.EDU

B. CORWIN
OAK RIDGE NATIONAL LABORATORY
P.O. BOX 2008
OAK RIDGE, TN 37831 USA
423-574-4648 FAX 423-574-5118
CORWINWR@ORNL.GOV

D. COUCILL
BRITISH NUCLEAR FUELS
SPRINGFIELDS WORKS, SALWICK
PRESTON, UK
44 1772 762085 FAX 44 1772 763888

M. COURTAUD
COMMISSARIAT A L'ENERGIE ATOMIQUE
17, RUE DES MARTYRS
GRENOBLE, CEDEX 9, 38054 FRANCE
33 4 76 88 36 60 FAX 33 4 76 88 51 79
COURTAUDDRN.CEA.FR

K. COZENS
NUCLEAR ENERGY INSTITUTE
1776 I ST., NW, SUITE 400
WASHINGTON, DC 20006-3708 USA
202-739-8085 FAX 202-785-1898

M. CUNNINGHAM
PACIFIC NORTHWEST NATIONAL LABORATORY
PO BOX 999
RICHLAND, WA 99352 USA
509-372-4987 FAX 509-372-4989
ME_CUNNINGHAM@PNL.GOV

C. CZAJKOWSKI
BROOKHAVEN NATIONAL LABORATORY
PO BOX 5000, BLDG. 830
UPTON, NY 11973-5000 USA
516-344-4420 FAX 516-344-4486
CJC@BNL.GOV

B. DE BOECK
AVN
AVENUE DU ROI 157
BRUSSELS, B-1190 BELGIUM
32-2-5368335 FAX 32-2-5368585
BDB@AVN.BE

F. DE PASQUALE
ATOMIC ENERGY CONTROL BOARD
280 SLATER ST.
OTTAWA, ONTARIO K1P5S9 CANADA
613-947-4018 FAX 613-995-5086
DEPASQUALE.F@ATOMCO.GA.CA

J. DeBOR
3630 NO. 21 AVE.
ARLINGTON, VA 22207 USA
703-524-3222 FAX 703-524-2427

D. DIERCKS
ARGONNE NATIONAL LABORATORY
9700 S. CASS AVE.
ARGONNE, IL 60439 USA
630-252-5032 FAX 630-252-4798
DR_DIERCKS@QMGATE.ANL.GOV

S. DOROFEEV
RRC KURCHATOV INSTITUTE
KURCHATOV SQUARE 1
MOSCOW, 123182 RUSSIA
7 095 196 9840 FAX 7 095 882 5801
DOROFEEV@ACPI.MSK.SU

J. DUCO
INSTITUT DE PROT. ET DE SURETE NUC.
CEA/FAR - BP6
FONTENAY AUX ROSES, CEDEX 92265 FRANCE
33 1 46 54 7068 FAX 33 1 46 54 4437
DUCO@BASILIC.CEA.FR

M. DURIN
INSTITUT DE PROT. ET DE SURETE NUC.
CEA FAR, BP NO. 6
FONTENAY AUX ROSES, CEDEX 92265 FRANCE
33-1-46-54-81-83 FAX 33-1-46-54-32-64

Z. ELAWAR
PALO VERDE NUCLEAR GENERATING STATION
PO BOX 52034, STA. 7527
PHOENIX, AZ 85072-2034 USA
602-393-5328 FAX 602-393-5467
ZELAWAR@APSC.COM

J.M. EVRARD
INSTITUT DE PROT. ET DE SURETE NUC.
CEA FAR, BP NO. 6
FONTENAY AUX ROSES, CEDEX 92265 FRANCE

M. EVRE
PECO NUCLEAR, FUEL & SERVICES DIV.
965 CHESTERBROOK BLVD., 62a-5
WAYNE, PA 19087-5691 USA
610-640-6829 FAX 610-640-6797

J. FIGUERAS
CONSEJO SEGURIDAD NUCLEAR
JUSTO DORADO, 11
MADRID, 28040 SPAIN
34 1 3460204 FAX 34 1 3460588
JMFC@CSN.ES

K. FOLK
SOUTHERN NUCLEAR OPERATING CO.
PO BOX 1295
BIRMINGHAM, AL 35201 USA
205 992-7385 FAX 205 992-5536
KEN.F.FOLK@SNC.COM

W. FORD
OAK RIDGE NATIONAL LABORATORY
BLDG. 4500-N, MS 6238 PO BOX 2008
OAK RIDGE, TN 37831-6238 USA
423-574-5272 FAX 423-574-9676
WEC@ORNL.GOV

L. FUGELSO
SANDIA NATIONAL LABORATORIES
PO BOX 5800
ALBUQUERQUE, NM 87185-0742 USA
505-845-3228 FAX 505-844-0955
JFUGEL@SANDIA.GOV

T. FUKETA
JAPAN ATOMIC ENERGY RESEARCH INST.
TOKAI, IBARAKI 319-11 JAPAN
81 29 282-6386 FAX 81 29 282-6160
TOYO@NSRRSUNL.TOKAI.JAERI.GO.JP

W. GALYEAN
IDAHO NATIONAL ENGINEERING LABORATORY
PO BOX 1625
IDAHO FALLS, ID 83415-3850 USA
208 526-0627 FAX 208 526-2930
WGJ@INEL.GOV

G. GAUTHIER
COMM. A L'ENERGIE ATOMIQUE
60-68 AV. DU GENERAL LECLERK
FONTENAY AUX ROSES, 92265 FRANCE
33 1 46 549174 FAX 33 1 47461016

J. GESSLER
JAPAN ELECTRIC POWER INFORMATION CENTER
1120 CONNECTICUT AVE, NW, #1070
WASHINGTON, DC 20036 USA
202-955-5610 FAX 202-955-5612
JGESSLER@JEPIC.COM

L. GOLDSTEIN
THE S.M. STOLLER CORPORATION
485 WASHINGTON AVE.
PLEASANTVILLE, NY 10570 USA
914-741-1200 FAX 914-741-2093
STOLLERP@COMPUTER.NET

M. GOMOLINSKI
INSTITUT DE PROT. ET DE SURETE NUC.
CEA / FAR - BP 6
FONTENAY AUX ROSES, CEDEX 92265 FRANCE
33 1 46 54 8177 FAX 33 1 46 54 8925

J. GORMAN
DOMINION ENGINEERING, INC.
6862 ELM ST.
MC LEAN, VA 22101 USA
703 790-5544 FAX 703-790-0027
DEI@US.NET

C.-GRANDJEAN
INSTITUT DE PROT. ET DE SURETE NUC.
CEA CADARACHE
ST PAUL LEZ DURANCE, 13108 FRANCE
33 04 42 25 4480 FAX 33 04 42 25 3555
GRANDJEAN@IPSNCAD.CEA.FR

G. HACHE
INSTITUT DE PROT. ET DE SURETE NUC.
CEA CADARACHE
ST PAUL LEZ DURANCE, 13108 FRANCE
33 42 25 2055 FAX 33 42 25 7679

R. HALL
BROOKHAVEN NATIONAL LABORATORY
BLDG. 130, PO BOX 5000
UPTON, NY 11973-5000 USA
516-344-2144 FAX 516-344-3957
REHALL@BNL.GOV

B. HALLBERT
OECD HALDEN REACTOR PROJECT
PO BOX 173, N-1751
HALDEN, NORWAY
47-69-18-31-00 FAX 47-69-18-71-09
BRUCE.HALLBERT@NRP.NO

N. HANUS
KNOLLS ATOMIC POWER LABORATORY
PO BOX 1072
SCHENECTADY, NY 12301 USA
518-395-7098 FAX 518-395-4422

O. HASCOET
EDF - SEPTEN
12 AV. DU DUTRIEVOZ
VILLEURBANNE, 69628 FRANCE
33-72-82-74-91 FAX 33-72-82-75-55
OLIVER.HASCOET@DE.EDFGDF.FR

P. HAYWARD
ATOMIC ENERGY OF CANADA LIMITED
WHITESHELL LABORATORIES
PINAWA, MANITOBA ROE 1LO CANADA
204-753-2311 ext. 2790 FAX 204-753-2455

J.Y. HENRY
COMM. A L'ENERGIE ATOMIQUE
60-68 AV. DU GENERAL LECLERK
FONTENAY AUX ROSES, 92265 FRANCE
33 1 46 54 8565 FAX 33 1 47 46 1014

R. HENRY
FAUSKE & ASSOCIATES, INC.
16W070 WEST 83RD ST.
BURR RIDGE, IL 60521 USA
630-323-8750 FAX 630-986-5481
HENRY@FAUSKE.COM

G. HEUSENER
FORSCHUNGSZENTRUM KARLSRUHE
WEBERSTRASSE 5
KARLSRUHE, 76133 GERMANY
0 7247 82 5510 FAX 0 7257 82 5508

J. HIGGINS
BROOKHAVEN NATIONAL LABORATORY
BLDG. 130, PO BOX 5000
UPTON, NY 11973-5000 USA
516-344-2432 FAX 516-344-4900
HIGGINS@BNL.GOV

K. HISAJIMA
NUCLEAR POWER ENGINEERING CORP.
2F 3-13, 4-CHOME, TORANOMON
MINATO-KU, TOKYO 105 JAPAN
03 3434-2450 FAX 03 3434-6786

R. HOBBINS
RRH CONSULTING
PO BOX 971
WILSON, WY 83014 USA
307-739-0604 FAX 307-739-0604
RHOBBINS@WYOMING.COM

P. HOFMANN
FORSCHUNGSZENTRUM, IMF-1
PO BOX 3640
KARLSRUHE, 76021 GERMANY
49 7247 82 2517 FAX 49 7247 82 4567
PETER.HOFMANN@IMF.FZK.DE

H. HOLMSTROM
VTT ENERGY, NUCLEAR
PO BOX 1604
ESPOO, 02044 FINLAND
358 9 456 5050 FAX 358 9 456 5000
HEIKKI.HOLMSTROM@VTT.FI

T. HSU
VIRGINIA POWER
5000 DOMINION BLVD.
GLEN ALLEN, VA 23060 USA
804-273-3095 FAX 804-273-2188
TOM_W._HSU@VAPOWER.COM

I. HWANG
SEOUL NATIONAL UNIVERSITY
SAN 56-1, RM 32-211, SHINLIM-DONG, GWANAK-KU
SEOUL, 151-742 KOREA
82 2 880-7215 FAX 82 2 889-2688
HWANGILS@ALLIANT.SNU.AC.KR

Y.D. HWANG
KOREA ATOMIC ENERGY RESEARCH INST.
KUKJIM 150, YOUSUNG
TAEJON, KOREA
82 42 868-8292 FAX 82 42 868-8990
YDHWANG@NANUM.KAERI.RE.KR

K. ISHIJIMA
JAPAN ATOMIC ENERGY RESEARCH INST.
TOKAI, IBARAKI 319-11
TOKAI, IBARAKI 319-11 JAPAN

J.J. JEONG
KOREA ATOMIC ENERGY RESEARCH INST.
KUKJIM 150, YOUSUNG
TAEJON, KOREA
82 42 868 2659 FAX 82 42 868 8362
JJJEONG@NANUM.KAERI.RE.KR

Y. JIN
KOREA ATOMIC ENERGY RESEARCH INST.
KUKJIM 150, YUSONG
TAEJON, KOREA
82 42 868 2756 FAX 82 42 868 8256
YHJIN@NANUM.KAERI.RE.KR

W. JOHNSON
UNIVERSITY OF VIRGINIA
115 FALCON DR.
CHARLOTTESVILLE, VA 22901 USA
804-982-5465 FAX 804-982-5473
WRJ@VIRGINIA.EDU

R. JONES
STRUCTURAL INTEGRITY, MAGNOX ELECTRIC
BERKELEY CENTRE
BERKELEY, GLOUCESTERSHIRE GL139PB UK
0-1-453-81-2479 FAX 0-1-453-81-2693

M. KAKAMI
JAPAN ELECTRIC POWER INFORMATION CENTER
1120 CONNECTICUT AVE, NW, #1070
WASHINGTON, DC 20036 USA
202-955-5610 FAX 202-955-5612
GENDER@JEPIC.COM

R. KARIMI
SCIENCE APPLICATIONS INT'L CORP.
20201 CENTURY BLVD.
GERMANTOWN, MD 20874 USA
301-353-8326 FAX 301-428-0145
ROY.KARMI@CPMX.SAIC.COM

E. KEE
HOUSTON LIGHTING & POWER
SO. TEXEX PROJ., FM 521
WADSWORTH, TX 77414 USA
512-972-8907 FAX 512-972-8081

M. KENJI
NUCLEAR POWER ENGINEERING CORP.
FUJITA KANKO TORANOMON BLDG. 8F 1
MINATO-KU, TOKYO 105 JAPAN
81-3-5470-5500 FAX 81-3-5470-5524

R. KENNEDY
RPK STRUCTURAL MECHANICS CONSULTING, INC.
18971 VILLA TERRACE
YORBA LINDA, CA 92886 USA
714-777-2163 FAX 714-777-8299

H.J. KIM
KOREA INSTITUTE OF NUCLEAR SAFETY
PO BOX 114 YUSONG
TAEJON, 305-600 KOREA
82 42 868 0230 FAX 82 42 861-1700

H.K. KIM
KOREA INSTITUTE OF NUCLEAR SAFETY
PO BOX 114 YUSONG
TAEJON, 305-600 KOREA
82-42-868-0224 FAX 82-42-861-0943
K113KHK@PINPOINT.KMS.RE.KR

K.T. KIM
KOREA INSTITUTE OF NUCLEAR SAFETY
PO BOX 114 YUSONG
TAEJON, 305-600 KOREA
82-42-868-0153 FAX 82-42-861-2535
K235KKT@PINPOINT.KINS.RE.KR

J. KNEELAND
CONSUMERS POWER COMPANY
27780 BLUE STAR MEMORIAL HWY.
COVERT, MI 49043 USA
616-764-2814 FAX 616-764-2060

J. KOHOPAA
IVO INTERNATIONAL LTD.
RAJATORPANTIE 8
VANTAA, 01019 FINLAND
358-9-8561-4420 FAX 358-9-563-0432
JYRKI.KOHOPAA@IVO.FI

S. KOMURA
TOSHIBA CORPORATION
8, SHINSUGITA-CHO, ISOGO-KU
YOKOHAMA, KANAGAWA-KEN 235 JAPAN
85-45-770-2032 FAX 85-45-770-2117
KOMURA@RDEF.IEC.TOSHIBA.CO.JP

D. KOSS
PENNSYLVANIA STATE UNIVERSITY
202A STEIDLE BLDG.
UNIVERSITY PARK, PA 16803 USA
814-865-5447 FAX 814-865-2917
KOSS@EMS.PSU.EDU

J. KRAMER
ARGONNE NATIONAL LABORATORY
9700 SO.CASS AVE, BLDG. 207
ARGONNE, IL 60439 USA
630-252-4583 FAX 630-252-3075
JMKRAMER@ANL.GOV

J. KUJAL
NUCLEAR RESEARCH INSTITUTE
REZ NEAR PRAGUE
250 68 CZECH REPUBLIC
422-685-79-60 FAX 422-688-20-29
KUJ@NRI.CZ

D. KUPPERMAN
ARGONNE NATIONAL LABORATORY
9700 S. CASS AVE.
ARGONNE, IL 60439 USA
630-252-5108 FAX 630-252-4798

K. KUSSMAUL
MPA UNIV. OF STUTTGART
PFAFFENWALDRING 32
STUTTGART, D-70569 GERMANY
49-711-685-3582 FAX 49-711-685-2635
KUSSMAUL@MPA.UNISTUTTGART.DE

P. LACY
UTILITY RESOURCE ASSOCIATES
SUITE 1600, 51 MONROE ST.
ROCKVILLE, MD 20854 USA
301-294-1940 FAX 301-294-7879

J. LAKE
IDAHO NATIONAL ENGINEERING LABORATORY
PO BOX 1625, MS 3860
IDAHO FALLS, ID 83415-3860 USA
208-526-7670 FAX 208-526-2930
JJL@INEL.GOV

J. LAMBERT
ARGONNE NATONAL LABORATORY
9700 S. CASS AVENUE
ARGONNE, IL 60187 USA
630 252-6695 FAX 630 252-4922
LAMBERT@FLICKER.FP.ANL.GOV

D. LAMPE
UTILITY RESOURCE ASSOCIATES
SUITE 1600, 51 MONROE ST.
ROCKVILLE, MD 20854 USA
301-294-1940 FAX 301-294-7879

P. LAROUERE
VIRGINIA POWER
5000 DOMINION BLVD.
GLEN ALLEN, VA 23060 USA
804-273-2269 FAX 804-273-3543
PAULA_J._LAROUERE@VAPOWER.COM

T. LEAX
WESTINGHOUSE BETTIS ATOMIC POWER LAB
PO BOX 79
WEST MIFFLIN, PA 15122 USA
412-476-6782 FAX 412-476-5151

J.H. LEE
KOREAN NUCLEAR FUEL COMPANY
150 DEOJIN-DONG, YUSUNG-CZY
TAEJON, 305-353 KOREA
82 42 868 1461 FAX 82 42 862 4790

S. LEE
KOREA INSTITUTE OF NUCLEAR SAFETY
PO BOX 114 YUSONG
TAEJON, 305-600 KOREA
82-42-868-0196 FAX 82-42-861-0943

Y. LEE
KOREA INSTITUTE OF NUCLEAR SAFETY
PO BOX 114 YUSONG
TAEJON, 305-600 KOREA
82-42-868-0007 FAX 82-42-861-2535

J. LEHNER
BROOKHAVEN NATIONAL LABORATORY
BLDG. 130, PO BOX 5000
UPTON, NY 11973-5000 USA
516-344-3921 FAX 516-344-5730
LEHNER@BNL.GOV

J. LEWI
INSTITUT DE PROT. ET DE SURETE NUC.
CEA CADARACHE
ST PAUL LEZ DURANCE, 13108 FRANCE
33-04-42-25-44-47 FAX 33-04-42-25-29-29

R. LIMON
COMISION FEDERAL DE ELECTRICIDAD
KM 43.5 CARRETERA CARDEL-NAUTLA
MUN. DE ALTO LUCERO, VERA CRUZ 91680 MEXICO
91 297 40700 EXT 4326 FAX 91 297 40109

C.J. LIN
ATOMIC ENERGY COUNCIL
67, LANE 144 KEELUNG RD., SEC. 4
TAIPEI, TAIWAN 106 ROC
886-2-363-4180 EXT 762 FAX 886-2-366-0535
CJLIN@CC22.AEC.GOV.TW

T. LINK
PENNSYLVANIA STATE UNIVERSITY
107 STEIDLE BLDG.
UNIVERSITY PARK, PA 16802 USA
814-863-3512
TML110@PSU.EDU

M. LIVOLANT
INSTITUT DE PROT. ET DE SURETE NUC.
CEA / FAR - BP 6
FONTENAY AUX ROSES, CEDEX 92265 FRANCE
1-46-54-71-79 FAX 1-42-53-89-90
COLLIN@LUCIGER.CEA.FR

R. LOFARO
BROOKHAVEN NATIONAL LABORATORY
BLDG. 130, PO BOX 5000
UPTON, NY 11973-5000 USA
516-344-7191 FAX 516-344-3957
LOFARO@BNL.GOV

P. LOPEZ
NATIONAL COMM. OF NUCLEAR SAFETY
DR. BARRAGAN NO. 779 COL. NARVARTE
MEXICO CITY, 03020 MEXICO
525 590 50 54 FAX 525 590 75 08

W. LUCKAS
BROOKHAVEN NATIONAL LABORATORY
BLDG. 130, PO BOX 5000
UPTON, NY 11973-5000 USA
516-344-7562 FAX 516-344-2613

S. MAJUMDAR
ARGONNE NATIONAL LABORATORY
9700 S. CASS AVE.
ARGONNE, IL 60439 USA
708-252-5136 FAX 708-252-4798
MAJUMDAR@ANL.GOV

T. MARGULIES
U.S. EPA
MAIL CODE 6602J
WASHINGTON, DC 20460 USA
202-233-9774

A. MARION
NUCLEAR ENERGY INSTITUTE
1776 I ST., N.W., SUITE 300
WASHINGTON, DC 20006-3708 USA
202 739 8081 FAX 202 785 1898
AM@NEI.ORG

C. MARUSKA
ONTARIO HYDRO
700 UNIVERSITY AVE.
TORONTO, ONTARIO M5G 1X6 CANADA
416-592-5688 FAX 416-592-4483
CMARUSKA@HYDRO.ON.CA

B. MAVKO
JOSEF STEFAN INSTITUTE
JAMOVA 39
LJUBLJANA, 1000 SLOVENIA
286-61-1885-330 FAX 386-61-374919
BORUT.MAVKO@IJS.SI

D. McDONALD
AEA TECHNOLOGY
RISLEY, WARRINGTON
CHESHIRE, ENGLAND
01925-254512 FAX 01925-254536
DAVE.MCDONALD@AEAT.CO.UK

D. McCABE
OAK RIDGE NATIONAL LABORATORY
PO BOX 2008
OAK RIDGE, TN 32831-6151 USA
423-574-8010 FAX 423-574-5118

I. McNAIR
HM NUCLEAR INSTALLATIONS INSPECTORATE
ST PETER'S HOUSE, BALLIOL RD
BOOTLE, MERSEYSIDE L20 3LZ UK
44-151-951-4242

T. McNULTY
HM NUCLEAR INSTALLATIONS INSPECTORATE
ST PETER'S HOUSE, BALLIOL RD
BOOTLE, MERSEYSIDE L20 3LZ UK
44-151-951-3624 FAX 44-151-951-4942

R. MILLER
WESTINGHOUSE CNFD
3968 SARDIS ROAD
MURRYSVILLE, PA 15668 USA
412 374 2291 FAX 412 374 2382

E. MONAHAN
WESTINGHOUSE/SMPD
881 FIFTH STREET
NORTH HUNTINGTON, PA 15642 USA
412 374 4576

S. MONTELEONE
BROOKHAVEN NATIONAL LABORATORY
BLDG. 130, PO BOX 5000
UPTON, NY 11973-5000 USA
516 344-7235 FAX 516 344-3957
SMONTELE@BNL.GOV

R. MONTGOMERY
ANATECH CORP.
5435 OBERLIN DR.
SAN DIEGO, CA 92121 USA
619-455-6350 FAX 619-455-1094
ROB@ANATECH.COM

K. MORIYAMA
JAPAN ATOMIC ENERGY RESEARCH INST.
2-4 SHIRAKATA-SHIRANE
TOKAI-MURA, IBARAKI-KEN 319-11 JAPAN
81-29-282-5871 FAX 81-29-282-5570
MORI@SUN2SARL.TAKAI.JAERI.GO.JP

A. MOTTA
PENNSYLVANIA STATE UNIVERSITY
DEPT OF NUCLEAR ENG, 231 SACKETT BLDG.
UNIVERSITY PARK, PA 16802 USA
814-865-0036 FAX 814-865-8499
ATM2@PSU.EDU

M. MUHLHEIM
OAK RIDGE NATIONAL LABORATORY
PO BOX 2009, BLDG. 9201-3
OAK RIDGE, TN 37831 USA
423-574-0386 FAX 423-574-0382
M8M@ORNL.GOV

D. MURTLAND
SCIENCE & ENGINEERING ASSOCIATES, INC.
7918 JONES BRANCH DR., SUITE 500
MCLEAN, VA 22102 USA
703-761-4100 FAX 703-761-4105
DMURTLAND@SEABASE.COM

R. NANSTAD
OAK RIDGE NATIONAL LABORATORY
PO BOX 2008, 4500 S, MS 6151
OAK RIDGE, TN 37831-6151 USA
423 574-4471 FAX 423 574-5118
NANSTADRK@ORNL.GOV

D. NAUS
OAK RIDGE NATIONAL LABORATORY
PO BOX 2009
OAK RIDGE, TN 37831-8056 USA
423 574-0657 FAX 423 574-0651
DJN@ORNL.GOV

U. NAYAK
WESTINGHOUSE COMMERCIAL NUC. FUEL DIV.
PO BOX 355
PITTSBURGH, PA 15230-0355 USA
412 374 2241 FAX 412 374 2452

H. NOURBAKHSH
BROOKHAVEN NATIONAL LABORATORY
BLDG. 130, PO BOX 5000
UPTON, NY 11973-5000 USA
516-344-5405 FAX 516-344-5730

D. O'HAIR
WESTINGHOUSE NSA
129 ALEXANDER DRIVE
IRWIN, PA 15642 USA
412 374-5994
OHAIRD@CECIL.PGH.WEC.COM

G. ODETTE
UC SANTA BARBARA
DEPT. OF MECHANICAL ENGINEERING
SANTA BARBARA, CA 93106 USA
805 893-3525 FAX 805 893-8651

A. OHTA
MITSUBISHI HEAVY INDUSTRIES
3-1, MINATOMIRAI 3-CHOME, NISHI-KU
YOKOHAMA, 220-84 JAPAN
81-45-224-9637 FAX 81-45-224-9970
OHTA@ATOM.HQ.MHI.CO.JP

N. ORTIZ
SANDIA NATIONAL LABORATORIES
PO BOX 5800
ALBUQUERQUE, NM 87185 USA
505-844-0577 FAX 505-844-0955
NRORTIZ@SANDIA.GOV

D. OSETEK
LOS ALAMOS TECHNICAL ASSOCS., INC.
BLDG. 1, SUITE 400, 2400 LOUISIANA BLVD, NE
ALBUQUERQUE, NM 87110 USA
505-880-3407 FAX 505-880-3560

K. OSHIMA
TOSHIBA CORPORATION
C/O GENE M/C 726, 175 CURTNER AVE.
SAN JOSE, CA 95125 USA
408-925-6592 FAX 408-925-4945
OSHIMA@RDES.IEC.TOSHIBA.CO.JP

O. OZER
ELECTRIC POWER RESEARCH INSTITUTE
PO BOX 10412
PALO ALTO, CA 94303 USA
415-855-2089 FAX 415-855-2774
OOZER@EPRINET.EPRI.COM

J. PAPIN
INSTITUT DE PROT. ET DE SURETE NUC.
CEA CADARACHE
ST PAUL LEZ DURANCE, 13108 FRANCE
33-42-25-3463 FAX 33-42-25-6143

M. PARKER
ILLINOIS DEPT. OF NUCLEAR SAFETY
1035 OUTER PARK DR
SPRINGFIELD, IL 62704 USA
217-785-9854 FAX 217-524-5671

S. PATI
ABB COMBUSTION ENGINEERING NUCLEAR OPERATIO
2000 DAY HILL RD.
WINDSOR, CT 06070 USA
860-687-8043 FAX 860-687-8051
SATYAV.PATI

J. PELTIER
INSTITUT DE PROT. ET DE SURETE NUC.
60-68 AV. DU GENERAL LECLERC, BP 6
FONTENAY AUX ROSES, 92265 FRANCE
33-1-46-54-84.45 FAX 33-1-46-54-10-43
PELTIER@LUCIFER.CEA.FR

B. PENN
BROOKHAVEN NATIONAL LABORATORY
BLDG. 197C, PO BOX 5000
UPTON, NY 11973-5000 USA
516-344-7213 FAX 516-344-3021
PENN@BNL.GOV

W. PENNELL
OAK RIDGE, LOCKHEED MARTIN ENERGY RESEARCH
ENG'G MECHANICS & THERMAL SYS
OAK RIDGE, TN 37831-8045 USA
423-576-8571 FAX 423-574-0651
PQ5@ORNL.GOV

A. PEREZ-NAVARRO
UNESA/UNIV. ALFONSO X
VILLANUEVA DE LA CANADA
28691 SPAIN
34-1-8109150 FAX 34-1-8109101
NAVARRO@.UAX.ES

K. PETTERSSON
KTH
STOCKHOLM, S-10044 SWEDEN
46-8-790-9194 FAX 46-8-207681
KJELLP@MET.KTH.SE

S. POPE
SCIENTECH
11140 ROCKVILLE PIKE, SUITE 500
ROCKVILLE, MD 20852 USA
301-468-6425 FAX 301-468-0883
SPOPE@SCIENTECH.COM

G. POTTS
GENERAL ELECTRIC CO.
PO BOX 780, CASTLE HAYNE RD, M/C K12
WILMINGTON, NC 28402-0780 USA
910-675-5708 FAX 910-675-6966

W.T. PRATT
BROOKHAVEN NATIONAL LABORATORY
BLDG. 130, PO BOX 5000
UPTON, NY 11973-5000 USA
516-344-2630 FAX 516-344-5730
PRATT@BNL.GOV

J. PUGA
UNESA
FRANCISCO GERVAS, 3
MADRID, 28020 SPAIN
34 1 567 4807

C. PUGH
OAK RIDGE NATIONAL LABORATORY
P.O. BOX 2009, MS-8067
OAK RIDGE, TN 37831 USA
423 574 0422 FAX 423 241 5005
PUG@ORNL.GOV

J. RASHID
ANATECH CORP.
5435 OBERLIN DR.
SAN DIEGO, CA 92121 USA
619-455-6350 FAX 619-455-1094
JOE@ANATECH.COM

S. RAY
WESTINGHOUSE
ENERGY CENTER, NOTHERN PIKE
MONROEVILLE, PA 15146 USA
412 374 2101 FAX 412 374-2045

R. REDA
GE NUCLEAR ENERGY
PO BOX 780, M/C J26
WILMINGTON, NC 28402 USA
910-675-5889 FAX 910-675-5879
REDAR@WLMPOL.WILM.GE.COM

K. REIL
SANDIA NATIONAL LABORATORIES
PO BOX 5800, MS 1139
ALBUQUERQUE, NM 87185-1139 USA
505-845-3050 FAX 505-845-3117
KOREIL@SANDIA.GOV

J. REITER
KNOLLS ATOMIC POWER LABORATORY
PO BOX 1032
SCHENECTADY, NY 12306 USA
518-395-4818

I. REMEC
OAK RIDGE NATIONAL LABORATORY
PO BOX 2008, BLDG. 6025 MS 6363
OAK RIDGE, TN 37831-6363 USA
423-574-7076 FAX 423-574-9619
I7R@ORNL.GOV

P. RICHARD
COMMISSARIAT A L'ENERGIE ATOMIQUE
BATTMENT 211 CE CADARACHE
ST PAUL LEZ DURANCE, 13108 FRANCE
33-62-25-31-54 FAX 33-42-25-47-59

D. RISHER
WESTINGHOUSE
P.O. BOX 355
PITTSBURGH, PA 15230 USA
412 374-5774 FAX 412 374-4011

G. ROCHAU
SANDIA NATIONAL LABORATORIES
PO BOX 5800, MS 0741
ALBUQUERQUE, NM 87185-0741 USA
505-845-7543 FAX 505-844-0955
GEROCHA@SANDIA.GOV

A. ROMANO
BROOKHAVEN NATIONAL LABORATORY
BLDG. 197C, PO BOX 5000
UPTON, NY 11973-5000 USA
516-344-4024 FAX 516-344-5266
ROMANO1@BNL.GOV

S. ROSINSKI
ELECTRIC POWER RESEARCH INSTITUTE
1300 HARRIS BLVD.
CHARLOTTE, NC 28262 USA
704-547-6123 FAX 704-547-6035
STROSMS@CHARLOTT.EPRI.COM

J. ROTHWELL
NUCLEAR SAFETY DIRECTORATE
ST. PETER'S HOUSE, BALLIOL RD.
BOOTLE, MERSYSIDE L20 3LZ UK
44-151-951-3751 FAX 44-151-951-3942

J. ROYEN
OECD NUCLEAR ENERGY AGENCY
LE SEINE ST GERMAIN, 12 BLVD DES ILES
ISSY LES MOULINEAUX, F 91130 FRANCE
33-1-4524-1052 FAX 33-1-4524-1110
JAQUES.ROYEN@OECD.ORG

D. SACCOMANDO
COMMONWEALTH EDISON
1400 OPUS PL, SUITE 500
DOWNERS GROVE, IL 60515 USA
630-663-7283 FAX 630-663-7155

O. SANDERVAG
SWEDISH NUCLEAR POWER INSPECTORATE
KLARABERGSVIADUKTEN 90
STOCKHOLM, 10658 SWEDEN
46-8-698-8463 FAX 46-8-661-9086
ODDBJORN@SKI.SE

Y. SASAKI
NUCLEAR POWER ENGINEERING CORP.
2F 3-13, 4-CHOME, TORANOMON
MINATO-KU, TOKYO 105 JAPAN
03-3434-4551 FAX 03-3434-9487

M. SATTISON
LOCKHEED MARTIN IDAHO TECH. CO., INEL
PO BOX 1625
IDAHO FALLS, ID 83401 USA
208-526-9626 FAX 208-526-2930
SBM@INEL.GOV

C. SAVAGE
JUPITER CORP.
2730 UNIVERSITY BLVD. W., SUITE 900
WHEATON, MD 20902 USA
301-946-8088 FAX 301-946-6539
BUZZ_SAVAGE@JUPITERCORP.COM

F. SCHMITZ
INSTITUT DE PROT. ET DE SURETE NUC.
CEA CADARACHE
ST PAUL LEZ DURANCE, 13108 FRANCE
33-42-25-7035 FAX 33-42-25-7679

S. SCHULTZ
YANKEE ATOMIC ELECTRIC CO.
580 MAIN STREET
BOLTON, MA 01740 USA
508 568-2131 FAX 508 568-3703
SCHULTZ@YANKEE.COM

M. SCHWARZ
INSTITUT DE PROT. ET DE SURETE NUC.
CEA CADARACHE
ST PAUL LEZ DURANCE, 13108 FRANCE

W. SHA
ARGONNE NATIONAL LABORATORY
9700 S. CASS AVE., BLDG. 308
ARGONNE, IL 60439 USA
630-252-3910 FAX 630-252-3250

R. SIMARD
NUCLEAR ENERGY INSTITUTE
1776 I ST., NW, SUITE 400
WASHINGTON, DC 20007 USA
202-739-8128

A. SINGH
ELECTRIC POWER RESEARCH INSTITUTE
3412 HILLVIEW AVE.
PALO ALTO, CA 94304 USA
415-855-2384 FAX 415-855-1026
AVSINGH@MSM.EPRI.COM

L. SLEGERS
SIEMENS/KWU
POSTFACH 101063
D 63067 OFFENBACH, GERMANY
06-91-807-3224 FAX 06-91-807-4567

J. SMITH
SANDIA NATIONAL LABORATORIES
PO BOX 5800
ALBUQUERQUE, NM 87185-0741 USA
505-845-0299 FAX 505-844-1648
JASMITH@SANDIA.GOV

K. SODA
JAPAN ATOMIC ENERGY RESEARCH INST.
2-2-2 UCHISAIWAICHO
CHIYODAKU, TOKYO 100 JAPAN
81-3-3592-2100 FAX 81-3-3592-2119
SODA@HEMS.JAERI.GO.JP

S. SONG
KOREA INSTITUTE OF NUCLEAR SAFETY
PO BOX 114 YUSONG
TAEJON, 305-600 KOREA
82-42-868-0222 FAX 82-42-861-0943
K056SSH@PINPOINT.KINS.RE.KR

K. ST. JOHN
YANKEE ATOMIC ELECTRIC CO.
580 MAIN ST.
BOLTON, MA 01740 USA
508-568-2133 FAX 508-568-3700
STJOHN@YANKEE.COM

P. STOOP
NETHERLANDS ENERGY RESEARCH FOUNDATION
WESTERDUJMWEG 3
PETTEN, 17552G NETHERLANDS
31-224-56-4342 FAX 31-224-56-3490
STOOP@ECN.NL

V. STRIZHOV
NUC. SAFETY INST., RUSSIAN ACADEMY OF SCI.
B. TULSKAYA 52
MOSCOW, 113191 RUSSIA
095 9580873 FAX 095 2302029

J. TAYLOR
BROOKHAVEN NATIONAL LABORATORY
BLDG. 130, PO BOX 5000
UPTON, NY 11973-5000 USA
516-344-7005 FAX 516-344-3957

T. THEOFANOUS
UCSB
SANTA BARBARA, CA 93106 USA
805-893-4900 FAX 805-893-4927
THEO@THEO.UCSB.EDU

C. THIBAULT
WYLE LABORATORIES
7800 HIGHWAY 20 WEST
HUNTSVILLE, AL 35806 USA
205-837-4411 FAX 205-837-3363

G. THOMAS
LAWRENCE LIVERMORE NATIONAL LABORATORY
PO BOX 808, 7000 EAST AVE
LIVERMORE , CA 94550 USA
510-423-3511 FAX 510-422-5497
THOMAS7@LLNL.GOV

O. THOMSEN
SOUTHERN CALIFORNIA EDISON
PO BOX 128
SAN CLEMENTE, CA 92672 USA
714-368-8087 FAX 714-368-8188

H. THORNBURG
CONSULTANT
901 S. WARFIELD DR.
MT AIRY, MD 21771 USA
301-829-0874 FAX 301-829-0874

P. TIPPING
SWISS FEDERAL NUCLEAR SAFETY INSPECTORATE (H
HSK, CH-5232
VILLIGEN, SWITZERLAND
41-56-310-3926 FAX 41-56-310-3855
TIPPING@HSK.PSI.CH

R. TREGONING
NAVAL SERVICE WARFARE CENTER
CODE G14
BETHESDA, MD 20084-5000 USA
301-227-4145 FAX 301-227-5576

P. TROY
MORGAN, LEWIS & BOCKIUS
1800 M ST., NW
WASHINGTON, DC 20036 USA
202-346-7536 FAX 202-467-7176
TROY7536@MLB.COM

J. TULENKO
UNIVERSITY OF FLORIDA
202 NUCLEAR SCIENCE CENTER, PO BOX 118300
GAINESVILLE, FL 32611-8300 USA
352-392-1401 FAX 352-392-3380
TULENKO@UFL.EPU

H. TUOMISTO
IVO INTERNATIONAL LTD.
RAJATORPANTIE 8
VANTAA, FINLAND
358-9-8561-2464 FAX 358-9-8561-3403
HARRI.TUOMISTO@IRO.FI

A. TURNER
DOMINION ENGINEERING, INC.
6862 ELM ST.
MC LEAN, VA 22101 USA
703 790-5544 FAX 703 790-0027
DEI@US.NET

H. UCHIDA
NUCLEAR POWER ENGINEERING CORP.
FUJITA KANKO TRANOMON BLDG. 6F
MINATO-KU, TOKYO 105 JAPAN
81-3-3438-3066 FAX 81-3-5470-5544

R. VALENTIN
ARGONNE NATIONAL LABORATORY
9700 S. CASS AVE., BLDG. 308
ARGONNE , IL 60439 USA
630-252-4483 FAX 630-252-3250

K. VALTONEN
FINNISH CENTRA FOR RADIATION & NUC. SAFETY
PO BOX 14
HELSINKI, 00881 FINLAND
358-0-759-881 FAX 358-0-7598-8382
KEIJO.VALTONEN@STUK.FI

M. VESCHUNOV
NUC. SAFETY INST., RUSSIAN ACADEMY OF SCI.
B. TULSKAYA 52
MOSCOW, 113191 RUSSIA
095 9552618 FAX 095 2302029

J. VILLADONIGA
CONSEJO DE SEGURIDAD NUCLEAR
JUSTO DORADO, 11
MADRID, 28040 SPAIN
34-1-3460240 FAX 34-1-3460588
JIVT@CSN.ES

G. VINE
ELECTRIC POWER RESEARCH INSTITUTE
2000 L ST NW, SUITE 805
WASHINGTON, DC 20036 USA
202-293-6347 FAX 202-293-2697
GVINE@MSM.EPRI.COM

N. WAECKEL
ELECTRICITE DE FRANCE SEPTEN
12-14 AV. DUTRIEVOZ
VILLEURBANNE, 69450 FRANCE
33-4-72-82-7571 FAX 33-4-72-82-7713

C. WELTY
ELECTRIC POWER RESEARCH INSTITUTE
3412 HILLVIEW AVE.
PALO ALTO, CA 94062 USA
415 855-2821 FAX 415 855-2774
CWELTY@EPRINET.EPRI.COM

K. WHITT
SOUTHERN NUCLEAR OPERATING CO.
40 INVERNESS CENTER PKWY
BIRMINGHAM, AL 35201 USA
205-870-6396 FAX 205-870-6108
KERMILT.W.WHITT@SNC.COM

D. WILKINSON
EPRI/NPG
3412 HILLVIEW AVENUE
PALO ALTO, CA 94303 USA
415 855-2426 FAX 415 855 2774

R. WITT
UNIVERSITY OF WISCONSIN - MADISON
531 ERB, 1500 ENGINEERING DR.
MADISON, WI 53719 USA
608 263 2760 FAX 608 262-6707
WITT@ENGR.WISC.EDU

G. WROBEL
ROCHESTER GAS & ELECTRIC CO.
89 EAST AVE.
ROCHESTER, NY 14649 USA
716-724-8070 FAX 716-724-8405

R. YANG
ELECTRIC POWER RESEARCH INSTITUTE
3412 HILLVIEW AVE.
PALO ALTO, CA 94304 USA
415-855-2481 FAX 415-855-2774
RYANG@EPRINET.EPRI.COM

L. YEGOROVA
RRC KURCHATOV INSTITUTE, NSI
KURCHATOV SQ. 1
MOSCOW, 123182 RUSSIA
7-095-196-7283 FAX 7-095-196-1702
ASMOLOV@OBAE.KIAE.SU

K. YOON
FRAMATOME TECHNOLOGIES
3315 OLD FOREST RD.
LYNCHBURG, VA 24503 USA
804 832-3280 FAX 804 832 3663
KYOON@FRAMATECH.COM

W.H. YOON
KOREA INSTITUTE OF NUCLEAR SAFETY
PO BOX 114 YUSONG
TAJEON, KOREA
82-42-861-4040 FAX 82-42-861-9945

R. YOUNGBLOOD
SCIENTECH
11140 ROCKVILLE PIKE
ROCKVILLE, MD 20852 USA
301-468-6425 FAX 301-468-0883
RYOUNG@SCIENTECH.COM

T. ZAMA
TOKYO ELECTRIC POWER CO.
1901 L ST., NW, SUITE 720
WASHINGTON, DC 20036 USA
202-457-0790 FAX 202-457-0810
ZAMA@WASH.TEPCO.CO

PROCEEDINGS OF THE
24TH WATER REACTOR SAFETY INFORMATION MEETING
OCTOBER 21-23, 1996

Contents - Volume 2

	Page
Abstract	iii
General Index	v
Registered Attendees	vii

Reactor Pressure Vessel Embrittlement and Thermal Annealing
M. Vassilaros, C. Fairbanks, Co-Chairs

Current Understanding of the Effects of Environmental and Irradiation Variables on RPV Embrittlement G. Odette, et al. (UCSB)	1
Neutron Radiation Embrittlement Studies in Support of Continued Operation, and Validation by Sampling of Magnox Reactor Steel Pressure Vessels and Components R. Jones, C. Bolton (Magnox Electric U.K.)	25
Collaborative Investigations of In-Service Irradiated Material from the Japan Power Demonstration Reactor Pressure Vessel W. Corwin, B. Broadhead (ORNL), M. Suzuki, A. Kohsaka (JAERI)	49
IAEA International Studies on Irradiation Embrittlement of Reactor Pressure Vessel Steels M. Bromovsky (NRI, Czech Republic), L. Steele (Consultant)	51
Annealing Behaviour of Loviisa-1 Surveillance Materials Measured with V-notched Specimens and the Current Status of Vessel Anneal M. Valo, K. Wallin, T. Planman (VTT), J. Kohopää, (IVO International Ltd., Finland)	81
Effects of Thermal Annealing and Reirradiation on Toughness of Reactor Pressure Vessel Steels R. Nanstad, S. Iskander, M. Sokolov (ORNL), A. Chernobaeva, et al. (RRC-Kurchatov Institute)	99
DOE's Annealing Prototype Demonstration Projects J. Warren (US DOE), J. Nakos, G. Rochau (SNL)	111

Page

NRC Assessment of the Department of Energy Annealing Demonstration Project 129
D. Jackson, S. Malik (NRC)

Reactor Vessel Lower Head Integrity
A. Rubin, Chair

Reactor Vessel Lower Head Integrity Session Overview 137
A. Rubin (NRC)

A Scaling and Experimental Approach for Investigating In-Vessel Cooling 141
R. Henry (Fauske & Associates, Inc.)

Studies on In-Vessel Debris Coolability in ALPHA Program 161
Y. Maruyama, et al. (JAERI)

In-Vessel Coolability and Retention of a Core Melt 173
T. Theofanous, et al. (UCSB)

In-Vessel Melt Retention as a Severe Accident Management Strategy
for the Loviisa Nuclear Power Plant 239
O. Kymäläinen, H. Tuomisto (IVO International Ltd., Finland),
T.Theofanous (UCSB)

A Scaling Law for the Local CHF on the External Bottom Side
of a Fully Submerged Reactor Vessel 253
F. Cheung, K. Haddad, Y. Liu (Penn State)

A Preliminary Assessment of the Effects of Heat Flux Distribution and Penetration
on the Creep Rupture of a Reactor Vessel Lower Head 277
T-Y Chu , J. Bentz, R. Simpson (SNL), R. Witt (U. Wisconsin)

Evaluation and Projection of Steam Generator Tube Condition and Integrity
J. Muscara, Chair

Overview of Steam Generator Tube Degradation and Integrity Issues 297
D. Diercks, W. Shack (ANL), J. Muscara (NRC)

Steam Generator Tube Integrity - U.S. Nuclear Regulatory Commission Perspective .. 313
E. Murphy, E. Sullivan (NRC)

Page

Modeling of Eddy Current Probe Response for Steam Generator Tubes 323
S. Bakhtiari, D. Kupperman (ANL)

Characterization of Flaws in a Tube Bundle Mock-up for Reliability Studies 343
D. Kupperman, S. Bakhtiari (ANL)

Steam Generator Tubing NDE Performance 355
G. Henry, C. Welty (EPRI)

Estimating Probable Flaw Distributions in PWR Steam Generator Tubes 365
J. Gorman, A. Turner (Dominion Engineering, Inc.)

Predictions of Structural Integrity of Steam Generator Tubes
Under Normal Operating, Accident and Severe Accident Conditions 389
S. Majumdar (ANL)

Modeling Local Chemistry in PWR Steam Generator Crevices 415
P. Millet (EPRI)

Current Understanding of the Effects of Environmental and Irradiation Variables on RPV Embrittlement

G. R. Odette, G. E. Lucas, B. Wirth, C.-L. Liu
Department of Mechanical and Environmental Engineering
University of California, Santa Barbara, CA 93106

ABSTRACT

Radiation enhanced diffusion at RPV operating temperatures around 290°C leads to the formation of various ultrafine scale hardening phases, including copper-rich and copper-catalyzed manganese-nickel rich precipitates. In addition, defect cluster or cluster-solute complexes, manifesting a range of thermal stability, develop under irradiation. These features contribute directly to hardening which in turn is related to embrittlement, manifested as shifts in Charpy V-notch transition temperature. Models based on the thermodynamics, kinetics and micromechanics of the embrittlement processes have been developed; these are broadly consistent with experiment and rationalize the highly synergistic effects of most important irradiation (temperature, flux, fluence) and metallurgical (copper, nickel, manganese, phosphorous and heat treatment) variables on both irradiation hardening and recovery during post-irradiation annealing. A number of open questions remain which can be addressed with a hierarchy of new theoretical and experimental tools.

INTRODUCTION

Embrittlement in reactor pressure vessel (RPV) steels, manifested by a shift in the transition temperature (ΔT) delineating ductile and brittle cleavage fracture regimes, is primarily caused by yield stress increases ($\Delta\sigma_y$) produced by the fine scale microstructural features that form under irradiation[1,2]. Semi-empirical, physically-based embrittlement models have been developed by linking: a) microstructural evolution as a function of the irradiation and metallurgical variables; b) the effect of the microstructure on yield stress increases; and c) the effect of the yield stress increases on transition temperature shifts. These models rationalize a number of complex embrittlement trends and have been very useful for developing engineering correlations[3]. This paper reviews the current state of understanding of these components of the embrittlement process.

MICROSTRUCTURAL EVOLUTION

The defect microstructures that evolve in RPV steels during neutron irradiation are primarily a consequence of radiation enhanced diffusion (RED) and defect clustering. Depending on the alloy and irradiation conditions, the accelerated decomposition of supersaturated solid solutions may produce copper-rich precipitates (CRPs) or copper-catalyzed, manganese-nickel rich precipitates (MNPs) and possibly alloy carbonitrides and/or phosphides. In addition, matrix defects (MDs) form during irradiation. The CRPs and MNPs are the dominant features in highly embrittled steels and are reasonably well understood. The MDs, while not fully characterized, are believed to be some form of defect cluster-solute complex and typically have been categorized based on their thermal stability under irradiation and during post irradiation annealing (PIA): namely, those that are thermally unstable (UMDs) or stable (SMFs) at the irradiation temperature.

CRPs and MNPs

Fine scale CRPs and MNPs are the dominant features in irradiated RPV steels that have copper contents greater than about 0.1%. The primary effect of irradiation is to greatly accelerate precipitation of this residual copper as a consequence of RED, producing a high number density ($N_{crp} \geq 10^{17}$ cm^{-3}) of small (~1 nm) coherent bcc CRPs. As illustrated in Figure 1 these processes can be modeled by combining thermodynamic models with more detailed treatment of solute clustering kinetics, and accounting for RED; the latter results from the excess flux of vacancies and interstitials produced by irradiation and mediated by the density of sinks and recombination sites in the lattice. Such calculations, applied to simple Fe-Cu alloys, show that the precipitates typically develop in overlapping regimes of nucleation, growth and coarsening (NGC) mediated by irradiation temperature (T_{irr}), neutron fluence (ϕt), and available copper. The radiation enhanced diffusion coefficient is constant over a modest temperature range, bounded by thermal-diffusion at high temperatures and a cluster-recombination-mediated regime at low temperatures. The thermodynamics of CRP evolution have been modeled based on extended regular solution theory[2], using empirical excess enthalpy and entropy formulations taken from the literature[4]. These calculations can also explicitly treat nonequilibrium effects of composition and precipitate size in more complex systems (e.g., Fe-Cu-Ni-Mn) due to the contribution of the CRP-matrix interface to the free energy. The resulting solute partitioning leads to different compositional paths depending on the bulk chemistry and irradiation temperature. In particular, MNPs are promoted by high Ni and Mn contents and low irradiation temperatures.

Figure 2 illustrates that a wide range of experimental data are in good agreement with the model calculations. A number of the general trends predicted by the model and supported by the data are also illustrated here, including: 1) the temperature and flux dependence of the radiation enhanced diffusion coefficient, 2) the coarsening of CRPs at high fluence, and 3) the predominance of MNPs at high Ni contents. The evolution of CRPs/MNPs has more recently been investigated using lattice Monte Carlo (LMC) atomistic methods. These results show that, as the Mn and Ni content are increased and the Cu content reduced, the precipitate evolves from a nearly pure Cu precipitate, to a precipitate with a Mn/Ni shell, to a compound precipitate with Cu-rich and ordered

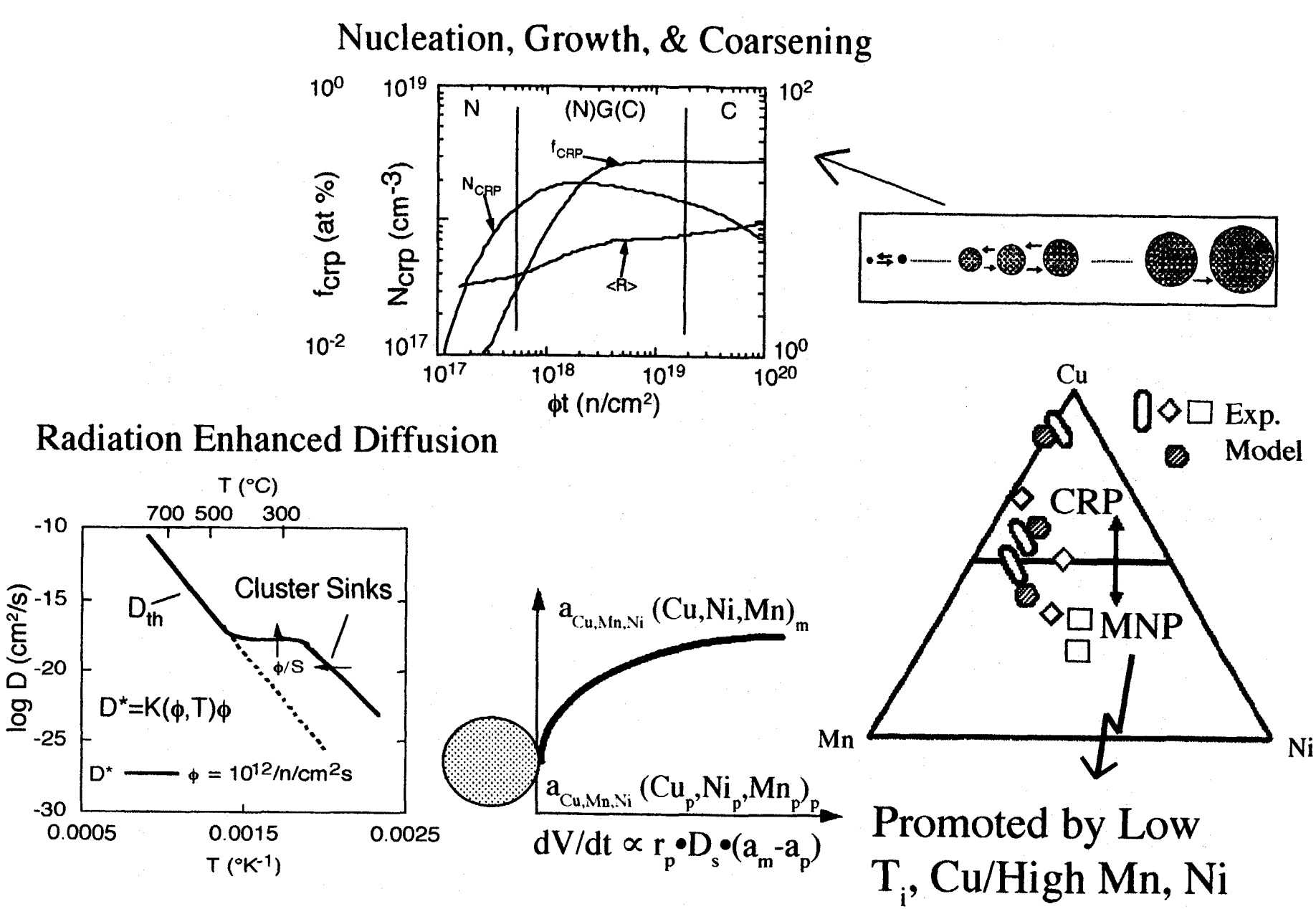

Figure 1 Illustration of the components of the model of CRP/MNP evolution.

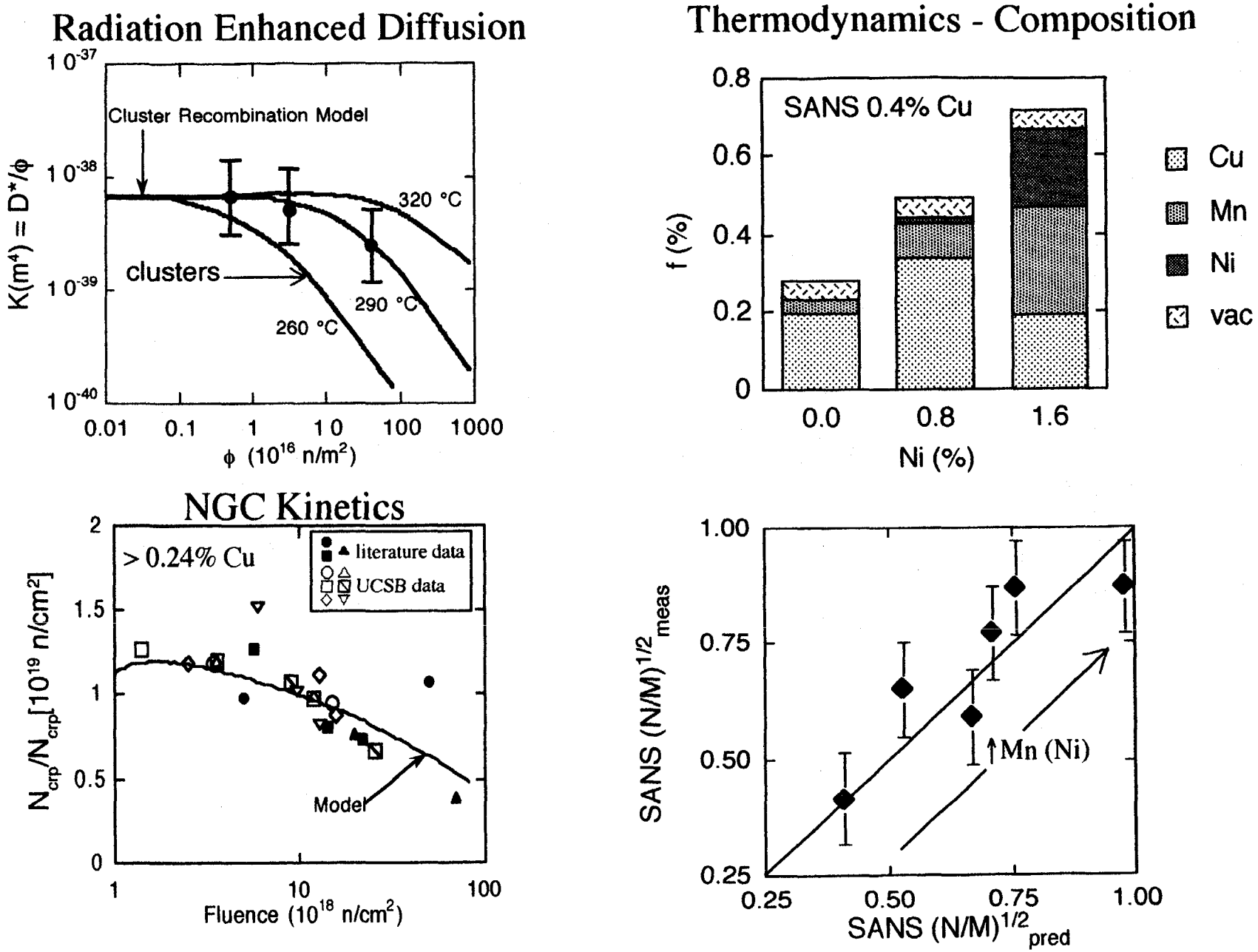

Figure 2 Comparison of CRP/MNP precipitation model predictions with experimental data.

Mn/Ni-rich components, to a MNP with a small amount of Cu required to drive the precipitation process. Moreover, simulations of the atom-probe (FIM/AP) analysis of these LMC-calculated precipitates are in good agreement with experiment[5], indicating that the features are really precipitates and not solute clouds. This is illustrated in Figure 3.

The contribution of CRPs/MNPs to hardening can be modeled by using the modulus interaction mechanism proposed by Russell and Brown (RB)[6] combined with a computer simulation of dislocation glide in an obstacle field (illustrated in Figure 4) and accounting for the size and composition of the precipitates as determined by SANS measurements. As shown in Figure 4, the predicted values of $\Delta\sigma_y$ are in good agreement with measurements. This hardening can in turn be used to estimate the transition temperature shift at the 41 J level in Charpy energy curves (ΔT_{41}) based on both theoretical and empirical analysis of the relationship between $\Delta\sigma_y$ and ΔT_{41}. Indeed, these same principles have been used to construct the irradiated Charpy curves from unirradiated Charpy data and measurements of $\Delta\sigma_y$[7]. This is also illustrated in Figure 4.

Hence, the evolution of CRPs and MNPs and their contribution to hardening and embrittlement are fairly well understood. Results suggest that the embrittlement associated with the formation of "late blooming" MNPs, even at very low Cu levels, may eventually equal or even exceed that produced by CRPs at high Cu levels. Such delayed embrittlement could produce a technical surprise that could have serious implications to pressure vessel operation and life extension, and hence some of the key assumptions used in determining the evolution of MNPs need to be verified.

Matrix Defects

The nature of UMDs and SMFs is not well understood since they have not been characterized in any detail. There is some evidence that displacement cascades play a key role in their formation. Candidates for UMDs include vacancy-solute complexes and detrapped mobile interstitial clusters. SMFs do not appear to be a single type of defect, but exhibit a range of thermal stabilities; candidates include precipitates and nanovoids or interstitial clusters complexed with solutes.

As illustrated in Figure 5, post-irradiation annealing (PIA) can be used to separate out the contributions to hardening of the UMDs, SMFs and CRPs. Hence, the evolution of these defect classes as a function of irradiation and metallurgical variables can be assessed. The example shown in Figure 5 illustrates that the contribution to hardening from the UMDs increases and that from the CRPs decreases with increasing neutron flux. Such data in turn provide an opportunity to develop and calibrate models for the formation of these defects. For instance, PIA data have been used to determine that the mean life of the UMDs is about 3×10^5 s at 290°C. This can be used to develop a quantitative estimate of the UMD number density as a function of flux and temperature[4]; by assuming that the UMDs serve as recombination sites for point defects, the rate of recombination can be incorporated into the model of RED giving rise to the flux and temperature sensitivity of RED. This self-consistent picture is illustrated in Figure 6.

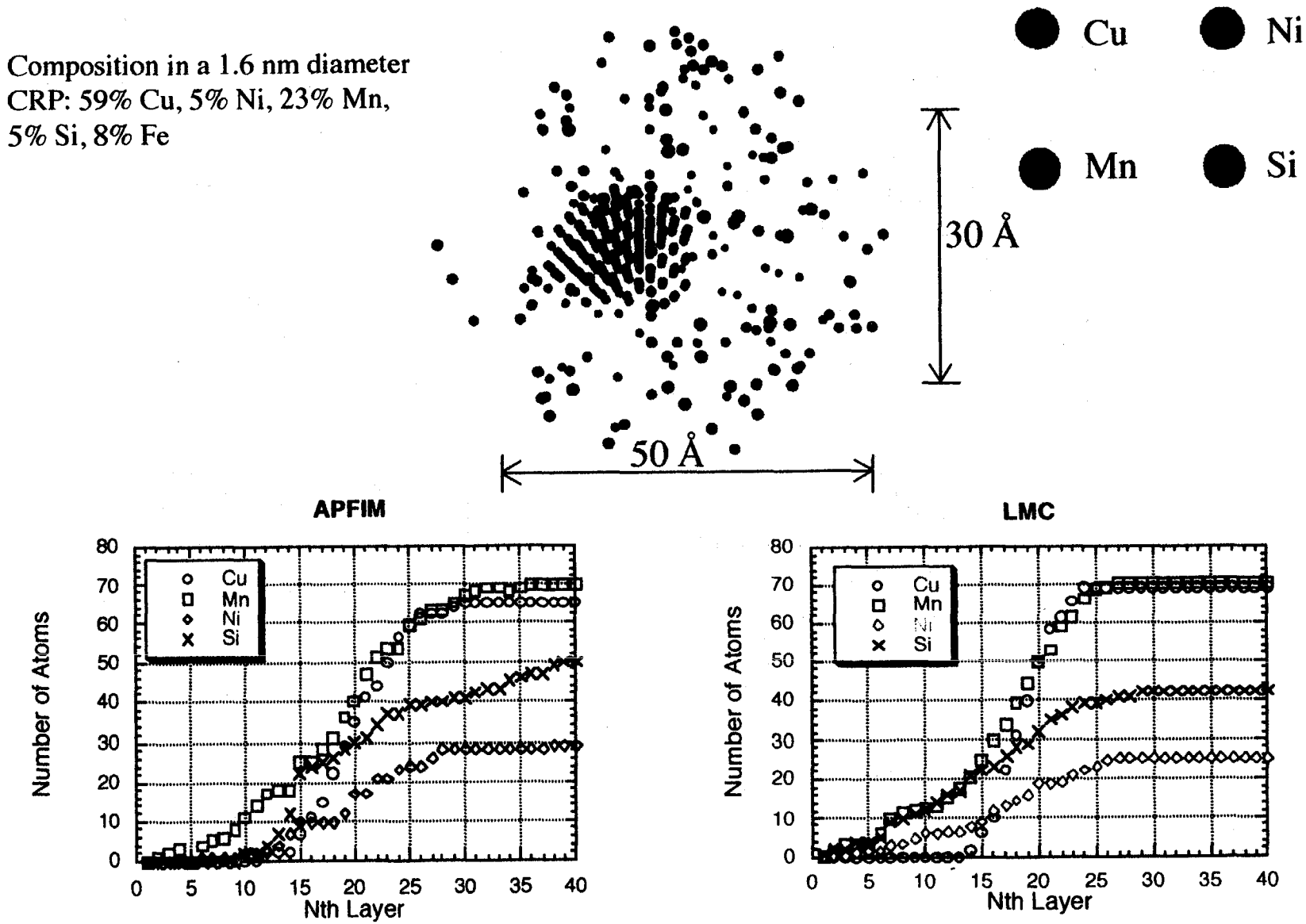

Figure 3 (Top) Illustration of a CRP determined by LMC. (Bottom) Comparison of experimental analysis (left) of the composition of atom layers evaporated in an FIM/AP examination of a CRP with (right) a simulated FIM/AP analysis of the LMC CRP.

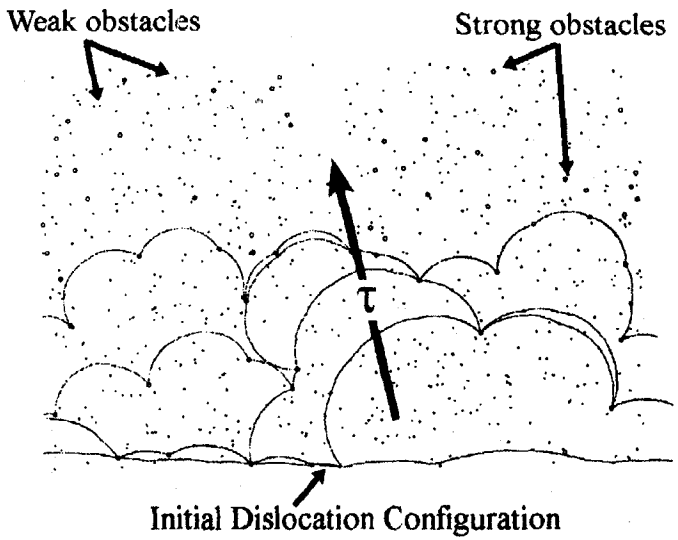

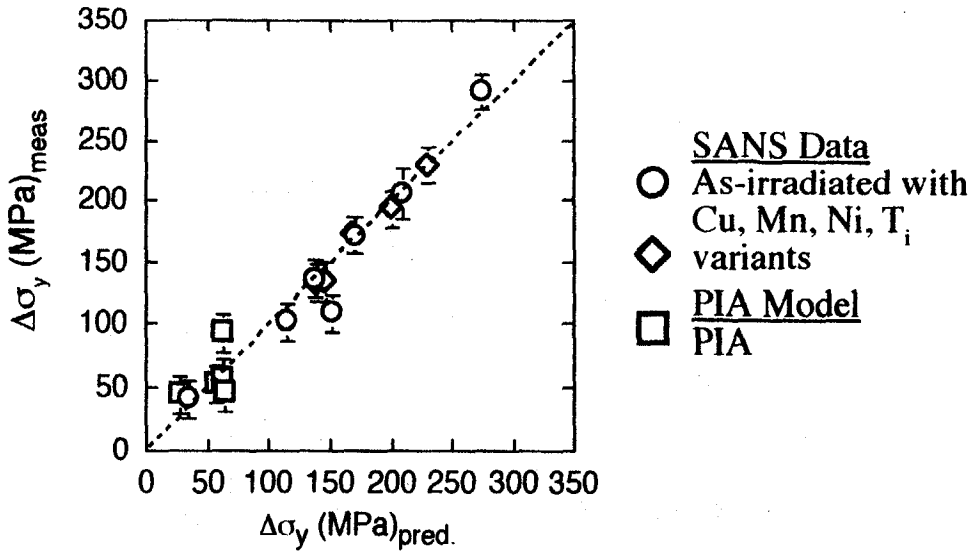

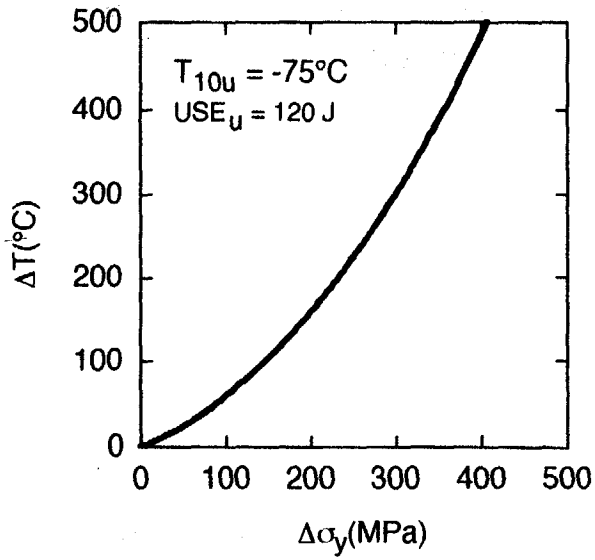

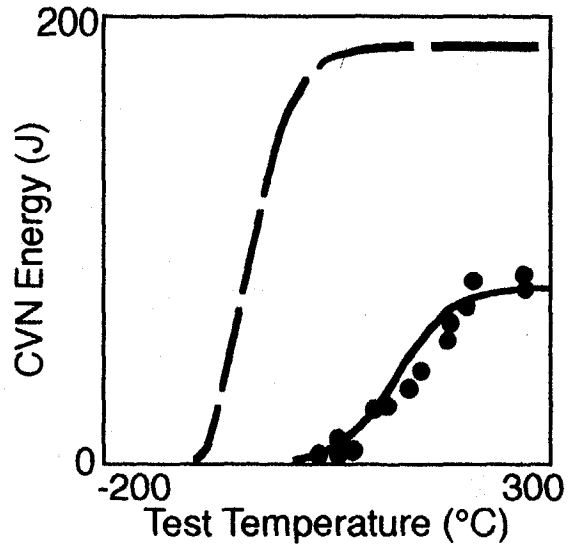

Figure 4 Illustration of computer-simulated dislocation glide in an obstacle field; predicted vs. measured $\Delta\sigma_y$; the relationship between ΔT_{41} and $\Delta\sigma_y$ for an RPV steel; predicted Charpy curve compared to the unirradiated curve and experimental data for an irradiated steel.

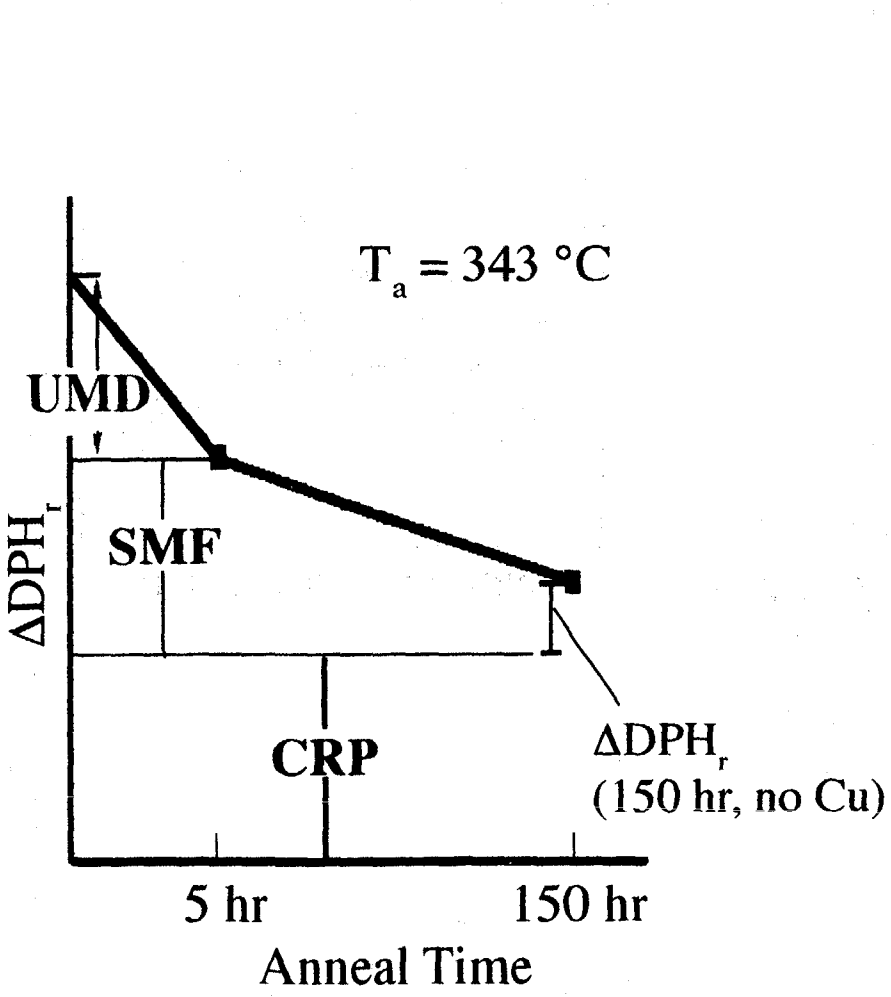

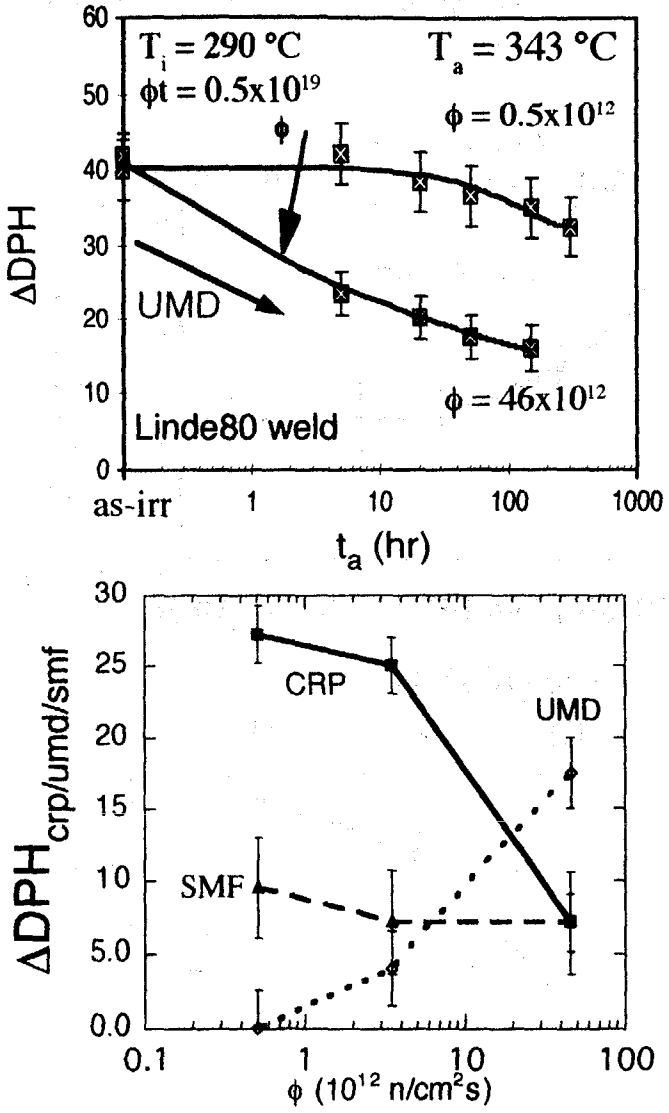

Figure 5 Illustration of the PIA recovery signatures of UMDs, SMFs and CRPs and the flux dependence of hardening from these features as determined by PIA studies.

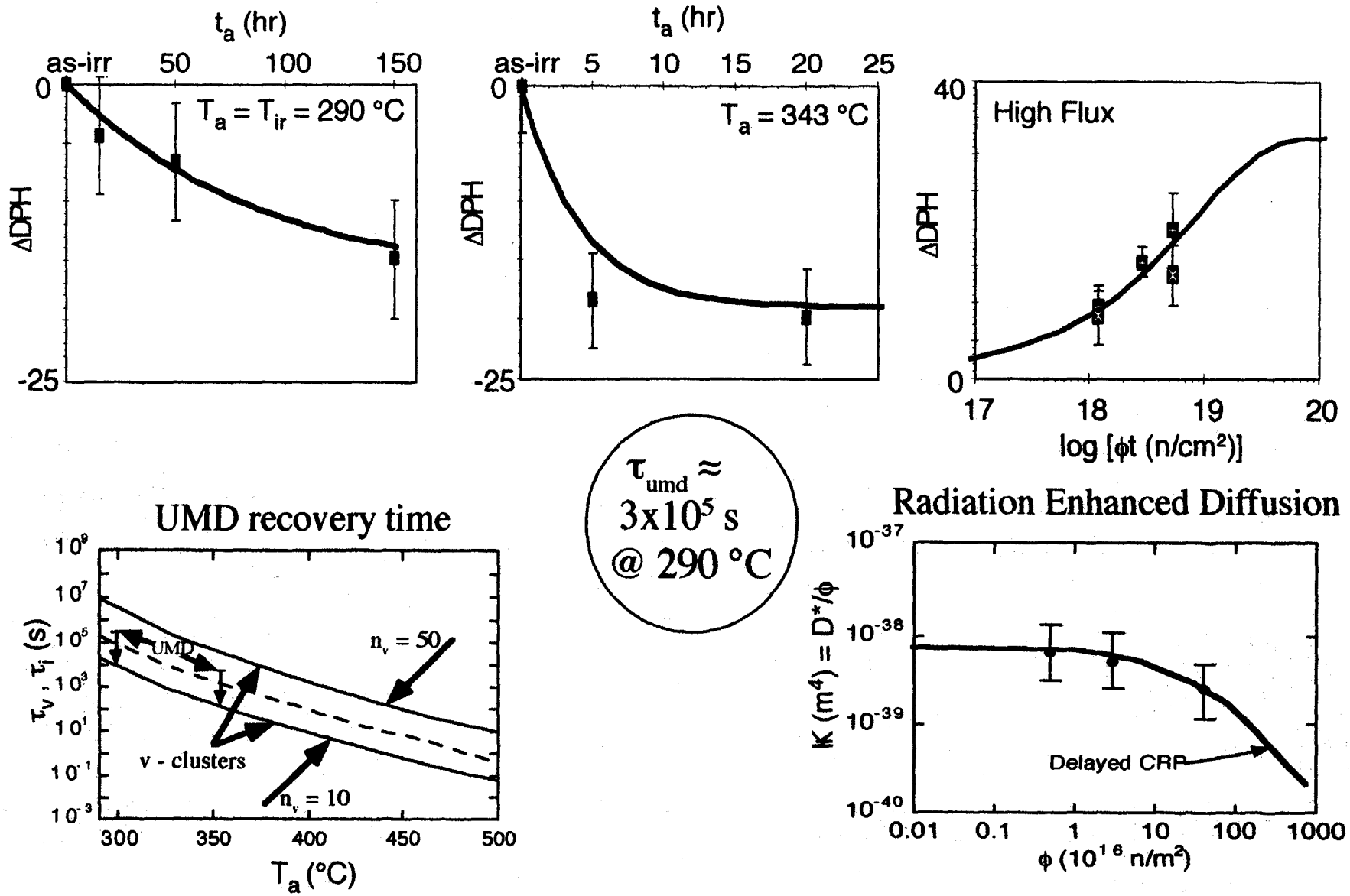

Figure 6 Illustration of the component of the self-consistent model accounting for the effect of flux on hardening.

The complexing between vacancies and solutes may also serve as the precursor to precipitate nucleation. For instance, recent kinetic LMC modeling of vacancies left in the wake of a cascade in an Fe-0.4Cu binary shows that binding between copper and vacancies or small vacancy clusters leads to the segregation of copper into a small clusters as the vacancies/clusters migrate. This is illustrated in Figure 7.

EMBRITTLEMENT VARIABLES

Embrittlement is mediated by the interaction between many metallurgical variables as well as environmental (radiation, PIA, re-irradiation) variables. Metallurgical variables include composition (Cu, Ni, Mn, P, others) and themomechanical history. Irradiation and re-irradiation variables include flux, spectrum, fluence, irradiation temperature, history, etc. PIA variables include annealing times and temperatures as well as the previous irradiation history. Coupling the understanding of the basic elements of embrittlement with models of microstructural evolution, hardening and embrittlement helps illuminate the basis for these interactions, and some examples of this are given below.

Effect of Flux

Empirical observations of the effect of flux (ϕ) on embrittlement have seemed contradictory. For example, as shown in Figure 8, high ϕ has been shown to increase hardening in low Cu steels and to decrease hardening in high Cu steels. This is now understood to result from the formation of UMDs (see Figure 5). At high ϕ, a large UMD population provides modest strengthening in low Cu steels. However, this contribution can be overcome in high Cu steels by the delay in RED-controlled evolution of the CRPs, since the UMDs act as sinks, thus enhance recombination. The UMD mechanism establishes a lower limit on the effect of ϕ. This lower limit on the ϕ-dependent regime decreases with decreasing T_{irr} and is estimated to be 5 to 10 x 10^{15} n/m^2-s at 290°C[8]. This suggests that ϕ does not normally play a significant role in embrittlement for either surveillance or actual vessel conditions, and opens the way to sensible use of accelerated test reactor data.

Irradiation Temperature

The T_{irr}-dependence of hardening can be understood and modeled based on a two feature concept. The CRP contribution is relatively athermal. In contrast, the SMF component increases with decreasing T_{irr}. The overall effect of T_{irr} depends on the balance of relatively athermal CRP to thermal SMF contributions. This has led to quantitative treatments of the effect of T_{irr} in terms of a fractional increase (lower T_{irr}) or decrease (higher T_{irr}) of hardening that depends primarily on the Cu content, with a secondary effect of P, apparently due to the effect of this element increasing the CRP number density[9]. This model has been derived from test reactor data; but, as shown in Figure 9, it is consistent with surveillance data trends.

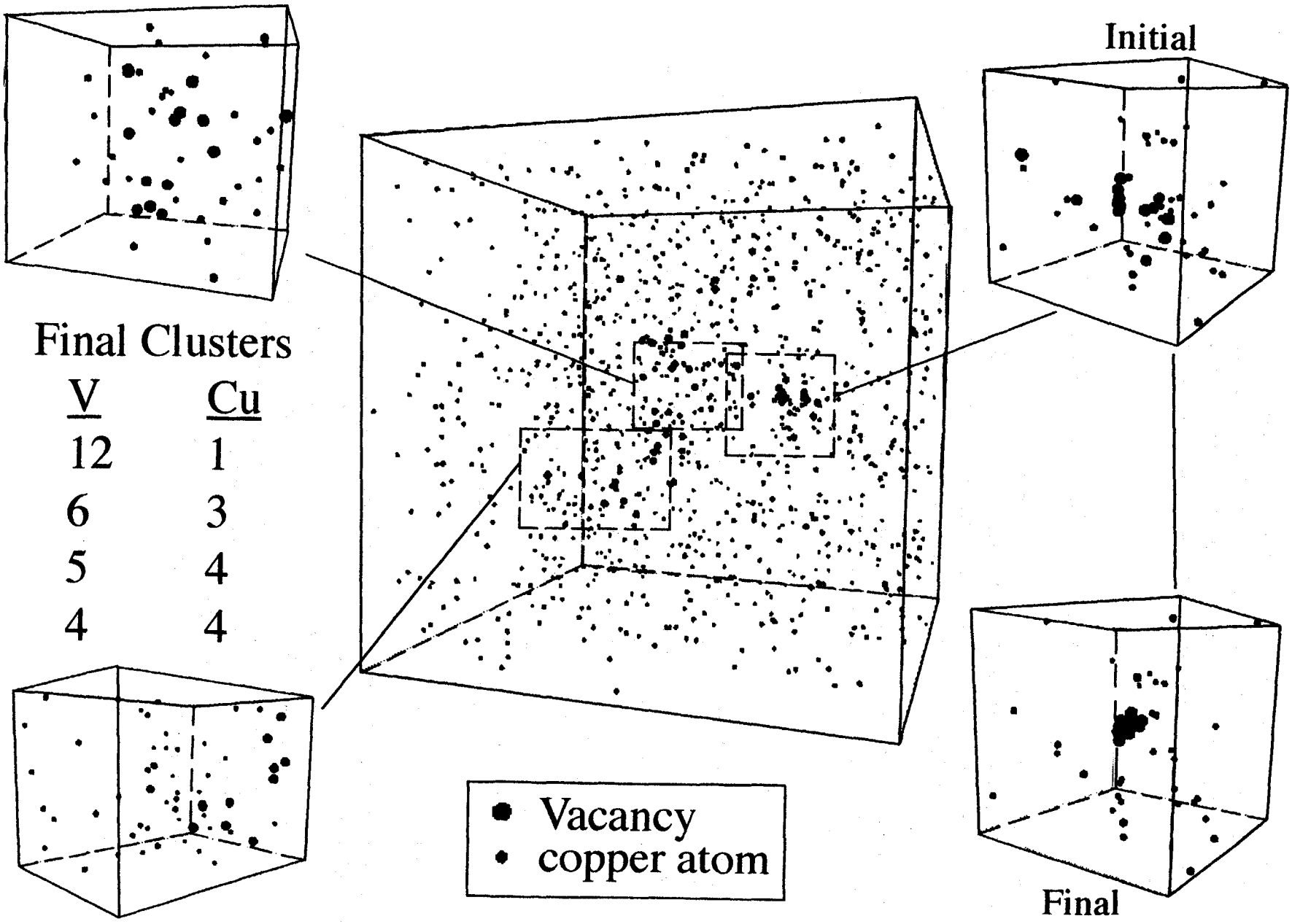

Figure 7 Examples of copper clustering promoted by binding to diffusing vacancies as seen in post-cascade kinetic lattice Monte Carlo simulations in an Fe-0.4Cu alloy.

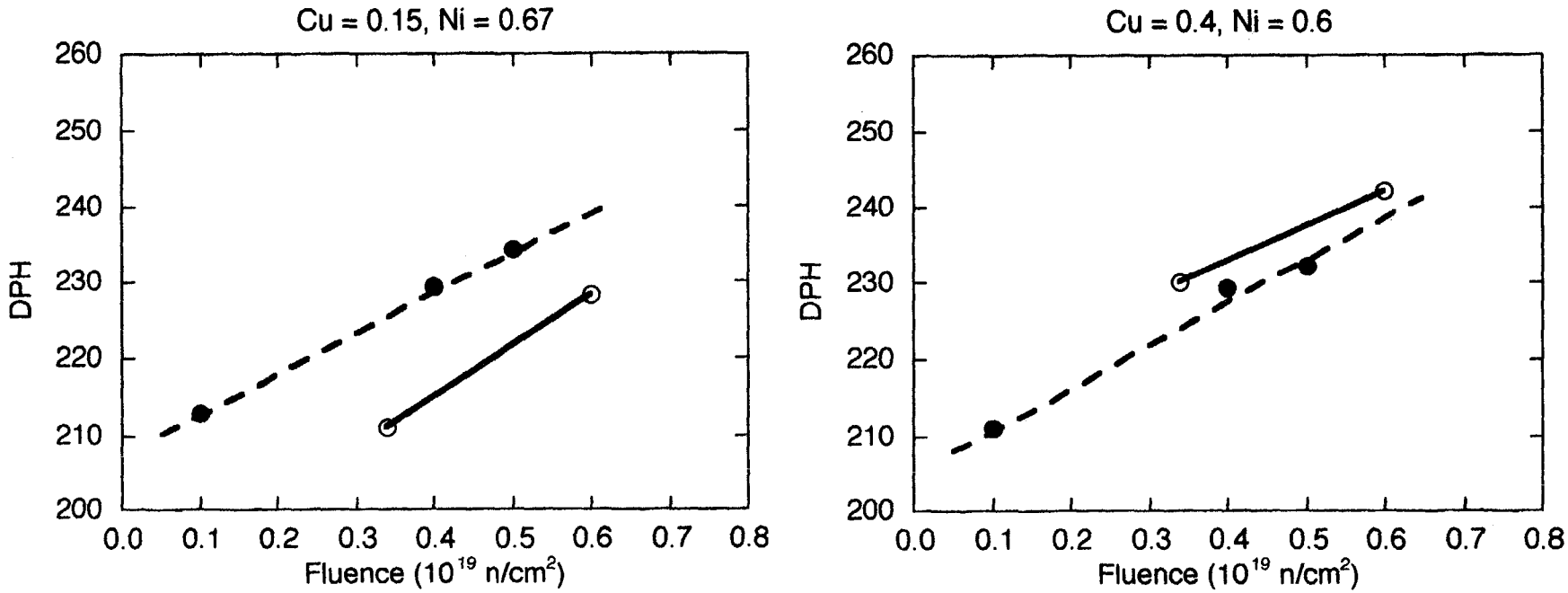

Figure 8 Variation of hardening with fluence for low and high Cu steels irradiated at low flux (solid lines) and high flux (dashed lines).

Copper Content and Heat Treatment

The basis for the variation of hardening/embrittlement with Cu is now well understood. At levels below about 0.1% Cu, CRP features do not form, and Cu has little effect. Likewise above about 0.3% Cu, variations in Cu have little effect due to pre-precipitation during stress relief treatments that leaves a maximum amount of Cu in solution near this level. The variation of hardening between 0.1 and 0.3% has a roughly $Cu^{0.5}$ dependence, as predicted by models of the precipitation hardening mechanism. These model predictions combined with $\Delta\sigma_y$-ΔT_{41} relations are also consistent with surveillance data trends, as shown in Figure 10. The data in Figure 10 illustrate the effect of heat treatment on limiting the availability of Cu. In this case, yield stress increases measured in irradiated specimens from split melt heats with various Cu contents and heat treatments have been converted to transition temperature shifts by the model described previously. Clearly the lower temperature-longer time heat treatment reduces ΔT due to pre-precipitation. The identification of practical upper limits on the effective Cu precludes the over-extrapolation of embrittlement trends from lower levels of Cu.

Ni and Mn Content

The independent effect of Ni is relatively weak, at least at low-to-intermediate ϕt. However, Ni increases the volume fraction of CRPs by increasing their Mn and Ni contents. This CRP alloying effect increases with decreasing T_{irr}, explaining the larger influence of Ni at lower T_{irr}. Both test reactor data and analysis of the surveillance data base shown in Figure 10 demonstrate that the Cu-Ni-Mn interaction is, by far, the dominant contribution to the compositional dependence of hardening and embrittlement. At very high Ni and Mn levels the CRPs are replaced by MNPs. Such MNP phases may form even at low Cu levels at sufficiently high ϕt. Early recognition of this possibility provides the opportunity to avoid a technical surprise when, and if, a severe re-acceleration of embrittlement is observed at high ϕt.

Post-Irradiation Annealing

The multi-feature model has also been very useful in developing physically-motivated correlations of post-irradiation annealing (PIA) recovery[10]. The MDs (UMDs plus SMFs) recover over a lower temperature range than the CRPs. The recovery of the CRPs only occurs at annealing temperatures above about 400°C, and depends on the Cu content. The effect of the MDs increases with decreasing T_{irr} and increasing ϕ (the UMD component). Thus recovery depends primarily on Cu, T_{irr} and ϕ, as well as the annealing time and temperature. This is illustrated in Figure 12.

High temperature annealing (T_a >400°C) dissolves small defect clusters and complexes, reduces the Mn and Ni content of CRPs, redissolves some of the Cu, and coarsens the CRPs. This is illustrated in Figure 13. The combined effects can be modeled by solving the rate equations for the UMD's (dissolution under thermal conditions with a mean life given previously), SMFs and CRPs (essentially clustering kinetics in reverse under thermal conditions, with appropriate corrections for the composition-dependent interface energy) and using a Russel-Brown model for hardening along

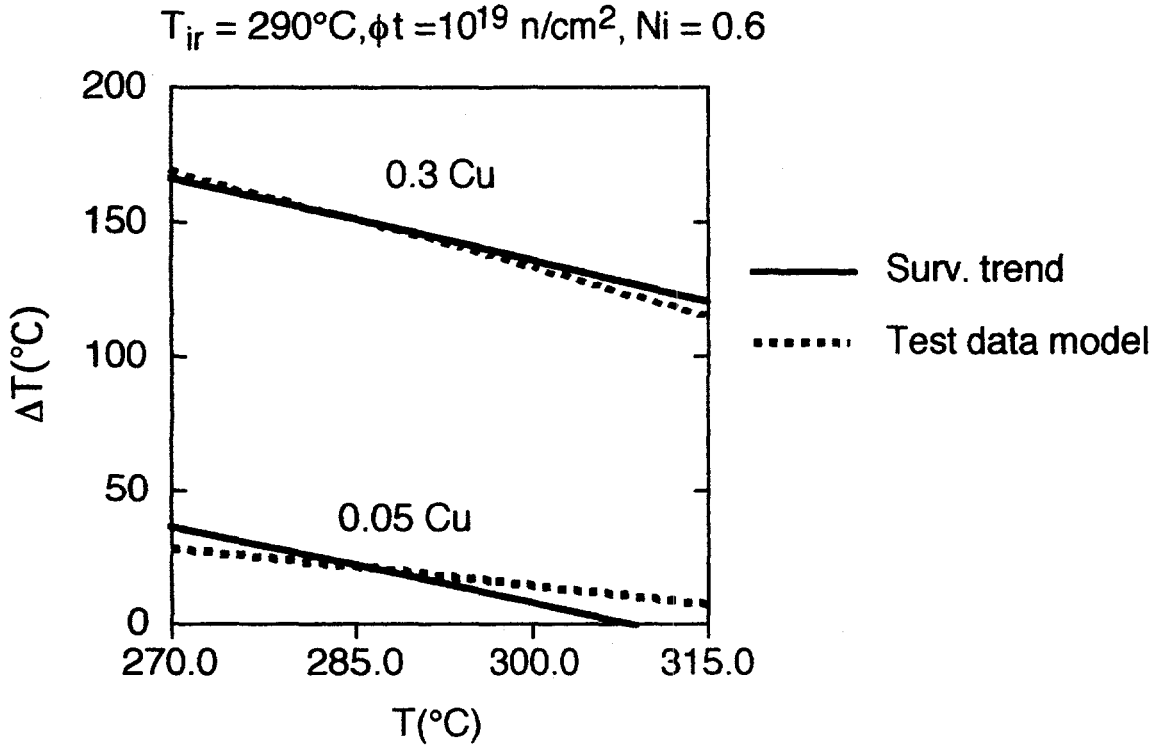

Figure 9 Transition temperature shifts versus irradiation temperature for high and low Cu steels as determined by the model (based on test reactor data) and surveillance data.

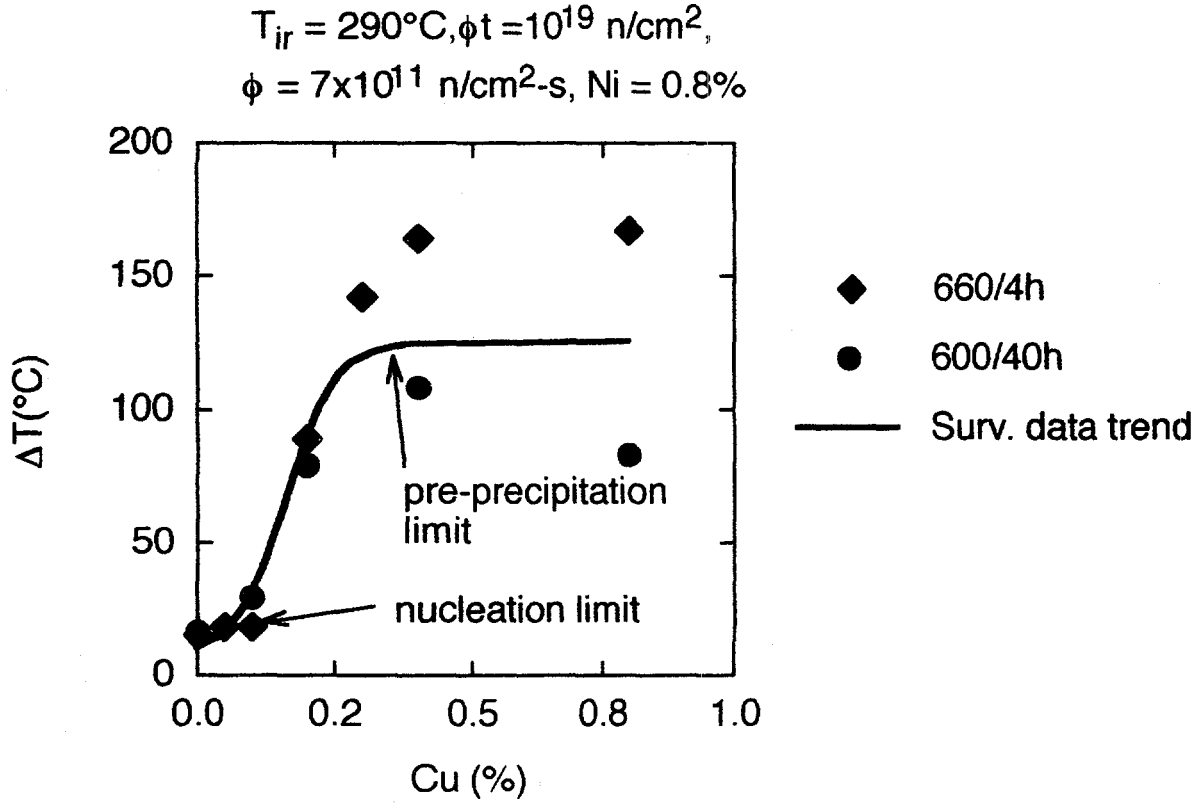

Figure 10 Variation of transition temperature shift with bulk Cu content. Data illustrate the effect of final heat treatment: with a higher temperature (660°C vs. 600°C) more copper is initially available in solution and hence hardening/shift is larger.

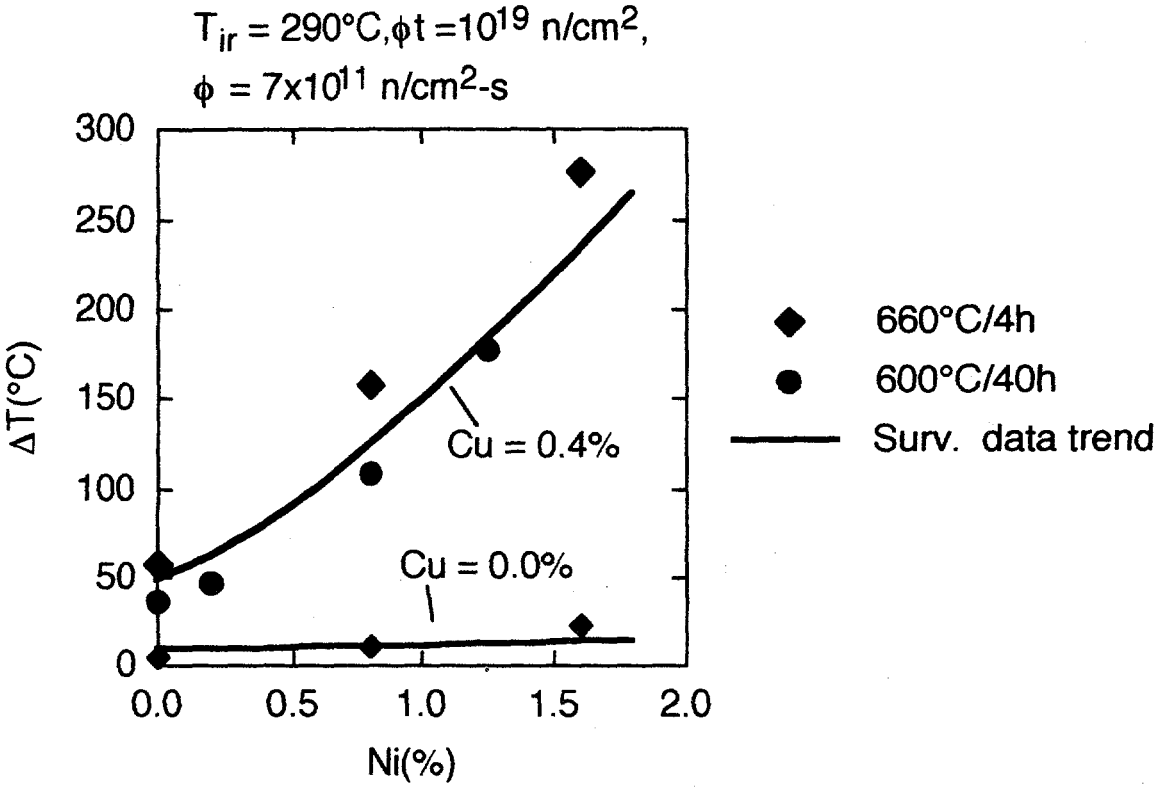

Figure 11 Variation of transition temperature shift with bulk Ni content at high and low Cu.

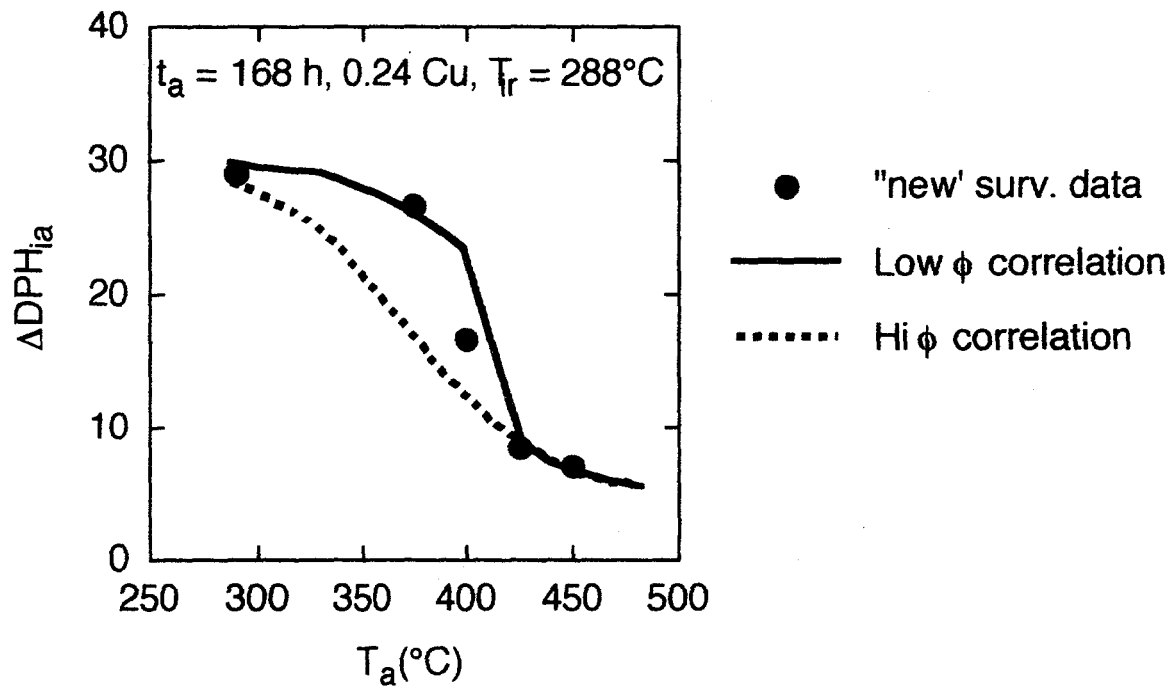

Figure 12 Variation of residual hardening with annealing temperature following PIA at 168h for a steel containing 0.24 Cu irradiated at 288°C.

- T_i=316 °C
- Cu=0.3 %
- Ni=0.86 %
- Mn=1.44 %
- $D_{Cu}=7x10^{-21}$ m²/s

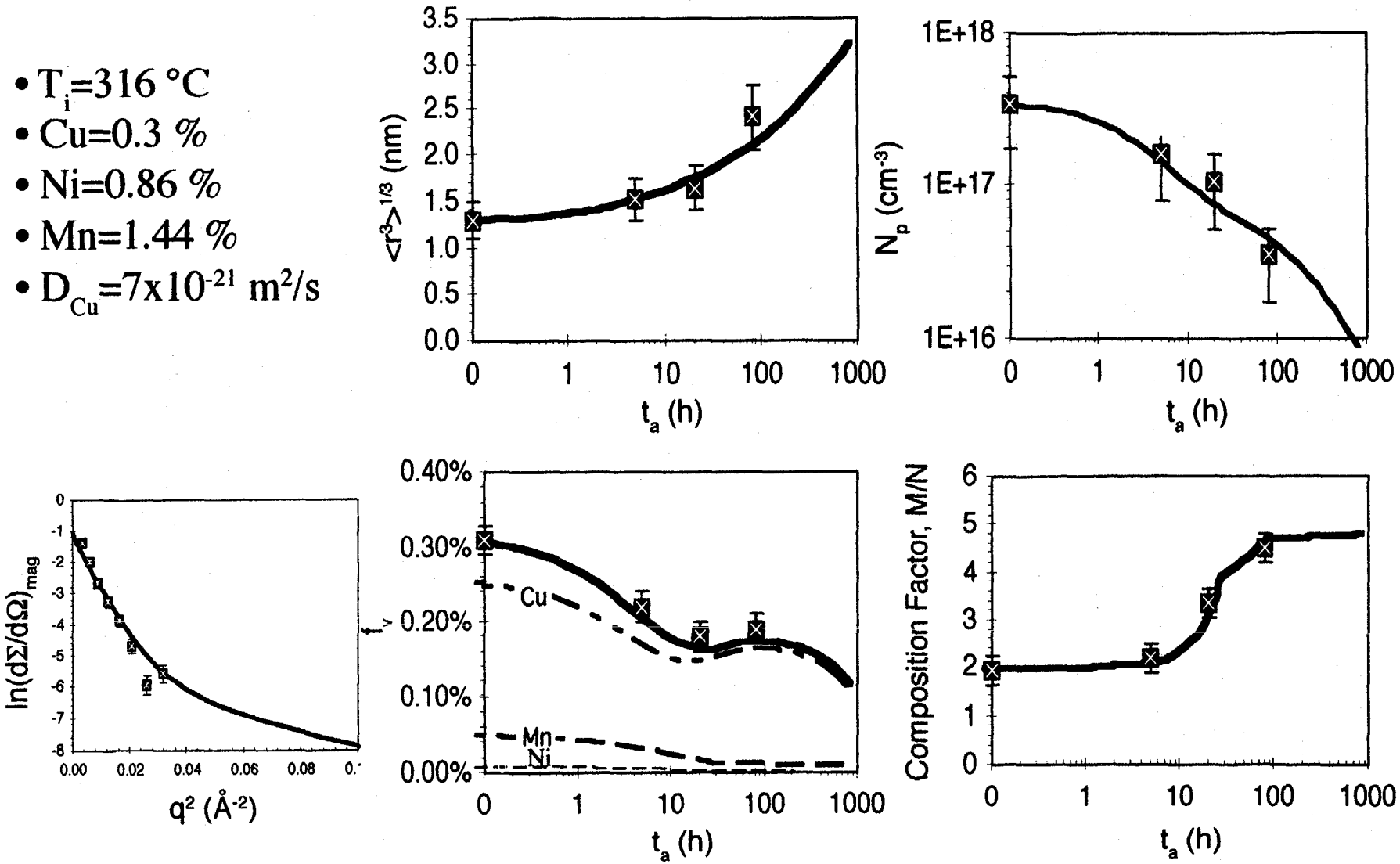

Figure 13 Examples of the variation of defect parameters with annealing time for a 0.3Cu-0.86Ni steel irradiated at 316°C and annealed at 450°C. (r = radius, N_p = number density, f_v = volume fraction, M/N = magnetic to nuclear scattering ratio in SANS)

with a computer-simulation-derived superposition law. The results are in good agreement with experimental measurements. Figure 14 illustrates this and shows some of the dominant trends of recovery as a function of metallurgical and annealing variables.

These results also have significant implications to re-irradiation embrittlement. For instance, following PIA at high temperatures and long times, Cu is sequestered in large stable precipitates but Mn and Ni are returned to solution. A variety of fates might be anticipated during re-irradiation. For instance, resolutioned or unprecipitated Cu (as well as Mn and Ni) may be partitioned to coarsened precipitates, may form new CRPs, or may help to form other matrix defects. While these issues remain to be explored, the defect evolution models provide an opportunity to explore this by using the post-PIA conditions to initialize the models for re-irradiation embrittlement modeling. Preliminary results shown in Figure 15 demonstrate the good agreement between model predictions of $\Delta\sigma_y$ in irradiated and PIA'd material, and that predicted embrittlement is reduced by an intermediate PIA treatment. Thus the possibility exists to identify optimum heat treatments to achieve the best combination of high recovery and low re-embrittlement rates. Experimental verification is planned.

Fluence

The fluence dependence of hardening can also be understood and modeled based on a two feature concept. The CRP contribution slows and ultimately saturates above ϕt levels of about $1\text{-}3\times10^{19}$ n/cm^2 due to exhaustion of Cu. In contrast, the SMF component varies roughly as $\phi t^{0.5\pm0.2}$. Hence, the SMFs become increasingly important at high ϕt. Thus, embrittlement does not completely saturate, but may appear to do so over limited ϕt intervals. This is illustrated in Figure 16. The contributions of late "blooming" MNPs to hardening and embrittlement are not yet known. However, models and limited data suggest the potential for large volume fractions of MNPs in low copper steels, restricted by slower nucleation kinetics compared to the CRPs. This may lead to severe embrittlement at high fluence, as illustrated in Figure 17 and shown for two examples taken from the literature[11,12].

MODELING FRACTURE

As noted earlier models based on the micromechanics of fracture have been used to derive relationships between $\Delta\sigma_y$ and ΔT_{41}. In principle, these models can be extended to treat the effect of irradiation on fracture toughness-temperature curves, $K_{Jc}(T)$, including constraint and statistical effects. This requires combining finite element method simulations of crack tip fields with rigorous micromechanical models and measures of local fracture conditions. However, it has been found that the simple equivalent σ_y treatments that are effective for modeling Charpy shifts overpredict toughness shifts at high $\Delta\sigma_y$ due to changes in the calculated shape of $K_{Jc}(T)$ curves that are not observed experimentally. Significant progress in resolving such outstanding issues as well as developing a better fundamental understanding of fracture and fracture mode transitions will depend on the application of advanced modeling and new experimental methods. The latter includes confocal microscopy-fracture reconstruction techniques (CM-FR), which provide

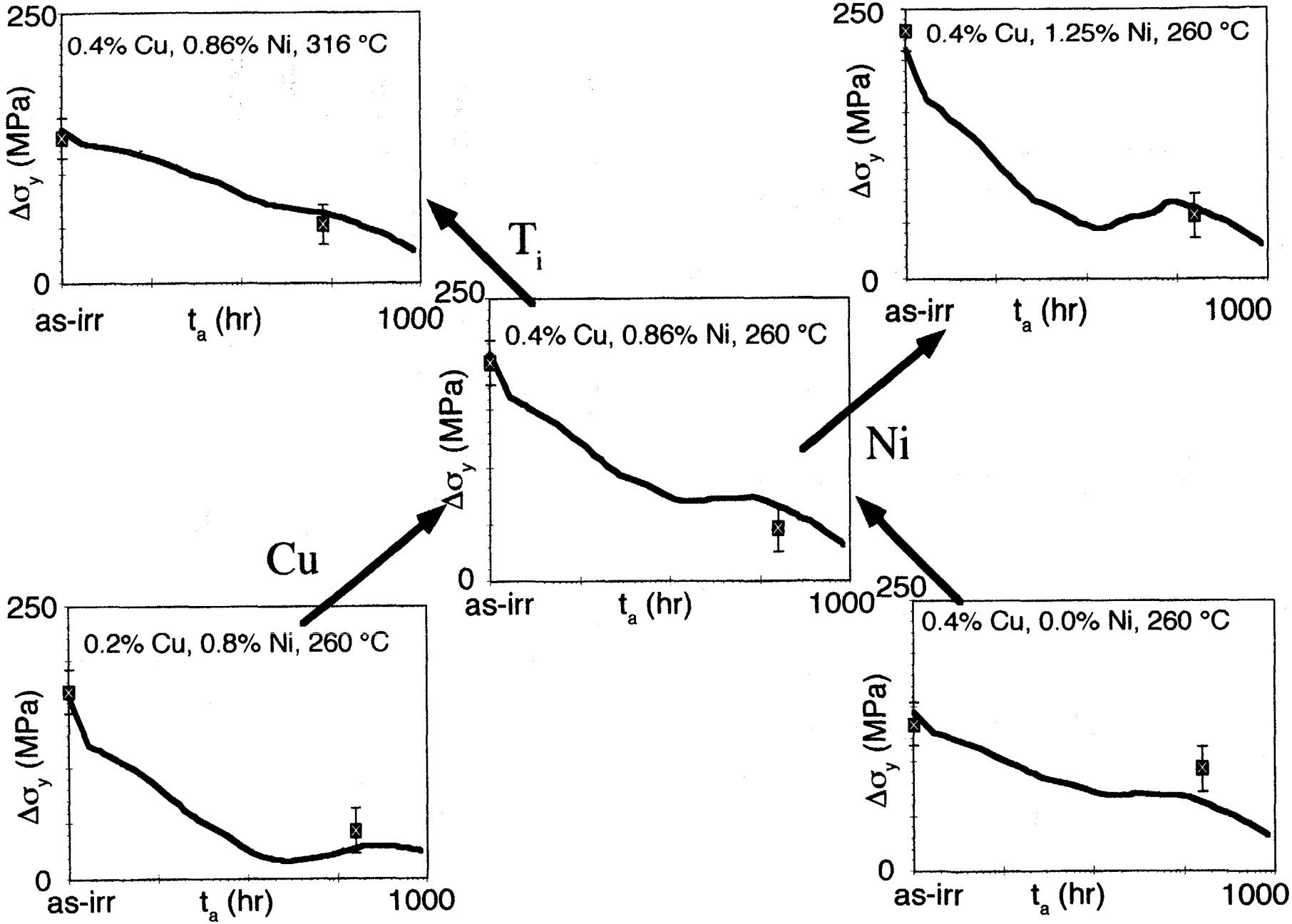

Figure 14 Comparison of the model predictions of residual hardening vs. annealing time with experimental data for various irradiation and metallurgical variables.

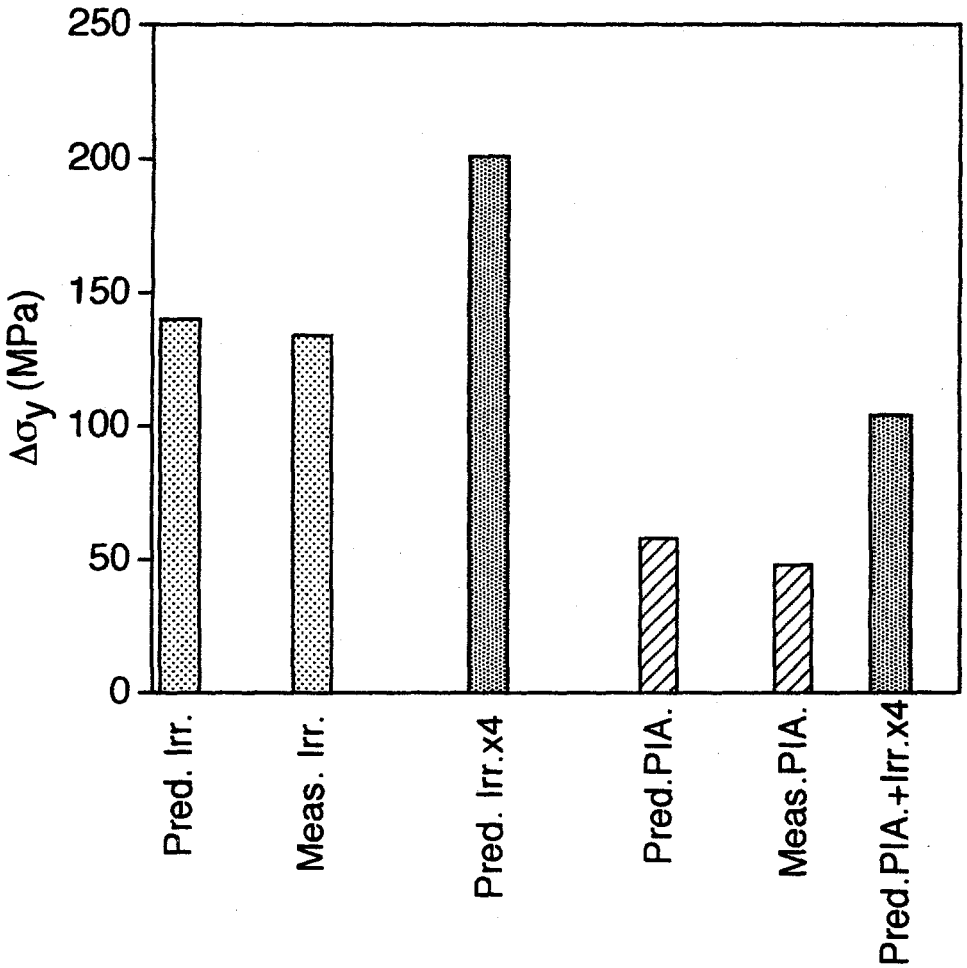

Figure 15 Comparison of measured and predicted hardening following irradiation, PIA and re-irradiation.

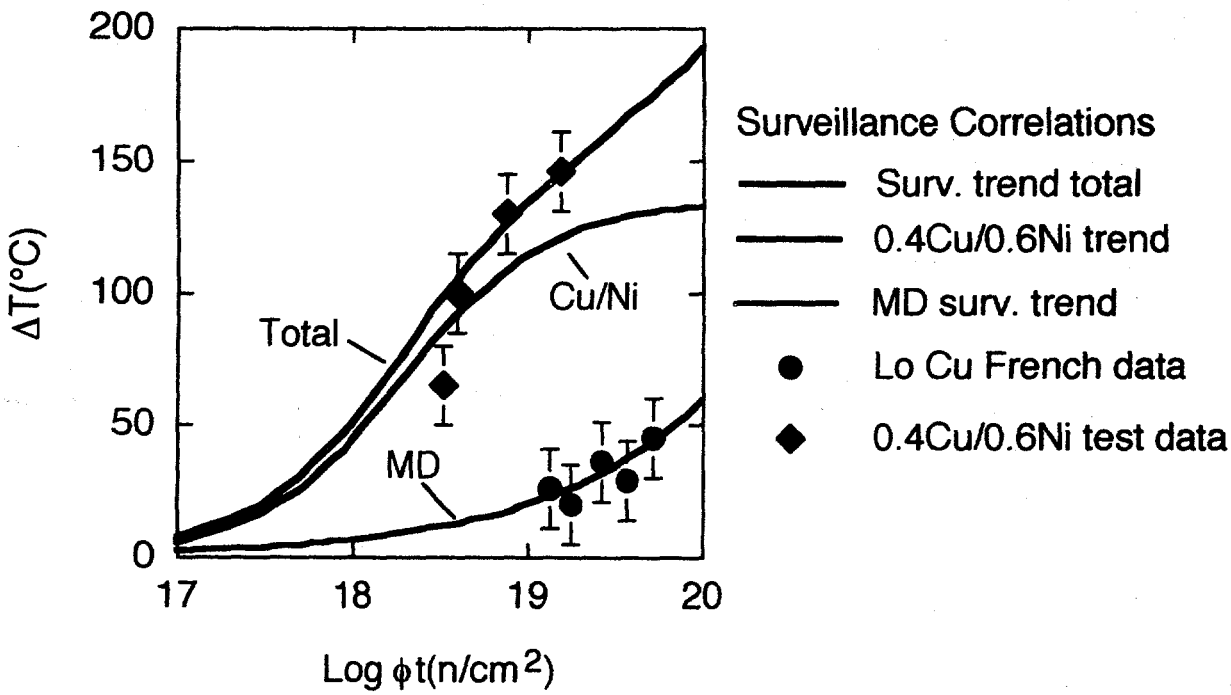

Figure 16 Variation of transition temperature shift with fluence illustrating the contributions from CRPs and MDs.

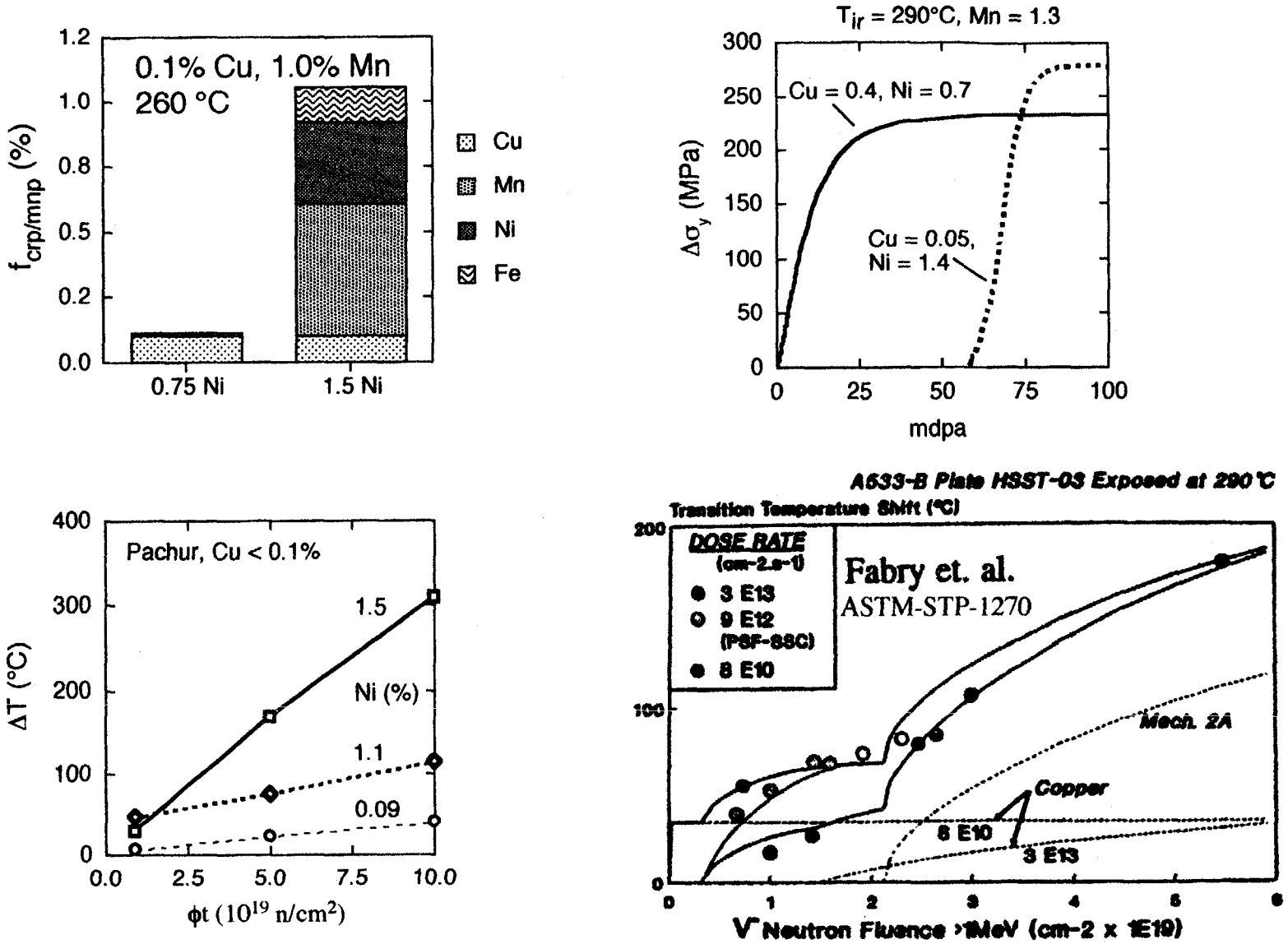

Figure 17 (Top) Illustration of the potential contribution of MNPs to accelerated embrittlement at high fluence in high Ni steels. (Bottom) examples of additional hardening at high fluence in the literature[11,12].

quantitative tomographic information on the sequence of deformation and damage development near the crack tip leading to fracture. However, these topics are beyond the scope of this paper and are discussed elsewhere.[13-17]

OPEN QUESTIONS AND FUTURE OBJECTIVES

Despite significant advances, there remain a number of unknowns in our understanding of irradiation embrittlement. Major questions and opportunities include the following:

- establishing the nature and etiology of the matrix defects and the effects of irradiation and metallurgical variables on their evolution.

- more precisely quantifying the lower limit of the flux-effects regime for a range of T_{irr}, and assessment of the potential for additional flux effects at very low flux levels due to contributions from anomalous thermal aging.

- quantifying the interactions between major embrittlement compositional variables (Cu-Mn-Ni and others) and the effects of time-temperature processing history on the distribution and availability of these species to participate in embrittlement.

- developing a model of high fluence embrittlement including new phases and features at low Cu contents, and devising experiments to calibrate and test the model.

- developing an integrated experimental description and physical model of microstructural evolution during irradiation , PIA and re-irradiation.

Although it was not the focus of this paper, there are also important opportunities to improve our understanding of fracture mechanics and application of fracture mechanics. Rather than relying on Charpy-based indexing of the reference toughness curve, it may be possible to use small specimen test methods to directly measure K_{Jc}. For instance, Charpy-sized or smaller specimens, including biopsies extracted from operating vessels, are sufficient to measure K_{Jc} up to 100 MPa$\sqrt{m}$; and a minimum number of (small) specimens is required to index a master curve of toughness on an absolute temperature scale, $K_{Jc}(T)$. However, this assumes a relatively constant shape of $K_{Jc}(T)$. Although a master-type curve is supported by observation, this behavior is not well understood. Moreover, the effective use of small specimens requires properly accounting for the size-dependence, including constraint and statistical effects. As noted above, the requisite understanding can be obtained by combining finite element calculations of crack tip stress and strain fields with local critical field conditions leading to failure (e.g., critical stresses/strains over critical volumes). Better understanding and models of these local fracture micromechanisms will come from the application of advanced micromechanical characterization methods, such as CM-FR.

ACKNOWLEDGMENTS

This work is supported by the USNRC, Contract Number NRC-04-94-049.

REFERENCES

1. G. R. Odette and G. E. Lucas, *An Experimental Investigation of Kinetic Aspects of Neutron Irradiation Embrittlement of Light Water Reactor Pressure Vessel Steels,* EPRI NP 6114, EPRI, Palo Alto (1989).

2. G. R. Odette, MRS Soc. Symp. Proc., 373 (1995) 137.

3. G. R. Odette and G. E. Lucas, ASTM-STP-909, American Society for Testing and Materials, Philadelphia, PA (1986) 206.

4. G. R. Odette, *Neutron Irradiation Effects in Reactor Pressure Vessel Steels and Weldments,* IAEA Technical Report Series, Vienna (in press).

5. P. Pareige, *Etude a la Sonde Atomique de l'Evolution Microstructurale Sous Irradiation d'Alliages Ferritiques FeCu et d'Aciers de Cuve de Reacteurs Nucleaires*, PhD Thesis, Universite de Rouen (1994).

6. K. C. Russell and L M. Brown, *Acta Met.,* 20 (1972) 969.

7. G. R. Odette, P.M. Lombrozo, P.M., R. A. Wullaert, ASTM-STP-870, American Society for Testing and Materials, Philadelphia, PA (1985) 841.

8. G. R. Odette, E. V. Mader, G. E. Lucas, W. J. Phythian, and C. A. English, ASTM-STP-1175, American Society for Testing and Materials, Philadelphia, PA (1993) 373.

9. G. R. Odette, G. E. Lucas, D. Klingensmith, ASTM-STP-1270, American Society for Testing and Materials, Philadelphia, PA, (1996) 606.

10. E. Eason, J. E. Wright, E. E. Nelson, G. R. Odette, E. Mader, *Proceedings of the 7th Int'l Symp. on Environmental Degradation of Materials in Nuclear Power Systems--Water Reactors*, NACE-ANS-TMS, Breckenridge, CO (1995).

11. D. Pachur and G. Seivers, *Irradiation Program for Pressure Vessel Steels.* KFA Julich, (1974).

12. A. Fabry, J. Van de Velde, J. L. Puzzolante, T. Va Ransbeeck, A. Verstrepen, E. C. Biemiller, R. G. Carter, T. Petrova, ASTM-STP-1270, American Society for Testing and Materials, Philadelphia, PA (1996) 138.

13. T. Kobayashi and D. A. Shockey, *Met. Trans.*, 18A (1987) 1941.

14. T. Kobayashi and D. A. Shockey, *Advanced Matls and Proc.*, 140-5 (1991) 28.

15. K. Edsinger, *Fracture Reconstruction and Advanced Micromechanical Modeling of Structural Steels,* PhD Thesis, Dept. of Chemical Engineering, UC Santa Barbara (1995).

16. K. Edsinger, G. R. Odette, G.E. Lucas, *Proceedings of the IEA International Symposium on Miniaturized Specimens for Testing Irradiated Materials,* KFA Julich, (1995) 150.

17. B. Wirth, K. Edsinger, G. R. Odette, G. E. Lucas, ASTM-STP-1270, American Society for Testing and Materials, Philadelphia, PA, (in press).

Neutron Radiation Embrittlement Studies in Support of Continued Operation, and Validation by Sampling of Magnox Reactor Steel Pressure Vessels and Components

By

R B Jones and C J Bolton

Magnox Electric plc,
Structural Integrity Branch,
Technology and Central Engineering Division,
Berkeley Centre, Berkeley, Glos, UK

Magnox steel reactor pressure vessels differ significantly from US LWR vessels in terms of the type of steel used, as well as their operating environment (dose level, exposure temperature range, and neutron spectra). The large diameter ferritic steel vessels are constructed from C-Mn steel plates and forgings joined together with manual metal and submerged-arc welds which are stress-relieved. All Magnox vessels are now at least thirty years old and their continued operation is being vigorously pursued. Vessel surveillance and other programmes are summarised which support this objective.

Our current understanding of the roles of matrix irradiation damage, irradiation-enhanced copper impurity precipitation and intergranular embrittlement effects is described in so far as these influence the form of the embrittlement and hardening trend curves for each material. An update is given on the influence of high temperature exposure, and on the role of differing neutron spectra. Finally, the validation offered by the results of an initial vessel sampling exercise is summarised together with the objectives of a more extensive future sampling programme.

Introduction

In 1996 the nuclear generation of electricity in the UK was reorganised. Magnox Electric plc was formed to manage the UK Magnox reactors formerly operated by Nuclear Electric plc and Scottish Nuclear plc. Magnox Electric generate about 8% of the electricity in the UK from the operation of twelve reactors. Four of the generating sites have twin reactors with steel pressure vessels. This paper addresses the work necessary to support the continued operation of these eight steel pressure vessels. Further information on the Magnox reactors is given in Table 1, from which it can be seen that all operating steel vessels are at least thirty years old (Ref 1).

Vessel Design and Construction

The steels used in vessel construction generally consisted of simple C-Mn ferritic plates, either Si-killed or Al-grain refined, in the normalised and stress relieved condition. Similar materials were used for nozzle and coolant gas duct forgings. The design requirements (Ref 2) were twofold: firstly that the steels should have good notch ductility during fabrication operations and

at start-of-life and that these properties should be maintained after service irradiation; secondly, that creep deformation should not exceed 0.2% combined with sufficient creep ductility to accommodate local deformation at stress concentrations and good general section stress rupture properties over a 20 year period at the highest vessel temperature envisaged (400°C).

Table 1 - Details of Magnox Reactor Steel Pressure Vessels

Station	Site Work Started	Commercial Power	Inner Diameter and Thickness	Type of C-Mn Steel Plate
Bradwell	1957	1962	20.3m, 76mm	Si-killed+alloy
Hinkley Pt A	1957	1965	20.4m, 76mm	Si-killed
Dungeness A	1960	1965	19.1m, 102mm	Grain refined
Sizewell A	1961	1966	19.4m, 105mm	Si-killed

Construction involved some factory prefabrication with final assembly at the site. At the factory, two or three curved plate panels were welded together to form a ring segment using a submerged-arc process with copper-coated welding rods. Holes were cut in some panels and duct forgings were attached by the submerged-arc welding process. At the site, the segments were welded to form ring sections using a manual metal-arc welding process. The pressure vessel was built by welding together differing sizes of ring section (shell courses) and attaching bottom and top domes; all these joints were circumferential and of the manual weld type. To complete vessel assembly, fuel access and control rod standpipes were attached by manual welding. Afterwards, the entire vessel was slowly heated, stress relieved for up to ten hours at temperatures within the range 600 ± 40°C, and slowly cooled at 2 - 5°C/hour (Ref 2).

Ambient temperature pneumatic proof testing was carried out on the finished vessel, generally at 1.5 times operating pressure (Ref 2). The total length of weld in a typical 20m diameter vessel has been estimated to be between 1000 - 2000m, depending on plate size, the majority of welds being of the manual type. All welds were radiographed before proof testing. Figure 1 shows the constructional features of a typical vessel including the position of the core, core support structure (diagrid), vessel internals and vessel support structure (Ref 2).

Surveillance Scheme

The mechanical property changes produced in each pressure vessel by thermal and irradiation effects during life have been monitored by a surveillance scheme that employed plate, weld and forging samples fabricated at the same time as the vessels. Table 2 shows the average, or range of, chemical compositions for the plates, manual metal-arc (MMA) welds, submerged-arc (SMA) welds and forgings respectively, as derived from the populations of vessel cut-outs ex-construction, surveillance samples and contemporary reproduction vessel materials.

Surveillance canisters, filled with standard Charpy impact and uniaxial tensile test samples of the vessel materials together with flux monitoring devices (nickel and cobalt wires), were exposed in the reactors in tubes (ducts) fitted at below-core and side-core positions and in baskets hanging

Table 2 - Chemical Composition of Magnox Vessel Materials (Wt %)

Material	C	Mn	Si	S	P	Cu
Plate	0.09- 0.17	1.04- 1.32	0.10- 0.60	0.02- 0.04	0.01- 0.04	0.03- 0.15
MMA	0.086	0.91	0.42	0.022	0.025	0.08
SMA	0.088	1.49	0.52	0.037	0.031	0.23
Forgings	0.18	1.30	0.36	0.024	0.024	0.10

Ni and Cr each < 0.1%; Mo, Sn, As and Ti each < 0.05%.

at other locations above the core. However, although plate was always present, not every canister contained all weld or forging materials, nor did every vessel have the full variety of surveillance locations. Figure 2 shows a typical arrangement of surveillance locations in-reactor (Ref 3).

The original operating conditions of the Magnox reactors comprised extremes of vessel temperatures from 165°C below-core to 360 - 392°C above-core. However, when an oxidation problem on ferritic bolting materials was detected after several years operation, the maximum temperature was reduced to 360°C. The thermal history of the surveillance samples also reflects these changes. The neutron dose experienced by the samples is affected by canister location. In the Magnox reactors the canisters generally have similar doses to the adjacent vessel (i.e. a "lead factor" of about one), but there are a few locations where the vessel has a higher dose than the appropriate surveillance canisters by a factor of about two. Expressing the dose in units of displacements-per-atom, for reasons that will become clear later on, it is possible to summarise the operating conditions of the surveillance canisters, see Table 3 below.

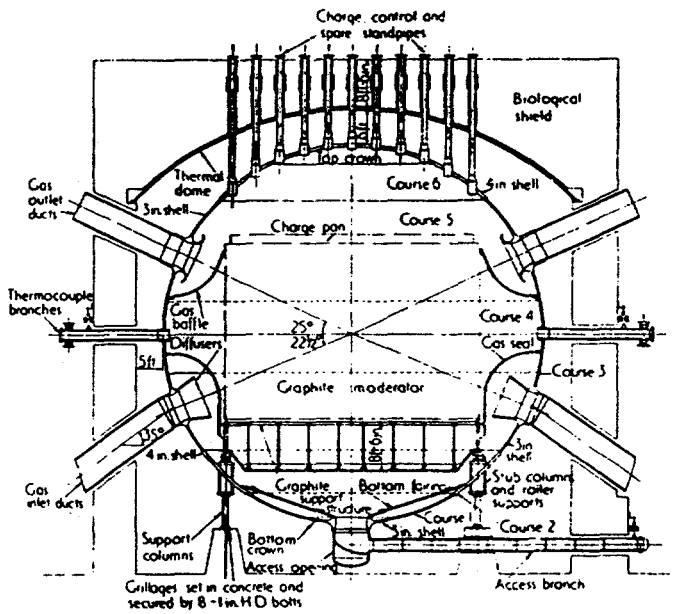

Figure 1 - Typical spherical reactor shell

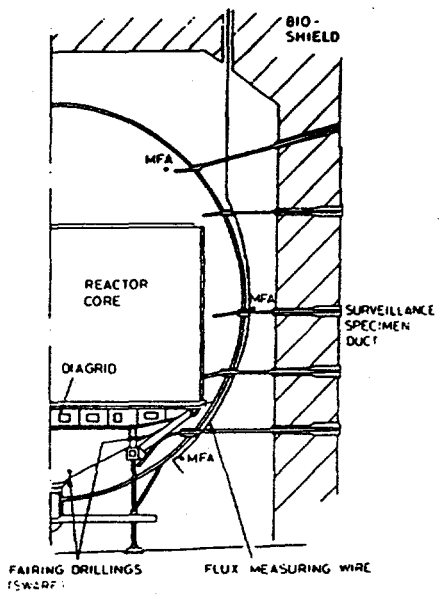

Figure 2 - Surveillance canister locations and dose validation positions

Table 3 - Exposure Conditions for Surveillance Canisters

Canister Location	Irradiation Temp °C	Irrad 'n Dose Rate dpa / sec	Max 30 Year Dose, dpa $x10^5$ *
Above core	330	4.4×10^{-13}	33
	392 / 360	$3.2 - 4.9 \times 10^{-13}$	24 - 37
Side core	198 - 201	2.0×10^{-12}	152
	221	7.3×10^{-13}	55
	297 - 301	2.6×10^{-12}	198
	314 - 355	1×10^{-12}	76
Sub-core	165	9.4×10^{-14}	7.1
	190	$1.5 - 3.5 \times 10^{-12}$	114 - 266
	221	$4.2 - 4.9 \times 10^{-12}$	320 - 374

* At 80% load factor

Vessel and Sample Doses

Originally the doses to the vessel were estimated from design calculations augmented by the dose measurements obtained from the surveillance canisters. Due to the complexity of the reactor internals it was realised that this procedure was inadequate. A significant improvement has been obtained over the last seven years by the use of modern neutron transport codes such as MCBEND (Refs 3, 4, 5 and 6). This 3D code is able to make explicit represention of graphite reflectors and reactor structural steelwork, including the surveillance ducts, can allow for the effects of temperature and irradiation on the structure, and for the attenuation in the CO_2 coolant and pressure vessel steel wall. Operating power history effects are also incorporated. The code generates neutron spectra at the inner surface of the vessel. Since the spectra vary considerably around the vessel the use of dose descriptors involving neutrons of specific energies, > 1 MeV for example, is considered to be inadequate since significant irradiation damage effects can occur in steels from neutrons with energies well below this value (Refs 3 and 4). Consequently the damage unit employed is displacements-per-atom (dpa), obtained by folding together the neutron spectrum and the ASTM dpa damage cross-section for iron (Ref 7). Initially the dpa results were calculated for neutrons with energies > 0.1keV (Ref 3), but as the work progressed it was realised that the dpa arising from low energy neutrons might also be important in the surface regions of the vessel (see later). Consequently "fast" dpa (for neutrons >1keV) and "thermal" dpa (neutrons < 1keV) are now regularly determined (Ref 6).

The code calculations are themselves validated by comparison with measurements (Ref 5). These come from the activation monitor materials in the surveillance canisters, from the activation of the steel surveillance samples themselves, from data obtained from specially installed multi-foil activation packs (MFA), from activation measurements obtained on steel swarf remotely drilled from reactor internals or from reactor debris (broken bolts, clamps etc), and, occasionally, from the activation profile along lengths of stainless steel wire wrapped around the outside of the

vessel; Figure 2 shows details of these methods. Agreement between calculation (C) and experiment (E) is quite good; mean C/E values for >1keV dpa in below core positions are typically 0.96 - 1.13, for side core 0.85 - 1.03 and for above core 0.99 - 1.19. For thermal dpa the agreement is less good; below core 0.50 - 1.47, side core 0.97 - 1.36 and above core 1.50 (Ref 6).

The aim of the dosimetry programme is to calculate the mean and 1 standard deviation doses at about 1° intervals around the vessel surface and to obtain values for individual surveillance samples. Figure 3 shows the angular distribution of fast and thermal dpa from the top of a typical vessel (Ref 6). At the top and bottom of the vessel the fast dpa dominate, due to the stronger attenuating effect of the structural steel in the charge pan and diagrid respectively on the thermal neutrons compared to fast neutrons (see Figure 1). At the side of the core the fast and thermal dpa are of similar magnitude, the exact contribution of the thermal dpa depending on the thickness of the graphite reflectors and the disposition of the steel in the vessel internals and core restraint structure. For the surveillance samples, the MCBEND calculations are used to produce location-dependent "scale factors" for fast dpa which are applied to the fission-equivalent flux from each canister's Ni activation monitors: these factors can vary by up to a factor of eight between locations. The thermal dpa are obtained from the thermal monitor activation via the 2200m/sec cross section.

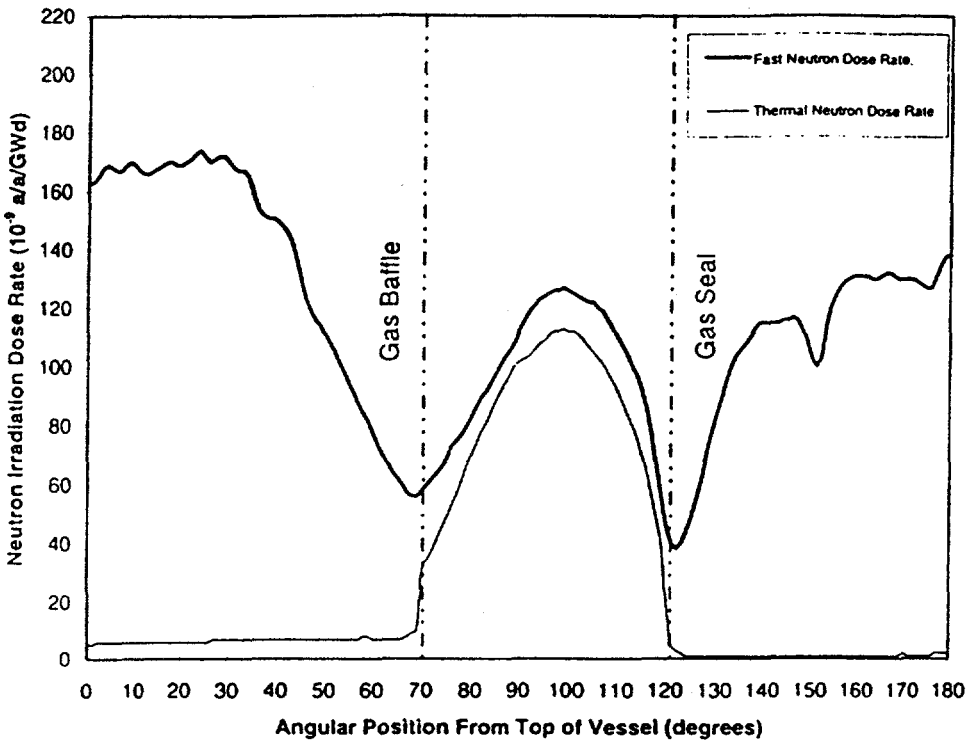

Figure 3 - Polar distribution of fast (E > 1 keV) and thermal (E < 1keV) dpa rates

Safety Case Methodology

In the 1960's the safety cases relied on the high quality of construction, the results of the radiographic inspection and the tolerance to large defects implied by survival of the proof test (Ref 8). At start-up a minimum operating temperature had to be exceeded before significant vessel pressurisation could commence. This minimum operating temperature was defined by the results of crack arrest tests on wide plate samples of full section-thickness (arrest temperature typically 30°C) combined with an estimated upward shift in arrest temperature due to approximately equal contributions from in-service aging and irradiation effects giving a total shift of 40°C (Ref 9). The magnitude of the shift was perodically checked by reference to the Charpy shifts determined in the surveillance programme. By the late 1970's it was clear that, after allowing for data scatter, the shift allowance had been exceeded. Furthermore, it was the submerged-arc welds, rather than the plates, that had the biggest shifts (Ref 10). Consequently changes to the operating rules were required.

The operation of reactor vessels during start-up and normal operation is governed by an operating rule of the type shown in Figure 4 (Ref 9). This permits both pressure margins and temperature margins to be maintained, at all vessel locations, between the rule and a "limit line". The latter is determined from considerations of both resistance to fast fracture and to plastic collapse using the R6 failure assessment diagram (Ref 11). Necessary inputs to the assessment are the size of the defects postulated to be present in the vessel, the operating stresses, the temperature dependence of the fracture toughness of the steel plate or weld metal, whichever is the lower, and the yield stress of the weakest material at the location being assessed (Ref 9).

Figure 5 schematically shows the effect of neutron irradiation on fracture toughness in Magnox pressure vessel steels (Ref 9). Changes to lower shelf toughness are minimal, transition toughness is shifted to higher temperature and upper shelf toughness is degraded. The upper shelf toughness

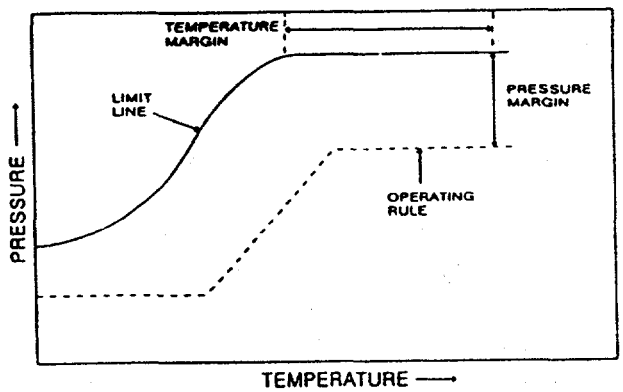

Figure 4 - Calculated limit line compared with the operating rule showing temperature and pressure operating margins

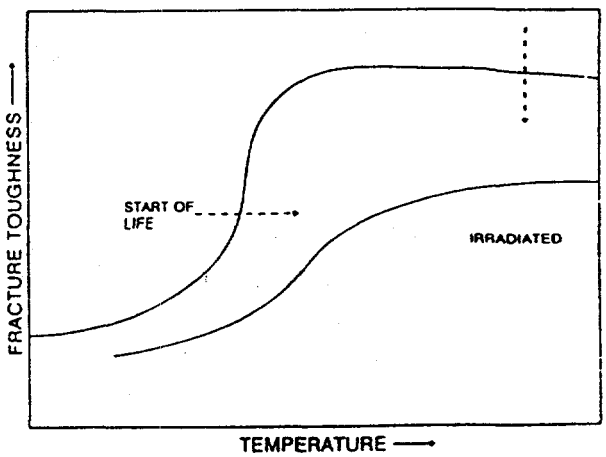

Figure 5 - Effects of neutron irradiation on start-of-life fracture toughness properties of a pressure vessel steel

in the unirradiated condition may be defined from tests on full section-thickness fracture toughness samples of plate and weld metal prepared from material recovered from the duct and standpipe cut-outs mentioned earlier. However, the degradation produced by irradiation is more difficult to define because the surveillance schemes only contained Charpy samples of 10mm section size. Although 3-point bend toughness tests could be performed in-cell at upper shelf temperatures on precracked irradiated Charpy samples (Ref 12), the validity of the result was often compromised by the limited section size. To mitigate this problem, the method finally adopted is to measure the dose-dependence of the relative change in upper shelf Charpy toughness, i..e. the ratio F_K = irradiated toughness / unirradiated toughness, and factor the unirradiated toughness of the full section-thickness samples accordingly. The dose-dependence of F_K is shown in Figure 6 (Ref 4) for submerged-arc weld metal in both surveillance and accelerated irradiation experiments; these welds show a modest degradation of properties. The other vessel materials showed no degradation of F_K over the dose ranges of interest for vessels.

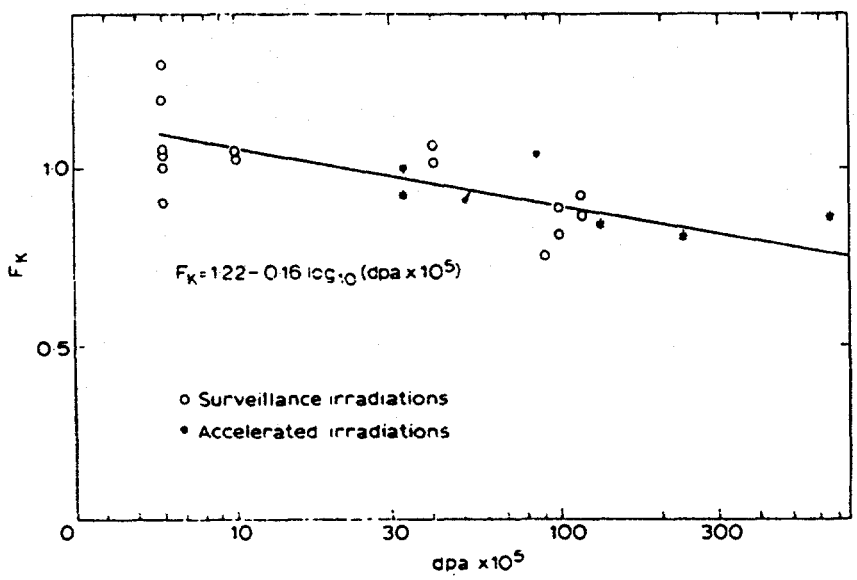

Figure 6 - Variation of F_k with dpa dose for submerged-arc weld metal

The lower bound yield strength properties at the operating temperature, for assessment of the pressure margins, may be obtained from knowledge of the room temperature yield stress properties of each material at start-of-life; these are adjusted to values appropriate to the operating temperature. To these values is added the corresponding irradiation-induced increase in ambient temperature yield strength for each material, as obtained from the surveillance programme. Over the range of use the irradiation shift is essentially independent of the application temperature.

For applications in the toughness transition region conventional Charpy testing is employed to obtain the irradiation-induced shift in 40J transition temperature; the Charpy impact energy/test temperature results being analysed using the *tanh* function. This temperature shift is identified

with the shift in the temperature for a toughness of 100 MPa√m, where the fracture toughness curve is assumed to exhibit no change in shape with irradiation (Ref 13). A number of 3-point bend tests have also been employed to directly determine the fracture toughness in the transition region for both irradiated and unirradiated materials and to derive the irradiation-induced shift. However direct fracture toughness testing has been limited by the use of the restricted supply of Charpy samples in each canister for impact testing, and, in addition, this procedure could not have been employed on any of the materials that were withdrawn early in life. Consequently, reliance has been placed on the toughness/Charpy correlation for Magnox materials, derived from data in Reference 10, that is shown in Figure 7 (Ref 14). This indicates that the T_{40J} and $T_{100\,MPa\sqrt{m}}$ temperatures, and hence the shifts, are linearly related. With the recent successful adoption of Charpy sample reconstitution techniques it is now feasible to re-use broken Charpy impact samples of both welds and plates for 3-point bend toughness testing on a regular basis and to extend the range of validation given by Figure 7. Ultimately the aim is to obtain sufficient data to derive a trend curve that directly relates the transition toughness to irradiation dose.

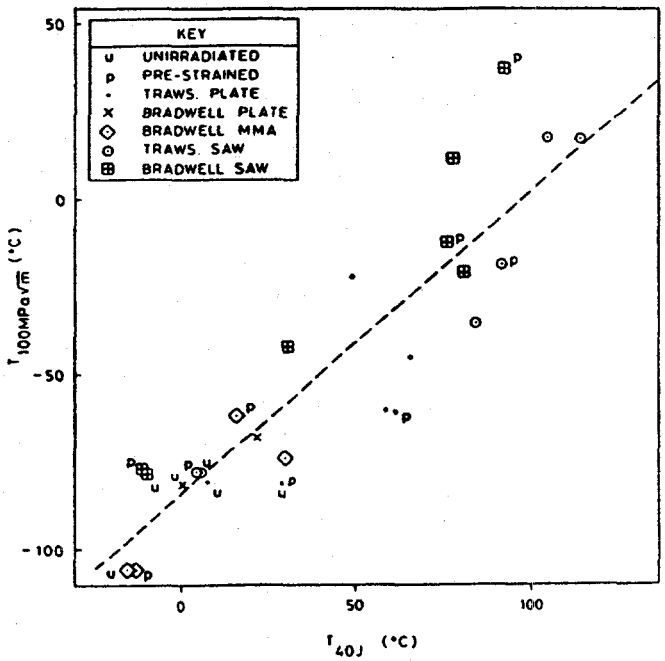

Figure 7 - Correlation between $T_{100MPa\sqrt{m}}$ and T_{40J} for Magnox plates and welds

In the calculation of the mean toughness shift and the 90% confidence interval on the data, it is important to combine the uncertainties in the start-of-life toughness data with those of the Charpy impact energy shifts. For each material there are contributions to the uncertainties in unirradiated properties from testing variables and from material variability, particularly for weld metals. For the irradiation shifts uncertainties arise from the Charpy tanh-fitting programs, from uncertainties in irradiation temperature and dose, and from the scatter in the irradiation response of a plate or weld due to variability in composition or microstructure. To calculate the mean and the 90% confidence interval for the toughness, and for other mechanical properties, a computer program

CUSURV has been developed which, after making assumptions about the independence of each source of uncertainty, samples and combines them using a stratified statistical sampling method (Ref 9).

Irradiation-Induced Changes in Strength and Transition Temperature

A key area in the assessment of the irradiated material properties is the method used to analyse the surveillance data. The development of dose-damage relationships, or "Trend Curves" describes the irradiation-induced changes in strength and transition temperature as functions of neutron dose and irradiation temperature. The method currently employed at Magnox Electric recognises the important advances made in understanding the mechanisms by which irradiation-induced changes in ferritic steels occur (Refs 15, 16 and 17). The advantage of this approach is that the relationships derived can be used with confidence when limited extrapolation is required into areas of neutron dose, dose rate, or irradiation temperature which are not specifically covered by the surveillance database. In short, the relationships adopted for the change in ambient temperature yield stress ($\Delta\sigma_y$),and the change in 40J Charpy transition temperature (ΔT_{40J}), are as follows:

$$\Delta\sigma_{y,Total} = \Delta\sigma_{y,Cu} + \Delta\sigma_{y,Matrix} \quad (1)$$

$$\Delta T_{40J,Total} = \Delta T_{40J,Cu} + \Delta T_{40J,Matrix} + \Delta T_{40J,GB} \quad (2)$$

where the various subscripts refer to the respective contributions to the total change arising from the irradiation-enhanced precipitation due to impurity copper, from the matrix irradiation damage due to lattice displacements in the steel, and to intergranular embrittlement effects due to grain boundary segregation of a deleterious element like phosphorus (Ref 18). Because the surveillance canisters represent effects over a wide temperature and dose range (Table 3) it then becomes necessary to define the dose and temperature dependence of each of the terms in equations (1) and (2).

In assessing the magnitude of the first term in equations (1) and (2) due to the influence of copper, it was found that a direct examination of the copper precipitation process was not feasible using transmission electron microscopy techniques because the precipitates were difficult to image, i.e. they were too small, ~1nm, and had insufficient contrast in relation to the matrix. However, from measurements made using the small angle neutron scattering technique (SANS) on unirradiated and irradiated submerged-arc welds, it was shown that under surveillance conditions, and at temperatures below about 300°C, copper-rich precipitates were quickly nucleated and grew to about 2 nm in diameter (Ref 19). At a constant volume fraction of copper this size corresponded to that calculated for maximum hardening (Ref 20). For doses between ~50 and 1200 x 10^{-5} dpa, and for a variety of dose rates and temperatures, the precipitate diameter remained essentially constant at 2nm, as in Figure 8 (Ref 19). The understanding of the mechanism of hardening by copper in α iron and C-Mn ferritic steel indicated that the hardening produced was inversely proportional to precipitate diameter, for a constant volume fraction of precipitate; therefore the hardening effect of copper would remain unchanged over the neutron

dose range (>50 $x10^{-5}$dpa) relevant to the Magnox steel pressure vessel applications. The magnitude of the effect due to copper has also been shown to depend on the copper content in solution in the steel at start-of-life. For the steel vessel heat treatment temperatures the soluble fraction corresponded to about 0.18±0.02% Cu (Ref 16). By this means the magnitude of the copper hardening term could be estimated as well as its dependence on reactor exposure parameters.

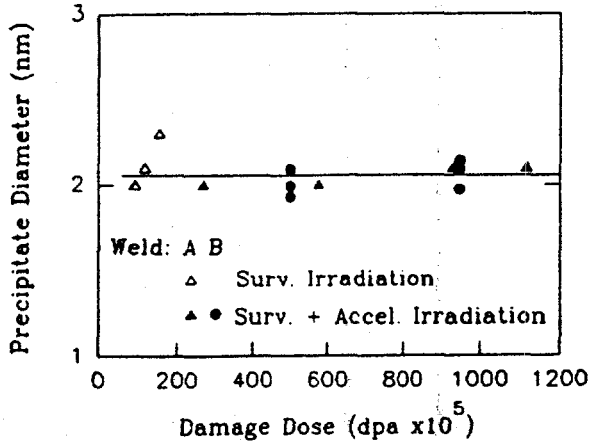

Figure 8 - Dose-dependence of Cu-rich precipitate diameter in submerged-arc welds

In regard to the matrix hardening and embrittlement damage effects, it is known that many measurements of irradiation hardening in steels and other materials have demonstrated that in the absence of solute precipitation effects the damage produced in the matrix by displaced atom debris (arranged in the form of defect clusters, interstitial or vacancy loops and voids) may be expressed as the square root of the neutron dose (Ref 21). A number of experiments on the hardening of ferritic steels at differing irradiation temperatures have been analysed (Ref 22) and, in the absence of significant precipitation, the increase in the yield stress due to dose (D) and irradiation temperature (T_i) may be expressed as

$$\Delta\sigma_y = A\, F_T \sqrt{D} \qquad (3)$$

The term F_T is included to allow for the effects of differing irradiation temperatures, i.e.

$$F_T = 1.869 - 4.57 \times 10^{-3}\, T_i \qquad (4)$$

as demonstrated in Figure 9 (Ref 22).

A number of experimental investigations have examined the dose rate dependence of hardening (Ref 21). In the absence of precipitation effects no influence of dose rate on irradiation hardening has been detected. Figure 10 demonstrates this over five orders of magnitude change in dose rate for C-Mn plate steels at an irradiation temperature of 200°C typical of Magnox applications (Refs 23 and 24). Equations (3) and (4) can therefore be used to define the dose, dose rate, and irradiation temperature dependence of the matrix damage hardening.

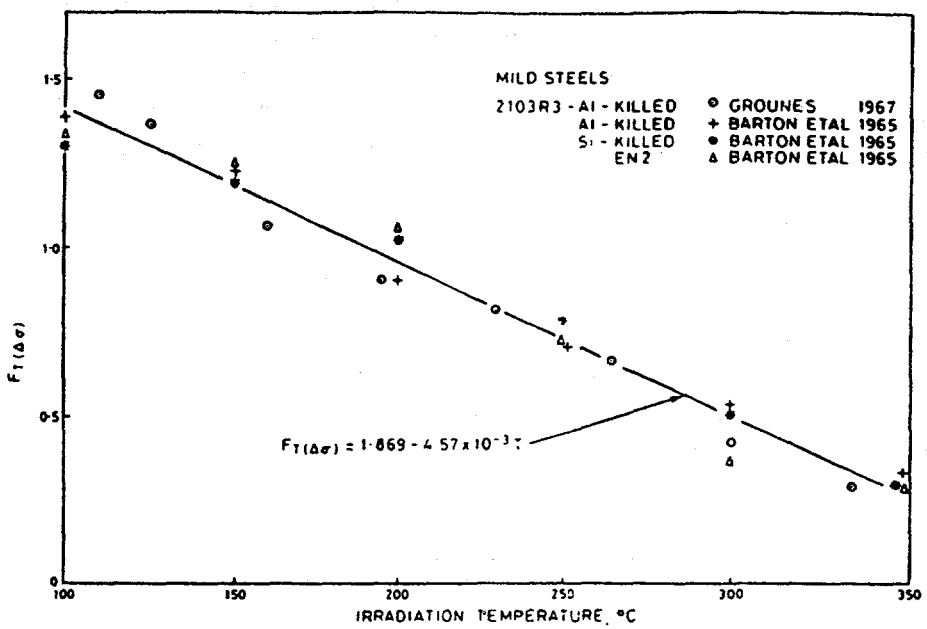

Figure 9 - Irradiation temperature dependence factor F_T for the irradiation hardening of C-Mn plate steels (Ref 22)

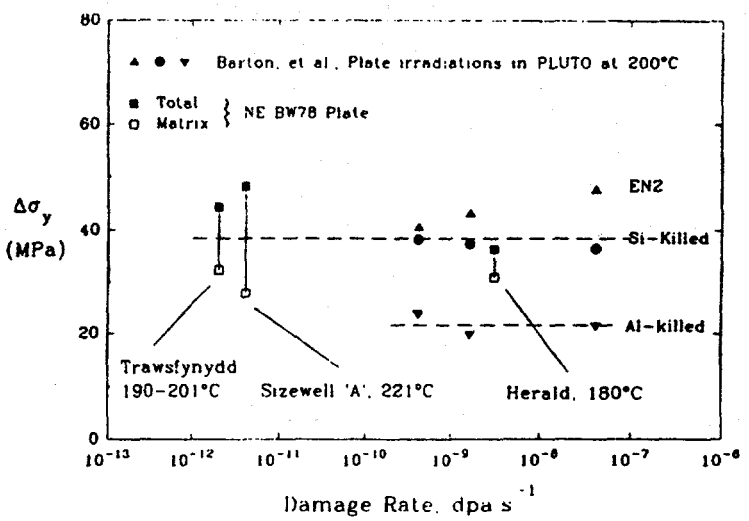

Figure 10 - Dose rate dependence of irradiation hardening at 31×10^{-5}dpa in BW78 Magnox vessel plate and in C-Mn plate steels studied by Barton et al (Ref 23)

Turning to the quantification of embrittlement effects (equation (2)), it is known that there are relatively frequent circumstances when the third term in equation (2) is negligible. Under these circumstances irradiation hardening and irradiation embritlement are linearly related by

$$\Delta T_{40J} = K \Delta\sigma_y \quad (5)$$

where K has typical values between 0.5 and 0.7 (Refs 16 and 25). Hence, it follows that irradiation embrittlement can also be described by similar types of expression to those for irradiation hardening, i.e. by combining equations (3), (4) and (5) it becomes possible to describe the dose, dose rate and temperature dependence of the matrix embrittlement term in equation (2).

Finally, by adding the expressions for matrix hardening or embrittlement to a constant copper term, at a level depending on the concentration of copper and the vessel heat treatment temperature, simple equations are obtained that describe the irradiaton hardening and embrittlement as functions of the dose, dose rate, irradiation temperature, and copper content. Such equations have been found to be satisfactory for describing the hardening and embrittlement behaviour of plates, forgings and manual welds and for the hardening of submerged-arc welds. Furthermore the magnitude of the parameters for copper and matrix hardening are physically reasonable.

There are a number of criteria for assessing when equation (5) is not obeyed and a third embrittlement term has to be included in equation (2). Experimentally, these may be recognised when (Ref 17):

(i) the embrittlement shift becomes larger than that expected on the basis of irradiation hardening alone, i.e when (after allowing for experimental uncertainty) the values of K in equation (5) become ≥ 1.0, and

(ii) the fracture surface of the Charpy sample contains significants levels of intergranular fracture (>5% by area), partly replacing the cleavage fracture mode, when tested on the lower shelf and in the transition range (Ref 18).

Our limited experience has been that submerged-arc welds are much more susceptible to the occurrence of intergranular fracture effects, with manual welds, plates and forgings showing minimal effects. To complicate matters, the susceptibility to intergranular embrittlement has been found to vary within the population of submerged-arc welds, for reasons that are not completely understood. This makes the derivation of an embrittlement trend curve rather more difficult. One method (Ref 17), characterises the SMA welds with a dummy variable (z) such that $z = 0$ for insensitivity and $z = 1$ for susceptibility to intergranular embrittlement. By augmenting the surveillance database to include experimental data on surveillance samples that have been re-irradiated under accelerated conditions to higher doses, it then becomes possible to derive a three term trend curve for those welds with $z = 1$, provided use is made of theoretical modelling of the dose rate dependence of intergranular embrittlement by phosphorus (Ref 26). However, if the use of the accelerated data is denied, then only a two term trend curve can be derived, based on the surveillance data alone (Fig 11); this subsumes any intergranular effects into a "matrix" term of a size that is significantly larger than before (by a factor of two). Consequently the present position is that the assessment of SMA weld embrittlement is performed using an empirical trend curve fitted only to the surveillance data (Fig 11). To develop a better understanding of the mechanisms operating requires further work on welds exposed at low dose rates; in this respect

results derived from high dose submerged-arc welds sampled from a decommissioned vessel wall will be of some benefit.

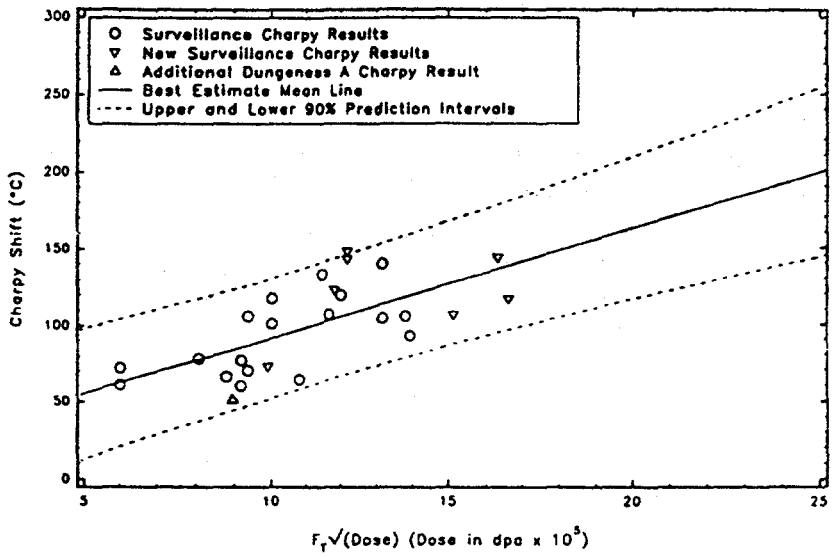

Figure 11 - Empirical trend curve for submerged-arc welds based on reactor surveillance data

New Developments

1 - Role of Thermal Neutrons

Recent neutron dosimetry calculations and measurements have demonstrated that high levels of thermal neutron flux can occur at pressure vessel side-core locations (see Figure 3). Although surveillance canisters had been intentionally located in side-core positions the actual thermal neutron dose received by the steel samples was not fully representative of the surface layers of the vessel because of the strong attenuation of thermal neutrons through steel, i.e. through the steel of surveillence canisters and the reactor duct holding the canisters. Consequently, to provide information on the possible hardening and embrittling effects on steel plates and welds a number of activities were started.

A comprehensive literature review was undertaken on the influence of thermal neutrons on steel mechanical properties. This showed that thermal neutron captures in (n,γ) reactions, mainly with ^{56}Fe, produced recoils of about 500 eV that generated a few atom displacements. In addition, atom displacements could be produced by the energetic ^{7}Li and ^{4}He products resulting from the thermal neutron-induced (n,α) transmutation of the ^{10}B isotope in natural boron present in ppm-levels in the steel. Analysis of published data enabled estimates to be made of the magnitude of these effects but showed that further experimental data were required.

As the available facilities in UK reactors did not have high enough fractions of thermal neutrons, a comprehensive accelerated experiment was mounted on pressure vessel plates, weldmetals and model ferritic alloys in the highly thermalised spectrum at the neutron shield of the Heavy Water

Reactor at Halden in Norway. The experiment aims to just exceed the worst combinations of thermal and fast dpa doses present in Magnox pressure vessels. The first stage of a three-stage experiment at 240°C has been completed and indicates that additional hardening and embrittlement can occur due to thermal neutron effects in some ferritic materials, with others apparently being less affected. Further data from the later experiments will be required to interpret all these effects satisfactorily.

2 - High Temperature Effects on Copper Precipitates

In an earlier section it was remarked that copper precipitate diameters were invariant under irradiation, but only up to irradiation temperatures of about 300°C. In Figure 12, evidence derived mainly from SANS measurements is presented showing the temperature variation of the copper precipitate diameter over a wider temperature range. The data are for pressure vessel submerged-arc welds and plate steels under surveillance or accelerated irradiations (Refs 19, 27 and 28) and in exposures where surveillance doses were enhanced by accelerated re-irradiations. Other information comes from a field-ion microscope measurement reported for a PWR surveillance submerged-arc weld (Ref 29), and from transmission electron microscope examinations of copper precipitates in materials from the pressure vessel high temperature surveillance canisters, from the ex-service mild steel of the cladding on Magnox control rods, from control rod shock absorber steel and from a number of short term accelerated irradiations or medium term thermal aging tests on Cu-containing iron alloys and steels (Refs 15 and 30).

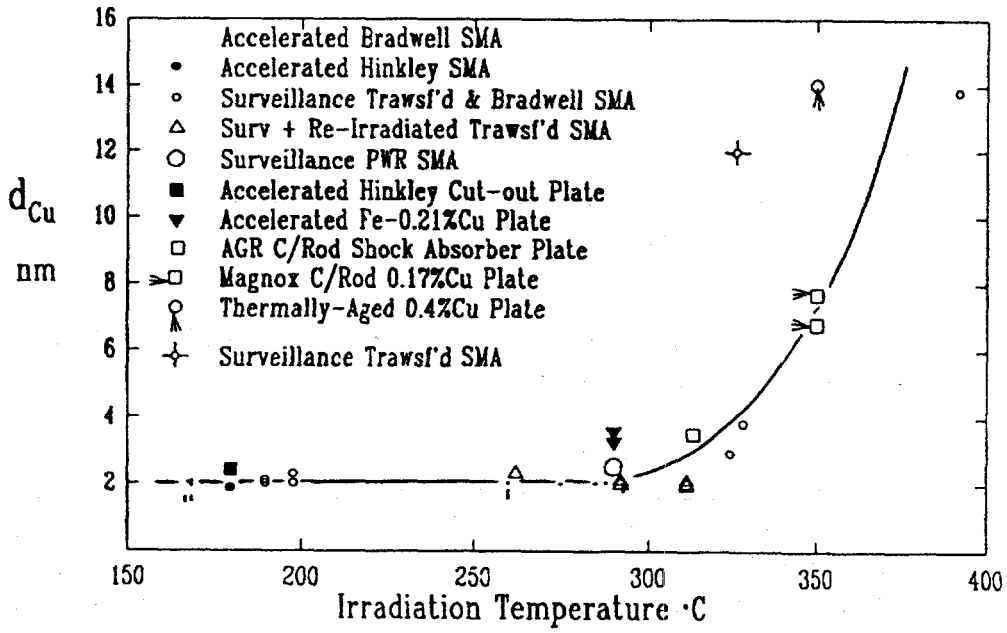

Figure 12 - Variation of Cu-rich precipitate diameter with irradiation temperature

The coarsening of copper precipitates (diameter d_{Cu}), at constant volume fraction (f_p) as is the case here, affects the strength of the iron matrix through modulus differences (E) between iron and copper (Ref 20), as below.

$$\Delta\sigma_y = C\,(f_p^{1/2} / d_{Cu})\,[\,1 - (E_{Cu} / E_{Fe})^2\,]^{3/4} \qquad (6)$$

Figure 13 shows that the observed strengthening behaviour due to copper precipitates, as measured by SANS on different submerged-arc weld tensile samples after high temperature surveillance irradiation, is linearly related to the inverse of the mean diameter of the copper precipitates, in accord with equation (6). As the aging temperature is known for each sample, and all had similar long exposure times, the diametral dependence can be converted to an effective temperature dependence of the hardening (or embrittlement) due to copper. This permits an irradiation temperature-dependence of the copper hardening and embrittlement terms to be incorporated into the trend curves for all materials above 300°C. This refinement describes the behaviour more precisely; in application it has the benefit of increasing the operating temperature margins (by reducing the transition temperature shifts) with the penalty of decreasing the pressure margins (which are yield stress dependent) in the safety assessments.

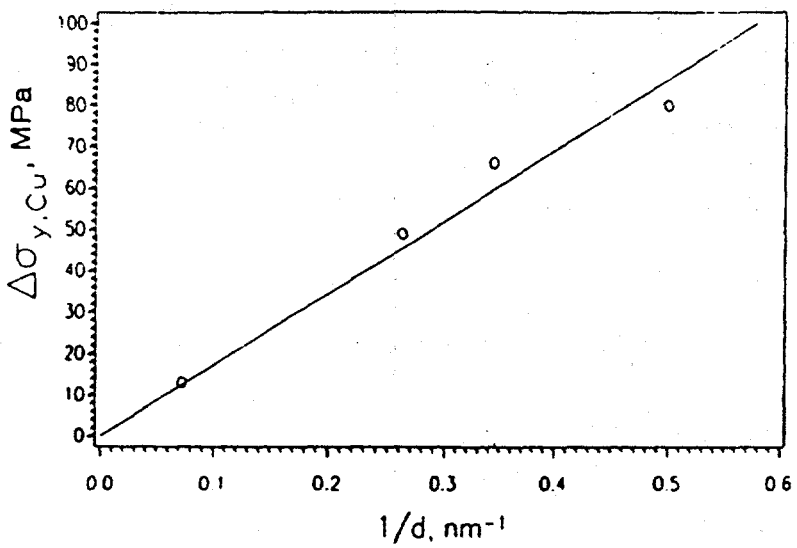

Figure 13 - Change in yield stress ($\Delta\sigma_y$) of submerged-arc welds as a function of the reciprocal of the Cu-rich precipitate diameter at constant volume fraction

3 - High Temperature Intergranular Fracture

Low dose surveillance results on submerged-arc welds after a two stage exposure at 392°C and 360°C showed large transition temperature shifts (90°C) but with only small changes to the associated yield stress (Ref 31). A smaller embrittlement shift was seen for manual weld metal but nothing was detected for plate; neither of these materials showed significant irradiation hardening. According to equation (4) the anticipated matrix irradiation embrittlement effect in the submerged-arc welds should be small at these temperatures and doses (only 3°C); the embrittling influence of the coarse copper precipitates would also be small (about 7°C). Both these expectations were confirmed after an additional high dose re-irradiation of some of the samples under accelerated conditions at high temperature; this produced a further increase in transition temperature of < 10°C. The small size of the anticipated irradiation-induced shifts, and the small

shifts detected in the accelerated experiment, were both in accord with the small magnitude of the yield stress changes observed. Consequently, from equation (2), the substantial surveillance embrittlement shifts could only result from the operation of a non-hardening embrittlement process. Examination of the fractured surveillance Charpy samples by scanning electron microscopy showed the presence of a large fraction (33%) of intergranular fracture for those samples tested in the transition region; Auger microscope analysis of in-situ fracture surfaces also indicated a high monolayer coverage of P at the grain boundaries.

As the occurrence of the intergranular embrittlement seemed to be associated with time-at-temperature, rather than irradiation dose, then an analysis of the time-dependence of the transition temperature was undertaken (Ref 31) using the equations for grain boundary solute segregation derived by McLean and others. A dependence on the square root of time fitted the data at both temperatures, see Figure 14. The reduction in the embrittlement kinetics following the lowering of the temperature to 360°C, enabled the apparent activation energy for the process to be calculated; this was 2.11eV and was smaller than the activation energy for P diffusion in ferritic steel (2.56 eV). This shortfall in the activation energy arose because there was also a countering influence of the increasing equilibrium segregation of P at the boundaries as the temperature was lowered. Using this information, a modified trend curve has been derived for high temperature applications that depends on the square root of time-at-temperature, rather than on the square root of dose.

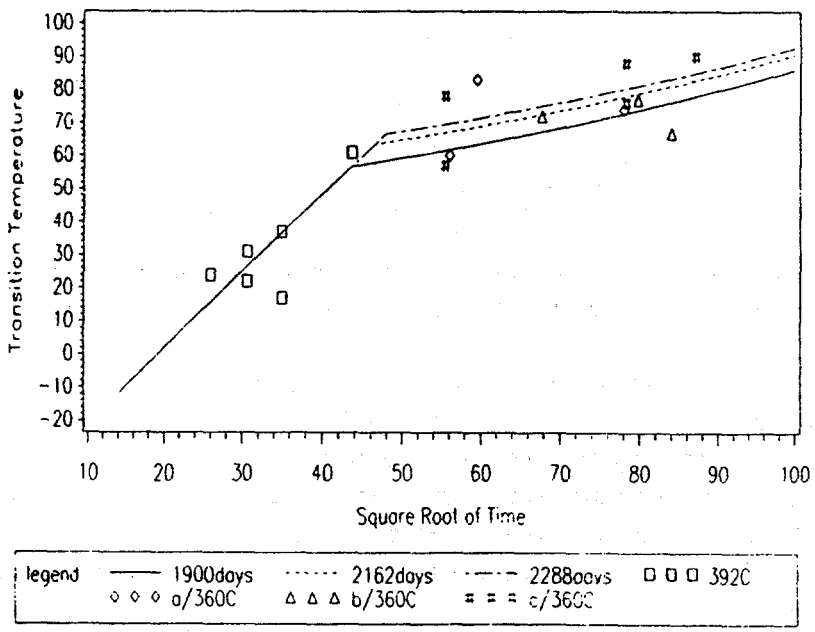

Figure 14 - Observed and calculated variation in transition temperature versus the square root of time (in days) for submerged-arc welds at high temperatures (Ref 31)

An interesting feature of the analysis was that at zero time the time-dependent transition temperature did not extrapolate back to the start-of-life transition temperature value; there was an incubation time period for the process. This has been interpreted as indicating that a certain

critical concentration of P had to be achieved on the boundaries before the intergranular fracture process could begin to develop beyond the small levels commonly found at start-of-life (Ref 32). From the kinetics observed the variation of this critical time with exposure temperature can be estimated, the result being shown in Figure 15 which also includes a compilation of all known aging data on submerged-arc welds at different temperatures (Ref 31). The line satisfactorily separates the intergranularly embrittled Magnox welds cited above from the rest of the data points; the latter fall below the line indicating an insensitivity to thermal intergranular embrittlement for the exposure times experienced. The line predicts that the incubation time becomes so long at low temperatures (300°C) that the possibility of thermal intergranular embrittlement of SMA welds in service can be ignored; however, for temperatures above about 330°C some effects might be detected for exposure times of about 30 years and longer.

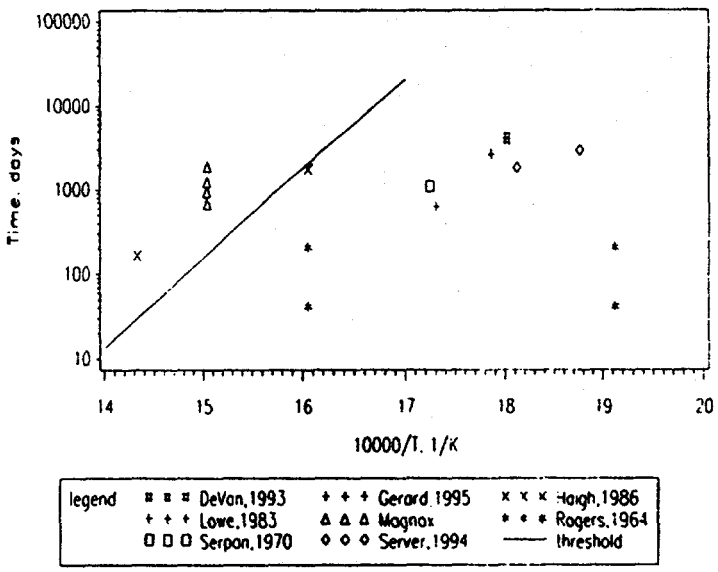

Figure 15 - Threshold time (logarithmic scale) for onset of intergranular embrittlement in submerged-arc welds as an inverse function of absolute temperature of exposure

It is clear that the chemical composition of the steel affects the development of thermal embrittlement susceptibility; in particular P, C and Mn have all been identified as playing a role in intergranular embrittlement experiments on three or four component systems based on iron (Ref 33). The susceptibility to embrittlement by P in an Fe-C-P-Mn system increases almost linearly with the Mn content; for the reactor welds a similar variation in susceptibility occurs between the manual welds and the submerged-arc welds which can be related to differences in Mn content (see Table 2).

There is a need for further results from long term aging data. A programme of sampling is being undertaken on service-aged vessels or components, to validate the analysis and trends outlined above.

Sampling of an Operational Pressure Vessel

In 1995 the inside surface of a Bradwell reactor vessel was sampled at a high temperature location to obtain material to validate the time-at-temperature embrittlement analysis outlined above. The samples taken were small because after sampling had been completed the vessel was returned to service. Small disc-shaped samples of diameter 24mm and 3.5mm maximum thickness were taken using the sample cutter shown in Figure 16. The cutter, rather like an "ice-cream scoop", has a rotating cutting head driven by a flexible drive and was introduced into the reactor, during a normal outage period, through a refuelling standpipe on the end of a "SNAKE", i.e. a flexible, articulated manipulator arm (Ref 34). The location of the standpipe was carefully chosen to enable three high temperature aged samples to be taken from both SMA and MMA welds. In addition, as shown in Figure 17, the standpipe was located on an MMA weld for which ex-manufacturing cut-out material was available and provided fully representative control samples. No such identical controls were available for the SMA weld samples which had to be compared with unexposed weld metal from other cut-outs from Bradwell. The SMA weld metal location had been visited before for non-destructive ultrasonic testing purposes. The samples were aligned to be no more than 5mm from the centre lines of each weld to ensure that both columnar and fine-grained microstructures were obtained.

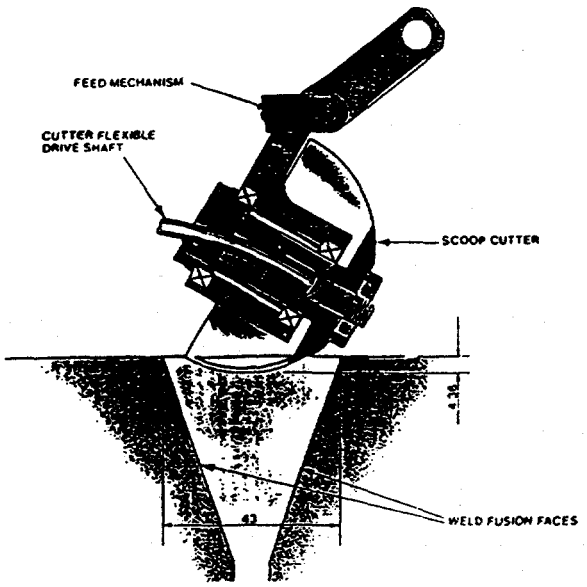

Figure 16 - Scoop sample cutting device

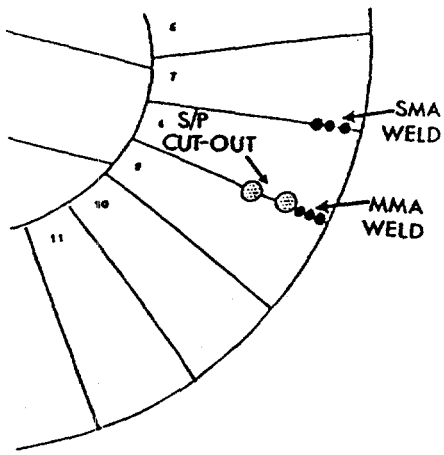

Figure 17 - Scoop sample locations in welds in top dome region of the pressure vessel

After removal the samples were subjected to a number of analyses to obtain information on neutron dosimetry (standard activation analysis), chemical composition (Electron Micro-Probe Analysis), microstructure (Optical and Transmission Electron Microscopy), fracture surface examination (Scanning Electron Microscopy) and grain boundary surface analysis for phosphorus and other elements (Auger Spectroscopy and High Spatial Resolution X-Ray Micro-Analysis in Scanning Transmission Electron Microscopy) (Ref 35). To provide the respective samples the scoops had to be carefully cut-up as shown in Figure 18. The fracture surface examination was

quantitative in that the proportions of intergranular fracture facets, cleavage facets, ductile micro-void coalescence fracture and other fracture features were determined by a counting technique (Ref 18).

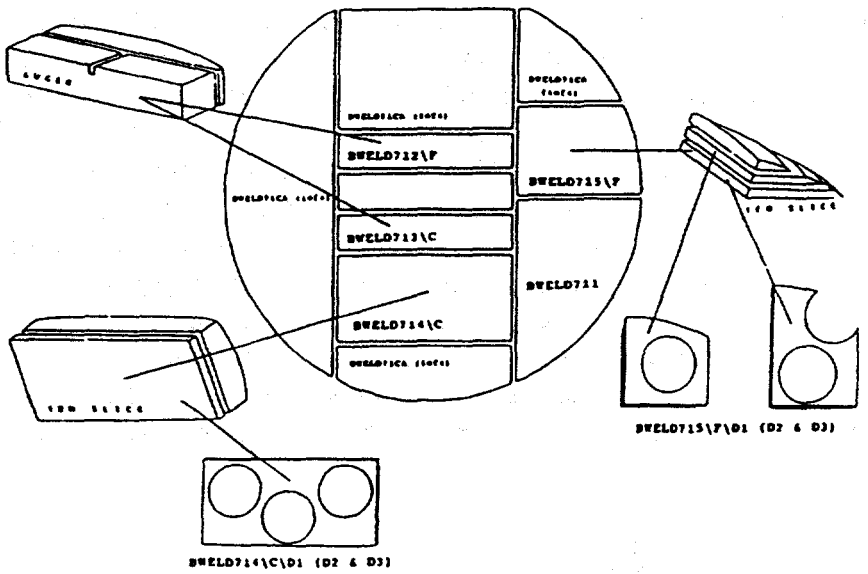

Figure 18 - Cutting diagram for scoop samples

The results from the dosimetry measurements agreed satisfactorily with the MCBEND predictions and the scoop sample chemical compositions compared well with the respective databases of manual and submerged-arc weld analyses. There was nothing unusual about the optical microstructure of the scoop samples and the dislocation densities determined from thin foils were similar to the levels observed in unirradiated welds. Cu precipitates were not detected in the manual welds either before or after irradiation but in the submerged-arc welds the reactor exposure had produced a significant population of large Cu precipitates (13nm mean diameter), in agreement with observations on surveillance SMA welds. Quantitative comparisons made between the unirradiated control welds and the weld scoop samples in terms of the fraction of intergranular failure (%IGF) and the grain boundary coverage by phosphorus (%IGP) showed that both SMA and MMA weld scoops exhibited significantly higher levels of both %IGF and %IGP than at start-of-life; both %IGF and %IGP were higher in SMA than in MMA welds. Evidence was found for an increase in Mn at the grain boundaries in the scoop SMA samples compared to values at start-of-life. There was a lower %IGP in the scoop SMA welds compared to surveillance SMA welds which could not be explained by a neutron dose effect, since the doses were similar. However, on the basis that the IGP% values are thermally induced then the difference could have arisen from exposure at a slightly higher temperature (by about 20°C) for the surveillance samples due to nuclear heating effects. Table 4 illustrates these comparisons in greater detail (Ref 35). The final conclusion is that the sampling was consistent with the proposed thermally activated high temperature embrittlement mechanism based on time-at-temperature.

Table 4 - Comparison of Weld Scoop Samples with Start-of-Life and Surveillance Data

Weld Type	Intergran'r Fracture %	Cleavage Fracture %	Ductile and Unclassified Fracture %	Neutron Dose dpa $x10^5$	Mean % Intergran'r Phosphorus
SMA					
Scoop 1	30	50	20	21.8	34, 19
Scoop 2	25	50	25	21.8	27, 23
Start-of-life	< 2			0	4, 2, 6, 4, 6
Surveillance	33	19	48	22.1	53
MMA					
Scoop 1	16	65	19	21.1	15, 14
Scoop 2	19	61	20	21.1	17, 14
Start-of-life	< 2			0	2, 2, 1, 6

Mean intergranular phosphorus has 1σ of 25-30% for irradiated welds and 50% at start-of-life.

Sampling of a Decommissioned Pressure Vessel

At one of the decommissioned Magnox reactors at the Trawsfynydd site, a more extensive sampling programme is currently underway on a region of the pressure vessel exposed at low irradiation temperature and high neutron dose. The objectives are:

(i) to obtain direct information on the fracture toughness of submerged-arc welds at doses which are beyond the present range covered by the surveillance programme but are representative of future conditions in operational pressure vessels,

(ii) to compare the service fracture toughness data with the fracture toughness curve predicted from the surveillance scheme,

(iii) to obtain chemical analysis data, to check mechanistic interpretations and enhance microstructural information, especially in respect of grain boundary phosphorus segregation and intergranular embrittlement,

(iv) to confirm predictions of the attenuation of neutron spectrum, dose and embrittlement through the pressure vessel wall.

The pressure vessel location chosen for sampling had to maximise the lengths of the available SMA welds which combined a relatively uniform neutron dose profile with a known and constant irradiation temperature. An inspection of the pressure vessel dose and temperature profiles (see Figure 19) indicated that an appropriate region was located below-core (region D in Figure 19) where the irradiation temperature was about 205°C and the mean dose was $350x10^{-5}$dpa. As access to these welds was from the outside of the pressure vessel, and from within the support skirt on which the reactor vessel sits, it was necessary to remove large amounts of vessel

insulation: Consequently a number of specialised remotely-operated vehicles have had to be constructed for bearing the cutting and manipulating tools. The cutting method selected for both insulation and pressure vessel steel was by a high power jet of abrasive particles suspended in water.

Four different lengths of SMA weld will be available for sampling and from each weld four quasi-cylindrical through-wall plugs will be removed (see Figure 20). From each plug eight Charpy-sized samples will be machined from the central region containing the weld, namely two Charpy samples from each of the four differently dosed layers through the wall thickness. Making use of sample reconstitution techniques on each half of failed Charpy test pieces a total of twenty four mechanical test results will be obtained from each layer (i.e. each dose) within each length of weld. In principle the number of welds sampled is insufficient to establish true "lower bound" properties even though the total possible number of weld/dose/test combinations will be 384. The test method selected is quasi-static three-point bend fracture toughness testing, permitting direct comparison with the predictive method used for calculating the toughness of the irradiated RPV material from the surveillance data. Current plans indicate that testing of the first welds will commence early in 1997.

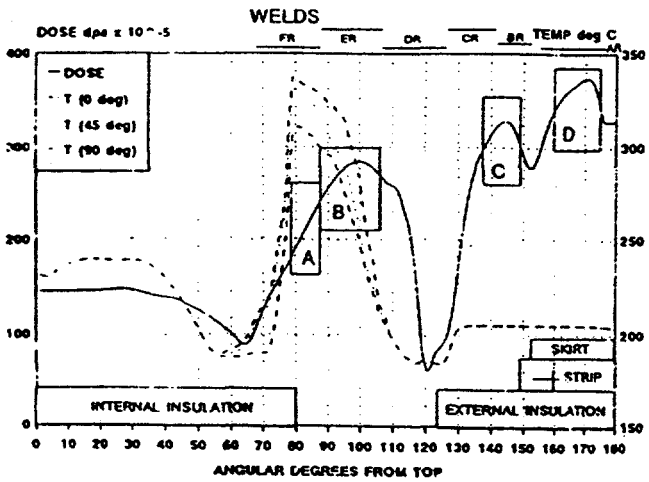

Figure 19 - Dose and irradiation temperature profiles for Trawsfynydd pressure vessel

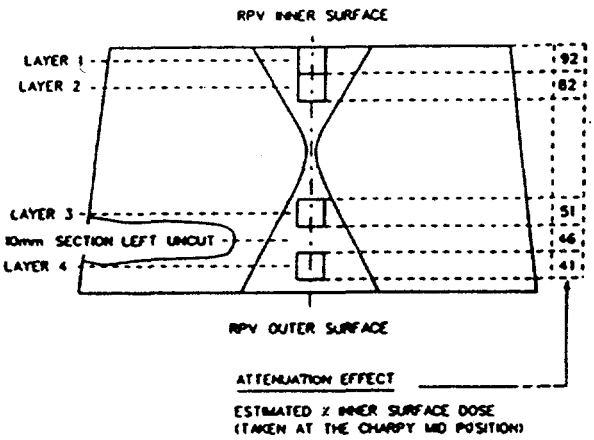

Figure 20 - Location of Charpy samples in through-wall plug taken from pressure vessel

Conclusions

1. Mechanistic studies of embrittlement and hardening have aided development of robust dose-damage equations for hardening, transition toughness behaviour and the degradation of upper shelf toughness which are used over wide irradiation temperature and dose ranges for the assessment of Magnox reactor pressure vessels

2. Copper impurity precipitation, irradiation damage by matrix atom displacement and grain boundary embrittlement by phosphorus all contribute to the degradation of mechanical properties of these pressure vessel steels.

3. Neutron spectrum effects are important in the damage assessments and displacements-per-atom is the preferred dose unit.

4. Results from the sampling of submerged-arc and manual welds in an operating pressure vessel have confirmed predictions of the effects of copper and phosphorus at high exposure temperatures.

5. Further sampling of a decommissioned pressure vessel is in progress to validate mechanistic predictions of the high dose, low exposure temperature behaviour of submerged-arc welds and to compare predicted and measured vessel toughness.

Acknowledgements

This paper is published by permission of the Director of Technology and Central Engineering Division, Magnox Electric plc. Information on Trawsfynydd pressure vessel sampling was provided by Dr P J E Bischler and is gratefully acknowledged.

References

1. B Watkins and A Cowan, Steels for Gas-Cooled Reactor Pressure Vessels; A Review of British Practice, Progress in Nuclear Energy, Series IV, Volume 5, pp 55 - 88, 1963.
2. W C Holliday and M J Noone, Metallurgical Problems Associated with the Construction of Gas-Cooled Reactor Pressure Vessels, Symposium on "Steels for Reactor Pressure Circuits", Iron and Steel Institute Special Report No 69, pp 207-239, 1961.
3. P J H Heffer, L T Jones, D A Thornton, A Avery, N Smith and K Ziver, Magnox Pressure Vessel Dosimetry - A New Assessment, 7th ASTM-Euratom Symposium on Reactor Dosimetry, Strasbourg, Kluwer Academic Publishers, 1990.
4. C A English, A J Fudge, R J McElroy, W J Phythian, J T Buswell, C J Bolton, P J H Heffer, R B Jones and T J Williams, Approach and Methodology for Condition Assessment of Thermal Reactor Pressure Vessels, International Journal of Pressure Vessels and Piping, Vol 54, pp 49-88, 1993.
5. J R Mossop, D A Thornton and T A Lewis, Validation of Neutron Transport Calculations on Magnox Power Plant, "Reactor Dosimetry", ASTM STP 1228, pp 384-391, 1994.
6. T A Lewis, S E Hopper, J R Mossop, D A Thornton and G S Whiley, The Prediction of Fast and Thermal Neutron Dose Rates for the Pressure Vessels of Magnox Power Plant, Proceedings of the 9th International Symposium on Reactor Dosimetry, Prague, Czech Republic, 2-6th September 1996, to be published.
7. ASTM Annual Book of Standards (1988), Part 45: Nuclear Standards, Standard Practice for Characterising Neutron Exposures in Ferritic Steels in Terms of Displacements -per-Atom, ASTM E693-79, Reapproved 1985.
8. C L Formby, Use of the Overpressure Proof Test to Indicate Fitness for Purpose of a Ferritic Pressure Vessel, International Journal of Pressure Vessels and Piping, Vol 19, pp 47-68, 1985.
9. P E J Flewitt, G H Williams and M B Wright, Integrity of Magnox Reactor Steel Pressure Vessels, Materials Science and Technology, Vol 9, pp 75-82, 1993.

10. C J Bolton, W Charnock and R H Priest, The Effect of Irradiation on Fracture Toughness Transition Temperature of Magnox Reactor Pressure Vessels, Proceedings of the International Conference on "Nuclear Power Plant Life Extension", Snowbird, Utah, USA, 1988.
11. I Milne, R A Ainsworth, A R Dowling and A T Stewart, Assessment of the Integrity of Structures Containing Defects, CEGB Report R/H/R6 Revision 3, Leatherhead, 1986.
12. B K Neale and R H Priest, The Unloading Compliance Method for Crack Length Measurement Using Compact Tension and Precracked Charpy Specimens, in "Elastic-Plastic Fracture Test Methods-The User's Experience", ASTM STP 856, pp375-393, 1985.
13. K Wallin, M Valo, R Rintamaa and R Ahlstrand, The Effect of Loading Rate Upon Irradiation Embrittlement Measured by Fracture Mechanical Properties, in "Effects of Radiation on Materials": 16th International Symposium, ASTM STP 1175, pp 156-171, 1993.
14. R H Priest and R B Jones, A Comparison of Irradiation-Induced Increases in Ductile-Brittle Transition Temperature as Measured from Charpy Impact and Fracture Toughness Tests, Nuclear Electric Report, TD/SEB/MEM/3044/92, 1993.
15. S B Fisher, J E Harbottle and N Aldridge, Radiation Hardening in Magnox Pressure Vessel Steels, Philosophical Transactions of the Royal Society of London, Vol A315, pp 301-332, 1985.
16. J T Buswell and R B Jones, The Modelling of Radiation Hardening and Embrittlement in Magnox Mild Steel Submerged-Arc Welds, in "Effects of Radiation on Materials": 16th International Symposium, ASTM STP 1175, pp 424-443, 1993.
17. C J Bolton, J T Buswell, R B Jones R Moskovic and R H Priest, The Modelling of Irradiation Embrittlement in Submerged-Arc Welds, in "Effects of Radiation on Materials": 17th International Symposium, ASTM STP 1270, pp103-118, 1996.
18. P J E Bischler and R K Wild, A Microstructural Study of Phosphorus Segregation and Intergranular Fracture in Neutron Irradiated Submerged-Arc Welds, in "Effects of Radiation on Materials": 17th International Symposium, ASTM STP 1270, pp 260-273, 1996.
19. J T Buswell, P J E Bischler, S T Fenton, A E Ward and W J Phythian, Microstructural Developments in Neutron Irradiated Mild Steel Submerged-Arc Weld Metal, Journal of Nuclear Materials, Vol 205, pp 198-205, 1993.
20. K C Russell and L M Brown, Dispersion Strengthening in the Iron-Copper System, Acta Metallurgica, Vol 20, pp 969-974, 1972.
21. E A Little, Neutron Irradiation Hardening in Irons and Ferritic Steels, International Metallurgical Reviews, Number 204, pp 25- 60, 1976.
22. R B Jones and T J Williams, The Dependence of Radiation Hardening and Embrittlement on Irradiation Temperature, in "Effects of Radiation on Materials": 17th International Symposium, ASTM STP 1270, pp 569-590, 1996.
23. P J Barton, D R Harries and I L Mogford, Effects of Neutron Dose Rate and Irradiation Temperature on Radiation Hardening in Mild Steels, Journal of the Iron and Steel Institute, Vol 203, pp 507-511, 1965.
24. R B Jones and J T Buswell, Influence of Neutron Dose Rate on the Irradiation Hardening

of C-Mn Reactor Pressure Vessel Steels, Verbal presentation to 17th ASTM International Symposium, "Effects of Radiation on Materials", Sun Valley, Idaho, USA, 1994.

25. S B Fisher and J T Buswell, A Model for PWR Pressure Vessel Embrittlement, International Journal of Pressure Vessels and Piping, Vol 27, pp 91-135, 1987.
26. S G Druce, C A English, A J E Foreman, R J McElroy, I A Vatter, C J Bolton, J T Buswell and R B Jones, The Modelling of Irradiation-Enhanced Phosphorus Segregation in Neutron Irradiated Reactor Pressure Vessel Submerged-Arc Welds, in "Effects of Radiation on Materials": 17th International Symposium, ASTM STP 1270, pp 119-137, 1996.
27. J T Buswell, C J Bolton, M R Wootton, P E J Bischler, R B Jones, L T Jones, W J Phythian and R R Sinclair, The Radiation Hardening and Embrittlement of a Mild Steel Submerged-Arc Weld, in "Effects of Radiation on Materials": 16th International Symposium, ASTM STP 1175, pp 332-351, 1993.
28. J T Buswell, E A Little, R B Jones and R R Sinclair, Analysis of Microstructural Changes in Irradiated Pressure Vessel Steels Using Small Angle Neutron Scattering, Proceedings of the Second International Symposium on "Environmental Degradation of Materials in Nuclear Power Systems - Water Reactors", ANS, pp139-152, 1985.
29. S P Grant, S L Earp, S S Brenner and M G Burke, Phenomenological Modelling of Radiation Embrittlement in Light Water Reactor Pressure Vessels with Atom Probe and Statistical Analysis, Proceedings of the Second International Symposium on "Environmental Degradation of Materials in Nuclear Power Systems - Water Reactors", ANS, pp 385-392, 1985.
30. P A Beavan, F Frisius, R Kampmann and R Wagner, SANS/TEM Studies of the Defect Microstructure of Test Reactor Irradiated Fe-Cu Alloys and Cu-Containing RPV Steels, Proceedings of the Second International Symposium on "Environmental Degradation of Materials in Nuclear Power Systems - Water Reactors", ANS, pp 400-408, 1985.
31. W B Beere, R S Fidler, C J Bolton, S T Fenton and R B Jones, The Ductile-Brittle Transition Behaviour of Submerged-Arc Weldments Following High Temperature Exposure, in "Effects of Radiation on Materials": 18th International Symposium, ASTM STP 1325, to be published.
32. K Abbott, R Moskovic, R K Wild and P E J Flewitt, Low Temperature Fracture of C-Mn Submerged-Arc Weld Metal, Materials Science and Technology, Vol 11, pp 572-578, 1995.
33. H J Grabke, K Hennesen, R Moller and W Wei, Effects of Manganese on the Grain Boundary Segregation, Bulk and Grain Boundary Diffusivity of Phosphorus in Ferrite, Scripta Metallurgica, Vol 21, pp 1329-1334, 1987.
34. P J E Bischler and J M Stump, The Development of Techniques to Examine RPV Scoop Samples Removed From Bradwell R1, presented at Plant Life Management and Plant Life Extension Meeting, Nice, France, sponsored by Nuclear Engineering International, 1995.
35. P J E Bischler, G Knowles, P Spellward, R J Scowen, B J Lee, J M Stump and S J Mowles, An Examination of Irradiated Steel Scoop Samples Removed From Bradwell R1 Reactor Pressure Vessel, presented at Plant Life Management and Plant Life Extension Meeting, Nice, France, sponsored by Nuclear Engineering International, 1995.

Collaborative Investigations of In-Service Irradiated Material from the Japan Power Demonstration Reactor Pressure Vessel*

W. R. Corwin and B. L. Broadhead
Oak Ridge National Laboratory
Oak Ridge, Tennessee, U.S.A.
and
M. Suzuki and A. Kohsaka
Japan Atomic Energy Research Institute
Tokai Research Establishment
Tokai, Japan

There is a need to validate the results of irradiation effects research by the examination of material taken directly from the wall of a pressure vessel that has been irradiated during normal service. Just such an evaluation is currently being conducted on material from the wall of the pressure vessel from the Japan Power Demonstration Reactor (JPDR). The research is being jointly performed at the Tokai Research Establishment of the Japan Atomic Energy Research Institute (JAERI) and by the Nuclear Regulatory Commission (NRC)-funded Heavy-Section Steel Irradiation Program at the Oak Ridge National Laboratory (ORNL).

The JPDR was a small boiling water reactor that began operation in 1963. It operated until 1976, accumulating ≈17,000 h of operation, of which a little over 14,000 h were with the original 45-MWTh core, and the remaining fraction, late in life, with an upgraded 90-MWTh core. The pressure vessel of the JPDR, fabricated from A 302, grade B, modified steel with an internal weld overlay cladding of 304 stainless steel, is approximately 2 m in diameter and 73 mm thick. It was fabricated from two shell halves joined by longitudinal seam welds located 180° from each other. The rolling direction of the shell plates is parallel to the axis of the vessel. It operated at 277°C and reached a maximum fluence of about 2.3 ¥ 10^{18} n/cm^2 (> 1 MeV). The impurity contents in the base metal are 0.10 to 0.11% Cu and 0.010 to 0.017% P with a nickel content of 0.63 to 0.65%. Impurity contents of the weld metal are 0.11 to 0.14% Cu and 0.025 to 0.039% P with a nickel content of 0.59%.

The JPDR pressure vessel has been cut into pieces, roughly 800 x 800 mm x the original local wall thickness by JAERI as part of the now completed decommissioning of the plant. Full-thickness trepans have been cut from sections of the vessel originally located at the core beltline and also near the upper flange, well away from the beltline. Trepans, each approximately 87 mm in diameter, were removed containing the longitudinal fabrication weld as were trepans

*Research sponsored by the Office of Nuclear Regulatory Research, U.S. Nuclear Regulatory Commission, under Interagency Agreement DOE 1886-8109-8L with the U.S. Department of Energy under contract DE-AC05-96OR22464 with Lockheed Martin Energy Research Corp.

located completely within the base metal from both sections. JAERI has shipped a portion of the irradiated material from the wall of the JPDR to ORNL. The trepans contain four types of material: weld metal and base metal, each in both the irradiated condition (from the beltline) and in nominally, thermally aged-only condition (from the near the upper flange).

The objectives of the JPDR pressure vessel investigations are to obtain materials property information on the pressure vessel steel actually exposed to in-service irradiation conditions and to help validate the methodology for aging evaluation and life prediction of reactor pressure vessels. The Japanese research associated with the evaluation of irradiation effects is composed of three parts: examination of material from the JPDR vessel in conjunction with a reevaluation of its exposure conditions, new test reactor irradiations of archival and similar materials, and reevaluation of data from irradiation surveillance and related programs. The focus of the research to be performed by ORNL on the JPDR material is the determination of irradiation-induced damage through the thickness of the vessel in the beltline region and its comparison with the properties and microstructural evaluations of the same material following the Japanese short, high-rate irradiations or with thermal damage only. Parallel determinations of exposure are being made by dosimetry measurements taken on the vessel material itself and by supporting neutron transport calculations.

Initial studies conducted at JAERI have focused on measurements of the level of neutron attenuation through the vessel using hardness and tensile testing through the full thickness of the vessel sections of base metal before and after their annealing. By comparing the results before and after annealing, as a function of through-wall position, and making the assumption that the change is due to recovery of irradiation damage, the through-wall attenuation in irradiation-induced hardening was evaluated. Good agreement was obtained between the tensile and hardness data for the base metal, showing a change of about 3.3 points in Vickers hardness for each 1 MPa change in yield strength. The data from the weld metal are currently being analyzed. Initial indications from the testing are that the attenuation is somewhat greater than would be predicted by the attenuation formula in *Regulatory Guide 1.99.* This trend will be further evaluated by both JAERI and ORNL in the continuation of this work.

IAEA INTERNATIONAL STUDIES ON IRRADIATION EMBRITTLEMENT OF REACTOR PRESSURE VESSEL STEELS

Milan BRUMOVSKÝ
Nuclear Research Institute Řež plc
250 68 Řež, Czech Republic
L.E.STEELE
Chief Scientific Investigator of the Programme
Consultancy
Highland Str.7624
Springfield, VA 22159-3931, USA

Abstract

In last 25 years, three phases a Co-operative Research Programme on Irradiation Embrittlement of Reactor Pressure Vessel Steels has been organized by the International Atomic Energy Agency. This programme started with eight countries in 1971 and finally 16 countries took part in phase III of the Programme in 1983.Several main efforts were put into preparation of the programme, but the principal task was concentrated on an international comparison of radiation damage characterization by different laboratories for steels of "old" (with high impurity contents) and "advanced" (with low impurity contents) types as well as on development of small scale fracture mechanics procedures applicable to reactor pressure vessel surveillance programmes. This year, a new programme has been opened, concentrated mostly on small scale fracture mechanics testing.

1. INTRODUCTION

PHASE 1

In 1971, the IAEA Working Group on **Engineering Aspects of Irradiation Embrittlement of Reactor Pressure Vessel Steels** elaborated and approved, as an initial step, a standard programme (Phase 1) of the Co-ordinated Research Programme on **"Irradiation Embrittlement of Reactor Pressure Vessel Steels"** which should be performed on a **reference steel ASTM A 533 Grade B Class 1 (HSST 03 Plate)** deriving from the Heavy Steel Section Technology Programme and provided to the IAEA by the Union Carbide Corporation, USA.

Eight IAEA Member States (nine institutions)participated in the Phase 1 programme: Czechoslovakia, Denmark, FRG, France, Japan, Sweden, UK, USA. The main goals were :

(1) To establish the basis for describing embrittlement, and for performing the measurement of neutron spectrum, fluence and mechanical properties was sufficiently standardized to permit direct intercomparison between international programmes without major adjustment of the data.

(2) To compare the embrittlement sensitivity of national steels with that of the standard steel- ASTM A 533-B Plate 03.

No major discrepancies were observed in the results in spite of the use of unique irradiation assemblies in nine different reactors with individual evaluations of neutron fluence and neutron spectra as it can be seen in **Fig.1**. Differences in mechanical test procedures and data interpretation might also have produced complications in the comparison and analysis of data. In fact, this proved not to be true and the differences in the results were probably due to neutron measurements. It is believed that further adjustment of experimental data for neutron spectrum variations or flux determination may reduce the scatter.

Main results from the programme including all reports from participated organizations were published in the IAEA Report "Co-ordinated Research Programme on Irradiation Embrittlement of Pressure Vessel Steels", IAEA-176, Vienna (1975).

PHASE 2

After a detailed review and discussion of Phase 1 of the CRP, it was agreed that there was a need to continue the research under an extension to Phase 1. The general goal would be **"to demonstrate that knowledge has advanced to the point that steel manufacture and welding for nuclear technology can routinely produce steels for reactor pressure vessels of high radiation resistance".** In December 1976, the new programme (Phase 2), entitled **"Analysis of the Behaviour of Advanced Reactor Pressure Vessel Steels under Neutron Irradiation"**, was formally initiated.

Many organizations and countries provided steels for Phase 2 and during 1977-1979 the participants received test materials from advanced steels and welds typical for current practice in France, the Federal Republic of Germany and Japan.

Nine IAEA Member States (ten organizations) participated in the programme: Czechoslovakia, Denmark, FRG, GDR, France, India, Japan, UK, USA

The main goal was to undertake a comparative study of the irradiation embrittlement behaviour of improved (advanced) steels produced in various countries. It was intended to demonstrate that careful specification of pressure vessel steel could eliminate or vastly reduce the problem of neutron irradiation embrittlement, and to show that knowledge had advanced to the point where steel manufacture and welding technology could routinely produce steel reactor pressure vessels of high radiation resistance.

Within this programme, which lasted from 1977 to 1983, **the following main conclusions were obtained :**

(1) The general aim of Phase 2 of the programme was to demonstrate that knowledge had advanced to the point where steel manufacture and welding for nuclear technology can routinely produce steels for reactor pressure vessels of high radiation resistance. Results from this programme show that modern pressure vessel materials (plates, forgings and welds) possess high resistance to neutron irradiation damage.

(2) In general, and for those mechanical tests which show a response of neutron irradiation, the results demonstrate that reducing the copper content (together with low phosphorus content) of steels leads to an improvement in their irradiation resistance. The copper content of modern steels is low, usually less than 0.1 mass % while phosphorus content is usually lower than 0.012 mass%. Charpy transition shifts of the modern steels were generally lower than those steels represented by the HSST 03 Plate - see **Fig.2.**

(3) Changes in tensile yield strength and hardness followed the Charpy transition temperature changes and the results support the recommendation to include such tests in any scheme to measure irradiation sensitivity.

(4) There was no systematic variation of Charpy upper shelf energy change (decrease) with neutron fluence. Indeed, all materials showed large variations in percentage change at a particular neutron fluence level. However, the actual levels of upper shelf energy for these modern steels are higher than those typified by the HSST 03 Plate. It is therefore considered to be more appropriate to consider absolute levels of upper shelf energy change (decrease) than the percentage approach of US NRC Regulatory Guide 1.99. Certainly on this basis the modern steels show an improved response when compared to the older generation of steels.

(5) The results of fracture toughness tests showed that modern steels are more resistant to neutron irradiation than the older pressure vessel steels. A good correlation was observed between the Charpy 41J transition temperature increase on irradiation and the shift in transition temperature, defined at the 100 MPa.$m^{1/2}$ level, from dynamic and static fracture toughness tests. No reasonable correlation was found between Charpy upper shelf energy decrease after irradiation and that determined from dynamic or static upper shelf fracture toughness determination. In the latter case, significant irradiation effect were apparent only at the higher neutron fluence examined. Because of the potentially crucial nature of dynamic upper shelf toughness for the assessment of operating vessel integrity, a more quantitatively coherent method must be found for future surveillance and other irradiation studies.

(6) The US NRC Regulatory Guide 1.99 (Rev.1), April 1977, was based primarily on the results of accelerated irradiation in materials testing reactors. More recent data for different compositions (including high-nickel) and from longer term surveillance capsule irradiations have led to a reconsideration and probable revision of the Regulatory Guide. Results from the present programme underline the shortcomings of the initial Regulatory Guide approach, in particular with respect to high nickel contents and the description of upper shelf Charpy fracture energy decrease. Additional data correlations based upon internally consistent materials, fluence measurements and fracture methods will be necessary to provide trend curves of bounds which describe the physical realities of steel embrittlement.

(7) From detailed transmission electron microscopy examinations no discernible evidence of neutron irradiation was found, even for an extreme case where Charpy transition shift of + 130 C had been observed.

Further progress in the application of the fracture mechanics approach to radiation damage assessment has been achieved in this programme. Improvement and unification of neutron dosimetry methods have provided better data with a smaller scatter.

All results together with their analysis and raw data were summarized in the IAEA Technical Report Series No. 265 "Analysis of the Behaviour of Advanced Pressure Vessel Steels under Neutron Irradiation", Vienna, 1986.

2. SCIENTIFIC SCOPE AND PROGRAMME GOALS OF PHASE 3

CRP representatives in June 1983 agreed that a third phase of the Co-ordinated Research Programme on neutron radiation effects on advanced pressure vessel steels be initiated.

Success achieved in these two earlier phases provides the background for consolidation and advancement of phase 3 to meet **the principal goal of optimizing reactor pressure vessel surveillance programmes and related methods of analysis** for

international application.

The main objective of this phase of the programme was to consolidate the now increasing body of knowledge on embrittlement and the technique used to determine its significance. It was intended to establish guidelines for surveillance testing which could then be used internationally. Surveillance for this purpose is the periodic assessment of the condition of nuclear power reactor vessel with the view toward assuring its structural integrity.

To achieve this, four principal goals were defined for this phase :

(1) Optimization of the means for measuring fracture resistance.
(2) Establishment of correlative methods for measuring irradiation response by using different mechanical tests.
(3) Seeking to understand the mechanisms responsible for embrittlement.
(4) Establishment of means for ameliorating embrittlement.

In line with the four principal goals the primary emphasis of all participants was toward the ultimate goal implicit in the agreed title - **"Optimizing Reactor Pressure Vessel Surveillance Programmes and Their Analyses"**. To this end, it was agreed to participate with a key focus upon advancing quantitative fracture mechanics methodology and assuring the extrapolation of qualitative fracture methods which have predominated in reactor vessel surveillance until recent years.

Inherent to these main goals are certain uniform procedures such as

(1) use of a reasonably uniform base of reference fluence irradiation,
(2) use of activation dosimeters for assessing the neutron environment,
(3) use of tensile and standard Charpy V-notch specimens to characterize the steels in conventional terms,
(4) adoption of one of two or both of the commonly accepted fracture mechanics tests,
(5) acceptance of an irradiation temperature of 290 C as the standard baseline temperature,
(6) acceptance of the idea of collectively **providing a data base** on "modern" steels with a tie by **use of a key reference steel** to the "first generation" pressure vessel steels and
(7) and agreement to encourage collaborative evaluation of research results so as to multiply the effectiveness of the collective research data.

From 32 steels offered by Japanese steelmakers, 27 were chosen for the study. Primary interest was centered upon the group of Japanese laboratory melts to assess composition effects and on a **"radiation sensitive" correlation monitor from Japan**. A crucial recommendation was to provide the latter which may serve as a reference for this programme and for future surveillance programmes throughout the world. This involved the procurement of a 20-25 ton heat of this steel produced as a special charge by Kawasaki Steel corporation in Japan, which was designated as **JRQ**. The sheer volume of steels to be stock-piled for study dictated careful review of the needs to assure stock was reasonably consistent with the programme scope and with funds available for the study.

The Phase 3 of the programme was realized between 1983 and 1994 by 16 participants - Member States: Argentina, Austria, Belgium, Czechoslovakia, FRG, France, finland, GDR, Hungary, India, Japan, Russia, Spain, Switzerland, UK, USA. Within this programme, 23 different materials (17 specially prepared materials for this phase by Japanese companies, 3 materials from phase 2 and 3 from national programmes) were irradiated and tested.

The composition of the materials tested is given in **Table 1**.

Irradiations were carried out in 20 different experimental and power reactors. These were mainly of the PWR type, i.e. irradiation was performed at 288 °C. In most cases irradiation capsules were located in reflector or near-core position, in some cases directly in

empty channels for surveillance specimens (mostly in WWER-440 type reactors with irradiation temperature equal to 270 °C). Irradiation temperatures were controlled and measured by thermocouples in cases of irradiation in experimental reactors, or determined by temperature monitors in cases of power reactors, mostly.

Neutron energy spectra were determined by calculation and/or experimental measurements using multiple foil techniques and spectrum unfolding evaluation methods. In cases of WWER-440 irradiations, results from mock-up experimental were also used for spectra determination and corrections. Neutron fluences were determined by means of a smaller (but sometimes up to 9 monitors including fission ones) quantity of foil detectors, usually Fe and Cu for fast neutrons and Co for thermal neutrons.

3. MAIN RESULTS OF THE PHASE III AND THEIR DISCUSSION

Taking into accound large amount of data obtained within the Phase III, only the most important ones are presented and discussed.

The most important directions of the programme can be found as follows:

- effect of copper, phosphorus and nickel contents on irradiation embrittlement of ASTM A 533-B type steel,
- comparison of experimental transition temperature shifts and upper shelf energy decreases with those predicted by different empirical formulae given in Guides or standards,
- comparison of Charpy and fracture toughness transition temperature shifts.

All experimental data from impact testing were analyzed using a unified procedure and software programme based on nonlinear regression of the formula

$$KV(T) = A_0 + B_0 \cdot \tanh\{(T-T_0)/C_0\}$$

where KV(T) - notch impact energy at temperature T

A_0, B_0, C_0, T_0 - material constants

3.1. Effects of elements contents in experimental heats

Main purpose of the study of experimental heats was to create a possibility for a study of an effect of main detrimental elements - phosphorus, copper and nickel - on radiation damage in steels of ASTM A 508/A 533 B type of steels.

Figures 3 to 5 show fluence dependence of transition temperature shifts; these diagrams are constructed in such a way that they comprise only heats with the same content of one of the detrimental elements : **Figure 3** with 0.006 % P, **Figure 4** with 0.017 % P and **Figure 5** with 0.16 % Cu. In most cases, transition temperature shifts increase with increasing neutron fluence. Reasons for a "negative" trend pronounced in some cases is not yet clear now.

Looking on **Figures 3 to 5** it seems very difficult to analyse behaviour of individual heats with respect to an effect of element content, if they were irradiated by different participants - in different conditions. Such an effect can be so tiny that irradiation in different conditions must not result in any reliable effect. Thus, more reliable way is to analyse only such heats which underwent similar conditions. Only one participant irradiated all heats in one condition - at 288 C by a fluence equal to 6×10^{22} n.m^{-2}.

Effect of phosphorus in **Figures 6 and 7** depends also on the content of other elements : this effect is very small if heats contain a medium copper content (0.16 % or less), but is very strong if nickel content is 0.82 % and higher. In the same time, threshold phosphorus content is lower than approx. 0.008 % which well correspond with the formula in RG 1.99, Rev.1.

Effect of copper, as it is shown in **Figures 8 to 10** an effect of copper is more

pronounced even for low contents. Copper content together with phosphorus content suppress an effect of nickel, either for constant phosporus contents (0.007 % P and 0.017 % P in **Figure 8**) or for constant nickel content (0.82 % in **Figures 9 and 10**).

Effect of nickel is less pronounced as an effect of phosphorus - only about 50 % increase is found for the increase of nickel content from 0.1 to 1.2 %, both for constant phosphorus and copper contents. Extraordinary transition temperature shift was found for very high copper content - 0.33 %(see **Figures 11 and 12**).

3.2. Comparison of experimental and predicted material changes

Transition temperature shift - ΔT_{41J}

The transition temperature shift, ΔT_{41J} , from Charpy tests is the most common measure of irradiation embrittlement and the following discussion will be conducted principally in terms of this parameter.

Assessment of reactor pressure vessels life is usually carried out using different formulae for prediction transition temperature shift based on chemical composition of materials and neutron fluence. These formulae strongly depend on set of data used for an analysis, in most cases obtained from surveillance specimens programmes. Thus, these national type formulae depend on model accepted but mostly on vessel materials requirements and technology used for an analysed set of experimental data. Most used formulae - US NRC Regulatory Guides 1.99, Rev.1 (RG1) and 2 (RG2), German (KTA), French (FIS and FIM) and Japanese (JAP) will be applied to all experimetal data and results compared. All these guides were established for irradiation temperature close to 290 C.

US NRC Regulatory Guide 1.99, Rev.1 from April 1997 is represented by the equation

RG1: $\Delta T_{41J} = (5/9)\,[40+1000(Cu-0.08)+5000(P-0.008)](Fx10^{-23})^{0.5}$
where Cu and P are the copper and phosphorus contents in mass per cent).

Some other results show that nickel could play a role in radiation damage. Thus, the Rev.2 of this Reg. Guide has been changed and used the following modified formulae:

RG2: $\Delta T_{41J} = (5/9)\,CF\,(Fx10^{-23})^{(0.28-0.1\,\ln F)}$
where CF - chemistry factor which depends on content of phosphorus and nickel and is different for base metals and weld metals.

German KTA 3203 from March 1984 takes into account copper and phosphorus contents and transition temperature shifts are given in graphical (and also table) form, only. This graph is valid for phosphorus content lower than 0.012 mass % P; for P larger than 0.012 %, each additional 0.002 % P is corrected by an additional 0.01 % Cu. Maximum copper content, for which this guide is constructed, is equal to 0.18 mass % and there is no recommendation for an assessment of radiation damage for higher copper contents.

French formulae have the following forms developed by Framatome from French reactor pressure vessel surveillance programmes:

FIS: $\Delta T_{41J} = 8+[24+1537(P-0.008)+238(Cu-0.08)+191(Ni^2.Cu)]\,(Fx10^{-23})^{0.35}$ **FIM:** $\Delta T_{41J} = [17.3+1537(P-0.008)+238(Cu-0.08)+191(Ni^2.Cu)]\,(Fx10^{-23})^{0.35}$

and the Japanese JEAC formulae have the following forms, different for base (BM) and weld (WM) metals :

BM: $\Delta T_{41J} = [-16 + 1210\,P + 215\,Cu + 77(Cu.Ni)^{0.5}]\,(Fx10^{-23})^{0.29-0.04\,\ln F}$

WM: $\Delta T_{41J} = [26 - 24\,Si - 61\,Ni + 301\,(Cu.Ni)^{0.5}]\,(Fx10^{-23})^{0.25-0.1\,\ln F}$

In the following part, an evaluation of applicability of all aforementioned formulae to the CRP experimental data will be performed and assessed.

US NRC Regulatory Guide 1.99, Rev.1 [1] :

Even though this revision of this guide was updated, it still has some meaning for the CRP programme, as it includes an effect of phosphorus, too.

Figure 13 compares calculated (predicted using this formula) transition temperature shifts of all tested materials with real experimental data. It is seen that some of experimental data, not only those irradiated at 270 C, are even higher than mean line + 1 sigma = 28 C for base metals. These differences between predicted and experimental data can reach values as high as 70 C, as it is shown in **Figure 14** which collects differences between calculated and experimental data as a function of neutron fluence. It seems that with increasing of neutron fluence these differences are also slightly increasing. The RG mostly overpredicted real damage but in some cases an underestimation as large as 60 C is also found.

Figure 14 gives comparison of these differences for all materials. Only the JRQ material was damaged much larger than predicted values but also many materials were overestimated, especially for lower neutron fluences. Looking on the effect of main important elements, then behaviour of materials with low phosphorus content (0.005 %) are well predicted, while materials with high contents (0.015 to 0.020 %) are sometimed underestimated - **Figure 15. Figures 16,17** show that copper content is better described by the used formula while nickel content should be better included.

Thus, formula in RG 1.99, Rev.1 does not fairly well predicted experimental transition temperature shifts, when maximum differences reach values up to 70 C in both directions.

US NRC Regulatory Guide 1.99, Rev.2 [2] :

This guide is the mostly used for predicting irradiation embrittlement of ASTM type steels. On the contrary with the previous Revision 1, it is including effect of nickel but neglecting effect of phosphorus. This step was supported by the detailed analysis of surveillance data of U.S. produced materials which, in general, contained low content of phosphorus according to requirements.

Figures 18 and 19 summarizes predicted and experimental transition temperature shifts for all tested materials using the formula (6.2). Generally, it cen be concluded that this formula mostly overestimated predicted shifts but there are many cases with a strong underestimation, up to 45 C.

Some base materials (JRQ, JPB, JPJ) reached higher shifts than can be predicted within the 1 sigma limit, but they are many others within this limit - **Figure 19** . It seems that fluence effect is relatively well included into the formula (6.2), while materials with higher content of phosphorus (approx. 0.017 to 0.020%) are slightly underestimated by the used formula while for low content (0.005 % P) its estimation is quite good- **Figure 20**. On the contrary, effect of copper is also quite well described while it can be concluded that synergestic effect of phosphorus and nickel evokes an underestimation of shifts values for such materials - **Figures 21 and 22**. The same conclusions can be made also from experimental heats. In the same time, is seems that neutron fluence part in the formula (6.2) slightly overestimates transition temperature shifts for increasing neutron fluences - **Figure 19**.

Different Chemistry Factor CF is defined in the equation (6.2) for weld metals. Comparison of predicted and experimental transition temperature shifts - **Figure 22** shows to a general overestimation by prediction with two excemptions - materials JWQ and BWA which could be also given by a high phosphorus content in materials (up to 0.026 % for JWQ).

This analysis of results supported the US NRC activity which is directed to an upgrading of the formula using an upgrading set of US surveillance data. In this connection, the whole analysis performed in this chapter must be taken with some sensitivity to the fact that the CRP contains mostly results from experimental reactors which sometimes cannot be compared with surveillance ones.

German KTA 3203 :

Test of the applicability of this approach will be also performed even though there are some limits of the use, mainly for high copper and phosphorus contents.

Figure 24 shows that this approach is, in general, very conservative, as most of experimental transition temperature shifts are lower than predicted ones. This is valid mainly for base materials where only materials with high phosphorus contents are the only ones that are underestimated by the prediction - **Figure25**. The largest underestimation was obtained for the JPA material which has not only high phosphorus content (0.018 %) but also high copper content (0.33 %) which falls behind the limits of the use of this formula which is fully understandable. This conclusion is also supported by results from experimental heats, as most of these heats are underestimated by the KTA formula. It can be discussed that fluence factor in the KTA formula is the factor that contributes by the largest portion to the overestimation of transition temperature shifts.

In general, KTA rule mostly, with only limited number of exceptions, overestimates transition temperature shifts of tested materials even though it has some limitation in detrimental elements content which was not fulfilled.

French FIS formula :

This formula takes into account influence of all three discussed element contents, e.g. of phosphorus, copper and nickel.

Summary of all experimental and predicted data is given in **Figure 26**. Similarly to KTA approach, only experimental heats JPB and JPJ as well as JRQ are underestimated, for all other materials a conservative prediction has been obtained. Underestimation is not only rare but also practically negligible - smaller than 10 C, on the other side, overestimation reaches values up to 95 C - **Figure 27**. It can be also preliminary concluded that fluence factor can be of those that play an important role in the overestimation of shifts. Behaviour of weld metals is predicted with a very high conservatism, independently on C, P and Ni contents - in all cases by about 25 C - **Figure 28.**

Thus, from the comparison of predicted and experimental transition temperature shifts can be concluded that FIS formula is highly conservative, practically for all tested materials.

French FIM formula [4]:

This formula can be taken as a modification of the previous - FIS - one, but results are not fully compatible with those.

Figure 29 summarizes comparison of predicted and experimental shifts for all tested materials - there are many points which are underestimated by the used formula. Even though this underestimation is not very large - up to about 30 C - it is larger than can be allowed. Degree of conservatism is also very high - up to 75 C, but mostly up to 50 C - **Figure 30**. It seems that factors describing an effect of all three elements - P, Cu and Ni - are equally responsible for the overestimation of shifts.These conclusion is also consistent with results for experimental heats. In addition, **Figure 30** shows to a underestimating effect of fluence factor in the equation. Relative good prediction is given for the JRQ material.

Generally, the FIM formula has lower ability to predict transition temperature shifts correctly comparing with the FIM one. All factors in the formula are probably responsible for an uncorrectness in prediction.

Japanese JEAC formula for base metals :

This formula takes also into account all three elements - P, Cu and Ni as the previous ones but with different importance.

Comparison of all predicted and experimental shifts is given in **Figure 31** where many experimental data lie over predicted ones. **Figure 32** shows that underestimation is up to 35 C but conservatism up to.70 C. These trends are not dependent on neutron fluence, but can be connected with factors describing phosphorus and copper effects in whole contents region and of nickel in contents higher than 0.8 % , in both directions. Relatively well is described the behaviour of the JRQ material where maximum differences lie between - 25 C and + 20 C.

JEAC formula was not established by only very high purity steels, but also some steels having a certain amount of impurities, such as JRQ. Another possible reason is the formula was derived from mainly surveillance data from power plants in Japan.

General conclusion from all this analysis of applicability of formula for predicting transition temperature shifts is as follows :

- not any of formulae gives satisfactory results in prediction of shifts values,
- reason of this fact can be found in sets of data that were used for the formulae construction - materials used for reactor pressure vessels are slightly/strongly differed even though they were manufactured according to similar ASTM standards, but using different technologies and different additional requirements to the material cleanness,
- relatively safest results have been obtained using KTA and FIS formulae - they give the most conservative values only exceptionally with underestimation of shifts,
- all these conclusions must be taken with some pracaution as most of experimental data were obtained in experimental reactors,
- nevertheless, any supplementary analysis of all accessible data are promoting, as this is the only way to describe an effect of all elements in a proper manner.

3.3. Decrease in upper shelf energy - Δ USE

Decrease in upper shelf energy is characterized mainly for welding metals. In some cases, for weldments with higher copper contents, resulting upper shelf energy can be as low as 68 J (50 ft-lb) or even lower. For such occasion, a special procedure has to be applied and additional calculations to be performed.

While in Reg.Guide 1.99, Rev.1 only graphical form for such an estimation was included, in Reg.Guide 1.99, Rev.2 some empirical formulae also exist. Decrease in upper shelf energy is defined in portion of the initial one, e.g. in percentage of the initial USE values.

Thus, the following formulae were defined :

upper limit for all materials :

$$\Delta USE\ (\%) = 42.39\ F^{0.1502}$$

lower limit for base metals :

$$\Delta USE\ (\%) = (100\ Cu + 9)\ F^{0.2368}$$

lower limit for weld metals :

$$\Delta USE\ (\%) = (100\ Cu + 14)\ F^{0.2368}$$

Figure 33 summarizes all data of upper shelf energy decrease for base metarials from the programme. In these diagrams, decrease in USE is taken as a negative one, correspondingly with real situation, while in the RG 1.99 their mark is opposite, e.g. positive instead of negative ones. Thus, upper bound in the RG means the lower bound of experimental values - no experimental value should lie below this line. This suggestion is well fulfilled in the figure, even for lower irradiation temperature (270 C). In **Figure 34** "lower limits"

for three different copper content are also added : for this situation the equations (6.8) does not well agree with experimental data as some experimental data lie below and some over these lines.Thus, these lower limits do not correspond to exact experimental values in most cases as they are mostly not conservative especially for low and medium copper content.The lower is copper contents in materials the larger is scatter of results with respect to lower limits of the corresponding content of copper.

Limited number of weld metals is not representative but **Figure 35** again approved the correctness of upper bound given in the equation (6.7). Nevertheless, lower bounds for both copper contents - 0.05 % and 0.26 %, resp. - are again not fully conservative.

As a conclusion, prediction of decrease in USE according to the RG 1.99, Rev.2 is not conservative in all cases - upper limit well corresponds to all experimental data, but lower bounds are not conservative for all experimental materials and irradiation conditions. Reason for such a discrepancy can be probably found in the effect of other elements, mainly of phosphorus which is not taken into account in both the equations.

3.4. Fracture mechanics tests and procedure

One of the key focuses is upon advancing quantitative fracture mechanics methodology and assuring the extrapolation of qualitative fracture methods which have predominated in reactor vessel surveillance until recent years. Another key research item was to seek understanding of the mechanisms responsible for the embrittlement.

One scope of the programme was fracture toughness testing. The participants performed a variety of different fracture toughness tests on many of the materials. The tests included static and dynamic testing.

The data included in the analysis were generally taken from the IAEA CRP 3 data base. The data was in all cases checked against and complemented fom the original national reports. Nine countries performed static fracture toughness testing out of which three performed also dynamic testing. In one case (dynamic), the irradiation was performed in Switzerland and the testing in Finland.

Before re-evaluation, the data was screened. Only data, deemed as descriptive of the true fracture toughness was included in the analysis. The prerequisite was that the fracture toughness is based on the elastic-plastic J-integral, or valid linear elastic (LEFM) fracture toughness K_{IC}.

The definition of ductile crack growth initiation toughness varied from laboratory to laboratory (lab-to-lab). Thus, the ductile fracture results showed such a large lab-to-lab variability that a comparative analysis of the results was impossible. Also, the quality of the data supplied to the data base was such that a systematic recalculation of the ductile initiation toughness was not possible. By necessity, the re-evaluation had to be restricted to brittle fracture initiation described by the elastic-plastic fracture toughness K_{JC}.

The statistical analysis was performed in accordance with the VTT method for assessment of fracture resistance. It is based on a statistical brittle fracture model, which gives for the scatter of fracture toughness

$$P\,[K_{IC} \le K_I] = 1 - \exp\left(-\left[\frac{K_I - K_{min}}{K_0 - K_{min}}\right]^4\right)$$

where $P[K_{IC} \le K_I]$ is the cumulative failure probability, K_I is the stress intensity factor, K_{min} is the theoretical lower bound of fracture toughness and K_0 is a temperature and specimen size dependent normalization fracture toughness, that corresponds to a 63.2 % cumulative failure probability being approximately 1.1 $\bar{K}_{IC}$ (mean fracture toughness). The model predicts a statistical size effect of the form

$$K_{B_2} = K_{min} + \left[K_{B_1} - K_{min}\right] \cdot \left(\frac{B_1}{B_2}\right)^{1/4}$$

where B1 and B2 correspond to respective specimen thickness (length of crack front).

For structural steels, a "master curve" describing the temperature dependence of fracture toughness has been proposed [5],

$$K_0 = 31 + 77.\exp\,(0.019.[T - T_0])$$

where T_0 is the transition temperature where the mean fracture toughness, corresponding to a 25 mm thick specimen, is 100 MPa $m^{0.5}$ and K_0 is 108 MPa $m^{0.5}$.

This equation gives an approximate temperature dependence of the fracture toughness for ferritic structural steels and it is comparatively well verified. Keeping the temperature dependence fixed, decreases the effect of possible invalid fracture toughness values upon the transition temperature T_0.

The use of the statistical treatment enabled the fracture toughness results to be described with only one parameter (T_0). The treatment is also in line with a new ASTM standard proposal for fracture toughness testing in the transition region.

The majority of the fracture toughness testing was performed on the reference material JRQ. To study the effect of specimen size, type and orientation, the data, in the form of T_0, was plotted as a function of specimen distance to the plate surface in **Figures 36 and 37.** The T_0 data include also the theoretical $\pm 1\ \sigma$ confidence limits for the estimate. The scatter in the results is comparatively large. It appear that estimates besed on less than 3 specimens are much too unreliable. Therefore, a second plot of the data, including only estimates based on three or more specimens, was made in **Figure 38** for L-T orientation. The result is a much reduced scatter in T_0 (especially for the L-T orientation). No systematic differences between different specimen types are visible. Neither is any size effects, in addition to the statistical size effect included in the analysis, to be seen. The L-T orientation seem to show a toughness gradient in the plate thickness direction, but not the T-L orientation. The data from the different countries are quite consistent.

The dynamic tests were all performed with 10 mm thick specimens, which made an examination of size effects impossible. The dynamic fracture toughness appear to, based on the limited data, to behave like the static fracture toughness, but being shifted on the average to a 30-40 °C higher temperature.

The irradiation response of the static fracture toughness was examined by fitting a power law equation for T_0

$$T_{0F} = T_{0n} + A\,(F \times 10^{-23})^m$$

After a preliminary study of the JRQ material, it was decided to fix the power m equal to 0.5. It was not felt that the data enabled a more aqqurate description of the irradiation response.

The results for the material JRQ (T-L & L-T) are presented in **Figures 39 -40.**

3.5. Correlation between different transition temperatures

Analysis of all experimental data within the CRP 3 programme shows that both initial transition temperatures and transition temperature shifts are in a very good linear correlation

- initial values are practically only shifted in temperature scale by some constant characterictic for a give relationship, independent on materials (at least for studied set of materials),
- shifts defined from impact tests are practical identical, with a very high correlation coefficient.

3.6. Correlation between fracture toughness and Charpy-V

A comparison between the static fracture toughness transition temperature shift $\Delta T_0$0 and the most common Charpy-V transition temperature ΔT_{41J} was made. The result is presented in **Figure 41.**

The result of the comparison is not very encouraging with respect to the reliability of the Charpy-V test. Only in one case (GWA), is the Charpy-V shift greater than the static fracture toughness shift. For the GWA material. the Charpy-V shift corresponds to the T-L orientation whereas the fracture toughness shift corresponds to the L-T orientation. The Charpy-V shift underestimates the facture toughness shift at maximum by approximately 70 °C (GFB). Based on the comparison, it can be concluded that the Chapy-V shift is not appropriate for the estimation of the static facture toughness shift.

In an attempt to improve the usability of the Charpy-V test, a direct correlation between the transition temperatures (no the shifts) was attempted. In this case many more results were available for the comparison. The result of the comparison is presented in **Figure 42.**

A clear difference in the correlation is seen between irradiated and non-irradiated materials. Considering the scatter, a 95 % "lower bound" correlation for the irradiated materials becomes, $T_0 \approx T_{41J} + 15$ °C. This relation, used together with the master curve, appears more applicable than the use of the Charpy-V shift combined with the ASME reference curve. Most favourable is, however, based on the analsysis, the direct determination of the static fracture toughness.

3.7. IAEA Reference Steel JRQ

Maximum results have been collected for JRQ material, of course. It is clearly seen that specimen depth plays the most important role, mainly between surface and 1/4 ot the plate thickness - see **Figure 43** : difference between surface and one-quarter (up to middle of thickness) transition temperatures is about 50 C. This difference depends not only on specimen depth but also on the other aforementioned two parameters. Effect of the testing standard (ISO vs. ASTM) and of specimen orientation (L-T vs. T-L) was also found. Similar dependencies of upper shelf energy on specimen depth are given in **Figure** 44.

Using statistical evaluation of all results the following mean values for specimens located in one quarter of the plate thickness have been found :

- T-L orientation gives higher transition temperature than L-T orientation by about 8 C:

  T_{41J} (T-L, 55 mm) = -15.9 ± 8.2 C
  T_{41J} (T-L, 55 mm) = -23.7 ± 4.8 C
  T_{41J} (55 mm) = -19.5 ± 7.8 C

- testing with ASTM type tup gives similar results to those obtained using ISO type tup (within a given scatter) ::

  T_{41J} (55 mm, ASTM) = -21.3 ± 6.7 C
  T_{41J} (55 mm, ISO) = -20.2 ± 8.2 C

- T-L specimen orientation gives lower values of upper shelf energy than L-T orientation by about 20 J :

  USE (T-L, 55mm) = 187.8 ± 11.1 J
  USE (L-T, 55mm) = 213.6 ± 12.2 J
  USE (55mm) = 198.6 ± 17.2 J

- and the effect of tup radius on upper shelf energy can be also found :

  USE (55mm, ASTM) = 200.3 ± 1.2 J
  USE (55mm, ISO) = 182.8 ± 9.1 J

The transition temperature shift ΔT_{41J} was chosen as a main parameter and a linear regression method used to evaluate the results, when possible within the whole programme. For this evaluation the following commonly used simplified expression was applied :

$$\Delta T_{41J} = A_F (F \times 10^{-23})^n$$

where A_F, n are material constants.

Relatively good results have been obtained for the JRQ material as it can be seen in **Figure 45.** Testing in different laboratories was carried out according two standards - ASTM and ISO which differs by tup geometry, in principle. There was also difference specimen/notch orientation used in different laboratories. While irradiation embrittlement of specimens with orientation L-T shows to a relatively small scatter of data (and to no difference between ASTM or ISO tup), its exponent of temperature dependence is unusually high. On the other side, specimens with orientation L-T show unormous scatter of transition temperature shifts with a very low correlation. Irradiation at 270 C is relatively consistent, maybe as a results of very close irradiation conditions in power WWER-440 type reactors.

Linear regression analysis of experimental data from impact testing has shown no significant dependence on the tup geometry (e.g. on the standard) but supprisingly to some dependence on specimen/notch orintations:

irradiation temperature ~ 290 C :

$$\Delta T_{41J}(T\text{-}L) = 57.7 (F \times 10^{-23})0.387$$

$$\Delta T_{41J}(L\text{-}T) = 22.5 (F \times 10^{-23})0.743$$

$$\Delta T_{41J} = 40.7 (F \times 10^{-23})^{0.511}$$

irradiation temperature ~ 270 C :

$$\Delta T_{41J} = 74.9 (F \times 10^{-23})^{0.326}$$

Results obtained show to different neutron embrittlement exponent n for different specimens orientation after irradiation at 290 C, only their mean value is close to 0.5. On the other side, this exponent after irradiation at 270 C is close to 0.3.

Comparison of transition temperature shifts in two reference materials - JRQ and HSSTP 03 Plate is shown in **Figure 46.** Mean trend lines were established in the following forms :

JRQ : $\Delta T_{41J} = 58.67 (F \times 10^{-23})^{0.342}$

03/1+2 : $\Delta T_{41J} = 26.87 (F \times 10^{-23})^{0.687}$

Comparison of results summarized in figures and analyzed by trend lines gives the follolwing conclusions :

- JRQ steel is more susceptible to irradiation damage - embrittlement in comparison with HSST 03 steel, thus, it can be well used as a potential "reference" material for future surveillance as well as research irradiation programmes,
- different exponent in trend lines of materials irradiated in the Phase 1 +2 and Phase 3, respectively have been determined :
  "old" and "advanced" materials from Phases 1 + 2 are characterized by the exponent value close to 2/3, while
  "reference" (e.g. old) JRQ material in Phase 3 is characterized by the exponent value close to 1/3.

4. CONCLUSIONS AND RECOMMENDATIONS

Within the framework of the IAEA co-ordinated research programme, a large amount of experimental wotk has been carried out. Fifteen organizations from fourteen (former fifteen) Member States took part in this programme which lasted from 1984 to 1993.

The following are the main conclusions :

(i) The general aim of Phase 3 of the programme was to consolidate the now increasing body of knowledge on embrittlement and the technique used to determine its significance. Results from this programme show that there is a comparable knowledge, experience, irradiation and testing facilities in the Member States which creates a well established worldwide comparable centres for evaluation of the behaviour of reactor pressure vessels under neutron irradiation damage.

(ii) In general, comparison of results from mechanical testing gives quite reproducible data suitable for a reliable assessment of reactor pressure vessel life.

(iii) Creation of a database of all experimetal results obtained within the programme has been found as a very usable instrument in analysis of all the data. This database will also serve as a initiative part of a wider IAEA database on surveillance programmes results.

(iv) Testing of "old" and "advanced" types of materials showed to an effective way of decreasing the material susceptiblity to radiation damage by decreasing phosphorus and copper contents. Study of the effect of phosphorus, copper and nickeal contents on specially preparede experimental heats supported existing models on radiation damage in this type of steels.

(v) Comparison of experimental transition temperature shifts and upper shelf energy decreases with those predicted by US, French, German and Japanese Guides show to the fact that no of them is fully applicable for the materials studied - they are partially conservative and partially strongly nonconservative (up to 70 C). This conclusion supported an effort of the creation of the IAEA surveillance database as only analysis of very large set of data from different manufacturers could determine effects of individual elements in a proper way.

(vi) Comparison of initial transition temperatures from impact Charpy as well as of static fracture toughness testing showed to a good linear correlation between inidividual parameters with a relatively small scatter of data.

(v) While transition temperature shifts from impact testing have been found practically identical, independent on the parameter determined, transition temperature shifts from static fracture toughness testing have found, in general, higher than compared with impact testing.

(vi) Specific heat treatment (annealing) used for material recovery was showed as a very useful tool - it sems that its mechanism is controlled by self-diffusion of iron.

(vii) Additional studies directed to understand mechanisms of radiation damage, hardening and embrittlement using different physical methods have been realized and results discussed.

(viii) Recommendation for a standard procedure for testing of small scale (pre-cracked Charpy type) specimens applicable for static fracture toughness determination within surveillance specimens programmes have been proposed and checked on results from the programme.

(ix) Specially manufactured material JRQ (with higher content of copper and phosphorus) has been studied by all participants. Analysis of the results obtained approved a suggestion for using this steel as a "reference steel" for future surveillance as well as research irradiation programme.

This material has been found as a well homogenous with reproducible results if recommended conditions are fulfilled : specimens depth equal to 1/4 (approx. 55 to 65 mm) of the thickness, proper orientation (L-T or T-L) and standard of testing (ISO or ASTM)

Mean trend lines have been determined for transition temperature shifts from impact testing as well as for yield strength increase tested at room temperature, all after

irradiation at 290, resp. 270 C.

(x) Progress in neutron dosimetry resulted in better instrumentation and characterization of irradiation experiments even though common uncertaintity in neutron fluence determination is still probably not better than 30 %. However, scatter of some results cannot be explained by any possible manner.
Difference between slope of trend lines of dependence of impact transition temperature shifts on neutron fluence received in Phases 1+2 and 3, respectively, cannot be also explained by any physical mechanism of damage; possible explanation can lie probably in neutron dosimetry but this effect is difficult to analyse and find.

Further progress in the application of the fracture mechanics approach to radiation damage assessment has been achieved in this phase of the programme. Nevertheless, improvement and unification of the method will be efficient way for improving precision and reliability of reactor pressure vessel life evaluation based on surveillance specimens programmes. Improvement and unification of neutron dosimetry methods have provided better data with a smaller scatter of data but further steps seems still to be necessary.

Thus, in September 1996, a new IAEA CRP on "Assuring Structural Integrity of Reactor Pressure Vessels" was founded, and more than 20 different countries are taking part in.

Table 1. Chemical composition of tested materials (Manufacturer´s data)

PHASE	CODE	C	Si	Mn	P	S	Cu	Ni	Cr	Mo	V	Al	NOTE
1	03	0.26	0.26	1.36	0.011	0.015	0.13	0.62	0,10	0,52		0.034	
2	JP	0.18	0.22	1.40	0.009	0.004	0.02	0.66	0.20	0.57	0.002	0.007	
	JF	0.18	0.24	1.38	0.007	0.007	0.04	0.75	0.11	0.49	<0.01	0.031	
	JW	0.08	0.36	1.24	0.009	0.007	0.04	0.71	0.07	0.48	0.009	0.010	
	FP	0.22	0.23	1.43	0.008	0.002	0.04	0.64	0.05	0.50	<0.005	0.010	WELD METAL
	FFA	0.15	0.24	1.36	0.009	0.009	0.063	0.68	0.24	0.46	0.008	0.031	
	FW	0.06	0.37	1.50	0.012	0.008	0.04	0.79	0.07	0.62	0.008	0.010	WELD METAL
	GWA	0.08	0.16	1.48	0.015	0.009	0.05	0.93	0.02	0.62	0.003	0.020	WELD METAL
3	JPA	0.18	0.27	1.47	0.018	0.002	0.33	0.82	0.15	0.54	0.01	0.018	LAB.HEAT
	JPB	0.18	0.26	1.42	0.017	0.001	0.01	0.83	0.15	0.54	0.01	0.016	LAB.HEAT
	JPC	0.18	0.27	1.45	0.007	0.002	0.01	0.81	0.15	0.54	0.01	0.021	LAN.HEAT
	JPD	0.19	0.27	1.45	0.006	0.001	0.16	0.10	0.15	0.55	0.01	0.019	LAB.HEAT
	JPE	0.17	0.27	1.45	0.006	0.001	0.16	0.39	0.15.	0.55	0.01	0.027	LAB.HEAT
	JPF	0.18	0.27	1.49	0.020	0.001	0.16	0.62	0.15	0.55	0.01	0.010	LAB.HEAT
	JPG	0.18	0.27	1.45	0.017	0.001	0.16	0.82	0.15	0.55	0.01	0.013	LAB.HEAT
	JPH	0.18	0.27	1.45	0.006	0.001	0.17	1.18	0.15	0.54	0.01	0.021	LAB.HEAT
	JPI	0.18	0.21	1.50	0.006	0.001	0.01	0.69	0.17	0.57	0.001	0.012	
	JPJ	0.18	0.21	1.41	0.005	0.001	0.05	0.64	-	0.50	<0.003	-	
	JFL	0.17	0.25	1.44	0.004	0.002	0.01	0.75	0.20	0.51	0.004	0.016	
	JFM	0.18	0.25	1.40	0.013	0.003	0.16	0.77	0.25	0.49	<0.01	-	
	JRQ	0.18	0.24	1.42	0.017	0.004	0.14	0.84	0.12	0.51	0.002	0.014	
	JWN	0.10	0.28	1.33	0.006	0.004	0.018	0.87	0.043	0.47	0.002	0.016	WELD METAL
	JWO	0.073	0.29	1.24	0.005	0.005	0.03	0.78	0.06	0.37	0.005	0.005	WELD METAL
	JWP	0.09	0.33	1.18	0.009	0.004	0.03	0.90	0.06	0.40	0.01	0.001	WELD METAL
	JWQ	0.09	0.30	1.29	0.026	0.005	0.26	1.10	0.04	0.48	0.002	0.011	WELD METAL
	GFA				0.022		0.26	0.74					LOW "USE"
	GFB				0.006		0.05	0.85					
	D4S	0.07		1.57			0.05	0.78	0.14	0.48	0.004		WELD METAL

Comments : F - forging P - plate W - weld
J - Japanese G - UK D - Denmark

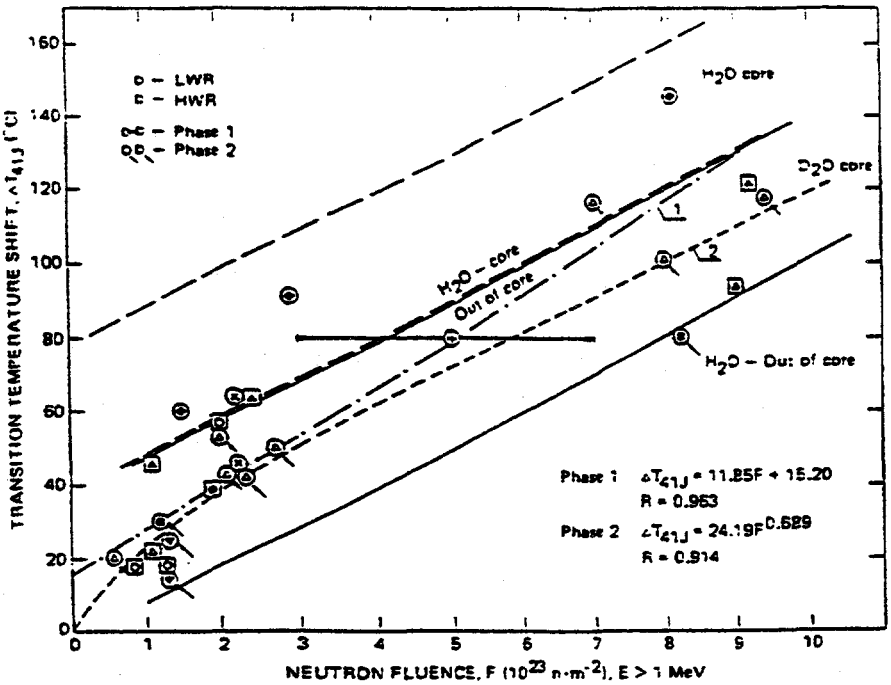
o – LWR
□ – HWR
Phase 1
Phase 2
H_2O core
D_2O core
H_2O – core
Out of core
H_2O – Out of core
Phase 1 $\Delta T_{41J} = 11.85F + 15.20$
R = 0.963
Phase 2 $\Delta T_{41J} = 24.19F^{0.589}$
R = 0.914
TRANSITION TEMPERATURE SHIFT, ΔT_{41J} (°C)
NEUTRON FLUENCE, F (10^{23} n·m^{-2}), E > 1 MeV

Fig. 1

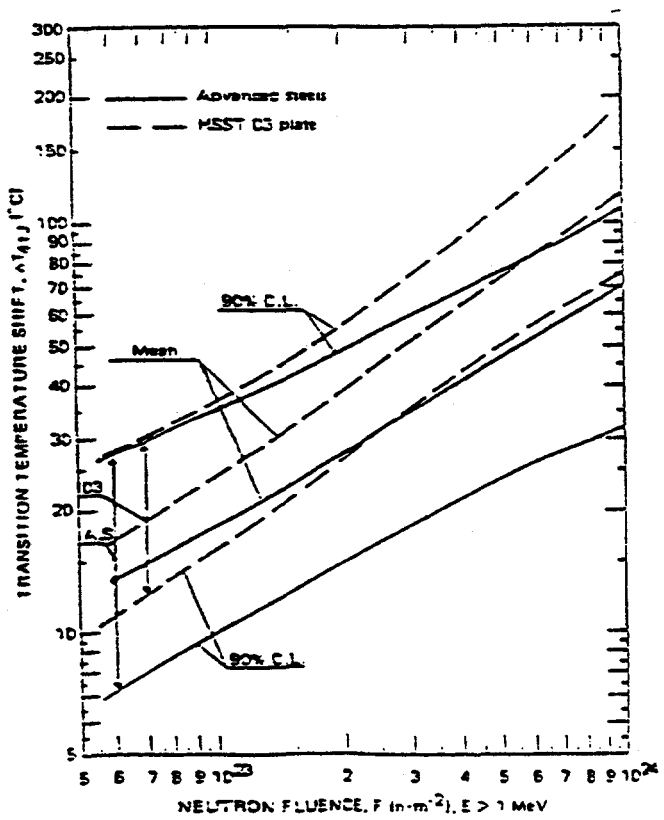
Advanced steels
MSST C3 plate
90% C.L.
Mean
90% C.L.
TRANSITION TEMPERATURE SHIFT, ΔT_{41J} (°C)
NEUTRON FLUENCE, F (n·m^{-2}), E > 1 MeV

Fig. 2

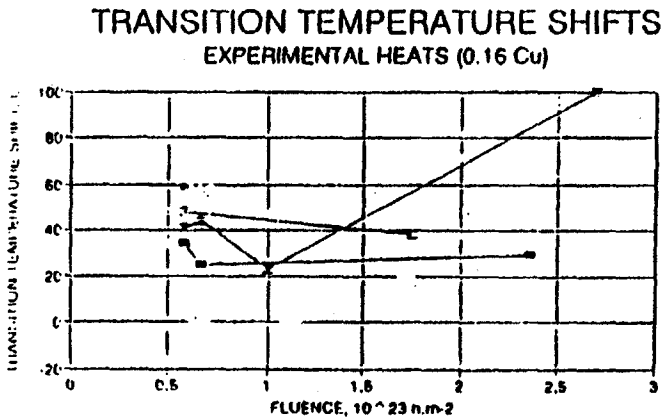

Fig. 3

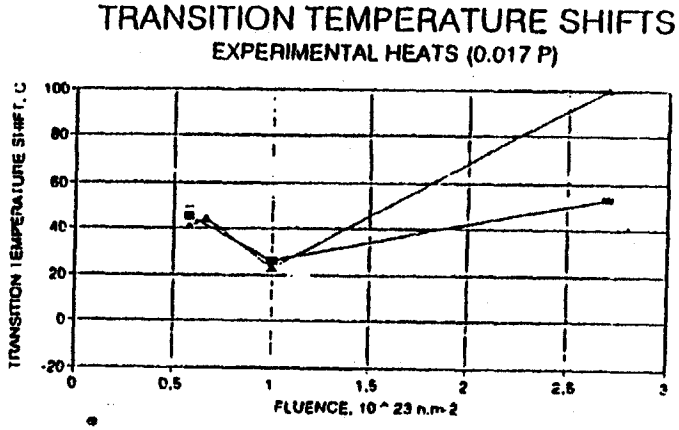

Fig. 4

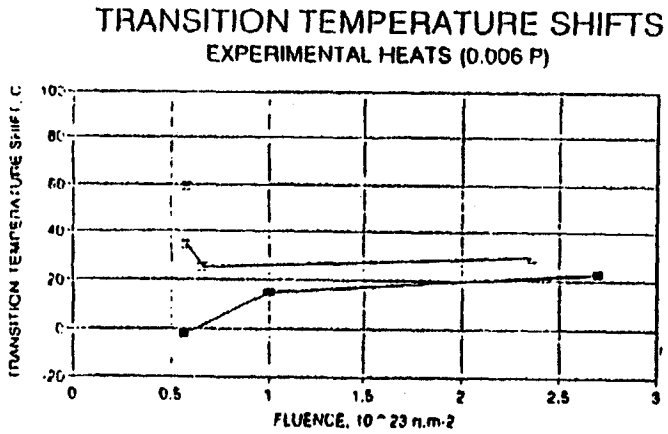

Fig. 5

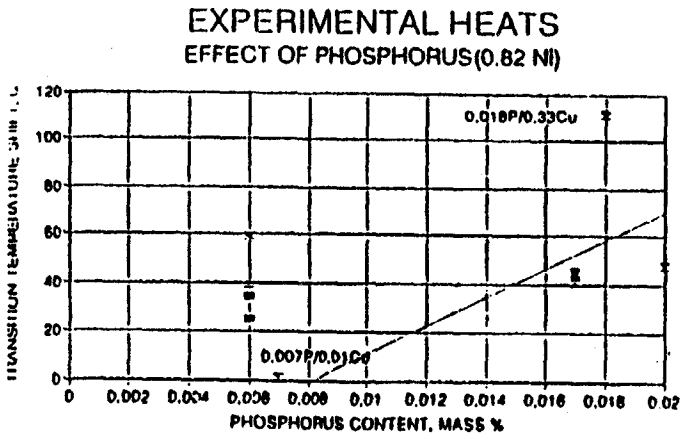

Fig. 6

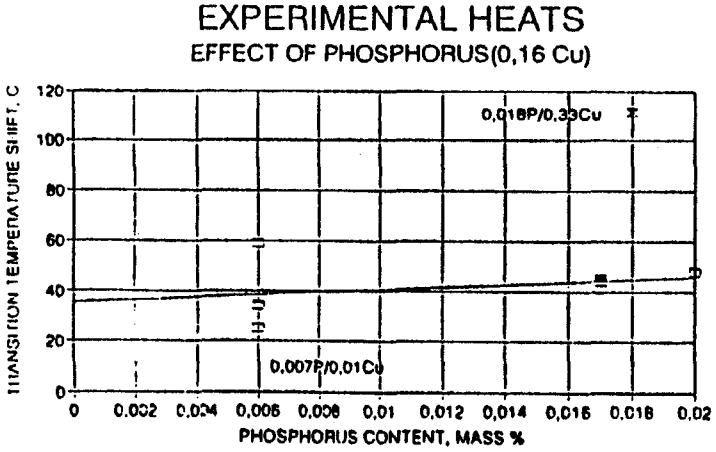

Fig. 7 ■ 0,01 Cu ⊏ 0,16 Cu ⧖ 0,33 Cu

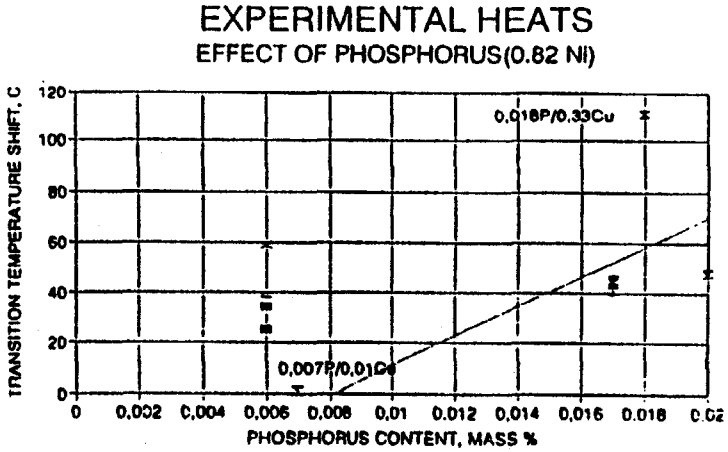

Fig. 8 ■ 0,10 Ni ⊏ 0,39 Ni ⧖ 0,82 Ni × 1,15 Ni

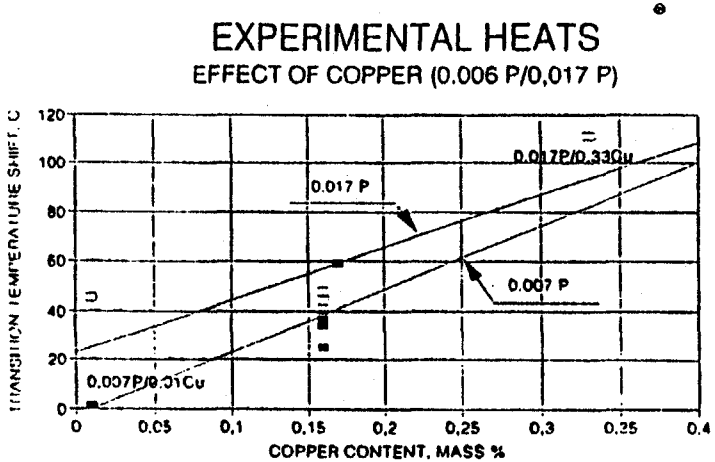

Fig. 9 ■ 0,006 P ⊏ 0,017 P

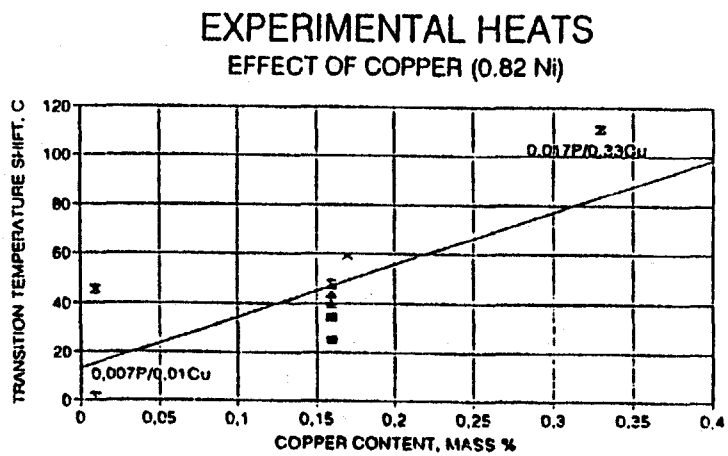

Fig. 10 ■ 0,10 Ni ⊏ 0,39 Ni ⧖ 0,82 Ni × 1,15 Ni

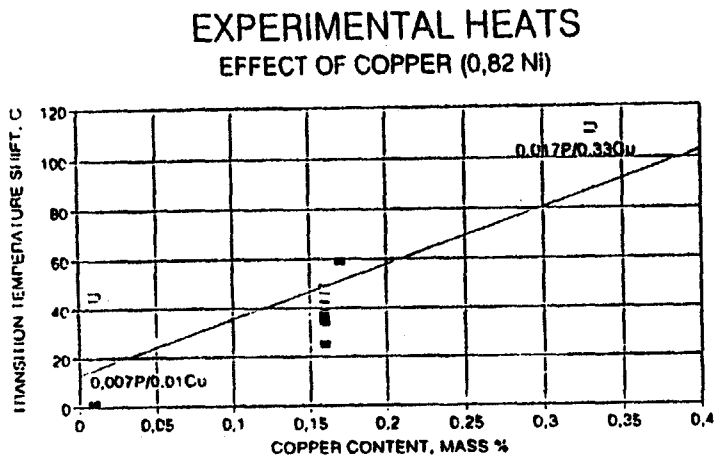

Fig. 11

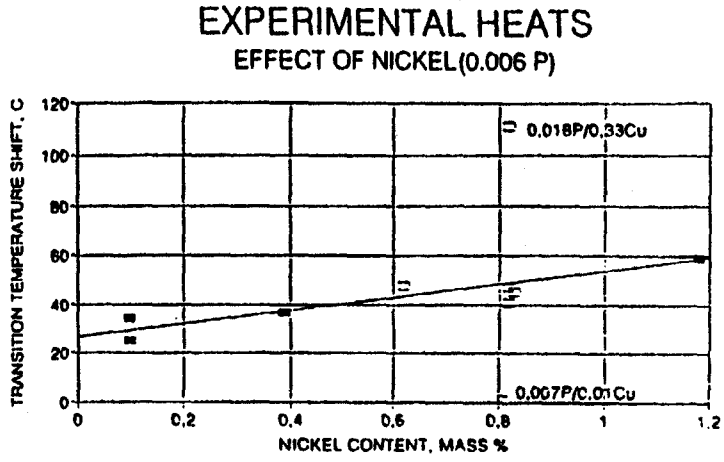

Fig. 12

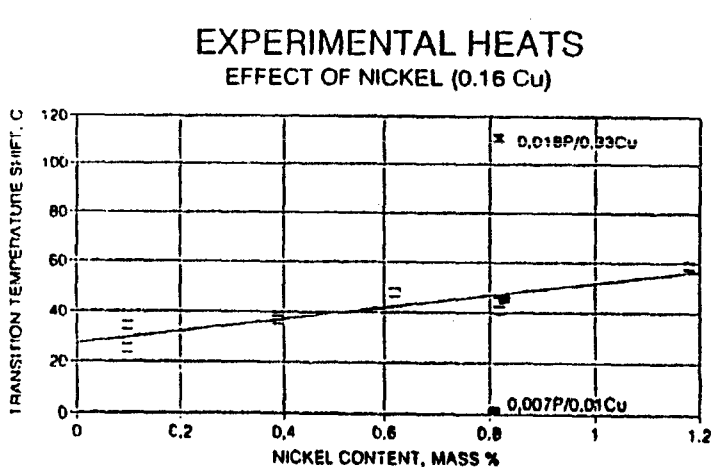

Fig. 13

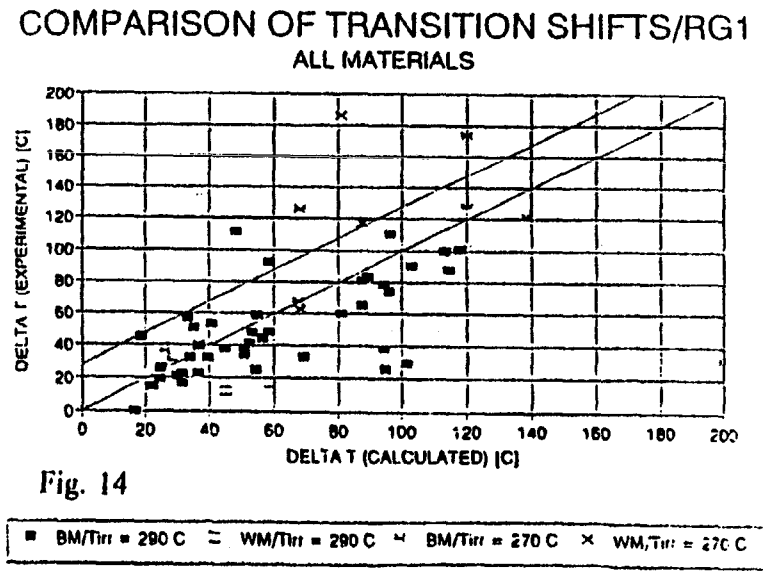

Fig. 14

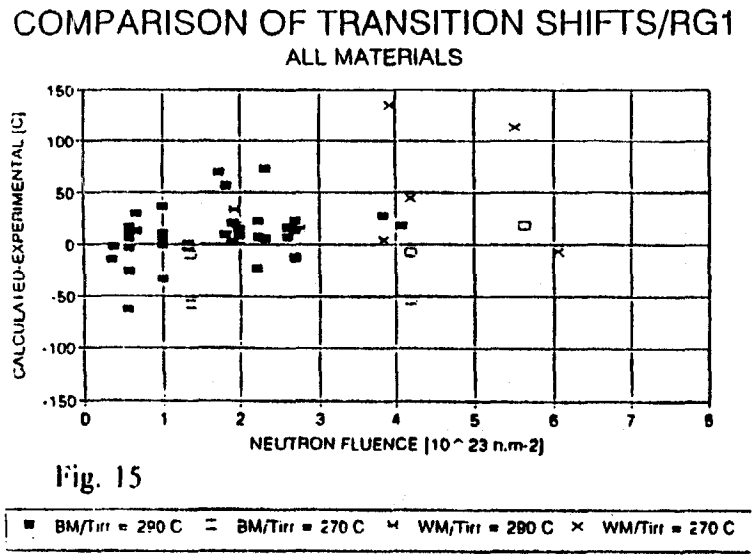

Fig. 15

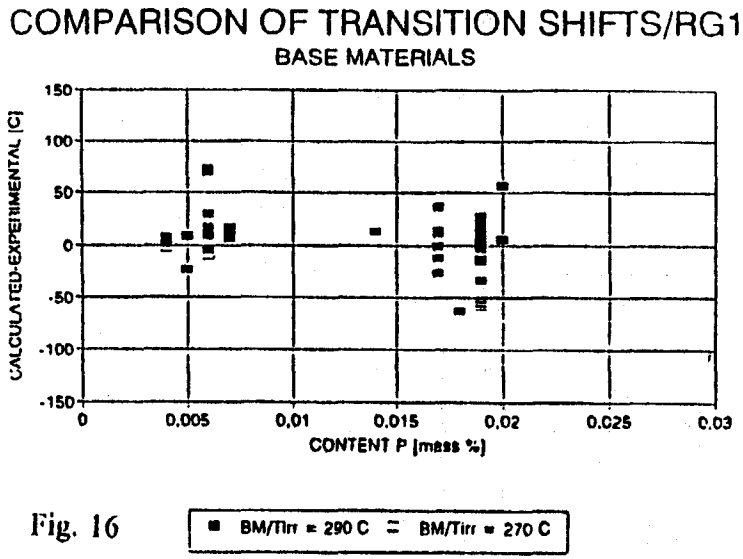

Fig. 16

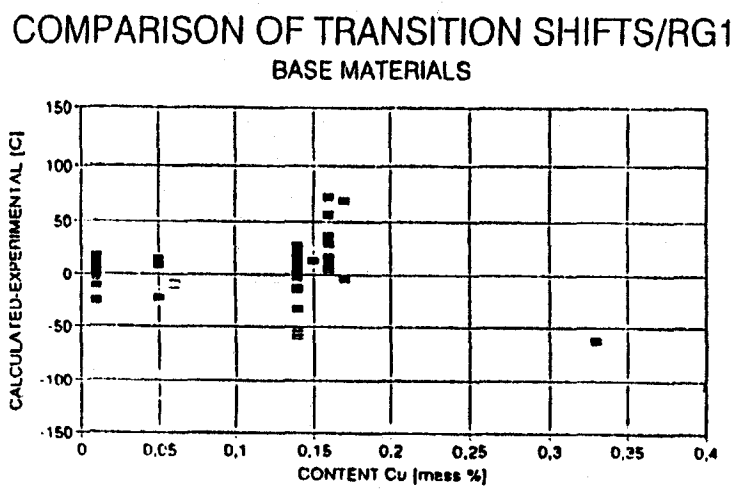

Fig. 17

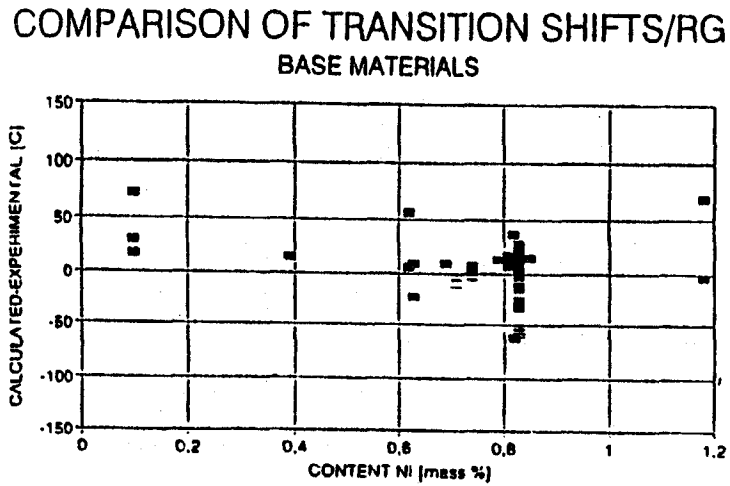

Fig. 18

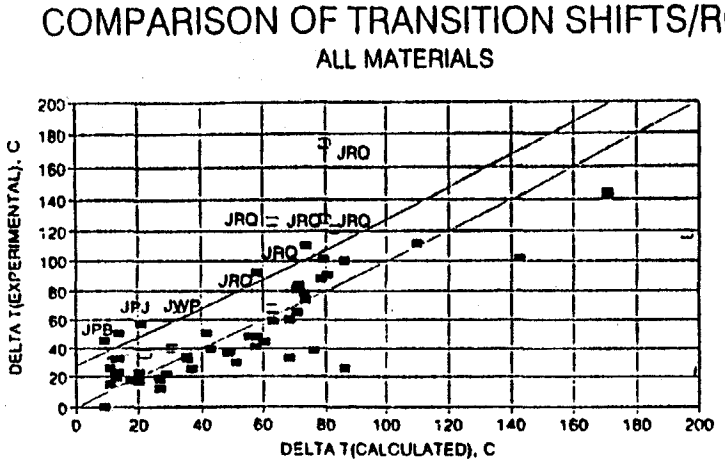

Fig. 19 ■ Tirr = 290 C = Tirr = 270 C

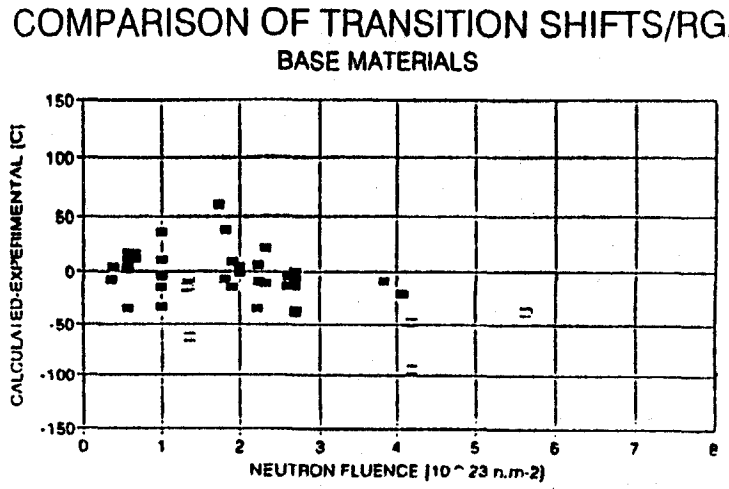

Fig. 20 ■ BM/Tirr = 290 C = BM/Tirr = 270 C

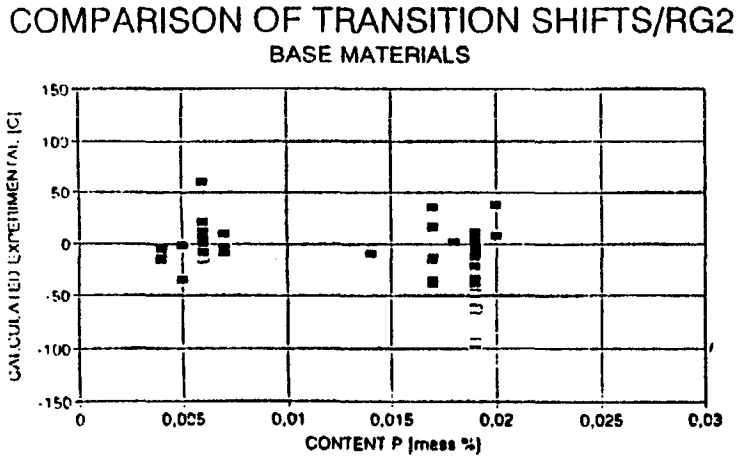

Fig. 21 ■ BM/Tirr = 290 C = BM/Tirr = 270 C

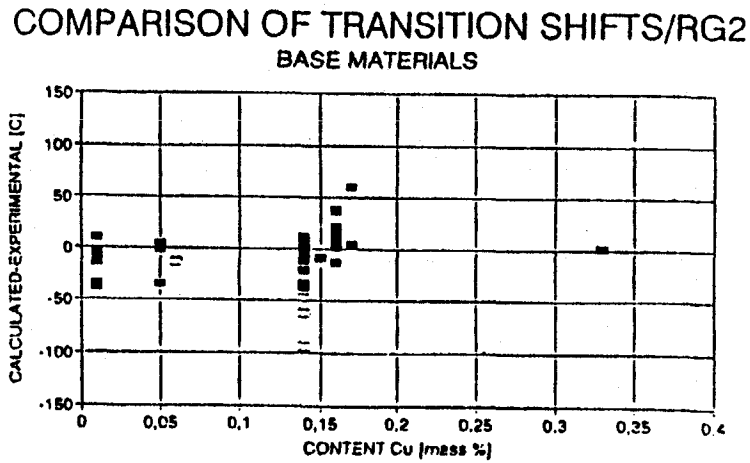

Fig. 22 ■ BM/Tirr = 290 C = BM/Tirr = 270 C

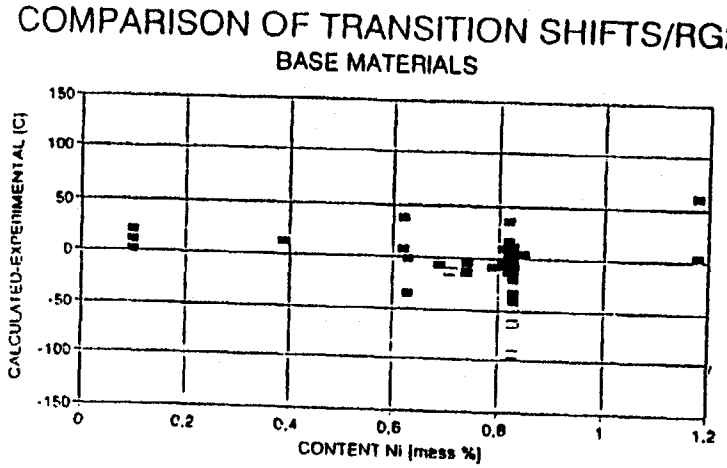

Fig. 23 ■ BM/Tirr = 290 C □ BM/Tirr = 270 C

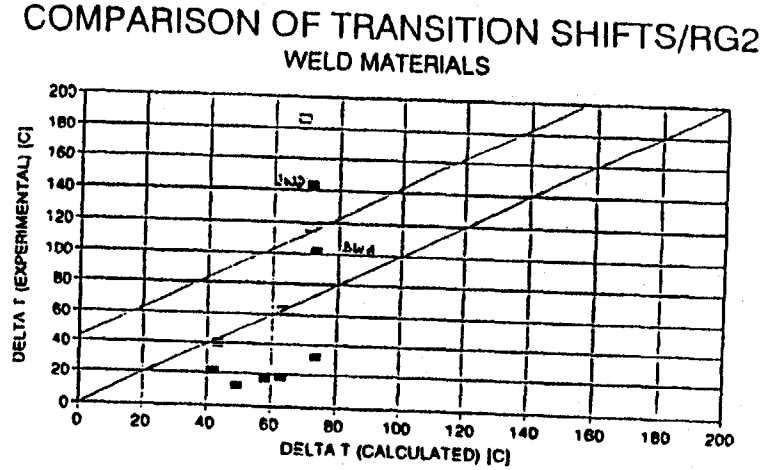

Fig. 24 ■ WM/Tirr = 290 C □ WM/Tirr = 270 C

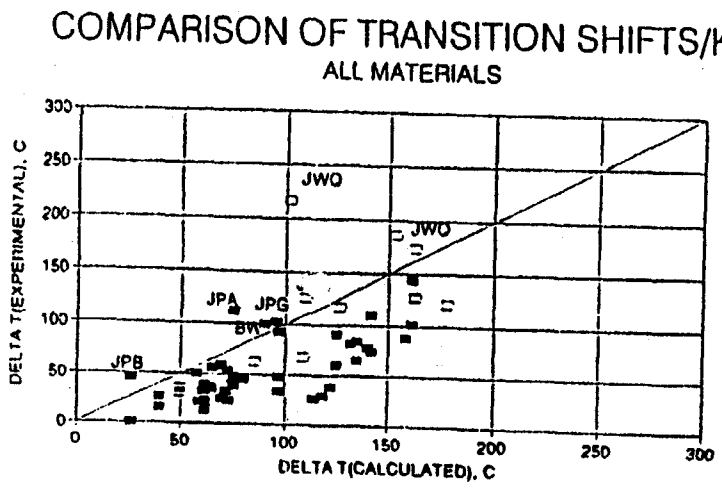

Fig. 25 ■ Tirr = 290 C □ Tirr = 270 C

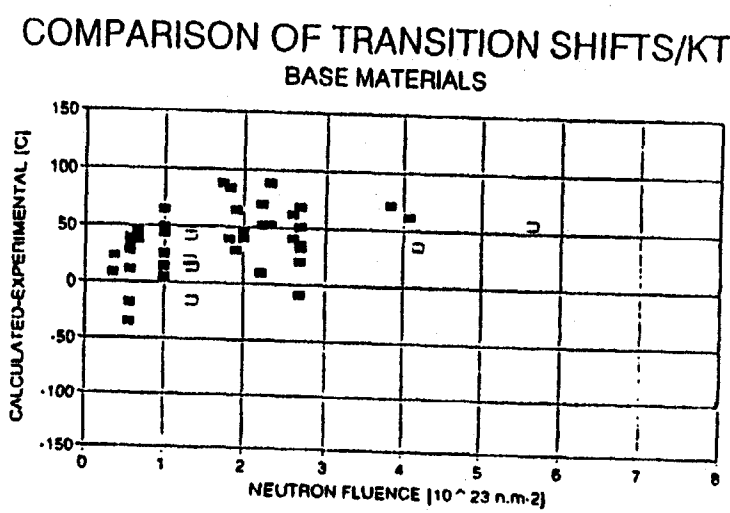

Fig. 26 ■ BM/Tirr = 290 C □ BM/Tirr = 270 C

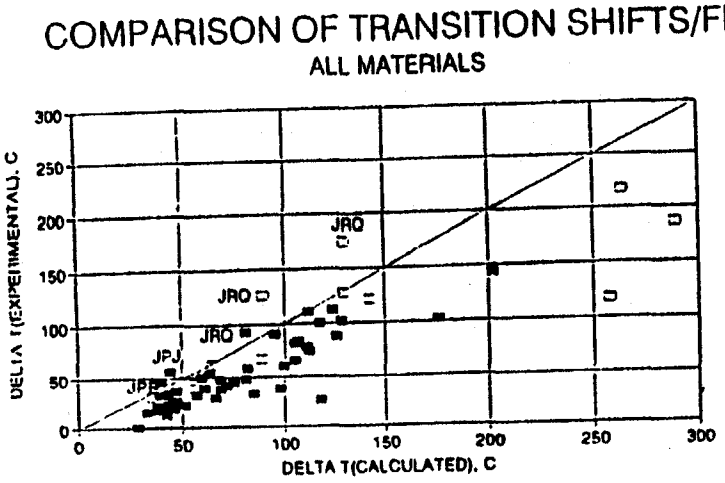

Fig. 27

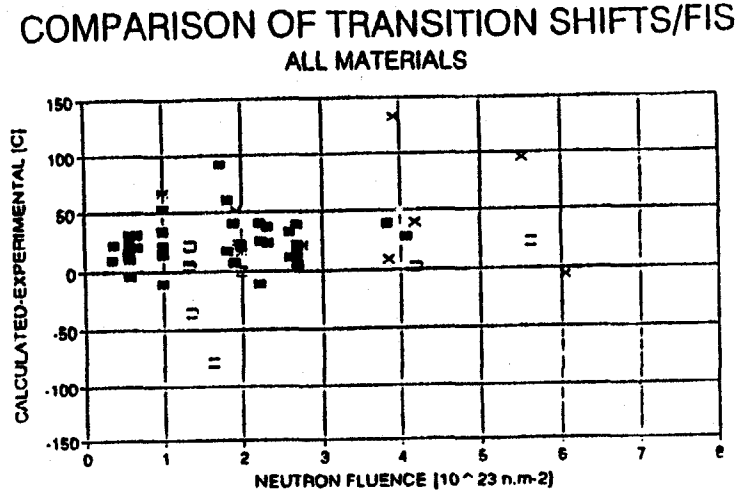

Fig. 28

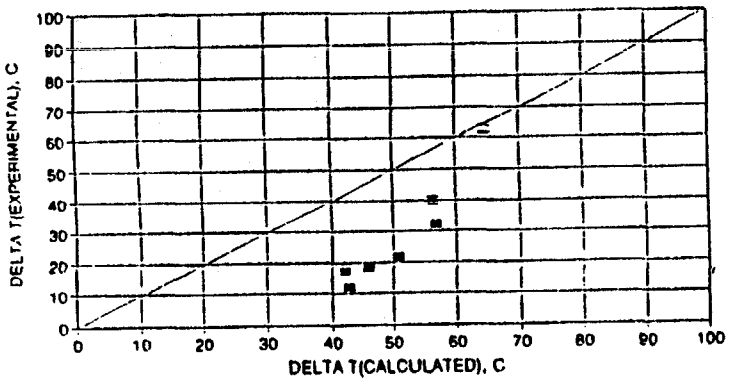

Fig. 29

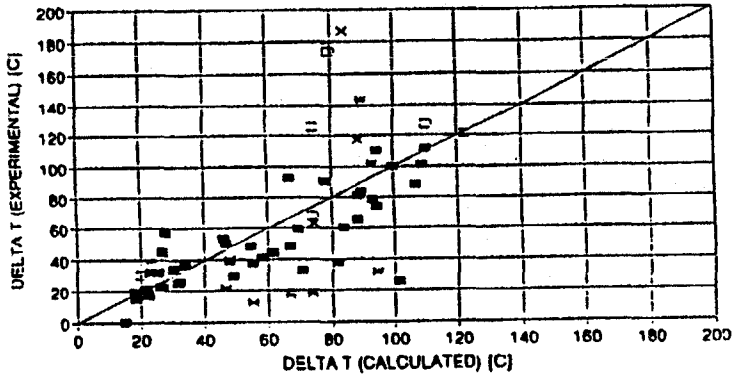

Fig. 30

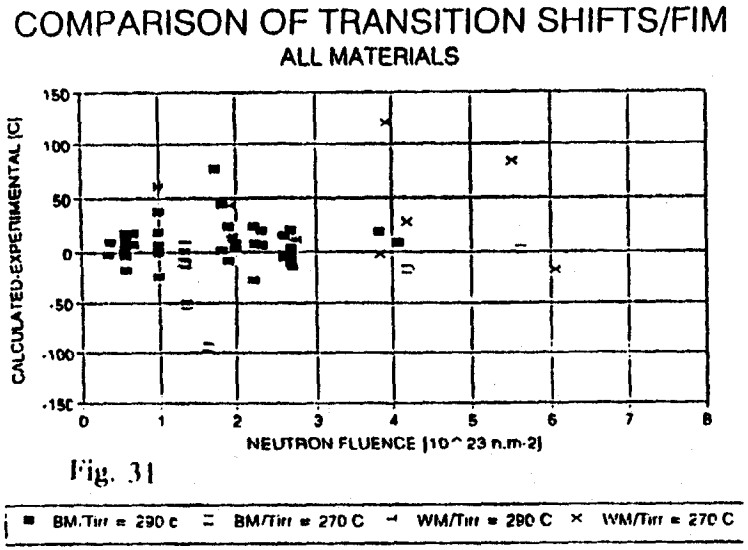

Fig. 31

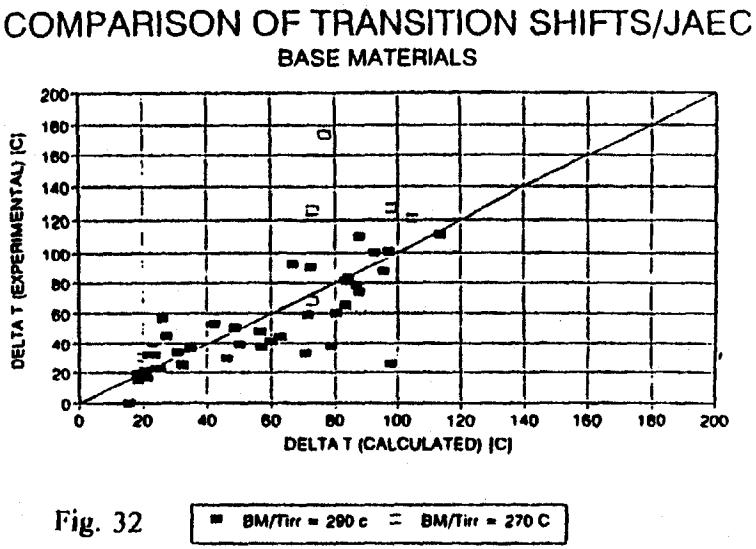

Fig. 32

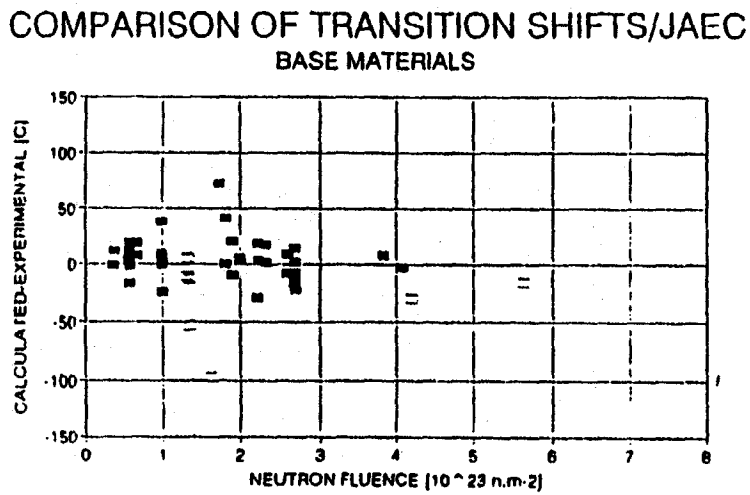

Fig. 33

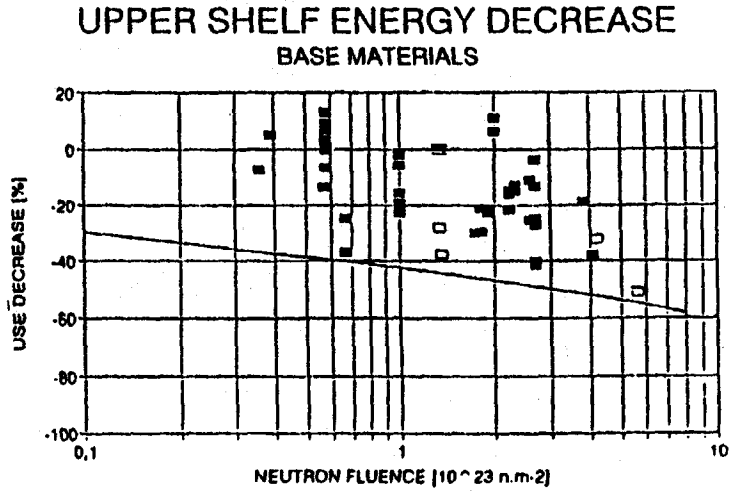

Fig. 34

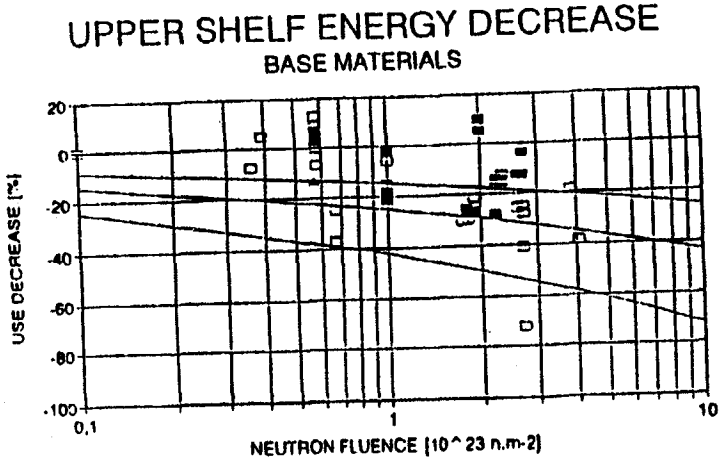

Fig. 35

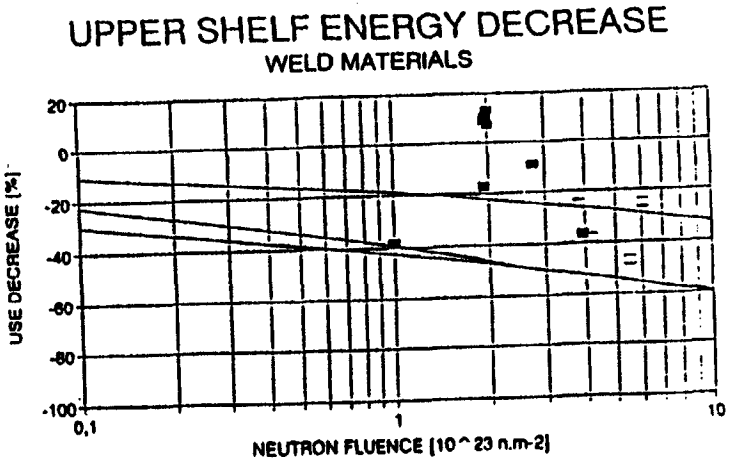

Fig. 36

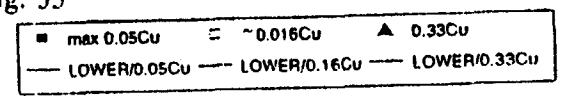

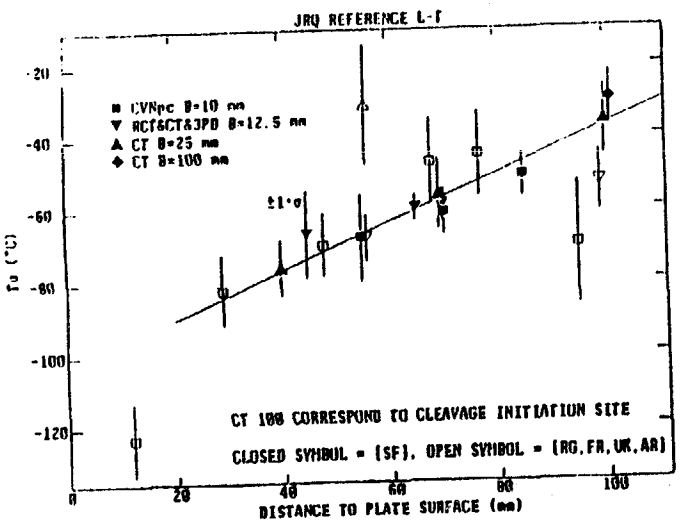

Fig. 37

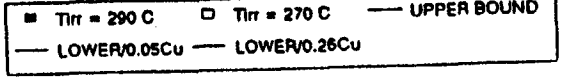

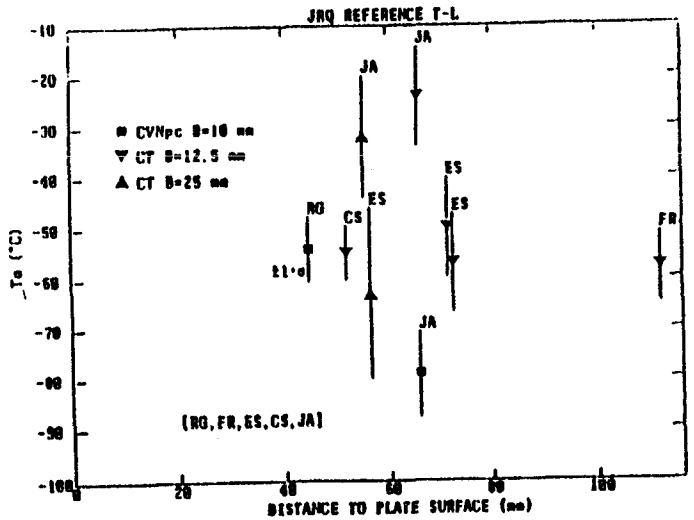

Fig. 38

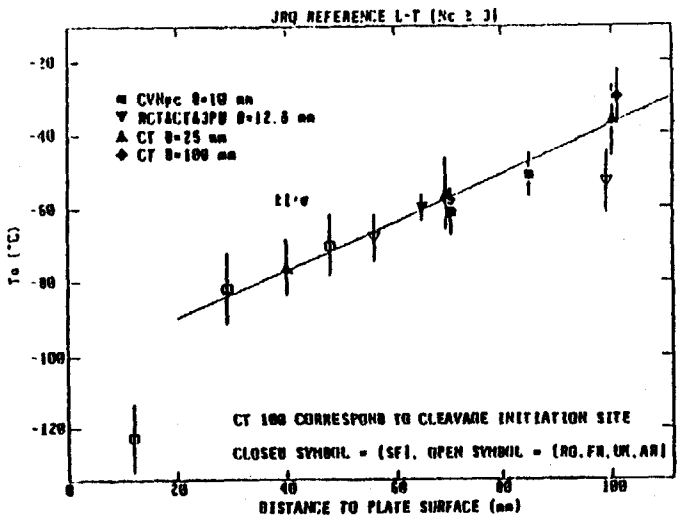

Fig. 39

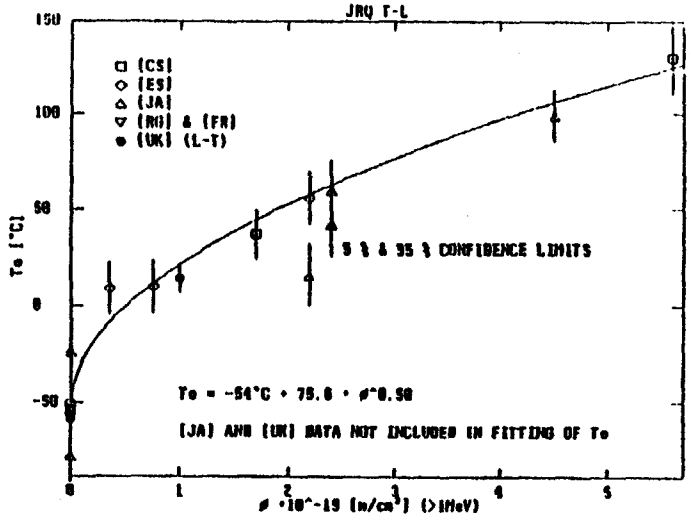

Fig. 40

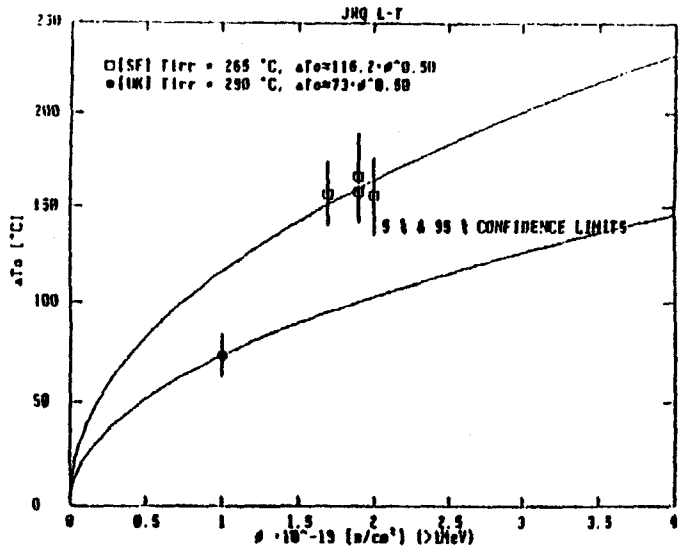

Fig. 41

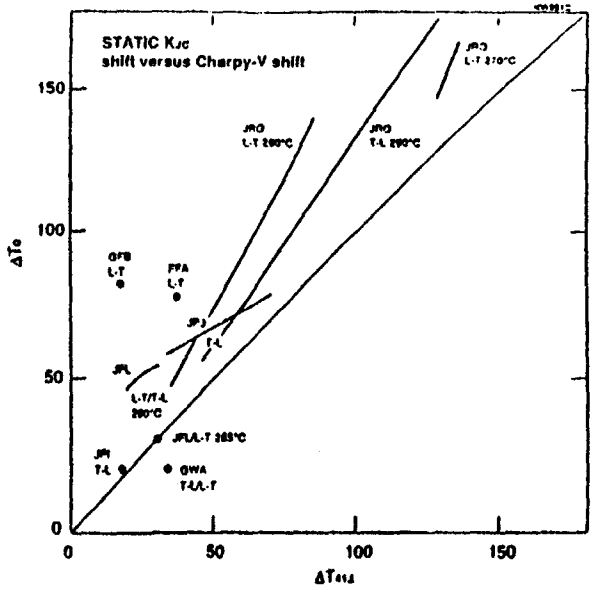

Fig. 42

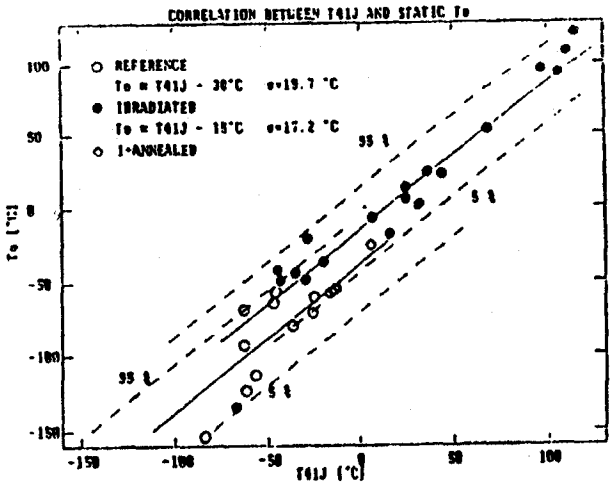

Fig. 43

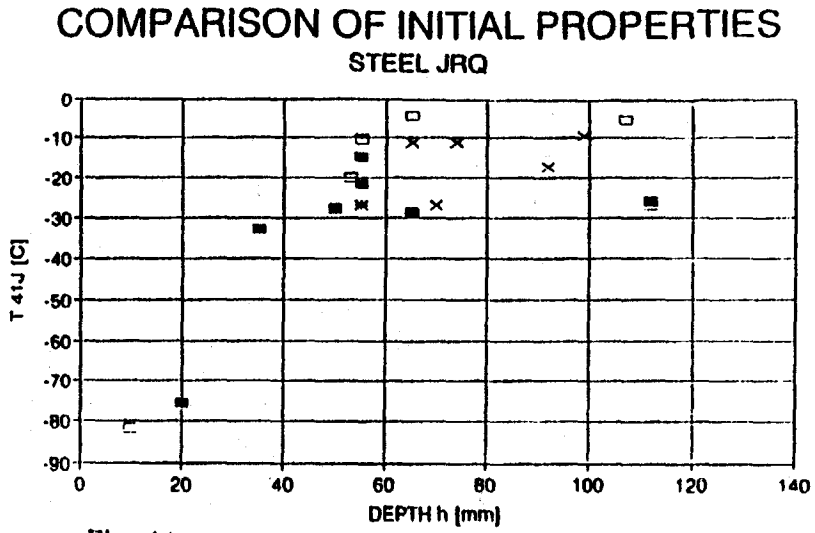

Fig. 44

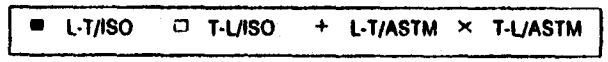

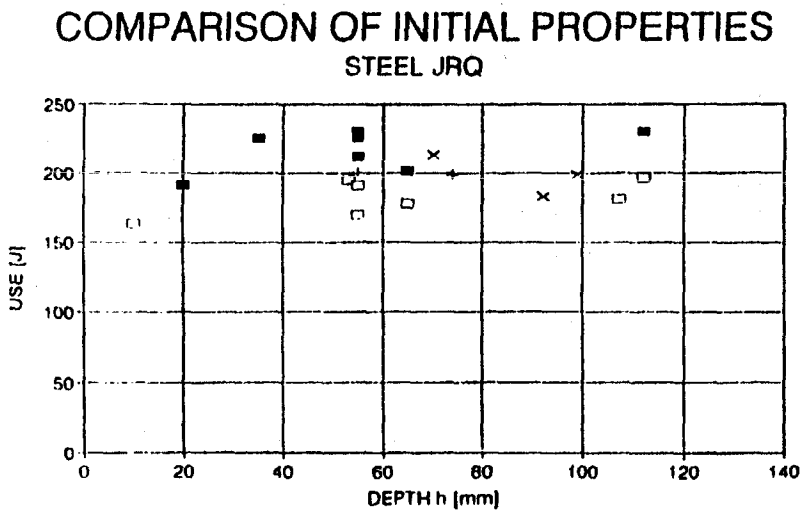

Fig. 45

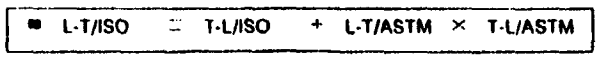

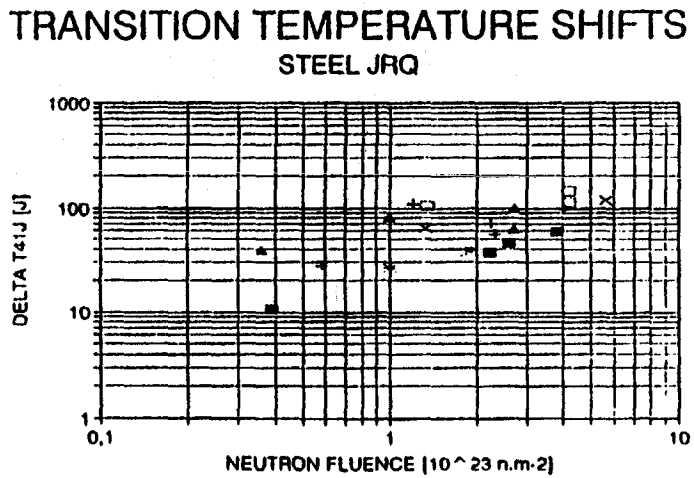

Fig. 46

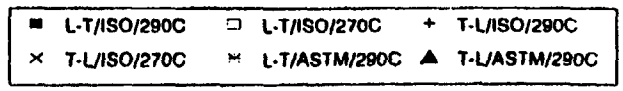

TRANSITION TEMPERATURE SHIFTS

ALL MATERIALS

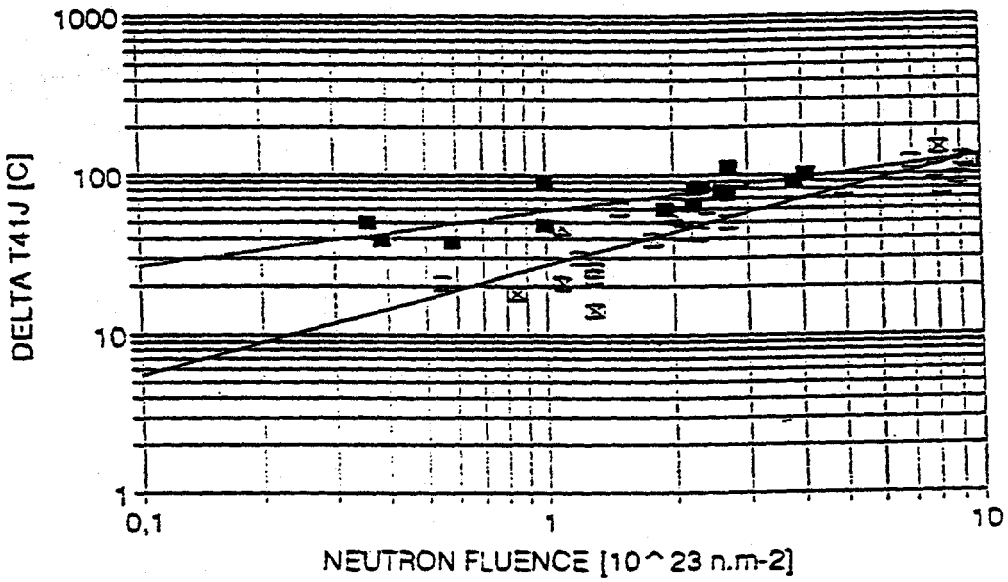

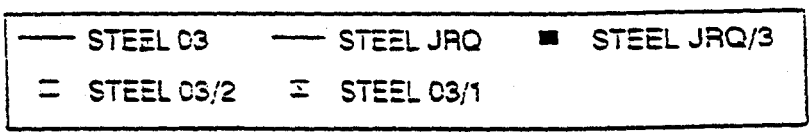

Fig. 47

ANNEALING BEHAVIOUR OF LOVIISA-1 SURVEILLANCE MATERIALS MEASURED WITH V-NOTCHED SPECIMENS AND THE CURRENT STATUS OF VESSEL ANNEAL

Matti Valo*, Jyrki Kohopää**, Kim Wallin* and Tapio Planman*

*VTT Manufacturing Technology, P.O. BOX 17042, 02044, Finland
**IVO International Ltd, 01019 IVO, Finland

ABSTRACT

The reactors of Loviisa NPP were the first WWER 440 type reactors, which had a plant specific surveillance programme. The higher than predicted irradiation embrittlement of the core weld material was discovered at an early stage of the reactor operation and in spite of the applied core reduction it was clear that vessel annealing could possibly be required for the later years of reactor operation. Annealing and reirradiation research programmes were started based on the available surveillance material. Due to the limited amount of material subsize specimens and specimen reconstitution had to be used in the studies. The effect of annealing parameters (time / temperature) on annealing recovery was studied with 3mm x 4mm x 27 mm subsize Charpy-V specimens. The range of variation of the annealing parameters was considerable wider than specified for a real vessel annealing in order to rule out any long term or unexpected effects. The annealing behaviour was also measured with ISO Charpy-size V-notched and fracture toughness specimens for the condition 475 °C / 100h, which was chosen to be applied in practice. Annealing recovery data is presented in the paper.

Loviisa Unit 1 was annealed in August 1996 after nineteen years of operation. The annealing is shortly described in the paper.

INTRODUCTION

The Loviisa Nuclear Power Plant owned by Imatran Voima Oy (IVO) consists of two WWER-440 units. The first unit was commissioned in 1977 and the second unit in 1980. The unexpectedly high embrittlement rate of Loviisa-1 weld material was observed in the first surveillance tests in 1980. Since then several plant modifications and other measures have been carried out by the utility in order to mitigate embrittlement and to ensure the integrity of the reactor pressure vessel.

In 1993 the utility decided to anneal the core weld of Loviisa-1 during the 1996 outage. IVO International Ltd started the preparation and licensing work for the annealing at the beginning of 1994. Licensing of the RPV annealing consists mainly of material investigations and the analyses of thermal and stress loads in the vessel during the annealing process.

MATERIAL RESEARCH PROGRAMMES

It is clear that the shortage of time and relevant materials complicated the creation of an annealing and reirradiation data. Because the irradiation history of the vessel wall materials can not be reproduced, extrapolations concerning the applied fluences and fluence rates have to be made. The operating licence is also issued for a limited time span, which means that the requirements on material data will change in time. At first data on material annealing behaviour is required, later on the reirradiation behaviour will be the dominating factor in defining the material properties and at a longer term it is conceivable that better theoretical understanding of fracture mechanisms and achievements in measuring techniques can introduce new requirements.

The material research programmes supporting the annealing and postannealing operation of Loviisa units are described in Table. 1.

The full programme is considered to provide the required information in due time. Because only relatively low fluence rate irradiations are considered relevant, the programme can not be accelerated.

Table 1. Material research programmes supporting the operation of Loviisa-1 after the vessel anneal.

programme	material	irradiation	number of irradiated specimens	material conditions to be measured	measured properties	duration*
extended surveillance	Lo-1 surv	Lo-surv	-	U, I, IA, IAI	CH-V, KLST, K_{JC}	-5 to +5
extended surveillance	Lo-2 surv	Lo-surv	-	U, I, IA, IAI	CH-V, KLST, K_{JC}	-5 to +5
accelerated surveillance for annealing	tailored weld HAZ+cladd	MTR**	292	U, I, IA, IAI, IAIA, IAIAI	CH-V, K_{JC}	-1 to +1
surveillance for annealing	tailored weld	Lo-surv	236	U, I, IA, IAI, IAIA, IAIAI	CH-V, K_{JC}	0 to +10

U unirradiated reference condition
I irradiated condition

A	annealing
IA	irradiated and annealed, etc.
CH-V	ISO Charpy-V
KLST	subsize Charpy-V
K_{Jc}	cleavage fracture toughness measured with ISO Charpy-size specimens
*	approximate duration of the programme in relation to vessel annealing
**	irradiated Dimitrovgrad by MOHT OTJIG

THE MEASURED ANNEALING BEHAVIOUR OF LO-1 SURVEILLANCE MATERIALS

Loviisa-1 surveillance material

The utilisation of the original surveillance material for annealing and reirradiation measurements is defined as extended surveillance. The purpose of the original surveillance was the measurement of irradiation response of the vessel materials. Further utilisation of the material requires the application of specimen reconstitution technique and the use of subsize specimens.

A good starting point for the extended surveillance is the rather large number of original surveillance specimens in Loviisa reactors. The number of irradiated surveillance specimens is given in Table 2. The weld portion in HAZ specimens is the same material as surveillance weld.

Table 2. Number of irradiated Charpy-size surveillance specimens in one Loviisa unit. Tensile specimens are not given because they were not reconstituted. In addition Charpy-size ageing specimens are available.

material	specimen type		number of sets	number of specimens
	CH-V	$CH_{PRECRACKED}$		
base	12	12	6	144
weld	12	12	6	144
HAZ	12	12	6	144
			total number	432

The cores of the units Loviisa-1 and Loviisa-2 were reduced after tree and one year of operation respectively. Most of the irradiation sets has experienced mixed fluence rate irradiations. After annealing the operation of Loviisa-1 will be continued with the reduced core. Hence the irradiation history of surveillance specimens and the reactor vessel is relatively complicated and the irradiation parameters are not mutually well comparable. The parameters characterising the neutron load histories are given in Table 3.

Chemical composition of the materials is given in Table 4.

Table 3. Neutron characteristics of the surveillance position and the inner pressure vessel wall near the weld seam. The numbers refer to circumferential or axial maximum.

core loading	surveillance position		vessel wall	
	fluence[1)]	fluence rate[2)]	fluence[1)]	fluence rate[2)]
full core	16 (3 years[3)])	20	0.9 (3 years[3)])	1.05
reduced core	2.1 (3 years)	2.4	1.5 (30 years[3)])	0.17

1) in units [10^{19} n/cm^2, E> 1 MeV]
2) in units [10^{11} n/cm^2 s, E> 1 MeV]
3) Loviisa-1 was operated 3 years with full core, outages included

Table 4. Chemical composition of Loviisa-1 surveillance materials.

material	C	Si	Mn	S	P	Cr	Ni	Mo	V	Cu
forging 12Х2МФА	0.15	0.30	0.49	0.017	0.010	2,56	0.15	0.67	0.34	0.16
Weld 10ХМФТ	0.05	0.39	1.20	0.010	0.030	1.38	0.17	0.48	0.22	0.14

Experimental test programme

Because material data for licensing the annealing of the pressure vessel had to be created in a relatively short time, the research programme was based on Charpy-V and fracture toughness measurements only. No modelling or fundamental studies were undertaken. Because the determination of the transition temperature requires relatively large number of specimens, subsize Charpy-V specimens were chosen for optimising the annealing parameters. The annealing behaviour using the optimum or nominal annealing condition was then checked with ISO Charpy size V-notched and precracked specimens.

Experimental techniques

The so called KLST specimen was chosen to be used as the subsize Charpy-V specimen because it allows a good yield of new specimens. The KLST specimen is shown in Figure 1. Six new KLST specimens can be prepared with an electric wire discharge machine from one broken half of an ISO Charpy-size specimen as shown in Figure 2. If the broken halves of the KLST specimens are reconstituted (one new specimen from one broken half, which is a moderate choice) altogether 32 subsize Charpy-V tests can be performed with one original ISO Charpy size specimen i.e. nearly three new transition curves can be generated.

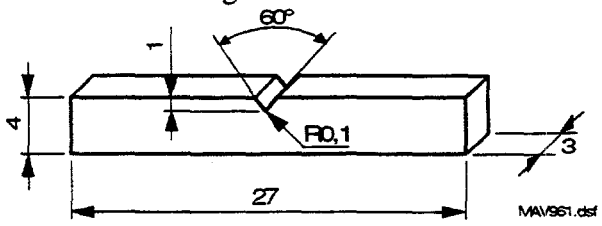

Figure 1. The KLST-specimen

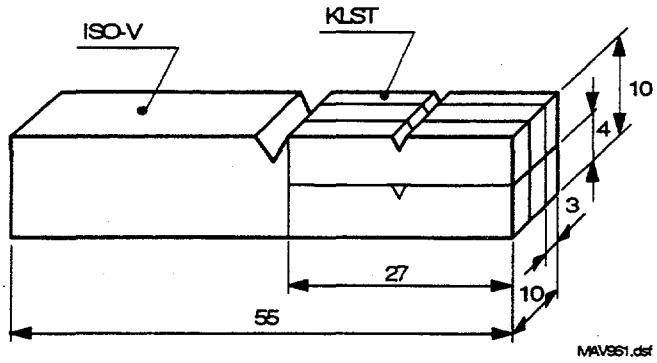

Figure 2. Sectioning of an ISO Charpy-V specimen into KLST specimens.

Specimen reconstitution using stud arch welding technique and subsequent specimen finishing with an electric discharge machine was applied in the study. Only one new Charpy-V specimen was prepared from one broken half of the original ISO or subsize specimen. Specimen reconstitution is described in detail elsewhere [1].

In the original HAZ surveillance specimens the V-notch was located relative to the fusion line with an allowance of < 1 mm, which caused considerable scatter in impact test values. The V-notch in the KLST specimens was carefully located just on the fusion line, which was identified for each specimen by etching. The accuracy in the positioning was better than 0.1 mm. The axis of the original specimens was aligned in the circumferential direction and hence the fusion line did not traverse the specimen in a rectangular way. Specimen alignment was kept in the KLST HAZ specimens but the position of the V-notch was chosen carefully in such a way that crack growth was facing the base metal as shown in Figure 4.

ISO Charpy-V tests were performed with a 300 J DIN hammer using the velocity 5.4 m / s and the KLST tests with a 15 J hammer using the velocity 3.85 m/s. Both impact hammers were instrumented. The Charpy-V transition curves were measured with 12 specimens with some exceptions.

Figure 4. Position of the V-notch in the KLST HAZ specimens.

The measured annealing behaviour

Only the behaviour of transition temperatures is considered because ductile tearing properties of Loviisa materials are of no concern. Transition temperature criteria $T_{E1.9J}$, $T_{E3.1J}$ and $T_{LE0.3mm}$ were used for KLST specimens and criteria T_{E42J}, $T_{LE0.89mm}$ and $T_{FA50\%}$ for ISO Charpy-V specimens.

HAZ in Figures 5-7. The residual embrittlement after annealing is given for the same materials in Figure 8-10.

The annealing response measured with ISO Charpy-V and KLST specimens for the 475 °C/100h annealing is given in Figures 11 and 12. The residual embrittlement after annealing for these materials is shown in Figures 13 and 14.

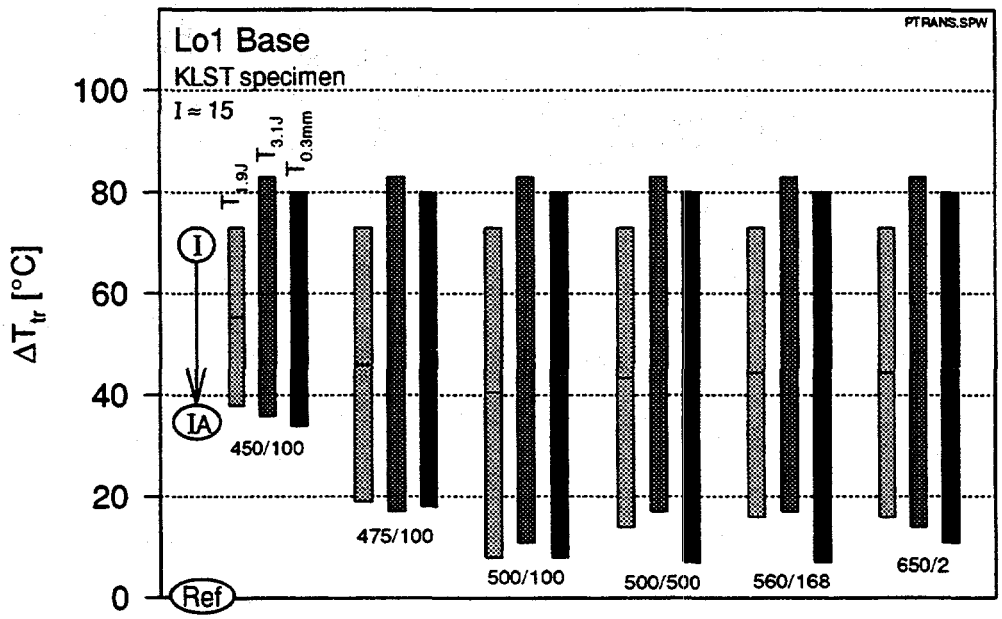

Figure 5. Transition temperature recovery in annealing for varying annealing conditions, base metal, subsize Charpy-V specimens, initial fluence 15 x 10 ^{19} n/cm^2, E> 1 MeV.

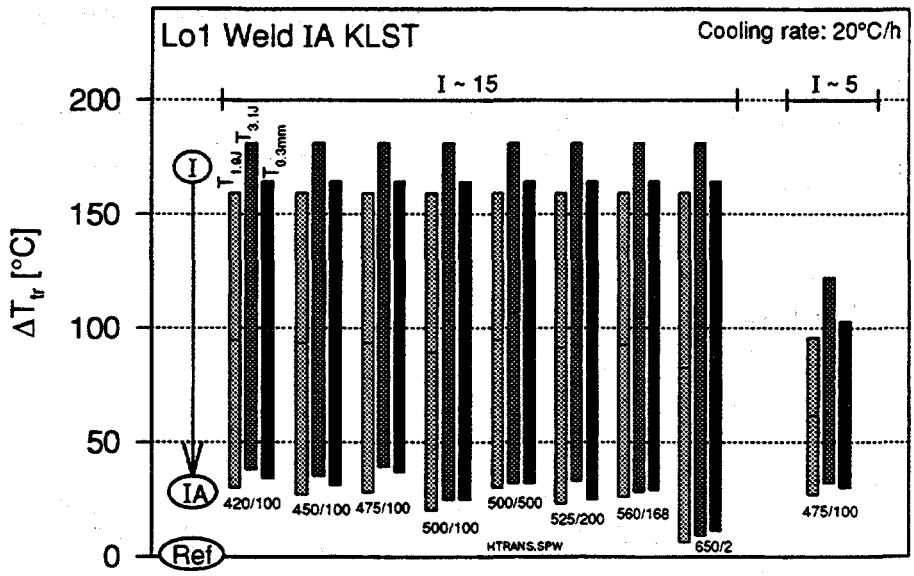

Figure 6. Transition temperature recovery in annealing for varying annealing conditions, weld, subsize Charpy-V specimens, initial fluences 5x and 15 x 10 [19] n/cm², E> 1 MeV.

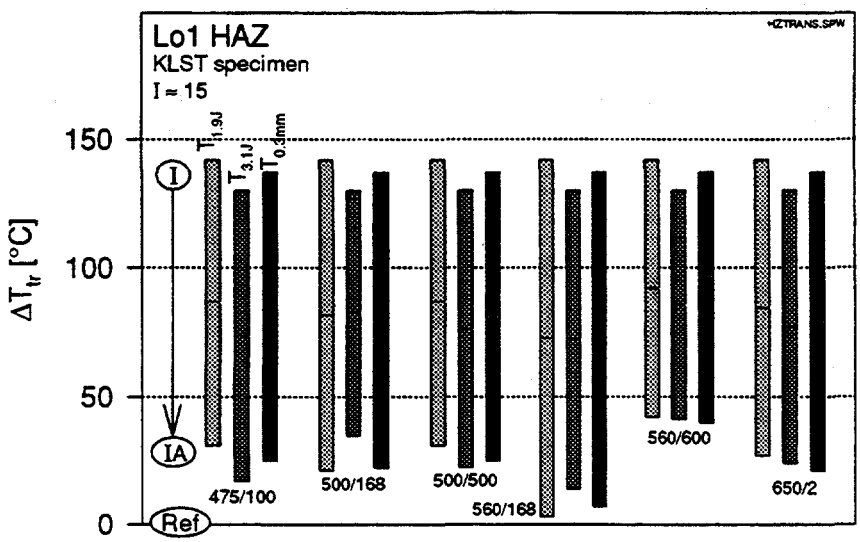

Figure 7. Transition temperature recovery in annealing for varying annealing conditions, HAZ, subsize Charpy-V specimens, initial fluence 15 x 10 [19] n/cm², E> 1 MeV.

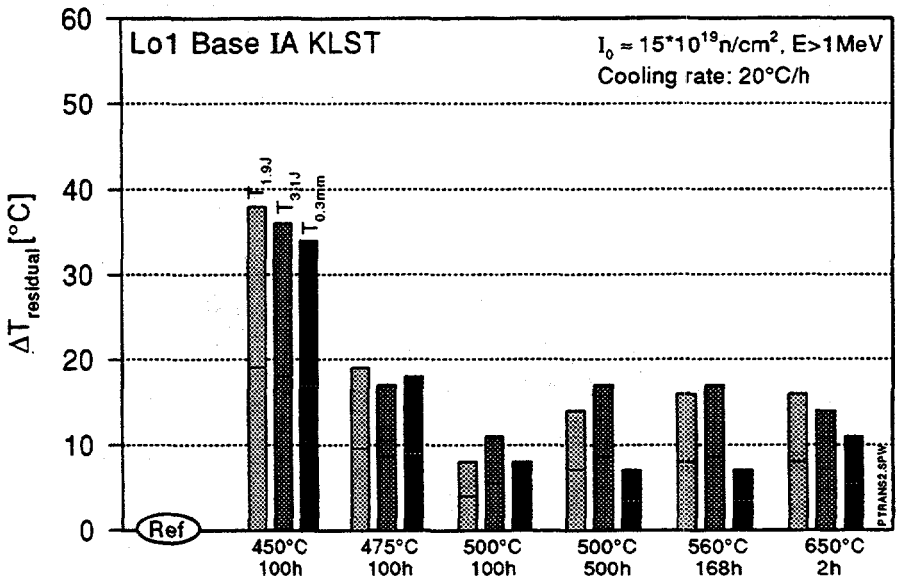

Figure 8. Residual embrittlement after annealing for varying annealing conditions, base metal, subsize Charpy-V specimen, initial fluence 15x10^{19} n/cm^2, E> 1 MeV.

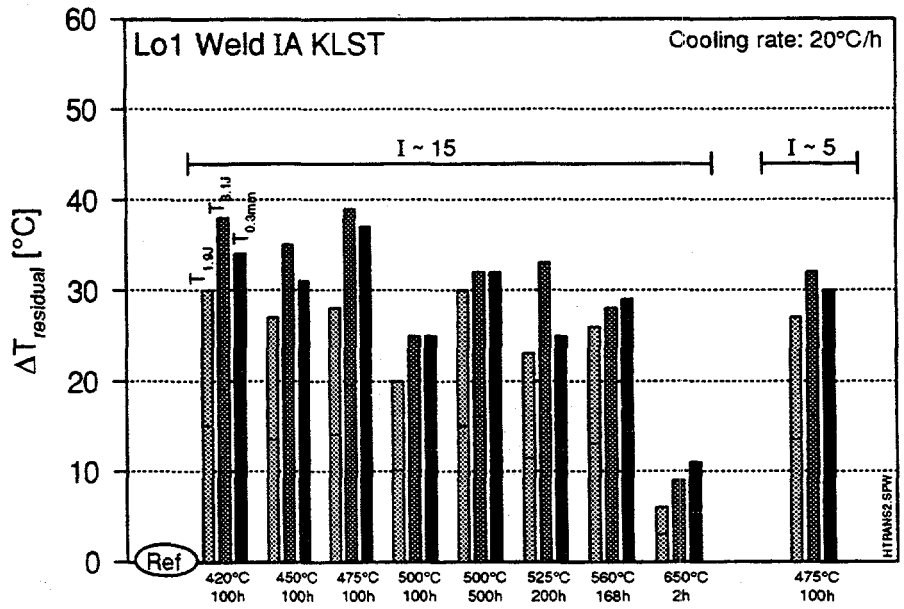

Figure 9. Residual embrittlement after annealing for varying annealing conditions, weld, subsize Charpy-V specimen, initial fluences 5x and 15x 10^{19} n/cm^2, E> 1 MeV.

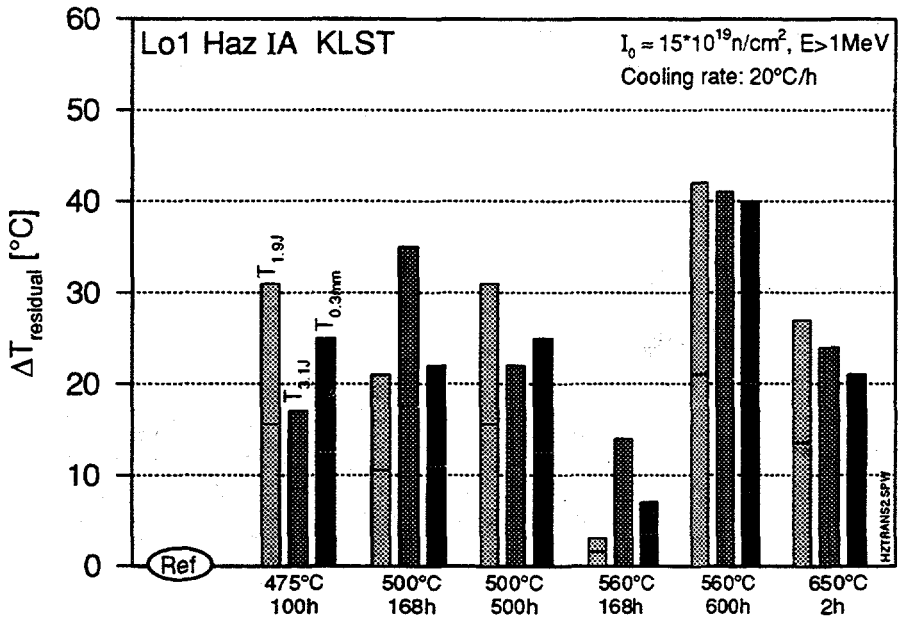

Figure 10. Residual embrittlement after annealing for varying annealing conditions, HAZ, subsize Charpy-V specimen, initial fluence 15x10^{19} n/cm^2, E> 1 MeV.

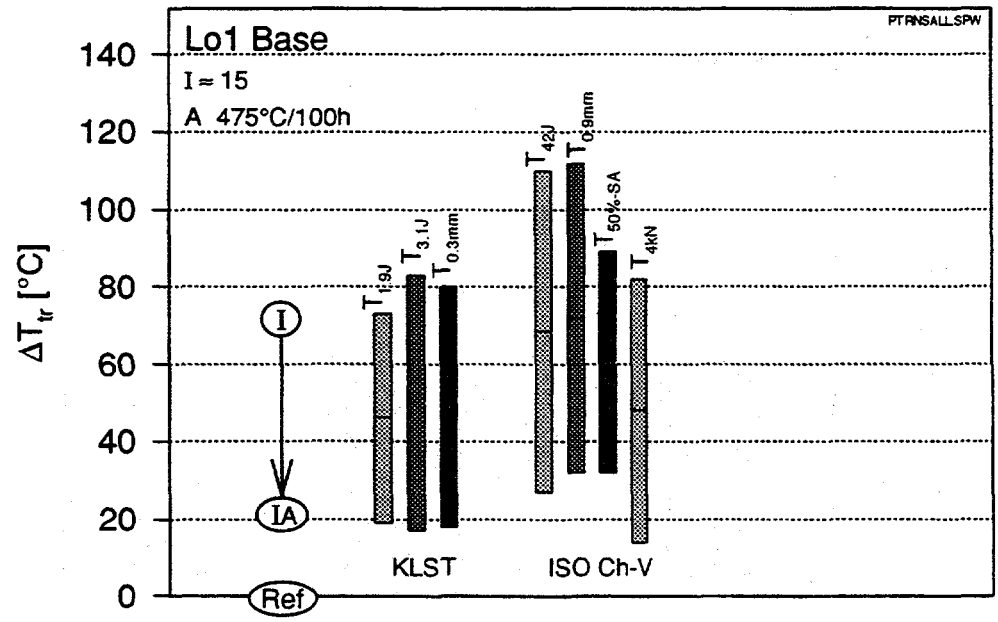

Figure 11. Comparison of annealing recovery measured with ISO Charpy-V and KLST specimens, base metal, annealing condition 475 °C / 100 h, initial fluence 15x 10^{19} n/cm^2, E> 1 MeV.

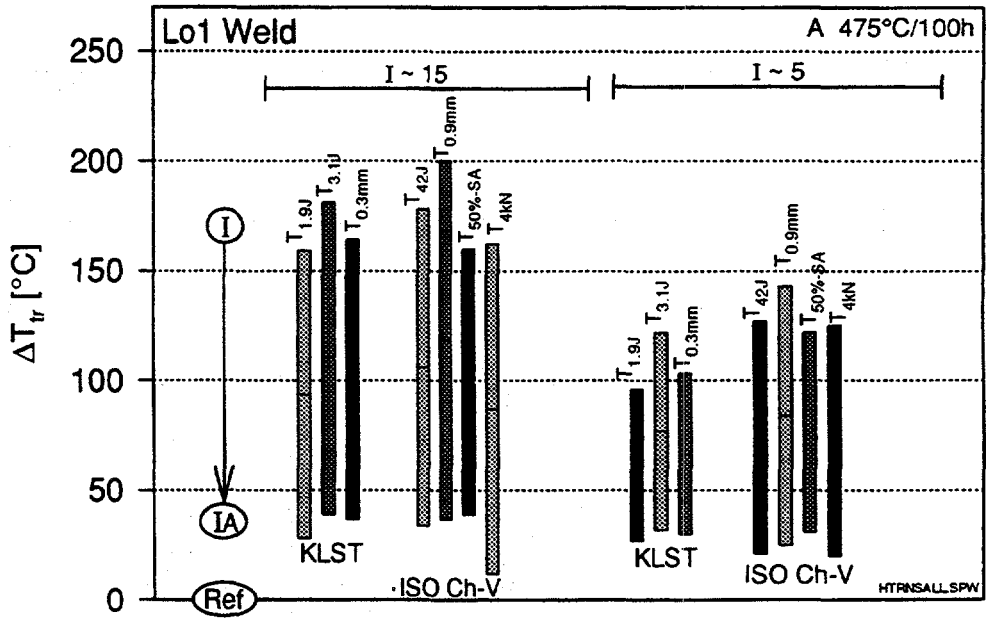

Figure 12. Comparison of annealing recovery measured with ISO Charpy-V and KLST specimens, weld, annealing condition 475 °C / 100 h, initial fluences 5x and 15x 10^{19} n/cm^2, E> 1 MeV.

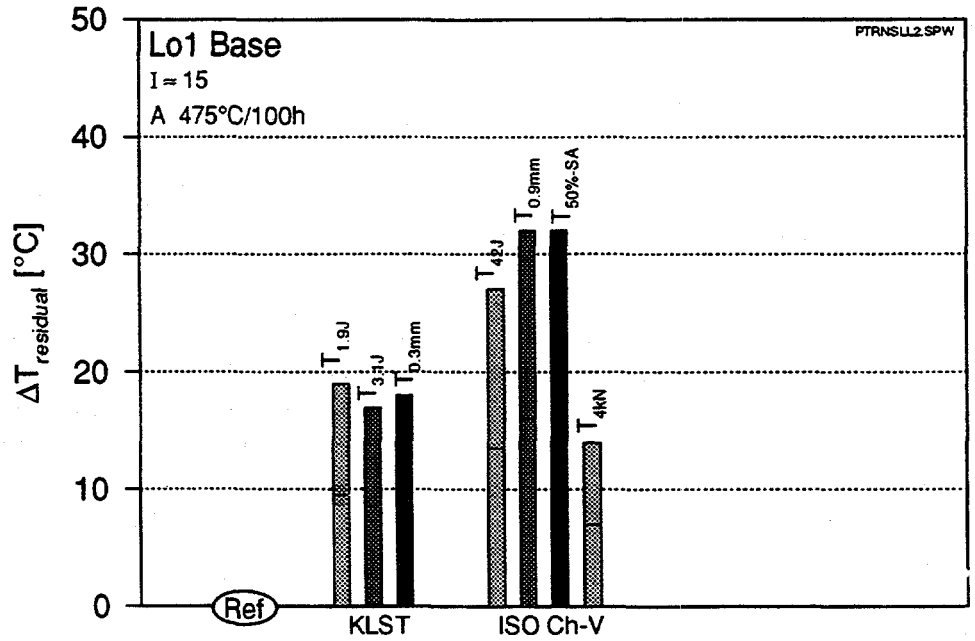

Figure13. Comparison of residual embrittlement after annealing measured with ISO Charpy-V and KLSTspecimens,base metal, annealing condition 475°C/100 h, initial fluence 15x10^{19}n/cm^2, E>1 MeV.

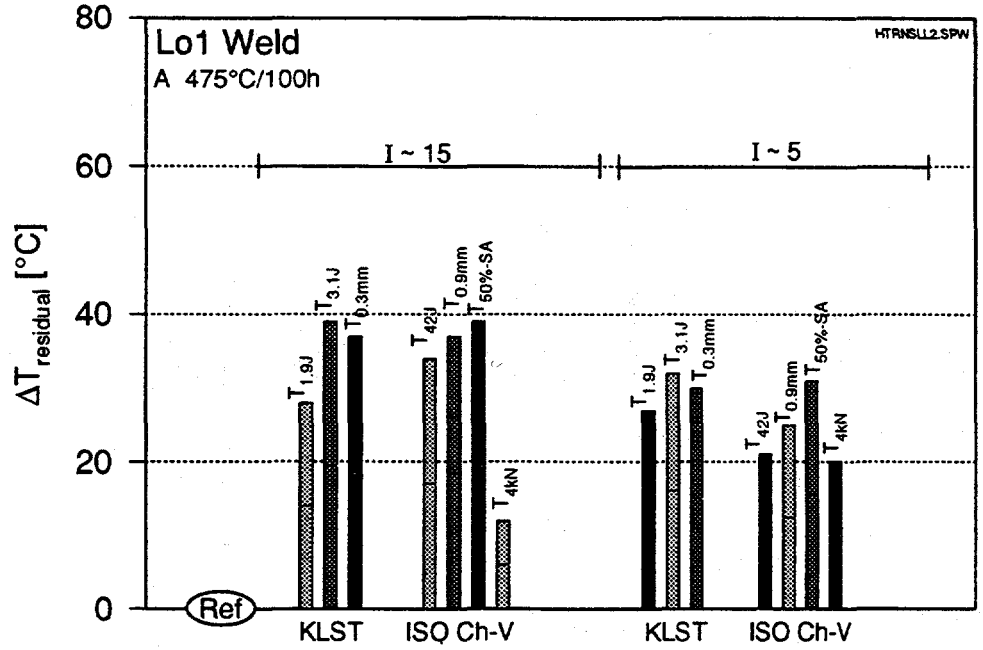

Figure 14. Comparison of residual embrittlement after annealing measured with ISO Charpy-V and KLST specimens, weld, annealing condition 475 °C/ 100 h, initial fluences 5x and 15x 10^{19} n/cm^2, E> 1 MeV.

DISCUSSION

Loviisa-1 pressure vessel materials recover rather well in thermal annealing as the Figures 5-7 indicate, the degree of recovery is approximately 80 %.

The residual shift after annealing measured with subsize Charpy-V specimens remains practically constant, when the annealing temperature is varied between 420 °C - 560 °C and the annealing time between 100 h - 500 h as shown by Figures 8-10. The residual shift values are approximately 10 °C for base metal, 30 °C for weld and 25 °C for HAZ. The measured ΔT_{res} for base metal in the 450 °C / 100h annealing is higher than for the other annealing conditions. However, this transition curve was measured with nine specimens only and the intrinsic scatter in base metal is considerably larger than in weld. Hence the higher value of ΔT_{res} measured in the 450 °C / 100h annealing for base metal is not considered to differ significantly from the other values. No optimum annealing condition could be found by varying the annealing parameters. The residual embrittlement measured within the variation range of the annealing parameters seems to be a characteristic material specific constant.

The measured value of ΔT_{res} for weld exceeds the upper limit $\Delta T_{res,\ max} = 20$ °C given earlier [ref. 2, page 14]. If the safety marginal of 20 °C proposed in the reference is taking into account, our measured values are within the proposed assessment limits.

Figures 12 and 14 indicate that for weld the residual shift is slightly dependent on neutron fluence and it is lower for lower initial fluences. When the irradiation fluences 5.1 x 10^{19} n/cm^2, E> 1 MeV and 15 x 10^{19} n/cm^2, E> 1 MeV are compared, the lower fluence gives for ΔT_{res} approximately 10 °C lower value, when measured with ISO Charpy-V specimens and app. 5 °C lower value, when measured with subsize Charpy-V specimens.

The annealing data do not reveal any clear indication of temper embrittlement in any of the pressure vessel materials. The heat treatment 560 °C / 600 h gave for HAZ ΔT_{res} = 40 °C, which is larger that the values for other heat treatment parameters. However, this variation can be accounted for the larger inherent scatter in HAZ data compared to base and weld data.

The annealing parameters measured with ISO Charpy-V and KLST specimens are compared in Figures 11-14. Several correlations accounting for the effect of specimen size on transition temperatures measured with V-notched specimens have been proposed. Siemens [3,4] has used the correlation (1) and VTT [5] has proposed the correlation (2).

$$T_{KLST} = T_{ISO\ CH\text{-}V} - 65\ °C \quad (1)$$

$$T_{KLST} = T_{ISO\ CH\text{-}V} - 38\ °C \quad (2)$$

The indexation parameters used in the correlations are given in Table 5.

Table 5. Transition temperature indexations used in the correlations.

specimen	Siemens			VTT	
	E		LE	E	LE
ISO CH-V	42 J	68 J	0.89 mm	28 J	equal
KLST	1.9 J	3.1 J	0.3 mm	3.15 J	equal

The data arranged according to Siemens correlation is given in Figures 14 and 15 and according to VTT correlation in Figures 16 and 17.

The VTT correlation gives a better description for the transition temperature shifts for weld than the Siemens correlation. Both correlations describe base metal shifts rather unsatisfactorily. For base metal the KLST specimens give smaller transition temperature shifts than the ISO Charpy-V specimens. For weld the shifts are nearly equal and hence KLST specimen is can monitor irradiation or annealing induced transition temperature shifts in Loviisa type weld at least for fluences used in the study.

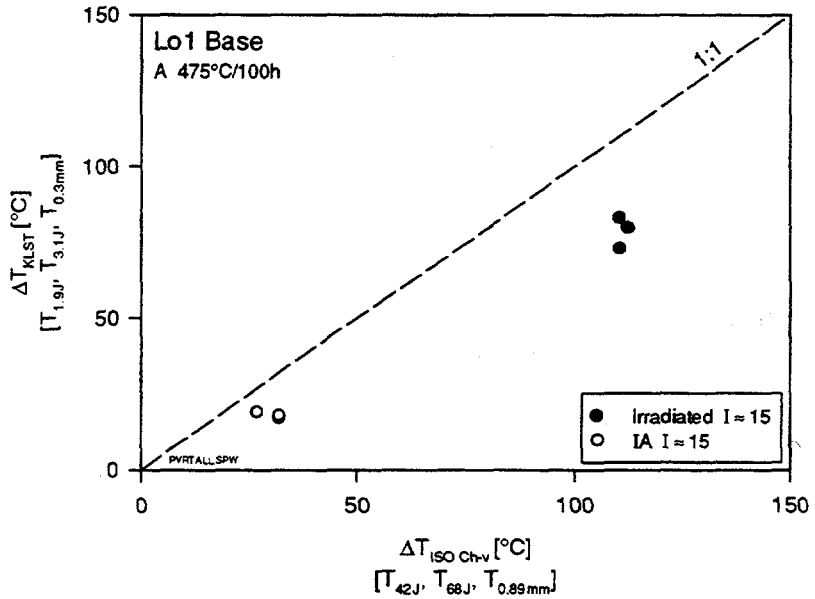

Figure 14. Comparison of transition temperature shifts measured with ISO Charpy-V and KLST specimen, base metal, irradiation fluence 15 x 10^{19} n/cm^2, E> 1 MeV, annealing parameter 475°C/ 100h. Transition temperature criteria proposed by Siemens are used.

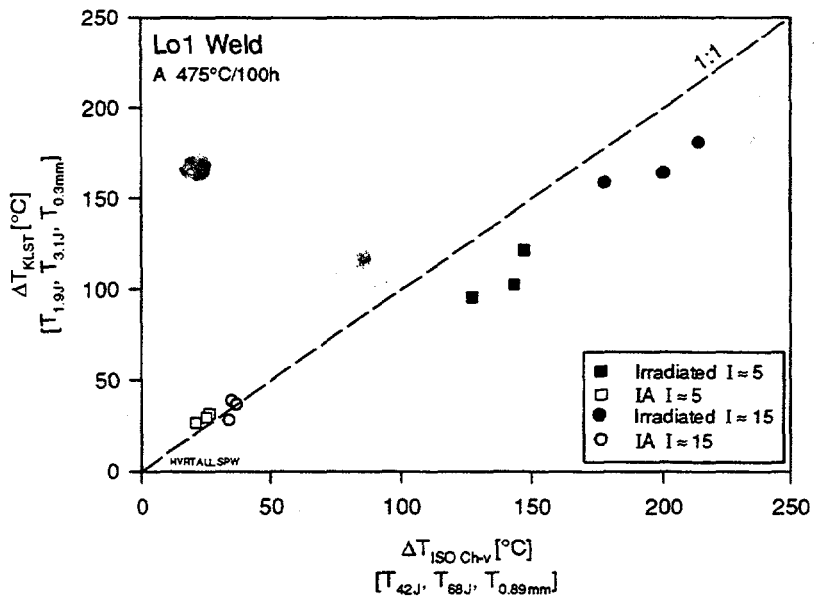

Figure 15. Comparison of transition temperature shifts measured with ISO Charpy-V and KLST specimen, weld, irradiation fluences 5x and 15 x 10 ^{19} n/cm^2, E> 1 MeV, annealing parameter 475°C/ 100h. Transition temperature criteria proposed by Siemens are used.

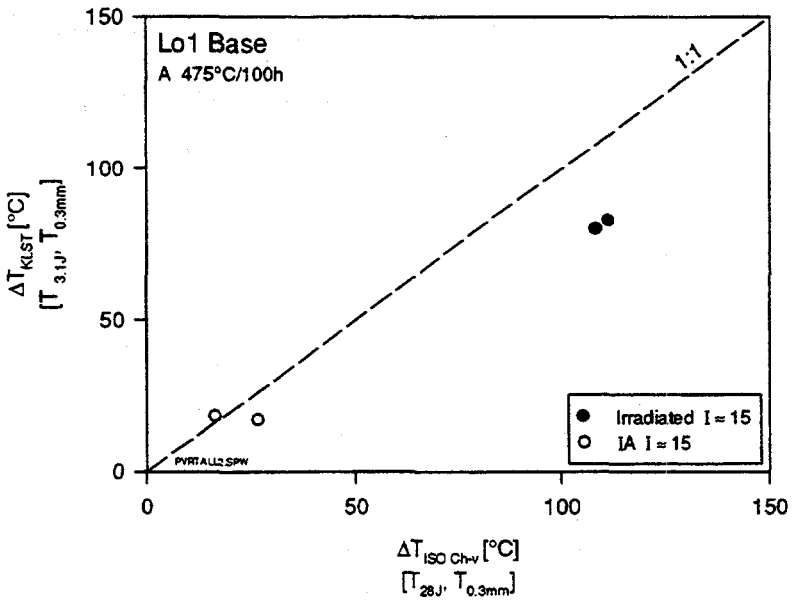

Figure 16. Comparison of transition temperature shifts measured with ISO Charpy-V and KLST specimen, base metal, irradiation fluence 15 x 10 19 n/cm2, E> 1 MeV, annealing parameter 475°C/ 100h. Transition temperature criteria proposed by VTT are used.

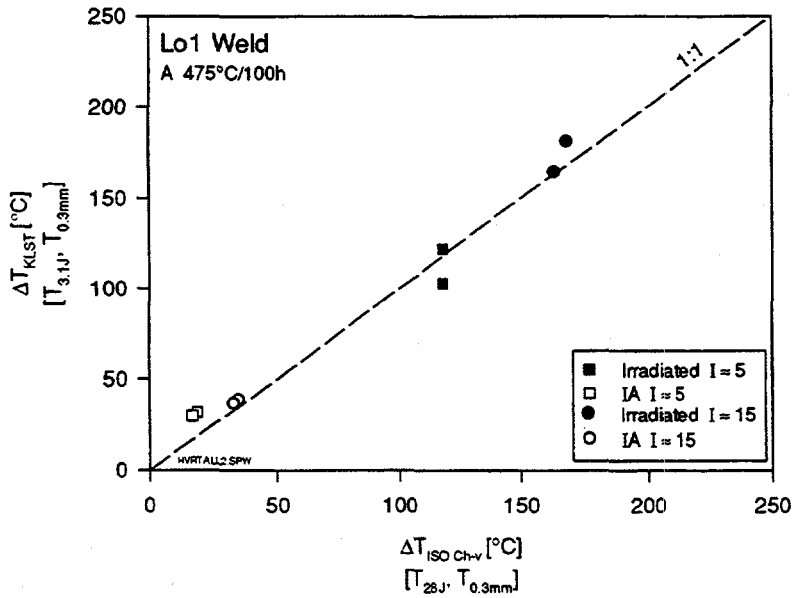

Figure 17. Comparison of transition temperature shifts measured with ISO Charpy-V and KLST specimen, base metal, irradiation fluences 5x and 15x 10 ^{19} n/cm^2, E> 1 MeV, annealing parameter 475°C/ 100h. Transition temperature criteria proposed by VTT are used.

The crack arrest fracture toughness $K_{ia}(T)$ is found to correlate surprisingly well with a temperature derived from crack arrest load measured in a ISO Charpy-V test [6]. The temperature

corresponding to a 4 kN arrest load is used for indexation. The correlation is shown in Figure 18. The recovery of the T_{4kN} crack arrest temperature is shown in Figures 11-12 and the respective residual temperatures in Figures 13-14. The residual shifts after annealing for the crack arrest temperature are clearly lower than the residual shift for the initiation temperature.

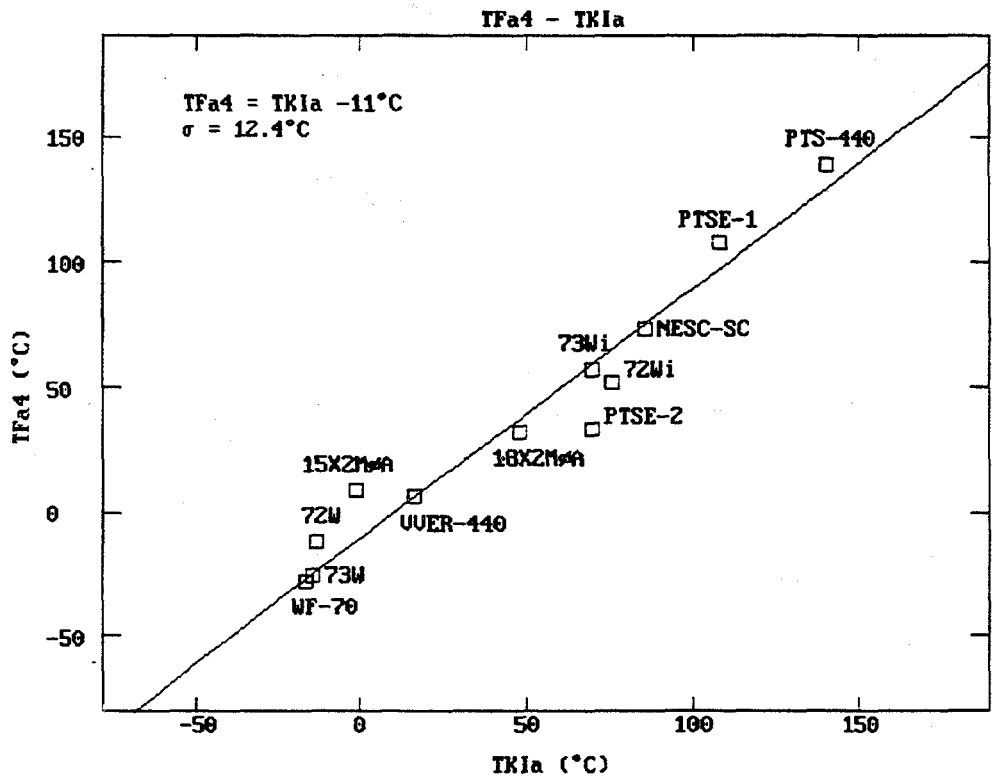

Figure 18. The K_{Ia}-T_{Fa4kN} correlation

VESSEL ANNEALING

The critical circumferential core area weld of Loviisa 1 reactor pressure vessel was annealed during the refuelling and maintenance outage in August 1996. The work was implemented by Skoda Nuclear Machinery Ltd as a main supplier representing consortium of Skoda Nuclear Machinery Ltd from Czech Republic and Bohunice Nuclear Power Plant from Slovak Republic.

The annealing parameters were established based on material investigations and stress analysis. A target value for the annealing temperature range was 465 - 505°C and for heating/cooling rate 20°C/h. According to the results of the material investigations about 80% recovery of the transition temperature shift caused by irradiation embrittlement can be achieved using the above mentioned annealing parameters.

The recovery annealing was performed using an electrical heating device owned by Bohunice NPP. The control system of the annealing device was accurate and the target annealing parameters were maintained on the inside and outside surfaces of the RPV wall with sufficient margins. During the 100 hours of dwell time the lowest measured temperature on the outside surface of the annealed core weld was 475°C and the highest measured temperature on the inside surface of the annealed weld was 500°C.

According to the on-line stress monitoring system used, stresses in the RPV wall caused by local heating of the weld area were less than 100 MPa including heating and cooling periods. Naturally, thermal stresses of the austenitic cladding were much higher and some plastic deformation occurred in the cladding material. There were about 40 thermocouples installed in different parts of RPV for establishing the correct temperature field for stress calculations.

After vessel annealing new sets of surveillance chains i.e. surveillance programme for vessel annealing was installed in the Loviisa 1 RPV. The same tailored weld, which was used in the accelerated vessel surveillance programme, is used also for the surveillance of vessel annealing. The new program will be used for following the re-embrittlement of the weld material and it will also provide data for a possible second annealing of the pressure vessel in the future. The scope of the surveillance program is given in Table 1.

CONCLUSIONS

The annealing studies performed with Loviisa-1 surveillance materials allow the following conclusions to be made.

- Toughness properties of Loviisa type pressure vessel materials recover well in annealing and the residual shift does not depend on the annealing parameter within a rather large range of parameter variation. Hence no optimum condition can be defined based on annealing behaviour only. It is clear that the reembrittlement after annealing will be the dominating factor, which defines material properties during the postannealing operation. Reembrittlement might well be more sensitive to the detailed annealing condition but this data was not available at the time of vessel annealing.

- No evidence of temper embrittlement was found in the annealing studies. However, it is also expected that temper embrittlement, if existing at all, will show itself in reirradiation.

- The KLST specimen is capable of monitoring transition temperature shifts in irradiation and annealing for weld metal equally well as ISO Charpy-V specimen, if VTT type of correlation is used. The ISO CH-V versus KLST transition tenmperature correlation does not work satisfactorily for base metal.

- There is a rather large inconsistency in the fluence-, fluence rate- and time in irradiation-parameters between the values, which the surveillance materials and the pressure vessel wall materials will experience. The applied core reduction also further complicated the irradiation histories. Hence post mortem studies of pressure vessel materials, which have experienced relevant operating conditions, are of great importance, when fracture properties of the operating

vessel will be assessed. The closed Greifswald plants are in most respects identical to the operating WWER 440 units.

REFERENCES

[1] Valo, M., and Ahlstrand, R.., "Application of Reconstitution Welding Technique for Studying Base Metal of a Novovoronesh Unit-1 Trepan Sample", *Small Specimen Test Techniques Applied to Nuclear Reactor Vessel Thermal Annealing and Plant Life Extension, ASTM STP1204*, W.R.Corwin,F.M.Haggag, and W.L.Server, Eds., American Society for Testing and Materials, Philadelphia, 1993.

[2] Report, WWER-440 MODEL 230 REACTOR PRESSURE VESSEL EMBRITTLEMENT AND ANNEALING, Extrabudgetary Programme on the safety of WWER NPPS, WWER-RD-72, September 9, 1994, IAEA, Vienna.

[3] Klausnitzer, E.N., Micro-specimens for mechanical testing. Materialprüfung **33** (1991) **5**, p.132-134.

[4] Amayev, A.D., Badanin, V.I., Kryukov, A.M., Nikolaev,V.A., Rogov, M.F., and Sokolov, M.A., " Use of Subsize Specimens for Determination of Radiation Embrittlement of Operating Reactor Pressure Vessels", Small Specimen Techniques Applied to Nuclear Reactor Vessel Thermal Annealing and Plant Life Extension, ASTM STP 1204, W.R.Corwin,F.M.Haggag, and W.L.Server, Eds., American Society for Testing and Materials, Philadelphia, 1993,pp.424-439.

[5] T.Planman, M.Valo, K.Wallin, Comparison of Impact Test Results on Small and ISO-V Type Charpy Specimens, IAEA Specialists` Meeting on Irradiation Embrittlement and Mitigation, 23-26 October 1995, Espoo, Finland.

[6] K. Wallin, R. Rintamaa, M. Valo, T, Planman and M. Nevalainen, The VTT method for assessment of fracture resistance for structural steels from small material samples, ECF 11, Mechanisms and Mechanics of Damage and Failure, VOL. III. Ed. J. Petit, EMAS, 1996, pp.2211-2216.

EFFECTS OF THERMAL ANNEALING AND REIRRADIATION ON TOUGHNESS OF REACTOR PRESSURE VESSEL STEELS

R. K. Nanstad, S. K. Iskander, and M. A. Sokolov
Oak Ridge National Laboratory
Oak Ridge, Tennessee

A. A. Chernobaeva, Y. A. Nikolaev, A. M. Kryukov, and Yu. N. Korolev
Russian Research Center-Kurchatov Institute
Moscow, Russia

ABSTRACT

One of the options to mitigate the effects of irradiation on reactor pressure vessels (RPV) is to thermally anneal them to restore the toughness properties that have been degraded by neutron irradiation. This paper summarizes recent experimental results from work performed at the Oak Ridge National Laboratory (ORNL) to study the annealing response, or "recovery," of several irradiated RPV steels; it also includes recent results from both ORNL and the Russian Research Center-Kurchatov Institute (RRC-KI) on a cooperative program of irradiation, annealing and reirradiation of both U.S. and Russian RPV steels. The cooperative program was conducted under the auspices of Working Group 3, U.S./Russia Joint Coordinating Committee for Civilian Nuclear Reactor Safety (JCCCNRS). The materials investigated are an RPV plate and various submerged-arc welds, with tensile, Charpy impact toughness, and fracture toughness results variously determined. Experimental results are compared with applicable prediction guidelines, while observed differences in annealing responses and reirradiation rates are discussed.

DESCRIPTION OF MATERIALS AND IRRADIATION-ANNEALING CONDITIONS

The materials used for the studies described here are commonly used for the fabrication of RPVs in U.S. and Russian pressurized water reactors. Three submerged-arc welds (weld 73W and the two Midland Reactor welds) and one plate of A533 grade B class 1 steel (HSST Plate 02) are representative of materials used in U.S. reactors and have been used in a number of irradiation studies at ORNL [1,2,3]. The two Russian welds are representative of those used in VVER-440 and VVER-1000 type reactors and have been used in other studies by the RRC-KI. Table 1 provides the chemical compositions for all six of the materials. The U.S. steels are generally designated Mn-Mo-Ni steels, while the Russian welds are similar to 1.5 Cr-0.5 Mo steels. With regard to radiation sensitivity, the U.S. welds are characterized primarily by relatively high copper and low phosphorous contents, while the Russian welds have relatively low copper but high phosphorous (VVER-440) or high nickel (VVER-1000) contents. Because the VVER-1000 reactor is a newer design than the VVER-440, the welds were designed with reduced phosphorous and copper contents based on experience within Russia as well as that from Western countries. Unfortunately, the high nickel content in the VVER-1000 welds may result in relatively high radiation sensitivity in spite of the reduced phosphorous and copper contents. HSST Plate 02 is similar to the U.S. welds in most respects except for its relatively lower copper content. A summary of some basic mechanical properties for the U.S. materials is provided in Table 2 and shows that the materials exhibit a fairly wide range of Charpy V-notch (CVN) upper-shelf energies (USE) and transition temperatures. The U.S. materials have generally lower strength than the Russian welds. All the materials were postweld heat treated prior to testing.

In the ORNL experiments, the U.S. materials were all irradiated in material test reactors at a nominal irradiation temperature of 288°C (550°F) to neutron fluences ranging from about 0.5 to 2.0 × 10^{19} neutrons/cm^2 (>1 MeV); the Russian welds were irradiated under similar conditions except the VVER-440 weld was irradiated at a nominal irradiation temperature of about 270°C (518°F) because that is close to the temperature at which the VVER-440 RPV operates. For the RRC-KI experiments, two U.S. steels (HSST Plate 02 and HSSI Weld 73W) were irradiated in the Novovoronezh-5 commercial power plant at a nominal irradiation temperature of 290°C (554°F) to various fluences from about 2 to 18 × 10^{19} neutrons/cm^2 (>1 MeV). The preliminary fluences (>1 MeV) reported for the RRC-KI irradiations are estimated from the measured fluences (>0.5 MeV) using a factor provided by RRC-KI and based on previous experience. Thermal annealing experiments at ORNL have concentrated on two temperatures, 343 and 454°C (650 and 850°F). These two temperatures have been reported as the most likely "wet anneal" and "dry anneal" temperatures, respectively, for U.S. reactors [4]. Annealing times investigated by ORNL range from 24 to 336 hours, with 168 hours (one week) considered the "standard" annealing time for U.S. practice. The RRC-KI annealing experiments were conducted at 454°C (850°F) for 72 hours, except for the two reirradiation experiments wherein the specimens were annealed for 150 hours for the first anneal and 72 hours for the second anneal. The RRC-KI also conducted post-anneal reirradiation experiments for the two U.S. steels under the same conditions used for the initial irradiations.

EXPERIMENTAL RESULTS

HSSI Weld 73W was irradiated to a fluence of about 1.5 × 10^{19} neutrons/cm^2 (>1 MeV) and exhibited a CVN 41-J temperature shift of 82°C. Figure 1 provides a summary of the results of thermal annealing of Weld 73W at 454°C for various times. The percent recovery of the transition temperature (ΔTT) and USE (ΔUSE) are referenced to the shift or drop, respectively, due to irradiation, as shown below:

$$\% \text{ Recovery } TT_{ia} = \frac{TT_i - TT_a}{TT_i - TT_{unirr}} \cdot 100 ,$$

$$\% \text{ Recovery } USE_{ia} = \frac{USE_a - USE_i}{USE_{unirr} - USE_i} \cdot 100 ,$$

where TT is the transition temperature at the 41-J energy level, USE is the average upper-shelf energy, and the subscripts "i, a, ia, and unirr" refer to "irradiated, annealed, irradiated and annealed, and unirradiated," respectively. A 100% recovery indicates that the property after annealing has fully recovered its unirradiated value. Although the 41-J TT recovery does reach nearly 100%, it appears to occur at a slower rate than that of the CVN USE. However, whereas the TT recovery increase is insignificant after 96 hours of annealing, the USE recovery continues to increase even up to 336 hours and reaches recovery levels of about 200%. Figure 2 provides a summary of the annealing experiments conducted by ORNL on the four U.S. steels (more detailed discussions are available in references 5 and 6). The results of annealing at 343°C for 168 hours resulted in TT recoveries from 10 to 50%, while annealing at 454°C for 168 hours resulted in TT recoveries from about 75 to 100%. In every case at 454°C, the USE recovery exceeded 100% (over recovery). Models have been developed by Eason et al. [7] for prediction of transition temperature and upper-shelf energy

recovery as a consequence of thermal annealing. Figure 3 shows a comparison of the ORNL annealing results with the predictions of the Eason et al. model. Most of the experimental results are within ±2 standard errors of the predicted results; for the few values which fall outside of the ±2 standard error bounds, the models provide conservative predictions. Regarding the over recovery of upper-shelf energy, Figure 4 shows a plot of published data (about 105 data) comparing the % recoveries of USE and 41-J TT. It is seen that much greater recoveries occur for the USE than for the 41-J TT; there are very few data for which the percent recovery of the USE is lower than that of the 41-J TT.

Regarding comparisons of annealing effects on fracture toughness with those on CVN toughness, Figure 5 provides one example of results for the low upper-shelf energy submerged-arc weld from the beltline region of the Midland Reactor. After annealing at 454°C for 168 hours, the residual transition temperature shifts of 24°C and 13°C for the CVN 41-J temperature and fracture toughness 100 MPa$\sqrt{m}$ temperature represent recoveries of 77 and 86%, respectively. Additional comparisons are shown in Figure 6(a) for HSST Plate 02. For annealing at 343°C, the CVN 41-J TT recovered about 50%, whereas, at a similar fluence, the fracture toughness TT showed no recovery. For annealing at 454°C, both CVN and fracture toughness TTs recovered substantially, although that for fracture toughness was somewhat less. There are very sparse data available for such comparisons.

The results of the Working Group 3, JCCCNRS cooperative experiments are shown in Figures 6 and 7. As mentioned earlier, the neutron fluences (>1 MeV) for the RRC-KI experiments are estimated from the measured fluences (> 0.5 MeV) and are considered preliminary at this time. In general, the irradiation and annealing experiments conducted by RRC-KI with HSST Plate 02 and HSSI Weld 73W show reasonable agreement with those by ORNL. A significant difference in the experiments is that those conducted by RRC-KI involved very high neutron fluences. These results are extremely important in that they show neither material exhibits unexpected radiation sensitivity at very high fluences and, further, that both highly irradiated materials show nearly full recovery of CVN toughness after annealing at 454°C. Moreover, the results of reirradiation experiments show that the so-called "lateral shift" method for prediction of reirradiation embrittlement is applicable for these steels. The dashed lines on Figures 6 (a) and (b) represent the predicted reirradiation response while the filled triangles (▲) show the measured reirradiation data. In Figure 7, the annealing results indicate a potentially increasing post-annealing residual transition temperature shift with increasing fluence for the VVER-440 weld, but the data are too sparse to draw a conclusion.

SUMMARY OF OBSERVATIONS

1. Annealing has resulted in various degrees of recovery of the transition temperature and upper-shelf energy that depend strongly upon the annealing temperature and to a somewhat lesser degree upon the annealing time.

2. Recovery at the lower annealing temperature investigated, 343°C (for 168 hours), resulted in recovering most of the upper-shelf energy, but the recovery of the 41-J transition temperature varied from insignificant to about 50%, depending upon the material.

3. The post-annealed recovery of the fracture toughness transition temperature appears to be somewhat less than that for the Charpy impact toughness, but the available data are too sparse to allow for a conclusion.

4. Irradiation and annealing experiments of both U.S. and Russian steels by ORNL and RRC-KI show generally good agreement.

5. For the RRC-KI experiments with HSST Plate 02 and HSSI Weld 73W in a Russian commercial nuclear plant, (a) neither material exhibits unexpected radiation sensitivity at very high fluences and, further, both highly irradiated materials show nearly full recovery of CVN toughness after annealing at 454°C; (b) the reirradiation embrittlement rates for both steels are conservative relative to the "lateral shift" method for reembrittlement prediction.

ACKNOWLEDGMENTS

Oak Ridge National Laboratory is managed by Lockheed Martin Energy Research Corporation for the U.S. Department of of Energy under Contract DE-AC05-96OR22464. The authors gratefully acknowledge the financial support and encouragement provided by the U.S. Nuclear Regulatory Commission, particularly Michael G. Vassilaros, present Heavy-Section Steel Irradiation Program Monitor, and Julia L. Bishop for preparation of the manuscript.

REFERENCES

1. Nanstad, R. K., McCabe, D. E., Haggag, F. M., Bowman, K. O., and Downing, D. J., "Statistical Analyses of Fracture Toughness Results for Two Irradiated High-Copper Welds," *Effects of Radiation on Materials, 15th International Symposium,* ASTM STP 1125, R. E. Stoller, A. S. Kumar, and D. S. Gelles, Editors, American Society for Testing and Materials, Philadelphia, 1992, pp. 270-291.
2. Nanstad, R. K., McCabe, D. E., Swain, R. L., and Miller, M. K., Oak Ridge Natl. Lab., *Chemical Composition and RT Determinations for Midland Weld WF-70,* USNRC Report NUREG/CR-5914 (ORNL-6740), December 1992.
3. McGowan, J. J., and Nanstad, R. K., "A Statistical analysis of Fracture Toughness of Irradiated Low-Alloy Steel Plate and Welds," *Influence of Radiation on Material Properties: 13th International Symposium (Part II),* ASTM STP 956, F. A. Garner, C. H. Henager, Jr., and N. Igata, Eds., American Society for Testing and Materials, Philadelphia, 1987, pp. 569-589.
4. Major, T. R., and Lott, R. G., *Thermal Annealing of an Embrittled Reactor Pressure Vessel,* EPRI NP-6113-M, Electric Power Research Institute, Palo Alto, Calif., January 1989.
5. Iskander, S. K., Sokolov, M. A., and Nanstad, R. K., "Effects of Annealing Time on the Recovery of Charpy V-Notch Properties of Irradiated High-Copper Weld Metal," *Effects of Radiation on Materials: 17th Volume,* STP 1270, D. S. Gelles, R. K. Nanstad, A. S. Kumar, and E. A. Little, Editors, American Society for Testing and Materials, Philadelphia, 1996, pp. 277-293.
6. Iskander, S. K., Sokolov, M. A., and Nanstad, R. K., "A Perspective on Thermal Annealing of Reactor Pressure Vessel Materials From the Viewpoint of Experimental Results," *Proceedings of the ASME-JSME 4th International Conference on Nuclear Engineering, Volume 1 - Part A,* Atam S. Rao, R. B. Duffey, and D. Elias, Editors, The American Society of Mechanical Engineers, New York, and The Japan Society of Mechanical Engineers, Tokyo, 1996.
7. Eason, E. D., Wright, J. E., Nelson, E. E., Odette, G. R., and Mader, E. V., Modeling and Computing Services, Boulder, Colo., *Models for Embrittlement Recovery Due to Annealing of Reactor Pressure Vessel Steels,* USNRC Report NUREG/CR-6327 (MCS 950302), May 1995.

Table 1. Average chemical composition of materials used in the annealing and reirradiation studies

Material	Composition (wt %)									
	C	Mn	P	S	Si	Cr	Ni	Mo	Cu	V
HSSI weld 73W	0.098	1.56	0.005	0.005	0.45	0.25	0.60	0.58	0.31	0.003
Midland beltline weld	0.084	1.61	0.017	0.007	0.62	0.10	0.57	0.41	0.21-0.34	0.004
Midland nozzle weld	0.088	1.57	0.015	0.010	0.56	0.11	0.58	0.39	0.37-0.46	0.008
HSST Plate 02	0.23	1.55	0.009	0.014	0.20	0.04	0.67	0.53	0.14	0.003
Weld 502-1 (VVER-440)	0.03	1.16	0.030	0.013	0.57	1.60	0.12	0.48	0.15	0.24
Weld 260-11 (VVER-1000)	0.08	0.85	0.009	0.015	0.30	1.83	1.59	0.61	0.07	---

Table 2. Mechanical properties of U.S. materials

Material	CVN impact USE (J)	CVN 41-J transition temperature (°C)	Room temperature tensile strength (MPa)	
			Yield	Ultimate
HSSI weld 73W (undersize)	118	–38	495	603
HSSI weld 73W (full size)	135	–40	495	603
Midland beltline weld	89	–9	407	586
Midland nozzle weld	88	–1	505	655
HSST Plate 02	164	–16	471	619

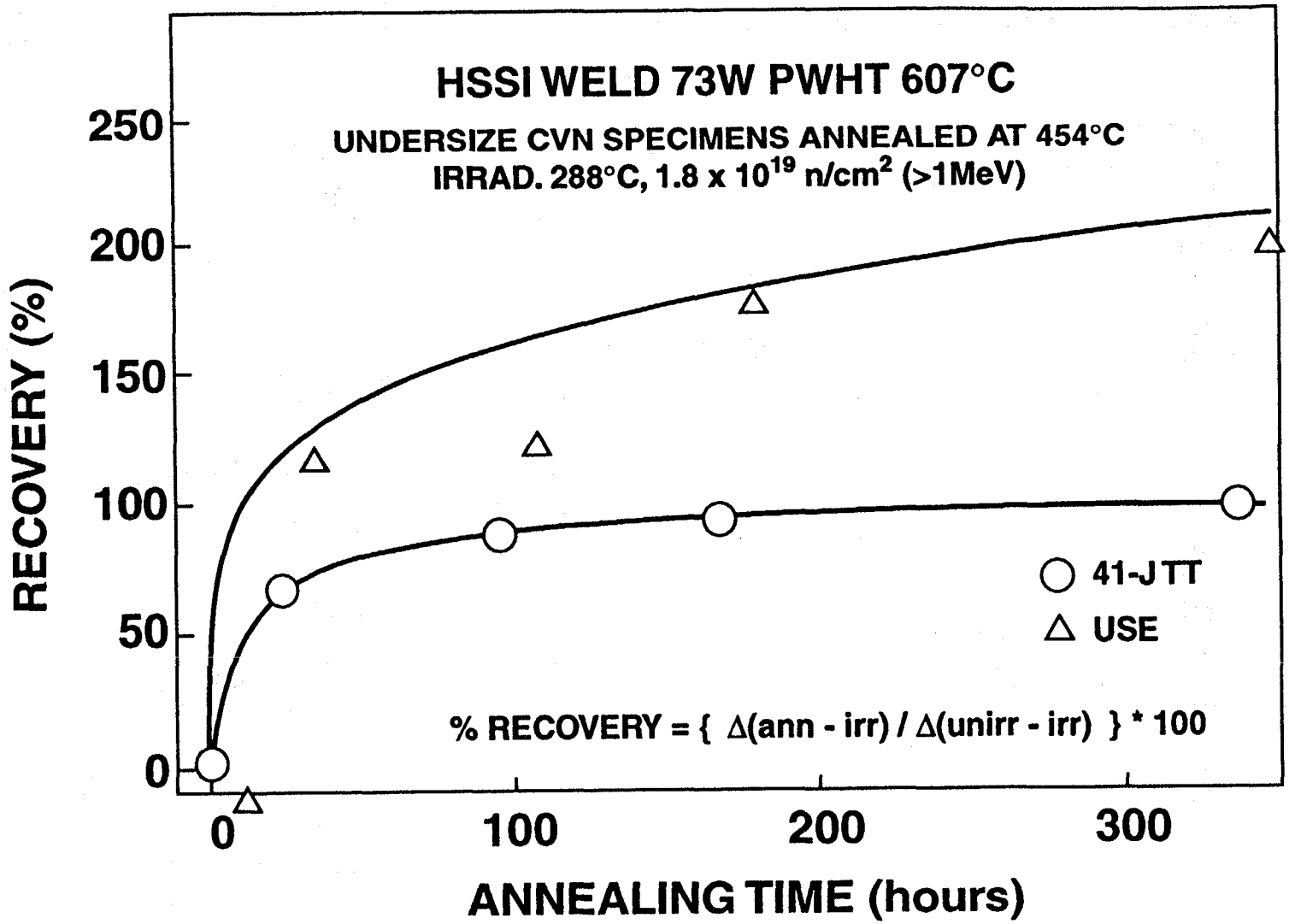

Figure 1. Upon thermal annealing at 454°C, HSSI Weld 73W exhibited rapid recovery of Charpy impact toughness. Diminishing returns of the transition temperature were observed after 96 hours, but the upper-shelf energy continued to increase even up to 336 hours.

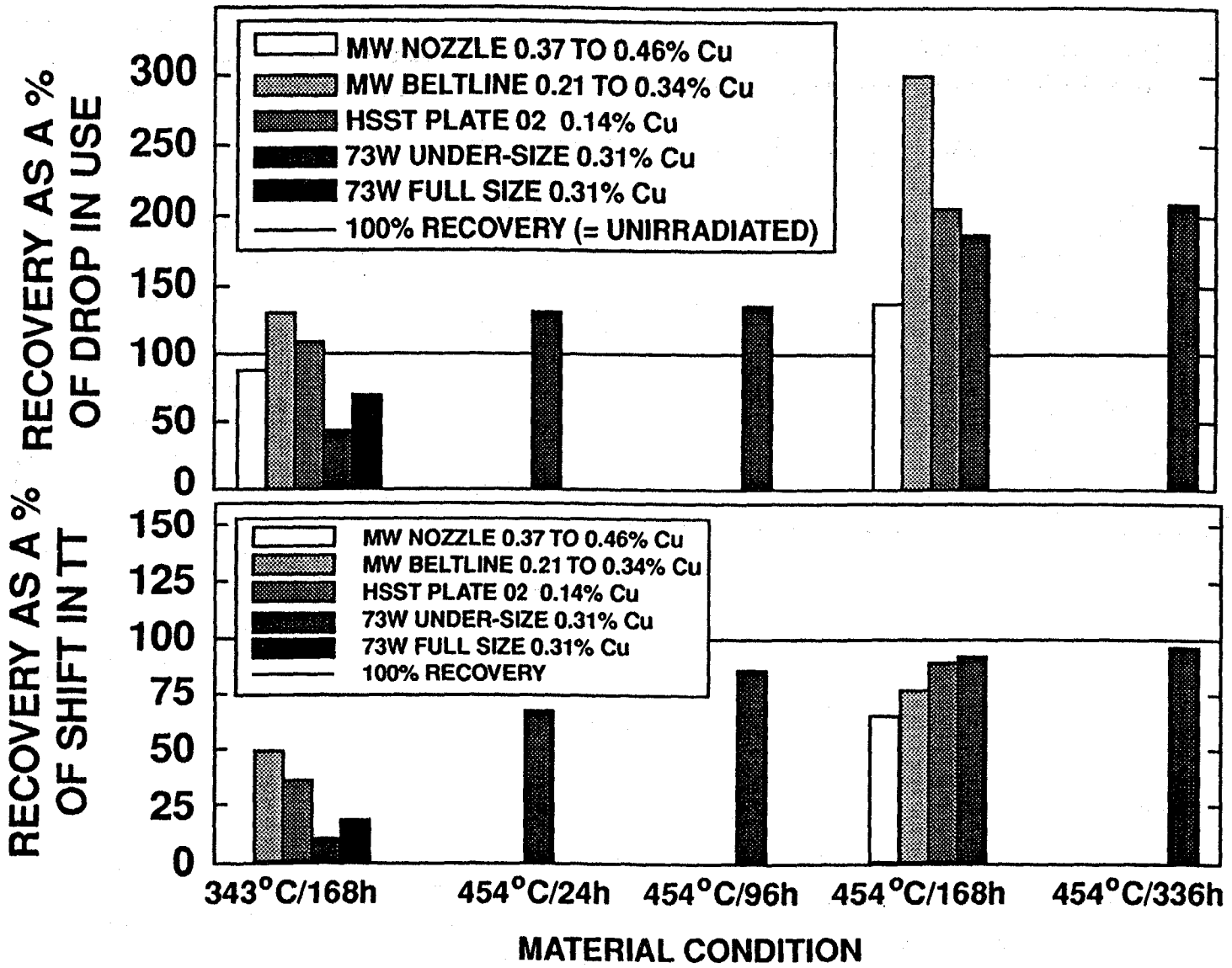

Figure 2. Percent recovery of Charpy upper-shelf energy and 41-J transition temperature for three submerged-arc welds and one plate following thermal annealing at various temperatures and times.

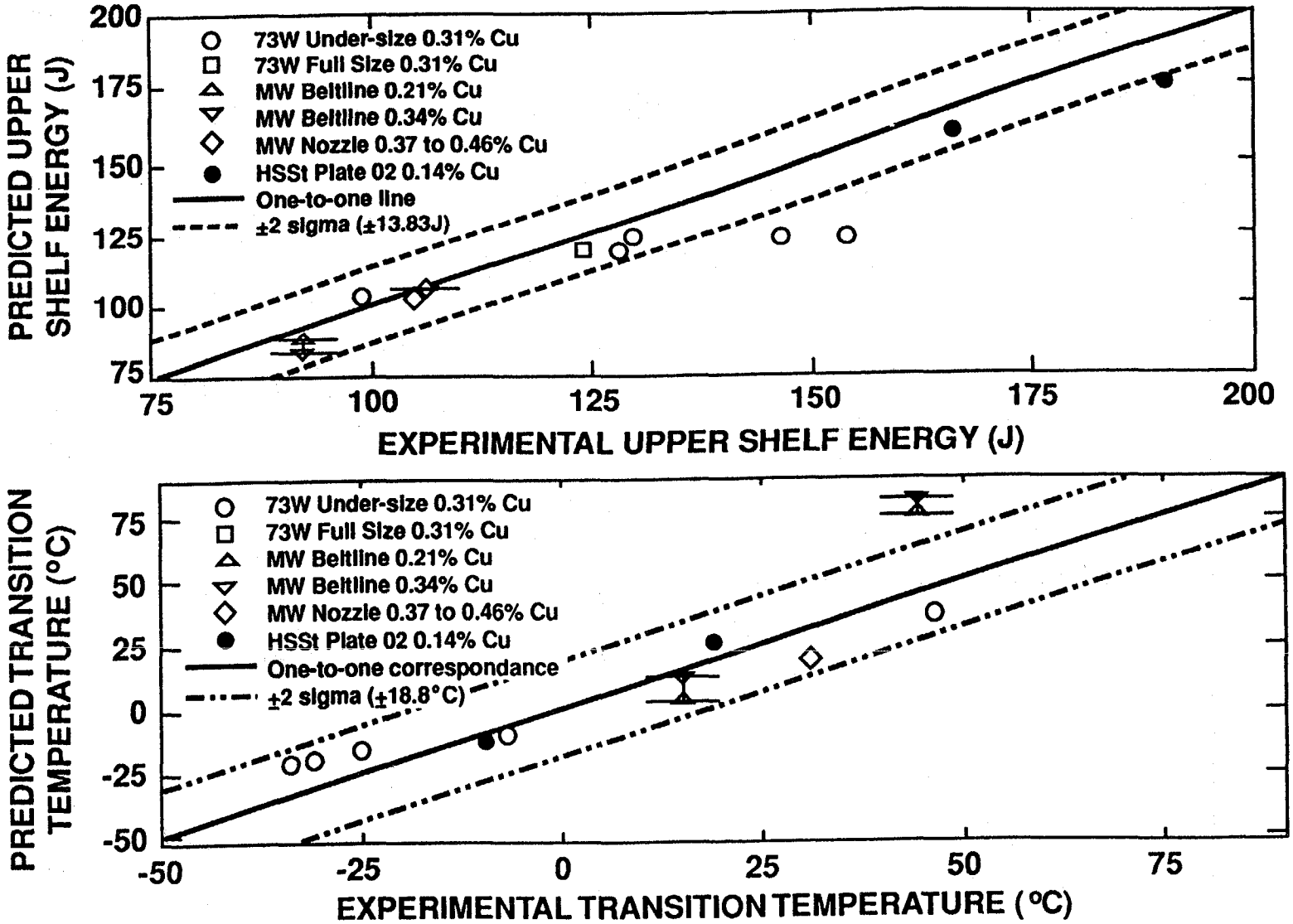

Figure 3. Comparison of annealing recovery measurements with the Eason et al., prediction models. For the materials and conditions investigated, the annealing recovery model has generally given, within ±2σ, good to conservative predictions of transition temperature and upper-shelf energy.

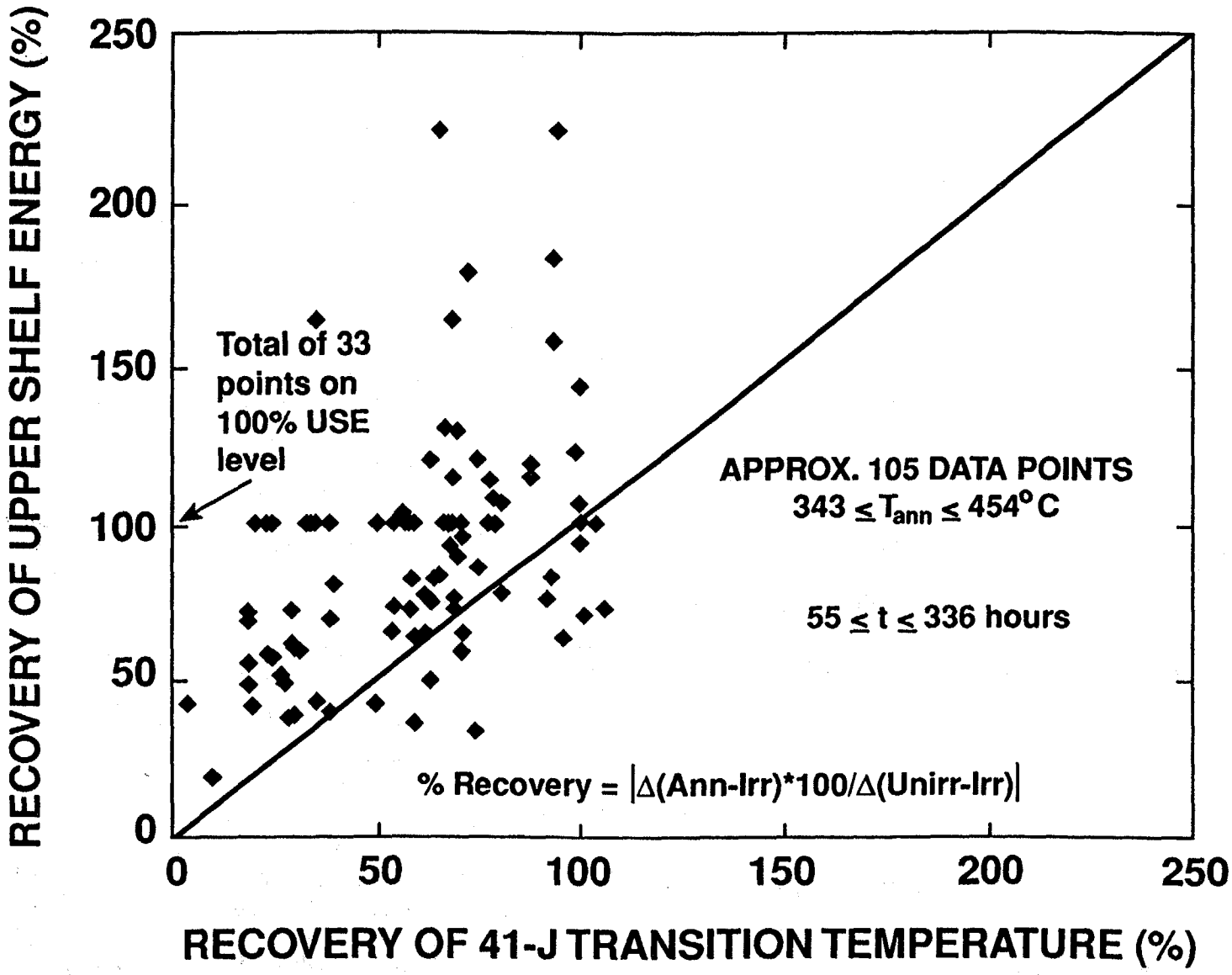

Figure 4. Comparison of Charpy upper-shelf energy and transition temperature recoveries following thermal annealing from published data.

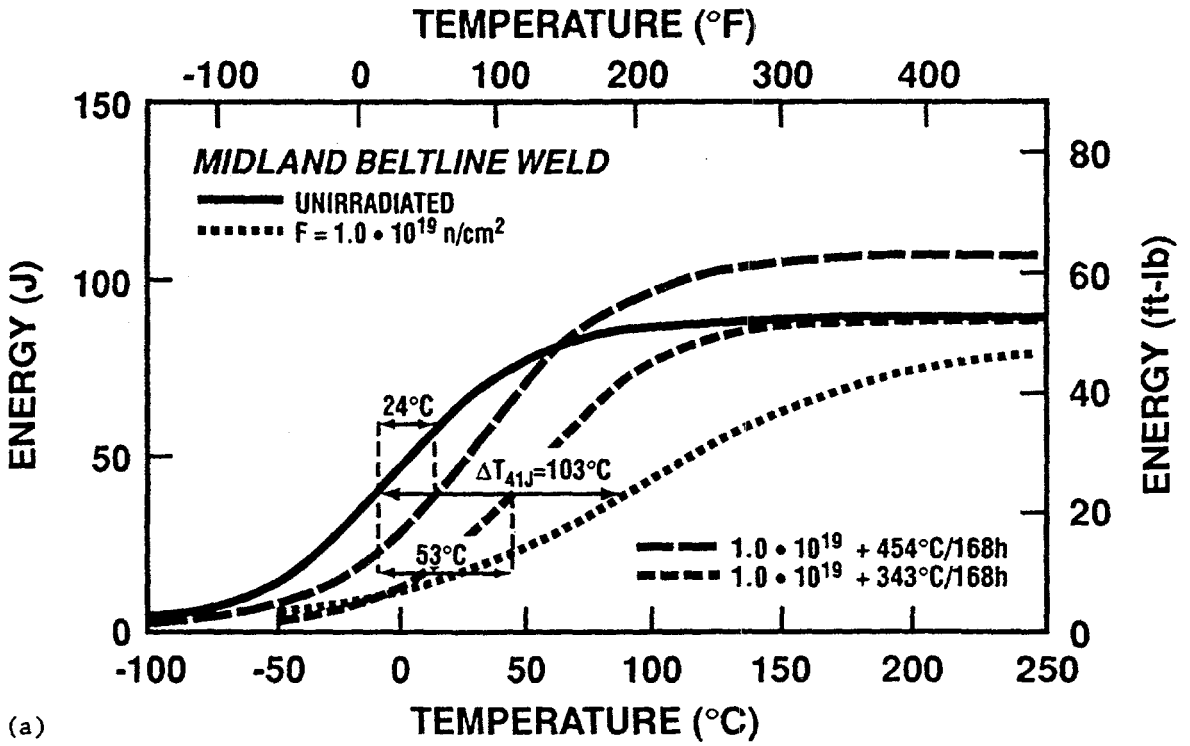

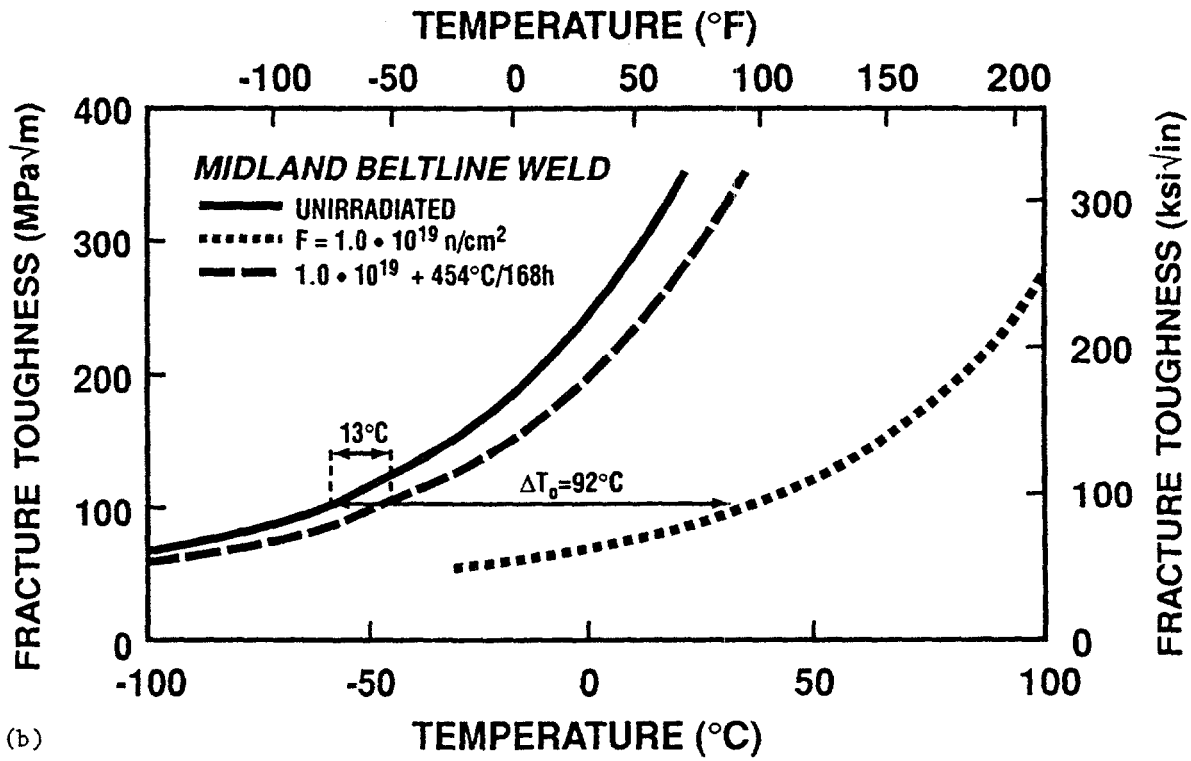

Figure 5. Results of thermal annealing experiments at 454°C for 168 hours with Midland Reactor beltline weld, showing (a) Charpy impact energy and (b) fracture toughness.

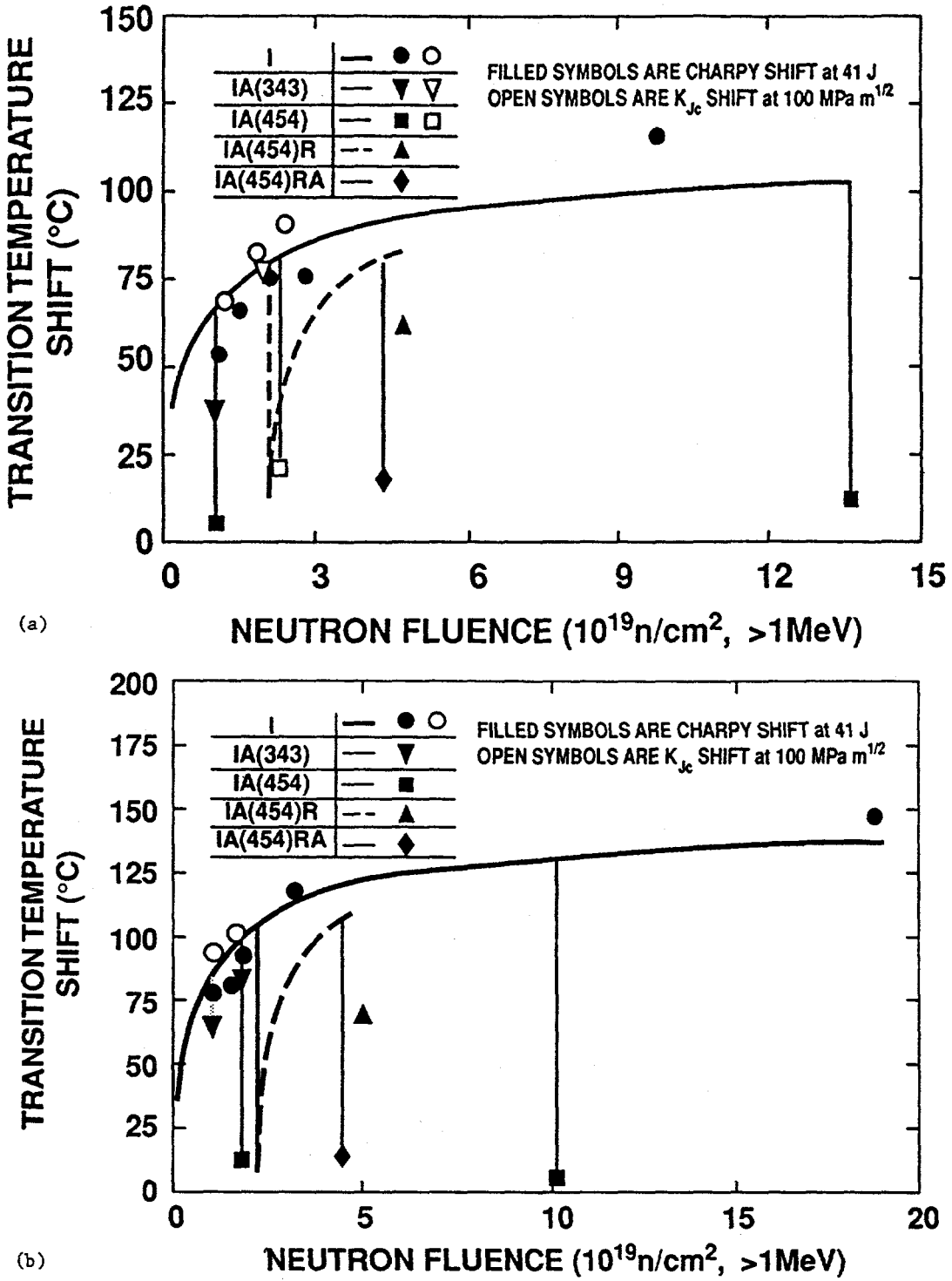

Figure 6. Results of irradiation, annealing, and reirradiation experiments with (a) HSST Plate 02 and (b) HSSI Weld 73W, by Oak Ridge National Laboratory and Russian Research Center-Kurchatov Institute.

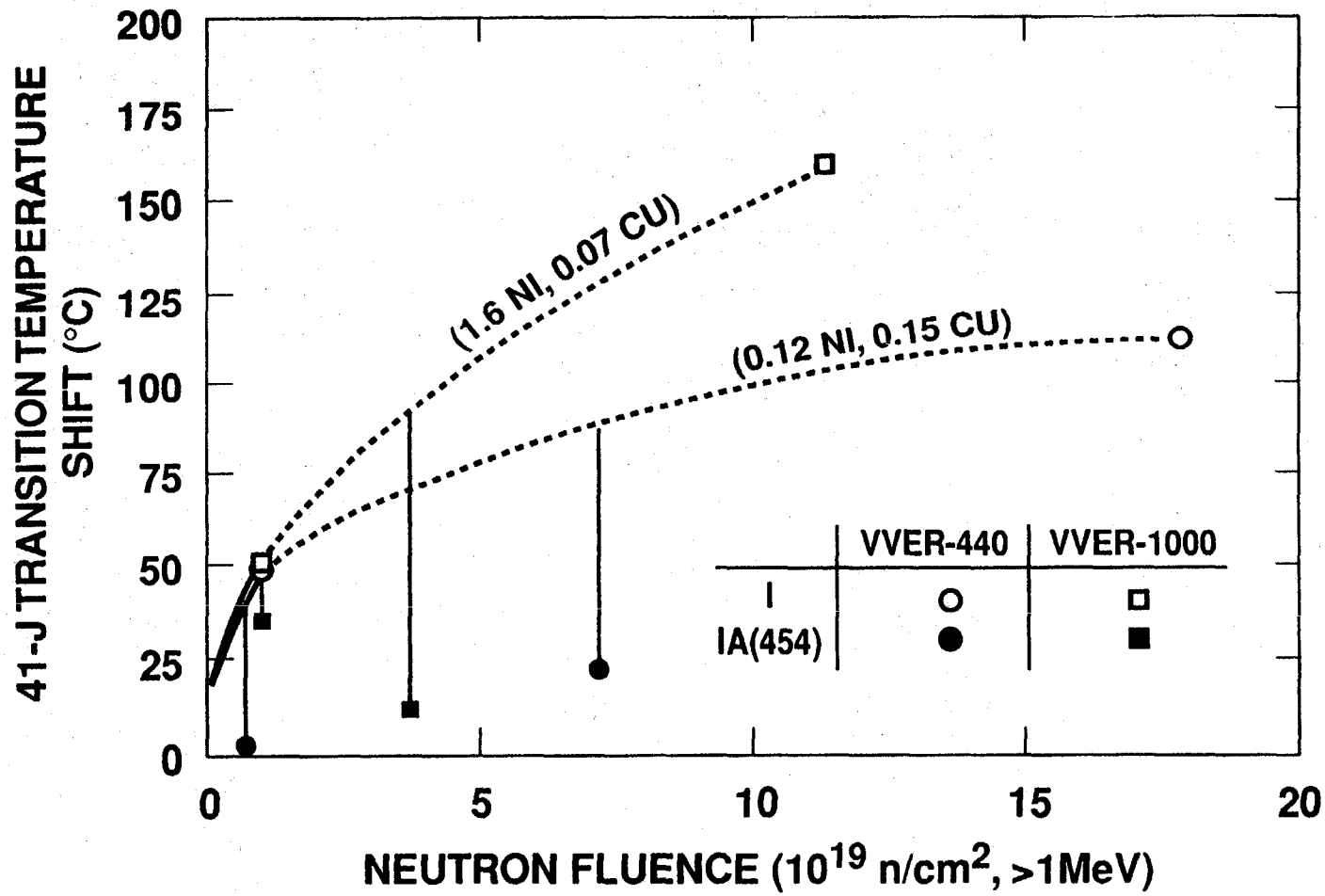

Figure 7. Results of irradiation and annealing experiments with Russian VVER-440 and VVER-1000 welds by Oak Ridge National Laboratory and Russian Research Center-Kurchatov Institute.

DOE's Annealing Prototype Demonstration Projects

John Warren
Commercial Light Water Reactor Programs
U.S. Department of Energy

and

Jim Nakos and Gary Rochau
DOE's Light Water Reactor Technology Center at
Sandia National Laboratories

Abstract

One of the challenges U.S. utilities face in addressing technical issues associated with the aging of nuclear power plants is the long-term effect of plant operation on reactor pressure vessels (RPVs). As a nuclear plant operates, its RPV is exposed to neutrons. For certain plants, this neutron exposure can cause embrittlement of some of the RPV welds which can shorten the useful life of the RPV. This RPV embrittlement issue has the potential to affect the continued operation of a number of operating U.S. pressurized water reactor (PWR) plants. However, RPV material properties affected by long-term irradiation are recoverable through a thermal annealing treatment of the RPV. Although a dozen Russian-designed RPVs and several U.S. military vessels have been successfully annealed, U.S. utilities have stated that a successful annealing demonstration of a U.S. RPV is a prerequisite for annealing a licensed U.S. nuclear power plant.

In May 1995, the Department of Energy's Sandia National Laboratories awarded two cost-shared contracts to evaluate the feasibility of annealing U.S. licensed plants by conducting an anneal of an installed RPV using two different heating technologies. The contracts were awarded to the American Society of Mechanical Engineers (ASME) Center for Research and Technology Development (CRTD) and MPR Associates (MPR) . The ASME team completed its annealing prototype demonstration in July 1996, using an indirect gas furnace at the uncompleted Public Service of Indiana's Marble Hill nuclear power plant in southern Indiana. The MPR team's annealing prototype demonstration was scheduled to be completed in early 1997, using a direct heat electrical furnace at the uncompleted Consumers Power Company's nuclear power plant at Midland, Michigan. This paper describes the Department's annealing prototype demonstration goals and objectives; the tasks, deliverables, and results to date for each annealing prototype demonstration; and the remaining annealing technology challenges.

Introduction

One of the important challenges U.S. electric utilities face in addressing technical issues associated with the aging of nuclear power plants is the long-term effect of plant operation on reactor pressure vessels (RPVs). These vessels, which contain the nuclear material in a reactor, are large, carbon steel structures that are about 15 feet in diameter, more than 40 feet in height, and about 8 inches thick. After many years of power plant operation, the carbon steel of a vessel in the beltline region can become less ductile and thus more brittle or *embrittled.* A key safety concern regarding embrittled RPVs is pressurized thermal shock (PTS) where the RPV is depressurized, and rapidly repressurized at temperatures lower than normal operating conditions. Should PTS occur, a severely embrittled RPV could conceivably crack and rupture.

The Nuclear Regulatory Commission (NRC) has promulgated a number of regulations to ensure the safety of RPVs. The NRC has defined a set of screening criteria by which a utility can project when its RPV would be embrittled to the point where actions to prevent a PTS failure may need to be taken (10 CFR 50.61, "Fracture toughness requirements for protection against pressurized thermal shock," May 15, 1991).

One of the actions that could be taken if an RPV does not satisfy NRC's PTS screening criteria is for the plant to anneal its RPV. The NRC has issued an Annealing Rule (10 CFR 50.66, "Thermal Annealing Rule," December 19, 1995) and Regulatory Guide 1.162 ("Format and Content of Report for Thermal Annealing of Reactor Pressure Vessels," February 1996) to provide a utility with guidance regarding how to obtain permission to anneal.

Annealing is the only known treatment for metals which reverses the deleterious effects of embrittlement. Embrittlement can be caused by a number of processes, e.g., high temperatures, welding, or exposure to neutrons. Figure 1 schematically shows how the neutrons from the nuclear fuel expose the beltline region of the RPV, which becomes the most embrittled. By heating the metal to a known temperature (e.g., 850°F) and holding at that temperature for a known period of time, most of the negative effects of embrittlement can be reversed. Figures 2 and 3 show how typical nozzle and skirt supported RPVs can be annealed to reverse the effects of neutron embrittlement.

There have been a number of successful anneals performed on pressurized water reactor (PWR) RPVs internationally as well as in the U.S. Over a dozen Russian VVER RPVs and two U.S. military reactor vessels have been successfully annealed. However, to date, annealing has never been used in the United States to repair an installed commercial reactor pressure vessel at a licensed nuclear power plant. Although the previous experience proved that annealing techniques could be successfully applied to large reactor vessels, the U.S. reactor pressure vessels designs are significantly different and require substantially larger anneal zones and heaters. These important differences dictate that much larger, heavier, and higher energy output heaters; much more complicated analyses which include the annealing temperature effects on nozzles and surrounding components, concrete, and structures; and different reactor designs and plant configurations as well as other technical and regulatory issues must be evaluated, understood, and resolved before a licensed U.S. pressure vessel can be annealed.

In February 1994, the Department of Energy (DOE) and the Electric Power Research Institute (EPRI) sponsored a Reactor Pressure Vessel Thermal Annealing Workshop to assemble

international experts and discuss the viability of annealing in the U.S. Although there was little to indicate there were any significant technical roadblocks to demonstrate that annealing U.S. RPVs would be viable, utility representatives attending the workshop clearly stated that there would be little chance of an actual anneal in the U.S. until it was demonstrated that major components (e.g., the RPV, reactor coolant system (RCS) piping, and concrete biological shield wall -- bioshield) would not be damaged during the annealing process.

DOE's Annealing Demonstration Project

With the above industry interest and the Department's desire to support activities that could affect the continued and safe operation of the existing U.S. commercial nuclear power plants, the Department initiated an Annealing Prototype Demonstration Projects (ADP) effort to evaluate, both technically and economically, the viability of thermal annealing as a reactor pressure vessel embrittlement management option. Technical guidance for this ADP evaluation effort was provided by joint government and industry teams which included both domestic and international participation. Also, the NRC participated as an independent observer of the ADP activities to support their confirmatory annealing analyses and other associated regulatory activities.

The primary program objectives of the Department's Annealing Prototype Demonstration Projects were as follows:

- Confirm that the thermally annealing process can be maintained within acceptable annealing parameters during the heatup, annealing soak, and cooldown phases of the anneal.

- Verify RPV dimensional stability during and after the anneal, including confirmation that there is no vessel distortion and that all internal RPV dimensions are within acceptable limits.

- Verify lack of damage during and after the anneal on key reactor components and systems, including the reactor cooling system piping, concrete reactor cavity wall, and bioshield.

- Instrument RPV, RCS piping, bioshield, and other key components; and acquire data during the anneal for annealing process and model verification.

- Provide and benchmark a 3-dimensional thermal and stress analysis model that accurately predicts the key annealing temperatures and stresses of the vessel and the affected, surrounding components during the anneal.

- Obtain realistic cost data for the various annealing processes and hardware.

ADP Teams, Sites and Heating Technology

In the spring of 1994, the Department directed Sandia National Laboratories to issue a request for quote (RFQ) to conduct the above ADP effort. Two viable proposals were received in response to the RFQ, one from ASME's CRTD and one from MPR. In May 1995, the Department

authorized the award of both contracts to minimize the overall risk of the effort and to make more information available to resolve regulatory technical and procedural issues associate with annealing. Each ADP was based on conducting an annealing demonstration of different PWR RPV designs -- a Westinghouse 4-loop nozzle supported design and a Babcock & Wilcox 2-loop skirt supported design -- and different heater technologies -- an electric resistance heater and an indirect gas-fired heater. Also, both ADPs used unirradiated, installed RPVs and nuclear steam supply system (NSSS) components and systems at uncompleted commercial nuclear power plants. Table 1 provides ADP information on the contractors and subcontractors, financial sponsors, the plant owners, plant locations, the RPV types, NSSS vendors, an estimation of the % completion of the units, and heating technologies. Table 2 provides information specific to each plant site, including type and status of the RPV, RPV supports, RPV support cooling, RPV insulation, RPV bottom head connections, steam generators, reactor coolant pumps, RCS piping and supports, branch piping and supports, and reactor cavity cooling system.

The ADP at the Marble Hill site was conducted from June 24, 1996 through July 8, 1996 and is complete except for analyzing the data and completing the final report. Preliminary data shows that the project was successful in that the anneal process was controlled within prescribed limits, the predicted and measured results agree, the appropriate RPV dimensions were within required criteria, and there was no damage to the RPV, RCS piping, bioshield or other important components. The Marble Hill annealing demonstration showed that annealing is a viable option for nozzle supported RPV type designs and is also likely to be viable for other RPVs as well.

At the beginning of FY 1997, all remaining Marble Hill and Midland ADP work was stopped due to restrictions concerning annealing work contained in the FY 1997 Energy and Water Development Appropriation Bill that was signed into Law. However, prior to work stoppage, a significant amount of progress on the Midland ADP was also made during the period from August 1995 through September 1996 on Tasks 1-4 as defined below. The Midland ADP team was assembled, funding was secured and a project plan was developed. The thermal/stress model was mostly completed with preliminary results being provided. Instrumentation was finalized and draft procedures developed. The furnace was almost completely assembled but not tested. The Midland site also underwent significant cleanup in preparation for the ADP.

ADP Contract Tasks and Deliverables

The ADP contracts were divided into the following six (6) tasks: Task 1 - Assemble team and manage project; Task 2 - Select and characterize site where the ADP would take place; Task 3 - Provide a thermal/stress model to predict the response of the RPV, RCS piping and concrete reactor cavity wall; Task 4 - Define and install instrumentation and assemble data acquisition system to obtain experimental data; Task 5 - Perform the ADP; and, Task 6 - Reduce and analyze test data and report all results.

Task 1 defined the project structure and the required routine reporting. The task specifically required the contractor to manage the project. Task 2 provided for the screening of possible sites and for documenting a clear definition of the site configuration for future reference. These two tasks provided the baseline structure and facility definition to allow detailed project planning and implementation to proceed.

Tasks 3 and 4 were essential to providing a clear strategy for fielding instrumentation and for obtaining sufficient high-integrity data. The thermal/stress model developed under Task 3 included the coupling of the heating system to the reactor vessel as well as identifying key areas for detailed examination and instrumentation. This model also provided "bracketing" information on stresses and strains to determine if refinements to the heating system design were needed and to determine critical areas for instrumentation.

Task 5, in addition to performing the annealing demonstration, required a risk assessment of the annealing system to determine failure modes and provide the basis for contingency planning. Specific areas of concern were the redundancy of critical systems to avoid interruption of the anneal, impact of component failures to the results of the anneal, and personnel safety.

Task 6 would, when completed, document the results of the projects. In particular, this task would document the exact procedures used, the results obtained, and would reconcile the results with the analytical model. Lessons learned from the ADPs would also be documented for consideration by future users to reduce cost, maximize safety, and minimize personnel radiation exposure.

Selected results from the Marble Hill Annealing Demonstration Project

Key technical objectives of the Marble Hill Annealing Demonstration Project were as follows:

- Predict the areas of greatest strain in a commercial scale reactor vessel during an in-situ anneal using an analytical model;
- Heat the annealing zone of a nozzle-supported pressure vessel to a minimum temperature of 800° F for a minimum of 168 hours; and
- Measure temperatures, displacements, and strains during the annealing cycle to demonstrate the validity of the process and model.

Specifically, the vessel would be heated and cooled at a rate of not greater the 25° F/hour to avoid strains that may cause damage to the reactor vessel or the associated loop piping. The vessel was to be heated to a nominal temperature of 850° $\pm$ 25° F on the inside of the vessel. This temperature range would provide for a minimum temperature in the anneal zone of 800° F to provide the maximum material recovery allowed by the Annealing Rule. The maximum temperature on the vessel was to be held below 900° F to prevent the vessel material from reaching temperatures that could cause any significant creep of the material and possibly thinning the vessel wall.

The Marble Hill Annealing Demonstration Project was performed in New Washington, Indiana at the Marble Hill Unit 1 owned by PSI Supply Company. Construction of Unit 1 was stopped at approximately 65% of completion. The reactor system is a Westinghouse 4-loop PWR with a reactor vessel manufactured by Combustion Engineering.

The Marble Hill ADP was implemented using a steering committee approach with all the project funding contributors serving as committee members. Primary funding of the project was supplied

by the U.S. Department of Energy, the principal Marble Hill ADP subcontractors (Westinghouse and Cooperheat), the Westinghouse Owners Group, and the Electric Power Research Institute. The membership of the steering committee is detailed in Figure 4.

The unique approach to annealing employed during the Marble Hill ADP was the use of an indirect gas-fired heater inserted into the reactor vessel. In the indirect gas-fired technique, air is heated to high temperatures outside of containment and piped through containment penetrations to a sealed heat exchanger which is placed inside the vessel and supported from the reactor vessel top flange. A schematic of the Marble Hill heat exchanger is shown in Figure 5. The advantage of this technique is that no active components are located inside the vessel so that critical components can be serviced during the annealing process. Another advantage is that the sealed can of the heat exchanger allows for easier decontamination of the heat exchanger after being used in a commercial PWR.

The specific application of indirect gas-fired heating technology at Marble Hill used propane-fueled burners to heat air to 1600° F. The 6,000,000 BTU/hr burners, Figure 6, were located outside of containment on the end of stainless steel ducts. Blowers, Figure 7, providing an air flow of up to 2,700 CFM to the burners, pushed the heated air through the ductwork to the sealed heat exchanger inside the vessel and exhausted it back through containment on the same route to the outside. The ducts, Figure 8, were insulated to minimize the heat load on the containment building.

The heat exchanger, Figure 9, was installed in the reactor vessel with an approximately 16" wide gap between the heat exchanger and the reactor vessel wall. The heat exchanger was divided into 5 independent zones with the three central zones spanning the anneal zone of the reactor vessel which was defined as extending 3" above and below the active fuel height of 12 feet (see Figure 5 for relative locations). The top and bottom zones of the heat exchanger were used to control the thermal gradient from the heated anneal zone to the unheated portions of the vessel. The heat exchanger had no provisions for azimuthal control of heating of the reactor vessel.

Thermal barriers were used to help contain heat inside the reactor vessel. Panels of insulation were placed at each of the eight loop openings in the vessel and at the top of the heat exchanger between the exchanger and the vessel wall. These panels prevented convective heat flow into the reactor coolant loops and into the top half of the reactor vessel. One special barrier (Figure 10) was designed and constructed to demonstrate the ability to remotely install these barriers in loops of a commercial reactor. The panels on top of the heat exchanger were remotely actuated from the top of the heat exchanger lid.

To verify that the annealing process did not physically damage the reactor vessel, physical measurements were made before and after the annealing cycle. There measurements consisted of dimensions required to replace the reactor internals and non-destructive techniques to examine the welds on the vessel. Special tooling was designed to measure the vessel diameters and verify alignment between the top and bottom keyways of the reactor vessel. No significant dimensional changes or weld flaws were found after the annealing cycle.

Thermocouples (TCs) and Resistance/Temperature Devices (RTDs) were used to measure temperatures during the anneal cycle throughout the Marble Hill facility. Fifty redundant pairs (Figure 11) of TCs were spot-welded directly to the inside surface of the reactor vessel making

the thermocouple junction directly on the surface of the vessel. Twenty-four retractable TCs were mounted on the heat exchanger and remotely extended to the vessel wall to demonstrate the process to be used in a commercial application. Sixty-eight RTDs were mounted on the outside of the vessel to measure the minimum temperature in the anneal zone and to measure the loop temperatures. Sixteen TCs were placed directly in the concrete of the bioshield wall to measure the concrete temperature, particularly in the region of the nozzle supports. All temperatures measured were within the predictions of the model and no TCs or RTDs failed during the anneal cycle. The concrete temperature in the bioshield wall never exceeded 150° F.

Strain and displacement gauges were placed at critical locations outside of the reactor vessel. The critical locations were defined by the model. All strains measured (Figure 12) were below the model predictions with no critical limits approached. The displacement measurements were all within expectations with the reactor vessel responding symmetrically during the anneal cycle.

Propane for the heating system was brought to the site in 11,000 gallon tankers (Figure 13). The two storage tanks on site provided a minimum of 48 hours of propane supply. Approximately 1/3 of the expected 90,000 gallons was used during the anneal. One minor problem was encountered with this system when the excess flow valves engaged during refueling and shut down the fuel to the burners during the soak portion of the anneal. These valves are installed on the tankers to prevent dumping of the propane during a fuel line break. The differential pressure between the tank and the fuel line pressure during refueling caused a surge of flow thus closing the valve when the storage tank was returned to the system. The valves are passive devices with no visible indications.

The heat up of the Marble Hill Reactor vessel was started on June 24, 1996 and achieved the nominal soak temperature of 850° F in 85 hours on June 28, 1996. The average heat up rate was 16° F/hour. The soak temperature was maintained for 173 hours until July 5, 1996. The vessel was cooled down to less than 200° F in 67 hours and the anneal cycle was complete on July 8, 1996. Though the average heat up rate was 16° F/hour, it approached 25° F/hour in portions of the vessel, particularly at the ends of the anneal zones since the heat exchanger did not couple heat energy to the top and bottom ends of the vessel as effectively as it did to the anneal zone. Several perturbations occurred during the anneal cycle, i.e. loss of power, component failure, loss of propane, but effective contingency planning prevented the cycle from being interrupted.

A new issue was raised regarding the annealing of the reactor vessel during the Marble Hill ADP. It was discovered during the heat up of the vessel that air leakage through the insulation on the reactor vessel was cooling one azimuthal location of the vessel through the entire length of the vessel. After extensive examination of the insulation, it was concluded that the air leakage was inherent to the design and installation of the Transco metal insulation. This preferential cooling introduced azimuthal temperature gradients which were not expected. The heat exchanger had sufficient capacity to accommodate the heat loss and stay within the temperature limits established for the anneal. This particular heat exchanger design has the capacity to remove energy with some zones while adding it in others. This feature was used to control the gradient by cooling the central portion of the anneal zone while heating the top and bottom zones.

The Marble Hill Annealing Demonstration Project was successfully completed without damage to the vessel or the associated loop piping. The anneal cycle was completed without interruption due to effective contingency planning. The indirect gas-fired process is capable of heating the

vessel and no indications were found to support the need for azimuthal heating control.

Conclusion

Reactor pressure vessel embrittlement caused by neutron irradiation can be a significant problem for some commercial operating nuclear power plants. The only known way to reverse neutron embrittlement damage to a reactor pressure vessel after years of operation is to heat the vessel material to a temperature of about 850° F for a period of four to seven days. Annealing is a common method for toughening steel, but has never been used in the United States to repair an installed reactor pressure vessel at a licensed commercial nuclear power plant. The Department of Energy, working in close cooperation with industry and the NRC, initiated an effort to demonstrate the economic and technical viability of thermally annealing U.S. type reactor pressure vessels. The Marble Hill annealing demonstration was completed in July 1996, and proved that thermal annealing is now a feasible option for installed U.S. commercial reactor pressure vessels at licensed plants. As with all new techniques and processes, some refinements, optimizations, and other considerations such as ALARA will undoubtably need to be undertaken prior to the first commercial RPV anneal. It is envisioned that many pressurized water reactors will make use this technology to extend their useful lives far into the future.

	Marble Hill	Midland
Contractors and Sub-contractors	ASME CRTD, Westinghouse, Cooperheat, Parsons Power (formerly Gilbert/Commonwealth), Power Generation Technologies	MPR Associates, MOHT Russian Annealing Consortium, Framatome Technologies (formerly BW Nuclear Technologies), Consumers Power
Sponsors	DOE, Westinghouse/Cooperheat, Westinghouse Owner's Group, Electric Power Research Institute (EPRI), Consumers Power Company, Duquesne Light Company, Central Research Institute of the Electric Power Industry (Japan), Electricité de France	DOE, Framatome, Consumers Power Co., Empire State Electric Energy Research Company, EPRI and Utilities through EPRI: GPU Nuclear and Tennessee Valley Authority, Central Research Institute of the Electric Power Industry (CRIEPI from Japan)
Plant Owner	PSI (Public Service of Indiana) Supply Company	Midland Cogeneration Venture (initially, Consumers Power Company)
Location	Southern Indiana	Central Michigan
RPV	Nozzle-supported, fabricated by Combustion Engineering	Skirt-supported, fabricated by Babcock & Wilcox
NSSS	Westinghouse, 4-loop, U-tube steam generators	Babcock & Wilcox, 2-loop, once-through steam generators
Construction (estimated)	~65% complete	~90% complete
Heating Technology	Indirect gas-fired	Electric resistance

Table 1: Annealing Demonstration Projects - Overall Team and Site Information

Component	Marble Hill		Midland	
	Type	Status	Type	Status
Reactor Pressure Vessel (RPV)	173"Ø fabricated by Combustion Engineering	Installed	171"Ø fabricated by Babcock & Wilcox	Installed
RPV Supports	Nozzle-supported	Installed	Skirt-supported	Installed
RPV Support Cooling	Original design: air cooled, backup: water cooled	Air cooling installed, water cooling not installed	Air cooled	Installed
RPV Insulation	Mirror insulation	Installed, except RPV bottom head and RCS piping. Will install insulation of equivalent R-value.	None	Will install insulation of equivalent R-value on RPV and RCS piping only through bioshield penetrations.
RPV Bottom Head Connections	Thimble tubes	Not installed	Instrumentation lines	Severed
Steam Generators (SGs)	Westinghouse U-tube design	Installed	Once-Through Steam Generators (OTSGs)	Hot leg severed
Pressurizer (PZR)	---	Installed	---	Installed
Reactor Coolant Pumps (RCPs)	---	Installed, except motor. Not all concrete grouting is in place.	---	Installed
Reactor Coolant System (RCS) Piping	4-loop, stainless and cast austenitic stainless steel piping (4 hot and 4 cold legs)	All piping ≥12"Ø installed, except pressurizer surge line	2-loop, stainless steel clad carbon steel (4 cold legs, 2 hot legs)	All piping installed -hot legs cut about 2/3 up the vertical run prior to the 180° return at the OTSG inlet, "windows" cut in all 4 cold legs near the bottom of the steam generators
RCS Piping (Permanent) Supports	---	All installed	---	Essentially all installed
Branch Piping	Stainless steel piping	All piping greater than 12"Ø installed, many branch lines removed including SG bypass	Stainless steel piping	Essentially all installed
Reactor cavity cooling system	Forced-air cooled	Installed for ADP	Forced-air cooled	Installed for ADP

Table 2: Annealing Demonstration Projects - Site Details

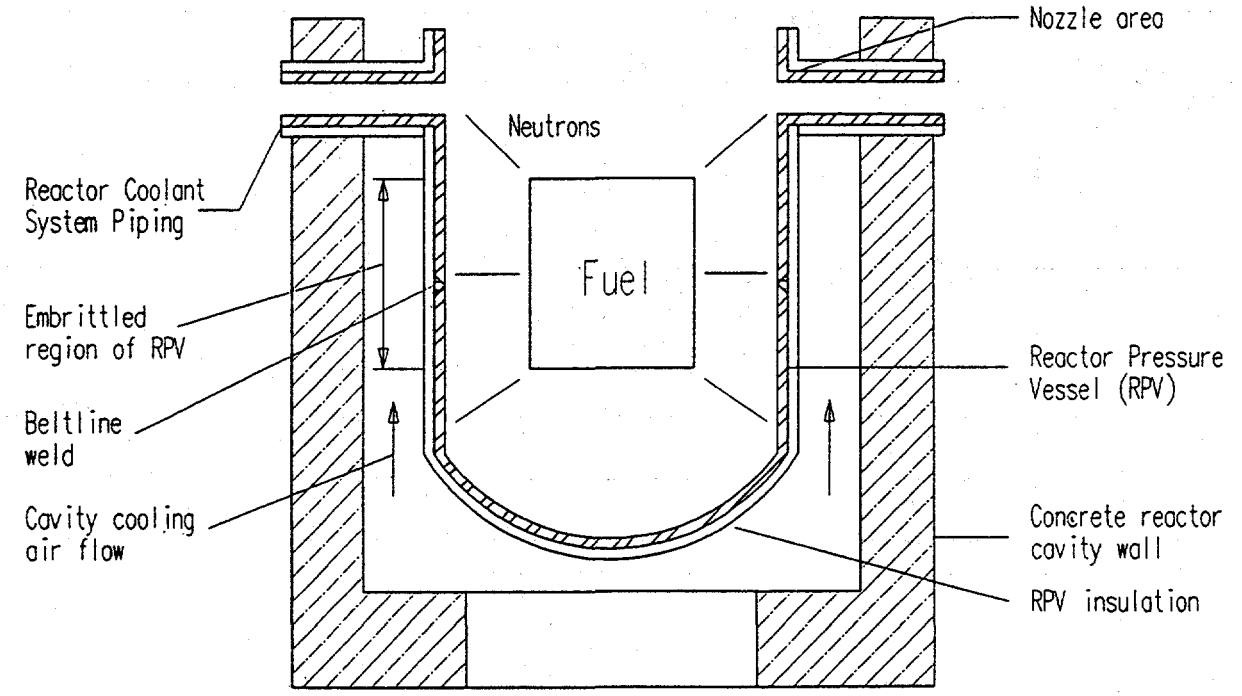

Figure 1. Schematic of Neutron Exposure of a PWR Reactor Pressure Vessel.

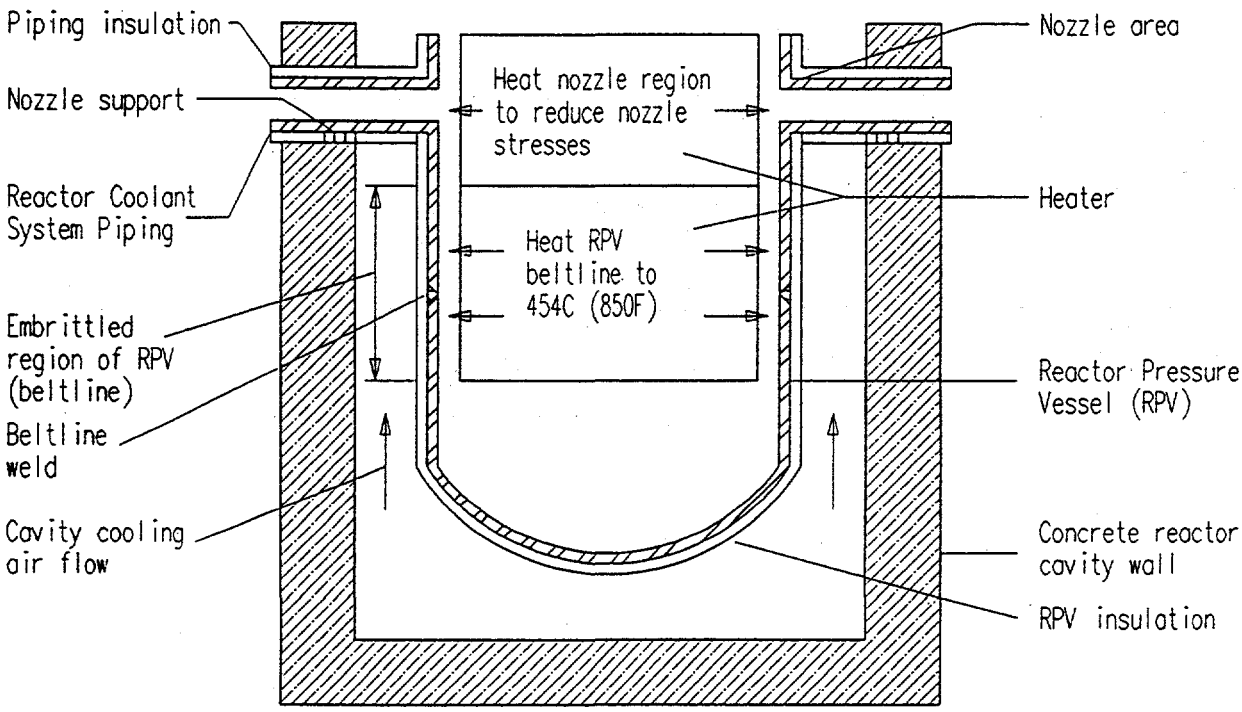

Figure 2. Schematic of PWR Reactor Pressure Vessel Annealing (Nozzle Supported RPV).

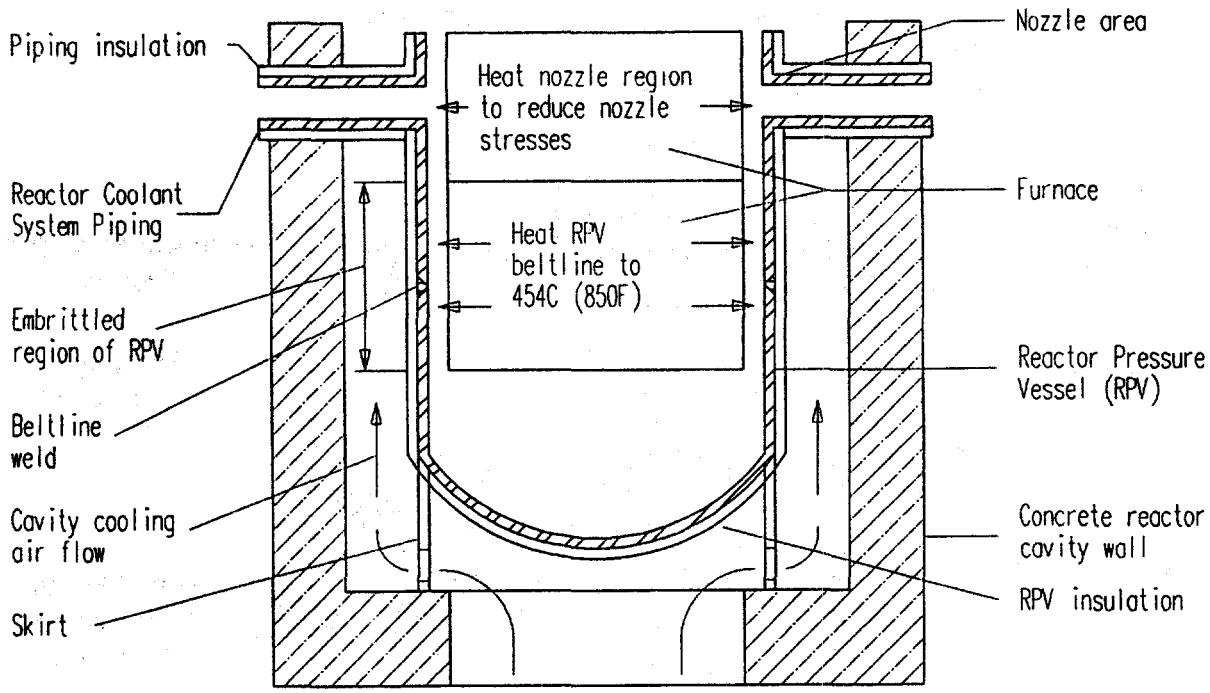

Figure 3. Schematic of PWR Reactor Pressure Vessel Annealing (Skirt Supported RPV).

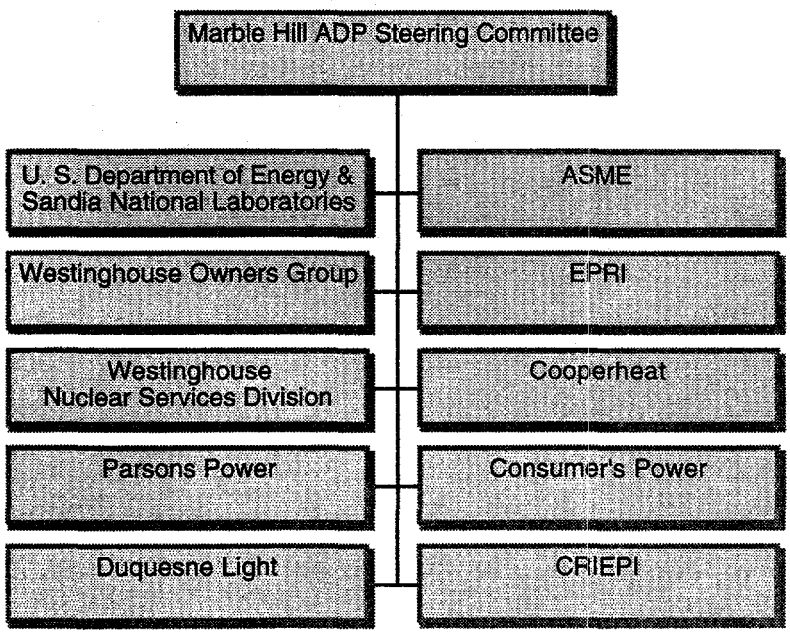

Figure 4. Marble Hill Annealing Demonstration Project Steering Committee.

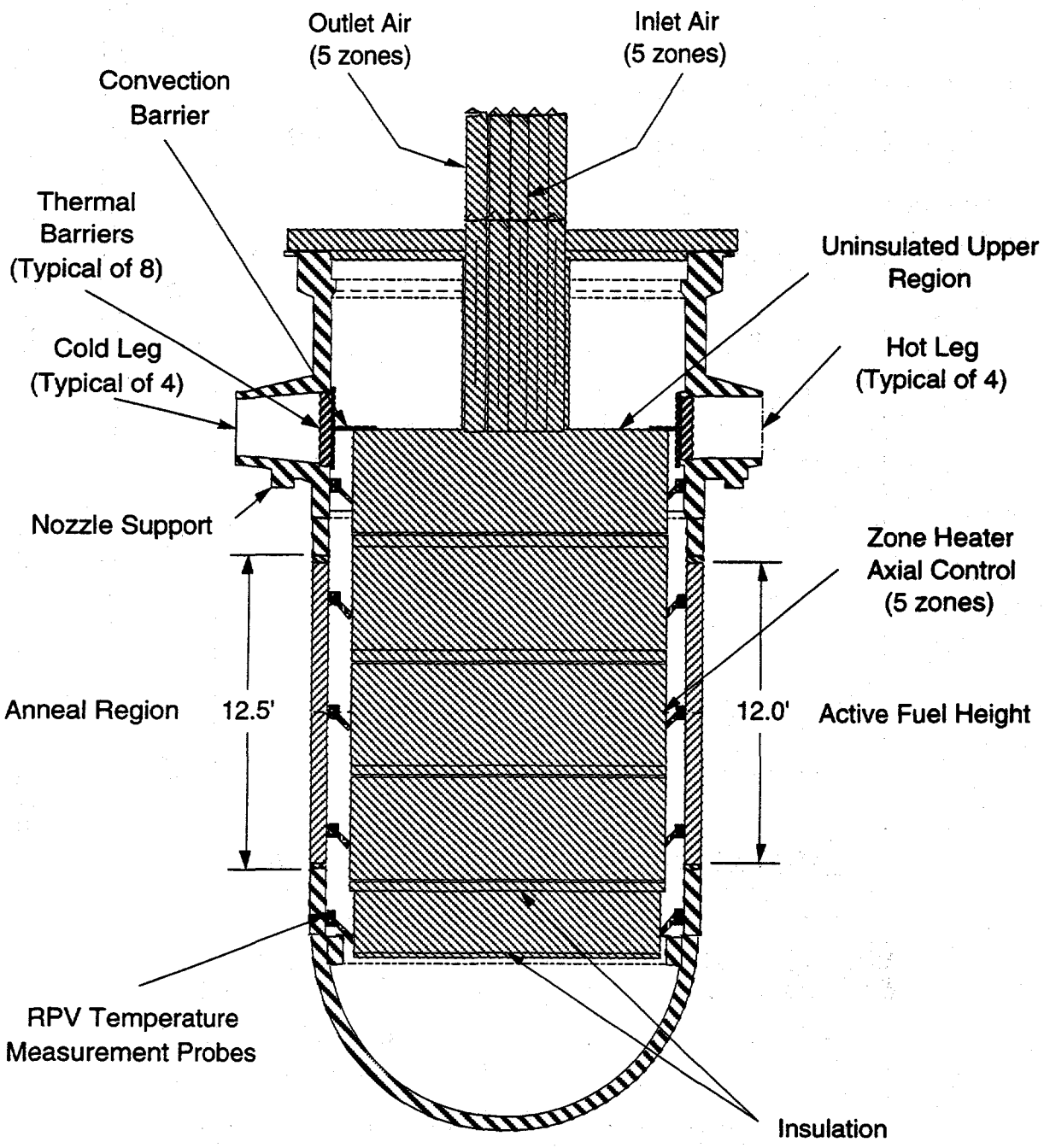

Figure 5. Schematic of Marble Hill ADP.

Figure 6. Cooperheat 6,000,000 BTU/hour Environmental Propane Burners.

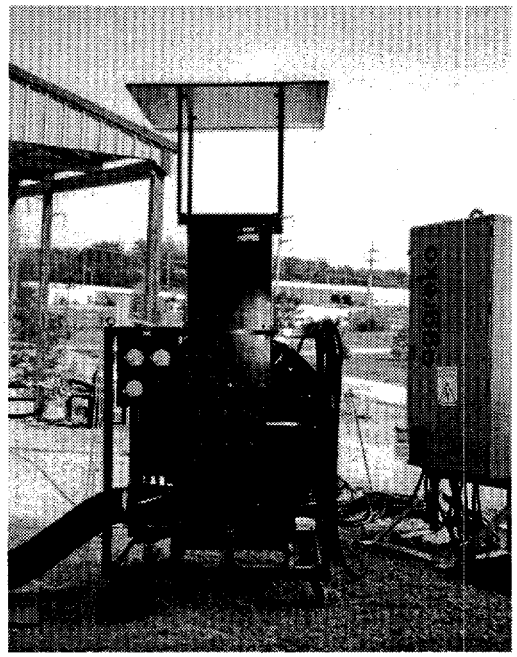

Figure 7. Cooperheat 2700 CFM Blower.

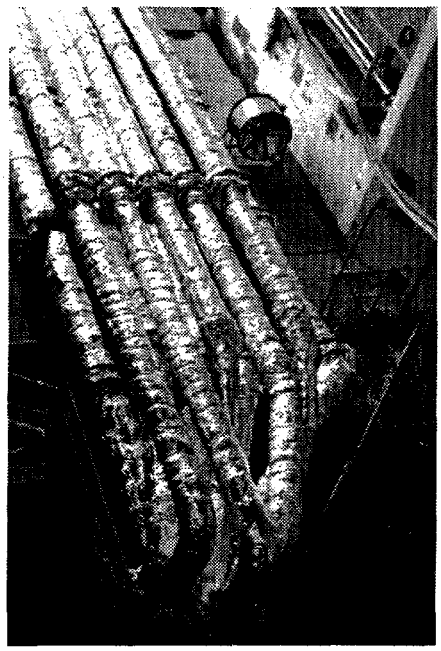

Figure 8. Inlet and Outlet Ductwork on Containment Floor leading down into the reactor cavity.

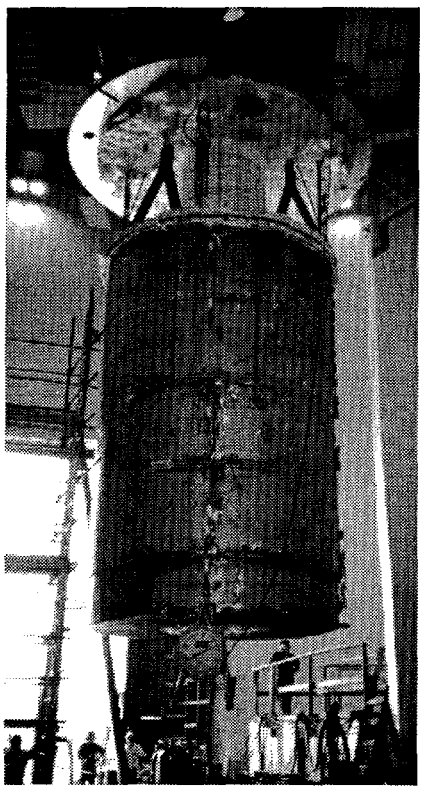

Figure 9. The Marble Hill Heat Exchanger - Reactor Assembly in route to the reactor vessel.

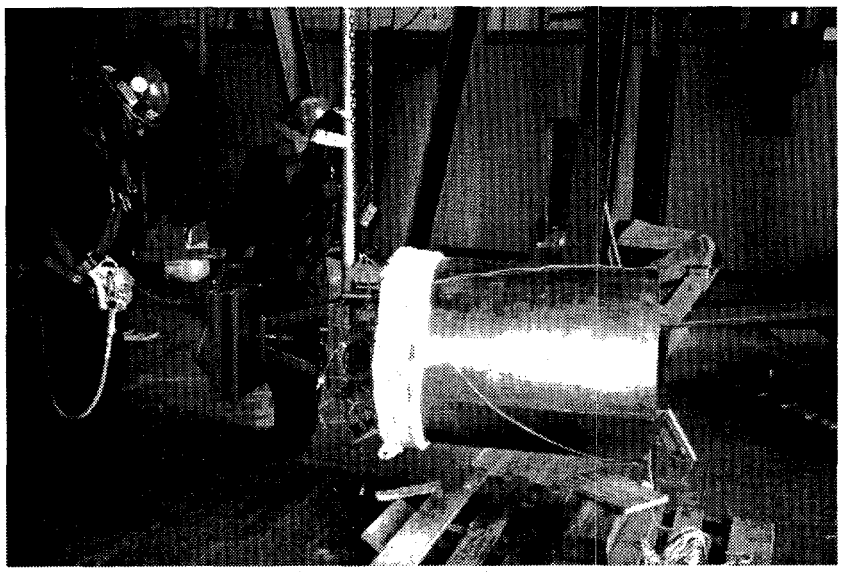

Figure 10. Field Thermal Barrier which was remotely installed into one of the reactor nozzles.

Figure 11. A pair of thermocouple junctions spot-welded on the inside surface of the reactor vessel.

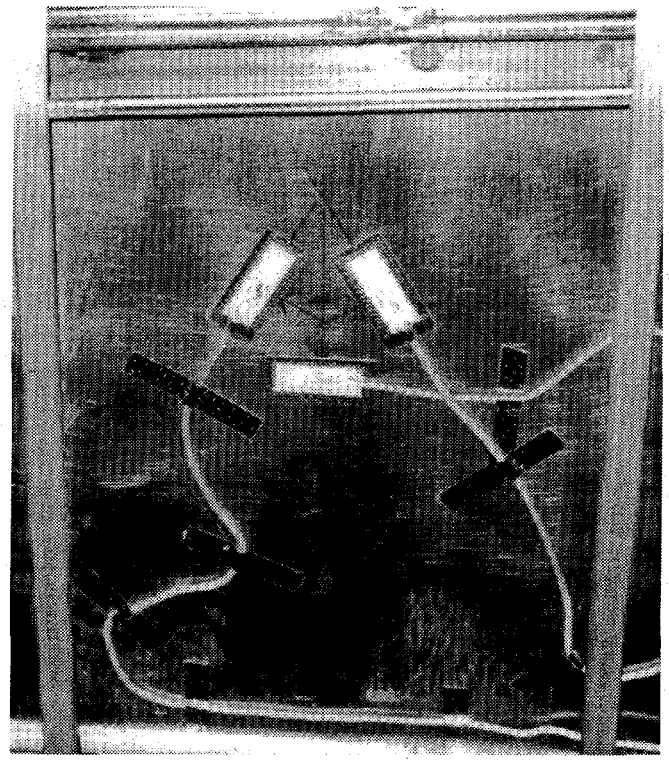

Figure 12. A high temperature strain gauge rosette directly mounted to the loop piping.

Figure 13. Refueling of propane storage tanks.

NRC ASSESSMENT OF THE DEPARTMENT OF ENERGY ANNEALING DEMONSTRATION PROJECT

Deborah A. Jackson and Shah N. Malik
Office of Nuclear Regulatory Research
U. S. Nuclear Regulatory Commission
Washington, DC 20555-0001

ABSTRACT

Thermal annealing is the only known method for mitigating the effects of neutron irradiation embrittlement in reactor pressure vessel (RPV) steels. In May 1996, the U.S. Department of Energy (DOE) in conjunction with the American Society of Mechanical Engineers, Westinghouse, Cooperheat, Electric Power Research Institute (with participating utilities), Westinghouse Owner's Group, Consumers Power, Electricite' de France, Duquesne Light and the Central Research Institute of the Electric Power Industry (Japan) sponsored an annealing demonstration project (ADP) at Marble Hill. The Marble Hill Plant, located in Madison, Indiana, is a Westinghouse 4 loop design. The plant was nearly 70% completed when the project was canceled. Hence, the RPV was never irradiated. The paper will present highlights from the NRC's independent evaluation of the Marble Hill Annealing Demonstration Project.

GENERAL BACKGROUND

Maintaining the structural integrity of reactor pressure vessels is fundamental to the safe operation of nuclear power plants. During the operating life of a nuclear power plant, neutrons escaping from the reactor core embrittle the reactor pressure vessel (RPV) beltline materials resulting in a reduction of the margins against vessel failure and a possible limit in the service life of a reactor vessel. Vessels embrittled by neutron irradiation are more vulnerable to failure due to operating and accident loads. U. S. Nuclear Regulatory Commission (NRC) (Refs. 1-3) requirements limit the permissible irradiation-induced embrittlement in the beltline region such that adequate fracture-prevention margins are maintained throughout the 40-year period of operation. Researchers in the U.S. and other countries are making progress in modeling neutron irradiation embrittlement and understanding the mechanisms that cause the embrittlement. However, the only known method for mitigating the effects of neutron irradiation is thermal annealing.

THERMAL ANNEALING PROCESS

Thermal annealing is a process in which the highly embrittled area of the vessel is heated significantly above the operating temperature for an extended period, usually one week. The elevated temperature causes a rearrangement of the metallurgical substructure of the RPV beltline materials, thereby relieving embrittlement damage to the vessel and restoring the fracture toughness and ductility to almost an unirradiated level. Restoring the fracture

toughness and ductility restores the margin against failure and, potentially, the service life of the vessels. The temperature must be elevated enough to restore the embrittled material to nearly its unirradiated level, but not elevated to the point to cause dimensional distortion and creep damage to the vessel, or affect the original heat treatment.

ANNEALING EXPERIENCE

Thermal annealing of a commercial reactor pressure vessel has never been accomplished in the United States. The Russians and East Europeans have obtained significant experience with thermal annealing of commercial RPVs. They have successfully performed 15 separate anneals of the VVER-440 design vessel (Novovoronezh Unit 3 was annealed twice). While their experience is useful, it does not address all of the relevant questions for the U.S. designs (Ref. 4).

DEVELOPMENT OF NRC REGULATORY DOCUMENTS

In anticipation of the possible need for thermal annealing of an operating plant, the U.S. Nuclear Regulatory Commission (NRC) published a Thermal Annealing Rule (Part 50.66, Code of Federal Regulations) on December 1995 and issued a Regulatory Guide 1.162, "Format and Content of Report for Thermal Annealing of Reactor Vessels," on February 1996. The thermal annealing rule addresses the critical engineering and metallurgical aspects of thermal annealing. The regulatory guide provides guidance on preparing a thermal annealing report for licensees seeking to anneal their pressure vessel. Additionally, the American Society of Mechanical Engineers (ASME) developed and approved Code Case N-557 (Ref. 5) on thermal annealing which addresses annealing conditions (temperature and duration), temperature monitoring, evaluation of loadings, stress and strain limits, and non-destructive examination techniques. Thus, the regulatory documents and codes/standards are in place to support a licensee's decision to anneal its RPV.

U.S. ANNEALING DEMONSTRATION PROJECT (ADP)

The U.S. Department of Energy (DOE) in conjunction with ASME, Westinghouse, Cooperheat, Electric Power Research Institute (with participating utilities), Westinghouse Owner's Group, Consumers Power, Electricite' de France, Duquesne Light and the Central Research Institute of the Electric Power Industry (Japan) sponsored an annealing demonstration project (ADP) at Marble Hill. The Marble Hill Plant, located in Madison, Indiana, is a Westinghouse 4 loop design. The plant was nearly 70% completed when the project was canceled. Hence, the RPV was never irradiated

Prior to the actual ADP, DOE and the NRC entered into a Memorandum of Understanding (MOU) (Ref. 6) in June 1995, which established the framework for cooperation and coordination of DOE and NRC activities during the ADP. The DOE established a multi-year strategy aimed at demonstrating thermal annealing of an RPV as a commercially viable option for managing the embrittlement of an RPV and restoring its material properties. The NRC participated in the portion of the DOE program addressing the annealing demonstration, as an independent observer. The NRC's objectives were to perform an independent assessment of the validity of engineering analysis methods in predicting the temperatures and thermally induced deformations and stresses induced in PWR

components due to thermal annealing, to evaluate the engineering issues associated with thermal annealing, and to develop an inspection procedure for use during the anneal of an actual plant.

NRC STAFF PARTICIPATION IN ADP

The Marble Hill ADP began in May 1996 and was completed in July 1996. NRC staff members and Oak Ridge National Laboratory (ORNL) personnel participated as observers in the project. Prior to arrival on site at Marble Hill, NRC and ORNL staff members identified the engineering issues that needed to be addressed for the ADP. The issues involved: 1) development of appropriate thermal and structural models for predicting limiting stress conditions and providing guidance for placement and quantity of instrumentation; 2) control of thermal gradients during heat up and cooldown to minimize stresses and deformations in the vessel and attached piping; 3) adequate instrumentation for monitoring the response of the RPV and piping to the anneal; 4) adequate onsite fire protection; and 5) protection of other equipment, components and structures potentially affected by the annealing. During an anneal at an operating plant the issues of radiation hazards and material property recovery would be addressed.

An observation procedure was developed by NRC staff for NRC and ORNL personnel. The observation procedure, provided background and objectives for NRC/ORNL staff while on site. The NRC/ORNL staff activities while on site were to observe all elements of the ADP particularly as they might apply to Palisades, exercise the staff observation procedure and gather information for revising the staff observation procedure into an inspection procedure. NRC staff and contractor participation in onsite activities included 11 NRC headquarters staff, three regional staff members and two staff members from Oak Ridge National Laboratory (ORNL).

PRELIMINARY RESULTS OF STAFF OBSERVATIONS

NRC staff members were on site to observe set up of the heater; installation and removal of the heater, ductwork and instrumentation; assembly and installation of the reactor vessel top cover; pre and post NDE inspections and dimensional checks, RPV measurements (upper flange, inlet/outlet nozzles, core support lugs), set up of burners, heat up and soak (850 degrees for seven days) of the vessel. NRC staff members would observe all or some of the previously mentioned activities during an actual anneal. The opportunity to observe these activities on an unirradiated RPV provided valuable insights into the accuracy and level of uncertainty that might be encountered for an irradiated RPV. Observations from the NRC staff and NRC contractors, with regard to the requirements of 10 CFR 50.66 and the guidance of RG 1.162, included the following: RPV dimensional stability, thermal and stress analyses, control of thermal gradients, protection of other equipment, structures, and components, adequacy of instrumentation, adequacy of fire protection, and radiation protection.

Preliminary results from the pre and post anneal non-destructive examination (NDE) inspections, and pre and post anneal dimensional measurements revealed no distortion to the vessel. NDE inspections of the RPV and associated loop piping resulted in no

reportable indications. Pre and post anneal dimensional measurements were within acceptable tolerance.

The NRC contracted with Oak Ridge National Laboratory (ORNL) to develop an independent thermal stress and deformation analysis model, select confirmatory instrumentation, and perform post-anneal analytical model validation for the ADP. The purpose of these analyses was to provide an independent assessment of the analytical modeling used in designing the annealing process, the accuracy of that modeling compared to measurements made during the anneal, and the design and implementation of the instrumentation package installed to monitor the annealing process. The effort did identify some differences in the analytical models used by the DOE/Industry team and ORNL. The key modeling differences are:

1. The NRC/ORNL thermal-hydraulics model of the ADP included both the radiant heating of the vessel by the gas-fired radiant heater as well as the effects of natural convection flow of hot air within the RPV, whereas the DOE/Industry analytical model considered only the radiant heating of the vessel.

2. The NRC/ORNL analytical model for the reactor vessel thermal stress analysis differed with the DOE/Industry model in that ORNL utilized the more accurate quarter-symmetry (90 degrees) model, whereas the DOE/Industry staff used an approximate 1/8th (45 degrees) model of the reactor vessel and associated inlet/outlet piping. The difference in the two analyses models predicted considerably different bending stresses in the inlet/outlet piping connected to the reactor vessel. Although, both models predicted the stresses and strains to be within allowable limits in the recently approved ASME Boiler & Pressure Vessel (B&PV) Code Case N557 on thermal annealing of RPVs.

Additionally, the results of the analyses identified one substantive difference in perspective on temperature limits that should be imposed during a thermal anneal. Specifically, the predicted concrete temperature in the RPV nozzle-support region was predicted by ORNL to be about 400 degrees F assuming no water or air cooling of the support. This is above the temperature limit (350 degrees F for short term exposure) as specified in paragraph CC-3440 of the ASME B&PV Code. The DOE/Industry analysis also found temperature above the ASME code allowable for the concrete in the nozzle-support region. However, the DOE/Industry team considered the concrete in the nozzle-support region to be "sacrificial," with the actual load being supported by the steel frame underneath the concrete.

Preliminary assessment of the measured temperature data shows a very sharp axial gradient extending from the vessel nozzle to the top of the RPV flange area. As shown in Figure 1, this temperature gradient is highly nonlinear and is expected to cause additional stresses in the vessel nozzle to flange area. Figure 1 also shows the ORNL pre-test prediction for the temperature gradient in that region. The post-test analysis is being carried out to determine the effect of this highly non-linear axial temperature. It is believed that the sharp gradient may be due to air flow leakage in the annular gap (0.5 inch) between the mirror insulation and the outside of the reactor vessel wall. This is being investigated further from the outside vessel wall temperature history data.

All monitoring instrumentation operated as specified. There were 228 temperature sensors located on the reactor vessel external surfaces, reactor coolant piping, cavity concrete, reactor vessel nozzles, flange, and internal surfaces, 22 displacement sensors located on reactor vessel external surfaces and reactor coolant piping and 14 strain sensors located on the reactor coolant piping and reactor vessel nozzle to pipe end welds. In addition, NRC confirmatory instrumentation consisted of two temperature detectors installed on RPV nozzle support area, four strain gages installed in the nozzle area and four displacement gages installed on the base of the steam generator and primary coolant pump. The objective of the NRC confirmatory instrumentation was to assist in resolving the differences in thermal and stress analysis models by DOE/Industry and NRC/ORNL.

The NRC and DOE/Industry teams have obtained measured test data from the instrumentation of the ADP and from the NRC confirmatory instrumentation. The data are presently being analyzed to perform post-test refinement of the respective analytical predictive models to validate the instrumentation required for an actual anneal of a similar plant.

NRC staff observations identified two areas which would be unacceptable during the anneal of an operating plant's RPV. The areas are fire protection and radiation protection. It should be noted that the Marble Hill ADP was a demonstration project and the fire protection and radiation protection findings did not present a problem for the Marble Hill ADP. In the area of fire protection there were three areas of concern, 1) proximity of potential ignition sources (electrical equipment) was a minor deviation from National Fire Protection standard No. 58 for Liquid Propane/Gas storage and use, 2) storage of propane tanks such that if the tanks were inadvertently ignited they would move toward safety related structures, 3) limited manual fire suppression capabilities (portable fire extinguishers and a single hose line connected to a hydrant).

Radiation protection issues resulted from the extended duration of certain activities. The specific activities were fabrication of the heater ductwork and installation of a remotely installed thermal barrier. The heater ductwork required extensive onsite engineering and fabrication. Similarly, a dimensional problem was encountered during installation of the non-simplified thermal barrier. The non-simplified thermal barrier, which was installed using a specially designed tool, had to be removed, machined and reinstalled. The other seven thermal barriers were installed manually. Both of these issues, heater ductwork and the thermal barrier, highlighted the importance that must be placed on detailed pre-anneal planning, inspections, and quality assurance checks to avoid unnecessary personnel exposures.

CONCLUSION

The NRC staff has concluded, conditioned on the data that are available at this time, that thermal annealing of a U. S. design reactor vessel can be accomplished without damage to other equipment, components, and structures in the plant. No significant problems were identified during the annealing process. However, there were some practical issues identified associated with assuring that personnel exposures would be minimized.

Additionally, some issues were identified associated with analytical modeling and how limits on temperature should be implemented. It is anticipated that these issues would be easily resolved as part of a thermal annealing program for an operating nuclear power plant.

Participation in this project provided the staff the opportunity to observe a realistic thermal annealing process on an unirradiated RPV, and provided valuable insights into the accuracy an level of uncertainty in the analytical modeling of the annealing process. The combination of the regulatory basis now in place for thermal annealing and the results of this engineering demonstration provide a sound technical and regulatory basis for performing a thermal anneal of an operating reactor pressure vessel of U.S. design.

MARBLE HILL ADP

THERMAL GRADIENTS IN THE UPPER SHELL REGION WERE LARGER THAN PREDICTED

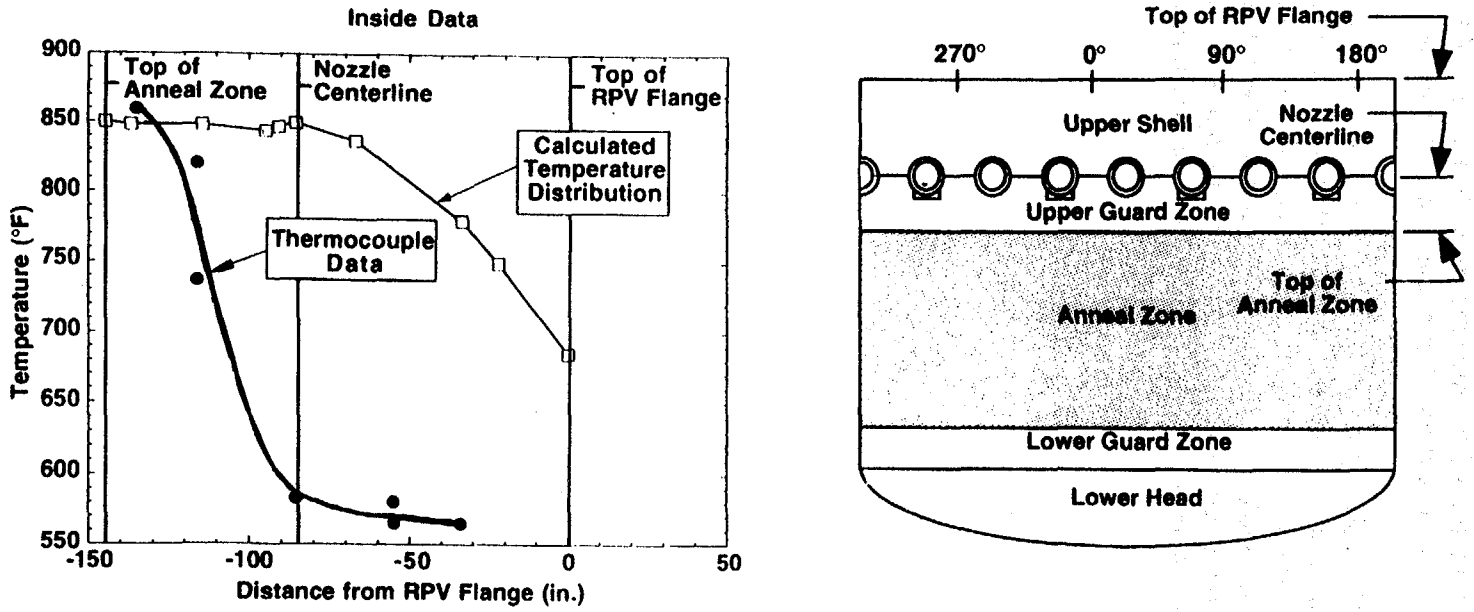

FIGURE 1: Axial Temperature Gradient in the Reactor Pressure Vessel Nozzles to Top Flange Region During the Steady-State Soak Period of the Thermal Anneal at Marble Hill Annealing Demonstration Project, and Pre-Test Prediction by Oak Ridge National Laboratory for NRC

REFERENCES

1. Title 10, Code of Federal Regulations, Section 50.60, "Acceptance Criteria for Fracture Prevention Measures for Lightwater Nuclear Power Reactors for Normal Operation.

2. Title 10, Code of Federal Regulations, Section 50.61, "Fracture Toughness Requirements for Protection Against Pressurized Thermal Shock Events."

3. Title 10, Code of Federal Regulations, Part 50, Appendix G, "Fracture Toughness Requirements."

4. R. Pelli and K. Torronnen, "State of the Art Review on Thermal Annealing," European Commission, DG XIII - Joint Research Centre, Institute for Advanced Materials, DG XI - Safety of Nuclear Installations, Aging Materials and Evaluation Studies (AMES) Report No. 2, December, 1994.

5. ASME Code Case N-557, "In Place Dry Annealing of a PWR Nuclear Reactor Vessel," March 1996.

6. Letter from J.M. Taylor, Executive Director for Operations, U. S. Nuclear Regulatory Commission, to Dr. T. R. Lash, Director - Office of Nuclear Energy, Science and Technology, U. S. Department of Energy, enclosing 2 copies of the Memorandum of Understanding for the DOE Annealing Demonstration Project, August 4, 1995.

REACTOR VESSEL LOWER HEAD INTEGRITY

SESSION OVERVIEW

by Alan M. Rubin

US Nuclear Regulatory Commission

On March 28, 1979, the Three Mile Island Unit 2 (TMI-2) nuclear power plant underwent a prolonged small break loss-of-coolant accident that resulted in severe damage to the reactor core. Post-accident examinations of the TMI-2 reactor core and lower plenum found that approximately 19,000 kg (19 metric tons) of molten material had relocated onto the lower head of the reactor vessel. Results of the OECD TMI-2 Vessel Investigation Project concluded that a localized hot spot of approximately 1 meter diameter had existed on the lower head. The maximum temperature on the inner surface of the reactor pressure vessel (RPV) in this region reached 1100°C and remained at that temperature for approximately 30 minutes before cooling occurred.

Even under the combined loads of high temperature and high primary system pressure, the TMI-2 RPV did not fail. (i.e., The pressure varied from about 8.5 to 15 MPa during the four-hour period following the relocation of melt to the lower plenum.) Analyses of RPV failure under these conditions, using state-of-the-art computer codes, predicted that the RPV should have failed via local or global creep rupture. However, the vessel did not fail; and it has been hypothesized that rapid cooling of the debris and the vessel wall by water that was present in the lower plenum played an important role in maintaining RPV integrity during the accident. Although the exact mechanism(s) of how such cooling occurs is not known, it has been speculated that cooling in a small gap between the RPV wall and the crust, and/or in cracks within the debris itself, could result in sufficient cooling to maintain RPV integrity. Experimental data are needed to provide the basis to better understanding these phenomena and improve models of RPV failure in severe accident codes.

The question of whether or not the RPV would fail or not during a severe accident is important from two standpoints. First, it has a direct impact on ex-vessel phenomena (e.g., high pressure melt ejection and direct containment heating, ex-vessel fuel-coolant interactions, molten core-concrete interactions). If the vessel does not fail, loads associated with these phenomena would not affect the containment. Second, the need to maintain water in-vessel, if possible, during a severe accident is relevant to accident management strategies. Specifically, knowing the effectiveness of adding water to the RPV before or after the reactor core has been damaged is particularly important. Flooding the cavity to provide ex-vessel cooling of the RPV is another accident management strategy that could be used to prevent the vessel from failing.

Many of the issues and questions mentioned above will be discussed during this session on Reactor Vessel Lower Head Integrity. The first paper, entitled "A Scaling and Experimental Approach for Investigating In-Vessel Cooling," discusses scaled experiments to obtain data on two mechanisms that could protect the vessel wall from overheating from relocating molten core debris. The first involves the lack of adhesion between melt material and the vessel wall that can create substantial contact resistance between the melt and the wall. The second mechanism involves creep of the RPV wall due to both internal pressure and elevated wall temperatures. The relative growth of the vessel wall can form a gap between the wall and the crust, thereby allowing water in the gap to enhance the cooling of the wall and the debris. The second paper, entitled "Studies on In-Vessel Debris Coolability in ALPHA Program," covers a different, but closely related, scaled experimental program to investigate phenomena related to enhanced in-vessel debris cooling with the presence of water in the plenum. The rough upper surface of the solidified debris, cracks in the debris surface, and the presence of a gap at the interface between the solidified crust and the vessel wall are discussed in the paper.

The next two papers in this session address the subject of in-vessel retention of core melt via ex-vessel flooding. The paper entitled "In-Vessel Retention of a Core Melt," presents results and conclusions from an extensive assessment of the concept of ex-vessel flooding of the reactor cavity to effect in-vessel core melt retention for an AP600-like reactor design. The fourth paper describes the implementation of an accident management strategy to flood the reactor cavity for the Lovissa Nuclear Power Plant in Finland. Modifications made to the plant and the technical bases for implementing this strategy are discussed.

The fifth paper, entitled "A Scaling Law for the Local Critical Heat Flux (CHF) on the Outer Surface of a Heated Hemispherical Vessel," presents results from scaled experiments on CHF and the application of a scaling law to apply the results of these experiments to full-scale reactor conditions. These data and analyses can be used to assess the heat removal capability and local CHF on the outer surface of a submerged reactor vessel lower head.

Each of the first five papers in this session addresses some aspect of whether or not molten core material can be retained in the RPV, either from in-vessel cooling with water in the lower plenum, or ex-vessel flooding. The last paper, entitled "A Preliminary Assessment of the Effects of Heat Flux Distribution and Penetration on the Creep Rupture of a RPV Lower Head," discusses scaled experiments on RPV failure. These experiments provide data on the strain behavior prior to creep rupture, rupture time, and the resulting rupture size from creep rupture of the lower head under the combined effects of thermal and pressure loads. The results of these experiments will be used to support the development and assessment of analytical models of RPV failure.

In conclusion, the papers in this session cover three major areas on RPV lower head integrity. The first area involves experiments on in-vessel debris cooling phenomena. Results of these experiments will help to determine if the behavior observed during the TMI-

2 accident is representative of all such accidents, or if it is specific to the TMI-2 accident sequence and RPV design. The second area covers ex-vessel flooding to maintain reactor vessel integrity during a severe accident. This includes experimental and scaling analyses for CHF, assessment of in-vessel melt retention for an advanced reactor design, and implementation of an ex-vessel flooding accident management strategy for an operating reactor. The final area covers creep rupture failure of the RPV under various combined pressure and thermal loads. The results of these papers can help to answer the following two key questions relating to RPV lower head integrity during severe accidents: (1) Under what conditions can molten core material be retained in the reactor pressure vessel through internal and/or external cooling (i.e., ex-vessel flooding)? and (2) If the RPV were to fail, what is the likely failure mode, location and timing of vessel failure?

A SCALING AND EXPERIMENTAL APPROACH FOR INVESTIGATING IN-VESSEL COOLING

Robert E. Henry
Fauske & Associates, Inc.

ABSTRACT

The TMI-2 accident experienced the relocation of a large quantity of core material to the lower plenum. The TMI-2 vessel investigation project concluded that approximately 20 metric tonnes of once molten fuel material drained into the RPV lower head. As a result, the lower head wall experienced a thermal transient that has been characterized as reaching temperatures as high as 1100°C, then a cooling transient with a rate of 10 to 100°C/min. This cooling process was the result of water in the reactor pressure vessel and may, or may not, be typical of all accident sequences in which water is added to the RPV after core damage occurs and before there is substantial relocation to the RPV lower planum.

Two mechanisms have been proposed as possible explanations for this cooling behavior. One is the ingression of water through core material as a result of interconnected cracks in the frozen debris and/or water ingression around the crust which is formed on internal structures (core supports and in-core instrumentation) in the lower head. The second focuses on the lack of adhesion of oxidic core debris to the RPV wall when the debris contacts the wall. Furthermore, the potential for strain of the RPV lower head when the wall is overheated could provide for a significant cooling path for water to ingress between the RPV and the frozen core material next to the wall. Such water ingression could provide for significant cooling of both the wall and the core debris.

To examine these proposed mechanisms, a set of scaled experiments have been developed to examine the potential for cooling. These are performed in a scaled system in which the high temperature molten material is iron thermite and the RPV wall is carbon steel. A thermite mass of 40 kg is used and the simulated reactor vessels have water in the lower head at pressures up to 2.2 MPa. Furthermore, two different thicknesses of the vessel wall are examined with the thicker vessel having virtually no potential for material creep during the experiment and the thinner wall having the potential for substantial creep. The experiment also includes the potential for substantial creep. Moreover, the experiment includes the option of having molten iron as the first material to drain into the RPV lower head or molten aluminum oxide being the only material that drains into the test configuration.

1.0 INTRODUCTION

Post-accident examinations of the TMI-2 reactor core, lower plenum and lower plenum wall illustrated that a substantial amount of molten core debris (approximately 20 tonnes) drained from the original core boundaries into the lower head at about 3 hours and 45 minutes into the accident. The net result of this was that a significant part of the RPV wall (approximately 1 meter in diameter) was overheated to temperatures approaching 1100°C. Metallographic information taken from the vessel wall samples illustrated that the wall cooled rapidly at this temperature in the range of 10 to 100°C per minute (Wolf et al., 1994). This aspect of the TMI accident is particularly relevant to accident management evaluations. More specifically, how effective is water that is injected into the RPV, as occurred in the TMI-2 accident, after the reactor core has been damaged? Is the behavior observed in the TMI accident representative of all such situations, or is it specific to the TMI accident sequence and reactor vessel design?

Accident management actions have two major goals:

- to stop the accident progression, and
- prevent, or mitigate, the release of fission products from the reactor coolant system and containment.

Of these, the first is the most important since it has a direct bearing on the second. Hence, any actions to limit the progression of an accident are of key interest to accident management personnel.

Once a severe accident has been initiated, the above goals can be described in terms of (1) debris barriers, and (2) fission product barriers. For those LWR reactor designs used in the U.S., Western Europe and the Far East, there are two debris barriers, i.e. the reactor vessel and the containment. Of these, retaining the damaged core material within the reactor vessel greatly reduces the uncertainties to be considered and addressed in managing the accident. Moreover, it reduces the mobility of fission products, thereby also aiding in preventing, or mitigating, the release of fission products.

Debris retention in the reactor pressure vessel requires that the RPV and eventually the debris be cooled. Cooling of the vessel wall can be accomplished with (a) water inside the RPV (b) by external cooling of the reactor vessel with no water in the RCS or (c) through both internal and external cooling. Of course using both mechanisms simultaneously, for those reactor systems where this can be accomplished, protects the RPV integrity, scrubs fission products and limits the accident progression. Cooling the debris and the RPV wall with water in the RPV, as was the case in the TMI-2 accident, would be the result of EOPs if the necessary systems are available. Furthermore, for some designs in-vessel cooling would be effective much faster since several hours are necessary to flood some containments to a level sufficient for RPV external cooling.

An experimental program has been developed and is being carried out to examine the possibility for in-vessel cooling of the RPV, thereby providing insights on protecting the RPV integrity. One explanation for the TMI-2 behavior proposed by Henry and Dube (1994) involves two fundamental responses in the RPV lower plenum; (1) the core material draining into the lower head does not "wet" or adhere to the RPV wall, and (2) if the vessel wall becomes hot, local material creep could create a small but significant cooling path between the debris and the RPV wall. This cooling path could have a characteristic dimension of 1 mm. While this is one explanation for the behavior in the TMI-2 accident, there may be other mechanisms which could aid or control the cooling process, for example water ingression through cracks in the core debris or small gaps between frozen core debris and internal structures (Rempe and Chavez, 1993).

The experiments performed in this study focus on the potential for an in-vessel cooling mechanism, either as a result of the mechanism proposed by Henry and Dube or water ingression through cracks, or a combination thereof. In any case, they focus on the question of whether core debris draining into a water filled lower plenum could be successfully cooled if water was continually available in the lower plenum. In essence, the experiments focus on whether the accident progression could be terminated inherently as long as a) water is maintained in the reactor lower plenum even though major core damage occurs, b) core debris drains into

the lower plenum and c) the RPV wall temperatures increase to values where the wall would have limited strength.

2.0 TECHNICAL BASIS FOR THE MECHANISM EXAMINED

2.1 Experimental Evidence in the Literature

For a configuration like that shown in Figure 2, high temperature molten core material draining onto the RPV lower head results in substantial overheating of the reactor vessel wall. If the molten material entered the lower plenum at a time when there was a significant water inventory, EPRI-sponsored experiments (Hammersley, et al., 1993 and Hammersley and Henry, 1994a and 1994b) and the TMI-2 experience suggests a significant contact interface resistance would be established as the debris submerges water-filled crevices in the RPV wall. Vaporization of this trapped water (Figure 3) would separate the wall and the debris, causing a contact resistance. This has been observed on repeated occasions, and not only controls the energy transfer from the melt to the wall, but also the adherence of the debris to the RPV wall.

It is interesting to note that many steam explosion experiments, such as those reported by Long (1957), observe that contact between the high temperature melt and an unpainted wall initiated explosive interactions. When the wall was painted, no such interactions occurred. This is an indirect but important indication that water trapped in surface cavities (unpainted surface) vaporizes quickly once contact occurs. (For Long's experiments this likely was the "trigger" to initiate an explosive interaction.) Furthermore, the fact that painted surfaces prevent such interactions indicates this mechanism is eliminated when wall cavities are not available. For the stainless steel cladded surfaces in an RPV, wall cavities would always be available. While elevated pressures have been shown to prevent steam explosions (Henry and Fauske, 1979), vaporization of water in the surface cavities would still occur immediately following contact of the high temperature debris. Hence, these additional observations are entirely consistent with the formation of a contact resistance at the wall.

The comparatively large scale, out-of-reactor FARO tests (Magallon and Hohmann, 1993) also provide insights with respect to debris accumulation on the lower plenum wall. These experiments poured molten debris (a combination of uranium dioxide and zirconium dioxide at temperatures of approximately 3000°K), through water onto a debris catcher mechanism. Post-test examinations showed that there were substantial accumulations of molten material on this debris catcher, clearly indicating that much of the material was molten when reaching this plate. However, there were no indications that the plate suffered any damage, which is consistent with the above discussions considering the lack of adherence between the debris and the steel structures.

As a result of stresses imposed by the internal pressure and the dead weight of the material, the RPV lower head may experience creep at elevated temperatures. As the material creeps, the brittle oxidic core material is not subject to the same pressure stresses, hence it would not experience the same creep and would tend to separate from the RPV surface. Consequently, if such a creep mechanism were established, the lack of adherence of the debris to the RPV wall and the differential structural response would result in a stretching of the RPV wall with respect to the core material as illustrated in Figure 4. (The extent of creep is greatly

exaggerated in this figure to clearly illustrate the mechanism.) This would then create paths for water to ingress between the debris and the RPV wall. This relative growth of the RPV wall compared to the core debris, while quite small (gap dimension of the order 100 μm), would be extremely important in terms of the thermal response of the RPV wall. Such relative growth could also open cracks between the debris and internal structures. This coolant ingression path may also be due to crust shrinkage as proposed by Rempe and Chavez (1993).

What information is available to assess the heat removal rate in narrow gaps? Monde, et al. (1982) have performed experiments for heat removal in narrow channels submerged in a water pool. While this is not the specific geometry of interest for lower head cooling and the length of the gaps are much shorter than would be the case in the reactor lower plenum, it provides an order of magnitude perspective on maximum rate of heat removal.

Typical data for this experiment are shown in Figure 5, again taken from Monde, et al. As illustrated, the heat removal rates can approach 1 MW/m^2 at atmospheric pressure. The data for the maximum heat removal were correlated by the authors using the standard formulation for the flat plate critical heat flux;

$$q/A)_{gap} = c\, h_{fg} \sqrt{\rho_g} \sqrt[4]{g\sigma\,(\rho_f - \rho_g)} \tag{1}$$

where

$$c = 0.16 \left[1 + 6.7\,(10^{-4}) \left(\frac{\rho_f}{\rho_g}\right)^{0.6} \left(\frac{\ell}{\delta}\right)\right]^{-1} \tag{2}$$

Here $q/A)_{gap}$ is the maximum heat removal rate from the heated surface, g is the acceleration of gravity, σ is the steam-water surface tension, with ρ_f, ρ_g and h_{fg} being the water density, steam density and the latent heat of vaporization respectively. Of particular note, δ is the gap width and ℓ is the gap length. These latter two parameters are of major interest in applying the results to the reactor system since the gap is the path whereby water could ingress downward to cool the RPV wall and ℓ represents the path length, which could be torturous depending on the gap dimension.

Next, let us consider how fast the RPV wall could creep at elevated temperatures, i.e. how long would it take to develop a sufficient gap to cool the wall. Figure 6 shows creep rupture data for the TMI-2 vessel wall as well as that taken by Maile et al. (1990). If the internal pressure is 10 MPa, the stress in the lower head would be approximately 78 MPa (11,000 psi). Using Figure 6, this indicates the RPV would fail in tens of seconds for these conditions. This is also consistent with the Larson-Miller (1952) approach. This suggests that both the thermal transient and the temperature profile in the wall are important in determining the gap size. Of course, these values are only approximate but they clearly indicate that a sufficient separation can develop quickly when the temperatures reach values of about 1100°C. It is also interesting to note that the temperature would not greatly increase above this value with an internal pressure of 10 MPa. Thus, the fact that the temperature reached this value in the TMI-2 accident, in and of itself, is strongly indicative of a creep related mechanism.

To address the need for a more directly applicable data base, FAI performed a set of quenching experiments in a narrow annular gap (Henry and Hammersley, 1996). A schematic of the test apparatus is given in Figure 7. As shown, the annulus is formed by two pipes, the inner one capped at the top and the annulus is sealed at the bottom. This configuration enables both the inner and the outer walls of the annulus to be instrumented with thermocouples to monitor the quenching process. A clam shell heater furnace was used to heat the entire apparatus to about 800°C. At this point, the test piece was removed from the furnace and installed in a vertical rig to keep the upright orientation. A loose fitting funnel was put in the top and saturated water was added through the funnel. This water accumulated above the top of the capped end of the inner pipe and penetrated into the narrow gap to quench the stainless steel walls forming the annulus. The cooling rate is the major experimental observation.

Figure 8 illustrates the typical thermal transient for a 2 mm radial gap. Several general observations can be made immediately:

1. The overall transient appears similar to any quenching process.

2. As soon as the water is added to test apparatus, the increased cooling rate is observed over the entire 0.25 m length of the narrow annulus. Hence, whatever the two-phase flow pattern and circulation may be in this unique geometry, it is effective throughout the gap.

3. The transition to nucleate boiling may occur first at the bottom of the gap and propagate upward from this location.

Considering the initial phase of the cooling process as "film boiling" is itself quite interesting. Since the gap dimension is smaller than the capillary dimension, what kind of flow pattern would exist when the wall is not wet by the water? One possible two-phase flow pattern is a dispersed droplet configuration with the droplet size smaller than the radial gap dimension. The capillary dimension (diameter) is given by

$$d = \sqrt{\frac{\sigma}{g(\rho_f - \rho_g)}} \approx \sqrt{\frac{\sigma}{g\ \rho_f}} \tag{3}$$

where σ is the steam-water surface tension, g is the acceleration of gravity, with ρ_f and ρ_g being the respective densities of saturated water and steam. At atmospheric pressure, this corresponds to a value of 2.3 mm; hence droplets in the gap would be smaller than the capillary dimension.

With the entire inner and outer walls cooling at approximately the same rate, we can analyze the data to assess the heat flux to the coolant. If the wall is sufficiently thin to consider a negligible temperature gradient through the wall, the heat flux at any location can be calculated by

$$q/A = \rho_w\ \delta_w\ c_w \left(\frac{dT_w}{dt} - \left(\frac{dT_w}{dt} \right)_o \right) \tag{4}$$

where ρ_w is the density of the wall, δ_w is the wall thickness, c_w is the specific heat of the wall material, T_w is the wall temperature and t is time.

The transition to nucleate boiling occurs at different times for various locations. To provide a meaningful value for integral analyses, we can construct an average cooling rate that quenches the apparatus when the last measurement reaches saturation. This is illustrated on Figure 8 for Test 37 and is typical of all the experiments performed on this test section. Such a rate is about 100,000 w/m^2 for each the inner and outer surface, which is about 60% of that calculated from the Monde correlation.

2.2 Application to the TMI-2 Accident

To investigate the relevance to the TMI-2 accident, consider a continuous segment (reconstituted region) of core material on the bottom of the RPV head with a diameter of about 1 m and a thickness of 0.2 m. Approximating this volume as a pancake corresponds to ~ 1600 kg of core material or about 1.6% of the total fuel. On a percentage basis, the energy generated in this portion of the core debris would be about 0.5 MW. Conservatively assuming that all of this power needed to be extracted in the gap between the debris and the RPV wall, the heat flux necessary to sustain cooling would be ~ 0.6 MW/m^2. Considering the primary system pressure to be 10 MPa, the correlation developed by Monde, et al. would yield this heat flux when the gap is ~ 240 microns, i.e. a value requiring very little strain of the RPV wall. (This strain would correspond to about 0.05% which would not be detectable in the post-accident vessel inspection program.) However, the major point of this example is not that the strain is 200 microns, rather that the strain is very limited. In this regard, let us consider the potential cooling if the gap were 1 mm for the same conditions listed above. In this case, the heat flux that could be removed from the gap is three times greater than the conservative estimate above. Hence, the inherent cooling mechanism is such that the strain would continue until there was sufficient water ingression to cool the RPV wall and stop the local creep of the steel wall. Even in the most conservative assessment of the cooling conditions required, the strain (gap) necessary for effective cooling is very small compared to the radius of the continuous debris layer accumulated on the lower head. Hence, this relative growth of the RPV wall compared to the core debris, while quite small, would be extremely important in terms of the thermal response of the RPV wall.

MAAP4 includes a gap model based on the Monde correlation and a representation of material creep. Figures 9 and 10 illustrate two of the key results of the MAAP4 benchmark calculation with the TMI-2 accident. First the model predicts ~ 25.5 tonnes to drain into the lower head at about 3.77 hours (226 mins.) into the accident (Figure 9). This is in agreement with the observations that about 19 tonnes drained into the lower plenum at 227 mins. Figure 10 illustrates the calculated RPV wall thermal transient, with TRV(1,1) being the inner surface temperature of the RPV wall at the bottom of the vessel and TRV(1,5) is the temperature of the vessel outer surface at this location. As shown, the inner wall temperature increases rapidly to a temperature of about 2150°F (1177°C) where the decreasing metal strength and stress redistribution results in material creep. Eventually this creep is sufficient to enable cooling of the RPV wall in the debris-wall gap as evidenced by the reversal of the temperature profile in the vessel wall. This peak temperature is consistent with the metallographic estimates of 1100°C in the TMI-2 Vessel Investigation Project (Wolf et al., 1994).

3.0 DESCRIPTION OF THE TEST APPARATUS

3.1 Scaling

As suggested by Zuber et al. (1991), bottom-up scaling is one essential component of the scaling process. The first elements to be addressed are those issues related to scaling for the fundamental mechanism being investigated. For this, it is necessary to examine one or more possible mechanisms and determine the fundamental characteristics, thus the scaling issues to assure that the mechanism can be investigated, then demonstrate how the experiment will address these issues. For the mechanism suggested by Henry and Dube (1994), debris adherence to the RPV wall for debris falling through water and contacting the wall is determined by the material properties and by the behavior of water in the wall cavities. Hence, it is important for the experiment to have approximately the same materials and wall surface cavity population as the reactor vessel. Surface cavity site population is generally determined by the material, i.e. metallic (crystalline), glass amorphous, etc. Thus, using a steel test vessel provides the influence of wall cavities that are consistent with the behavior observed in the TMI-2 accident, i.e. the debris did not adhere to the RPV wall (Wolf et al., 1994).

The EPRI sponsored experiments (Hammersley and Henry, 1994), which examined the response of lower head penetrations, observed that when either molten Al_2O_3 was used alone or when both the iron and alumina were poured through water, the debris did not adhere to the test vessel wall. This was demonstrated by a lack of adherence between both types of frozen debris and the carbon steel wall in post-test examinations, as well as a contact resistance that influenced the heat transfer from the melt to the test vessel wall. Note that when the melt was poured into a dry vessel, the iron was welded to the carbon steel wall for those tests where the iron was not separated out. Consequently, water in the lower plenum had a dramatic influence on the contact behavior which is consistent with the TMI-2 behavior and the proposed mechanism. Table 1 describes these issues of scale, with Phenomenon 1 addressing the wall cavity scaling size, typically millimeter or submillimeter. Hence, an experimental apparatus with a carbon steel inner surface and a water inventory sufficient to submerge the RPV wall and the debris as it drains into the test element would be sufficient to satisfy this aspect of the scaling consideration.

The second phenomenon in the proposed mechanism is the potential for material creep of the test vessel wall at elevated temperatures. Table 1, Phenomenon 2, summarizes the considerations with respect to the scaling issues for material creep. To address this consideration, it is again necessary to have a steel vessel with significant internal pressure; carbon steel is preferable. For this, the experiment needs to achieve elevated wall temperatures (approaching 1100°C) to develop the potential for local material creep in the wall.

Third, the system must have the potential to cool the RPV wall and the debris, i.e. quench the material from temperature approaching 1100°C. This is also summarized in Table 1, as Phenomenon 3, and the scaling consideration means that the experiment must have a sufficient water inventory to extract the heat from the debris and the test vessel wall after significant overheating has occurred.

Another aspect to be modeled is the potential for water ingression. Since aluminum

oxide is part of the experimental system, the experiments will investigate the general behavior associated with rapid freezing of oxidic material, including the potential for forming interconnected cracks to enable water ingression. Like uranium dioxide, $A\ell_2O_3$ exhibits substantial contraction upon freezing and cooling and has demonstrated a significant porosity in previous experiments. While this cannot be directly scaled with the reactor system, this experimental test series will investigate the potential for water ingression by carrying out post-test examinations of the water ingression potential through both the central part of the oxidic material and that near the vessel wall.

3.2 Test Apparatus

Figure 11 is a schematic of the typical experimental configuration in which thermite is melted in the crucible, released through the melt plug (M1) and discharged into the test element. To disrupt the potential for molten jet attack, the melt is distributed by internal steel structures submerged in the water, fabricated as two parallel disks with holes that do not provide a line-of-sight path. As long as water is available, this disrupts the potential for jet attack. To achieve the necessary internal stress, the system pressure (the test vessel and thermite melting chamber) imposed can be as high as 2.9 MPa, with the pressure in the containment vessel being 0.1 MPa. As shown in Figure 11, the containment vessel has some water in the bottom to protect this part of the facility. Note that the containment water level is well below the test vessel such that there was no external cooling of the vessel due to water submergence. Furthermore, sacrificial material (fire bricks) cover the floor to protect the containment vessel if the test vessel should fail.

The iron oxide and aluminum powders (commercially available thermite) are intimately mixed, heated to a temperature sufficient to initiate the exothermic reaction, which results in aluminum oxide and iron with sufficient energy liberated to melt both reaction products. This molten material achieves temperatures of ~ 2400K, well above the melting temperature of aluminum oxide and far above that of iron.

Since the iron is more dense than the alumina, the two separate to a large extent during the thermite burn and the first material to drain out of the thermite melting chamber is molten iron. Since this has a superheat of ~ 600°C, it has the potential for substantial melt ablation. Hence, both the water and the internal structures in the simulated lower plenum are an important means of breaking up a coherent jet. As mentioned before, the debris did not adhere to the carbon steel wall in the EPRI sponsored tests when there was water in the test vessel even when superheated molten iron was the first material drained. In the reactor system, as observed in the post-TMI-2 investigations, the initial core material that would drain into the lower plenum would be oxidic as a result of the core melt progression. Therefore, experiments with molten iron represent a more aggressive melt than the reactor system in terms of vessel wall heating and attack since the first material descending into the lower head is a superheated metal. Hence, this component of the experimental program is performed in a conservative, non-prototypic manner. Table 2 provides some of the physical properties of iron and aluminum oxidic (alumina), showing that alumina provides a reasonable representation of the oxidic core debris. On the other hand, iron has a much larger thermal conductivity and thermal diffusivity than UO_2. Thus, it is useful for demonstrating the principal but not for simulating core material and RPV response.

The principle measurements for these experiments are the wall temperatures. In particular, these give a clear indication of the potential for material creep of the vessel wall as well as the nature of the cooling process. It is important to have measurements of the wall temperature variations through the vessel wall, as well as at various azimuthal positions in the test vessel lower head from the bottom center to locations above the equator. Figure 12 illustrates the thermocouple locations for Test 1, which is the experiment with the thin lower head (1.17 cm). (A similar pattern was used for tests 3 and 4.) Also shown in this figure is the linear voltage displacement transducer (LVDT) used in the three experiments with a thin lower head. This transducer measures downward deflection of the test vessel lower head. It is noted that this transducer measures the axial growth of the entire test vessel as it experiences an increase in the temperature from room temperature to saturated water at the particular pressure for a given experiment. Table 3 is an instrument list for the tests. This instrument designator given in this table can be used as a reference for all data plots in this report for the instrument type and location.

3.3 Test Matrix

For the proof-of-principle tests (Phase I), a sufficient mass of high temperature melt should be used to fill the test vessel lower plenum in the absence of water. Such proof-of-principle experiments investigate the potential for freezing the melt as it contacts the test vessel lower head, providing sufficient energy to the vessel wall to undergo substantial heating and growth due to strain of the vessel lower head. Thereby, this creates a condition for investigation of cooling from the inside as a result of opening a gap between the frozen core debris crust and the vessel wall. The test matrix used to investigate these conditions is illustrated in Table 4.

With this test matrix, the influence of wall thickness was addressed, even though it is understood that a thicker wall would not likely strain under the test conditions. Even so, Test 1 was very interesting in terms of both the wall thermocouple response and the post-test examination, particularly with respect to the capabilities for water to drain into the vessel lower head and out through holes drilled in the bottom of the test vessel. Moreover, the experiments investigated the potential for straining of a thin vessel wall at elevated pressures as well as at half that pressure for the same size of thermite charge. Consequently, this test matrix was sufficient to explore the basic nature of the wall strain/in-vessel cooling postulate.

4.0 CONCLUSIONS

Mechanisms have been proposed to describe the reason for successful cooling of the core material in the TMI-2 lower plenum. An experimental program has been developed, including bottom-up scaling, to investigate two of the proposed mechanisms. Of these, one of the mechanisms involves limited material creep in the RPV wall once temperatures of the wall reach a level where such deformation could occur. Since the test apparatus can investigate both experiments with oxidic and metallic components, it can also address the potential variations that have been considered for some different types of accident in which metallic constituents could be included in the molten debris.

5.0 REFERENCES

Hammersley, R. J., Merilo, M. and Henry, R. E., 1993, "Experiment to Address Lower Plenum Response Under Severe Accident Conditions", Prob. Safety Assessment, Intl. Topical Mtg., Clearwater Beach, FL, pp. 193-198.

Hammersley, R. J. and Henry, R. E., 1994a, "Experiments to Address Lower Plenum Response Under Severe Accident Conditions, Volume 1: Technical Report", EPRI Report TR-103389-V1.

Hammersley, R. J. and Henry, R. E., 1994b, "Experiments to Address Lower Plenum Response Under Severe Accident Conditions, Volume 2: Data Report", EPRI Report TR-103389-V2.

Henry, R. E. and Fauske, H. K., 1979, "Nucleation Processes in Large-Scale Vapor Explosions", ASME Journal of Heat Transfer, 101, p. 280-287.

Henry, R. E. and Dube, D. A., 1994, "Water in the RPV: A Mechanism for Cooling Debris in the RPV Lower Head", paper presented at the OECD-CSNI Meeting on Accident Management, Stockholm, Sweden.

Henry, R. E. and Hammersley, R. J., 1996, "Quenching of Metal Surfaces in a Narrow Annular Gap", paper presented at the 5th International Conference on Simulation Methods in Nuclear Engineering.

Larson, F. R. and Miller, J., 1952, "A Time-Temperature Relationship for Rupture and Creep Stress", Trans. ASME, pp. 765-775.

Long, G., 1957, "Explosions of Molten Aluminum in Water - Cause and Prevention", Metal Progress, May Issue.

Magallon, D. and Hohmann, H., 1993, "High Pressure Corium Melt Quenching Test in FARO", Paper Presented at the CSNI-FCI Specialists Meeting, Santa Barbara, California, January 5-8.

Maile, K., et al., 1990, "Load Carrying Behaviour of the Primary System of BWRs for Loads Beyond the Design Limits, Part 2: Creep and Failure Behaviour of the Piping Section Under Internal Pressure and High Temperature", Nuclear Engineering and Design, 119, pp. 131-137.

Monde, M., Cusuda, H. and Uehara, H., 1982, "Critical Heat Flux During Natural Convective Boiling in Vertical Rectangular Channels Submerged in Saturated Liquid", Trans. ASME, Journal of Heat Transfer, Vol. 104, pp. 300-303.

Rempe, J. L. and Chavez, S. A., 1993, "Studies to Investigate Cooling of a Continuous Mass of Relocated Debris", Paper Presented at 1993 Japanese Nuclear Technology Workshop.

Wolf, J. R., et al., 1994, "TMI-2 Vessel Investigation Project Integration Report", NUREG/CR-6197, TMI V(93)EG10 EGG-2734.

Zuber, N. et al., 1991, "An Integrated Structure and Scaling Methodology for Severe Accident Technical Issue Resolution", EG&G Idaho Report, NUREG/CR-5809, EGG-2659.

Table 1 Issues of Scale			
Basic Phenomena to be Included	Properties (Dimensions) to be Scaled	Demonstration	
		Test Apparatus (Iron Thermite)	Reactor System
1. Water soaked wall cavities/contact resistance/non-adherence.	Submillimeter.	Lower plenum test, steel surface, no adherence of the melt.	TMI-2, steel surface, no adherence of the melt.
2. Material creep.	• Steel material. • Need to achieve wall temperatures approaching 1100°C with a significant normal stresses.	a. Use carbon steel. b. Hot enough - long enough. c. Vessel will be pressurized. d. Do tests with and without water.	• Carbon steel. • Temps. > 1100°C (TMI-2). • TMI-2 RPV was pressurized. • Water in the lower plenum.
3. Quenching from 1100°C.	Sustained water inventory to submerge the debris.	Experimental design.	TMI-2.

Table 2 Comparison of Physical Properties of $A\ell_2O_3$ and UO_2				
		Physical Properties of $A\ell_2O_3$	Physical Properties of UO_2	Physical Properties of Fe
Melting Temp.	T_{mp}	2047°C	2850°C	1535°C
Heat of Fusion	h_{fs}	1.16×10^6 J kg^{-1}	2.80×10^5 J kg^{-1}	2.7×10^5 J kg^{-1}
Specific Heat	c_s	1300 J kg^{-1} K^{-1}	540 J kg^{-1} K^{-1}	678 J kg^{-1} K^{-1} (100°C)
Thermal Conductivity	k_s	7.5 J m^{-1} s^{-1} K^{-1}	3.35 J m^{-1} s^{-1} K^{-1}	80 J m^{-1} s^{-1} K^{-1} (100°C)
Density	ρ_s	3800 kg m^{-3}	9800 kg m^{-3}	7000 kg m^{-3}
Thermal Diffusivity	α_s	1.5×10^{-6} m^2 s^{-1}*	6.33×10^{-7} m^2 s^{-1}	1.7×10^{-5} m^2 s^{-1}
Coefficient of Thermal Exp.	β	1.7×10^{-4} K^{-1}	4.0×10^{-5}K^{-1}	10^{-5} K^{-1}

Table 3 Instrument List and Designators	
Instrument Designator	Instrument Location
THERMOCOUPLES	
±1	Thermite igniter.
M1	Melt plug lower surface.
C1	Crucible spool piece.
CV1, CV2	Containment vessel gas.
TE11, 12, 13	Test element hemisphere.
TE21, 22, 23	Test element hemisphere.
TE31, 32, 33	Test element hemisphere.
TE41, 42, 43	Test element hemisphere.
TE51, 52, 53	Test element hemisphere.
TE61, 62, 63	Test element wall (near hemisphere).
TE71, 72, 73	Test element wall (near hemisphere).
CT1, CT2, CT3	Catch tank water.
TS1, TS2, TS3	Test element wall (above hemisphere).
PRESSURE TRANSDUCERS	
P1	Crucible gas space.
P2	Containment vessel.
P4	Steam generator gas space.
P5	Steam generator level.
P3	Catch tank pressure.
MOTION TRANSDUCERS	
XB1	Test element bottom.

Table 4 Proof-of-Principle Test Matrix				
Test No.	Vessel Wall Thickness (cm)	Vessel Insulated	Thermite Mass (kg)	Maximum Pressure (MPa)
1	3.3	No	40	2.9
2	1.1	No	40	2.9
3	1.1	Yes	40	1.5
4	1.1	Yes	40	1.5

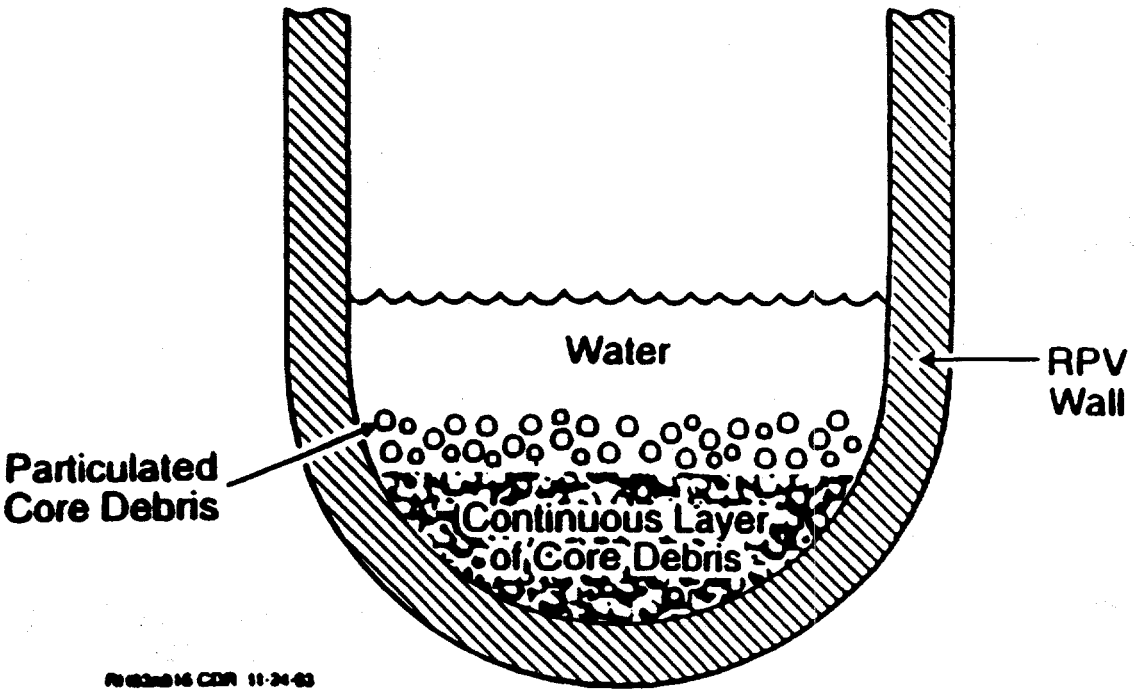

Figure 2 Accumulation of core debris on the RPV lower head.

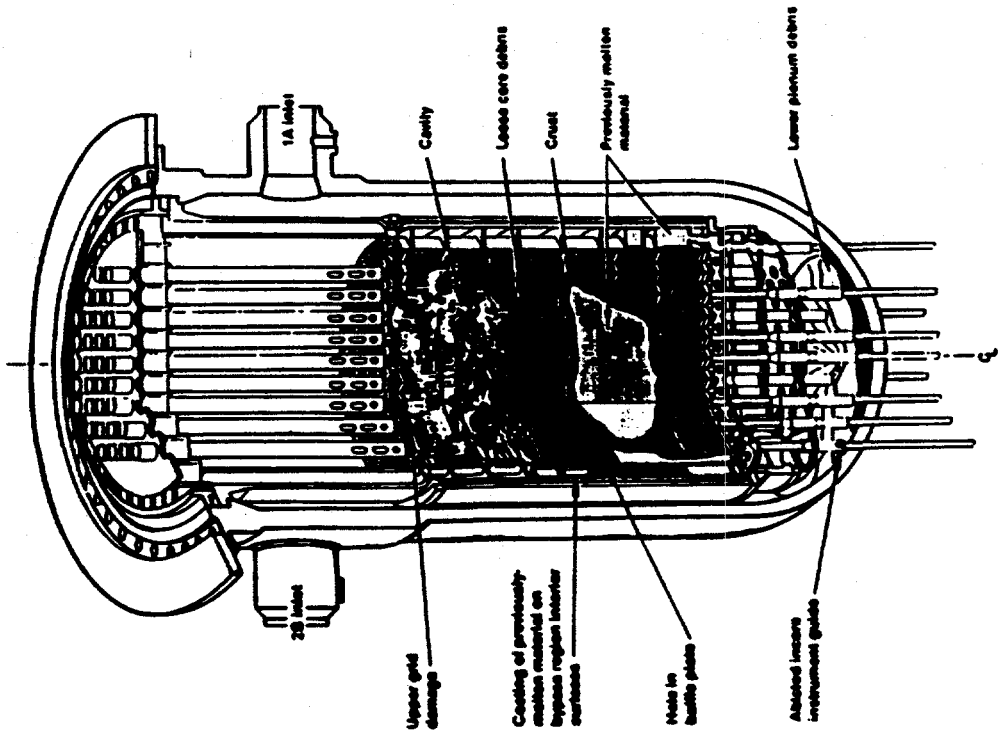

Figure 1 TMI-2 reactor vessel end-state configuration (as represented by Wolf et al., 1994).

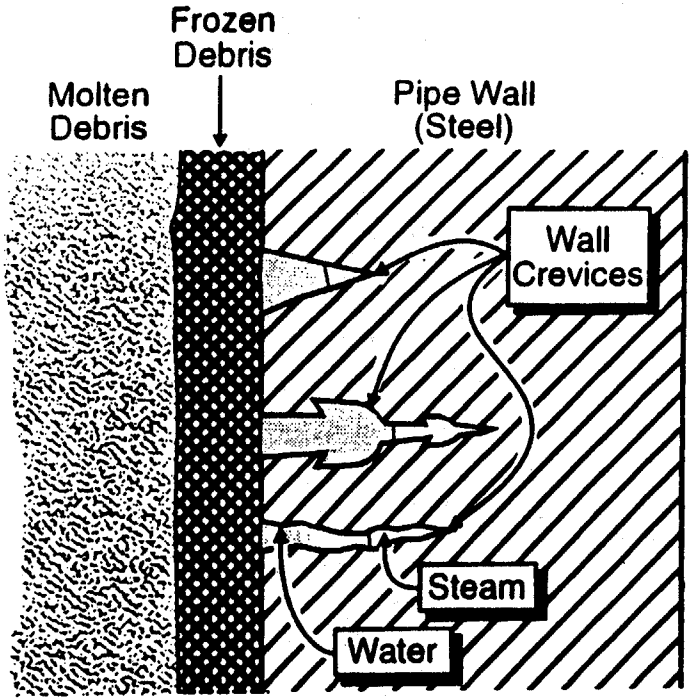

- Pipe is Initially Water Filled.
- Interface Temperature on Contact is:
  - Much Greater than the Critical Temperature for Water,
  - Sufficient to Freeze the Molten Debris,
  - Insufficient to Melt the Steel Wall.

Figure 3 Possible mechanism for developing a thin steam layer (contact resistance).

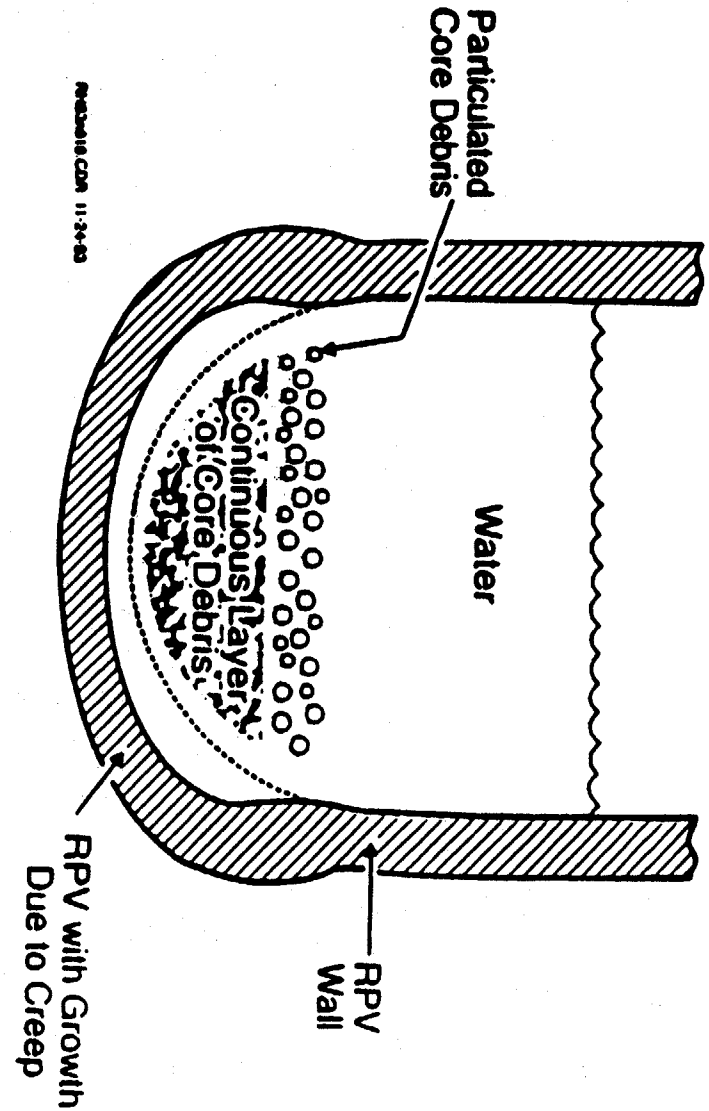

Figure 4 Schematic of relative growth due to creep.

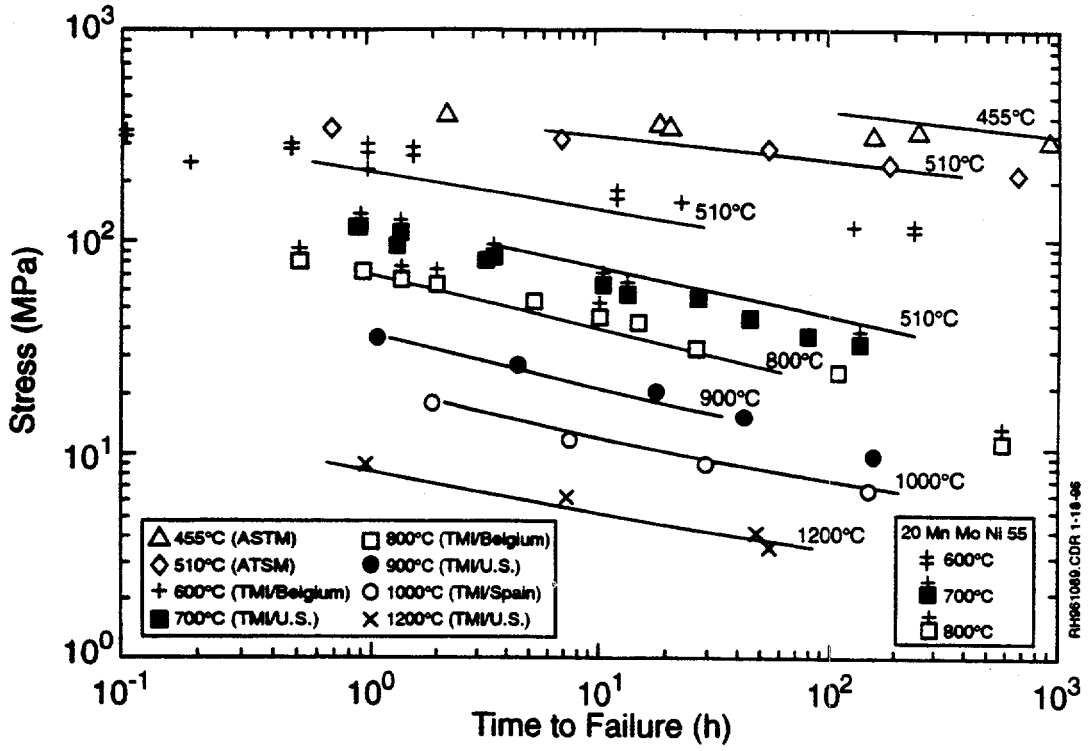

Figure 6 Master creep rupture curve for 316 stainless steel. Note T is in degrees Rankine and t_r is in hours.

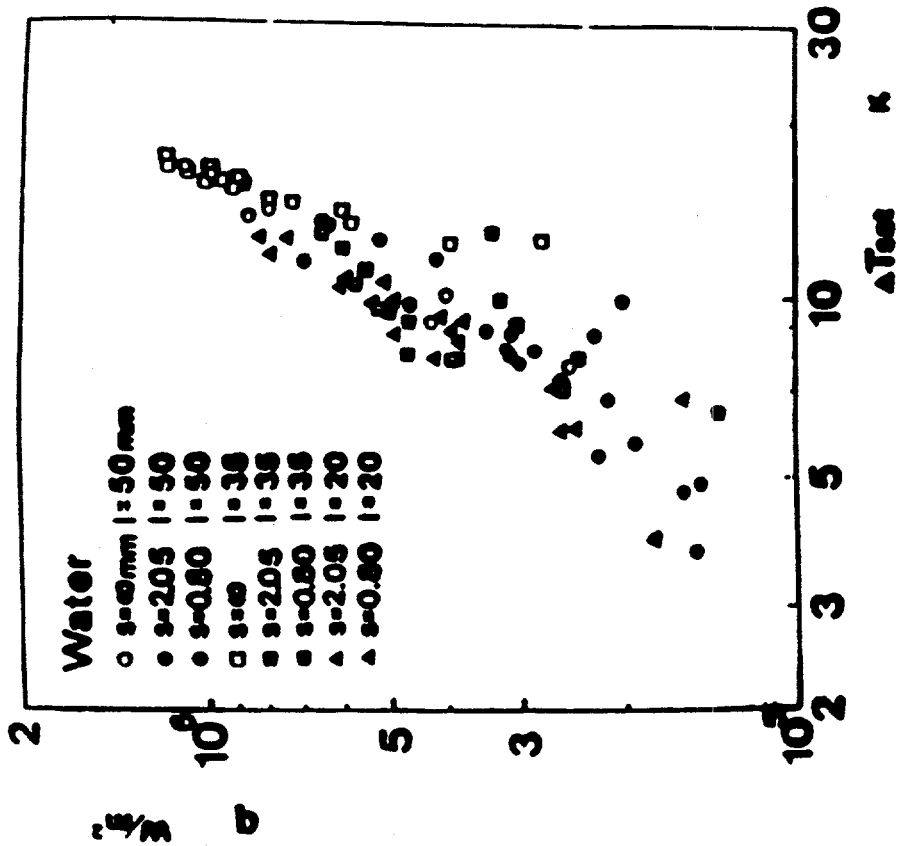

Figure 5 Nucleate boiling data (taken from Monde et al., 1982).

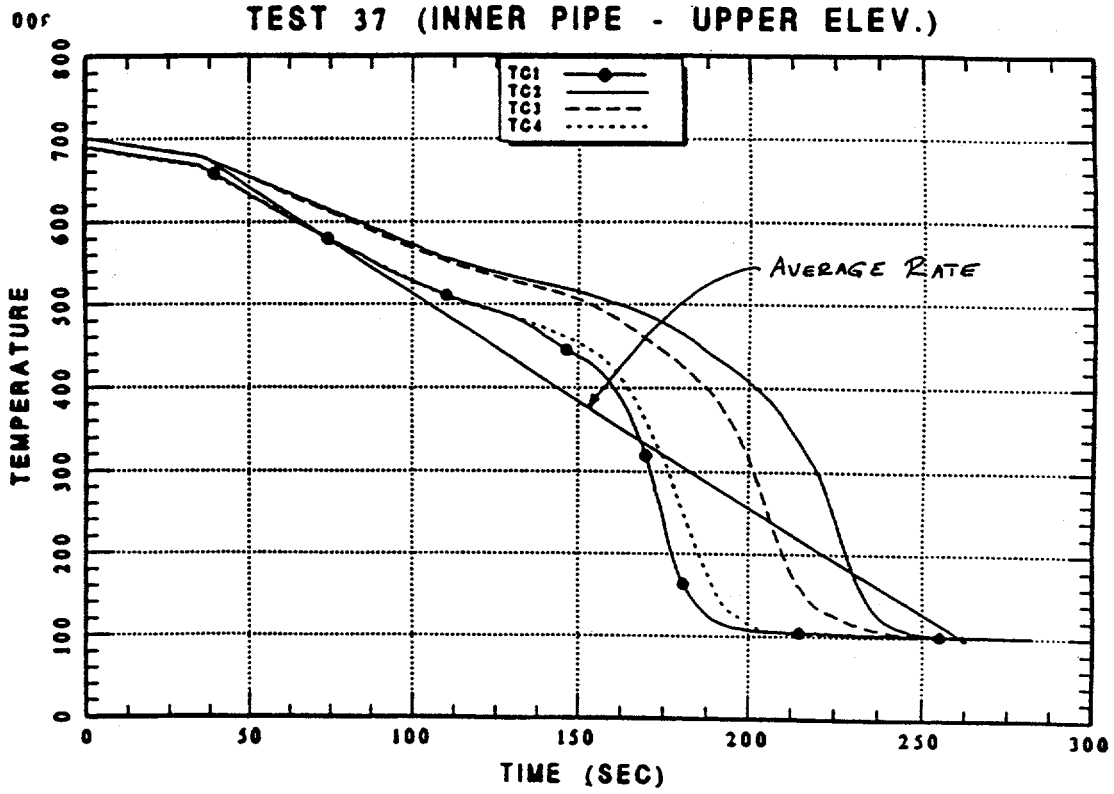

Figure 8 Measured quenching history for Test 37.

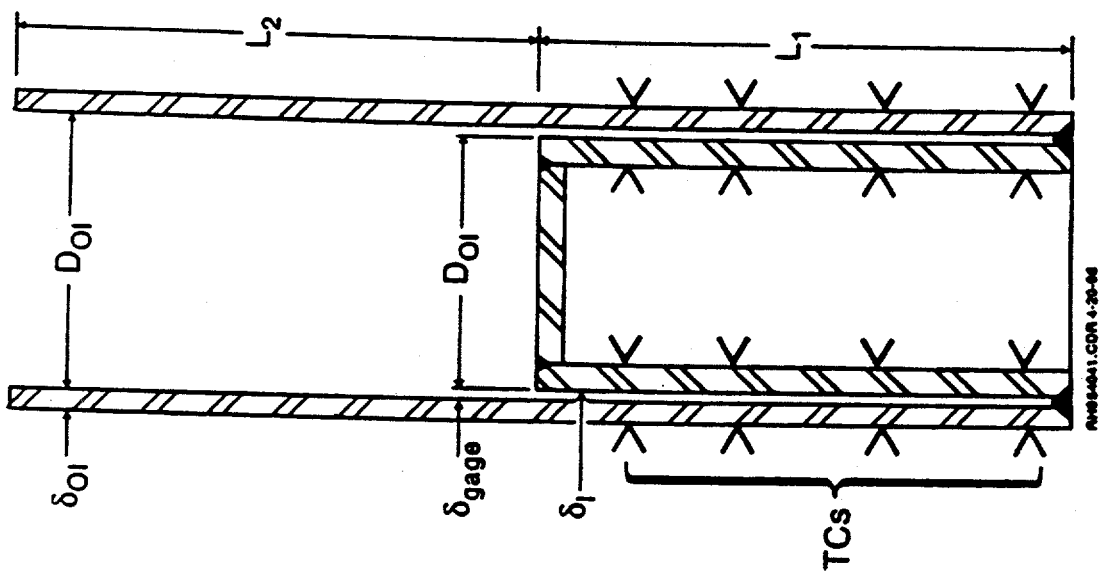

Figure 7 Configuration used for narrow gap cooling test.

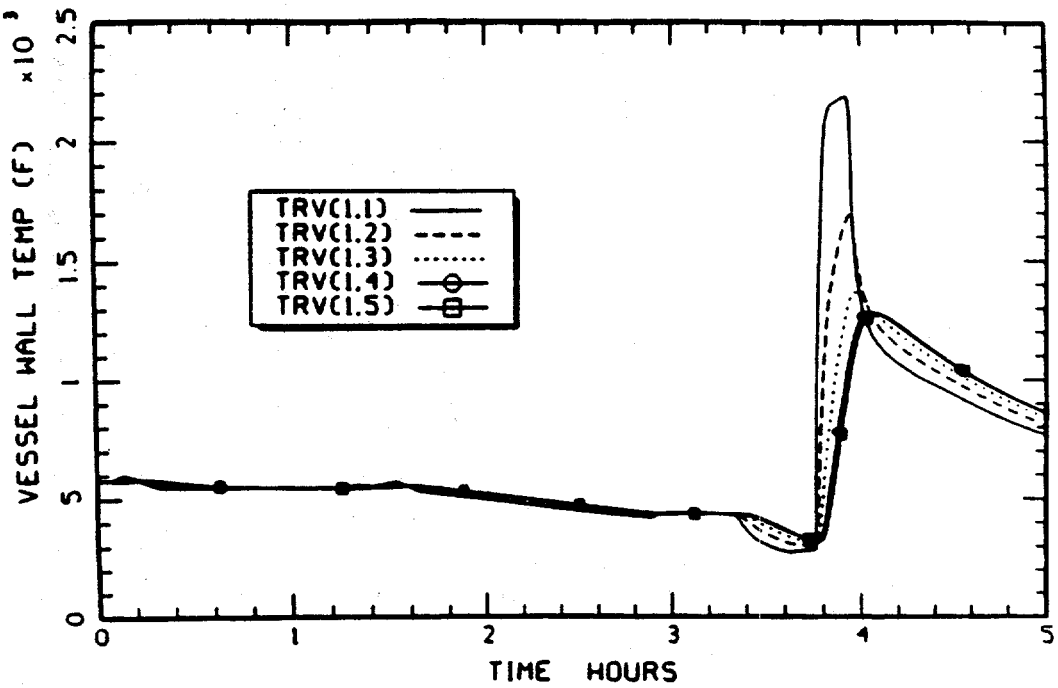

Figure 10 Calculated RPV wall thermal transient due to debris relocation for the MAAP4 TMI-2 benchmark.

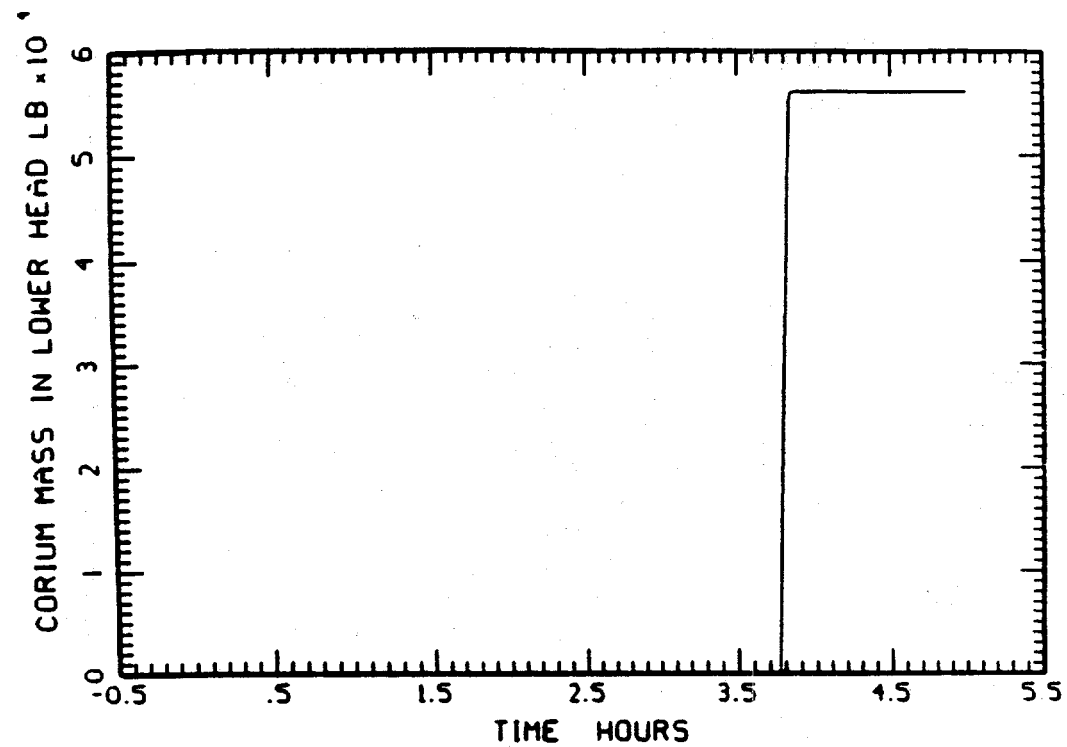

Figure 9 Mass of core debris relocating to the lower head in the MAAP4 TMI-2 benchmark.

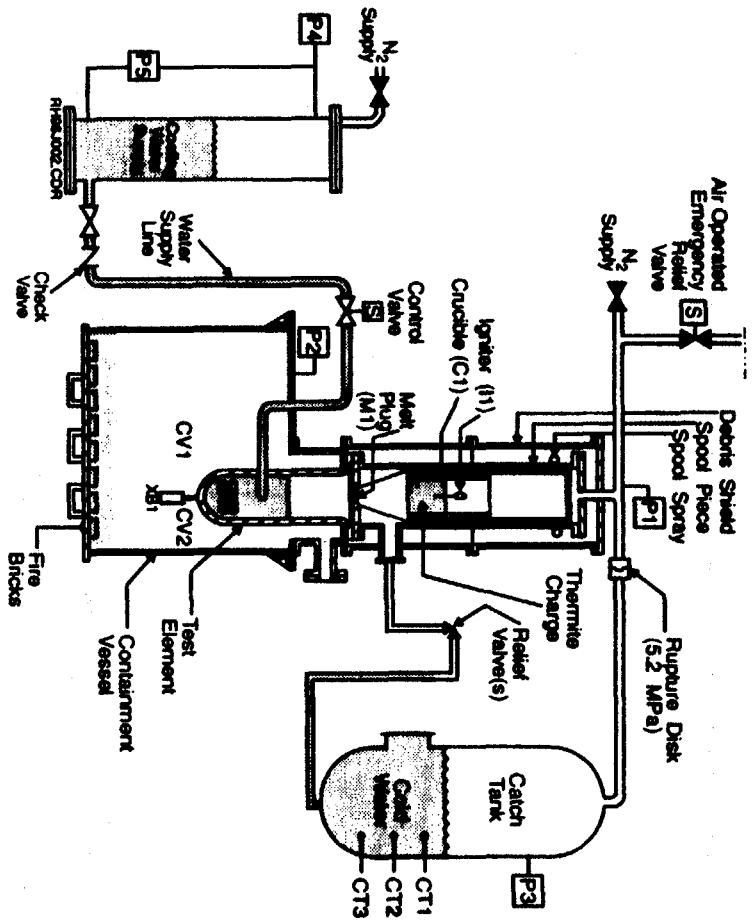

Figure 11 Schematic of the experimental configuration used for the proof-of-principle tests.

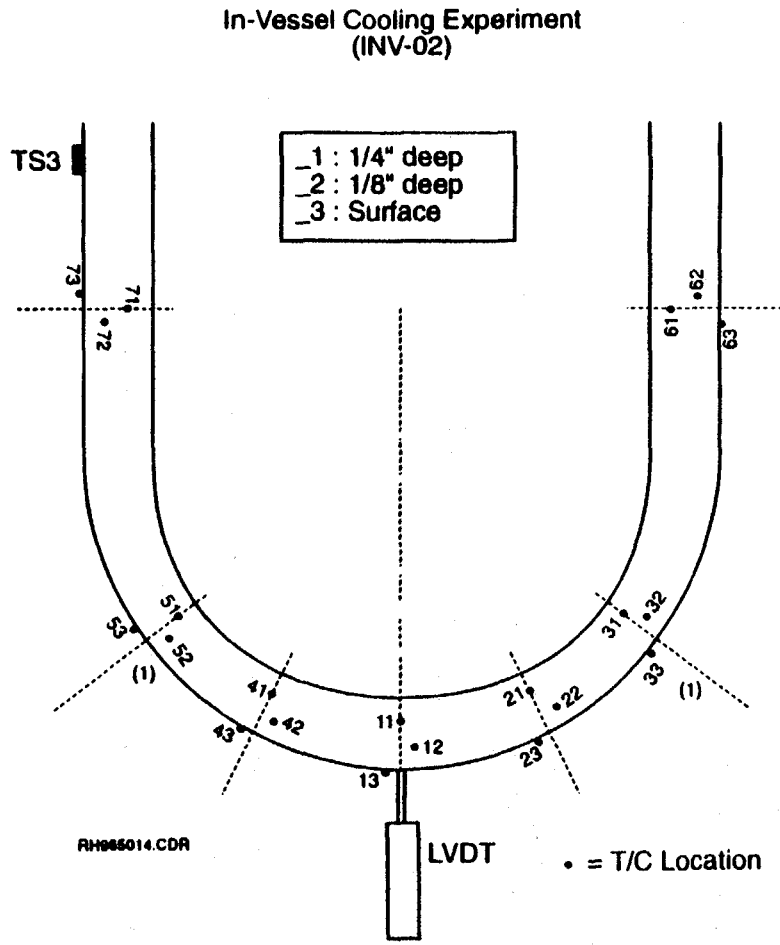

(1) Rotated 90° into plane of other thermocouples.

Figure 12 Location of thermocouples for Tests 2, 3 and 4.

STUDIES ON IN-VESSEL DEBRIS COOLABILITY IN ALPHA PROGRAM

Yu Maruyama, Norihiro Yamano, Kiyofumi Moriyama,
Hyun Sun Park, Tamotsu Kudo and Jun Sugimoto

Japan Atomic Energy Research Institute
2-4 Shirane, Shirakata, Tokai-mura, Naka-gun, Ibaraki-ken, 319-11, Japan
tel: +81-29-282-6163, fax: +81-29-282-5570
e-mail: maruyama@sun2sarl.tokai.jaeri.go.jp

ABSTRACT

In-vessel debris coolability experiments have been performed in ALPHA Program at JAERI. Aluminum oxide (Al_2O_3) produced by a thermite reaction was applied as a debris simulant. Two scoping experiments using approximately 30 kg or 50 kg of Al_2O_3 were conducted. In addition to post-test observations, temperature histories of the debris simulant and the lower head experimental vessel were evaluated. Rapid temperature reduction observed on the outer surface of the experimental vessel may imply that water penetration into a gap between the solidified debris and the experimental vessel occurred resulting in an effective cooling of once heated vessel wall. Preliminary measurement of a gap width was made with an ultrasonic device. Signals to show the existence of gaps, ranging from 0.7 mm to 1.4 mm, were detected at several locations.

1. INTRODUCTION

Severe damage of the reactor core followed by the relocation of the molten debris into the lower plenum region was realized in the event of Three Mile Island Unit 2 (TMI-2) accident[1]. It was identified through activities in TMI-2 Vessel Investigation Project (TMI-VIP) that approximately 19 tons of the debris was accumulated on the pressure vessel lower head[2,3]. The results obtained from metallurgical examinations[4] showed that temperature of the lower head was locally elevated up to approximately 1373 K (1100 °C) and this temperature was sustained for approximately 30 minutes. It was evaluated that the locally heated area was cooled with a temperature reduction rate of 10 to 100 K/s.

Analytical activities have been performed for the evaluation of margin-to-failure of the TMI-2 lower head[5,6]. The analyses implied that additional experimental data should be obtained in order to reduce the uncertainties related to the debris cooling and a lower head failure. A possible

debris cooling mechanism within a lower plenum region was proposed by Henry and Dube . Water migration into gaps formed between a solidified debris and a lower head plays an important role in their model. Unfortunately, the proposed mechanism has not been validated with experimental aspects. Several programs such as SONATA-IV in Korea[8,9] are in progress to clearly identify debris cooling mechanisms.

The evaluation of the in-vessel debris coolability is crucial for further clarification of the severe accident progression and establishment of accident management measures to mitigate a severe accident within a reactor pressure vessel. An experimental series on the in-vessel debris coolability was initiated in ALPHA (Assessment of Loads and Performance of Containment in a Hypothetical Accident) Program conducted at Japan Atomic Energy Research Institute (JAERI). Phenomenological understanding of the debris coolability and development of models regarding debris cooling mechanisms based on the experimental results are primary objectives of the in-vessel debris coolability experiments. Construction and installation of major components of the experimental apparatus were completed at the end of March, 1996. An overview of the experiments and the results of scoping experiments are described in the present paper.

2. DESCRIPTION OF EXPERIMENTS

2.1 Experimental Apparatus and Procedures

A conceptual diagram of the in-vessel debris coolability experiments is shown in Fig. 1. The experiments have been performed in a model containment vessel of the ALPHA facility, which has an inner diameter, a height and a volume of approximately 4 m, 5 m and 50 m^3, respectively. The experimental apparatus is mainly composed of a thermite melt generator, a lower head experimental vessel (LHEV), and water and nitrogen supply systems. The experiments were performed under elevated pressure and nearly saturated water conditions to suppress the occurrence of an energetic steam explosion.

Only an Al_2O_3 part produced by the thermite reaction of Al with FeO and Fe_2O_3 is used as a molten debris simulant. The thermite melt generator is designed to generate and deliver 50 kg of Al_2O_3. The entrance of a melt delivery nozzle of the thermite melt generator, whose diameter is 0.11 m, is plugged with a layer of thick papers in order to assure the desired period of time (approximately 45 seconds) for separation between Al_2O_3 at the top and Fe at the bottom of a melt layer due to the density difference. After ablation or burning out of the paper layer, the melt is gravitationally introduced into the LHEV. The vertical distance between the exit of the melt delivery nozzle and the bottom of the LHEV is 0.65 m.

The LHEV is made of carbon steel with stainless steel liner, and is composed of semispherical and cylindrical parts with an inner diameter of 0.5 m. Structure and the major dimensions of the LHEV are illustrated in Fig. 2. Water supply and drain lines are connected on the wall of the cylindrical part. The LHEV is covered with a layer of thermal insulator to minimize heat loss to the model containment vessel atmosphere. The temperatures of Al_2O_3, a water layer and the LHEV wall are measured by type-K (C/A) or W/Re thermocouples. Locations of type-K thermocouples on the LHEV outer surface are also shown in Fig. 2. Additional two type-K thermocouples are embedded in the LHEV wall on the same radial axes with TV2 and TV3. These two thermocouples are located at 1.0 cm from the outer surface. The signals from the thermocouples as well as the other measurements such as ambient pressure and temperature of

the model containment vessel are recorded in a data acquisition system.

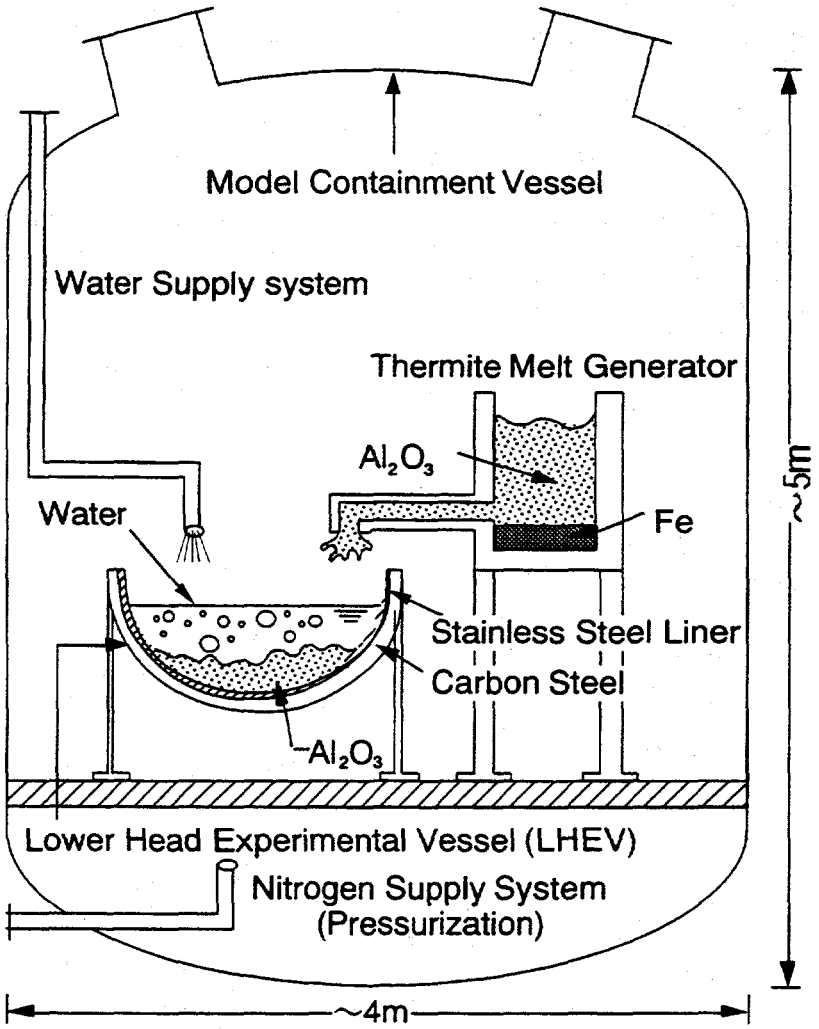

Fig. 1 Conceptual diagram of in-vessel debris coolability experiments in ALPHA Program

The model containment vessel was initially pressurized by nitrogen up to 1.6 MPa. The saturated water was supplied into the LHEV through the water supply line from a steam generator of the ALPHA facility and drained. This feed and drain procedure was repeated to heat-up the LHEV. After the temperature of the LHEV reached a target, the LHEV was filled with hot water up to an overflow level. A part of heat loss from the LHEV was compensated by supplying saturated steam into a water layer. Since maintaining water saturation temperature at the initial pressure was not possible, the model containment vessel was depressurized in order to establish a nearly saturated condition.

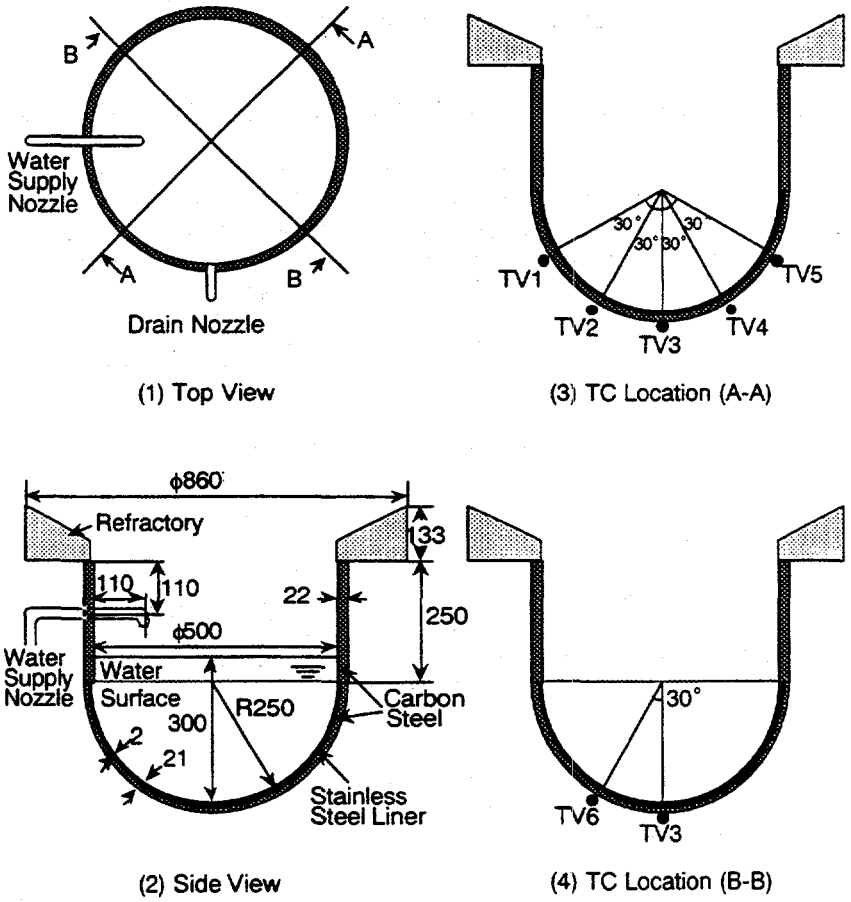

Fig. 2 Structure of lower head experimental vessel and thermocouple locations on outer surface

2.2 Experimental Conditions

Applicability of Al_2O_3 as a debris simulant and an experimental scale were investigated through calculations on heat loss from the molten debris and characteristics of crust formation at the debris upper surface for geometries of the ALPHA experiments and the TMI-2 lower head[10]. Based on the results from the calculations and the limitations of available space in the model containment vessel, the LHEV radius and the depth of Al_2O_3 were determined to be 0.25 m and 0.15 m, respectively. Approximately 50 kg of Al_2O_3 could form a 0.15 m depth debris layer at the LHEV center axis.

Two scoping experiments, IDC001 and IDC002, have been performed. The major experimental conditions are listed in Table 1. Water temperature and level in the LHEV and the ambient pressure in the model containment vessel at Al_2O_3 entry were similar in both experiments. These were approximately 450 K, 0.3 m and 1.3 MPa, respectively. Approximately 30 kg of Al_2O_3 in

IDC001 and 50 kg in IDC002 were poured into the LHEV. The temperature of the thermite melt was separately measured with a pyrometer, resulting in approximately 2700 K at the Al_2O_3 surface immediately after the completion of the thermite reaction[11].

Table 1 Major conditions of in-vessel debris coolability experiments in ALPHA program

	Debris Mass (kg)	Initial Water Depth (m)	Initial Water Temperature (K)	Ambient Pressure (MPa)
IDC001	~30	0.3	445	1.3
IDC002	~50	0.3	450	1.3

3. EXPERIMENTAL RESULTS AND DISCUSSIONS

3.1 Post-Test Observations

Post-test visual observations indicated that debris particles with generally smooth surfaces rested on the top of a continuous layer of the solidified debris. The debris particles size was ranged from several millimeters to several centimeters. The mass of the debris particles was approximately 2.0 kg for IDC001 and 2.6 kg for IDC002, corresponding to 6.7 % and 5.2 % to the total amount of Al_2O_3 poured into the LHEV, respectively. It was not possible to identify whether those were formed during a penetration stage of the debris jet or by quick solidification of delayed debris droplets. The surfaces of the solidified debris in both experiments were extremely rough. This surface roughness resulted in the augmentation of surface area which could promote heat transfer from the debris to the overlying water layer.

Formation of cracks was also recognized through the post-test observations. The cracks were not uniformly distributed over the surface of the solidified debris. Several cracks having a long horizontal length on the surface were found. This nature of the crack formation suggested that the cracks were developed at weaker locations of the crust during the beginning stage of crust formation to release the thermal stress imposed on the crust. Once cracks were formed, the stress concentration at a tip of the cracks would accelerate crack penetration into the solidified debris.

3.2 Preliminary Measurement of Gap Width

As described earlier, water migration into a gap between the solidified debris and the lower head wall was proposed as a debris cooling mechanism in a lower plenum region. A gap seemed to exist along the inner surface of the LHEV at the debris upper surface. Unfortunately, penetration of the gap into the deeper location has not been confirmed in the post-test visual observations. Preliminary attempts using an ultrasonic device were made to identify the spatial distribution of the gap width for the LHEV used in IDC002. The principle of the gap width measurement with an ultrasonic technique is shown in Fig. 3. An ultrasonic wave emitted into the LHEV wall from the outer surface is partly reflected at the LHEV inner surface and partly transmitted into the gap. Transmitted fraction is increased when the gap is filled with water. This behavior is generally realized at the interface between two different materials. The wave reflection is repeated within

the gap, and the reflected waves at the solidified debris surface arrive at the LHEV outer surface with a constant interval (t in Fig. 3). It is possible to detect the interfacial gaps in case that the initial intensity of an ultrasonic is sufficiently high and a gap width is more than a detectable limit.

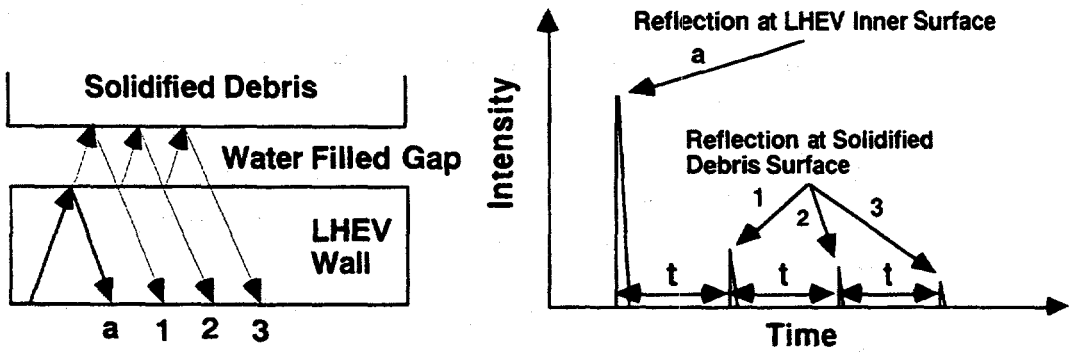

Fig. 3 Principle of gap width measurement with ultrasonic technique

Using the ultrasonic wave with a frequency of 5 MHz, signals to show the reflection at the solidified debris surface were detected at several locations of the LHEV wall, following the highest signal reflected at the LHEV inner surface. The time interval for the detection of these reflected waves was quite constant. The gap width was evaluated to be ranged between 0.7 mm and 1.4 mm, based on the detection interval and a sound velocity in water (approximately 1500 m/s). However, it should be noted that no signals were detected at some areas on the LHEV outer surface. The preliminary measurement with the ultrasonic technique implied that the gaps could be formed between the solidified debris and the LHEV wall and the gap width was largely ununiform. Further discussion will be possible after detailed measurement on the gap width and examinations of the solidified debris surface facing to the LHEV wall.

3.3 Debris Temperature History

Debris temperature histories measured by W/Re thermocouples are shown in Fig. 4. The debris temperature was measured at the vicinity of the LHEV center axis. Measurement location was approximately 5 cm and 10 cm from the LHEV bottom in IDC001 and IDC002, respectively. During the initial period of the debris cooling phase, the measured temperature was widely scattered. Despite smaller amount of the debris, the temperature reduction rate in IDC001 was quite similar to that of IDC002 after the stable measurement was established and the temperature in IDC001 was slightly higher than IDC002. The temperature reduction rate between 500 seconds and 1500 seconds was approximately 1 K/s. Assuming this temperature reduction rate was a representative for the whole solidified debris, corresponding energy release rate from the debris was roughly evaluated to be 37.5 kJ/s for IDC001 and 62.5 kJ/s for IDC002 by using 1250 J/kg•K as a specific heat of solidified Al_2O_3.

A ratio of the energy release rate between two experiments (IDC001/IDC002) was smaller than

that of available area for heat transfer (approximately 0.32 m^2 for IDC001 and 0.42 m^2 for IDC002 neglecting surface roughness of the solidified debris). This indicated that relatively effective cooling of the debris simulant could be established in IDC002. Unfortunately, a detailed quantitative discussion was not possible due to insufficient locations for temperature measurement and different measurement location between the two experiments.

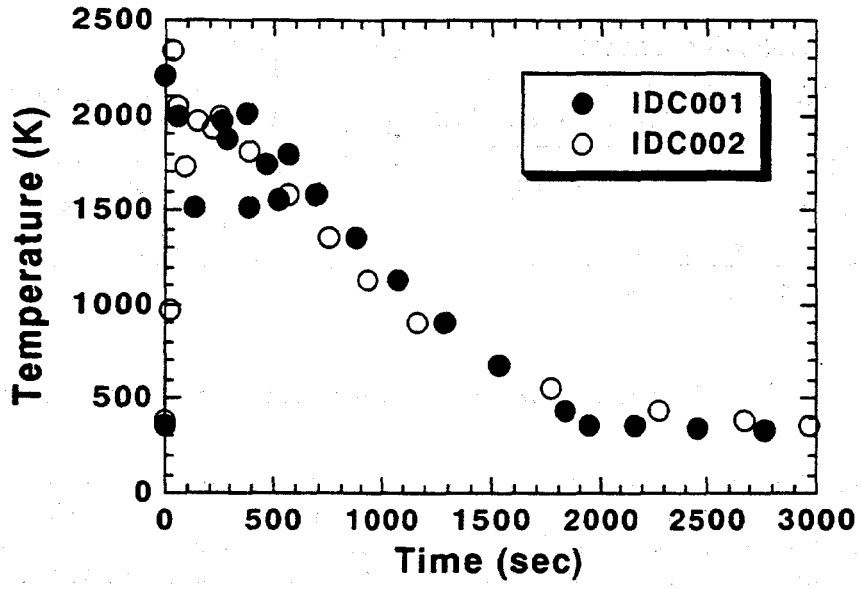

Fig. 4 Observed history for debris simulant temperature

3.4 Thermal Responses of LHEV Wall

Temperature histories on the outer surface of the LHEV are shown in Fig. 5 for IDC001 and in Fig. 6 for IDC002. In both experiments, the highest temperature was observed by the thermocouple on the center axis of the LHEV (TV3). Duration of higher temperature period depended on the location of the LHEV and lasted for approximately 350 seconds in IDC001 and 550 seconds in IDC002 at the center axis. The final temperature of the LHEV outer surface was nearly identical with the water saturation temperature to the ambient pressure.

In spite of the same distance from the center axis, three thermocouples, TV2, TV4 and TV6, showed different timing to initiate temperature decrease. In addition, the temperature reduction rate observed by TV2 in IDC001 was much slower than the other two locations. Unaxisymmetric configuration of the solidified debris, which was confirmed in the post-test visual observations, influenced on this behavior. No remarkable temperature increase was observed by TV1 and TV5 in IDC001 since the debris depth was too shallow to affect these thermocouples.

Temperature on the outer surface of the LHEV began to decrease earlier at the locations farther from the center axis. Generally, slightly faster temperature reduction was observed in IDC001

than in IDC002. The temperature reduction rate during the initial stage was roughly estimated to be 4 K/s for IDC001 (except TV4) and to be 3 K/s for IDC002 (except TV1 and TV6). Temperature measurement by thermocouples embedded in the LHEV wall showed the almost identical temperature reduction rate. The observed temperature reduction could not be qualitatively explained by a consideration of heat conduction within the solidified debris and the LHEV wall and heat loss to the surrounding atmosphere. The reasons were; 1) the LHEV was covered with a thermal insulator layer to minimize heat loss from the outer surface, 2) the debris was maintained at higher temperature during temperature reduction period of the outer surface, and 3) circumferential heat transfer through the wall of the LHEV semispherical part by conduction was supposed to be much smaller than that required for the rapid cooling of the LHEV wall due to a small cross section available for the heat conduction.

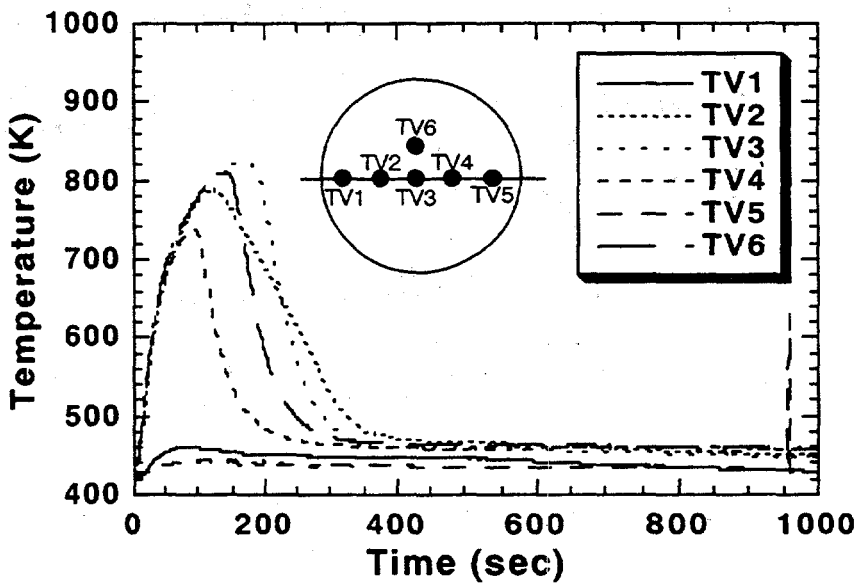

Fig. 5 Temperature history on outer surface of LHEV for IDC001

The above described rapid temperature reduction on the LHEV outer surface suggested that some cooling mechanisms acted at the interface between the solidified debris and the LHEV wall. A possible mechanism could be water penetration into a gap formed at the interface as proposed by Henry and Dube[7]. Once a gap was developed upon the contact, the gap width could be enlarged due to the thermal expansion of the LHEV wall resulting in augmentation of the water migration into the gap (radial enlargement was approximately 1 mm assuming uniform temperature of the LHEV wall at 800 K and no restriction for deformation). The observed difference for the temperature reduction timing on the LHEV outer surface may suggest that the cooling started from the edge of the solidified debris. The experiments were performed without an internal pressure load onto the LHEV wall and elevated temperature was not maintained for a long time. Therefore, a creep deformation of the vessel was not expected to develop a narrow space for the water migration. This imply that the effective cooling of the debris within a lower

plenum region can be realized even in low pressure accident sequences.

Using the observed temperature reduction rates on the outer surface of the LHEV (4 K/s for IDC001 and 3 K/s for IDC002) and the facing area of the LHEV inner surface to the solidified debris, an averaged heat flux at the LHEV inner surface was estimated. Approximately 0.4 MW/m^2 for IDC001 and 0.3 MW/m^2 for IDC002 were obtained from the estimation.

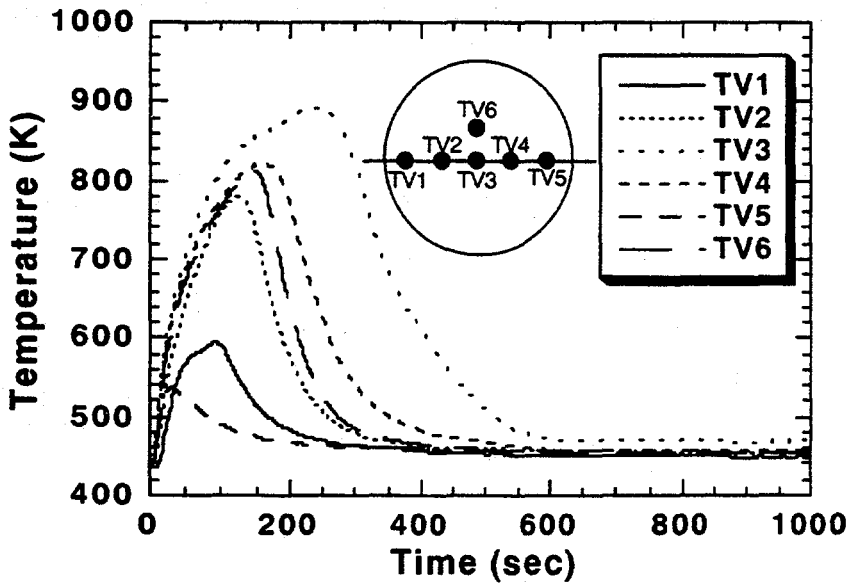

Fig. 6 Temperature history on outer surface of LHEV for IDC002

These heat fluxes were compared with predictions by correlations for critical heat flux within a narrow gap. The correlations developed by Katto and Kosho[12] for a gap between two horizontal disks and by Monde, et al.[13] for a gap between two vertical plates were applied. The calculated critical heat flux as a function of a gap width is shown in Fig. 7. The circumferential distance from the LHEV bottom to the upper edge of the solidified debris (approximately 0.25 m for IDC001 and 0.3 m for IDC002) was used as a representative length in both correlations. As clearly shown in the figure, critical heat flux within a narrow gap strongly depended on the geometries. The calculated critical heat flux for a horizontal gap was much smaller than for a vertical one. Both correlations predicted larger critical heat flux for IDC001. This prediction was consistent with the faster temperature reduction of the LHEV wall in IDC001.

As previously mentioned, the measurement with an ultrasonic device suggested the existence of the interfacial gap during the cooling phase of the experiments. The comparison with the correlation by Monde, et al. indicated that the observed heat flux could be reproduced if the gap having the measured width (0.7 through 1.4 mm) was formed over the whole area of the interface. However, applicability of this correlation should be further investigated, since a semispherical geometry was used and heat flux was given to water from the both sides (solidified debris and LHEV wall)

in the experiments, and the gap width was spacially ununiform.

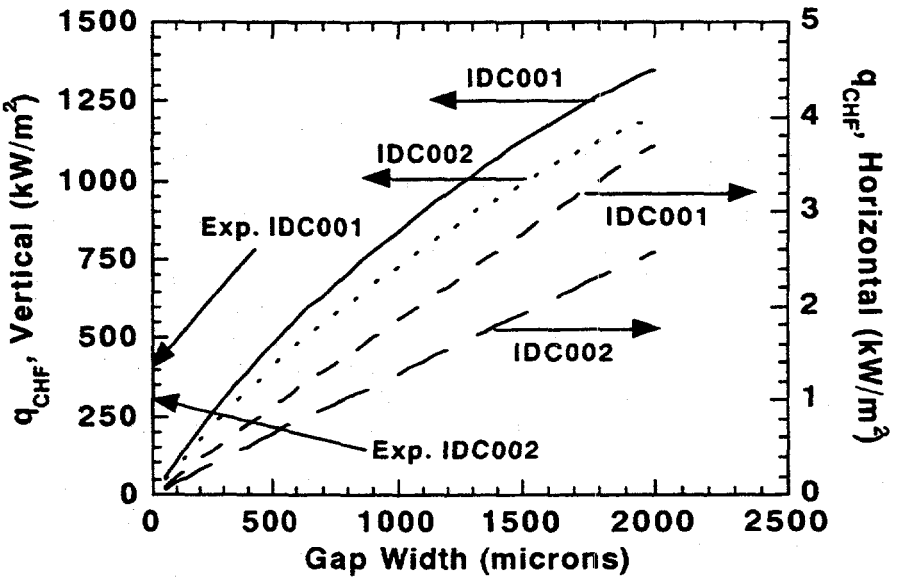

Fig. 7 Calculated critical heat flux for narrow gaps and comparison with experimental results

4. FUTURE PLAN

In the scoping experiments, the debris simulant was quenched in the water filled LHEV. In order to evaluate the long term cooling of the debris, the simulation of the decay heat generation is planned in future experiments. Detailed measurements on the temperature distribution in a debris simulant and an LHEV, the gap width, the steam generation rate and the structural response of the LHEV such as deformation and strain will be provided to further understand mechanisms for the in-vessel debris coolability. Application of materials with lower melting temperature than Al_2O_3 is also planned. It is expected that the temperature of the debris simulant is easily measured and the influence of material properties is examined by using these materials. A candidate is a mixture of CaO and Al_2O_3, which was used in WETCOR-1 experiment on ex-vessel debris coolability[14]. This mixture with 45 % CaO and 55 % Al_2O_3 in mole has solidus and liquidus temperatures of approximately 1640 K and 1700 K, respectively. Viscosity is augmented when the molten materials is in the range between solidus and liquidus temperatures due to the formation of a solid-liquid two phase mixture. The influence of the viscosity augmentation on the debris cooling through natural convection will be evaluated in the future experiments.

In parallel with the experiments, the development of a computer code is now under progress. WINDFLOW code[15], which has been developed at JAERI for the analysis on thermo-fluiddynamics of a compressive fluid flow in a reactor coolant piping system, is being modified to be applied to

the debris coolability issues. The first version of the code will be completed by the end of March, 1997. Analytical capabilities for natural convection with the internal heat generation, solid-liquid phase change, thermal interaction between the debris and the lower head are included in this version. The code will be validated using available experimental aspects including the experiments in ALPHA program.

5. SUMMARY

In-vessel debris coolability experiments have been performed in ALPHA program at JAERI. Aluminum oxide produced by a thermite reaction between aluminum and iron oxides was applied as a debris simulant. The applicability and an experimental scale were evaluated by simple scaling calculations on heat loss from the debris and characteristics of crust formation at the top of the debris. Two scoping experiments were conducted, in which approximately 30 kg or 50 kg of aluminum oxide was poured into a pool of nearly saturated water formed in a lower head experimental vessel (LHEV). The LHEV was composed of a semispherical and a cylindrical part made mainly of carbon steel. The inner surface of the semispherical part was covered with 2 mm thick stainless steel liner. A wall thickness and an inner diameter of the LHEV were approximately 20 mm and 500 mm, respectively. The ambient pressure was elevated up to approximately 1.3 MPa in order to suppress the occurrence of an energetic steam explosion.

It was confirmed from the post-test visual observations that surface of the solidified debris was rough and several cracks were formed. Temperature histories of the debris and the LHEV wall were measured. Sharp temperature decrease on the LHEV outer surface, 3 K/s through 4 K/s, was observed while the debris was sustained at high temperature. The observed temperature decreasing rate was more rapid than that expected by heat conduction to the overlying water through the vessel wall. This fact can be understood by assuming that a gap was formed at the interface between the solidified debris and the vessel wall and water penetrated into the gap resulting in the effective heat removal from the vessel. Heat flux on the inner surface of the vessel facing to the debris was evaluated to be 0.3 MW/m^2 to 0.4 MW/m^2 using the observed temperature decreasing rate. The evaluated heat flux was compared with predictions by available correlations for critical heat flux within a narrow gap. Preliminary measurements for the gap width were carried out by using an ultrasonic device with a frequency of 5 MHz. Periodic appearance of reflected waves at the solidified debris surface was detected at several locations of the LHEV outer surface. The measurements indicated that the gap width at these locations was in the order of a millimeter (0.7 to 1.4 mm) .

The modification of the experimental facility is planned in order to provide capability of using other materials as debris simulants and simulating decay heat generation. Detailed measurements will be made on temperature distribution within debris simulants and the LHEV wall, steam production rate and structural response of the experimental vessel. In parallel with the experiments, development of a computational code is in progress by improving WINDFLOW code. The first version of the code will be completed by the end of March, 1997.

ACKNOWLEDGMENTS

Authors would like to gratefully acknowledge the excellent work in preparation of the experiments and operation of the experimental facility by Mr. H. Itoh, Mr. K. Komori and Mr. H. Sonobe of Safety Facility Engineering Services Division in JAERI, and by Mr. M. Nogami, Mr. M. Kojima

and Mr. T. Suzuki of Nuclear Engineering Corporation.

REFERENCES

1. J. M. Broughton, et al., "A Scenario of the Three Mile Island Unit 2 Accident", Nucl. Technol. 87(1), pp. 34-53, (1989).
2. J. R. Wolf, et al., "TMI-2 Vessel Investigation Project Integration Report", NUREG/CR-6197 TMI V(93)EG10 EGG-2734, March 1994.
3. A. M. Rubin and E. Beckjord, "Three Mile Island - New Findings 15 Years After the Accident", Nuclear Safety, 35(2), pp. 256-268, (1994).
4. D. R. Diercks and G. E. Korth, "Results of Metallographic Examinations and Mechanical Tests of Pressure Vessel Samples from the TMI-2 Lower Head", Nuclear Safety, 35(2), pp. 301-312, (1994).
5. L. A. Stickler, et al., "Calculations to Estimate the Margin to Failure in the TMI-2 Vessel", NUREG/CR-6196, February 1994.
6. J. Rempe, et al., "Margin-to-Failure Calculations for the TMI-2 Vessel", Nuclear Safety, 35(2), pp. 313-327, (1994).
7. R. E. Henry and D. A. Dube, "Water in the RPV: A Mechanism for Cooling Debris in the RPV Lower Head", Proc. Specialist Meeting on Selected Containment Severe Accident Management Strategies, pp. 93-104, Stockholm, Sweden, 13-15 June, 1994.
8. K. Y. Suh and C. K. Park, "SONATA-IV Simulation Of Naturally Arrested Thermal Attack In Vessel", Proc. Int. Conf. on PSA Methodology and Applications, pp. 453-460 Seoul, Korea, November 26-30, 1995.
9. K. Y. Suh, et al., "The SONATA-IV Project In Pursuit of In-Vessel Defence-in-Depth Against a Severe Accident", Proc. 11th KAIF/KNS Annual Conf., pp. 841-853, Seoul, Korea, April 11-12, 1996.
10. Y. Maruyama, et al., "In-Vessel Debris Coolbility Experiments in ALPHA Program", Proc. of PSA'96, Park City, UT, September 29-October 3, 1996.
11. Y. Maruyama, et al., "Evaluation of Specific Heat and Temperature of Thermite Melt Used in Melt Coolant Interaction Test of ALPHA Program", JAERI-M 93-096, March, 1993 (in Japanese).
12. Y. Katto and Y. Kosho, "Critical Heat Flux of Saturated Natural Convection Boiling in a Space Bounded by Two Horizontal Coaxial Disks and Heated from Below", Int. J. Multiphase Flow, Vol. 4, pp. 219-224, 1979.
13. M. Monde, et al., "Critical Heat Flux During Natural Convective Boiling in Vertical Rectangular Channels Submerged in Saturated Liquid", Trans. ASME, J. Heat Transfer, Vol. 104, pp. 300-303. 1982.
14. R. E. Blose, et al., "Core-Concrete Interactions with Overlying Water Pools, The WETCOR-1 Test", NUREG/CR-5907 SAND92-1563, November 1993, Sandia National Laboratories.
15. Y. Maruyama, et al., "Three-Dimensional Thermo-Fluiddynamic Analysis of Gas Flow in Straight Piping with WINDFLOW Code", Proc. ASME/JSME 4th Intenat. Conf. on Nucl. Eng., Vol.1, Part B, pp.997-1008, New Orleans, LA, March 10-14, 1996.

IN-VESSEL COOLABILITY AND RETENTION OF A CORE MELT

T.G. Theofanous, C. Liu, S. Additon,
S. Angelini, O. Kymäläinen and T. Salmassi
Center for Risk Studies and Safety
University of California, Santa Barbara

ABSTRACT

The efficacy of external flooding of a reactor vessel as a severe accident management strategy is assessed for an AP600-like reactor design. The overall approach is based on the Risk Oriented Accident Analysis Methodology (ROAAM), and the assessment includes consideration of bounding scenarios and sensitivity studies, as well as arbitrary parametric evaluations that allow the delineation of the failure boundaries. The technical treatment in this assessment includes:

(a) new data on energy flow from either volumetrically heated pools or non-heated layers on top, boiling and critical heat flux in inverted, curved geometries, emissivity of molten (superheated) samples of steel, and chemical reactivity proof tests,

(b) a simple but accurate mathematical formulation that allows prediction of thermal loads by means of convenient hand calculations,

(c) a detailed model programmed on the computer to sample input parameters over the uncertainty ranges, and to produce probability distributions of thermal loads and margins for departure from nucleate boiling at each angular position on the lower head, and

(d) detailed structural evaluations that demonstrate that departure from nucleate boiling is a necessary and sufficient criterion for failure.

Quantification of the input parameters is carried out for an AP600-like design, and the results of the assessment demonstrate that lower head failure is "physically unreasonable." Use of this conclusion for any specific application is subject to verifying the required reliability of the depressurization and cavity-flooding systems, and to showing the appropriateness (in relation to the database presented here, or by further testing as necessary) of the thermal insulation design and of the external surface properties of the lower head, including any applicable coatings.

1. INTRODUCTION

This paper addresses a severe accident management concept known as "in-vessel retention," and it has been put together with two purposes in mind: one, to demonstrate the effectiveness of the concept for an AP600-like design; and two, to provide a readily adaptable path for its consideration for other designs.

The accident management strategy is to flood the reactor cavity, submerging the reactor vessel. The concept is based on the idea that the lower head, cooled externally, will be able to arrest the downward relocation of a degraded (melting) core. The related issue before us, then, is whether

lower head integrity can be maintained subject to the thermo-mechanical loads created during such a situation.

These loads are created because of the presence of the high temperature melt (~3000 K for the oxidic, ~1800 K for the metallic) on the inside. The mechanisms leading to such melts can span a wide range of behavior, from that associated with the initial portion of the relocation, through a series of intermediate states, to a final quasi-steady state, where essentially all the core materials have been relocated and are found on the lower head. Correspondingly, the process is initially dominated by forced convection, eventually reverting through a series of mixed regimes, to a purely natural convection one. Lower head integrity can be compromised by meltthrough, or by a combination of wall thinning and mechanical loading (including any internal pressure and/or thermal stresses developed as a result of the heating on the inside and cooling on the outside) that can cause structural failure.

In addition, mechanical loads can be created due to thermal interactions of the melt with any coolant present in the lower head. Such contact can arise either during the core relocation process, or later on if, upon regaining injection capability, water was to be supplied on top of the molten pool in the lower head. Of particular concern in this respect are energetic interactions, also known as steam explosions, especially in the relocation regime as it is capable of setting up conditions for "premixed" explosions.

The overall problem, as described above, is depicted in Figure 1.1. This figure also introduces the terminology to be used for the various loads, failure criteria, and corresponding loading "regimes." There are three such regimes. The "thermal regime" constitutes the subject of this paper, and this portion of Figure 1.1 will be taken up again below. For now, suffice it to say that: (a) $q_w(\theta)$ and $\delta_w(\theta)$ denote the heat flux through, and wall thickness of, the lower head at any angular position θ (see Figure 1.2); and (b) integrity is to be assessed by comparing these "load" values with corresponding failure criteria; that is, the critical heat flux, $q_{CHF}(\theta)$, and the minimum wall thickness, δ_F needed to ensure structural integrity. The other two regimes in Figure 1.1 refer to the consequences of melt-coolant interactions, and they are addressed separately by Theofanous et al. (1996a).

Briefly however, a key distinction (that gives rise to the subdivision of melt-coolant interactions into two regimes) with some bearing on the present effort needs to be made at this time. Namely, that energetic interactions can be of concern mainly in premixed explosions, (melt and water intermixed at coarse scales) as they might arise, for example, during the early stages of the core relocation, while interactions in a stratified configuration, concerning late water injection, are relatively benign. The key implication then is that integrity in the potentially energetic "Steam Explosion Regime" can be assessed against the full lower head capability (normal wall thickness), while in the benign "FCI Regime" any wall thinning, as a result of the thermal loads considered in the present work, must be taken into account. The other point made in Figure 1.1 is that due to the reduced wall structural capability in the FCI Regime, the static (or quasi-static) primary system pressure rise (to a peak pressure P_{max}) as a result of the steam produced, but not immediately vented, in the melt-coolant interaction might also have to be considered against a failure level, P_F, consistent with wall thickness, $\delta_w(\theta)$, and prevalent thermal stresses. Finally, in both melt-coolant interaction regimes, the main structural consideration is indicated in Figure 1.1 in terms of the delivered impulse, I, against the failure criteria I_F and $I_{F'}$. This is illustrative only of the key global consideration; the actual assessment is likely to require additional details, such as the space-time distribution character of the loads.

So far, the subject has been approached only from the standpoint of the Thermal Regime in the long term, and all this work is relatively recent. The technical feasibility of the idea was first demonstrated for the Loviisa nuclear power plant, a Russian VVER-440 in Finland (Theofanous,

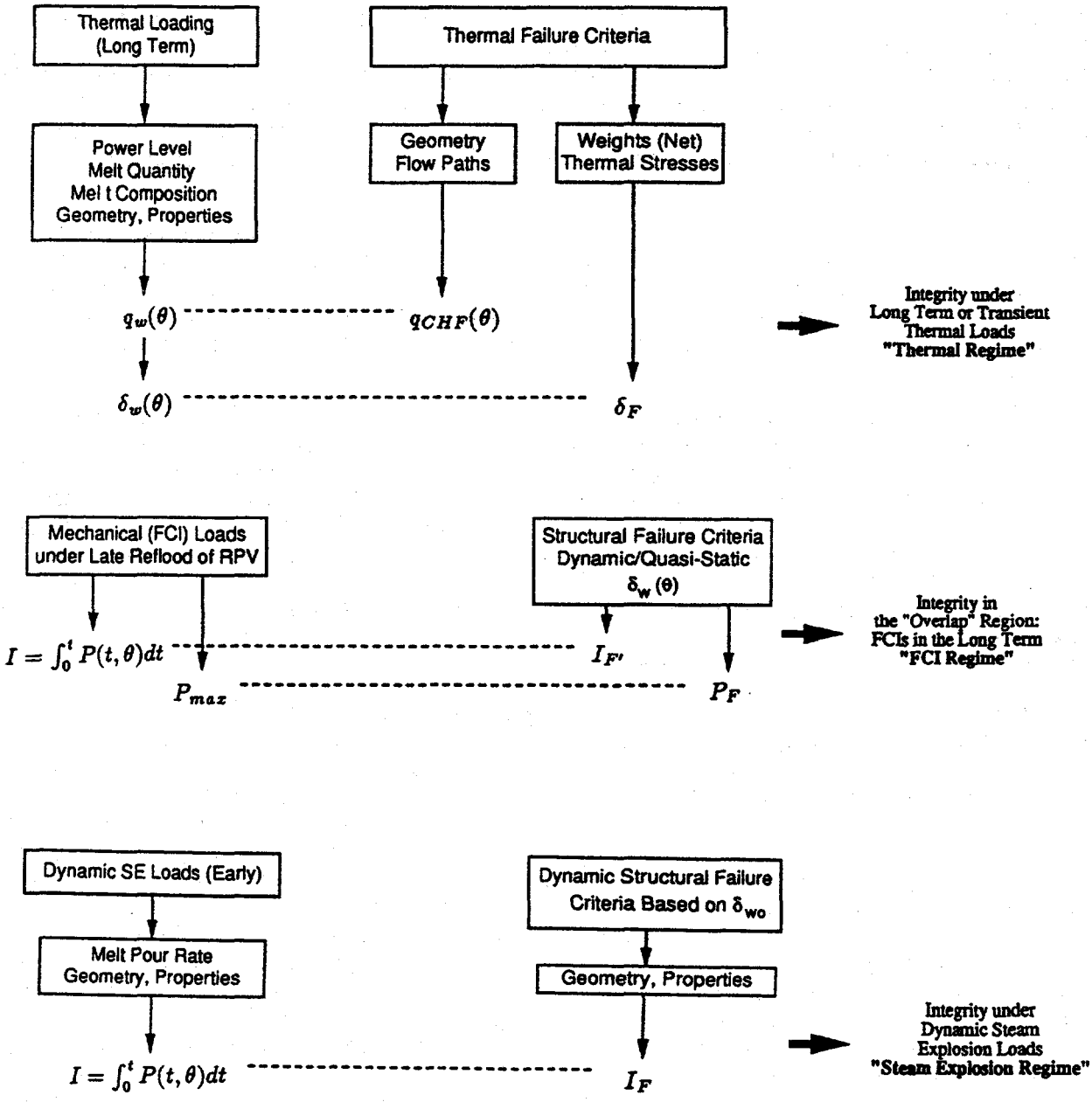

Figure 1.1. An overall view of the in-vessel retention issue.

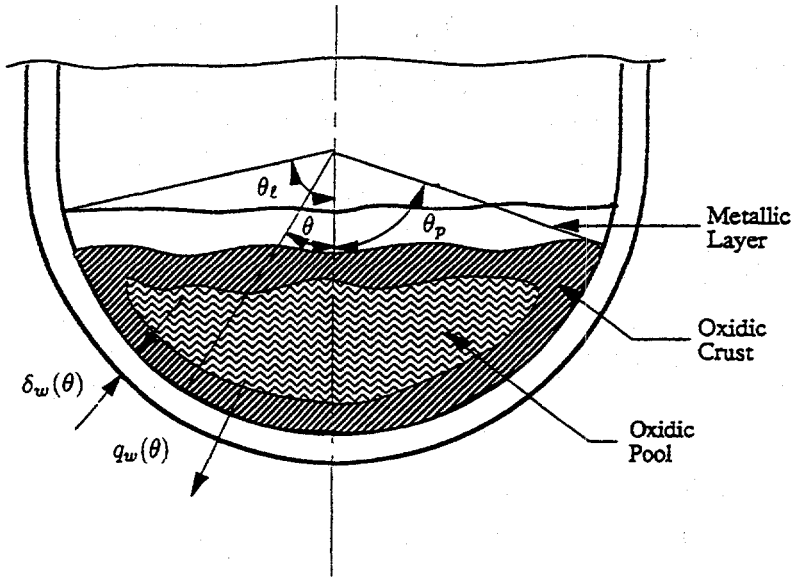

Figure 1.2. The basic geometry and nomenclature of in-vessel retention in the long-term, natural convection-dominated, thermal regime.

1989). This reactor is equipped with a Westinghouse ice condenser containment, and the cavity design happens to be, both in size and location, subject to flooding by the ice melting during the course of any severe accident. Thus, in-vessel retention formed the cornerstone of severe accident management in Loviisa (Tuomisto and Theofanous, 1994), and a related research program has been going on for the past several years (Kymäläinen et al., 1992; Kymäläinen et al., 1993). The complete assessments (Kymäläinen, 1994; Kymäläinen, et al., 1996), representing the culmination of these efforts, has been approved recently by the Finnish regulatory authority, STUK. The present effort for an AP600-like design evolved in close relation to this Finnish work, including the sharing of some facilities and personnel (Theofanous et al., 1994a; Theofanous et al., 1994b). More recently this informal bilateral effort has been expanded to a formal agreement to include the Italian utility ENEL and the Electric Power Research Institute (EPRI) for the purpose of furthering the confirmatory basis of the current assessments and extending the application to larger reactor designs.

Independently, the idea of in-vessel retention has been pursued also by Henry and co-workers (Henry et al., 1991; Henry and Fauske, 1993), by Hodge (1991), and it has been critically examined by Park and Dhir (1991), Park et al. (1992), and Hawkes and O'Brien (1991). Interest around the world developed rapidly; a number of new research programs are in place; and a CSNI-sponsored specialists meeting on the subject took place recently in Grenoble, France. The summary of this meeting, prepared for the CSNI by the participating experts, provides the most recent and comprehensive status report on the subject (CSNI, 1994). More detailed reviews of the technical issues involved, and of the various experimental programs worldwide, also have been prepared by groups of experts for the CSNI (Okkonen, 1993; Rougé and Seiler, 1994). By virtue of this large, international activity the problem can now be considered to be ripe for decisive steps, such as those needed in the regulatory context, toward resolution. This is the intent of the present document. It is important to emphasize, however, that such a task must be approached on a reactor-specific basis—the design of interest here is that of the Westinghouse advanced passive design: the AP600.

This paper consists of six main technical sections. Two sections (3 and 4) address the failure criteria: the q_{CHF} and δ_F, as identified in Figure 1.1 already, while the remaining four contain the development of the thermal loads. Namely, Sections 5, 6, and 7 address the long-term natural-

convection-dominated regime, while Section 8 is devoted to the consideration of forced convection effects. The overall aim of these sections and their interrelations are explained as a part of the overall approach and methodology in Section 2. The paper comes to an end with the conclusions and recommendations presented in Section 9. This paper derives from a report published and peer reviewed as DOE/ID-10460 (Theofanous et al., 1996b). Reference to this document is made for technical details, provided therein in the form of appendices.

2. PROBLEM DEFINITION AND OVERALL APPROACH

We begin with the basic assumptions that if core degradation takes place, the primary system will be depressurized and the lower head will be fully submerged in cavity water prior to the arrival of core debris on the lower head. Further, we assume that the water level in the cavity would be maintained indefinitely. Detailed consideration of these inherent aspects of the AP600 design are beyond the scope of this work, but the design attention given to the assurance of their validity is summarized in Appendix M of DOE/ID-10460. Their consequences can be listed as follows:

(a) Prior to being exposed to the melt the lower head is quenched down to the saturation temperature of water at ~1 bar: ~100 °C.

(b) In the absence of significant primary pressures, only a very small fraction of the lower head thickness is needed to support the dead-weight loads—thermal stresses and creep are the primary failure mechanisms to be considered instead.

(c) With the lower head fully submerged, the outside surface will remain in nucleate boiling (at ~100 °C) provided the critical heat flux is not exceeded at any point on it—a significant aspect of this requirement is that the thermal insulation allows sufficient flow paths for water to flow in and vapor to escape. The design of the thermal insulation for the AP600 has not been completely finalized yet, but as discussed in Appendix K of DOE/ID-10460, no difficulties in principle are anticipated.

Additional attractive features of the AP600, relative to this accident management strategy, are that its lower head is free of any penetrations, and its core power density is rather low.

To predict the thermal loadings on the lower head in all their detail, one would need the complete sequence of thermal states of the core and other internal structures throughout the core degradation and melt relocation processes. Rather than getting immersed, and perhaps lost, in such details, our approach is based on the identification of certain dominant features of these complex scenarios, and the detailed study of the loads in certain well-defined material and thermal state configurations. Our aim is to thus envelop the behavior, with regard to loads, and we will argue that this indeed has been achieved. Quantification of uncertainties will be emphasized in the detailed analysis carried out for each of these representative, enveloping configurations. The overall philosophical/methodological approach follows the risk oriented accident analysis methodology (ROAAM), which is described in Appendix A of DOE/ID-10460 (see also Appendix A of DOE/ID-10541 by Theofanous et al., 1996a). The scenario-independence stated above, and explained below, will be recognized as a Grade B approach, which is desirable in realizing the high confidence assessment sought here. This approach is conservative, but not unduly so, and it is consistent with the existence of a wide range of bifurcating behavior possible in such phenomenologically complex situations.

In the same vein we restrict our attention to scenarios in which failure to supply coolant into the reactor vessel persists indefinitely. This is clearly a limiting case, especially in light of the recovery that took place in Three Mile Island, Unit II (TMI-2). The unexpected arrest of lower head heatup and eventual quenching was key to the survival of the vessel (Strickler et al., 1994; Turland et al., 1993), and it is currently pursued mechanistically as yet another potentially important approach to

arresting a severe accident in-vessel (Henry and Dube, 1994). (Still, for another perspective on the likelihood of passive reflood in AP600, and its effect on the accident scenarios and failure margins, see Section 4.4 of DOE/ID-10541.)

The basic geometry can be represented in rather general terms in the manner shown in Figure 2.1. It consists of the lower head with some of the core debris on it, the rest of the reactor pressure vessel not in direct contact with core debris, and the core barrel, the reflector, and the core support plate, with any remaining core debris on it, as the key internal components. This figure also indicates the various pathways for the flow of thermal energy generated by radioactive decay processes within the core debris. These energy flows occur in accordance with the driving potential (temperature differences) and corresponding resistances. We have a strongly coupled problem here in that any imbalance between production and dissipation (heat input and heat loss) is accommodated by an increase in the driving potential which, in turn, gives rise to phase change (heat sinks) and convective losses either by relocation or by enhanced natural convection.

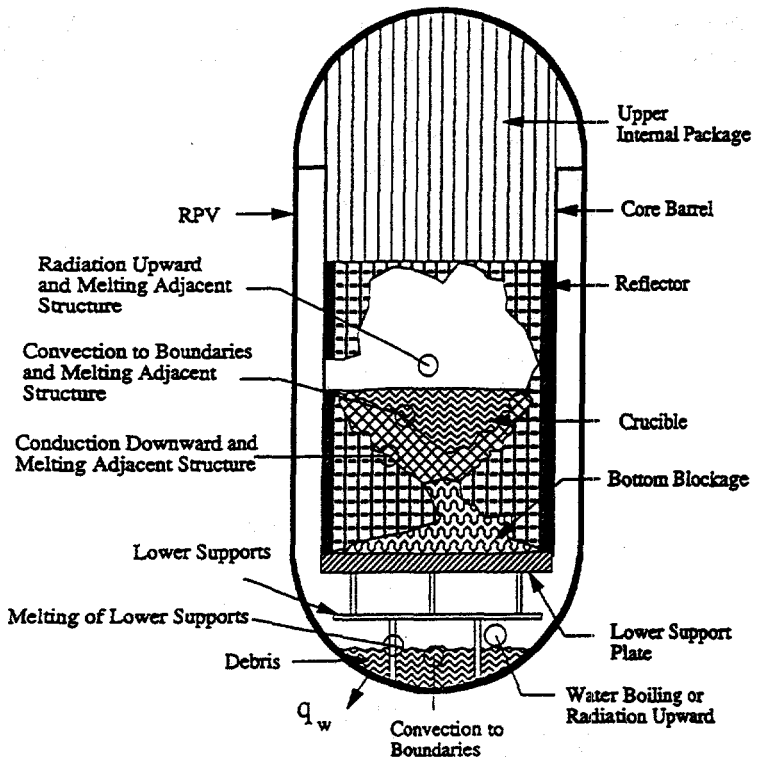

Figure 2.1. Material configuration and heat transfer processes at an intermediate state of the melt progression—after the initial, major relocation event, and before the attainment of a final steady state.

Considering the natural convection process, in this context, first, the thermal load to the lower head is maximized when:

(a) The debris pool has reached a steady thermal state,

(b) The heat generating (fuel) debris volume has been maximized, and

(c) The thermal resistance along the upward thermal radiation path has been maximized.

Indeed, for any given volumetric heat source, steady state implies that all internal heat sinks have been eliminated (melt-out of steel structures in the lower plenum), and that the pool temperature reached the highest value, as needed to exactly balance production by natural convection to the boundaries (see also Section 6). What occasionally has been mentioned as a slow approach to steady state is really attributable to the thermal capacitance of the pool rather than to unsteadiness in the natural convection process. In particular, in Appendix D of DOE/ID-10460 it is shown that boundary layer effects dominate, so that the behavior of such pools is readily predictable even under non-stationary conditions. What this means is that thermal loads to the pool boundaries throughout the time period of a heat-up transient are bounded by the thermal loads in the final steady state.* The effect of debris volume (item (b) above) is due primarily to the reduction in surface-to-volume ratio as the pool level rises in a hemispherical geometry. Finally, the effect of the thermal resistance along the radiation path is straightforward—as the resistance increases the metal layer must reach a higher temperature to reject the same amount of heat, which causes an increase in the thermal loading to the vessel walls.

Thus we arrive at the first configuration appropriate for detailed examination and quantification. It is schematically illustrated in Figure 2.2, and its key elements can be listed as follows:

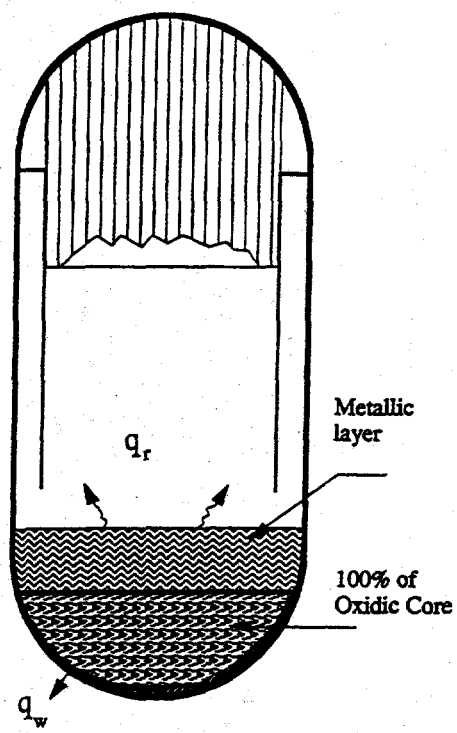

Figure 2.2. Materials configuration in the natural convection, steady state, extreme.

(a) All the core debris is contained, as either a solid oxidic crust or a molten oxidic pool, at steady state in the lower head.

* But as discussed in Sections 5 and 7 and Appendices O and P of DOE/ID-10460, the focusing effect due to a "thin" metal layer on top must be considered separately.

(b) A molten steel layer on top of the crust of the oxidic/pool, made up of all the "light" components of the core region, the reflector and core support plate, at least a portion of the core barrel, as well as all lower (plenum) internal structures.

In Section 7 (and in Appendix O of DOE/ID-10460), we demonstrate that the incorporation of the structural elements listed under item (b) above into the molten steel layer is a necessary consequence of the existence of a molten pool of significant size in the lower plenum.

This configuration is of fundamental significance in assessing the problem at hand, not only because it bounds all intermediate states, but also because it represents the final state that would actually be realized in any in-vessel retention scenario. (See also Appendix O of DOE/ID-10460.)

The bounding nature of the configuration described above could be violated only in the presence of significant forced convection effects. Such effects can arise as core debris relocates into the lower plenum, throughout the core degradation sequence, and most notably so during the major, initial discharge. This discharge would be expected to occur upon failure of a core-internal crucible that forms as a consequence of the melting–freezing phenomena—melting in the inner, higher power density region, and freezing as the melt relocates in the outer, colder boundaries. As it happened in TMI-2, the tight PWR bundle geometry favors the formation of such internal crucibles and the accumulation of significant melt quantities in them prior to their failure. The explanation for this TMI-2 behavior was first given by Epstein and Fauske (1989). In the AP600 such behavior is further favored by the bundle inlet geometry and the solid zirconium slug in each pin in the entrance region—an additional heat sink—and by the substantial steel reflector component that surrounds the core inside the core barrel. These, together with the thermal load distribution at the boundaries of a volumetrically heated pool, as discussed in Section 5, guarantee that in the AP600 failure will occur at the core side and that the initial discharge will involve a sizeable fraction of the core (something like 30%) (Sienicki and Theofanous, 1995).

Clearly, then, this is the second configuration of major interest for thermally loading the lower head. It is illustrated in Figure 2.3, and involves a "wall jet" released from near the top of the molten core pool, through the downcomer, and into the lower plenum. Subsequent to this initial release, melting and relocation occur in a much more gradual fashion, and melt and crusts already on the lower head further reduce the impact of these forced convective effects. Thus we can see that this second configuration provides an appropriate bound for all convective effects as they are found in the intermediate core degradation states.

To summarize, we have identified two specific configurations (as described by debris mass and thermal state), one dominated by natural convection and the other by forced convection and impingement effects. We take the position that these configurations bound the thermal loads on the lower head with respect to any other intermediate state that can reasonably be expected in the time interval between, and including, the initial major relocation event and the final steady state where all debris is contained in the lower head. The terms "natural convection" and "impingement" will be used to describe these two extreme thermal loading configurations. They are covered in Sections 5 through 7 and Section 8, respectively.

3. THERMAL FAILURE CRITERIA

The principal and, as we will show in the next section, most limiting failure mechanism of the lower head is the boiling crisis (BC). It occurs when the heat flux through it exceeds the critical heat flux (CHF) at the same location, and it results in a sudden transition of the flow regime from nucleate to film boiling. Film boiling is characterized by considerably lower heat transfer coefficients, and as a consequence the surface temperature rises to considerably higher values in order to accommodate the imposed thermal load from the inside. For example, for a heat flux of 400 kW/m^2 the surface

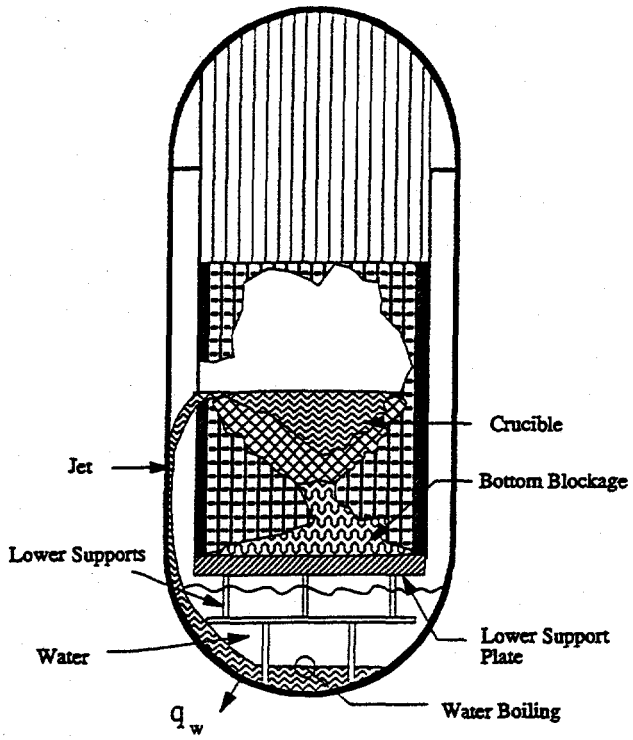

Figure 2.3. Materials configuration, in the forced convection, jet impingement extreme, associated with the major core relocation event.

temperature must rise to ~1200 °C in saturated water, while subcooling can only modestly moderate this rise (i.e., ~1100 °C for 20 °C subcooling). At such temperatures the steel loses essentially all of its strength, and it becomes susceptible to creep, and structural instability, even under the modest mechanical loads of interest to this problem. Moreover, the thermal gradient in the wall at the same flux level is 160 °C/cm which, considering a wall liquidus of 1300 °C (see Section 7) indicates a wall thickness of only 6.0 mm. As we will see in Section 6, heat fluxes on the lower head can considerably exceed the 400 kW/m^2 level considered in the above example. By contrast, nucleate boiling heat transfer coefficients are so high that any flux level, up to the CHF (but prior to BC), can be accommodated with only a few "tens" of degrees in wall superheat (temperature above the coolant saturation temperature). Nominally, therefore, in nucleate boiling the outer surface of the lower head is at ~100 °C.* This is very significant for the structural stability of the lower head, and it is taken up again in the next section. In the remainder of the present section our task is to discuss the boiling crisis and come up with reliable estimates of the heat fluxes necessary to cause its occurrence.

The key features of the problem can be seen with the help of Figure 3.1. Considering first the "local" aspects, we will note that the downward-facing geometry lends itself to the formation of a two-phase boundary layer that is "squeezed" upon the heating surface by gravity forces. This "squeeze" is moderated by turbulent mixing (including interfacial instabilities and entrainment) as

* Note that the vessel wall will cool from the inside during depressurization of the reactor coolant system, so that nucleate boiling will occur without any delay when the lower head comes in contact with cavity water on the outside.

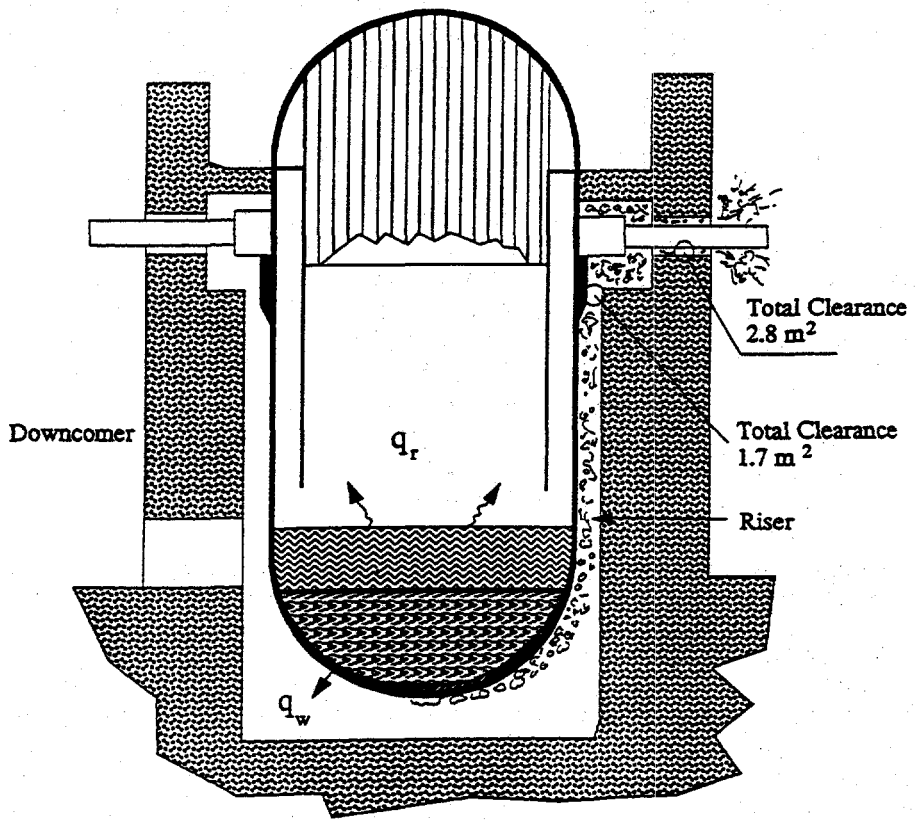

Figure 3.1. Key geometric features of cavity flooding and venting paths. Illustration of the two-phase boundary layer on the lower head. Thermal insulation not shown.

buoyancy drives the steam past the heating surface and the surrounding water. The balance between these two mechanisms is quite different in the various regions around the lower head. This gives rise to widely different two-phase flow regimes, and as a consequence, we can expect significant variations of the critical heat flux and perhaps even of the underlying mechanism(s) for it. For example, in the vicinity of the stagnation point ($\theta \sim 0°$) the vapor velocities are very low and the surface orientation, relative to the gravity vector, drives the maximum phase separation with the vapor "squeezed" up against the wall. We expect periodic formation of relatively large bubbles, growth, and escape. Under such flow conditions we can expect that boiling crisis will occur if the underlying thin liquid film dries out, within one such period, and if the surface temperature rises to high enough levels to prevent rewetting when the liquid rushes back-in following bubble escape. As a consequence, surface wetability (controlling the behavior of the thin film) and wall thickness (controlling the rate of heatup following the dryout of this film) should be important. Aspects that could affect the behavior of these bubbles, including any convection in the free-stream water (see global behavior discussed below) and its subcooling, should also be important. On the other hand, near the equator of the lower head hemisphere ($\theta \sim 90°$), we expect that cumulative vapor generation from all the upstream positions will give rise to high vapor, and entrained liquid, flow velocities, and in addition, the vapor "squeeze" effect described above would be minimal in the near-parallel orientation of the surface to the gravity vector. As a consequence, we expect a highly turbulent two-phase flow within a relatively "diffuse" boundary layer. Correspondingly, the BC mechanism would be convection-dominated. However, phase separation and perhaps even

capillarity may continue to have some bearing on the mechanism in this regime, as well. Evidently, intermediate (or mixed) mechanisms can be envisioned as we go from the stagnation region to the equator with the details of this transition region being strongly dependent upon the power (input) shape.

Let us turn next to the global aspects. In a fully-flooded cavity, as indicated in Figure 3.1, the gravity head would be ~7 meters, which corresponds to ~14 °C subcooling with saturated water at the top. The supply of this subcooled water to the cavity depends on any flow restrictions on the flow path, and on the gravity head developed due to the two-phase flow in the riser. Moreover, the availability of any subcooled water in the immediate vicinity of the heating surface would depend on the **local** mixing and flow patterns as described above. This coupling of the local to the global behavior is quite important in that it indicates a truly conjugate behavior. The situation is less so at a flooding level low enough to interrupt the natural circulation flow path; still, level swell is important in determining the extent of the cooled portion of the reactor vessel. Such partially flooded conditions are of limited interest only, as discussed in Appendix M of DOE/ID-10460; however, as demonstrated later on, the resulting "pool boiling" provides a low (conservative) estimate of the critical heat flux under fully flooded conditions. Back to a fully flooded condition, the key mechanism is void drift in the riser, and the void fraction distribution depends on the power input (including shape), the subcooling, and on the flow losses along the natural circulation path—especially on any inlet or outlet restrictions. The following clarifications need to be made: (a) power is also supplied along the riser section, it being the radiative heat flow conducted through the side wall of the reactor vessel; (b) in the AP600, as indicated in Figure 3.1, the flow path into the reactor cavity is wide open; and (c) key aspects of the flow geometry would be dictated by the thermal insulation design (and response in a severe accident) as discussed in Appendix K of DOE/ID-10460. In addition, the dynamics of the natural circulation loop, such as flow and pressure oscillations may be important (i.e., loop elasticity), especially on the bubble regime discussed above.

Mechanistically, these are behaviors unlike any CHF situations considered previously. Considering also the status of fundamental understanding in the extensively investigated problem of BC on a horizontal, upwards facing plate (Lienhard, 1994), we chose to pursue an experimental approach **that faithfully simulates the reactor in all the key aspects of the phenomena involved**. Based on the above discussion, these key aspects include:

1. **Heater length scale and shape.** To properly represent the two-phase boundary layer behavior, especially in the intermediate region, we need a full-length geometry, including the correct curvature.

2. **Heating surface thermal inertia.** In the reactor, the lower head thickness could vary from its initial value of 15 cm (for most of the region), to a low value of a few centimeters due to thinning by melt attack near the equator (see Section 7). Therefore, a minimum of a few centimeters in heated thickness is needed to properly represent the thermal inertia.

3. **Power shape.** In conjunction with the above item 1, a correct power history in the upstream region is necessary to represent the two-phase boundary layer conditions in the reactor. In addition, the total power shape, including that in the riser, must be represented to simulate void distribution and natural circulation flow behavior.

4. **Heating surface wetability.** The reactor lower head is designed to be made of forged carbon steel (SA 508), machined to 200 r.m.s. mean roughness. Even though it is to be painted in situ, the paint might be expected to flake off in boiling water, and the exposed steel surface to be well-wetted. This surface condition must be confirmed and matched experimentally.

5. **Loop length scale and hydraulic diameter.** To properly represent subcooling due to gravity head we need a full-length loop (~7 m). The annular gap in the reactor is ~20 cm, and a

similarly large cross sectional length scale (diameter) is needed in a one-dimensional geometry to allow proper simulation of the vapor drift.

The ULPU facility was built to embody all of the above key characteristics, allowing, therefore, a full-scale simulation capability. The facility, experimental program, and results obtained are described in detail in Appendix E of DOE/ID-10460. Here, we present the main results as summarized in Figures 3.2 and 3.3. The results in Figure 3.2 were obtained in experiments carried out with a limited submergence and absence of natural circulation (pool boiling). As noted above, these conditions are of limited, if any, significance to the problem at hand, but the results provide interesting perspectives in comparison to those of Figure 3.3 obtained under almost full submergence ($\sim$6 m) and natural circulation. This Figure 3.3 is the result appropriate for quantifying the thermal failure criteria. Further experiments in ULPU demonstrated a rather weak dependence on power shape and natural circulation flow rate, and verified the conservative bound of Figure 3.3 in tests including a channel-like geometry (created by the thermal insulation), and prototypic wall material and finish (see Theofanous and Syri, 1996).

The line in Figure 3.3 can be expressed by

$$q_{cr}(\theta) = 490 + 30.2\,\theta - 8.88 \cdot 10^{-1}\theta^2 + 1.35 \cdot 10^{-3}\theta^3 - 6.65 \cdot 10^{-5}\theta^4 \quad \text{kW/m}^2 \qquad (3.1)$$

and from an evaluation of uncertainties, as discussed in Appendix E in DOE/ID-10460, we expect this result to be good within a few percent, so that CHF can be excluded outside a rather narrow range around it. In Section 7 we will see that the margins to failure are so significant that they totally dwarf this uncertainty in this failure criterion.

In concluding this section we would like to mention certain others' past and on-going efforts addressing CHF in relation to lower head integrity.

1. The CYBL experiment (SNL). A full-sized, stainless steel vessel with torospherical lower head of 1 cm thickness. Radiant heating applied internally (to the lower head) with peak flux capability of about 200 kW/m^2. Experiments showed persistent nucleate boiling up to this level of heat flux. This work was carried out for the DOE's Advanced Reactor Severe Accident Program as a complement to that in ULPU. For more details see Appendix F of DOE/ID-10460. It is interesting to note that the periodic bubble formation and departure observed in CYBL was found also in ULPU—about 2 Hz at 200 kW/m^2.

2. The FAI experiments (Henry et al., 1991; Henry and Fauske, 1993). These were carried out in a 32 cm diameter (outer) pipe cap, with thermite as the heat source, in a transient mode. Peak fluxes of $\sim$1 MW/m^2 were measured. The effect of reflective thermal insulation was assessed, both experimentally and analytically, and it was found to introduce no important limitation to coolability.

3. The SULTAN experiments (CEN, Grenoble). The test section consists of a long, straight channel in an adjustable orientation relative to the gravity vector. Experiments are in progress (Bonnet et al., 1994).

4. The Penn State experiments. These NRC-sponsored experiments involve steel hemispheres up to 30 cm in diameter (1/24- to 1/10-scale) and are on-going.

5. Other small scale work. This involves quite a few experiments with centimeter-scale heating surfaces, or very narrow channels, carried out primarily in connection with cooling of electronic components. This work is not relevant to the present problem and thus is not mentioned explicitly.

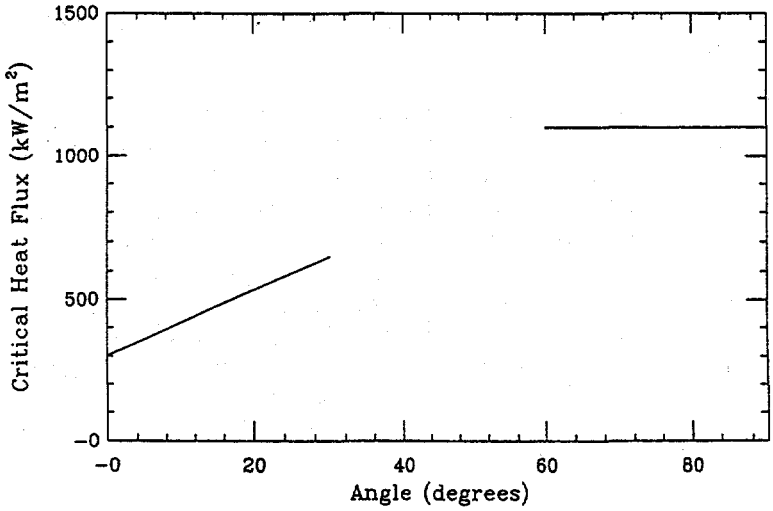

Figre 3.2. Critical heat flux as function of position on the lower head; from ULPU, in pool boiling.

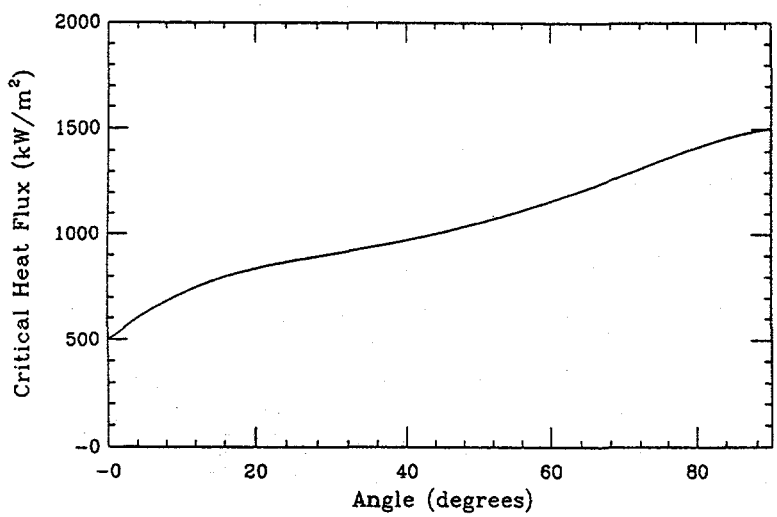

Figure 3.3. Critical heat flux as function of position on the lower head; from ULPU under full submergence and natural convection.

4. STRUCTURAL FAILURE CRITERIA

In this section we examine the behavior of the lower head under thermal loads severe enough to cause extensive wall thinning, and we show that structural failure cannot occur unless there is boiling crisis. In other words, we will endeavor to demonstrate that the thermal failure criteria discussed in the previous section are both necessary and sufficient for assessing lower head integrity. Under the low pressure conditions of interest here there are sufficient margins in the consideration to allow a basic-principles approach while avoiding the actual determination of structural failure. Other situations involving higher pressures may require detailed numerical simulations of the type illustrated in Appendix G of DOE/ID-10460, and for them, the so-derived structural failure criteria may become more limiting (than CHF). The purpose of this material is, in addition to this illustration, to provide further perspectives confirmative of the basic-principles approach pursued here.

We have already shown in the previous section that boiling crisis is a sufficient condition for lower head failure. Now, we wish to demonstrate that this is also the necessary condition; that is, unless BC occurs, there can be no failure. For this purpose it is adequate to demonstrate that a CHF-limited wall thickness is sufficient to support the lower head and its contents. The CHF-limited wall thickness can be readily obtained from Figure 3.3, using the steel thermal conductivity referenced together with other useful properties in Appendix L of DOE/ID-10460, and a steel liquidus temperature (see Section 7) of 1300 °C (1573 K). The result is shown in Figure 4.1. The critical region is around $\theta \sim 90°$, and the integrity of this region must now be examined in detail. Interestingly enough, this is the region revealed to be the most limiting from the thermal margins point of view as well (see Section 7).

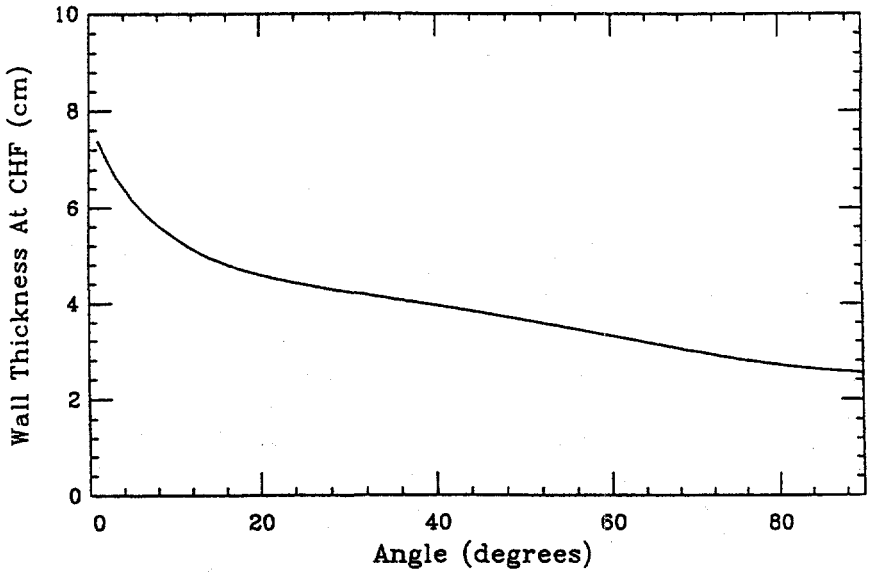

Figure 4.1. Maximum wall thicknesses allowed to accommodate the critical heat fluxes at various angular positions around the lower head, subject to 400 K and 1573 K temperature boundary conditions at the outside and inside boundaries respectively.

The physical situation is illustrated in Figure 4.2, and the following key points can be made regarding the state of stress in the segment shown.

1. Deadweight and Buoyancy. These two forces nearly cancel each other out. Take, for example, a melt layer 2 m deep, in the lower head, and a vessel submerged up to the hot leg nozzle elevation (~7 m from the bottom of the lower head). With a melt density of 8000 kg/m^3 we have a melt weight of 134 tons, a lower head weight of 29 tons, and a buoyancy force of 92 tons due to the effective hydrostatic head of 6.33 m on the lower head outer surface. The net force of 71 tons ($7 \cdot 10^5$ N) would require a wall thickness of 0.15 mm to reach the yield stress of this steel at full strength (355 MPa). In Figure 4.2 we can see that this region of full strength (i.e., below 900 K), under the heat flux condition of interest is 1.1 cm, and thus able to comfortably carry the applied stress.

2. Thermal Stress. As a result of the steep temperature gradient, the inner region is in compression, and the outer region is subject to tension at levels that, on an elastic basis, would significantly exceed the yield stress. A basic characteristic of thermal stresses is that they are self-equilibrating, i.e., in the absence of other stresses, thermal stresses must integrate to a net zero force

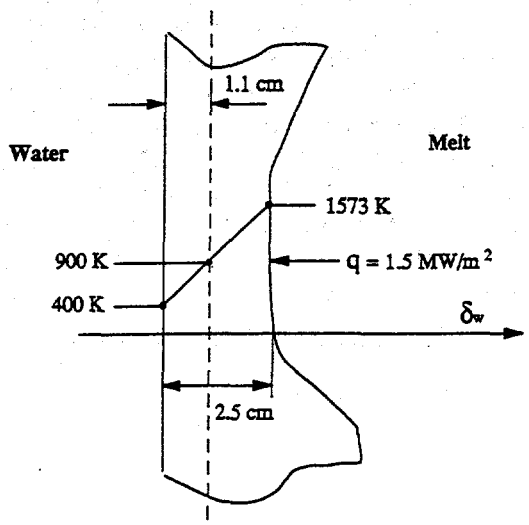

Figure 4.2. Illustration of conduction-limited wall thickness, and of the full-strength outer region ($T < 900$ K), under an imposed heat flux of 1.5 MW/m^2.

on any freebody section of the structure. Material plasticity would cause the temperature stresses to relax and redistribute to a profile that is bounded by the temperature-dependent tensile strength of the materials. In order to satisfy the self-equilibrating property, the thermal stress must redistribute to a profile that exhibits high tensile stress over a relatively narrow external (colder) portion of the vessel wall and a low compressive stress on the remainder of the wall. This thermal stress redistribution, when superimposed on stresses from other sources such as the differential internal pressure discussed under item 1 above, would result in the enhancement of the tensile stresses with the final stress distribution remaining at or below the temperature dependent flow stress of the material. Thus, the load carrying capacity of the vessel will be governed by the outer thickness of the wall that is under tension. Below, we will show that for the conditions of this problem, this outer region has a thickness of about one-fifth the wall thickness; that is, it is ~5 mm thick for the limiting case considered in Figure 4.2. It is easy to see that this elastically stressed portion of the wall is more than sufficient to carry the stress levels due to the externally imposed forces (as discussed under item 1).

In carrying out the quantitative demonstrations indicated above, we take a three-step approach. The first is idealized enough to allow an analytical result showing the basic features and extent of the tensile-stress region. We assume a linear dependence of the yield stress on temperature and a perfectly plastic behavior. The second step makes use of a simple numerical model and actual temperature-dependent material properties to show the relief mechanism described above and the load carrying capability of the outer tensile region. In Appendix G of DOE/ID-10460—finally, the third step—we can find that incorporation of creep confirms these results and that structural integrity is assured even under relatively significant primary system pressure. A detailed evaluation of ductile tearing has also been made, as described in Chapter 4 of DOE/ID-10460.

To illustrate the first step let us consider the thermal stresses in a cylindrical wall subject to a linear temperature distribution with a total temperature difference across it of magnitude ΔT. For a wall thickness, δ_w, small compared to the vessel radius, the analytical solution for the stress distribution (the azimuthal, σ_θ, axial, σ_z, and radial, σ_r, stresses) in the elastic region can be

simplified to:

$$\sigma_\theta = \sigma_z \sim \frac{\beta' E \Delta T}{2(1-\nu')} \left\{ 1 - 2\frac{r}{\delta_w} \right\} \qquad \sigma_r \sim 0 \tag{4.1}$$

where β', E, and ν' are the linear thermal expansion coefficient, Young's modulus of elasticity, and the Poisson ratio, respectively, and r is the distance from the outer boundary. The resulting equivalent (von Mises) stress is shown in Figure 4.3. Note that because the response is still elastic the midpoint is at zero stress and a region around it is subject to a low stress level. As T and ΔT increase the stresses in the extreme outer and inner regions reach yield, and assuming a perfectly plastic behavior, the situations obtained would be as illustrated in Figure 4.4. Clearly, the size of the elastic core decreases as the applied T and ΔT increase, and the elastic stress gradient increases with it.

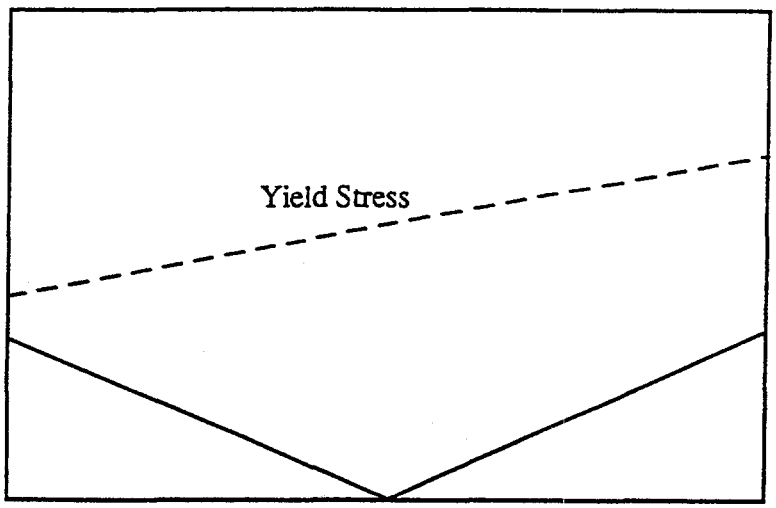

Figure 4.3. Equivalent (von Mises) stress distribution due to temperature gradient across the thickness of a vessel wall. Note that the yield stress is assumed to be linear with temperature.

For the second step, we make use of a finite element model of the whole reactor vessel (see Figure 4.5) Calculations were carried out with the code ABAQUS (version 5.2) and material properties accounting for the variation of the yield stress with temperature according to the recent data of Chavez et al. (1994). These data (for steel SA 106B, which is quite similar to that specified for the AP600) extend to 1150 K, and they were extrapolated linearly to zero at the steel liquidus ($\sim$1500 K). A wall thickness of 5 cm was taken in the calculation. The result is shown in Figure 4.6. Again, the tensile zone, which consists of an elastic core and a plastic outer region add up to about one-fifth of the wall thickness. The effect of yield variation with temperature is to shift this tensile zone toward the outside while much of the inside is seen to have relaxed to a near stress-free level.

In concluding this section we emphasize again that boiling crisis is the limiting failure criterion only at primary systems pressures near ambient (containment atmosphere). In fact, at some higher pressure level we would expect that control passes over to structural failure criteria, for which the computational approach of Appendix G in DOE/ID-10460 is appropriate and should be applied (with due consideration of uncertainties). Note that in this respect (of uncertainties) the present

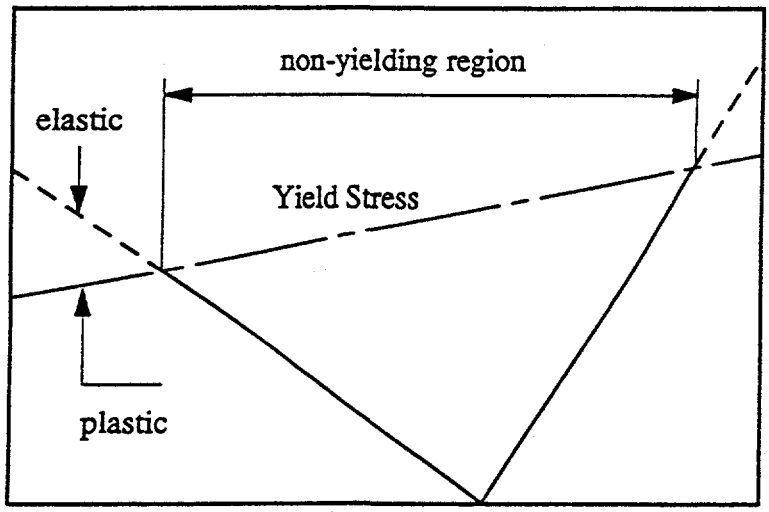

4.4. Equivalent stress distribution due to temperature gradient across the thickness of a vessel wall. The continuous line represents the stress distribution for elastic plastic behavior.

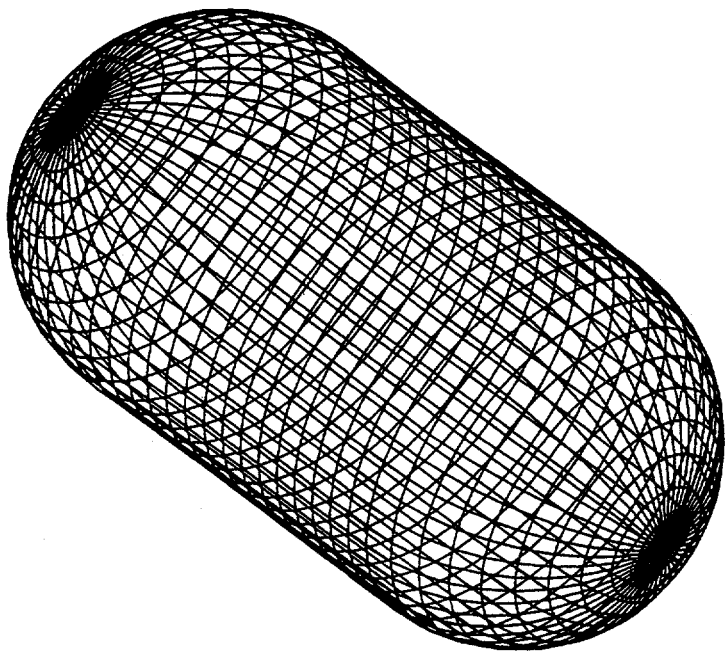

Figure 4.5. The finite element model utilized in the computations.

case is rather straightforward: boiling crisis is a conservatively limiting structural failure criterion. That is, structural failure margins are larger than margins to boiling crisis, which in turn are very large compared to uncertainties in this criterion (see Sections 3 and 7).

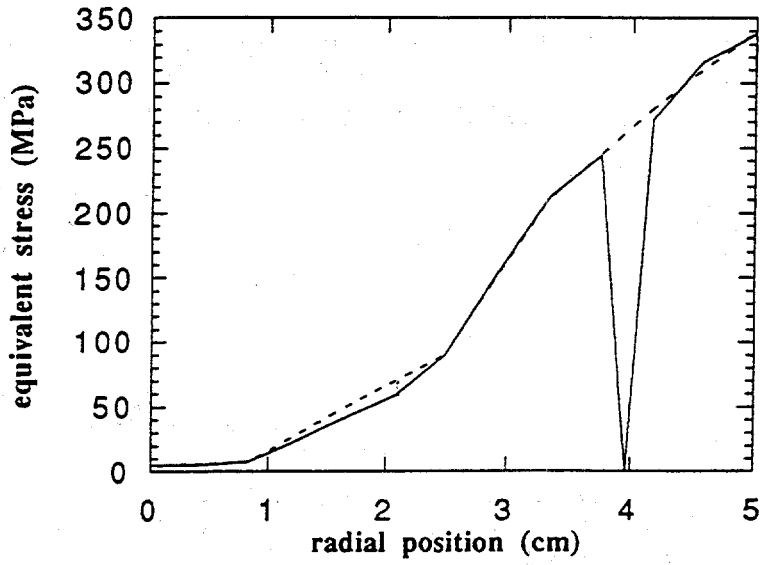

Figure 4.6. Equivalent stress distribution in the most critical section of the vessel from an ABAQUS calculation. Dashed line represents yield data at the temperatures corresponding to the various positions along the wall (from Chavez et al., 1994).

5. PARTITION OF THERMAL ENERGY FLOW BY NATURAL CONVECTION

In this section we consider the configuration dominated by natural convection phenomena and seek to determine the heat flow distribution at the boundaries of the volumetrically heated pool and of the steel layer. This is the key aspect of the overall model described in the next section, and therefore it is treated here separately. The physical situation is depicted in Figure 5.1, and its main characteristics can be listed as follows:

1. The hemisphere is almost full ($\theta_p \sim 75°$) with the oxide pool and the metal layer on top ($\theta_\ell \sim 90°$). This means that the effect of the "fill level" can be considered negligible for our purposes.
2. The oxide pool contains the oxidic components of the core melt (mainly UO_2 and ZrO_2), with a liquidus of ~2973 K. Because of this very high liquidus relative to the cooling capability at all boundaries (see Section 6) this pool is surrounded completely by crusts.
3. The crusts are thin enough not to appreciably alter the shape of the enclosure, and they impose a uniform temperature boundary condition—the melt liquidus. As a consequence, the pool-internal heat transfer problem is uncoupled from what goes on outside, (as long as the crusts do not vanish from any part of the boundary). This means that the internally imposed heat flux, together with thermal resistances and sink temperatures, determine the crust thickness distribution all around the pool boundary.
4. The metallic layer is of a large aspect ratio (thin compared to its diameter) and with its sidewalls almost vertical. It is heated from below and cooled from above and its sides. Again, natural convection drives the heat flow distribution, but now only the side boundary temperature is fixed—at the liquidus of the metal layer of ~1300 °C (see Section 6).

The nomenclature to be employed is as follows: From the oxide pool we have an "up" to "down" energy flow split. These two heat flows will be characterized by the average heat fluxes over the

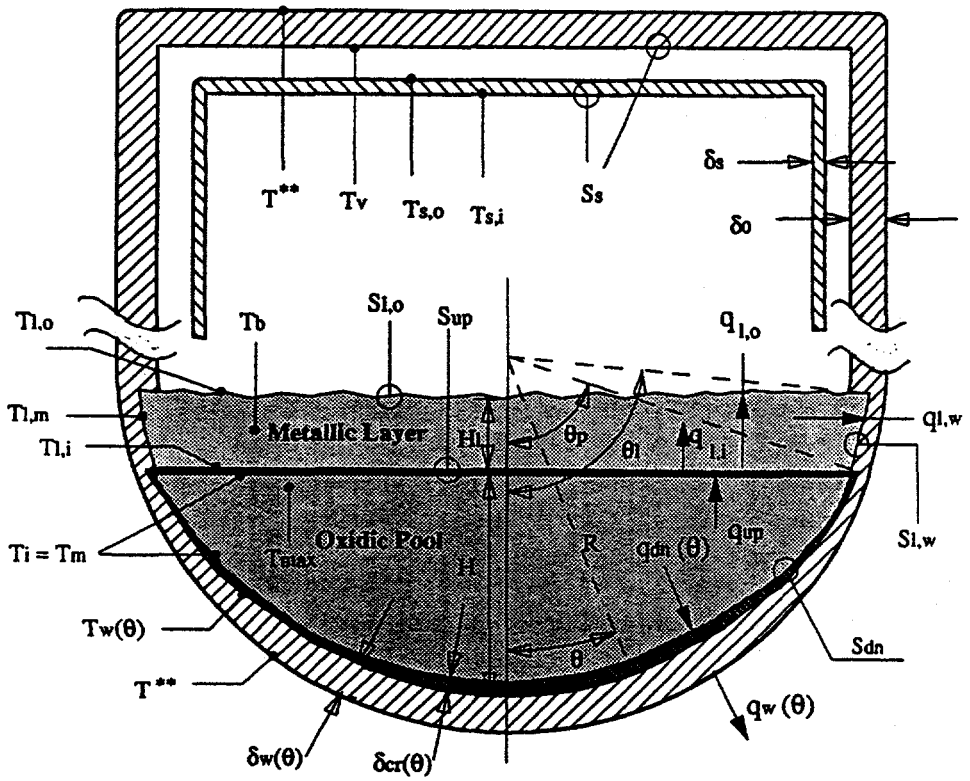

Figure 5.1. Schematic of the physical model used to quantify energy partition, and thermal loads in the long-term, natural convection thermal regime. Also shown is the nomenclature used in the formulation of the mathematical model.

horizontal and hemispherical boundaries of the pool (q_{up} and q_{dn}) respectively. Local values on the hemisphere will be defined by the angular position as indicated in Figure 5.1. Note that $q_w(\theta)$ contains $q_{dn}(\theta)$ plus the contribution of the heat generated in the crust at angular position θ. The heat flows "into" and "out" of the horizontal boundaries of the steel layer will be characterized by the average fluxes $q_{\ell,i}$ and $q_{\ell,o}$, respectively. The average heat flux through the side boundary of the steel layer will be denoted by $q_{\ell,w}$. The quantities of primary interest to the task of this section are those that directly affect lower head integrity; that is, $q_w(\theta)$ and $q_{\ell,w}$. However, these quantities can only be obtained from an integral analysis (presented in the next section) which makes use of all the heat fluxes defined above. The formulation necessary for this purpose is provided below.

Natural convection phenomena can be scaled in terms of the Grashof, Gr, and Prandtl, Pr, numbers, and in the presence of volumetric heating the Dammköhler, Da, number is also needed. These numbers are expressed as (Mayinger et al., 1975)

$$\mathrm{Gr} = \frac{g\beta(T_{max} - T_i)H^3}{\nu^2} \quad \mathrm{Pr} = \frac{\nu}{\alpha} \quad \mathrm{Da} = \frac{\dot{Q}H^2}{k(T_{max} - T_i)} \tag{5.1}$$

where $\dot{Q}$ is the volumetric heat generation rate, H is a characteristic dimension of the region in the vertical direction (i.e., pool depth), and β, k, ν, and α are the fluid thermal expansion coefficient,

thermal conductivity, kinematic viscosity, and thermal diffusivity, respectively. The overall heat transfer phenomenon is characterized by the Nusselt number, Nu, defined by

$$\mathrm{Nu} = \frac{qH}{k(T_{max} - T_i)} \tag{5.2}$$

where q is the average heat flux over a boundary of interest kept at uniform temperature T_i, and T_{max} is the maximum temperature in the pool. (In the absence of volumetric heating the "bulk" temperature (T_b) is used in place of T_{max}.) That is, the behavior can be characterized by correlations in the form

$$\mathrm{Nu} = \mathcal{F}\,(\mathrm{Gr}, \mathrm{Pr}) \qquad \text{no volumetric heating} \tag{5.3}$$

$$\mathrm{Nu} = \mathcal{G}\,(\mathrm{Gr}, \mathrm{Pr}, \mathrm{Da}) \qquad \text{with volumetric heating} \tag{5.4}$$

which can be obtained from model experiments or numerical simulations. Experience indicates that most, if not all of the effect of the Prandtl number is to be found in combination with the other dimensionless groups in the form of the Rayleigh, Ra, or "internal" Rayleigh, Ra′, numbers given by

$$\mathrm{Ra} = \mathrm{Gr}\,\mathrm{Pr}, \qquad \mathrm{Ra}' = \mathrm{Gr}\,\mathrm{Pr}\,\mathrm{Da} \tag{5.5}$$

such that

$$\mathrm{Nu} = \mathcal{F}\,(\mathrm{Ra}, \mathrm{Pr}^m) \tag{5.6}$$

$$\mathrm{Nu} = \mathcal{G}\,(\mathrm{Ra}', \mathrm{Pr}^n) \tag{5.7}$$

where m and n indicate a small (or zero) dependance. Our task, then, is to determine the functions $\mathcal{G}$ and $\mathcal{F}$ (and the exponents m and n) for the oxidic pool and metal layer, respectively. A key point, of course, is "similarity"—that is, these functions should be appropriate for the Ra, Ra′, and Pr number ranges of interest in the reactor. For the present application these ranges are:

$$\text{Oxidic Pool}: \quad 10^{15} < \mathrm{Ra}' < 6 \cdot 10^{15} \qquad \mathrm{Pr} \sim 0.6 \tag{5.8}$$

$$\text{Metallic Layer}: \quad 5 \cdot 10^{9} < \mathrm{Ra} < 2 \cdot 10^{10} \qquad \mathrm{Pr} \sim 0.1 \tag{5.9}$$

Another key point regarding similarity is the relationship of the final, truly steady state, to the sequence of transient states leading up to it. Finally, any correlation scheme has to be explicit on the "effective" temperature at which the various thermophysical properties are to be evaluated—normally the "film" temperature, i.e., the average value between the bulk and wall, is used, but because experiments so far related to Eq. (5.7), have been carried out with relatively small $(T_{max} - T_i)$, this is still an open question. Molecular diffusion considerations indicate that multicomponent effects on density and resulting natural convection cannot provide any sustainable influence, especially at high Rayleigh numbers. This was demonstrated experimentally by Schneider and Turland (1994).

5.1. The oxidic pool

The basic features of the flow regime in the oxidic pool are indicated in Figure 5.2. They consist of steep boundary layer regions adjacent to the isothermal boundary, a well-mixed upper pool volume, and a broadly stratified lower pool portion. These regions can be expected from consideration of basic principles of natural convection and have been demonstrated by the interferograms of Jahn and Reineke (1974) in a slice (semicircular) geometry. The upper mixed region is created by the cold "plumes" detaching continuously from the upper boundary layer, and the lower stratified region is the result of the downflowing boundary layers along the curved boundary and the induced bulk motion; that is, a combination of entrainment all along the outer edge of the boundary

layer, and a turnover process in the bulk (due to the wall-plume penetration). The transition from the well-mixed to the stratified region is controlled by the interplay between the mixing process from above and the bulk-convection (turnover) from below. The Ra′ numbers of interest are high enough to ensure turbulent motions for which we generally expect little or no effect of the length scale. This means correlations of the form

$$\mathrm{Nu} \sim \mathrm{Ra}'^{0.2} \tag{5.10}$$

from which the length scale just cancels out. As a consequence, regarding the behavior at the upper (flat) boundary we can also bring to bear results from fluid geometries enclosed between two horizontal boundaries, with at least the upper one held isothermal (i.e., the lower boundary can be isothermal or adiabatic). This is fortunate because this geometry has received wider attention than the hemispherical one, and available data for it extend to higher values of the Ra′ number. The following material in this section is arranged in three segments. In the first two we consider the upper (flat) and lower (curved) boundaries, respectively, while in the third we pursue certain interesting deductions from their interrelationship.

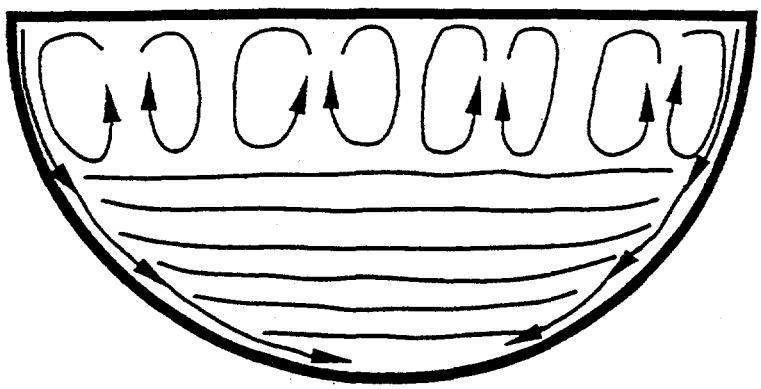

Figure 5.2. Illustration of the natural convection flow and stratification patterns in the oxidic pool.

The best known correlations for the upper boundary have derived from the experiments of Kulacki and Emara (1975) and Steinberner and Reineke (1978). The correlations and respective ranges of the experimental variables can be summarized as follows:

$$\text{Kulacki–Emara} \qquad \mathrm{Nu}_{up} = 0.34\,\mathrm{Ra}'^{0.226} \tag{5.11}$$
$$2 \cdot 10^4 < \mathrm{Ra}' < 4.4 \cdot 10^{12} \qquad \mathrm{Pr} \sim 7$$

$$\text{Steinberner–Reineke} \qquad \mathrm{Nu}_{up} = 0.345\,\mathrm{Ra}'^{0.233} \tag{5.12}$$
$$10^7 < \mathrm{Ra}' < 3 \cdot 10^{13} \qquad \mathrm{Pr} \sim 7$$

The experiments were carried out in rectangular geometries, under relatively small temperature differences. Kulacki and Emara also attempted to identify an independent Prandtl number effect (the n in Eq. 5.7) and wrote:

$$\mathrm{Nu}_{up} = 0.2\,\mathrm{Pr}^{0.239}\,\mathrm{Ra}'^{0.233} \tag{5.13}$$

which, interestingly enough, gives the same Ra′ number dependance as Eq. (5.12). However, it has been recognized that the data base was inadequate to support the Pr number dependance. Using a Pr number of 7 in Eq. (5.13), we obtain

$$\mathrm{Nu}_{up} = 0.32\,\mathrm{Ra}'^{0.233} \tag{5.14}$$

which can only be seen as an independent confirmation of the correlation by Steinberner and Reineke (1978).

More recently, the COPO experiments (see Appendix B of DOE/ID-10460) extended the Rayleigh number range to $1.5 \cdot 10^{15}$. The COPO data were obtained with hot water (Pr ~2.5), in a large-scale facility ($H = 0.8$ m), and were found to be in excellent agreement with Eq. (5.12) up to a Ra′ of $6 \cdot 10^{14}$. However, an apparent rapid transition occurred at this value of Ra′ number that produced a relatively consistent ~30% underprediction at the upper end of the range investigated. The authors of Appendix B (DOE/ID-10460) express some caution that such a transition is not understood and that its existence needs further investigation. The UCLA data (Appendix C of DOE/ID-10460) were obtained with Freon (Pr ~8) in a medium-sized hemispherical test section ($R = 0.4$ m). Both data points are below Eq. (5.12), one by 37% and the other, at $\mathrm{Ra}' = 9 \cdot 10^{13}$, by 17%. It should be noted, however, that due to the experimental arrangement the values reported pertain only to the outer position of the upper boundary.

Finally, the subject has been approached theoretically by Cheung (1980), who concluded that the asymptotic dependance for large Ra′ numbers is to the 1/4 power, and that at low Pr numbers there is a separate dependance (on Pr) to the 1/4 power as well. For the intermediate Pr number range (which is of interest here) he found that

$$\mathrm{Nu} = \frac{\mathrm{Ra}'^{1/4}}{B_1\,\Delta - B_2\,\mathrm{Pr}^{-1/3}\,\mathrm{Ra}'^{-1/12}} \tag{5.15}$$

where B_1, B_2, and Δ are all functions of the Pr number. He then used the data of Kulacki and Emara to show that the above formulation is consistent with "fitting" correlations of the form of Eq. (5.12) to data over limited ranges of the Rayleigh number, and that the exponent would be expected to increase asymptotically to the 0.25 value. In particular, he proposed that

$$\mathrm{Nu}_{up} \sim \mathrm{Ra}'^{0.227} \qquad \text{for} \quad \mathrm{Ra}' < 10^{11} \tag{5.16}$$

$$\mathrm{Nu}_{up} \sim \mathrm{Ra}'^{0.245} \qquad \text{for} \quad 10^{12} < \mathrm{Ra}' < 10^{22} \tag{5.17}$$

Note that this is consistent with Eq. (5.12), and its potential applicability up to the range of our interest ($\mathrm{Ra}' \sim 10^{16}$). However, he did not consider the Kulacki-Emara data adequate for extracting the Pr number dependance.

In light of the above, the basic issues regarding our present needs can be summarized as follows:

1. Validity of Eq. (5.12) to a Ra′ numbers range extended by 3 orders of magnitude. Besides the basic requirement for data support, we have the doubt cast on it by the COPO data and even (to a much lesser extent, however) by the UCLA data. It should be noted here that due to the importance of q_{up} on the behavior of the steel layer (see the next section), even a 30% discrepancy could be potentially rather significant to our conclusions.

2. Independent Prandtl number effect. Since our case requires an extrapolation (of the main data base) by about one order of magnitude (from ~7 to ~0.6) even a small dependance could produce a significant effect. For example, the dependance in Eq. (5.13) would produce a reduction by almost a factor of 2! Now, the COPO data indicate that such a strong effect is unlikely, since a Pr ~3 could have produced a 20% effect, rather than the excellent agreement found for $Ra' < 6 \cdot 10^{14}$. However, the discrepancy found for $Ra' > 6 \cdot 10^{14}$ prevents this issue from being considered closed.

The mini-ACOPO experiments, described by Theofanous and Liu (1996) and in Appendix D of DOE/ID-10460, have been carried out for the purpose of addressing these issues. They were carried out in a medium-scale (R ~0.4 m) hemispherical geometry, using water or freon as the working fluids. The experimental ranges covered were

$$10^{12} < Ra' < 7 \cdot 10^{14} \qquad 2.6 < Pr < 10.8 \tag{5.18}$$

and pool-to-wall temperature differences ranged up to 70 K. The main results for the upper boundary are summarized in Figures 5.3 and 5.4. Figure 5.3 shows the comparison with the Steinberner–Reineke correlation.* The agreement in the region of overlap with their data ($10^{12} < Ra' < 3 \cdot 10^{13}$) is excellent, which confirms the experimental approach in the mini-ACOPO. The agreement of the extended correlation with the data for Ra′ numbers that reach up toward prototypic values is also excellent. In Figure 5.4 we show the same data in a form suitable for detecting any Prandtl number effect. None can be seen, and we can thus see no problem for using this correlation under a small extrapolation down to Pr ~0.6.

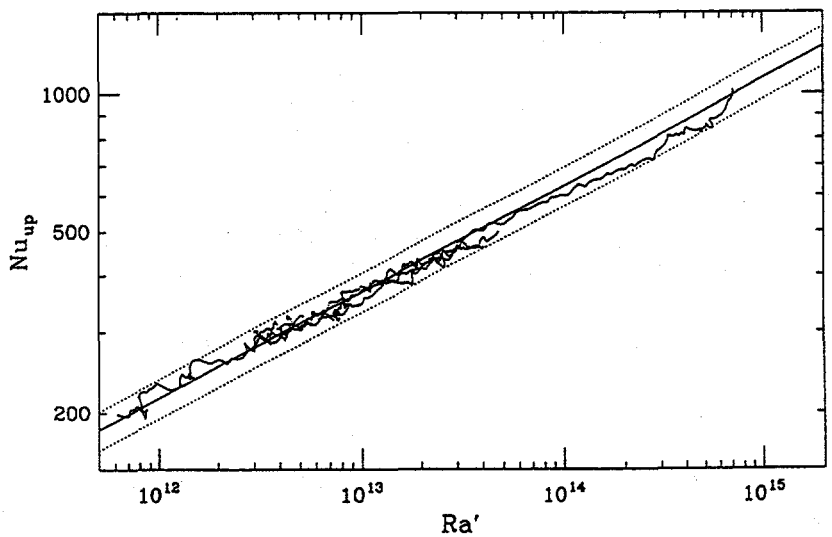

Figure 5.3. The mini-ACOPO results for upward heat transfer against the Steinberner and Reineke (1978) correlation. Data in the range $3 \cdot 10^{13} < Ra' < 7 \cdot 10^{14}$ are from run A16, the last Freon run, and the rest of the data are from runs B1, B2 and B3, carried out with water at various temperature ranges. Properties evaluated at "film" temperature.

* For the latest information on this subject, see Appendix V-2. of DOE/ID-10460.

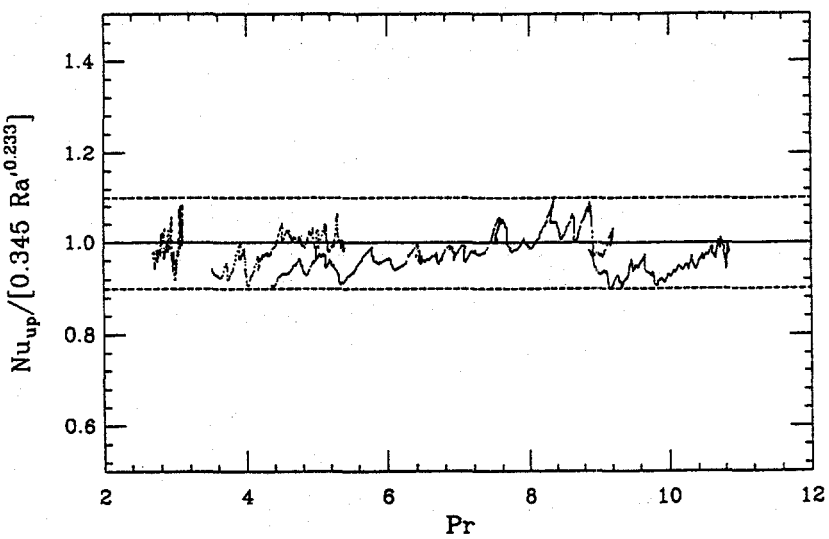

Figure 5.4. Mini-ACOPO data normalized according to the correlation in Figure 5.3, shown against the applicable Prandtl numbers.

Finally, it is worth mentioning the numerical simulations of Mayinger et al. (1975) and of Kelkar et al. (1993), mainly because they appear to have actually produced correct **predictions** for the **downward** heat flux (see below). Both calculations were carried out for a hemisphere. Mayinger et al. covered the range $7 \cdot 10^6 < \mathrm{Ra}' < 5 \cdot 10^{14}$, using a Prandtl number of 0.5 and fitted the results (for the upward heat flux) by

$$\mathrm{Nu}_{up} = 0.4\,\mathrm{Ra}'^{0.2} \tag{5.19}$$

It can be readily seen that this result at a Ra′ of 10^{15} would under-predict Eq. (5.12) by a factor of 3. The numerical simulations of Kelkar et al., were run with the low Reynolds number turbulence model of Jones and Laurder and included a "wall correction" due to Yap. Results were given for $10^8 < \mathrm{Ra}' < 10^{16}$ and a Prandtl number 1. They can be well fit by

$$\mathrm{Nu}_{up} = 0.18\,\mathrm{Ra}'^{0.237} \tag{5.20}$$

which can be seen to be essentially parallel to Eq. (5.12), but to provide a consistent under-prediction by almost a factor of 2.

Experiments for the hemispherical boundary (downwards heat transfer) have been problematic because of the difficulty in producing uniform heating. Thus, a slice (semicircular) geometry has been favored, even though it cannot reproduce the converging effect of the boundary layers present in the full geometry. The experiments of Jahn and Reineke (1974) were run with water (Pr ~7), covered the range $10^7 < \mathrm{Ra}' < 5 \cdot 10^{10}$, and produced

$$\mathrm{Nu}_{dn} = 0.54\,\mathrm{Ra}'^{0.18}\left(\frac{H}{R}\right)^{0.26} \tag{5.21}$$

The measurement also provided local heat fluxes and an indication of the peaking at higher polar angles. Equation (5.21) was confirmed by the COPO experiments and thus extended to $4 \cdot 10^{12} <$

$Ra' < 1.8 \cdot 10^{13}$ and Pr ~3. Data were also provided for the local heat fluxes on the vertical and lower boundaries. Mayinger et al. (1975) were able to reproduce Eq. (5.21) using the Navier–Stokes equations with an eddy diffusivity model, which was then applied to an axisymmetric geometry to produce

$$Nu_{dn} = 0.55\ Ra'^{0.2} \tag{5.22}$$

for $7 \cdot 10^6 < Ra' < 5 \cdot 10^{14}$ and Pr = 0.5. These as well as the COPO data were also interpreted by means of a turbulence model, incorporating an empirical modification of the eddy diffusivity via the Richardson number (Dinh and Nourgaliev, 1994). Kelkar et al., (1993) in the calculations mentioned above provided predictions for Pr = 1 and Ra' numbers up to 10^{16} which can be fit by

$$Nu_{dn} = 0.1\ Ra'^{0.25} \tag{5.23}$$

This is a quite different trend than that in Eq. (5.22), but interestingly enough, at a Ra' number of 10^{15} a discrepancy between these two equations is only ~2%!

The UCLA experiments mentioned above, and described in Appendix C of DOE/ID-10460, also provided data for the lower boundary of the hemisphere. Two data points on the average fluxes obtained at Ra' numbers of $3 \cdot 10^{13}$ and $9 \cdot 10^{13}$ are in good agreement (15% higher) with Eq. (5.22), and the local fluxes were correlated by

$$\frac{h(\theta)}{h} = c_1\ sin\ \Theta - c_2\ cos\ \Theta \qquad \text{for } 0.75 < \frac{\theta}{\phi} \leq 1 \tag{5.24}$$

where

$$c_1 = -1.25\ cos\ \phi + 2.6$$

$$c_2 = -2.65\ cos\ \phi + 3.6$$

and

$$\frac{h(\theta)}{h} = 1.17\ sin^4\ \Theta + 0.23 \qquad \text{for } 0 < \frac{\theta}{\phi} < 0.75 \tag{5.25}$$

where ϕ is the polar angle at the pool surface, and $\Theta = \frac{\theta}{\phi}\frac{\pi}{2}$. These experiments are encouraging in tying in with Eqs. (5.22) and (5.23); however, there are several aspects in relation to the present application that require further clarification. They can be summarized as follows:

1. Based on the highest UCLA data point, the present use would require an extrapolation on the Ra' number by nearly two orders of magnitude. The higher trend in Eq. (5.23) than from Eq. (5.22) (with Ra' number) then becomes of concern, especially as Kelkar et al. noted that (due to this trend) the downward heat flux approaches the upward flux at the high Ra' number range of interest here. As noted previously, their upward fluxes are underestimated by a factor of 2, which weakens this conclusion but does not eliminate the concern.
2. Although there is adequate experimental basis now (as explained above) that any independent Pr number effect is slight enough to be negligible at the upper (flat) boundary, indicating a high likelihood that the same is true for the curved boundary, this is still tentative and subject to experimental verification. (Both UCLA data points were obtained at Pr = 8.2.)
3. The microwave radiation heating technique employed in the UCLA experiments requires a slightly coupling medium (freon) in order to obtain uniformity over the scale of the experiment.

This low heating rate forced operation at rather low temperature differences ($T_{max} - T_i$), while conduction resistance through the glass wall produced a non-uniformity in T_i of similar magnitude as the ($T_{max} - T_i$) itself. For example, the run at Ra$' \sim 9 \cdot 10^{13}$ involved a ($T_{max} - T_i$) of 1.9 K at the top and a ($T_{max} - T_i$) of 5.8 K at the bottom of the pool, while the T_i varied by 4.5 K from the equator to the bottom of the hemisphere (Asfia, 1994). This could raise concerns about the appropriateness of the comparison with Eq. (5.22), or the validity of Eq. (5.24) to an isothermal boundary situation. (However, current efforts at UCLA are directed at obtaining freezing at the boundaries which would ensure an isothermal boundary—in this case the flux distribution can be obtained from the variation of crust thickness.)

4. Transient effects. While heat transfer at steady state occurs with a stable stratification pattern as indicated in Figure 5.2, consideration of transient behavior, besides pool thermal inertia effects, also needs to be concerned with timewise variation of this stratification pattern. In particular, starting from a uniform pool, this final pattern would be approached from a sequence of more uniform (than the final) states, and one might ask how this would affect the up-to-down energy flow split and the flux distribution over the curved boundary. Clearly, there is a potential here for significantly higher (than at steady state) thermal loads at lower positions on the lower head. Given the shape of the critical heat flux (Figure 3.3), it is immediately obvious that this topic constitutes a major open issue.

The mini-ACOPO experiment mentioned above was built and operated to address this different set of issues as well. Again, the experimental ranges covered were

$$10^{12} < \text{Ra}' < 7 \cdot 10^{14} \qquad 2.6 < \text{Pr} < 10.8 \tag{5.26}$$

and the pool-to-wall temperature differences ranged up to 70 K. The main results for the downward heat transfer are summarized in Figures 5.5 and 5.6. As seen in Figure 5.5, the data are tightly correlated by

$$\text{Nu}_{dn} = 0.048\,\text{Ra}'^{0.27} \qquad 10^{12} < \text{Ra}' < 3 \cdot 10^{13} \tag{5.27}$$

$$\text{Nu}_{dn} = 0.0038\,\text{Ra}'^{0.35} \qquad 3 \cdot 10^{13} < \text{Ra}' < 7 \cdot 10^{14} \tag{5.28}$$

Even though an overall correlation

$$\text{Nu}_{dn} = 0.02\,\text{Ra}'^{0.3} \qquad 10^{12} < \text{Ra}' < 7 \cdot 10^{14} \tag{5.29}$$

would still fit quite well, the use of the upper branch (Eq. (5.28)) is deemed preferable for this application. In Figure 5.6 we show the data in a form suitable for detecting any independent Pr number effect. None can be seen, and we can thus conclude that Eq. (5.28) is applicable under the modest extrapolation to a Pr number of 0.6.

Another interesting perspective can be obtained from Figure 5.7, containing the present data and correlations, Mayinger's correlation (Eq. 5.22), the numerical results of Kelkar et al., and the UCLA data. We can see that all of these results are mutually reinforcing. While in the range expected to dominate the thermal loads in this application ($10^{15} < \text{Ra}' < 5 \cdot 10^{15}$), the Mayinger correlation provides a lower bound, the present correlation provides an upper one (the trends of the UCLA data and Kelkar et al. simulations indicating an intermediate behavior). The effect of using the lower bound in the analysis is examined in a sensitivity study in Section 7.

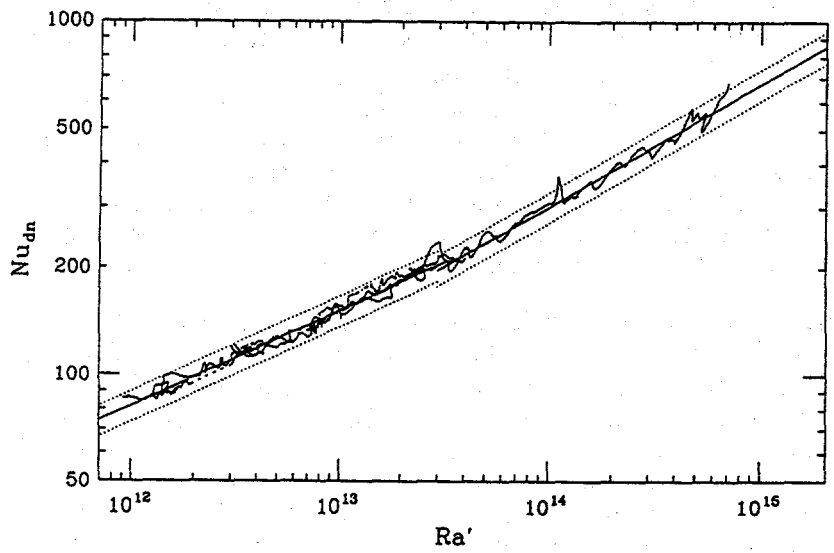

Figure 5.5. The mini-ACOPO results for downward heat transfer shown against Eqs. (5.27) and (5.28) Shown are: run A16, the last Freon run, and runs B1, B2 and B3 carried out with water at various temperature ranges. Properties evaluated at "film" temperature.

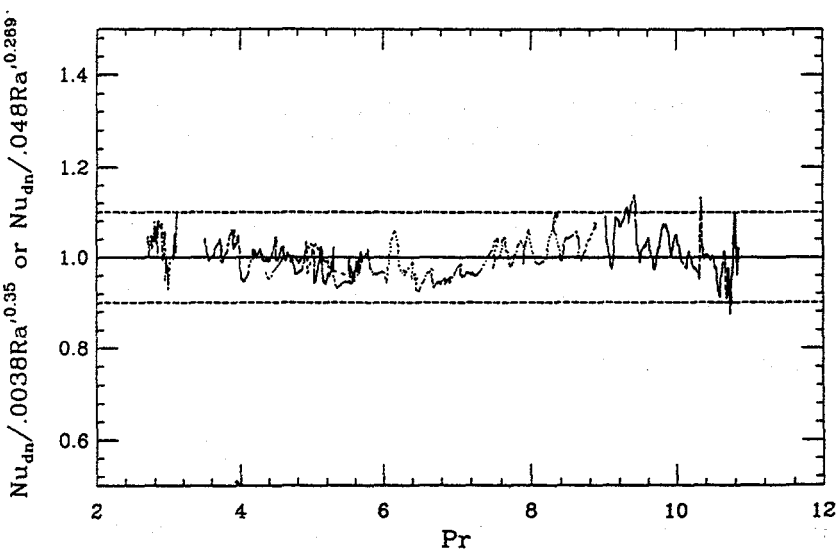

Figure 5.6. Mini-ACOPO data normalized according to the correlations in Figure 5.5, shown against the applicable Prandtl numbers.

Now, revisiting the four issues being addressed here, the mini-ACOPO data show that even under the most extreme transient conditions (as in run A16), the boundary layers and overall stratification patterns develop quickly enough to exhibit an average behavior quite consistent with steady-state behavior. However, these data also show a finer structure of stratification pattern adjustment, as a result of the transient, that produces some variation of the heat flux distribution. This is illustrated in Figure 5.8, containing all the mini-ACOPO data, and including for comparison

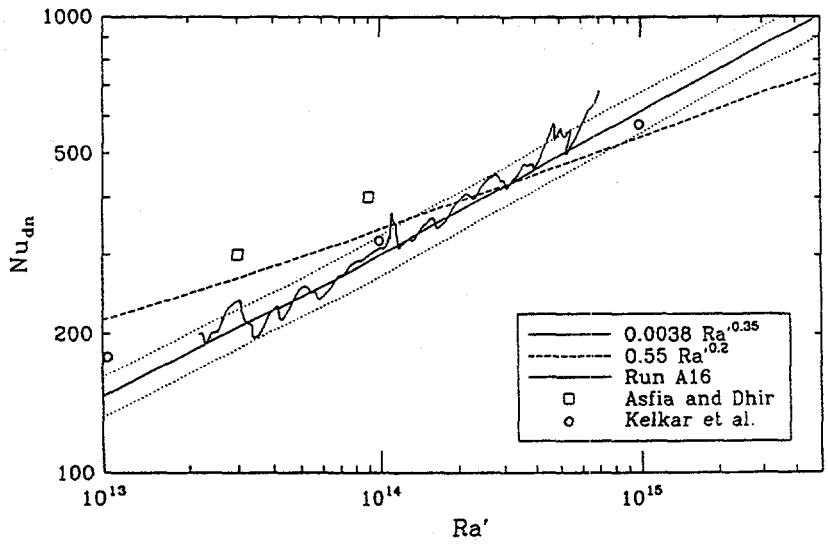

Figure 5.7. The mini-ACOPO data (downward heat transfer) and correlation obtained from them (Eq. (5.28)), shown against the Mayinger et al. (1975) correlation, the UCLA data, and the results of the numerical simulations by Kelkar et al. (1993).

the UCLA correlation and the shape found by Jahn (Mayinger et al., 1975) in a slice geometry at an Ra′ number of $1.2 \cdot 10^{10}$. This figure also shows that

$$\frac{\mathrm{Nu}_{dn}(\theta)}{\mathrm{Nu}_{dn}} = 0.1 + 1.08\left(\frac{\theta}{\theta_p}\right) - 4.5\left(\frac{\theta}{\theta_p}\right)^2 + 8.6\left(\frac{\theta}{\theta_p}\right)^3, \qquad 0.1 \le \frac{\theta}{\theta_p} \le 0.6 \qquad (5.30a)$$

$$\frac{\mathrm{Nu}_{dn}(\theta)}{\mathrm{Nu}_{dn}} = 0.41 + 0.35\left(\frac{\theta}{\theta_p}\right) + \left(\frac{\theta}{\theta_p}\right)^2, \qquad 0.6 < \frac{\theta}{\theta_p} \le 1 \qquad (5.30b)$$

reasonably represents the mini-ACOPO data. Although this correlation was derived with full hemisphere, it remains adequately normalized, and we expect it to be reasonably valid for $60° < \theta_p < 90°$. The UCLA correlation exhibits a somewhat more peaked distribution, and it will be used in a sensitivity study in Section 7. Also shown in Figure 5.8 is the result of the numerical simulations ($\mathrm{Ra}' = 10^{14}$ and 10^{16}) of Kelkar et al. (1993). It exhibits a trend more uniform than any of the experiments and, in fact, in the important upper regions it provides a lower bound.

Further confirmation of the treatment proposed here was obtained with the ACOPO experiment, as described in Appendix V-2 of DOE/ID-10460. Operating at a 4 times larger scale than the mini-ACOPO it affords a much longer "internal time scale" and hence full exploration of the stratification adjustment effects discussed above. The key characteristics of this experiment have been summarized in Table 5.1, and put into perspective with the mini-ACOPO, and the other ongoing experiments at UCLA (currently efforts to obtain freezing at the boundaries), and at IVO (currently directed to a semicircular slice geometry, with freezing at the boundaries). In addition, the BALI experiment at CEN, Grenoble (similar in concept and scale to the COPO, but including additional capabilities, such as gas or liquid injection at the boundaries), expected to be operational in the near future, should be mentioned (Bonnet et al., 1994).

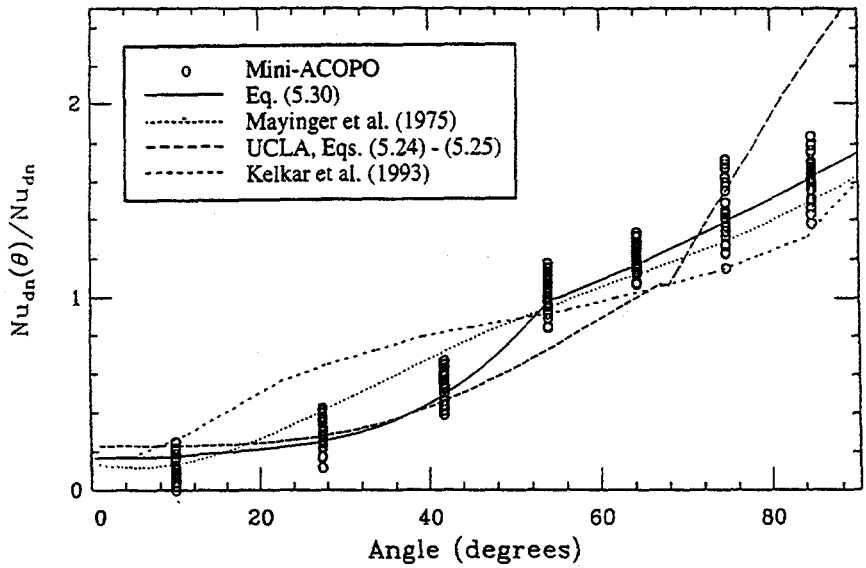

Figure 5.8. The mini-ACOPO data and the correlation obtained from them (Eq. (5.30)), for heat flux distribution as function of the angular position, shown against the UCLA correlation. Also shown is a line through the data obtainby by Jahn (Mayinger et al. 1975), for $Ra' \sim 2 \cdot 10^{10}$, renormalized (by area averaging) to an axisymmetric geometry, and the result of numerical simulations by Kelkar et al. (1993), for $10^{14} < Ra < 10^{16}$.

Table 5.1. An Overall View of Recent Work with Volumetrically Heated Pools

Experiment Concept	Scale/Shape Dimensionality	Working Fluid	$T_{max} - T_i$ (K)	Pr	Ra′
COPO Joule Heating	1/2 Torospherical 2-D slice	Water	10	$2 < Pr < 3$	$1 \cdot 10^{14} < Ra' < 8 \cdot 10^{15}$
UCLA Microwave Heating	1/8 Semispherical Axisymmetric	Freon-113	2 to 8	$8.2 < Pr < 9.5$	$4 \cdot 10^{11} < Ra' < 1 \cdot 10^{14}$
Mini-ACOPO Cooldown	1/8 Semispherical Axisymmetric	Freon-113 Water	40 100	$7 < Pr < 11$ $2 < Pr < 10$	$2 \cdot 10^{13} < Ra' < 7 \cdot 10^{14}$ $1 \cdot 10^{11} < Ra' < 3 \cdot 10^{12}$
ACOPO Cooldown	1/2 Semispherical Axisymmetric	Freon-113 Water	40 100	$7 < Pr < 11$ $2 < Pr < 10$	$1 \cdot 10^{16} < Ra' < 2 \cdot 10^{17}$ $4 \cdot 10^{13} < Ra' < 2 \cdot 10^{16}$

Finally, it is instructive to consider what can be learned from Eqs. (5.12), (5.28), and (5.30), regarding energy partition from the oxidic pool, and resulting local thermal loads at the curved boundary. First, the ratio of the up-to-down heat fluxes can be obtained from:

$$R' \equiv \frac{Nu_{up}}{Nu_{dn}} = 90\, Ra'^{-0.117} \tag{5.31}$$

which for $Ra' \sim 5 \cdot 10^{15}$ gives a ratio of 1.31. Using Eq. (5.22) in place of Eq. (5.28), on the other hand, we obtain

$$R' \equiv \frac{Nu_{up}}{Nu_{dn}} = 0.63\, Ra'^{0.033} \tag{5.32}$$

which for the same Ra' yields a ratio of 2.1. Now, from an overall energy balance on the oxidic pool (of volume V) we have

$$\dot{Q}V = S_{up}q_{up} + S_{dn}q_{dn} \tag{5.33}$$

which for an hemisphere can be written as

$$q_{dn} = \dot{Q}V \left\{2\pi R^2(1 + 0.5R')\right\}^{-1} \tag{5.33'}$$

where R' is the ratio defined above (Eq. (5.31) or (5.32)). This allows a simple estimate of q_{dn}, for Ra' numbers around the $5 \cdot 10^{15}$ value utilized in the derivation, and using it to estimate the flux shape (from Eq. (5.30)), and q_{up} (from the value of the Ra'). In the next section we will show how the complete solution for the steel layer can be obtained after q_{up} is known. (For cases where the Ra' is significantly different than $5 \cdot 10^{15}$, the same procedure can be utilized, after solving Eq. (5.33) for the Ra' number, as discussed in Section 6.) For example, supposing that $\dot{Q} = 1.3$ MW/m^3 and $V = 10$ m^3 (typical values for the AP600), and with $R = 2$ m, we obtain q_{dn} as 313 kW/m^2 or 252 kW/m^2 depending on whether the R' is obtained from Eq. (5.31) or (5.32), respectively. We can see that the sensitivity is only ~25%. We can also see that even with a bounding peak-to-average value of 2 (see Figure 5.8) we cannot expect local values much in excess of 626 kW/m^2 at $\theta \sim 90°$, which shows a margin of safety by over a factor of 2 (see Figure 3.3). The 10 m^3 do not quite fill the hemisphere and use of Eq. (5.33') is only approximate. Using Eq. (5.33), we obtain $q_{dn} = 391$ kW/m^2, as compared to the 313 kW/m^2 quoted above. On the other hand, using the complete numerical solution according to Section 6, we have $q_{dn} = 357$ kW/m^2.

5.2. The metallic layer

Available work in this area has considered only situations without side wall cooling; that is, liquid layers heated from below and cooled on the top. Our approach is to make use of this work in conjunction with heat transfer to a vertical wall, in a manner that conservatively represents this most important, for our purposes, component. The discussion proceeds in three steps. In the first we summarize available results for natural convection through liquid layers. In the second we consider natural convection to a vertical, cooled wall from an ambient fluid. Finally, in the third step, we explain how the previous two components can be put together to treat conservatively the role of the metal layer in the model that integrates the heat transfer behavior. This third step is also supported by a simple simulant experiment, run specifically for this purpose (Appendix N of DOE/ID-10460).

On the first step, let us begin with the widely used Globe and Dropkin (1959) correlation,

$$Nu = 0.069\, Ra^{1/3}\, Pr^{0.074} \tag{5.34}$$

incorporating data with various fluids ($0.02 < Pr < 8750$) at Rayleigh numbers in the range $3 \cdot 10^5 < Ra < 7 \cdot 10^9$. For the relevant Prandtl number (~0.13) the above correlation reduces to:

$$Nu = 0.059\, Ra^{1/3} \tag{5.35}$$

On the other hand, there is considerable evidence in the literature that for turbulent flow (high Ra) the Rayleigh number exponent should be less than 1/3. In fact, works by Silveston (1958) and O'Toole and Silveston (1961) recommend, respectively,

$$\mathrm{Nu} = 0.1\,\mathrm{Ra}^{0.31}\,\mathrm{Pr}^{0.05} \quad \text{and} \quad \mathrm{Nu} = 0.104\,\mathrm{Ra}^{0.305}\,\mathrm{Pr}^{0.084} \tag{5.36}$$

while Goldstein and Chu (1969) determined an exponent of 0.294 for air (Pr$\sim$1). For Pr = 0.13 Eqs. (5.36) reduce to

$$\mathrm{Nu} = 0.09\,\mathrm{Ra}^{0.31} \quad \text{and} \quad \mathrm{Nu} = 0.088\,\mathrm{Ra}^{0.305} \tag{5.37}$$

which are in apparent difference with Eq. (5.35). In fact, at the range of Rayleigh numbers of interest here, Ra $\sim 10^{10}$, these results are quite close, as can be seen by forcing Eq. (5.35) to a 0.31-type dependence on the Rayleigh number; that is,

$$\mathrm{Nu} = 0.1\,\mathrm{Ra}^{0.31} \tag{5.38}$$

Based on these considerations we can be quite confident in using Eq. (5.35), which is therefore selected for the analysis carried out in the next section.

For the second step, the situation is one of heat transfer to an isothermal vertical plate, and the appropriate driving force is **the bulk liquid temperature minus the plate temperature.** The heat transfer coefficient can be obtained according to Churchill and Chu (1975) from

$$\mathrm{Nu}^{1/2} = 0.825 + \frac{0.387\,\mathrm{Ra}^{1/6}}{\left\{1 + (0.492/\mathrm{Pr})^{9/16}\right\}^{8/27}} \tag{5.39}$$

which is valid for any Prandtl number and Ra $< 10^{12}$. Again, the properties are to be evaluated at the "film" temperature. For Pr = 0.13, the reduced form of the above equation is

$$\mathrm{Nu} = 0.076\,\mathrm{Ra}^{1/3} \tag{5.40}$$

Note the similarity of this to Eq. (5.35) above; however, also note that Eq. (5.35) is based on a ΔT that involves two, rather than one, boundary layers. Flux shape effects, along the length of the plate, are considered in Chapter 5 of DOE/ID-10460 and are found to be negligible.

As we proceed now onto the third step it is appropriate to first consider the role of the metal layer qualitatively. For a given thermal load at the lower boundary of this layer (note that this is determined solely from the natural convection processes within the oxidic pool) the behavior is controlled by the thickness of this layer and the radiative emission properties of the upper boundary. The basic trend is easy to see: as the thickness and/or the emissivity decrease, the layer temperatures must reach higher and higher levels, and since the thermal boundary conditions at the vessel wall must remain fixed (at the melt liquidus), the heat fluxes into it must increase correspondingly. This "focusing" effect can be counteracted only by one mechanism, owing to the rather large aspect ratio (layer diameter to height) at which this focusing effect begins to become important. That is, eddy diffusion limitations in the bulk, and the development as a consequence of a significant lateral temperature gradient. This mechanism has been confirmed in the experiment discussed in Appendix N of DOE/ID-10460, and we expect to quantify it in the large ACOPO experiment in the

near future. For now, we will make the conservative assumption that the layer is well mixed in the bulk.

In addition, recognizing that the situation described by the Globe-Dropkin correlation is symmetrical (two boundary layers of equal magnitude in temperature drop), we can "specialize" Eq. (5.35) to either of the two boundaries as

$$h = 0.15\,k \left\{ \frac{g\beta}{\alpha\nu} \Delta T' \right\}^{1/3} \tag{5.41}$$

where $\Delta T' = T_{\ell,i} - T_b$ or $\Delta T' = T_b - T_{\ell,o}$, and T_b is the "bulk" temperature, and where properties are evaluated at the "film" temperature of the respective boundary layers. In Section 6 this equation is used in conjunction with Eq. (5.40) to describe the metal layer. That this formulation is appropriate and conservative has been demonstrated experimentally, as discussed in Appendix N of DOE/ID-10460.

To gain some general perspectives here on the role of this metallic layer, we make use of these equations together with the following simplifying assumptions (to eliminate second order effects):

1. The property group in Eqs. (5.40) and (5.41) has the same value at all three boundaries.
2. The upper and lower boundaries of the layer have the same area (thin layer, at ~90°).
3. The crust between the oxidic pool and metallic layer is thin.
4. The energy radiated from the surrounding cavity to the layer is negligible.

From energy balance considerations and for a nearly full hemisphere ($H \sim R$),* we then have (see Figure 5.1 for nomenclature):

$$(T_{\ell,i} - T_b)^{4/3} = (T_b - T_{\ell,o})^{4/3} + \frac{H_\ell}{R} (T_b - T_{\ell,m})^{4/3} \tag{5.42}$$

$$0.15k \left\{ \frac{g\beta}{\alpha\nu} \right\}^{1/3} (T_b - T_{\ell,o})^{4/3} = \epsilon\sigma T_{\ell,o}^4 \tag{5.43}$$

$$q_{up} = 0.15k \left\{ \frac{g\beta}{\alpha\nu} \right\}^{1/3} (T_{\ell,i} - T_b)^{4/3} \tag{5.44}$$

that is, three equations in the three unknowns T_b, $T_{\ell,i}$, and $T_{\ell,o}$. The $T_{\ell,i}$ can be eliminated by substitution from Eq. (5.44), and the T_b can be solved explicitly in terms of $T_{\ell,o}$ from Eq. (5.43) to obtain:

$$T_b = T_{\ell,o} + \left(\frac{\epsilon\sigma}{A} \right)^{3/4} T_{\ell,o}^3 \tag{5.45}$$

and

$$q_{up} = (\epsilon\sigma) T_{\ell,o}^4 + A \left(\frac{H_\ell}{R} \right) \left\{ (T_{\ell,o} - T_{\ell,m}) + \left(\frac{\epsilon\sigma}{A} \right)^{3/4} T_{\ell,o}^3 \right\}^{4/3} \tag{5.46}$$

* For $R/2 < H < R$, the ratio H_ℓ/R in Eq. (5.42) can be approximated well by H_ℓ/R_c, where R_c is the radius of the circular segment at position H.

where

$$A = 0.15k\left(\frac{g\beta}{\alpha\nu}\right)^{1/3} \tag{5.47}$$

This system of equations reveals a characteristic temperature for this problem given by

$$\tilde{T} = \left(\frac{A}{\epsilon\sigma}\right)^{3/8} \tag{5.48}$$

from which we can also define a characteristic heat flux,

$$\tilde{q} = \epsilon\sigma\tilde{T}^4 \tag{5.49}$$

Based on these quantities we can define the dimensionless variables:

$$T_b^* = \frac{T_b}{\tilde{T}} \quad T_{\ell,o}^* = \frac{T_{\ell,o}}{\tilde{T}} \quad T_{\ell,m}^* = \frac{T_{\ell,m}}{\tilde{T}} \quad q_{up}^* = \frac{q_{up}}{\tilde{q}} \tag{5.50}$$

and the above system becomes:

$$T_b^* = T_{\ell,o}^* + T_{\ell,o}^{*3} \tag{5.51}$$

$$q_{up}^* = T_{\ell,o}^{*4} + \left(\frac{H_\ell}{R}\right)\left\{T_{\ell,o}^* + T_{\ell,o}^{*3} - T_{\ell,m}^*\right\}^{4/3} \tag{5.52}$$

and the heat flux to the sidewall can then be written as:

$$q_{\ell,w}^* = \frac{1}{2}(T_b^* - T_{\ell,m}^*)^{4/3} \tag{5.53}$$

where the independent parameters of the problem, A, ϵ, $T_{\ell,m}$, and q_{up}, have been recast in terms of q_{up}^* and $T_{\ell,m}^*$ only. The other independent parameter, H_ℓ/R, remains the same.

The solution of the above system of equations can be obtained numerically, once and for all, and it is shown in Figures 5.9 and 5.10. From these, the sidewall heat flux can be obtained using Eq. (5.53), and the result is shown in Figure 5.11. When q_{up} is less than the value at which $T_{\ell,o}^* = T_{\ell,m}^*$ freezing of the upper boundary is predicted, and a closed form solution for the sidewall heat flux can then be simply obtained as:

$$q_{\ell,w} = \frac{1}{2}q_{up}\left\{1 + \frac{H_\ell}{R}\right\}^{-1} \tag{5.54}$$

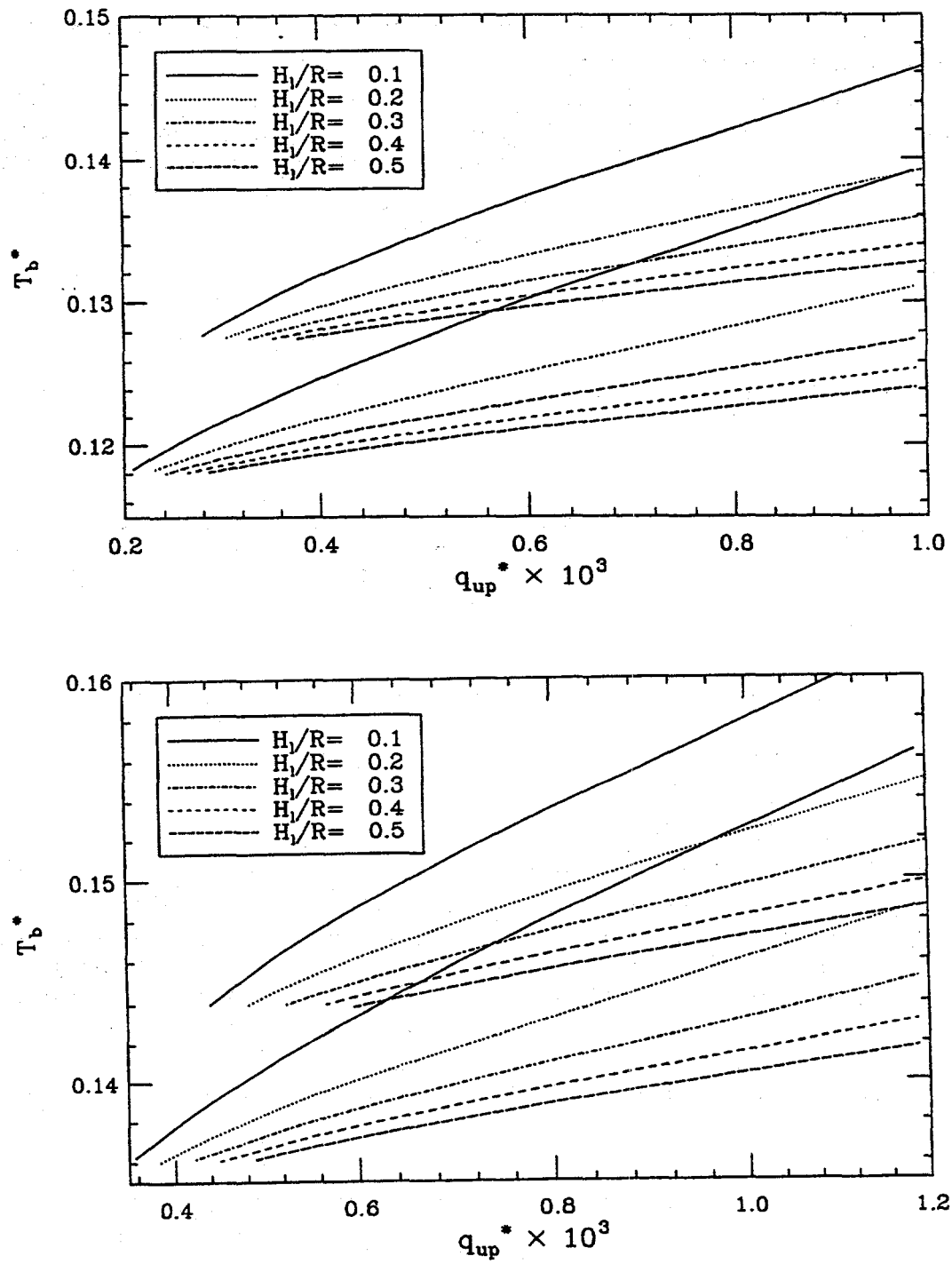

Figure 5.9. Solution to the system of Eqs. (5.51) and (5.52) for T_b^*, with H_ℓ/R and $T_{\ell,m}^*$ as the parameters. Each group of H_ℓ/R lines is for one value of $T_{\ell,m}^*$. Before using these figures first identify the $T_{\ell,m}^*$ values of each of the four groups of lines in Figure 5.10, and then proceed to Figure 5.9, recognizing that the four groups are similarly placed. Also note that corresponding lines (same $T_{\ell,m}^*$) start at the same value of the coordinate (q_{up}^*).

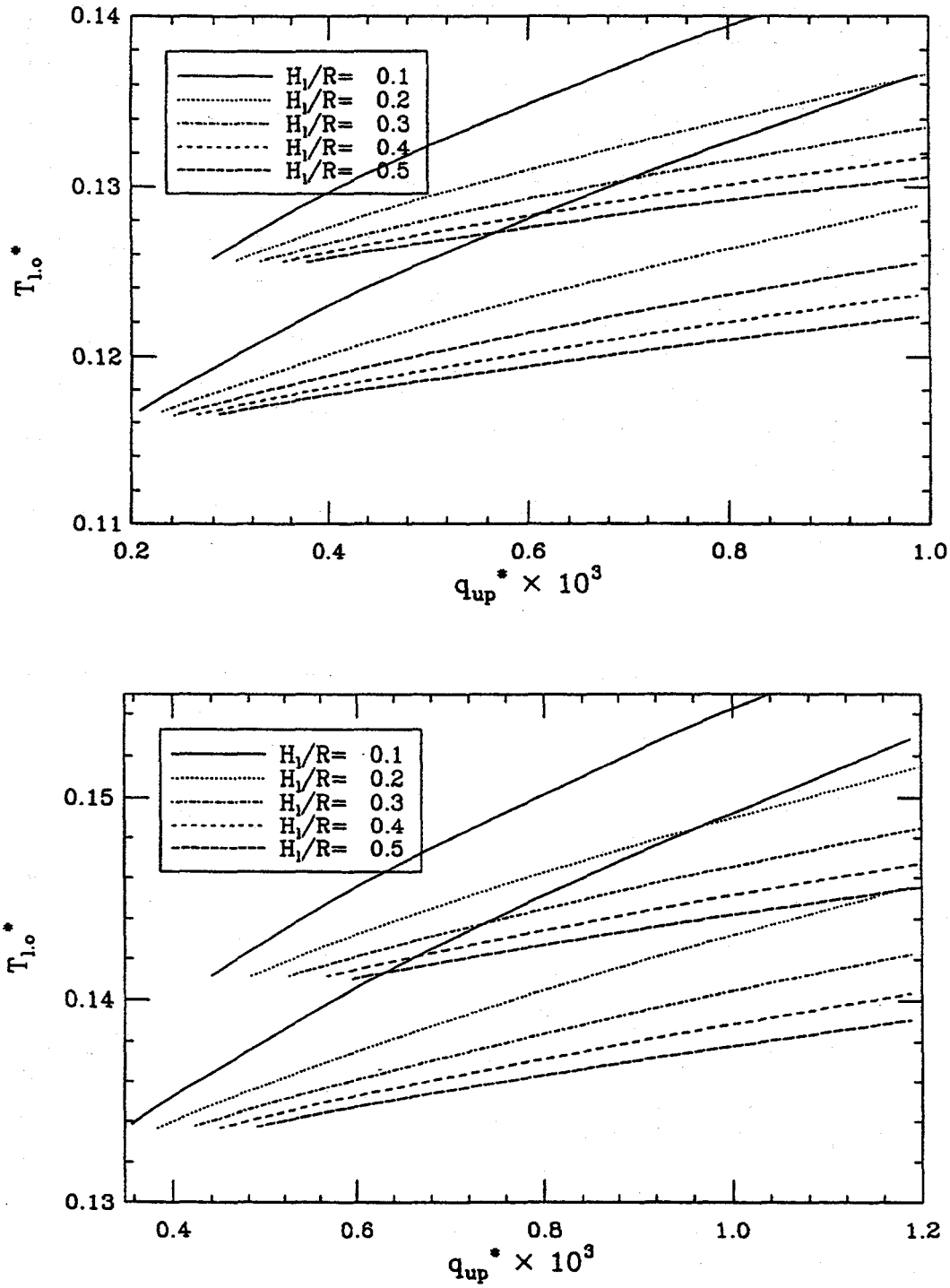

Figure 5.10. Solution to the system of Eqs. (5.51) and (5.52) for $T^*_{\ell,o}$, with H_ℓ/R and $T^*_{\ell,m}$ as the parameters. Each group of H_ℓ/R lines is for one value of $T^*_{\ell,m}$—it can be read from the position at which the lines stop. As noted in the text, the lines stop when there is freezing at the upper boundary, that is, when $T^*_{\ell,o} = T^*_{\ell,m}$. There are four such groups.

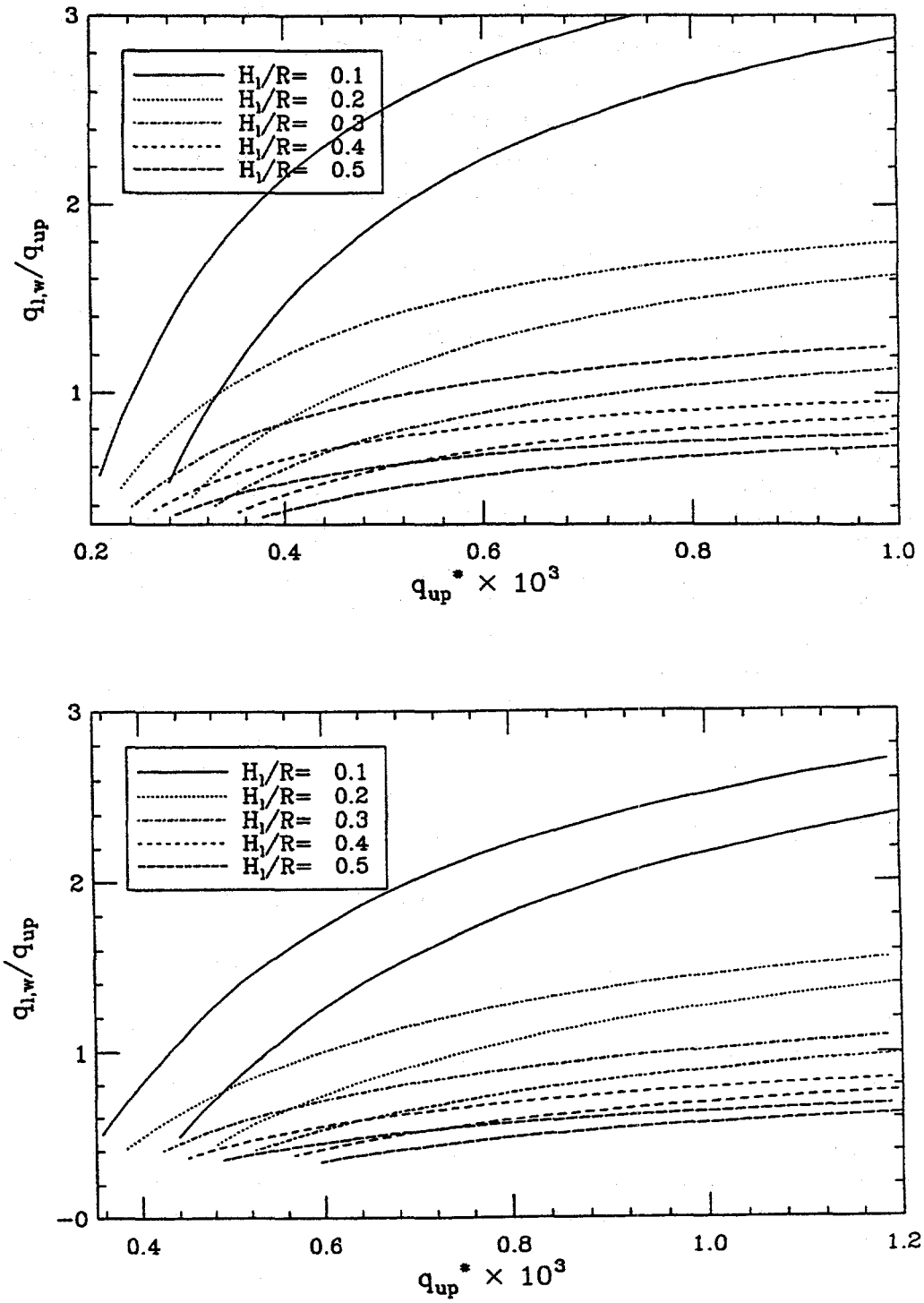

Figure 5.11. The heat flux to the sidewall, in contact with the metallic layer, obtained from the solutions in Figure 5.10 and Eq. (5.53). Again, each group of H_ℓ/R lines corresponds to one value of $T^*_{\ell,m}$. Note that the $T^*_{\ell,m}$ can be found in each case with the help of Figure 5.10 (by locating the corresponding minimum value of q^*_{up})

As an example of using these solutions, consider the following typical values of the parameters: $A = 2764$ W/m$^2 \cdot$ K$^{4/3}$, $\epsilon = 0.45$, $T_{\ell,m} = 1600$ K, $q_{up} = 600$ kW/m^2, and suppose that $H_\ell/R = 0.4$. From Eqs. (5.48) and (5.49) we obtain $\tilde{T} = 1.37 \cdot 10^4$ K, and $\tilde{q} = 9.1 \cdot 10^5$ kW/m^2, from Eq. (5.50) we obtain $T^*_{\ell,m} = 0.116$ and $q^*_{up} = 0.66 \cdot 10^{-3}$, and from Figures 5.9 and 5.10 we read $T^*_b = 0.12254$ and $T^*_{\ell,o} = 0.12078$. Then, from Eq. (5.53) we calculate $q^*_{\ell,w} = 5.58 \cdot 10^{-4}$, which finally gives $q_{\ell,w} = 508$ kW/m^2 (this can also be read directly off Figure 5.11). Moreover, from Figure 5.10 we find that freezing of the upper boundary will occur for an H_ℓ/R value of 0.3, if $q_{up} = 220$ kW/m^2 ($q^*_{up} = 0.24 \cdot 10^{-3}$); in this case the sidewall heat flux would be (from Eq. (5.54)) 85 kW/m^2, and for any larger value of H_ℓ/R the side heat flux could be obtained from

$$q_{\ell,w} = 110 \left\{ 1 + \frac{H_\ell}{R} \right\}^{-1} \text{ kW/m}^2 \qquad \text{for} \quad \frac{H_\ell}{R} > 0.3 \tag{5.55}$$

Finally, the above results can be used to determine in a rather general way the metal layer thickness below which the sidewall heat flux will exceed the peak heat flux from the oxidic pool boundary (at the uppermost end of it). Again, the above typical values of A, ϵ, and $T_{\ell,m}$ can be used, so that we have only one "free" parameter—the q_{up}. A given value of q_{up} implies a pool Rayleigh number (from Eq. 5.12), which in turn gives q_{dn} (from Eq. 5.28), and the peak flux at $\theta \sim 90°$, from Eq. (5.30). This value is then set equal to $q_{\ell,w}$ and making use of the procedure in the previous paragraph, in reverse, we can determine the corresponding value of H_ℓ/R. That is, calculate $\tilde{T}$, $T^*_{\ell,m}$, and $\tilde{q}$, use q_{up} and $q_{\ell,w}$ to get q^*_{up} and $q^*_{\ell,w}$, use Eq. (5.53) to get T^*_b, and from Figure 5.10 read (or interpolate) the H_ℓ/R value that satisfies this solution. A graphical depiction of the solution in dimensional variables, and including the just-discussed "threshold" values of H_ℓ/R (the "threshold" marks the transition from oxidic pool to melt layer heat flux dominance) is provided in Figures 5.12 and 5.13.

6. FORMULATION OF THERMAL LOADS UNDER NATURAL CONVECTION

The purpose of this section is to explain how the key transport processes discussed in the previous section are integrated into an overall computational scheme. In addition to these processes, the thermal radiation/conduction path to and through the core barrel and vessel wall to the water outside is considered explicitly. Since the model and the computer programming work are straightforward, we took a special purpose approach; that is, emphasizing simplicity of presentation through approximations quite acceptable in this application, rather than generality. Checks in the calculations, as described below, ensured that the error due to these approximations is less than a few percent and always on the conservative side.

We are given the volumes V and V_ℓ of the oxidic pool and the metallic layer respectively, their compositions, and the volumetric heat generation rate, $\dot{Q}$, and we seek to find $q_w(\theta)$ as a function of position all around the lower head. From the volumes we can calculate the heights, H and H_ℓ, and polar angles, θ_p and θ_ℓ, using:

$$V = \frac{1}{3}\pi H^2(3R - H) \quad \text{for} \quad V \leq \frac{2}{3}\pi R^3 \tag{6.1}$$

$$V + V_\ell = \frac{1}{3}\pi(H + H_\ell)^2(3R - H - H_\ell) \quad \text{for} \quad V + V_\ell \leq \frac{2}{3}\pi R^3 \tag{6.2}$$

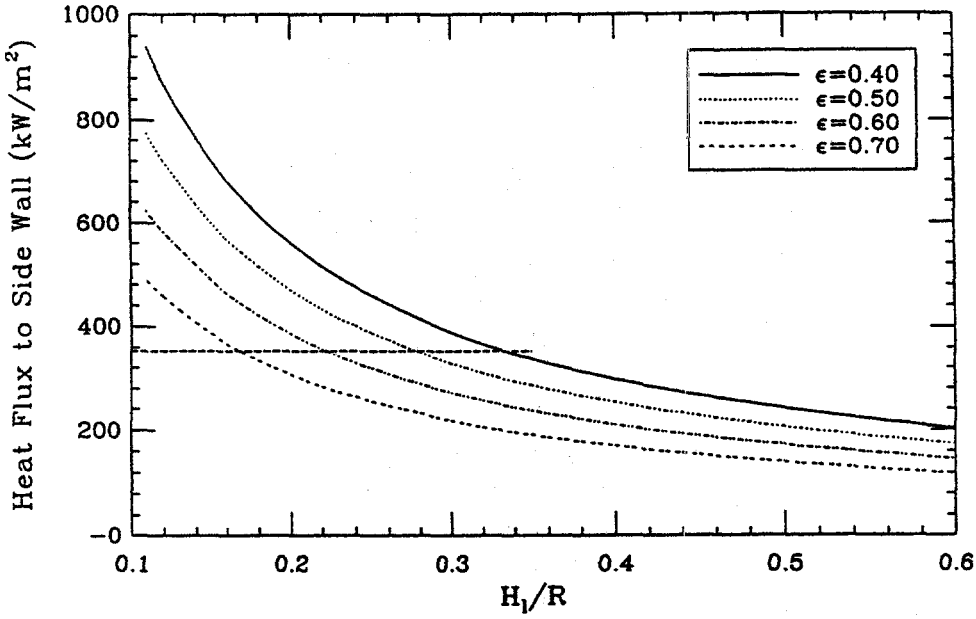

Figure 5.12. Solution to the system of Eqs. (5.51) and (5.52) in physical variables, with the emissivity as the parameter. $q_{up} = 400$ kW/m^2, and $A = 2764$ W/m$^2\cdot$ K$^{4/3}$. For the chosen value of q_{up}, the peak heat flux at the edge of the oxidic pool is 350 kW/m^2, and the intersections shown represent the threshold values of H_ℓ/R for the various emissivities.

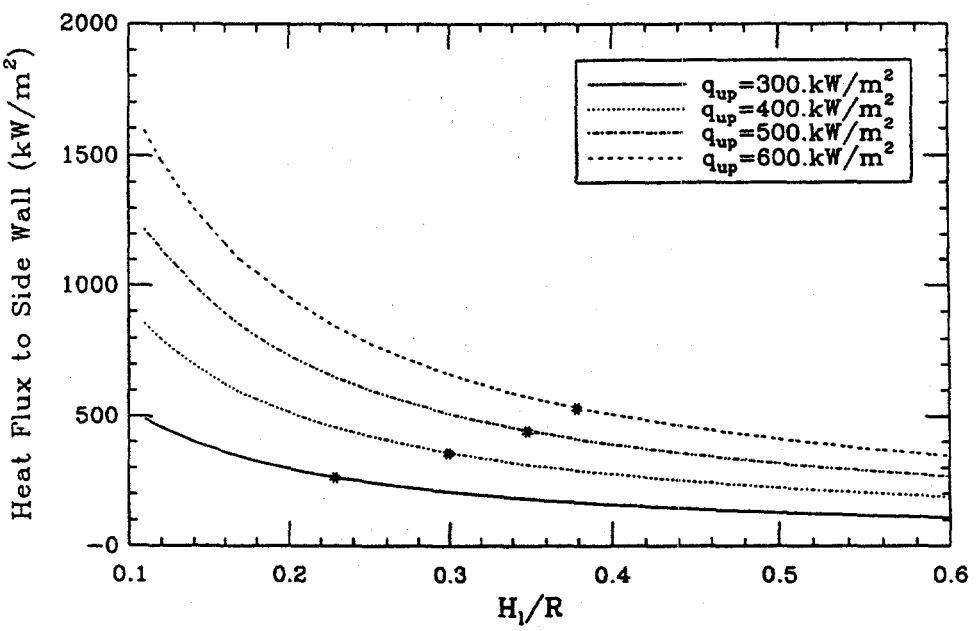

Figure 5.13. Solution to the system of Eqs. (5.51) and (5.52) in physical variables, with the imposed upward heat flux as the parameter. $\epsilon = 0.45$, $A = 2764$ W/m$^2\cdot$ K$^{4/3}$. The threshold values of H_ℓ/R, obtained as in Figure 5.12, are shown by the $*$'s.

and

$$cos\,\theta_p = \frac{R-H}{R}, \quad cos\,\theta_\ell = \frac{R-H-H_\ell}{R} \tag{6.3}$$

The above apply for volumes less than that of the hemisphere ($\frac{2}{3}\pi R^3$), which is always true for V. When this is violated for $V+V_\ell$ all that is needed is H_ℓ, which can be obtained by adding the height in the cylindrical portion of the vessel to the metal height in the hemisphere (i.e., $R-H$).Using the compositions we can obtain the thermophysical properties from Appendix L of DOE/ID-10460 and the liquidi from the phase diagrams in Figures 6.1 and 6.2. The heat generation rate is assumed to be uniformly distributed throughout the oxidic pool (including crusts). In reality, some of this decay energy will escape the pool as gammas, to be deposited in the vessel wall or the metallic layer, while some will escape the system altogether. Scoping and sensitivity calculations have indicated that such effects are quite negligible. We now proceed to solve for the pool, the metal layer, and the radiative/conduction path, in that order.

The oxidic pool maximum temperature (T_{max}) is obtained from an energy balance, which, ignoring the crusts, can be written as:

$$\dot{Q}V = q_{up}S_{up} + q_{dn}S_{dn} \tag{6.4}$$

where S_{up} and S_{dn} are the flat and curved areas respectively of the surface of the hemispherical segment.

The q_{up} and q_{dn} are obtained from:

$$q_{up} = h_{up}(T_{max} - T_m) \quad \text{and} \quad q_{dn} = h_{dn}(T_{max} - T_m) \tag{6.5}$$

with h_{up} and h_{dn} given by Eqs. (5.12) and (5.28) respectively. As we will see in the next section, the H/R is greater than 0.8, which makes the factor $(H/R)^{0.25}$ (see Eq. 5.21) greater than 0.95, indicating that it can be ignored—however, it is accounted for in parametric cases with lower H/R values. T_m is the oxidic material liquidus temperature. Once T_{max} is found the fluxes are also known from Eqs. (6.5). The q_{up} will be used (further below) as an input to the treatment of the metallic layer, while q_{dn} is now used to obtain the crust thickness, $\delta_{cr}(\theta)$, and the heat flux into the vessel wall, $q_w(\theta)$, as functions of θ.

This can be done by means of a local energy balance as:

$$q_w(\theta) \equiv q_{dn}(\theta) + \dot{Q}\delta_{cr}(\theta) = k_w \frac{T_w(\theta) - T^{**}}{\delta_w(\theta)} \tag{6.6}$$

and consideration of conduction within the crust

$$T_m - T_w(\theta) = \frac{\dot{Q}\delta_{cr}^2(\theta)}{2k_{cr}} + \frac{\delta_{cr}(\theta)}{k_{cr}} q_{dn}(\theta) \tag{6.7}$$

where T_m is the effective thermal conductivity of the wall accounting for temperature dependence, $q_{dn}(\theta)$ is obtained from q_{dn} and the shape function given by Eq. (5.30), and $T_w(\theta)$ is set equal to the wall liquidus, $T_{w,m}$, if it is found to be above it.* Thus, Eqs. (6.6) and (6.7) constitute a system

* Also, in the above, by "crust" we mean an "effective" crust that includes the so-called "mushy" zone with temperatures between the liquidus and solidus.

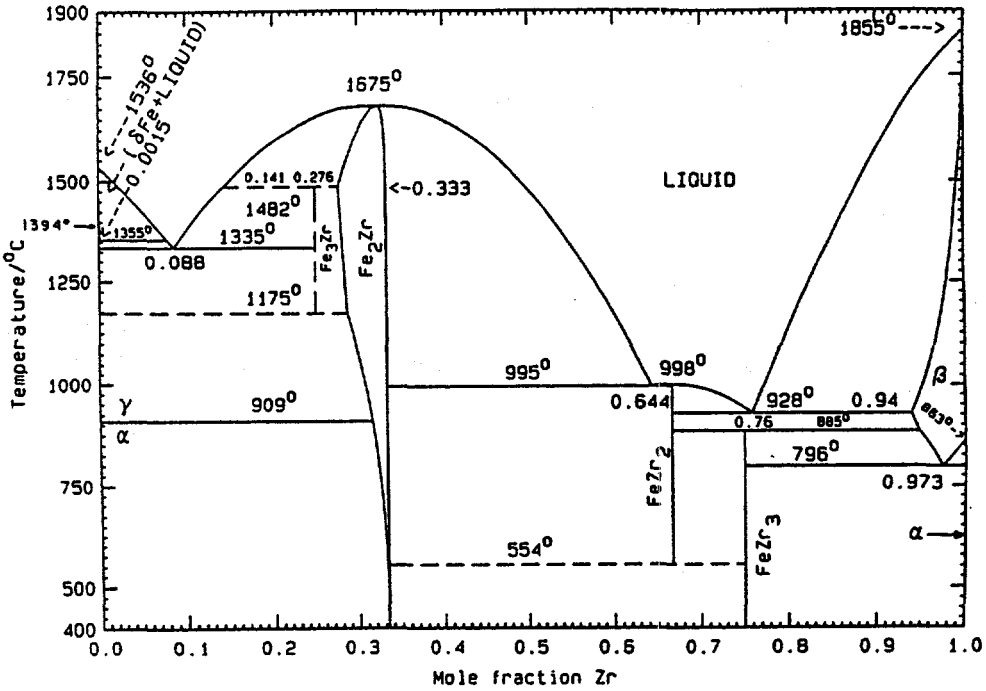

Figure 6.1. The iron-zirconium phase diagram (Pelton et al. 1994).

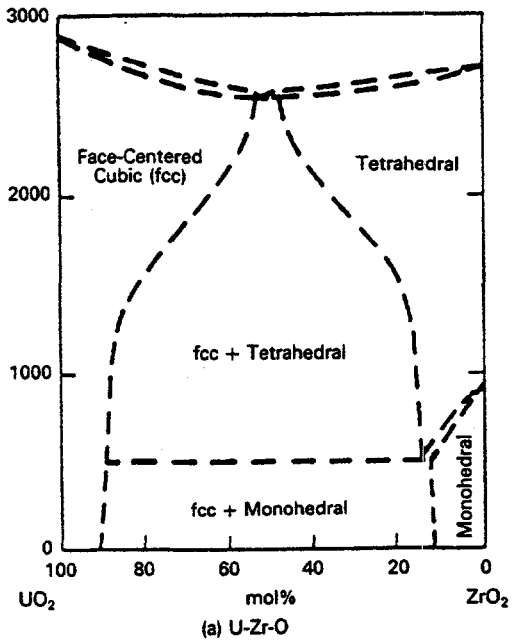

Figure 6.2. The UO_2–ZrO_2 phase diagram (Butterman and Foster, 1967).

of two equations in two unknowns, $\delta_{cr}(\theta)$ and $T_w(\theta)$ or $\delta_w(\theta)$, depending on whether there is wall melting. At the conclusion of this calculation we compute

$$\int_0^\theta \delta_{cr}(\theta')2\pi R\cos\theta d\theta \tag{6.8}$$

and have thus ensured that it is always less than a few percent of V (the oxidic pool volume) in this application.

Now, having q_{up}, the metallic layer is treated in the manner described by Eqs. (5.42) to (5.44) except for three additions: (a) accounting for the area difference between the upper and lower boundaries, (b) accounting for variations of thermophysical properties with temperature, and (c) representing the radiation/conduction path. Thus, we have:

$$cos^2\,\theta_p A_{\ell,i}(T_{\ell,i}-T_b)^{4/3} = cos^2\,\theta_\ell A_{\ell,o}(T_b-T_{\ell,o})^{4/3} + \frac{2H_\ell}{R}A_{\ell,m}(T_b-T_{\ell,m})^{4/3} \tag{6.9}$$

$$A_{\ell,o}(T_b-T_{\ell,o})^{4/3} = \sigma(T_{\ell,o}^4-T_s^4)\left\{\frac{1}{\epsilon}+\frac{1-\epsilon_s}{\epsilon_s}\frac{S_{\ell,o}}{S_s}\right\}^{-1} \tag{6.10}$$

$$q_{up} = A_{\ell,i}(T_{\ell,i}-T_b)^{4/3} \tag{6.11}$$

and

$$\sigma(T_{\ell,o}^4-T_{s,i}^4)\left\{\frac{1}{\epsilon}\frac{S_s}{S_{\ell,o}}+\frac{1-\epsilon_s}{\epsilon_s}\right\}^{-1} = k_s\frac{T_{s,i}-T_{s,o}}{\delta_s} = \epsilon\sigma(T_{s,o}^4-T_v^4) = k_w\frac{T_v-T^{**}}{\delta_o} \tag{6.12}$$

where

$$A_{\ell,j} = \mathcal{F}(\mathrm{Pr}_{\ell,j})k\left\{\frac{g\beta}{\alpha\nu}\right\}_{\ell,j}^{1/3} \qquad j = i,\ o,\ \text{or}\ m$$

the index indicating the boundary layer at whose "film" temperature the properties are to be evaluated, and the function $\mathcal{F}(\mathrm{Pr}_{\ell,j})$ indicating the Prandtl number dependence in Eqs. (5.34) and (5.35) for $j = i$ or o and $j = m$ respectively. This system of equations is solved by using T_s as an iteration parameter. That is, with a value of T_s assumed, Eqs. (6.9) to (6.11) are solved; with the $T_{\ell,o}$ thus found, $T_{s,i}$ and $T_{s,o}$ are computed from the first two equations in Eq. (6.12); with these values the third equation is checked to determine whether it is satisfied, and the procedure is repeated until this is so. Once the temperatures are known the heat flux to the sidewall, $q_{\ell,w}$, can be computed by

$$q_{\ell,w} = A_{\ell,m}(T_b-T_{\ell,m})^{4/3} \tag{6.13}$$

and the existence of an oxidic crust between the pool and the metallic layer is verified by the conditions that the quadratic

$$T_m - T_{\ell,i} = \frac{\dot{Q}\delta_{cr}^2}{2k_{cr}} + \frac{\delta_{cr}}{k_{cr}}q_{up} \tag{6.14}$$

has one positive root as long as $(T_m - T_{\ell,i}) > 0$. That this crust is thin is verified by the condition:

$$0 < \frac{\delta_{cr}\dot{Q}}{q_{up}} < 0.03 \tag{6.15}$$

Finally, at the conclusion of a computation the Rayleigh numbers are computed at the appropriate film temperature properties to ensure that the correlations have been applied within their designated ranges.

Before carrying out the detailed quantification with this model it is interesting to determine the effect of the additional effects included in the treatment of the metallic layer, in relation to the simpler model described at the end of Section 5. For this purpose, we have carried out a series of calculations, spanning relevant ranges of the parameters for this application, and plotted the results in the manner of Figures 5.12 and 5.13 (see DOE/ID-10460). The results are essentially indistinguishable for $0.4 < \epsilon < 0.5$, which constitutes the main range of interest to this study. Some difference appears for higher values of the emissivity, but it remains less than 12% even for the extreme case of $\epsilon = 0.7$, $H_\ell = 0.1$. Note that on this basis the whole problem can be reduced to a hand calculation. Specifically, once Eq. (6.4) is solved for $(T_{max} - T_m)$, the q_{up} and q_{dn} can be found via Eqs. (6.5), and then the solution for the metal layer can be simply read off Figures 5.9 through 5.11. This may be convenient for the reader, in exploring thermal loads under any specific conditions of interest. Our calculations in the next section are carried out with the full model put into a relatively straightforward computer program.

7. QUANTIFICATION AND ASSESSMENT OF THERMAL LOADS UNDER NATURAL CONVECTION

7.1 Quantification of input parameters

In this section we take on the numerical implementation of the formulation provided in Section 6. But first it is appropriate to briefly discuss some methodological aspects, and this is done with reference to Appendix A of DOE/ID-10460. We recognize that we have a deterministic model, fully supported by experiments and scaling considerations, and therefore modelling uncertainty can be considered negligible in relation to the margins inherent in the definition of this one bounding configuration. Also, we have seen that there is no scenario dependence. Thus, the model is appropriate for a Grade B assessment (as defined in Appendix A of DOE/ID-10460).

The parameters are basically deterministic, except for the decay power, the quantity of zirconium oxidized (this affects the volumes and compositions in the metallic layer and oxidic pools), and the quantity of steel in the metallic layer (this affects the depth). All three quantities are to some (minor) degree intangible and, therefore, their values and uncertainties will be considered very carefully. Our approach is to provide reasonably bounding distributions in the ROAAM sense using Table A.1 (DOE/ID-10460) as a guide. More of an intangible is the possibility of an oxidic "film" on top of the metallic layer, a film that is thick enough to make the conduction resistance overtake the improved radiation emissivity due to it. This is approached by means of a sensitivity study. Also approached by sensitivity studies is the use of Mayinger's correlation instead of Eq. (5.28), and of the UCLA flux shape correlation instead of Eq. (5.30). Finally, we have uncertainties on thermophysical properties, as described in Appendix L of DOE/ID-10460; they are of minor significance, but included anyway by means of Gaussian distributions with two standard deviations at the uncertainty intervals quoted in Appendix L of DOE/ID-10460. These parameters, their mean values, and their 2σ values, are summarized in Table 7.1. In this table is included also the emissivity value used for the steel layer, as measured in the laboratory (see Appendix I of DOE/ID-10460).

While any small amount of oxides and/or impurities would tend to produce higher values, such effects are difficult to judge, and the conservatively bounding value for a perfectly clear surface is preferred for these calculations. The emissivity of the "sink" surface (upper reactor inner boundaries), ϵ_s, is taken as 0.8, as is appropriate for high temperature (oxidized) solid stainless steel. Because of the very large areas involved, the effect of any reasonable variation in this parameter is negligible.

Table 7.1. Property Values and Uncertainty Intervals Used in the Computations

Property	Oxide Phase	Metallic Phase
Melting Point (K)	2973	1600
Density (kg/m^3)	Volume Averaged $\rho_{UO_2} = 8740$ $\rho_{ZrO_2} = 5990$	Volume Averaged $\rho_{Fe} = 7020$ $\rho_{Zr} = 6130$
Thermal Conductivity (W/k·m)	5.3 ± 1.6 ($\pm 30\%$)	25 ± 6.3 ($\pm 25\%$)
Viscosity (Pa·s) $\times 10^{-3}$	$\frac{5.3}{33.4}\ exp\left(\frac{10430}{T}\right) \pm 2.5$	$\frac{4.1}{37.0}\ exp\left(\frac{5776}{T}\right) \pm 1.1$
Specific Heat (J/kg·K)	Mass Averaged $c_{p,UO_2} = 485$ $c_{p,ZrO_2} = 815$	Mass Averaged $c_{p,Fe} = 835$ $c_{p,Zr} = 458$
Volume Thermal Expansion Coefficient (1/K) $\times 10^{-4}$	1.05 ± 0.12 ($\pm 11\%$)	1.1 ± 0.18 ($\pm 16\%$)
Effective Thermal Conductivity (W/k·m)	2.8 ± 0.4 ($\pm 14\%$) Crust	32.0 Vessel Wall

The decrease of the radioactive decay power with time is shown in Figure 7.1. From this we have to subtract the volatile component; however, this cannot be done as a constant fraction because the volatiles are decaying faster. Thus, in Figure 7.2 we show how the volatile component fraction changes with time (Schnitzler, 1981), and in combination with Figure 7.1, we obtain the decay power for the non-volatile components as a function of time (also shown in this figure). We now proceed to quantify the fraction of the zirconium oxidized and, with this plus all the above information, to arrive at probability distributions that characterize the volumes (and heights) of the oxidic pool and metallic layer, and the volumetric heat generation rate. The various materials inventories within the reactor vessel are listed in Table 7.2.

Available information on zirconium oxidation in a severe accident includes: the TMI-II accident, a large number of out-of-pile experiments such as those in the CORA facility in KfK, and a large number of special purpose models and code calculations. All this evidence points strongly to a heavy zirconium oxidation, and this is easy to see especially because of the open core geometry in a PWR. Thus, we assign a most likely expected value, for the fraction oxidized, in the range 40 to 60%, one unlikely range (the 10^{-1} level) in the 10% interval immediately above this range, and one highly unlikely (10^{-2}) in the 20% interval beyond. Higher values may be appropriate with recovery, but our interest here, obviously, is for unrecovered cases. (Also, higher values would

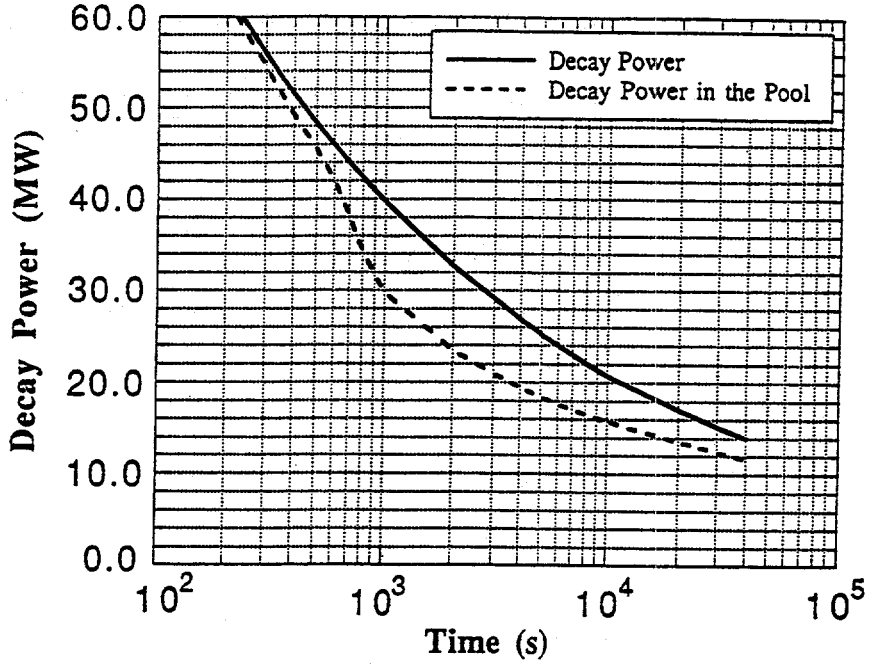

Figure 7.1. The decay power as a function of time after shutdown (AP600, 1994). The "in pool" curve accounts for loss of volatiles, their contribution being as in Figure 7.2. The rated power of the AP600 is 1933 Mw.

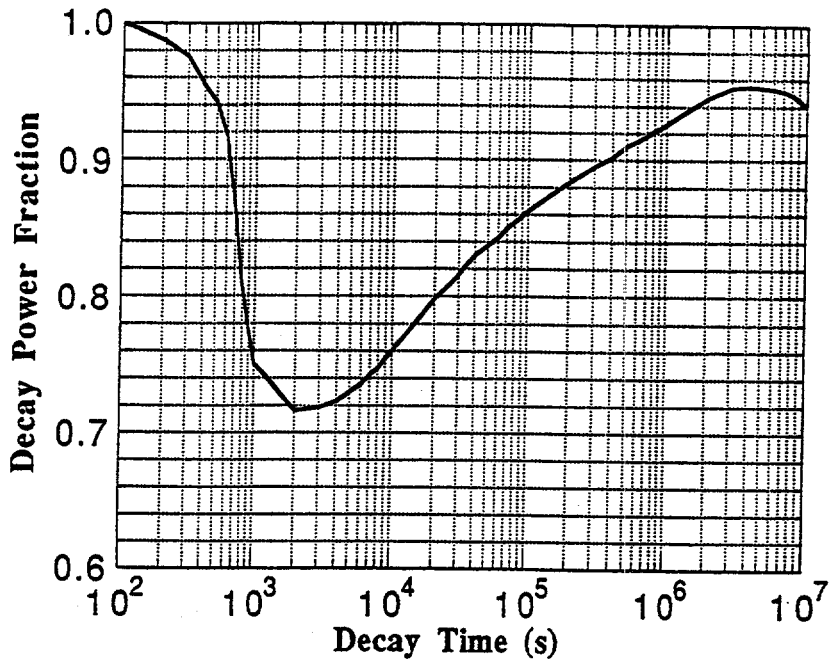

Figure 7.2. Fraction of total decay power remaining in pool, accounting for volatile fission product release as a function of time after shutdown.

Table 7.2. Material Inventories in the Reactor Vessel

Component	Material	Mass (kg) $\times 10^{-3}$	Volume[1] (m^3)
Fuel	UO_2	75.9	8.68
Core Cladding	Zircalloy	15.8	2.58
Peripheral Cladding[2]	Zircalloy	3.4	0.56
Control Rods	Silver/Indium/Cadmium	2.9	0.43
Lower Internals Package (LIP) — Estimated			
Core Barrel	Stainless	40	5.70
Lower Support Plate[†]	Stainless	25	3.56
Lower Supports	Stainless	2	0.29
Reflector	Stainless	40	5.70
Upper Internals Package (UIP) — Estimated			
Upper Support Plate	Stainless	23	3.38
Support Columns	Stainless	4	0.57
Rod Guides	Stainless	8	1.14
Lower Guide Tubes	Stainless	8	1.14
Upper Core Plate	Stainless	3.5	0.5

[1] In liquid state

[2] Mostly at the core entrance, as 7.5 cm-long pellets, at the lower end of the fuel rods

[3] Including inlet nozzles

reduce the decay power density, and hence the thermal loads.) This quantification is shown in Figure 7.3 in the form of a probability density function.

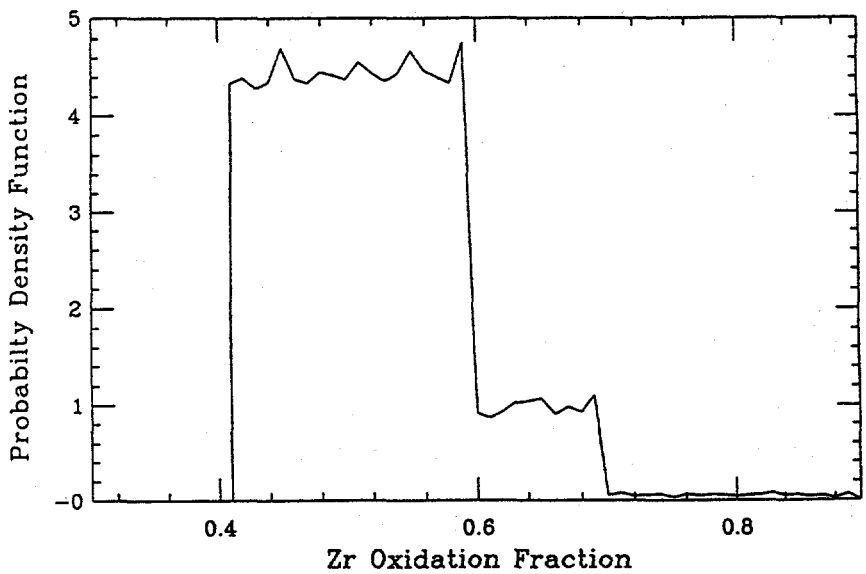

Figure 7.3. Specification of the fraction of zirconium oxidized, as a probability density function.

Using these fractions and the total quantity of zirconium present we can obtain the quantities of ZrO_2 to be mixed with UO_2 in the oxidic pool, and the quantity of Zr metal to be mixed with steel in the metallic layer. For the UO_2 we use the whole inventory which leads directly to the probability distribution of the oxidic pool height, shown in Figure 7.4. Since the radius of the vessel is 2 m, these heights correspond to polar angles in the range $75° < \theta < 81°$; that is, a nearly full hemisphere, as mentioned already.

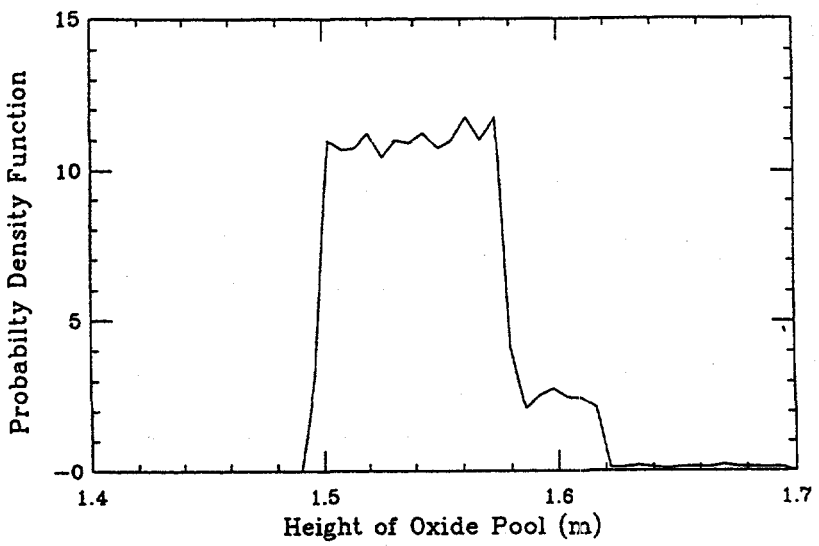

Figure 7.4. The oxide pool height probability distribution resulting from a UO_2 volume of 8.68 m^3, a hemisphere radius of 2 m, and the specification of Figure 7.3.

For the metallic layer, we note that the lower (or core) support plate is positioned at a height of 1.5 m (its bottom face), and according to the above, it would be in contact with the oxidic pool. This implies that the metallic layer cannot form until this plate (25 tons) melts in, which would also release any remaining (not yet melted) portions of the reflector (40 tons), and the lowest portions of the core barrel (a total of 40 tons). The metallic layer should also have to include all the lower internal structures (2 tons). Thus, the only intangible aspect is the extent of involvement of the upper internal structures, and the probability assignments are made as follows: a likely range ($\sim 10°$) for 67 to 72 tons (to include 1 m of core barrel), an unlikely range ($\sim 10^{-1}$) for 72 to 77 tons (to include 2 m of core barrel), and a very unlikely range ($\sim 10^{-2}$) for 77 to 87 tons (to include a small portion of the upper internals). The probability density function corresponding to this specification is shown in Figure 7.5. With these values added to the amounts of unoxidized zirconium, we can obtain the probability distribution of the metallic volume, and hence the layer height, as shown in Figure 7.6. Note that in constructing this figure we had to combine also Figure 7.4, to account for the actual position of the layer's lower boundary.

Finally, for the volumetric heat generation rate, besides the volume of the oxidic pool (Figure 7.4), we must consider the timing for the formation of the configuration under investigation. We wish to do so in a manner that is generally conservative (i.e., minimizing this timing), and not relying on detailed aspects of code calculations (to maintain the Grade B rating). Rather, we proceed from a general perspective of severe accident initiators, as provided by the level 1 PRA for AP600, to a selection of bounding, from the point of view of timing, scenarios of interest here, and finally to an understanding of what controls this timing. All non-negligible contributors to severe core

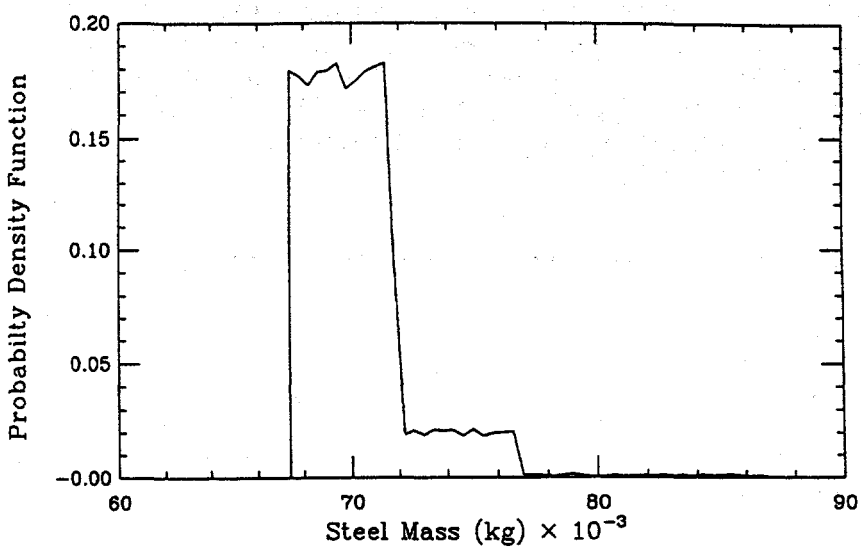

Figure 7.5. Specification of the steel mass in the metallic layer, as a probability density function.

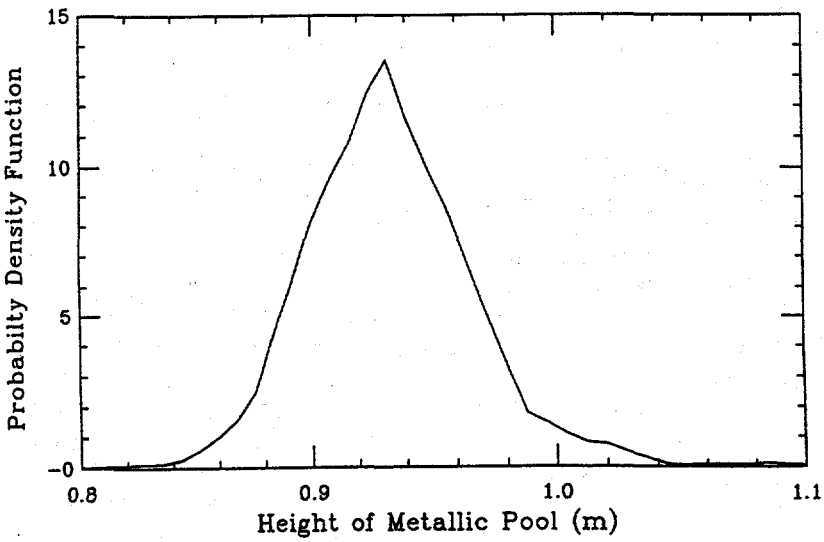

Figure 7.6. The metallic layer height probability distribution resulting from the specifications in Figures 7.3 and 7.5.

damage, found in the AP600 PRA (submitted to the NRC) are listed in Table 7.3. This table also lists the time for the first relocation event into the lower head (as calculated with the MAAP code) and includes comments on each case relevant to the present usage. The term "Not Relevant to IVR" was applied to cases 1AC, 1APC, 3BRC and 3C on the following basis:

- Case 3BRC. This variant of a large break LOCA accident leads to recovery and arrest prior to any debris relocation.

Table 7.3 Accidents Contributing to Core Damage Frequency (CDF) of the AP600 as Developed in the Level 2 PRA with Update Level 1 Quantification (AP600, 1995)

Case I.D.	% of CDF[1]	Timing of First Debris Relocation (hr)	Accident Description and Comments
1AC	1.9	~5.5 hr	• Core damage following transient or small LOCA[2] at high pressure; manual ADS[3] failure. • Some relevance to IVR[4] if hot leg nozzle ruptures and depressurizes system.
1APC	0.4	~10.5 hr	• Like 1AC, except PRHR operating. • Some relevance to IVR; less decay heat than 3BE; partially pressurized (<5 a.).
3BE	50	~4+ hr	• Core damage following large LOCA or other event with full depressurization (injection failure); may reflood through break as cavity floods. • Of main interest to IVR.
3BRC	~29	N/A	• Core damage following LOCA with early accumulator and CMT[5] failures or any other sequences where manual depressurization leads to reflood from IRWST[6] and recovery in-vessel. • Typically, not relevant to IVR
3C	4.1	N/A	• Vessel rupture. • Not relevant to IVR.
3DC	13	~22+ hr	• Non-large LOCA with partial depressurization. • Of interest to IVR, but less decay heat than 3BE.
6E	2.3	~22+ hr	• Core damage after steam generator tube rupture. • Of interest to IVR, but less decay heat than 3BE
3BE.cc0	N/A	~3 hr	• Sensitivity case for 3BE without cavity flooding. • Bounds IVR timing uncertainty

[1] CDF = Core Damage Frequency
[2] LOCA = Loss of Coolant Accident
[3] ADS = Automatic Depressurization System
[4] IVR = In-Vessel Retention
[5] CMT = Core Makeup Tank
[6] IRWST = In-Containment Refueling Water Storage Tank

- Case 3C. This is clearly outside the scope of IVR, and subject to meeting a screening frequency criterion.
- Cases 1AC and 1APC. Such high pressure accidents are expected to fail the hot leg nozzle and depressurize in any case. For the passive AP600 it is expected that failure to depressurize will meet the screening frequency criteria, such as to be negligible. It is inherent in these accidents to proceed at a slower rate (due to lower rate of coolant loss) as compared to large LOCAs—see Table 7.3—thus a depressurization too late to recover the accident still can be covered, conservatively, under case 3DC. (As one can see in Figure 7.1, the decay power at 10 hrs is only 80% of that at 4 hrs.)

The term "of Some Interest to IVR" was applied to cases 3DC and 6E in recognition that even though small contributors to CDF, these cases could be readily accommodateable in the IVR. The long term evolution is inherent of coolant availability and passive cooling design feature in these accidents; at 22 hrs the decay heat is only 67% of that at 4 hrs, and the so-reduced thermal loads are expected to accommodate structurally at least part (if not all) of such higher pressure scenarios—with a fourth stage ADS failure the pressure would be under 100 psi— (see Appendix G of DOE/ID-10460). Finally, and in light of the above, we are left primarily with case 3BE, which therefore has been termed "of Main Interest to IVR." It is the simplest, and fastest, scenario, thus it is of good bounding quality for timing the decay power. Both the core makeup tanks and the accumulator will passively inject to quench the core down to ~400 K and leave the primary system essentially full of water. A severe accident from this condition requires failure of the gravity-driven injection system, depletion of the in-vessel coolant inventory, and core heatup. Material relocation to the lower head in addition requires core melting with significant melt accumulation to cause side failure(s) through the reflector (minimum thickness 13 cm) and core barrel (minimum thickness 5 cm). A rough assessment of the timing of all these phenomena indicates (see Appendix O of DOE/ID-10460) that the relevant time frame final, steady, IVR case examined here would be 4+ hours, and this is in agreement with a more thorough, recent evaluation in DOE/ID-10541. Thus, we assign the main probability interval (~10°) between 4 and 5 hours, an unlikely range (~ 10^{-1}) between 5 and 6 hours, and a very unlikely range (10^{-2}) between 6 and 7 hours. As a perspective on the insensitive nature of this quantification, note, from Figure 7.1, that from 3 to 5 hours' shutdown time the decay power changes from 15 to 14 MW, that is, by less than 7%. The resulting probability density function from the above specification of the shutdown time is shown in Figure 7.7. The probability density function for the decay power density is then obtained by combining Figures 7.1, 7.3 and 7.7. The result is shown in Figure 7.8.

Note that the primary quantification carried out above is contained in Figures 7.3, 7.5, and 7.7, and they are independent of each other, as will be explained in the next paragraph. The quantities H, H_ℓ, and $\dot{Q}$ (Figures 7.4, 7.6, and 7.8) were derived using a Monte Carlo sampling program from these primary quantifications. These are **not** independent of each other, thus they are not convenient as inputs to the main calculation; rather, they were derived to provide some transparency of the quantification since any values from these figures can be used to directly read off the answers (heat fluxes) as described already in Section 5. In carrying out the calculations with the model we use the primary quantifications as above, but each sample is carried through the model to calculations of the heat flux distribution at the outer boundary of the lower head. Thus, the result is the probability distributions of the thermal loads at all angular positions in contact with the oxidic pool and the steel layer. As noted already, the distributions of property values are also sampled simultaneously.

Before displaying the results of these calculations, let us address the question of independence between quantities shown in Figures 7.3, 7.5 and 7.7. They are independent because each quantity is governed by completely different aspects of the melt progression sequence. Starting with the timing τ, the primary consideration is in the early portion of the sequences (as discussed above),

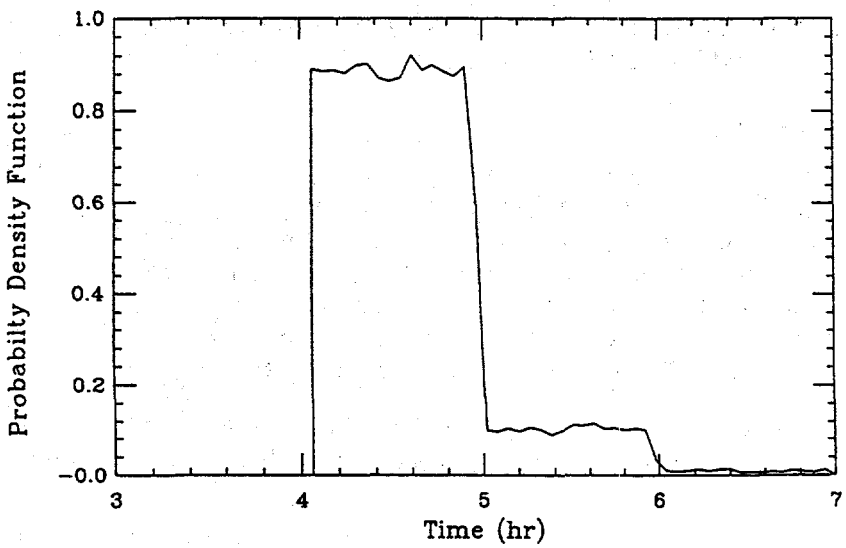

Figure 7.7. Specification of the shutdown time (for use in estimating decay power), as probability density function.

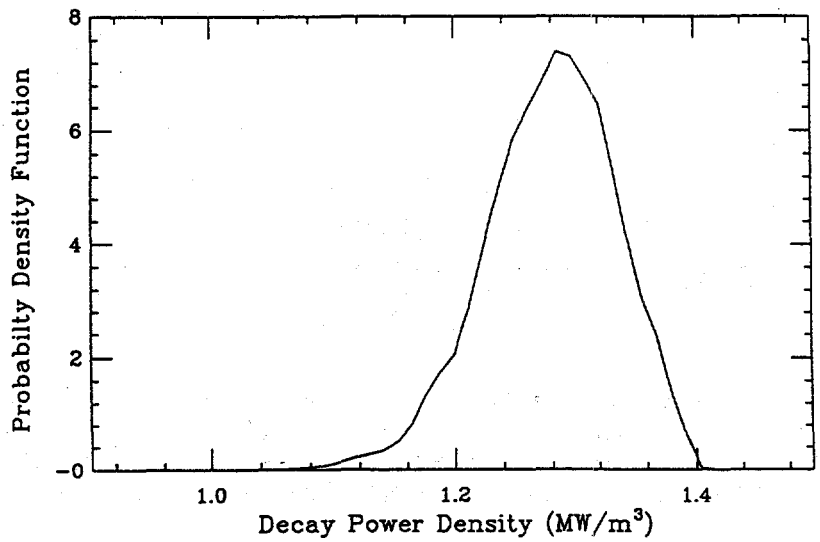

Figure 7.8. The decay power density probability distribution resulting from combination of Figures 7.1, 7.3, and 7.7.

prior to core uncovery, and the starting of degradation, which draws heavily on the likelihoods of various accidents leading to core melt, and thermal-hydraulic assessments (and systems codes) that operate in relatively "well-charted' space. The zirconium oxidation is related primarily to the early portion of severe accident sequences—during core uncovery—and it is clearly quite independent

of τ. Finally, the quantities of upper internals melted, **at low pressure** as in the case here would be rather limited, depending primarily on the phenomenology of the late phases of the core melt scenario, timing of core relocation, and heat transfer processes (radiation/conduction, primarily) between the upper core and the upper internal structures.

7.2. The main results

The results of the calculations are summarized in Figures 7.9 and 7.10. The detailed results are given in Appendix Q of DOE/ID-10460. Figure 7.9 shows the cumulative probability distributions of the heat fluxes at various angular positions around the lower head, while in Figure 7.10, the same results are presented as probability density functions of the heat fluxes at selected positions, divided by the corresponding critical heat flux value at the same position. This second manner of presentation makes the margins to failure immediately evident, and it is interesting to note that contrary to widely held opinion these margins are greatest at the lower positions ($\theta \sim 0°$) of the lower head. However, even at the high positions the margins-to-failure are sufficiently comfortable to lead to the conclusion that failure is "physically unreasonable." This conclusion is further buttressed by the numerous sensitivity and parametric calculations presented immediately below.

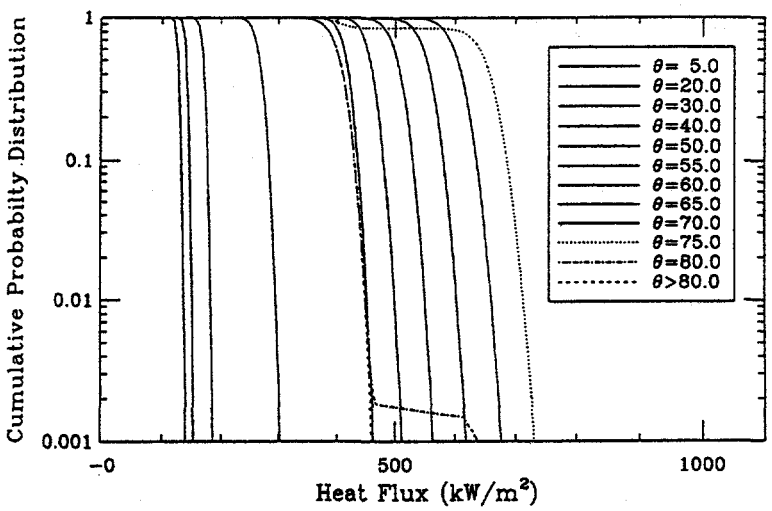

Figure 7.9. Probability distributions of the heat fluxes at various angular positions around the lower head. Over the region of the oxidic pool, fluxes increase monotonically with angle (all solid lines). The lines corresponding to the metallic layer are identified separately. The stepwise behavior at positions $\theta = 75°$ and $80°$ arises because of "sharing" the oxidic pool and metallic layer contact.

7.3. Sensitivity and parametric studies

One group of sensitivity and two groups of parametric studies have been performed to make apparent:

(a) The effect of shifts in the input distributions, namely:

- Fraction of Zr oxidized: Shift the distribution of Figure 7.3 to the right by 0.1
- Time: Shift the distribution in Figure 7.7 to the left by 1 hr.

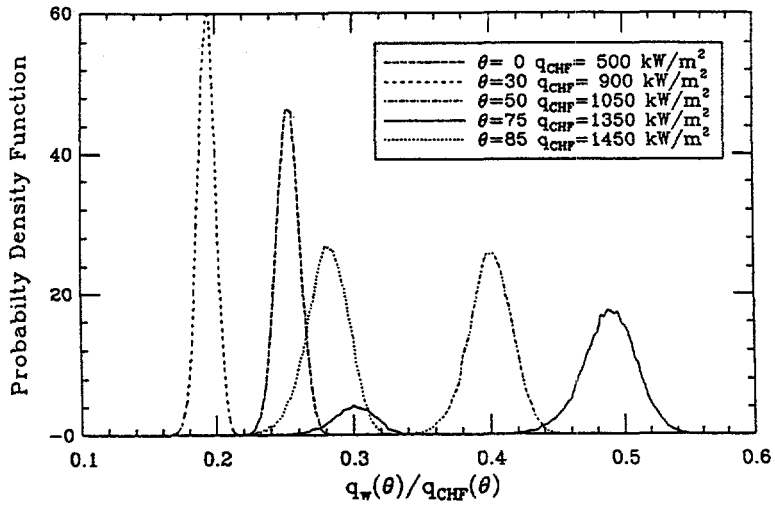

Figure 7.10. Probability distribution of the heat fluxes normalized by the local critical heat fluxes, for selected positions around the lower head. The position $\theta = 85°$ corresponds to the metallic layer. The double-hump behavior at position $\theta = 75°$, arises because of "sharing" the oxidic pool and metallic layer contact.

(b) The effect of using different correlations for:

- Downward heat transfer: Eq. (5.12) instead of Eq. (5.28)
- Flux shape: Eqs. (5.24) and (5.25) instead of Eq. (5.30).

both done in conjunction with assuming a 1 cm-thick oxide crust on top of the metal layer, or an adiabatic upper boundary.

(c) The extreme specification necessary to approach failure:

- Assuming that the lower support plate is intact,

Each group is presented and discussed, in turn, in the following.

The distribution shifts are straightforward, and the results are displayed in Figures 7.11 and 7.12. We see no significant effect on the margins understood from the base case results. Note that the double-hump is not present in Figure 7.11 because, with the oxide volume increase (due to added ZrO_2), the metal layer shifted higher, while the slight shift to higher q/q_{CHF} values is due to the correspondingly thinner metallic layer. As additional sensitivity on the base case, we also considered the effect of dividing the coefficient in the Globe–Dropkin correlation by a factor of 2, and of reducing the wall melt temperature by 100 K (i.e., 1500 K instead of 1600 K). The effect of both of these variations was slight.

The calculations using the various correlation options were carried out with $H = 1.6$ m, $H_\ell = 0.8$ m, and $\dot{Q} = 1.4$ MW/m^3. The results are displayed in Figures 7.13 through 7.15. In Figure 7.13 we see that even with an adiabatic upper boundary the metallic layer is quite sufficient to dissipate the heat load over its side boundary, still leaving significant margins to failure. In Figure 7.14 we see that use of the UCLA flux shape produces a 20% more peaking at $\theta \sim 80°$, but still a significant margin to failure remains. Finally, in Figure 7.15 we see that the use of Mayinger's

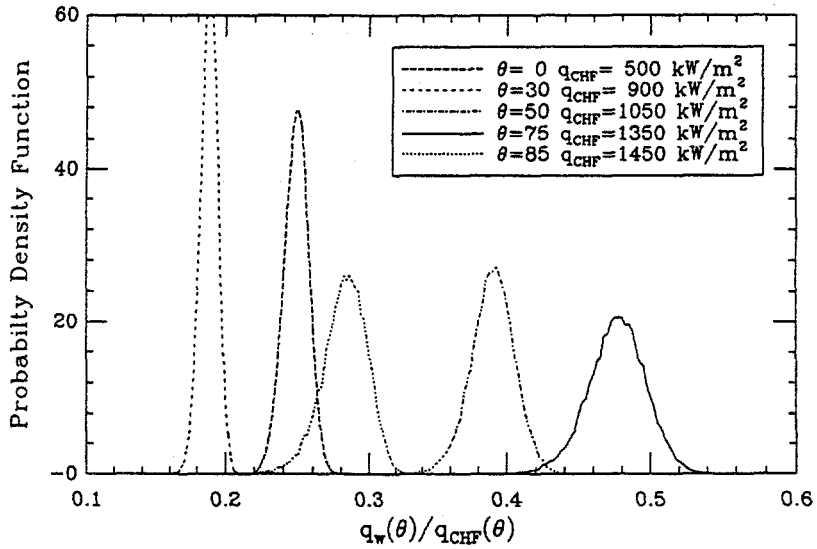

Figure 7.11 The results of a sensitivity study, specified by shifting the distribution for the zirconium fraction oxidized to higher values by 10%. All other inputs as in base case.

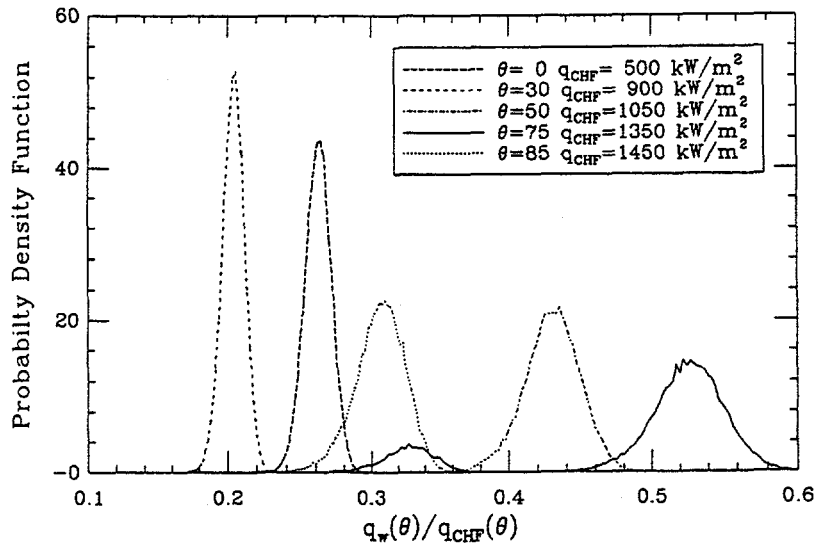

Figure 7.12. The results of a sensitivity study, specified by shifting the distribution of the shutdown time to lower values by 1 hr. All other inputs as in base case.

correlation biases the flux upward over the steel layer portion of the boundary by ~15% only. This rather low sensitivity was predicted already in Section 5.

From all the above we can conclude that there is no way to cause failure over the oxidic pool boundary. Thus, as we are left to seek "the limits to failure," in an arbitrary parametric study using the "focusing" mechanism due to the steel layer, described in Section 5. For this to occur, the top of the metal layer must be below the lower support plate. The metallic layer will then consist of only the lower support structures and the molten metals that relocated together with the fuel. To

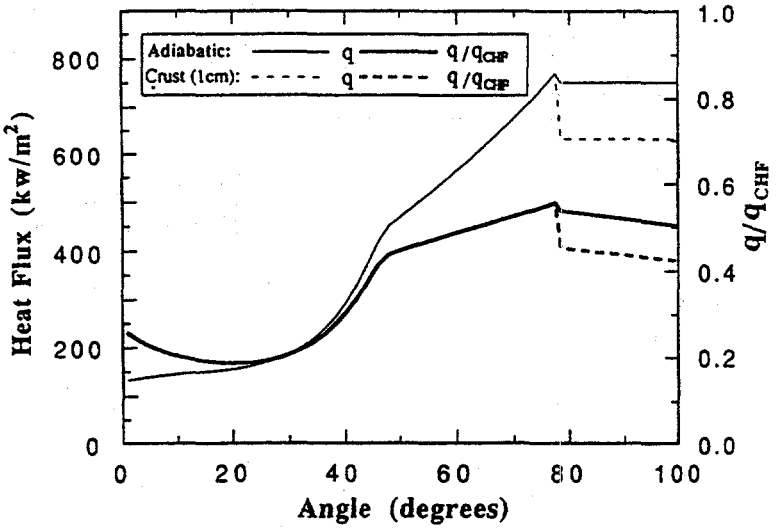

Figure 7.13. Results of a parametric study using an "adiabatic" boundary or a 1-cm-thick oxidic crust on top of the metallic layer. Values for H, H_ℓ, and $\dot{Q}$ were fixed at 1.6 m, 0.8 m, and 1.4 MW/m^3, respectively.

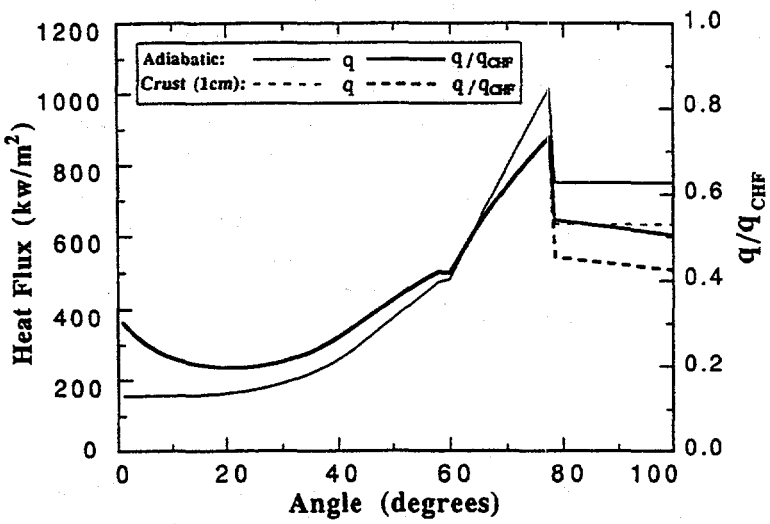

Figure 7.14. Results of a parametric study specified as in Figure 7.13 but using the UCLA flux shape (Eq. 5.24) in place of Eq. (5.30).

create a significant thermal load this fuel must be in excess of 70% of the core, which implies a rather extensive melt attack on the reflector and the core barrel. (Note that failure of both of these boundaries (see Figure 2.2) is required for the relocation of molten core materials to the lower plenum.) The reflector will supply ~10 tons of steel per axial meter melted, and the core barrel similarly ~5 tons per meter. One axial meter corresponds to 25% of the core height, and it can be considered (together with the 2 tons from the lower support structures) as a reasonable lower bound

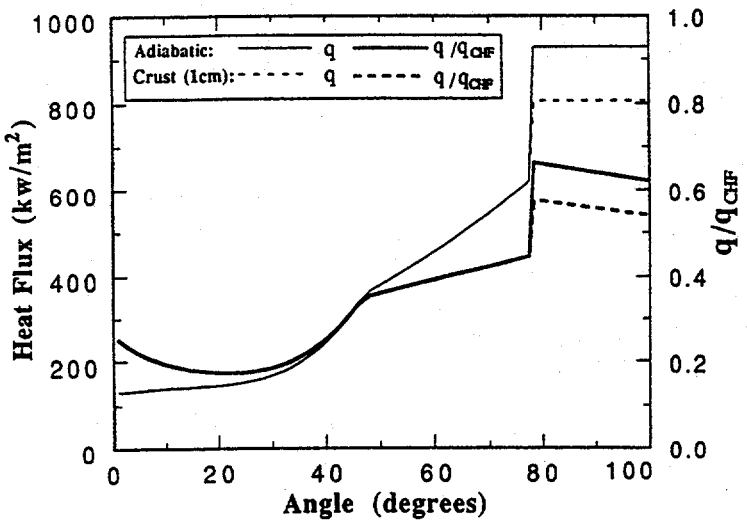

Figure 7.15. Results of a parametric study specified as in Figure 7.13 but using the Mayinger et al. (1975) correlation (Eq. 5.22) in place of Eq. (5.28).

of the metallics available to form a layer on top of the oxidic pool. That is, a total of 17 tons, which if made to just touch the bottom face of the lower support plate (1.4 m from the bottom of the lower plenum) would produce a depth of 22 cm, and would allow a maximum oxidic pool depth of 1.18 m. (Note that these are conservative limits in that no account was taken of the metallic zirconium that participated in the relocation, nor of the thermal expansion and creep in the core barrel—see also Appendix O of DOE/ID-10460.) Using these depths together with the upper bound in the decay power, which from Figure 7.8 is seen to be 1.4 MW/m^3, we obtain the results shown in Figure 7.16. Marginal failure is indicated; however, it is doubtful that even this extreme specification could in reality produce failure. This is because in addition to ignoring zirconium in the metal layer and elongation (and possible failure) of the core barrel, as just mentioned, this calculation has ignored 2-D effects due to (a) eddy diffusion in the bulk of the metal layer, and (b) conduction in the vessel wall. In addition, the effect of the highly localized thermal loads on the critical heat flux, also expected to be mitigative, has been ignored.

7.4. Discussion

As stated in Section 6, all these calculations were checked to verify that the conditions expressed by Eqs. (6.8) and (6.15) are satisfied. In addition, to check the applicability of the heat transfer correlations we computed the Ra and Ra′ numbers in the metal layer and oxidic pool respectively. The results from the base case calculation, shown in Figure 7.17 and 7.18, respectively, indicate that for the AP600 the relevant ranges are

$$5 \cdot 10^9 < \mathrm{Ra} < 2 \cdot 10^{10} \qquad 10^{15} < \mathrm{Ra}' < 6 \cdot 10^{15}$$

These also encompass the cases considered in the sensitivity and parametric studies:

$$\mathrm{Ra} = 1.1 \cdot 10^{10} \qquad \mathrm{Ra}' = 4 \cdot 10^{15}, \qquad \mathrm{Ra} = 2 \cdot 10^{8} \qquad \mathrm{Ra}' = 10^{15}$$

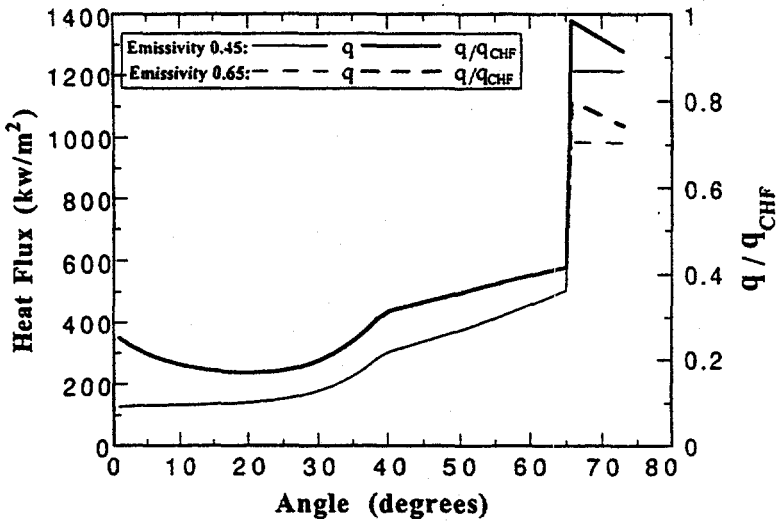

Figure 7.16. Results of an extreme parametric study carried out to "test the failure boundaries." $H = 1.18$ m, $H_\ell = 0.22$ m, and $\dot{Q} = 1.4$ MW/m^3. **See text for explanation.**

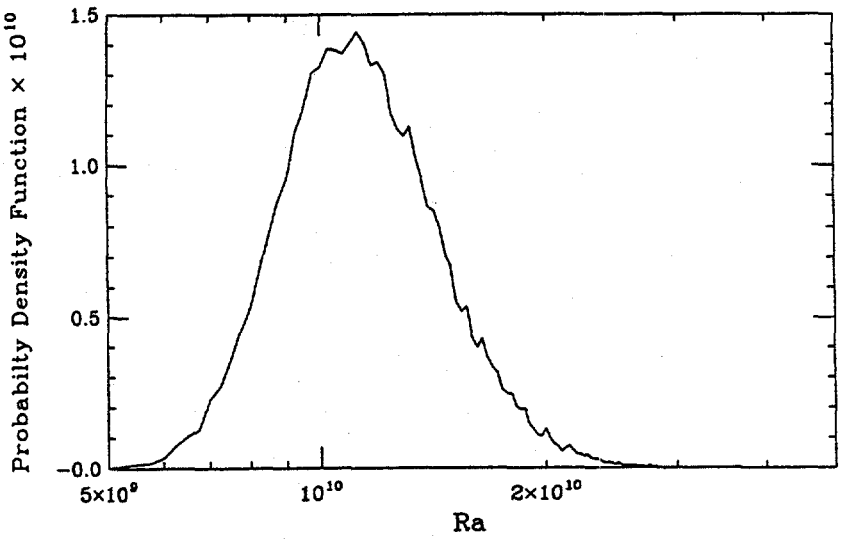

Figure 7.17. The Ra number distribution found in the calculations of the base case.

and are to be compared to the experimental ranges, which for convenience are repeated here again:

Globe–Dropkin:	$3 \cdot 10^5 < \mathrm{Ra} < 7 \cdot 10^9$
Chu–Churchill:	$\mathrm{Ra} < 10^{12}$
Present (mini-ACOPO):	$10^{12} < \mathrm{Ra}' < 7 \cdot 10^{14}$

We can see that in all three cases we are essentially where we need to be. There is a less than one order of magnitude extrapolation of the Globe–Dropkin correlation which besides being modest, it pertains to the thickest range of metal layers, which is uninteresting from a thermal loads point of view. On

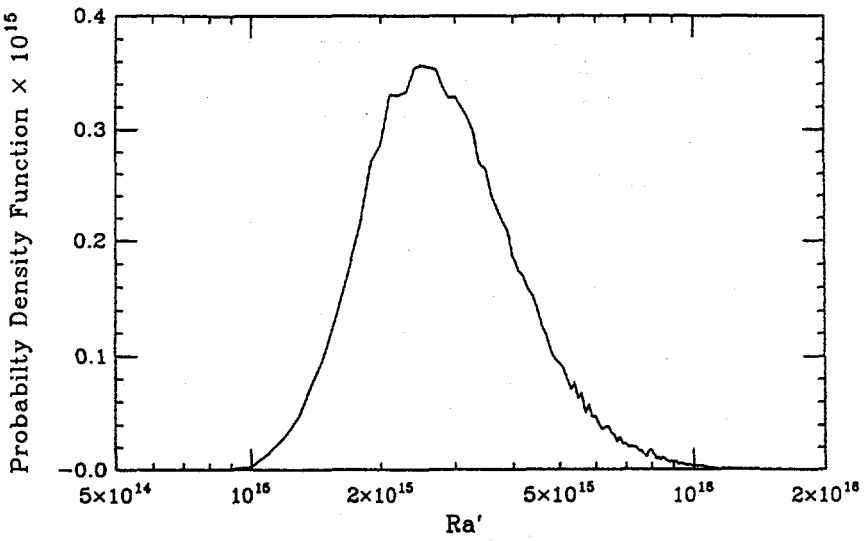

Figure 7.18. The Ra′ number distribution found in the calculations of the base case.

the simulation of the oxidic pools the mini-ACOPO revealed no significant surprises, and hence the extrapolation by about one order of magnitude can be considered modest also. This conclusion was confirmed by the recently-conducted main ACOPO tests, which reached $Ra' = 2 \cdot 10^{16}$ (see Appendix V-2 of DOE/ID-10460).

Additional information on the AP600 thermal insulation design, undertaken in conjunction with the present effort, on an updated design of the cavity flooding system and its reliability, and on vessel material RTNDT specifications, can be found in DOE/ID-10460.

8. QUANTIFICATION AND ASSESSMENT OF THERMAL LOADS UNDER JET IMPINGEMENT

In this section we examine the potential extent of local thermal attack on the lower head during the initial core relocation event. This is the second bounding configuration discussed in Section 2. In this consideration we ignore the cooling and dispersive effect of water on the relocating melt—ignoring both effects is clearly conservative and useful in obtaining the simple, yet bounding argument sought here. Further, we assume jet impingement occurs even though TMI vessel inspection found no evidence of such impingement (i.e., no wall attack). A complementary perspective on this problem, including consideration of these effects, is provided in Appendix H of DOE/ID-10460.

The situation then can be described as one involving a superheated oxidic melt of diameter D_j impinging on the lower head with the velocity U_j. The fundamental consideration is that molten oxide cannot exist next to a steel boundary even under strongly convective conditions; accordingly, the potential driving steel melting is the jet superheat. This idea was originally established by Epstein and co-workers (Epstein et al., 1980). More recently it was further validated and refined by Saito et al. (1990). In particular, they demonstrated experimentally the important effect of turbulence (in high Reynolds number jets) in enhancing the ablation rate significantly above that obtained in the laminar regime considered by Epstein et al. The experiments were carried out with molten salt ($NaC\ell$) at temperatures up to 1140 °C (Pr ~1) impinging on tin plates; the condition covered jet velocities up to 5 m/s, diameters up to 3 cm and Reynolds numbers up to $\sim 3 \times 10^5$. Two

runs were also carried out with $A\ell_2O_3$ at 2200 °C impinging on a steel plate at room temperature. In this case the Prandtl number is 5.46 and the Reynolds numbers were around 2×10^3. The data yielded a heat transfer correlation indicative of turbulent convection

$$\mathrm{Nu}_j = 0.0033\,\mathrm{Re}_j\,\mathrm{Pr}_j \tag{8.1}$$

and from it an ablation rate

$$\dot{Z} = 0.0033 \frac{\rho_j c_{pj}(T_j - T_m)}{\rho_w[\lambda + c_{pw}(T_{w,m} - T_{so})]} U_j \tag{8.2}$$

agreeing well with all the data that could be obtained. According to Eq. (8.1) the minimum required UO_2 temperature to prevent crust formation on steel is ~4400 K (Saito et al., 1990). This is significantly lower than the 6400 K obtained for laminar flow, but still well above any temperature of interest in the present application. We make use of Eq. (8.2), therefore, directly.

Using the material properties and a melt superheat of 200 K, Eq. (8.2) can be written as:

$$\dot{Z} = 4 \times 10^{-4} U_j \tag{8.3}$$

which can be integrated, assuming U_j is constant, over the duration of the relocation, τ, to yield the total ablation depth

$$Z_\tau = 4 \times 10^{-4} U_j \tau \tag{8.4}$$

The U_j and τ quantities are related by the total volume of relocated material and an effective jet diameter by

$$V_r = \frac{\pi}{4} D_j^2 U_j \tau \tag{8.5}$$

and if the principal variables are V_r and D_j Eq. (8.4) becomes

$$Z_\tau = 5.1 \times 10^{-4} \frac{V_r}{D_j^2} \tag{8.6}$$

This result, for a relocated volume of 2.5 m^3 (~ 1/3 of the fuel volume), as a function of D_j is shown in Figure 8.1.

An equivalent pour (jet) diameter of 10 cm is considered to be an extreme lower bound for such massive pours; still, it is seen to be unable to produce lower head penetration. Actually, we would expect the pour rate to increase with time as the breech on the core side boundary is enlarged by ablation (i.e., Sienicki and Theofanous, 1995).

These numbers are indicative of the rather intense and prolonged thermal loading required to produce local failures, and provide important perspectives on the even greater margins present in considering other transient phenomena, such as subsequent relocations into an existing corium pool. Such relocations would be expected to create "sinking" (cold) plumes, and in fact, Mayinger et al. (1980) measured the heat transfer rates in the impinging region of such plumes. Clearly, however, even ignoring the effects of crusts, momentum interactions in the corium pool, and turbulence would produce cooling and deceleration effects, thus making the wall interactions much more benign than those considered above.

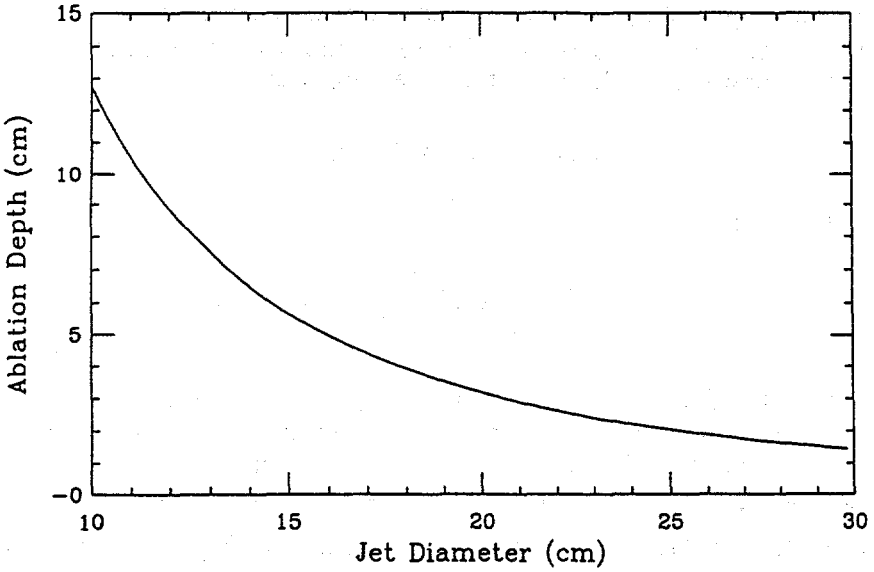

Figure 8.1. Wall ablation depth as function of jet diameter, for a melt pour of 2.5 m^3 ($\sim$1/3 of the fuel volume).

Based on the above, we can conclude that under no circumstance of a physically meaningful relocation scenario can we see local wall failures due to jet impingement. Under some extremely prolonged pours there may be some local attack and perhaps even a temporary CHF, if the ablation exceeds $\sim$3 cm at $\theta \sim 0°$, or $\sim$9 cm at $\theta \sim 30°$. However, due to the local nature of the thermal load, the dried out region would be expected to quench quickly after the temporary thermal load terminates.

Turland (1994) also concluded that jet attack does not provide a viable mechanism for lower head penetration, even for pours as large as 1/2 the core inventory.

9. CONCLUSIONS AND RECOMMENDATIONS

The major conclusion of this study is that thermally-induced failure of an externally flooded, AP600-like reactor vessel is "**physically unreasonable.**" In making use of these results for a specific AP600-like reactor, it is important to ascertain, or verify if appropriate, the following key system's features:

- Reliability of the depressurization and cavity flooding systems (valves) to ensure that failures can be classified in the "below-screening-frequency" category.
- Thermal insulation design that allows sufficient access of water to the bottom of the lower head and not subject to clogging, and venting of a steam/water mixture on the top. Further, based on this geometry (and available clearances), the dynamic behavior of the two-phase natural circulation flow should be assessed, and experimentally tested if necessary (i.e., if significantly different than the cases considered already in this study).
- Lower head external surface characteristics (finish, coatings, oxidation) that do not impair critical heat flux performance.

We believe that with appropriate attention in the design, none of these key features present serious difficulty in realizing this "in-vessel retention" concept.

The key mechanistic features for this favorable conclusion in AP600-like reactor designs can be listed as follows:

- A low power density core. In fact it is easy to see from the results of this study that at the decay power levels appropriate to this reactor it is virtually impossible for the oxidic pool to impose threatening thermal loads on the lower head, under **any** circumstances.
- A periodic bubble formation and detachment mechanism at the position of horizontal tangency ($\theta \sim 0°$) on the lower head, that, in combination with the large thermal inertia of it, allows very significant margins to critical heat flux. At higher positions, the thermal loads increase faster than the critical heat flux and, depending on the thickness of the metal layer, there may be locally even an essentially discontinuous further increase in the thermal load. That is, the margins to CHF decrease monotonically as we move from the center to the equator; however, they remain comfortable under all practically conceivable circumstances.
- Reactor vessel internals design that virtually prohibits the formation of superheated, thin, metallic layers on top of the oxidic pool. (Such layers would provide the only mechanism—a"focusing" in energy flow—that could conceivably compromise lower heat integrity.) This design includes:
  (a) a core inlet geometry (with large heat sinks) that would arrest downward relocation, allowing the formation of a core-wide crucible, and sideward failure through the reflector and core barrel,
  (b) massive reflector and core barrel components, extensively ablated and incorporated in the melt—that is, a significant metallic constituent with the relocating melt and
  (c) a massive lower (or core) support plate positioned such as to be subsummed in a large molten pool contained in the lower head.

Presently, this "focusing" mechanism has been conservatively treated by ignoring internal transport limitations (2D effects) due to the exceedingly large aspect ratio ($\sim$20) in such thin layers i.e., less than 20 cm. Eliminating the conservatism may provide important (needed) relief in assessing larger, and/or higher power density reactors.

Other ideas to improve the assessment basis, or the in-vessel retention performance for large and/or higher power density reactors can be listed as follows:

- Extend the database for heat transfer in volumetrically heated pools up to Rayleigh numbers of $\sim 10^{17}$. This is presently underway in the COPO (IVO) and the ACOPO (UCSB) experiments, which will also investigate thin metallic layers.
- Extend the CHF database to include reactor-specific thermal insulation, and relief path designs. This is ongoing in the ULPU experiment. Also under investigation (in ULPU) are surface treatment, lower head penetrations (as in existing reactors), and structural modification to enhance CHF performance. The surface treatment is more germane to the region $\theta \sim 0°$, and the structural modification (such as "fins") are oriented more to the upper region ($50° < \theta < 90°$ and including the vertical wall).
- Design reactor internals that effectively prohibit the formation of thin, superheated metallic layers on the top of a molten oxidic pool of significant size. The desired trend refers to availability of steel around the core and position of the lower support plate in the lower plenum, as discussed above.
- Examine the potential for fouling effects on CHF under long term operation.

Needless to say, slow accident progression to allow decreasing of the decay power to low levels, comfortable times for primary system depressurization and cavity flooding, and a water return flow path would continue to be important.

ACKNOWLEDGEMENTS

This work was supported under the ROAAM program carried out for the US DOE's Advanced Reactor Severe Accident Program (ARSAP), under ANL subcontract No. 23572401 to UCSB. The authors are grateful to Mr. Sterling Franks III (Associate Director, Engineering and Technology Development, Office of Nuclear Engineering, Science, and Technology) and his staff, W. Pasedag, R. Neuhold, R. Moore, and S. Sorrell (DOE Idaho Operations Office). For ANL the contract was managed by Dr. L. Baker, and his cooperation significantly facilitated the authors' focusing on the technical aspects of the work.

This has been a multifaceted technical effort that was enriched significantly by interactions with several individuals in other organizations outside UCSB. These include: J. Scobel (Westinghouse), J. Sienicki (ANL), J. Rashid (ANATECH), V.K. Dhir (UCLA), T.Y. Chu (SNL), C. Chu (ANL), and R. Hammersley (FAI). Thanks are also due to the following individuals affiliated with UCSB: M. Frye, J. Smith and G. Wang.

Last but not least we wish to acknowledge Ms. Eileen Horton, Administrative Assistant of CRSS, for her unhesitating devotion to this project, from contractual matters to budgeting and accounting to the preparation of the manuscript, often under very tight schedules.

The work was brought to a fruitful conclusion thanks to the participation of 17 experts, engaged independently through Argonne National Laboratory. They contributed (see DOE/ID-10460) not only by setting forth an in-depth record of scrutiny on essentially all aspects of the work, but also by providing further insights and otherwise enriching the technical bases of the work. The authors are grateful for their diligence and cooperation.

NOMENCLATURE

A	property group evaluated at "film" temperature, $\equiv 0.15k\{(g\beta)/(\alpha\nu)\}^{1/3}$
c_p	heat capacity
D	diameter
Da	Dammköhler number, $\equiv \dot{Q}H^2/k(T_{max}-T_i)$
E	Young's modulus of elasticity
Gr	Grashof number, $\equiv g\beta(T_{max}-T_i)H^3/\nu^2$
g	acceleration of gravity
H	depth of oxidic pool
h	heat transfer coefficient
I	Impulse
k	thermal conductivity
Nu	Nusselt number, $\equiv (qH)/k(T_{max}-T_i)$
P	pressure
Pr	Prandtl number, $\equiv \nu/\alpha$
$\dot{Q}$	volumetric heat generation rate
q	average heat flux at pool boundaries
$\tilde{q}$	characteristic heat flux, $\equiv \epsilon\sigma\tilde{T}^4$
q^*	dimensionless heat flux, $\equiv q/\tilde{q}$
q_{CHF}	critical heat flux

$q_{\ell,w}$	heat flux at vessel wall in contact with metal layer
$q_w(\theta)$	local heat flux across the vessel wall, at angular position θ
R	reactor vessel, hemisphere radius
Ra	Rayleigh number, $\equiv \{g\beta(T_{max} - T_i)H^3\}/(\alpha\nu)$
Ra′	Rayleigh number (internal), $\equiv (g\beta\dot{Q}H^5)/(k\nu\alpha)$
Re	Reynolds number, $\equiv (UD)/(\nu)$
r	radial coordinate
S	surface area
T	temperature
T^*	dimensionless temperature, $\equiv T/\tilde{T}$
T^{**}	water saturation temperature
$\tilde{T}$	characteristic temperature, $\equiv (A/\epsilon\sigma)^{3/8}$
T_m	oxidic pool liquidus
T_{max}	maximum (or "bulk," if uniform) pool temperature
U	velocity
V	volume of oxidic pool
Z_τ	total thickness of ablated wall following a relocation event
$\dot{Z}$	wall ablation rate

Greek letters

α	thermal diffusivity
β	thermal expansion coefficient
β'	linear thermal expansion coefficient
δ	thickness
ϵ	emmisivity
θ	polar angle on the lower head (see Fig. 2.1)
θ_ℓ	polar angle of metal layer top
θ_p	polar angle of oxidic layer top
λ	latent head of fusion
ν	kinematic viscosity
ν'	Poisson Ratio
ρ	density
σ	stress or Stefan–Boltzman constant
τ	duration of main relocation event

Subscripts

b	bulk value
CHF	critical heat flux
cr	crust value
dn	downward (over the hemispherical boundary)
F	failure condition
i	boundary value
j	based on jet properties
ℓ	metal layer
ℓ, i	inner metal layer boundary value
ℓ, m	liquidus of the vessel wall in contact with metal layer
ℓ, o	outer metal layer boundary value
ℓ, w	at vessel wall in contact with metal layer
m	liquidus
r	core relocation quantity, or radial coordinate
s	radiative sink value

s,i	inner radiative sink surface value
s,o	outer radiative sink surface value
up	upward (over the flat boundary of the oxidic pool)
v	inner vessel wall (upper vessel only)
w	vessel wall value
z	axial coordinate
0	initial value
θ	azimuthal coordinate

REFERENCES

1. AP600 (1994) "AP600 Probabilistic Risk Assessment," Prepared for U.S. Department of Energy, DE-AC03-90 SF18495, Rev. 1, July 22, 1994.
2. Asfia, J. Personal Communication (1994).
3. Asfia, J. and V.K. Dhir, An experimental study of natural convection in a volumetrically heated spherical pool bounded on top with a rigid wall, NED 163 (1996) 333–348.
4. Bonnet, J.M., S. Rougé and J.M. Seiler (1994) "Large Scale Experiments for Core Melt Retention — BALI: Corium Pool Thermalhydraulics SULTAN: Boiling Under Natural Convection," Proceedings, OECD/CSNI/NEA Workshop on Large Molten Pool Heat Transfer, Nuclear Research Centre, Grenoble, France, March, 9–11.
5. Butterman, W.C. and W.R. Foster (1967) *Am. Minerologist*, **52**, 884.
6. Chavez, S.A., G.E. Korth, D.M. Harper and T.J. Walker (1994) "High-Temperature Tensile and Creep Data for Inconel 600, 304 Stainless Steel and SA106B Carbon Steel," *Nuclear Engineering and Design* **148**, 351-363.
7. Cheung, F.B. (1980) "Heat-Source-Driven Thermal Convection at Arbitrary Prandtl Number," *J. Fluid Mech. 97*, part 4, p. 743.
8. Churchill, S.W. and H.H.S. Chu (1975) "Correlating Equations for Laminar and Turbulent Free Convection from a Vertical Plate *Int. J. Heat Mass Transfer* Vol. 18, 1323-1329.
9. CSNI (1994) Proceedings of the Workshop on Large Molten Pool Heat Transfer. Organized by OECD Nuclear Energy Agency in collaboration with Centre d'Etudes Nucleaires de Grenoble (France), 9-11 March, NEA/CSNI/R(94)11.
10. Dinh, T.N. and R.R. Nourgaliev (1994) "Numerical Analysis of Two-Dimensional Natural Convection under High Ra Number Conditions in Volumetrically Heated Corium Pool," Proceedings, OECD/CSNI/NEA Workshop on Large Molten Pool Heat Transfer, Nuclear Research Centre, Grenoble, France, March, 9–11.
11. Epstein, M., et al. (1980) "Simultaneous Melting and Freezing in the Impingement Region of a Liquid Jet," AIChE **26**, 5, p. 743.
12. Epstein, M. and H. Fauske (1989) *Nuclear Technology* **87**, 1021–1035.
13. Globe, S. and D. Dropkin (1959) *J. Heat Transfer* **81**, 24.
14. Goldstein and Chu (1969) *Prog. Heat Mass Transfer* **2**, 55.
15. Hawkes, G.L. and J.E. O'Brien (1991) "ARSAP AP600 In-Vessel Coolability Thermal Analysis Final Report," DOE/ID-10369, December.

16. Henry, R.E., J.P. Burelback, R.J. Hammersley, C.E. Henry, and G.T. Klopp (1991) "Cooling of Core Debris Within the Reactor Pressure Vessel Lower Head," ANS Summer Meeting, Orlando, Florida.

17. Henry, R.E. and H.K. Faùske (1993) "External Cooling of a Reactor Vessel Under Severe Accident Conditions," *Nuclear Engineering and Desing* **139**, 31.

18. Henry, R.E. and D.A. Dube (1994) "Water in RPV: A Mechanism for Cooling Debris in the RPV Lower Head," OECD-CSNI Severe Accident Management Specialists Meeting, Stockholm, June 1994.

19. Hodge, S.A. (1991) "Identification and Assessment of BWR In-Vessel Accident Management Strategies," ANS Trans. **64**, 367.

20. Jahn, M. and H.H. Reineke (1974) "Free Convection Heat Transfer with Internal Heat Sources," Proceedings of the Fifth International Heat Transfer Conference, Vol. 3, p.74.

21. K.M. Kelkar, K.K. Khankari, and S.V. Patankar (1993) Computational modelling of turbulent natural convection in flows simulating reactor core melt, Innovative Research Inc. Report submitted to Sandia National Laboratories.

22. Kulacki, F.A., and A.A. Emara (1975) "High Rayleigh Number Convection in Enclosed Fluid Layers with Internal Heat Sources," U.S. Nuclear Regulatory Commission Report NUREG-75/065.

23. Kymäläinen, O., H. Tuomisto and T.G. Theofanous (1992) "Critical Heat Flux on Thick Walls of Large, Naturally Convecting Loops," ANS Proceedings1992 National Heat Transfer Conference, San Diego, CA, Aug. 9-12, 1992, Vol. 6, 44–50.

24. Kymäläinen, O., H. Tuomisto, O. Hongisto and T.G. Theofanous (1993) "Heat Flux Distribution from a Volumetrically Heated Pool with High Rayleigh Number," Proceedings NURETH-6, Grenoble, October 5-8. [or *Nuclear Engineering & Design* **149**, 401-408, 1994.]

25. Kymäläinen, O. (1994) "Loviisa 1 & 2, In-Vessel Retention of Corium During a Severe Accident," IVO Int'l, Ltd. Report L01-GT1-64.

26. Kymäläinen, O., H. Tuomisto, and T.G. Theofanous (1996) "In-Vessel Melt Retention as a Severe Accident Management Strategy for the Loviisa Nuclear Power Plant, Proceedings 24th Water Reactor Safety Meeting, October 1996.

27. Lienhard, J.H. (1994) "Snares of Pool Boiling Research: Putting our History House," Proceedings of International Heat Transfer Conference, UK.

28. Mayinger, F., M. Jahn, H. Reineke, and U. Steinberner (1975) "Examination of Thermohydraulic Processes and Heat Transfer in a Core Melt," Final Report BMFT RS 48/1. Technical University, Hannover, W. Germany. As reviewed by F.A. Kulacki, Ohio State University, for the US NRC, march 31, 1976.

29. Mayinger, F., et al. (1980) "Theretische und Experimentelle Untersuchung des Verhaltenseines Geschmolzenen Kerns im Reaktorbehälter und auf dem Betonfundament," BMFT RS 166-79-05, Band V.

30. Okkonen, T. (1993) "In-Vessel Core Debris Cooling Through External Flooding of Reactor Pressure Vessel," Report by Group of Experts, Final Draft. To be published by CSNI.

31. O'Toole, J.L. and P.L. Silveston (1961) AIChE Chem. Eng. Prog. Symp. Ser. 57(32), 81.

32. Park, H. and V.K. Dhir (1991) "Steady State Thermal Analysis of External Cooling of a PWR Vessel Lower Head," AIChE Symp. Series, No. 283, Vol. 87, p.1.

33. Park, H., J. Lee, V.K. Dhir and A.K. Mal (1992) "Thermal Stresses and Creep Rupture Analysis for a PWR Vessel Lower Head During External Flooding," Proceedings 1992 National Heat Transference Conference, San Diego, CA, Aug. 9-12.

34. Pelton, A.D., L. Leibowitz and R.A. Blomquist (1994) *J. Nucl. Matter* (in press).

35. Rougé, S. and J.M. Seiler (1994) "Core Debris Cooling with Flooded Vessel or Core-Catcher: Heat Exchange Coefficient under Natural Convection," OECD/CSNI/PWG4, October 1994.

36. Saito, M., et al. (1990) "Melting Attack on Solid Plates by a High Temperature Liquid Jet – Effect of Crust Formation," *Nuclear Engineering and Design* **121**, 11-23.

37. Schneider, S.B. and B.D. Turland (1994) "Experiments on Convection and Solidification in a Binary System," Proceedings, OECD/CSNI/NEA Workshop on Large Molten Pool Heat Transfer, Nuclear Research Centre, Grenoble, France, March, 9–11.

38. Schnitzler, B.G. (1981) "Fission Product Decay Heat Modelling for Disrupted Fuel Regions (FRECAY)," EG& G Report EGG-PHYS-5698, Dec. 1981.

39. Sienicki, J.J. and T.G. Theofanous (1995) Draft material for Appendix O of DOE/ID-10460, made available in the July 1995 version.

40. Silveston, P.L. (1958) Forsch. Ingenieurwes **24**, 29, 59.

41. Squire, H.B. (1938) in **Modern Developments in Fluid Dynamics**, S. Goldstein, Ed., Oxford University Press, London, Vol. II, p. 641.

42. Steinberner, U. and H.-H. Reineke (1978) "Turbulent buoyancy convection heat tansfer with internal heat sources," Proc. Sixth International Heat Transfer Conf., Toronto, Canada, Aug 1978.

43. Stickler, L.A., et al. (1994) "Calculations to Estimate the Margin of Failure in the TMI-2 Vessel," NUREG/CR-6196, U.S. Nuclear Regulatory Commission.

44. Theofanous, T.G. (1989) "Some Considerations on Severe Accidents at Loviisa," Theofanous & Co., Inc. January 1989, IVO Proprietary Report.

45. Theofanous, T.G., S. Syri, T. Salmassi, O. Kymäläinen and H. Tuomisto (1994a) "Critical Heat Flux Through Curved, Downward Facing, Thick Walls," OECD/CSNI/NEA Workshop on Large Molten Pool Heat Transfer, Nuclear Research Centre, Grenoble, France, March, 9–11 [or *Nuclear Engineering and Design* **151** No. 3].

46. Theofanous, T.G., C. Liu, S. Angelini, O. Kymäläinen, H. Tuomisto and S. Additon (1994b) "Experience From the First Two Integrated Approaches to In-Vessel Retention Through External Cooling," OECD/CSNI/NEA Workshop on Large Molten Pool Heat Transfer, Nuclear Research Centre, Grenoble, France, March, 9–11.

47. Theofanous, T.G., W.W. Yuen, S. Angelini, J.J. Sienicki, K. Freeman, X. Chen and T. Salmassi (1996a) "Lower Head Integrity Under In-Vessel Steam Explosion Loads," DOE/ID-10541, June 1996.

48. Theofanous, T.G., C. Liu, S. Additon, S. Angelini, O. Kymäläinen and T. Salmassi (1996b) "In-Vessel Coolability and Retention of a Core Melt," DOE/ID-10460, Vols. 1 and 2, October 1996.

49. Theofanous, T.G., C. Liu, J. Scott, D. Williams and T. Salmassi (1996) "Natural Convection in Hemispherical Enclosures at Internal Rayleigh Numbers up to 7×10^{14}," Appendix D of DOE/ID-10460.

50. Theofanous, T.G. and S. Syri (1996) "The Coolability Limits of a Lower Reactor Pressure Vessel Head," Appendix E of DOE/ID-10460.

51. Turland, B.D., N.A. Johns and M.P. Owens (1993) "The Implications of the TMI-2 Vessel Investigation Project for Lower Head/Melt Interactions," AEA Technology Final Report AEA RS 7771, October 1993.

52. Turland, B.D. (1994) "In-Vessel Phenomena Relevant to the Achievement of Debris Coolability by Ex-Vessel Flooding for a PWR," Proceedings, OECD/CSNI/NEA Workshop on Large Molten Pool Heat Transfer, Nuclear Research Centre, Grenoble, France, March, 9–11.

53. Tuomisto, H. and T.G. Theofanous (1994) "A Consistent Approach to Severe Accident Management," *Nuclear Engineering and Design*, **148** 171-183 (1994). [see also Proceedings Specialist Meeting of Severe Accident Management Programme Development, ENEA/DISP, Rome, Italy, Sept. 23-25, 1991, 133-151.]

IN-VESSEL MELT RETENTION AS A SEVERE ACCIDENT MANAGEMENT STRATEGY FOR THE LOVIISA NUCLEAR POWER PLANT

Olli Kymäläinen and Harri Tuomisto
IVO International Ltd.
Rajatorpantie 8, Vantaa
FIN-01019 IVO, Finland
phone +358 9 8561 5388
fax +358 9 8561 3403

T.G. Theofanous
Department of Chemical and Nuclear Engineering
University of California
Santa Barbara, CA 93106, USA
phone (805) 893 4900
fax (805) 893 4927

Abstract

The concept of lower head coolability and in-vessel retention of corium has been approved as a basic element of the severe accident management strategy for IVO's Loviisa Plant (VVER-440) in Finland. The selected approach takes advantage of the unique features of the plant such as low power density, reactor pressure vessel without penetrations at the bottom and ice-condenser containment which ensures flooded cavity in all risk significant sequences. The thermal analyses, which are supported by experimental program, demonstrate that in Loviisa the molten corium on the lower head of the reactor vessel is coolable externally with wide margins. This paper summarizes the approach and the plant modifications being implemented. During the approval process some technical concerns were raised, particularly with regard to thermal loadings caused by contact of cool cavity water and hot corium with the reactor vessel. Resolution of these concerns is also discussed.

1. INTRODUCTION

In-vessel retention of corium (IVR) has been selected to be the key element of the severe accident management (SAM) strategy for IVO's Loviisa Plant. In-vessel retention was first proposed for Loviisa by Theofanous 1989 [1]. After extensive amount of work, the coolability of corium inside the reactor pressure vessel (RPV) has been demonstrated with high level of confidence [2] and the

approach has also recently been approved by the Finnish safety authorities. Presently, the implementation phase, including backfittings at the plant, has been started.

The goal of in-vessel retention of corium is to prevent the meltthrough of the reactor pressure vessel in case of a hypothetical core melt accident by flooding the reactor cavity and transferring the decay heat from the molten corium on the lower head of the RPV into the water surrounding the vessel. The heat transfer must be efficient enough such that at least part of the thickness of the RPV wall maintains its structural properties and is able to support the mechanical load due to the weight of the corium and the lower head and due to possible pressure inside the RPV. An obvious benefit of the in-vessel retention is the fact that all ex-vessel phenomena such as direct containment heating (DCH), ex-vessel steam explosions and corium-concrete interactions could be avoided.

The original idea that initiated the pursuit of in-vessel coolability as a major part of the SAM strategy was to fully exploit the numerous unique features of the Loviisa Plant [3]. At Loviisa (two VVER-440 units), the reactor cavity is small in size and in practice a dead ended volume. Therefore, the coolability of corium on the floor of the reactor cavity could be difficult to demonstrate. On the other hand, the Loviisa reactors have several features which favor in-vessel coolability of corium by external flooding of the reactor cavity. For example, the power density is relatively low and the water volumes both in the primary and secondary circuits are large meaning long time delays in case of an accident. Also, there are no penetrations at the bottom of the RPV. Finally, the plant is equipped with ice condenser containments which ensure flooded reactor cavity in most accident scenarios.

Whereas the thermal and heat transfer aspects of the issue are presented in reference [2], the purpose of this paper is to discuss the role of IVR in the overall SAM strategy for Loviisa and its implementation at the plant. Also, one section (section 4) of the paper is reserved for discussing an issue which was raised during the approval process concerning thermal loadings caused by contact of cool cavity water and hot corium with the reactor vessel.

2. THE ROLE OF IN-VESSEL RETENTION IN THE OVERALL SAM STRATEGY

IVO's approach for severe accident assessment and management is based on four successive levels [3],[4]. The first level of the approach is to ensure that severe accidents can be prevented with high probability. The quantitative targets for the overall core damage frequency (CDF) obtained from PSA level 1 are 10^{-4} /reactor year for existing plants (and 10^{-5} / reactor year for new plants).

The second level is to show a very low fraction of overall CDF for those classes of accident sequences which can be assumed to lead directly to a large release. Such sequences are the ones with impaired containment function, high pressure sequences and reactivity accidents leading to core damage. The goal which has been set for the conditional containment failure probability in these classes is 10^{-2}. In the case of Loviisa, the classes of sequences to be prevented also include

the ones in which successful IVR can not be guaranteed, because of, for example, significant amount sump water lost from the containment.

On the third level of the approach, the focus is on physical phenomena capable of threatening the containment integrity. The challenge to the containment integrity due to any physical phenomena should be excluded either by excluding the phenomenon itself as physically unreasonable or by showing that the loads caused by the phenomenon are tolerable. Generally, the phenomena that need to be addressed include, for example, in-vessel and ex-vessel steam explosions, hydrogen burns, direct containment heating, missiles, slow overpressurization due to steaming and generation of noncondensable gases, core-concrete interaction, recriticality of the degraded core and core debris, and temperature loadings of the containment. In Loviisa, the ex-vessel phenomena are addressed by preventing RPV failure with IVR. Instead of traditional PSA level 2 type of approach, IVO has treated the main phenomenological, Loviisa specific questions along the lines of the ROAAM (Risk Oriented Accident Analysis Methodology) proposed originally by Theofanous [5].

After successful exclusion of the containment system and structural failures, the fourth and final level of the approach is to define the radioactive releases through containment leakages. The releases during the managed accident sequences should stay below the acceptable criteria concerning acute health effects and land contamination.

For Loviisa, the approach translates to ensuring the following top level safety functions:

- depressurization of the primary circuit in order to initiate bleed and feed function as the ultimate means of preventing core damage or in order to ensure RPV integrity during external cooling in case the "feed"-component is not available;
- absence of energetic events, which in practice translates into prevention of energetic hydrogen combustion events by controlled recombination or burning the hydrogen,
- coolability and retention of molten core on the lower head of the reactor vessel,
- long term containment cooling with external spraying of the dome of the steel containment.

A more detailed description on how the goals of the aforementioned four levels have been met is given in a recent publication [6].

3. PROOF OF IN-VESSEL RETENTION FOR LOVIISA

3.1. The approach

The heat transfer and mechanical phenomena occurring during the relocation of corium from the core area down to the RPV lower head, during the formation of a molten pool on the lower head as well as during the final (quasi) steady state are highly complex and do not thus allow to be simulated in a detail level. It is therefore necessary to use bounding estimates, find the essential questions and focus the main attention to them.

When assessing the in-vessel retention for Loviisa, questions regarding reliable submergence of the RPV in water and regarding efficiency of the heat transfer from fully molten corium pool into the reactor cavity were classified as subissues of first priority. These subissues need to be resolved in a satisfactory way for each accident sequence or scenario for which in-vessel retention is planned for.

The second category of subissues consists of those potential threats which could possibly jeopardize the cooling in certain individual accident scenarios. After the first category issues are resolved, the second category subissues need to be tackled one by one. Such issues include, for example, in-vessel steam explosions or jet impingement effects during relocation of corium, brittle fractures of the RPV bottom in specific transient situations or stratified steam explosions after starting ECCS injection onto a molten corium pool. Some of these subissues are highly plant specific. For example, brittle behavior is practically no issue for modern RPVs [7] whereas it has to be taken into consideration for some older plants such as Loviisa.

A prerequisite for consideration of in-vessel retention as a part of severe accident management strategy is that the fraction of core damage frequency (CDF) of those accident sequences in which the RPV would not be submerged in water "fast enough" can be made low. It should be noted that the RPV needs to be submerged at least up to the level of the RPV support structures (level of cold legs). After this prerequisite is fulfilled, it has to be shown that the RPV can withstand the thermal and mechanical loads due to the molten corium. The main task is clearly to show that the heat loads from the corium pool can be transferred through the vessel wall without increasing the temperature of the wall to such values that the structural capabilities of the wall would be lost

The formation of solid crust at the boundaries of the molten corium pool efficiently decouples the heat transfer problem into two parts. Since the boundaries of the molten pool are always isothermal, the convective behavior of the molten pool determines the heat flux into the crust and thereby into the wall. On the other hand, the flow conditions outside the RPV determine the heat transfer mode at the outer surface of the wall. It can be easily seen that the crucial question regarding ex-vessel heat transfer is whether the heat transfer mode on the outer surface is nucleate boiling or film boiling. In nucleate boiling, the heat transfer coefficient is always high enough to keep the outer layers of the RPV wall at low temperatures so that meltthrough or creep failures need not be considered. On the other hand, if the critical heat flux is exceeded for a prolonged period, the wall will, in practice, always fail. Therefore, it has to be shown that the actual heat flux into the water at the outer surface of the RPV wall is always and everywhere below the critical heat flux at the corresponding location. Additionally, of course, assuming that critical heat flux is not exceeded, it has to be checked that the structural capabilities of the intact part of the wall are enough to support the mechanical loads.

It seems evident that the most limiting condition regarding the thermal loads occurs when the corium on the lower head is fully molten (except for the boundary crust) and no decay power is consumed in melting or heating up the debris or the structures. Therefore, in the thermal analyses carried out for Loviisa, steady state condition is assumed.

3.2. Ex-vessel coolant circulation and heat transfer

For the ex-vessel part of the heat transfer, the first task is to ensure that enough water for flooding the cavity and submerging the RPV up to the level of the RPV support structures is available in all relevant accident sequences. This task obviously includes ensuring that the water can pass the thermal and radiation shields and get into contact with the RPV outer surface and that the possible steam produced can freely escape to the other parts of the containment.

The present geometry around the Loviisa RPV is schematically shown in Figure 1. From the steam generator level, the water originating from the break, from the emergency core cooling system (ECCS) or from the ice-condensers can drain through several small routes down to the reactor cavity. In the cavity, the bottom part of the RPV is presently covered by a thermal and neutron shield which leaves only a narrow gap (less than 20 mm) between itself and the RPV wall. At the center part, the RPV is surrounded by an annular, 30 cm wide gap between the wall and the heat insulation. The steam formed in the annulus must escape upwards through the narrow gaps between the support structures of the RPV. This creates a strong exit restriction for the boiling flow. As well known, this kind of natural circulation flow loop is prone to two-phase flow oscillations.

For Loviisa it can be calculated that in all accident scenarios in which primary coolant or the sump water is not lost outside the containment, the amount of water in the primary circuit and in the hydroaccumulators and the minimum amount of ice which is expected to melt is sufficient to flood the cavity and submerge the RPV well upto its support structures.

In case the reactor cavity is flooded, the next requirement is that boiling crisis is avoided and the heat transfer mode on the outer surface of the vessel wall remains in nucleate boiling (or possibly single phase liquid convection). If the heat transfer mode permanently changes to film boiling, the surface temperature of the wall increases dramatically which sooner or later leads to failure of the RPV.

Based on the above discussion, an obvious question is whether the restriction in the flow area at the upper end of the annulus would create such flow oscillations which could significantly reduce the value of the critical heat flux (CHF). Two phase flow instabilities have been studied extensively in the past, but the present configuration differs significantly from the ones used in previous studies. First, the natural circulation loop is very large, several meters tall, so that hydrostatic pressure differences are significant. Second, the heating surface (the RPV wall) is thick and has a large thermal inertia, which is likely to influence the coupling between heat transfer and the flow rate when CHF is approached.

The first ULPU experiments, reported in [8], were carried out for studying the two-phase flow behavior (especially the oscillations) and the critical heat flux at vertical wall in a geometry corresponding to the one at Loviisa. In the ULPU facility, the cross-sectional flow area was scaled as 1:214. The height of the facility was approximately the same as in the prototypic case. The main finding in the ULPU experiments was that critical heat flux could not be exceeded with the power source available. The maximum heat flux used was about 1200 kW/m^2. The experiments also revealed three different oscillation modes with different periods, none of which

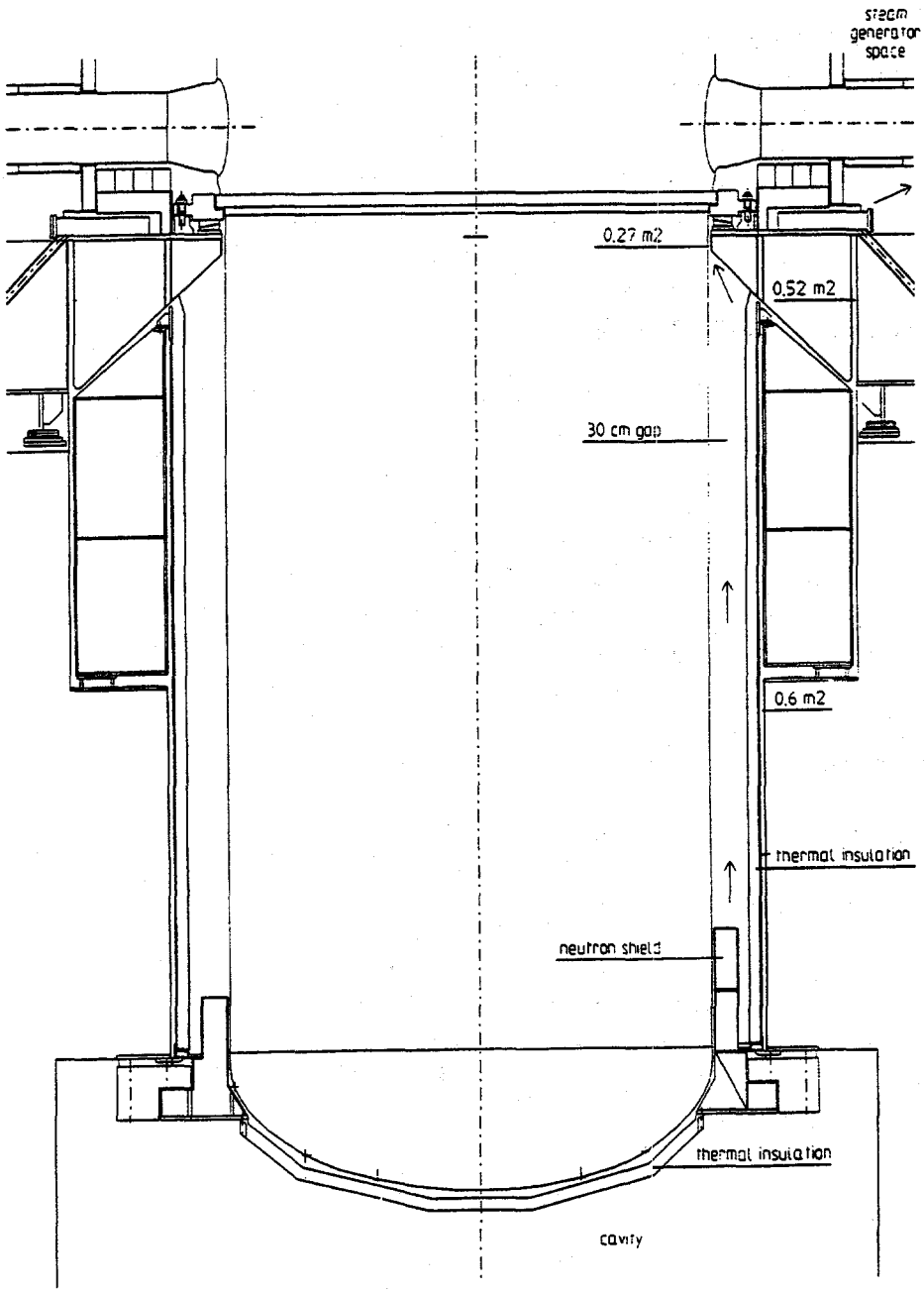

Figure 1. The flow routes around the Loviisa RPV.

however were able to induce CHF with exit restriction areas relevant at Loviisa. It should be mentioned that in the design of the ULPU facility, it was assumed that plant modifications for ensuring sufficient clearance between the RPV wall and the lower thermal and neutron shield and for ensuring efficient coolant circulation will be implemented.

As for the critical heat flux at the bottom of the vessel, an estimate can be found based on the ULPU-2000 experiments (continuation project of ULPU, financed by US DOE), in which the CHF was measured as a function of location at the curved boundary of the RPV bottom in a geometry corresponding to AP600 [9]. The experiments indicate that the CHF at the bottom of the vessel, even at zero subcooling and without global circulation in the flow loop is at least 300 kW/m^2. In reality the water in reactor cavity would be subcooled by ~17°C due to the hydrostatic head, even if the water at the sump level was saturated. Tests with ULPU-2000, configuration II in which global circulation of the flow loop was allowed, the value CHF increased to about 400 kW/m^2 [10].

In the assessment for Loviisa [2], the value of critical heat flux at the RPV surface was based on the ULPU and ULPU-2000 experiments.

3.3. In-vessel phenomena

The critical heat flux distribution on the surface of the RPV must be compared to the corresponding distribution of the actual heat flux. The actual heat flux is determined by the behavior of the corium inside the RPV. In the assessment done for Loviisa, it was assumed that the maximum heat fluxes are obtained in the final (quasi) steady state when the heat flows out from the RPV match the decay power in the corium and no decay power is consumed in heating up or melting the debris.

The geometry considered in the base case included a stratified molten corium pool, consisting of two layers. The lower, oxidic layer consisted mainly of UO_2 and ZrO_2 whereas the upper metallic layer included the unoxidized zirconium and molten stainless steel from the RPV internals.

The thermal analyses were based on the COPO experiments [11] and on the previous experimental data and correlations by Mayinger [12]. The results of the analyses, which are described in reference [2], indicated that the maximum heat flux through the wall occurs at the location of the molten metallic layer and that in the base case assuming a 70 cm thick metallic layer its value is below 500 kW/m^2.

3.4. Quantification

For the purpose of integrating the in-vessel retention into the overall severe accident management approach for Loviisa it was necessary to explicitly address the phenomenological uncertainties in some of the main parameters of the thermal analyses. This was done using a ROAAM type [5] of process. Since a large part of the work was done in parallel with the work for AP600-like reactors within the ARSAP program [7], the probabilistic ROAAM framework used for Loviisa resembled closely the one used in the ARSAP-report. The dominating parametric uncertainties and thus the ones quantified for the probabilistic framework were the amount of corium in the pool, the power density of the corium, the thickness of the metallic layer and the emissivity of the surface of the metallic pool. The results, which are presented in reference [2], indicate that failure of the RPV during external cooling is physically unreasonable.

4. TRANSIENT THERMAL LOADS ON THE WALL

During the approval process, an issue concerning potential brittle behavior of the RPV wall and especially the welds in the bottom head of the vessel was raised. This is clearly a plant specific question depending on the properties of the filler metal, and would probably be of no concern for newer reactor types such as AP600.

In external cooling, the outer surface of the reactor pressure vessel (RPV) lower head is in contact with water while the inner surface may be at temperatures as high as the steel melting point. Therefore, thermal stresses in the wall may become significant, which has raised concern about the possibility of a brittle fracture. The issue is further complicated by the fact that high temperatures combined with fast cooling rates create potential for phase transformations in the steel.

On the other hand, it can be noted that, even though the temperature gradients in the wall during external cooling of a corium pool are large, severe accident scenarios differ from typical (design basis) pressurized thermal shock (PTS) sequences in several ways, which tend to reduce the risk of a brittle fracture. First, because of the low neutron fluence, the embrittlement in the welds of the lower head is minimal. Furthermore, due to the molten corium involved in the transients, the temperatures, at least in part of the wall, are high, clearly above the brittle-to-ductile transition temperature. Finally, in a core melt accident, the pressure in the primary circuit is low, which means that the thermal stresses dominate and that there will most likely always be a region (hot part) where the wall is under compression. Clearly, rather complicated thermal sequences would, thus, be needed in order to create a global crack which could threaten the integrity of the lower head.

In the final (quasi) steady-state, when the decay power of the corium pool matches the heat losses into the water, the wall temperature decreases from melting point on the inner surface (at least near the top of the pool) down to approximately 100°C on the outer surface. In this case, propagation of possible cracks is not of concern since most of the wall material is at high temperatures and thus ductile.

Therefore, the potentially threatening scenarios must be looked for among transient situations. During external cooling of the RPV, the outside surface of the wall remains colder than the inner surface throughout all sequences. Since the pressure is low, the inner surface will typically remain under compression. Furthermore, due to the temperature difference, the inner surface is more ductile than the outer surface. Therefore, the crack initiation could potentially be a threat only for the outer surface. The only complication on the inner surface that cannot be excluded right away concerns possible phase transformation (hardening) of the steel.

Altogether three transient scenarios were identified to be investigated more closely. These three transients were considered to bound the whole spectrum of potential brittle fracture threats during external cooling. One of the scenarios involves an outer surface crack with fast temperature

transient. The other two cases consider possible phase transformation of the RPV steel assuming inner or outer surface cracks.

The first case considered was the initial transient when a relatively large amount of corium contacts the cold RPV wall for the first time. If a crack growth on the cool outer surface would be initiated, the crack might be able to propagate close to the inner surface of the wall until it would be stopped by the ductile high temperature front. Later on in the accident, however, the wall might get molten from inside with the molten region reaching the tip of the crack so that the crack would then extend through the wall.

In the second case, it was assumed that a limited amount of molten material first relocates to the lower head, but is subsequently quenched by the surrounding water. The wall also first heats up, but is rapidly cooled down after that. The danger in this situation is the possibility of creating a hardened (martensitic) steel layer on the inner surface of the wall. The hardened layer is very brittle and, furthermore, its density is lower than that of ferritic steel (expansion). The potential threat is connected 1) to inner surface cracks during the transient itself due to the embrittlement of the wall close to the inner surface or 2) to outer surface cracks due the possibly increased outer surface tension caused by the expansion of the hardened steel especially after new molten material has relocated onto the lower head.

The third scenario resembles the second one by involving also a martensitic transformation at the inner surface. In the third scenario it is assumed that the emergency core cooling system starts injecting water onto a molten corium pool, and rapidly cools down the wall just above the pool surface thus hardening the wall. Both inner surface and outer surface cracks need to be considered. This scenario involves only that portion of wall which remains above the corium pool. When starting coolant injection after temporary dry out of the RPV, the wall below the pool surface can be neglected from hardening point of view, since if the debris bed is not fully molten, the wall cannot be heated up to temperatures high enough for significant hardening. On the other hand, after a molten pool has been formed (with a metallic layer on top), the coolant will either not penetrate at all in between the crust and the wall, or the penetration and the resulting cooldown will be very slow. It may be noted that even though the lower head of the TMI-2 was cooled down fast possibly by the coolant between wall and crust [13], the situation is entirely different here. First, because of the low pressure and external cooling of the wall, no creeping of the wall is expected. Second, due to the low pressure and thus low density of steam, much wider gaps would be needed between the wall and the crust than at TMI.

Fracture mechanical analyses were carried out for the first scenario involving outside cracks and relocation of a large amount of corium. The analyses were carried out using very conservative boundary conditions especially at the inner surface. The results indicated that an outer surface crack of size 15 mm × 30 mm (which is detectable by large margins) cannot be initiated if the outside water temperature is 35°C, which can be regarded as a realistic minimum value for sump water temperature in accident conditions

The second scenario, in which the RPV wall was assumed to get hardened due to relocation and subsequent quenching of a limited amount of corium, is possible only if the amount of relocating

corium is small enough to allow rapid quenching of the corium and adjacent wall, and if the corium relocates through the downcomer. However, as these two assumptions seem to be mutually exclusive, it was concluded that the scenario is very unlikely. Therefore, no detailed structural analyses were carried out. However, simplified one-dimensional thermal conduction analyses showed that even in the imaginary case of 20 - 30 cm thick hot corium layer contacting the wall, the hardening depth in the low alloy steel would be limited to only about 20 mm, which could not be expected to cause any significant threat of brittle fracture.

In the third case it was assumed that coolant injection on top of a molten corium pool was started leading to fast cooling and hardening of the RPV wall above the pool surface. Two-dimensional thermal and structural analyses carried out showed that the disturbance caused by the hardening of the inner surface on the stress distribution of the wall was very local. Therefore, the impact on possible outer surface cracks is not significant. The inner surface remains under compression which prevents crack initiation.

5. IMPLEMENTATION

In order to ensure efficient natural circulation of coolant outside the RPV, some plant modifications are considered necessary. The modifications are schematically shown in Figure 2.

Presently, the smallest gap between the RPV wall and the lower neutron shield and the thermal insulation of the RPV bottom is less than ~20 mm. Taking into account thermal expansion of the vessel, this gap would be reduced even further. Coincidentally, the location of smallest gap is also the location of the highest heat flux through the vessel wall. Therefore, modifications in the lower shield were deemed necessary. The shield will be modified by changing its support mechanism so that the shield will be supported by a hydraulic cylinder. The hydraulic cylinder holds the thermal and neutron shields in place during normal operation, whereas in case of a severe accident the cylinder can be depressurized and the shield structure lowered down. The shield will be lowered after core uncovery has been detected from the measurements of core exit temperatures. Other alternatives, such as modification or partial removal of the thermal and neutron shield were also considered, but the aforementioned approach was found to have a clear advantage over other possibilities, since it does not impede normal operation (for example inspection of the RPV wall from outside) in the cavity and it does not degrade efficiency of the radiation shields.

At the upper end of the boiling channel modifications are needed, too, in order to ensure that the steam-water mixture can freely escape into the steam generator compartment. For this purpose, passively operated valves will be installed into the thermal insulation surrounding the RPV vessel.

As for the downcomers which bring water from the steam generator compartment down to the reactor cavity, the existing flow routes are rather narrow so that a clear danger of clogging them by loose debris (e.g., fibrous insulation material) exists. Additional downcomers are therefore needed. The additional channels will be created by installing passively operated valves in ventilation channels leading from the steam generator compartment down to the reactor cavity.

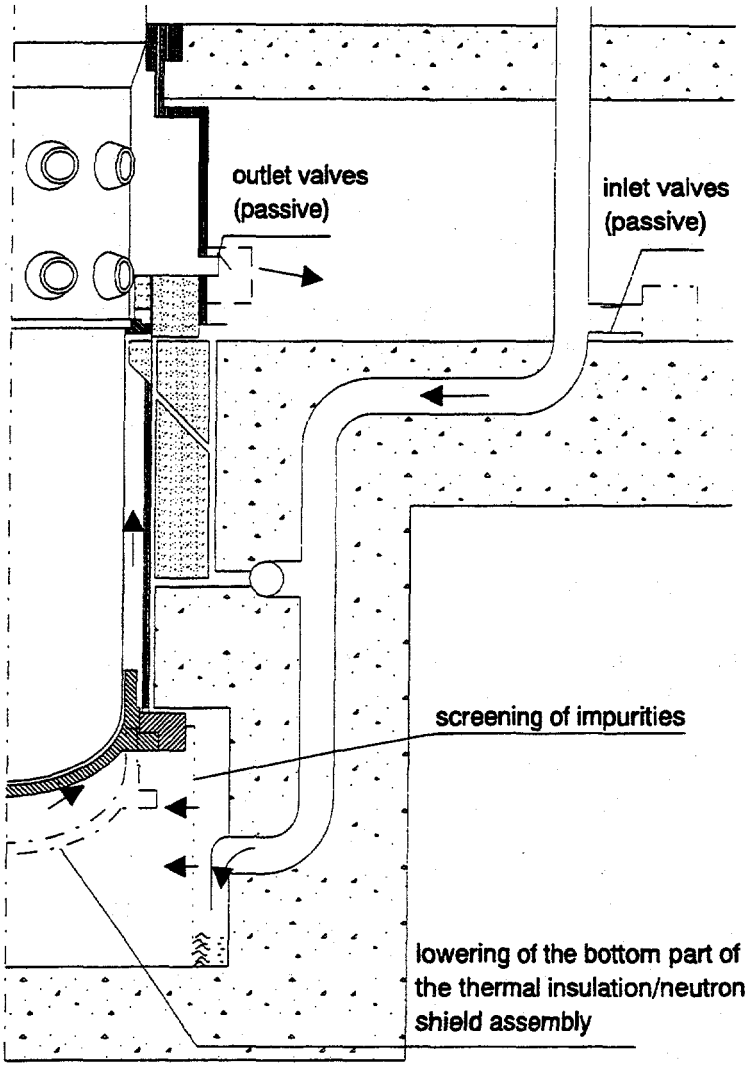

Figure 2. Modifications at Loviisa for implementing in-vessel retention.

In an accident situation debris from fibrous thermal insulation and other impurities will be flowing along with the coolant. Since the flow paths especially at the upper end of the boiling channel, are rather narrow, it is imperative to screen out the impurities from the coolant. In principle, two alternative locations for the location of the screening equipment could be imagined: either at the steam generator compartment in order to prevent the impurities from entering the reactor cavity or at the reactor cavity in order to trap the impurities there and thus keep the coolant entering the boiling channel clean. Out of these two alternatives the latter one turned out to be preferable, especially in view of missile protection and space limitations for construction in steam generator compartment. The final design of the strainers to be placed in the reactor cavity will be determined based on tests at IVO's Hydraulic Laboratory. Furthermore, the selected design will be confirmed in new tests planned to be carried out with the ULPU facility.

The aforementioned plant modifications are proposed and principally approved by the safety authorities. The final design and implementation schedule are to be worked out in near future.

Finally, it can be mentioned that the primary system depressurization capability to be installed at Loviisa in 1996 is a necessary modification also regarding in-vessel retention of corium. Primary circuit depressurization ensures that the mechanical loads to the degraded RPV walls remain tolerable and also that enough water (primary system inventory + accumulators + ice condensers) is available in time in the reactor cavity to submerge the RPV in all relevant accident scenarios.

6. CONCLUSIONS

In-vessel retention of corium by external cooling of the reactor pressure vessel is a key element in severe accident management strategy for Loviisa Plant. A ROAAM type of approach has been used to show that the RPV failure is physically unreasonable in all risk significant classes of accident sequences. This result eliminates the need to consider ex-vessel phenomena such as ex-vessel steam explosion or core-concrete interaction.

The implementation of in-vessel retention requires several backfitting measures to be done in order to ensure efficient coolant circulation in the channel surrounding the RPV. The detailed design of the backfittings is currently underway.

ACKNOWLEDGEMENTS

The contributions of Mr. L.Pietikäinen and Mr. J.Pullinen, both from IVO International, in solving the mechanical and structural challenges are gratefully acknowledged.

REFERENCES

[1] T.G. Theofanous, Some Considerations on Severe Accidents at Loviisa. Theofanous & Co., Inc. January 1989. IVO Proprietary Report.

[2] O. Kymäläinen, H. Tuomisto and T.G. Theofanous, In-Vessel Retention of Corium at the Loviisa Plant. Accepted for publication in Nuclear Engineering and Design, 1996.

[3] H. Tuomisto, T.G. Theofanous, A Consistent Approach to Severe Accident Management. Nuclear Engineering and Design 148 (1994) 171-183.

[4] H. Tuomisto, In Pursuit of Consistency of Completeness in the Severe Accident Assessment and Management. OECD Specialist Meeting on Severe Accident Management Implementation, Niantic, Connecticut, USA, 12-14 June 1995.

[5] T.G. Theofanous, H.Yan, ROAAM: A risk-oriented accident analysis methodology, Proc. Int. Conf. on Probabilistic Safety Assessment and Management (PSAM), Beverly Hills, CA, February 4 - 7, 1991, vol. 2, pp. 1179 - 1185.

[6] P. Lundström, H. Tuomisto and T.G. Theofanous, Integration of Severe Accident Assessment and Management to Fulfill the Safety Goals for the Loviisa NPP. International Topical Meeting on Probabilistic Safety Assessment PSA'96. Park City, Utah, September 29 - October 3, 1996.

[7] T.G. Theofanous, C. Liu, S. Additon, S. Angelini, O. Kymäläinen and T. Salmassi, In-Vessel Coolability and Retention of Core Melt. U.S.Department of Energy, Advanced Reactor Severe Accident Program. DOE/ID-10460, 1995.

[8] O. Kymäläinen, H. Tuomisto and T.G. Theofanous, Critical Heat Flux on Thick Walls of Large, Naturally Convecting Loops, ANS Proceedings of 1992 National Heat Transfer Conference, San Diego, CA, USA, 9-12 August 1992. ANS HTC Vol.6, 44-50.

[9] T.G. Theofanous, S. Syri, T. Salmassi, O. Kymäläinen and H. Tuomisto, Critical Heat Flux Through Curved, Downward Facing Thick Walls," Nuclear Engineering and Design, vol.151 (1994), no.3.

[10] T.G. Theofanous and S. Syri, The Coolability Limits of a Reactor Pressure Vessel Lower Head, Proceedings of the 7th International Topical Meeting on Nuclear Reactor Thermal Hydraulics (NURETH-7), Saratoga Springs, New York, 10-15 September 1995. NUREG/CP-0142.

[11] O. Kymäläinen, H. Tuomisto and T.G. Theofanous, Heat Flux Distribution from a Volumetrically Heated Pool with High Rayleigh Number. Nuclear Engineering and Design 149 (1994) 401-408.

[12] M. Jahn and F. Mayinger, Holographische Untersuchungen der Freien Konvektion in einer Kernschmelze. Institut für Verfahrenstechnik de T.U.Hannover. BMFT - Forschungsvorhaben RS 48/1, 1975.

[13] R.E. Henry and D.A. Dube, Water in the RPV: A Mechanism for Cooling Debris in the RPV Lower Head. OECD/NEA/CSNI Specialist Meeting on Selected Containment Severe Accident Strategies. Stockholm, Sweden, 13-15 June 1995.

A SCALING LAW FOR THE LOCAL CHF ON THE EXTERNAL BOTTOM SIDE OF A FULLY SUBMERGED REACTOR VESSEL

F.B. Cheung, K.H. Haddad and Y.C. Liu
Department of Mechanical Engineering
Pennsylvania State University
University Park, PA

ABSTRACT

A scaling law for estimating the local critical heat flux on the outer surface of a heated hemispherical vessel that is fully submerged in water has been developed from the results of an advanced hydrodynamic CHF model for pool boiling on a downward facing curved heating surface. The scaling law accounts for the effects of the size of the vessel, the level of liquid subcooling, the intrinsic properties of the fluid, and the spatial variation of the local critical heat flux along the heating surface. It is found that for vessels with diameters considerably larger than the characteristic size of the vapor masses, the size effect on the local critical heat flux is limited almost entirely to the effect of subcooling associated with the local liquid head. When the subcooling effect is accounted for separately, the local CHF limit is nearly independent of the vessel size. Based upon the scaling law developed in this work, it is possible to merge, within the experimental uncertainties, all the available local CHF data obtained for various vessel sizes under both saturated and subcooled boiling conditions into a single curve. Applications of the scaling law to commercial-size vessels have been made for various system pressures and water levels above the heated vessel. Over the range of conditions explored in this study, the local CHF limit is found to increase by a factor of two or more from the bottom center to the upper edge of the vessel. Meanwhile, the critical heat flux at a given angular position of the heated vessel is also found to increase appreciably with the system pressure and the water level.

INTRODUCTION

In recent years, the concept of external passive cooling of core melt in the lower head of a reactor vessel by cavity flooding has been considered a viable strategy of severe accident management. In this concept, water is made available on the bottom side of the reactor vessel by flooding the reactor cavity during a severe core-meltdown accident. As the lower head is heated by the pool of core melt resulting from the accident, the decay heat generated in the melt is removed from the external bottom surface of the reactor vessel by boiling of the water in the flooded cavity. If this mode of passive cooling is effective in the post-accident stage, then thermal failure of the reactor vessel can be prevented and the radioactive core melt can be retained within the reactor vessel. The feasibility of the cavity-flooding concept depends, however, heavily on the critical heat flux distribution on the external bottom surface of the reactor vessel under downward facing pool boiling conditions. To develop a suitable scaling law for estimating the critical heat flux distribution provides the major motivation for this study.

The mechanism responsible for the occurrence of CHF in pool boiling has been the subject of extensive investigation and debate in the past several decades (Katto 1985, Carey 1992). Notable studies include those of Kutaleladze (1948), Zuber (1959), Lienhard and Dhir (1973), Lienhard and Hasan (1979), and Haramura and Katto (1983). In all the existing CHF models, however, the critical heat flux was treated constant and uniform over the entire heating surface. Thus far, no attempt has ever been made to predict the spatial variation of the critical heat flux. While the assumption of a uniform critical heat flux is a good approximation for upward facing surfaces, it is not a valid assumption for downward facing surfaces. In the latter case, a two-phase boundary layer flow is likely to be induced by the boiling process owing to the downward facing orientation of the heating surface. With the development of a boundary layer flow along the heating surface, the local critical heat flux could be substantially modified by the flow, thus leading to a significant spatial variation of the CHF values along the heating surface in the flow direction. Conceivably, none of the existing CHF models is applicable to pool boiling on a downward facing heating surface. It should also be noted that correlations for the maximum pool boiling heat flux have been restricted to the geometrically averaged CHF value for the heating objects, as summarized by Carey (1992). The reported data on the spatial variation of CHF for pool boiling are limited to those by Theofanous et al. (1994), Cheung and Haddad (1994, 1995), Haddad, Liu and Cheung (1995), and El-Genk and Glebov (1995).

Most recently, Cheung and Haddad (1996) developed a hydrodynamic critical heat flux model to predict the CHF limit for saturated pool boiling on the outer surface of a heated hemispherical vessel. They considered the existence of a micro-layer underneath an elongated vapor slug on the downward facing curved heating surface. The micro-layer was treated as a thin liquid film with numerous micro-vapor jets penetrating through it. Local dryout was considered to occur when the supply of fresh liquid from the two-phase boundary layer to the micro-layer is not sufficient to prevent depletion of the liquid film by boiling. A boundary layer analysis, treating the two-phase motion as an external buoyancy-driven flow, was performed to determine the liquid supply rate and thus the local critical heat flux. The model provided a clear physical explanation for the spatial variation of the CHF observed in experiments.

In this study, the hydrodynamic CHF model of Cheung and Haddad (1996) is employed to develop a suitable scaling law for estimating the critical heat flux variation on a hemispherical vessel, taking into account the effects of vessel size and liquid subcooling. The validity of the scaling law is demonstrated by comparison with experimental data obtained for vessels of different sizes. The validated scaling law is applied to commercial-size vessels covering the anticipated ranges of system pressures and water levels above the vessel.

BACKGROUND

Subscale boundary layer boiling (SBLB) experiments were recently conducted by Cheung and Haddad (1994, 1995) and Haddad, Liu and Cheung (1995) to observe the critical heat flux phenomenon and the two-phase boundary layer flow on the outer surface of a heated

hemispherical vessel submerged in a large pool of water. In their experiments, the local wall heat flux was varied from 0.05 MW/m^2 up to the vicinity of the local CHF limit. At these high-heat-flux levels, a cyclic vapor ejection process was clearly observed. Large and elongated vapor masses or slugs, being squeezed up against the vessel wall by the local buoyancy force, were found to grow periodically on the downward facing curved heating surface. They were then ejected violently upward in all directions. The ejected vapor masses carried away the local vapor bubbles but tended to by-pass those large vapor slugs growing on the heating surface in the downstream locations, resulting in a two-phase boundary layer flow. A close-up view of the vapor slugs revealed the existence of a thin liquid film, i.e., a micro-layer, underneath each elongated vapor slug. The small vapor masses that were generated by boiling at numerous discrete locations on the heating surface were fed in a continuous manner to the large vapor slug through the liquid film in the micro-layer. These small vapor masses had the shape of micro-vapor jets. Apparently, it was the thin liquid film underneath the large vapor slug that prevented local dryout of the heating surface from occurring.

Near the local CHF limit, the characteristic frequency of the vapor ejection cycle was found to be approximately 4 Hz. Thus the cycle duration was about 0.25 s. This value was similar to the one observed by Chu, Bentz and Simpson (1995) on the outer surface of a heated torispherical vessel. Over 90% of this duration, the heating surface was covered by the vapor slugs. The waiting period was less than 10% of the cycle duration. High-speed photographic records indicated that the statistically averaged void fraction was very close to 0.915 as the CHF limit was approached. At the bottom center of the vessel, only a single large elongated vapor mass having an aspect ratio (i.e., length-to-thickness ratio) of approximately four, was present in the local boundary layer region. However, in the downstream locations, two or three large vapor slugs could be present in the local boundary layer region at the same time. Upon departure, a vapor slug tended to flow around those that were growing on the heating surface in the downstream locations. The local boundary layer thickness increased considerably from the bottom center to the upper edge of the heated vessel. No apparent changes in the vapor dynamics and cyclic ejection process were observed as the CHF point was attained. The vapor/liquid morphology and the local flow behavior were essentially the same throughout the high-heat-flux regime up to the CHF point, although the characteristic frequency of the vapor ejection cycle tended to increase with the heat flux level. Clearly, the CHF point is a continuation of the nucleate boiling region and simply represents the upper limit of the high-heat-flux regime. Throughout the entire high-heat-flux region including the CHF point, nucleate boiling is subject to Helmholtz instability. It is based upon this experimental observation that a new hydrodynamic CHF model was developed by Cheung and Haddad (1996) for pool boiling with the formation of a two-phase boundary layer on the heating surface.

THEORETICAL MODELING

Most existing hydrodynamic CHF models were developed primarily for upward facing surfaces. The critical heat flux was treated as a peculiar point that was different radically from the nucleate boiling regime. Helmholtz instability was assumed to act on the CHF point only,

causing a sudden collapse of the vapor removal path. The validity of these conventional models for downward facing surfaces is highly skeptical. The nucleate boiling phenomenon on the outer surface of a heated hemispherical vessel observed by Cheung and Haddad (1994, 1995) and Haddad, Liu and Cheung (1995) clearly indicated that throughout the entire high heat flux regime, nucleate boiling was subject to Helmholtz instability with cyclic ejection of large elongated vapor masses or slugs from the downward facing curved heating surface. Underneath each vapor slug was a micro-layer consisting of a continuous liquid film with numerous micro-vapor jets penetrating through it. The size of the micro-jets was dictated by Helmholtz instability. The CHF limit was reached as a result of insufficient supply of liquid from the two-phase boundary layer to the micro-layer, leading to depletion of the liquid film, i.e., local dryout of the heating surface. In view of this, the CHF point is a continuation of the nucleate boiling region in the high-heat-flux regime. Based upon this important new feature, an expression for the local thickness, δ_m, of the micro-layer was derived by Cheung and Haddad (1996) as

$$\delta_m = C_1 \sigma \rho_g \left(1+\frac{\rho_g}{\rho_\ell}\right)\left(\frac{\rho_g}{\rho_\ell}\right)^{0.4}\left(\frac{h_{fg}}{q''_{NB}}\right)^2 \tag{1}$$

where C_1 is a proportionality constant, σ the surface tension, ρ_g the vapor density, ρ_ℓ the liquid density, h_{fg} the latent heat of vaporization, and q''_{NB} the local nucleate boiling heat flux. The above expression for δ_m was derived from the physical argument that for the micro-jets to be hydrodynamically stable, the height of the jets must be smaller than the Helmholtz wavelength.

By considering local dryout of the liquid film to occur when the local rate of liquid supply from the two-phase boundary layer becomes smaller than the local rate of liquid depletion by boiling, an expression for the local critical heat flux, q''_{CHF}, was derived. This is

$$q''_{CHF} = \rho_\ell h_{fg} u_\ell (\delta_m)_{CHF} / C_2 \delta_0 \tag{2}$$

where C_2 is a proportionality constant, $(\delta_m)_{CHF}$ is the local thickness of the micro-layer at the CHF limit and u_ℓ is the local liquid velocity in the boundary layer.

Since the CHF point is a continuation of the nucleate boiling region in the high-heat-flux regime, Helmholtz instability is acting upon the micro-layer throughout the entire high-heat-flux nucleate boiling regime including the CHF point. Hence, equation (1) should be applicable to the CHF limit. By setting q''_{NB} equal to q''_{CHF}, equation (1) becomes

$$(\delta_m)_{CHF} = C_1 \sigma \rho_g \left(1+\frac{\rho_g}{\rho_\ell}\right)\left(\frac{\rho_g}{\rho_\ell}\right)^{0.4}\left(\frac{h_{fg}}{q''_{CHF}}\right)^2 \tag{3}$$

Substitution of Equation (3) into (2) gives

$$q''_{CHF} = B\rho_g h_{fg}\left[\frac{\sigma u_\ell}{\rho_\ell \delta_0}\left(1+\frac{\rho_g}{\rho_\ell}\right)\left(\frac{\rho_g}{\rho_\ell}\right)^{-1.6}\right]^{1/3} \tag{4}$$

where $B = (C_1 / C_2)^{1/3}$ is a new constant. Evidently, the local critical heat flux varies according to the 1/3 power of the local liquid velocity. This local flow quantity, which is expected to increase significantly along the heating surface in the flow direction, needs to be determined along with the local boundary layer thickness by treating the two-phase boundary layer motion as an external buoyancy-driven flow.

It should be noted that the dependence of the CHF limit on the local liquid velocity in the two-phase boundary layer given by equation (4) is similar to the one observed for forced convection boiling of the external flow type where the critical heat flux is proportional to the 1/3 power of the mass velocity of the ambient liquid flow (Haramura and Katto 1983). This similarity clearly shows the rather unconventional features associated with the present boundary-layer-type pool boiling process. Although it is a pool boiling phenomenon, the process exhibits flow boiling characteristics. Physically, this is because of the formation of the two-phase boundary layer along the downward facing curved heating surface in the present pool boiling case. Owing to the effect of the two-phase boundary layer, the CHF phenomenon at a given downstream location exhibits the same characteristic behavior as the one observed for external flow boiling.

To determine the local CHF limit, the boundary layer thickness δ_0 and the liquid velocity u_ℓ appearing on the right hand side of equation (4) need to be determined from the two-phase boundary layer flow behavior. According to Cheung and Epstein (1987), the momentum relation for the vapor-liquid mixture in the two-phase boundary layer is governed by the following differential equation applicable to any location θ measured from the bottom center in the upward direction along the hemispherical heating surface:

$$\begin{aligned}&\frac{d}{d\theta}\left\{\left[\rho_g \alpha u_g{}^2 + \rho_\ell (1-\alpha) u_\ell{}^2\right]\delta \sin\theta\right\} \\ &= \alpha\delta R g(\rho_\ell - \rho_g)\sin^2\theta - (\tau_w + \tau_i) R \sin\theta\end{aligned} \tag{5}$$

where R is the radius of the vessel, α the local void fraction of the two-phase boundary layer, u_g the local vapor velocity parallel to the heating surface, g the gravity constant, and τ_w and τ_I the wall and the interfacial shear stresses, respectively. The latter two quantities are given by (Cheung and Epstein 1987):

$$\tau_w + \tau_i = 0.5 C_f\left[\alpha u_g + (1-\alpha)u_\ell\right]\left[\rho_g \alpha u_g + \rho_\ell (1-\alpha) u_\ell\right] \tag{6}$$

where C_f is a friction coefficient having the value of 0.005.

A mass balance on the liquid phase across the thickness of the two-phase boundary layer at any location θ gives

$$\frac{d}{d\theta}\left[(1-\alpha)u_\ell \delta \sin\theta\right] = j_\ell R \sin\theta \tag{7}$$

where j_ℓ is the net liquid velocity entrained from the ambient fluid into the two-phase boundary layer at θ. Physically, the quantity j_ℓ represents the "entrained" component of the liquid mass swept into the boundary layer by the two-phase motion, excluding the "suction" component of the liquid mass due to liquid depletion by boiling on the heating surface.

Similarly, a mass balance on the vapor phase across the thickness of the two-phase boundary layer under saturated boiling conditions at any location θ gives

$$\frac{d}{d\theta}\left[\alpha u_g \delta \sin\theta\right] = \frac{q''_{CHF} R \sin\theta}{\rho_g h_{fg}} \tag{8}$$

where u_g is the local vapor velocity in the two-phase boundary layer. In deriving the above expression, the local wall heat flux on the heating surface has been assumed equal to the local critical heat flux. This corresponds to the critical heating condition for which the local CHF limit is reached in all upstream locations on the outer surface of the hemispherical vessel. This situation gives rise to the maximum local vapor velocity and boundary layer thickness that can possibly be attained at a given downstream location θ. Physically, the use of q''_{CHF} in equation (8) is consistent with the notion that CHF represents the upper bound of the excellent state of nucleate boiling. Beyond this upper limit, dryout will occur on the heating surface.

To close the governing system, an independent expression is needed for the relative velocity between the liquid and vapor phases. This is obtained by assuming that once the vapor mass departs from the heating surface, it would attain its terminal rise velocity relative to the liquid phase in the two-phase boundary layer. It follows that from Wallis (1969) that

$$u_g = u_\ell + 1.53\left[\frac{\sigma g \sin\theta(\rho_\ell - \rho_g)}{\rho_\ell^{\,2}}\right]^{1/4} \tag{9}$$

where $g \sin\theta$ represents the local gravitational force tangential to the heating surface.

Inspection of equations (4) to (8) indicates that the following local boundary layer variables, namely, the dimensionless critical heat flux, Q_{CHF}, dimensionless boundary layer thickness, Δ, dimensionless vapor velocity, U_g, and dimensionless liquid velocity, U_ℓ, can be introduced to simplify the governing system:

$$q''_{CHF} = \rho_g h_{fg}\left[\frac{\sigma g(\rho_\ell - \rho_g)}{\rho_g{}^2}\right]^{1/4}\left(1+\frac{\rho_g}{\rho_\ell}\right)^{1/3} Q_{CHF} \tag{10}$$

$$\delta = \left[\frac{\sigma R^2}{g(\rho_\ell - \rho_g)}\right]^{1/4}\left(\frac{\rho_g}{\rho_\ell}\right)^{-0.1}\Delta \tag{11}$$

$$u_g = \left[\frac{Rg(\rho_\ell - \rho_g)}{\rho_g}\right]^{1/2}\left(\frac{\rho_g}{\rho_\ell}\right)^{0.1} U_g \tag{12}$$

$$u_\ell = \left[\frac{Rg(\rho_\ell - \rho_g)}{\rho_\ell}\right]^{1/2} U_\ell \tag{13}$$

In terms of the dimensionless local variables, equations (4) to (9) can be written as

$$Q_{CHF} = B(U_\ell / \Delta_0)^{1/3} \tag{14}$$

$$\frac{d}{d\theta}\left\{\left[\alpha U_g{}^2 + \left(\frac{\rho_g}{\rho_\ell}\right)^{-0.2}(1-\alpha)U_\ell{}^2\right]\Delta\sin\theta\right\}$$

$$= \alpha\Delta\sin^2\theta\left(\frac{\rho_g}{\rho_\ell}\right)^{-0.2} - 0.5C_f L_b{}^{-1/2}\left(\frac{\rho_g}{\rho_\ell}\right)^{0.1}\sin\theta\left[\alpha U_g + \left(\frac{\rho_g}{\rho_\ell}\right)^{-0.6}(1-\alpha)U_\ell\right] \tag{15}$$

$$\left[\alpha U_g + \left(\frac{\rho_g}{\rho_\ell}\right)^{0.4}(1-\alpha)U_\ell\right]$$

$$\frac{d}{d\theta}\left[(1-\alpha)U_\ell\Delta\sin\theta\right] = J_\ell\left(\frac{\rho_g}{\rho_\ell}\right)^{0.1} L_b{}^{-1/2}\sin\theta \tag{16}$$

$$\frac{d}{d\theta}\left[\alpha U_g\Delta\sin\theta\right] = Q_{CHF}\sin\theta \tag{17}$$

$$U_\ell = \left(\frac{\rho_g}{\rho_\ell}\right)^{-0.4} U_g - 1.53(L_b{}^2\sin\theta)^{1/4} \tag{18}$$

where

$$\Delta_0 = \left[\frac{\sigma R^2}{g(\rho_\ell - \rho_g)}\right]^{-1/4} \left(\frac{\rho_g}{\rho_\ell}\right)^{0.1} \delta_0 \tag{19}$$

$$J_\ell = \left[\frac{Rg(\rho_\ell - \rho_g)}{\rho_\ell}\right]^{-1/2} j_\ell \tag{20}$$

$$L_b = \frac{1}{R}\left[\frac{\sigma}{g(\rho_\ell - \rho_g)}\right]^{1/2} \tag{21}$$

Physically, the dimensionless parameter L_b represents the length ratio between the intrinsic bubble size and the vessel radius.

Assuming the boundary-layer flow quantities to be nearly constant over the bottom-center region where $0 \le \theta \le \theta_0$ and that $d\Delta / d\theta = 0$ at $\theta = \theta_0$, equation (15) can be integrated to give

$$\alpha U_{g_0}{}^2 + \left(\frac{\rho_g}{\rho_\ell}\right)^{-0.2} (1-\alpha) U_{\ell_0}{}^2$$

$$= \frac{\alpha \theta_0{}^2}{3}\left(\frac{\rho_g}{\rho_\ell}\right)^{-0.2} - 0.25 C_f L_b^{-1/2}\left(\frac{\rho_g}{\rho_\ell}\right)^{0.1} \theta_0 \left[\alpha U_{g_0} + \left(\frac{\rho_g}{\rho_\ell}\right)^{-0.6} (1-\alpha) U_{\ell_0}\right] \tag{22}$$

$$\left[\alpha U_{g_0} + \left(\frac{\rho_g}{\rho_\ell}\right)^{0.4} (1-\alpha) U_{\ell_0}\right]$$

where the approximation of $\sin \theta_0 = \theta_0$ for small values of θ_0 has been employed in deriving the above equation.

SPATIAL VARIATION OF THE CHF LIMIT

Equations (14) to (18) form a complete set of coupled equations governing the local variations of the critical heat flux, Q_{CHF}, the vapor and liquid velocities U_g and U_ℓ respectively, the boundary layer thickness, Δ, and the void fraction, α. This set of equations have been solved numerically by Cheung and Haddad (1996), with the universal constant B in equation (14) being determined by experimental data. Results are shown in Figures 1 to 5. For all values of L_b, the boundary layer thickness increases considerably from the bottom center to the upper edge of the vessel (see Figure 1). However, the dimensionless boundary layer thickness is a weak function of the physical size of the vessel. The size effect is important only when the vessel diameter is very small. The actual boundary layer thickness, on the other hand, is a strong function of L_b. For $L_b < 0.05$, however, δ is almost inversely proportional to the square root of L_b. Thus for vessels larger than 0.1 m in diameter, δ would vary according to the square root of the vessel diameter whereas Δ is essentially independent of the vessel size.

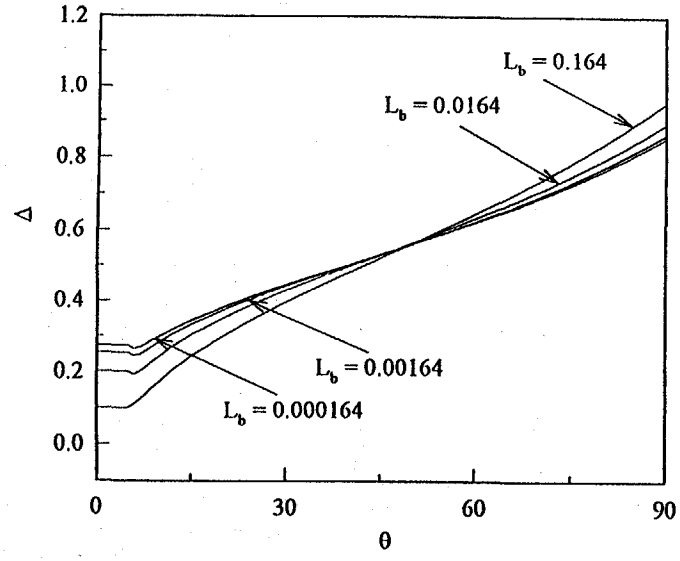

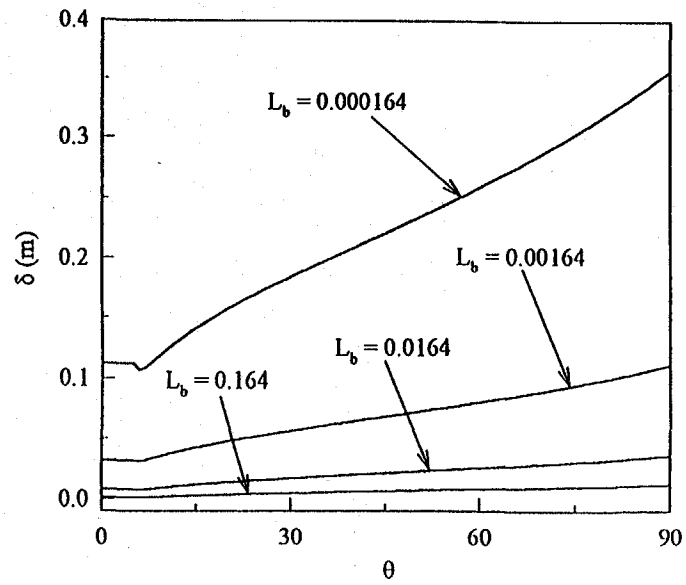

Figure 1. Spatial Variation of the Boundary Layer Thickness.

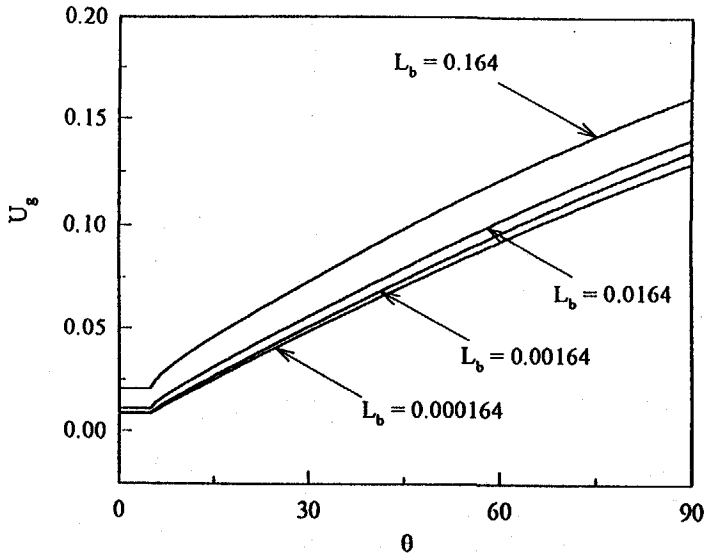

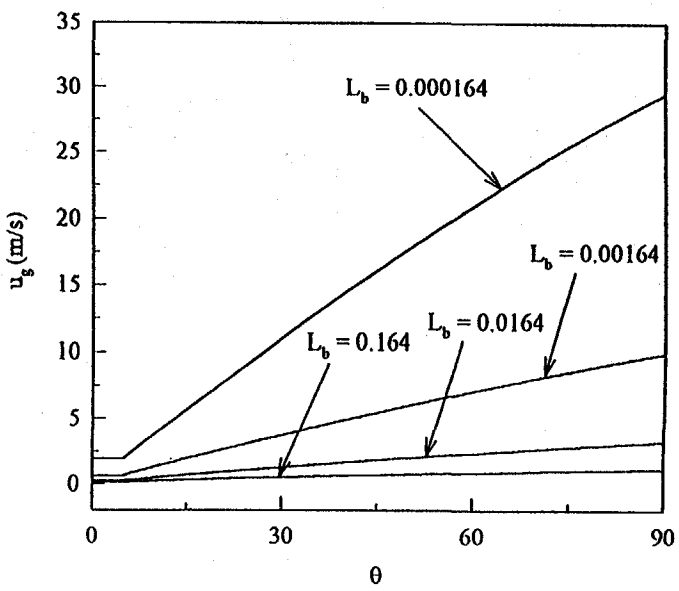

Figure 2. Spatial Variation of the Local Vapor Velocity.

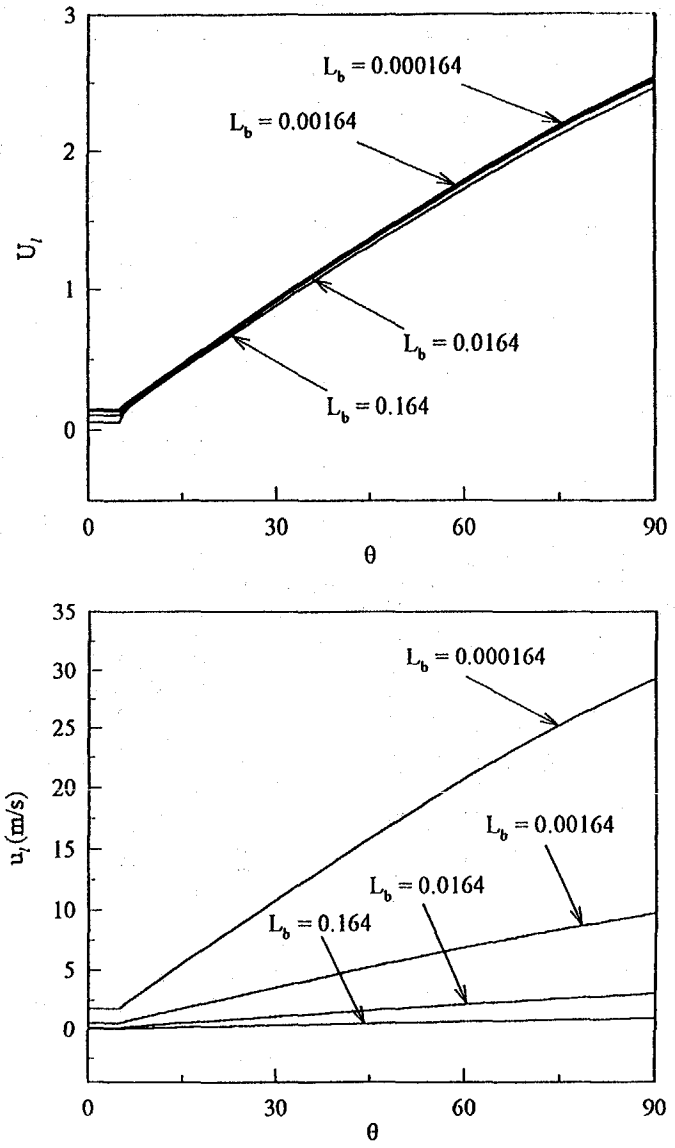

Figure 3. Spatial Variation of the Local Liquid Velocity.

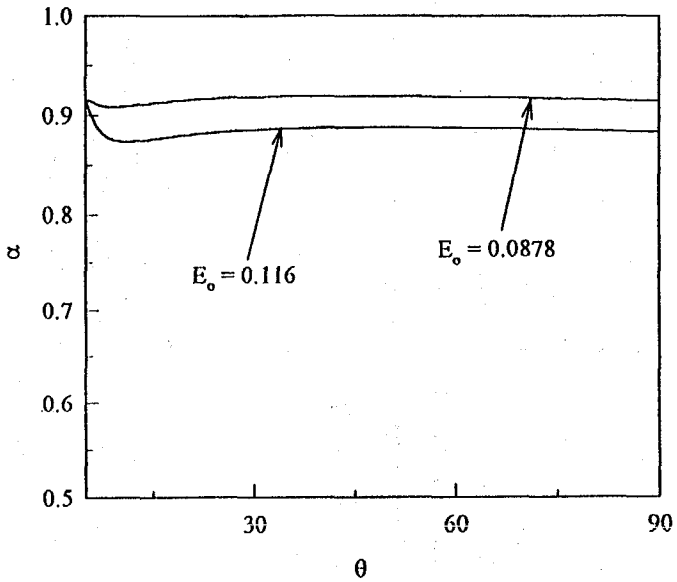

Figure 4. Spatial Variation of the Local Void Fraction.

The spatial variations of the vapor and liquid velocities are presented in Figures 2 and 3. For all values of L_b, the vapor and liquid velocities increase by more than an order of magnitude from the bottom center to the upper edge of the vessel. The relative velocity between the liquid and vapor phases is on the same order of the vapor and liquid velocities when θ is small. For large values of θ, the relative velocity is an order of magnitude smaller than the liquid and vapor velocities. The effect of L_b is quite strong on u_ℓ and u_g but very weak on the dimensionless quantities U_ℓ and U_g. For $L_b < 0.05$, both u_ℓ and u_g are almost inversely proportional to the square root of L_b. Thus for vessels larger than 0.1 m in diameter, u_ℓ and u_g would vary according to the square root of the vessel diameter whereas U_ℓ and U_g are essentially independent of the vessel size.

The local variations of the void fraction have been calculated by fixing the value of L_b at 0.0164, corresponding to a vessel diameter of 12" (0.305 m), which is the same as the vessel size employed in the experimental work of Cheung and Haddad (1994, 1995). Meanwhile, various values have been assumed for the entrainment coefficient by setting E_0 equal to 0.116 C_5, where C_5 is a constant factor having a value varying from 0.5 to 1.0. The value of $C_5 = 1.0$ (i.e., $E_0 = 0.116$) has been used by Morton (1965) for turbulent jets and by Cheung and Epstein (1987) for two-phase boundary layer flows. In the present case, however, E_0 is expected to be smaller than 0.116 because of the configuration of the downward facing curved heating surface and the wall effect on liquid entrainment. For all values of $0.5 \leq C_5 \leq 1.0$ employed in the calculations, the local void fraction was found to be nearly constant over the length of the hemispherical heating surface. Results for two special cases are presented in Figure 4. For the case of $E_0 = 0.116$ (i.e., $C_5 = 1.0$), the local void fraction is bounded within $\pm$ 2.5% of 0.892, whereas for the case of $E_0 = 0.0878$ (i.e., $C_5 = 0.75$), α is bounded within $\pm$ 0.5% of 0.915. These results clearly indicate that the constant-void-fraction postulation is a valid approach as it complies with the conservation of liquid mass, i.e., the liquid continuity equation. Based on the value of $\alpha = 0.915$ observed in the experimental work of Cheung and Haddad (1994, 1995), the entrainment coefficient for the present two-phase boundary layer flow is determined to be $E_0 = 0.0878$.

Figure 5 shows the spatial variations of the dimensionless critical heat flux and the actual critical heat flux. Both Q_{CHF} and q''_{CHF} are weak functions of the size parameter L_b for the cases of L_b equal to or less than 0.0164. This clearly demonstrates the fact that for heated vessels with diameters considerably larger than the characteristic bubble size, the critical heat flux is weakly dependent on the vessel size. As shown in equation (4), the local critical heat flux is given by the 1/3 power of the ratio between the local liquid velocity and the local boundary layer thickness. For $L_b < 0.05$, both u_ℓ and δ vary according to the square root of the vessel diameter. Thus the size effect on u_ℓ and δ_0 cancels out and q''_{CHF} becomes almost independent of L_b. Note that the local critical heat flux increases by more than 100% from the bottom center to the upper edge of the vessel. This result is similar to the spatial variations of CHF observed experimentally by Cheung and Haddad (1994, 1995), Haddad, Liu and Cheung (1995), and Theofanous et al.

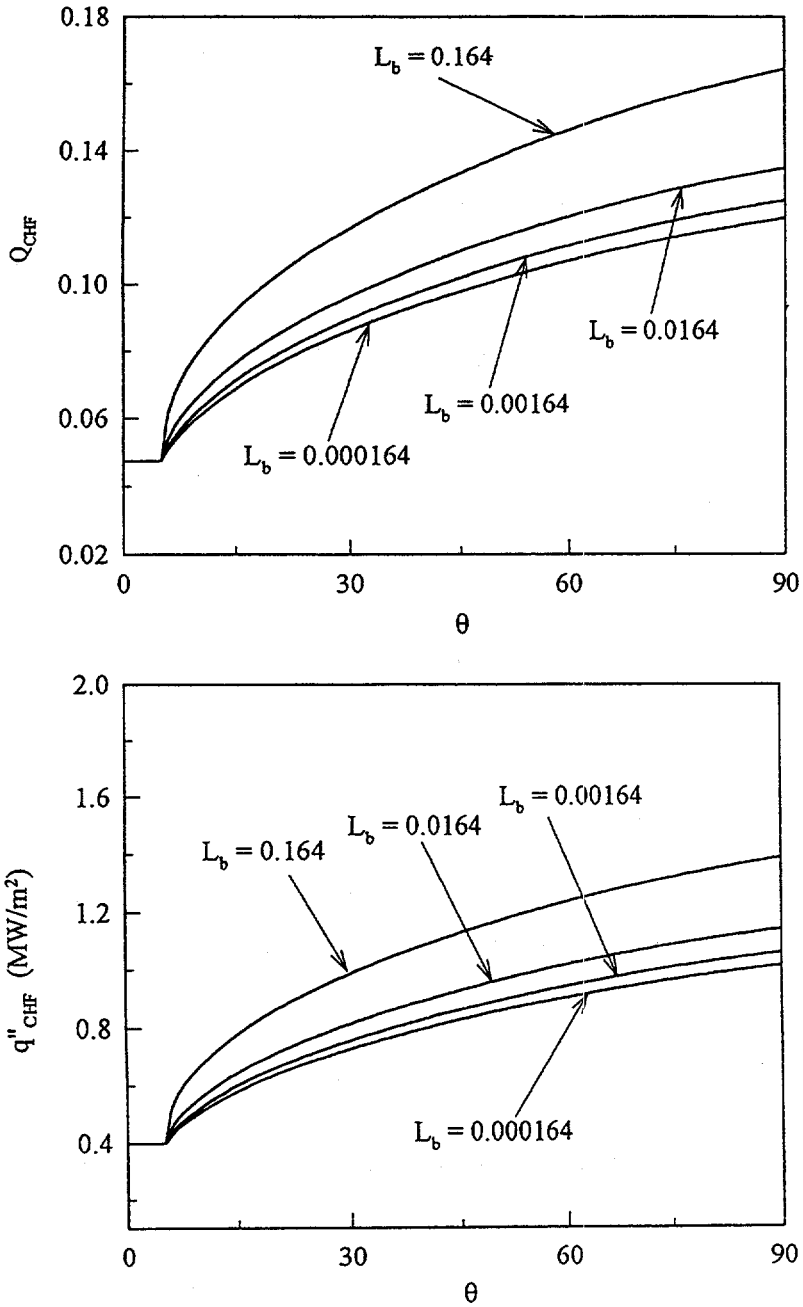

Figure 5. Spatial Variation of the Critical Heat Flux on the Outer Surface of a Hemispherical Vessel.

(1994). However, it is opposite to the CHF variation observed by El-Genk and Glebov (1995). Physically, this is because of the two-phase boundary layer flow effect, which was present in the experiments by Cheung and Haddad (1994, 1995), Haddad, Liu and Cheung (1995), and Theofanous et al. (1994) but not present in the transient experiments by El-Genk and Glebov (1995). In the latter case the heating surface was too small (~50 mm) for a two-phase boundary layer to develop.

DEVELOPMENT OF THE SCALING LAW

Saturated Boiling Conditions

From equations (14) to (18), it can be seen that for saturated boiling the dimensionless local critical heat flux Q_{CHF}, is a function of the vapor size-to-vessel radius ratio, L_b, and the angular position, θ, of the hemispherical vessel. For all vessel sizes, the spatial variations of Q_{CHF} with θ are quite similar, as shown in Figure 5. Morever the local value of Q_{CHF} tends to approach asymptotically to a constant value as L_b approaches zero. This functional behavior of Q_{CHF} indicates that

$$Q_{CHF} = F_{L_b}(L_b,\theta)\,F_\theta(\theta) \tag{23}$$

and

$$\lim_{L_b \to 0} F_{L_b}(L_b,\theta) = 1 \tag{24}$$

where $F_{L_b}(L_b,\theta)$ is a size correction factor and $F_\theta(\theta)$ is a spatial variation function. In view of the fact that the local buoyancy force that is parallel to the curved heating surface is proportional to $g\sin\theta$, the effect of vessel size is expected to vary with the local angular position, θ. Thus the size correction factor, F_{L_b}, is dependent upon both L_b and sin θ. Using a power-law expression, the following functional form of F_{L_b} that satisfies equation (24) is proposed:

$$F_{L_b}(L_b,\theta) = \exp\left[A\,L_b{}^m(\sin\theta)^n\right] \tag{25}$$

where the coefficient A and the indices m and n are positive constants. It follows from equations (23) and (25) that

$$Q_{CHF}\left\{\exp\left[A\,L_b{}^m(\sin\theta)^n\right]\right\}^{-1} = F_\theta(\theta) \tag{26}$$

If A, m and n are truly universal constants, then a plot of Q_{CHF} / F_{L_b} versus θ is a single curve for all values of L_b. From the four sets of numerical data of Q_{CHF} shown in Figure 5, the values of A, m and n that best merge all four curves into one are found to be A = 0.8, m = 1/2, and n = 1/3. Equation (25) thus becomes

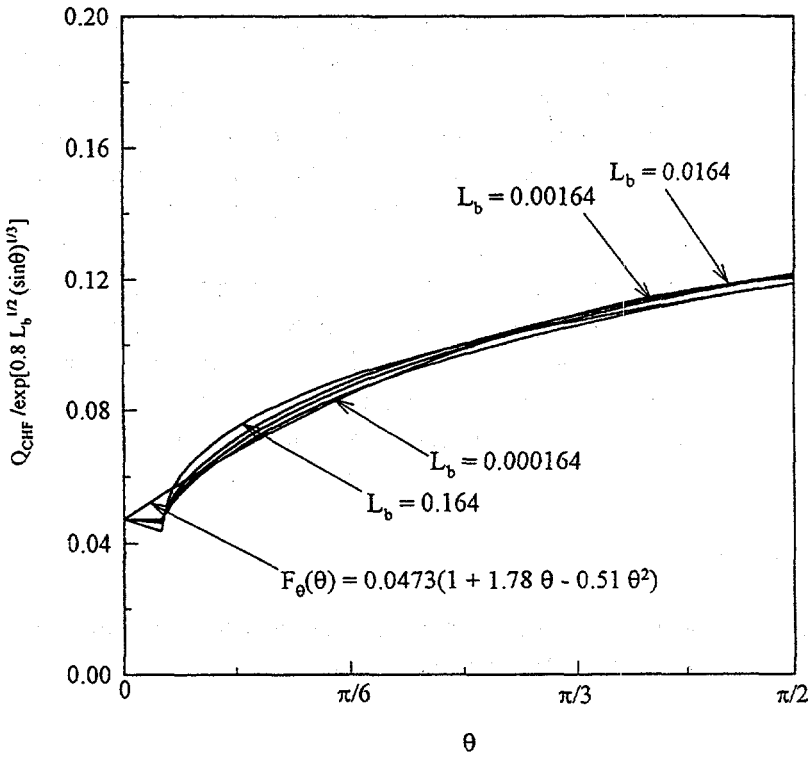

Figure 6. Scaling of the Vessel Size Effect on the CHF Limit.

$$F_{L_b}(L_b,\theta) = \exp\left[0.8\ L_b^{1/2}(\sin\theta)^{1/3}\right] \tag{27}$$

Results are shown in Figure 6. Even though L_b varies by four orders of magnitude, the spatial variation function varies less than ± 5%. A least-square fit gives

$$F_\theta(\theta) = 0.0473\ (1 + 1.78\,\theta - 0.51\,\theta^2) \tag{28}$$

where θ is in radians.

From equations (10) and (23), the local critical heat flux, $(q''_{CHF})_{SAT}$, for saturated boiling can be written as the product of three functional groups. This is

$$(q''_{CHF})_{SAT} = F_p(P)\ F_{Lb}(L_b,\theta)\ F_\theta(\theta) \tag{29}$$

where $F_p(P)$ is the property or pressure function given by

$$F_p(P) = \rho_g\, h_{fg}\left[\frac{\sigma g(\rho_\ell - \rho_g)}{\rho_g^{\,2}}\right]^{1/4}\left(1+\frac{\rho_g}{\rho_\ell}\right)^{1/3} \tag{30}$$

The value of F_p depends on the fluid properties. For a given fluid, F_p would vary with the system pressure. From equations (27) to (30), it can be seen that the local critical heat flux is a strong function of the vessel size for L_b on the order of 0.1 or higher. For vessels much larger than the characteristic vapor mass (i.e., for L_b on the order of 0.01 or smaller), the local critical heat flux is a weak function of the vessel size. To demonstrate this point, the scaling law given by equation (29) is compared with the experimental data of Cheung and Haddad (1994, 1995), Haddad, Liu and Cheung (1995), and Theofanous et al. (1994) in Figure 7. The heating surface employed in the work of Theofanous et al. was an order of magnitude larger than the heating surface employed in the work of Cheung and Haddad. However, all CHF data shown in the figure compare reasonably well with the scaling law. The relatively large differences between the ULPU natural convection boiling data and the spatial variation function is believed to be due to the effect of subcooling associated with the liquid head that was present in the experiments performed by Theofanous et al. This point will be further discussed in the next section.

Subcooled Boiling Conditions

It is widely recognized that subcooling enhances the critical heat flux limit (Katto 1985, Carey 1992). For pool boiling, the effect of subcooling can be represented as a linear function of the Jakob number, Ja, as

$$q''_{CHF} = (1 + b\ Ja)(q''_{CHF})_{SAT} \tag{31}$$

where q''_{CHF} is the local critical heat flux under subcooled boiling conditions and b is a proportionality constant. The Jakob number is simply the sensible-to-latent heat ratio defined by

$$\mathrm{Ja} = C_p \Delta T_{sub} / h_{fg} \tag{32}$$

where C_p is the specific heat of the liquid and ΔT_{sub} the degree of subcooling. From the CHF data of Cheung and Haddad (1994, 1995), the constant b is found to be 19.25. Results are shown in Figure 8, where except one data point at $\mathrm{Ja} = 1.87 \times 10^{-2}$, all the saturated and subcooled data obtained at different spatial locations can be correlated nicely by equation (31) with $b = 19.25$. For given fluid and vessel size, the CHF data when accounted for the subcooling effect, is practically a function of θ only, as demonstrated in the figure.

From equations (27) to (31), a generalized scaling law can be obtained. The local critical heat flux on the outer surface of a hemispherical vessel can be expressed by the product of four functional groups. This is

$$q''_{CHF} = F_p(P)\, F_{L_b}(L_b, \theta)\, F_{Ja}(\mathrm{Ja})\, F_\theta(\theta) \tag{33}$$

where F_p, F_{L_b} and F_θ are given respectively by equations (30), (27), and (28), and F_{Ja} is the correction factor given by

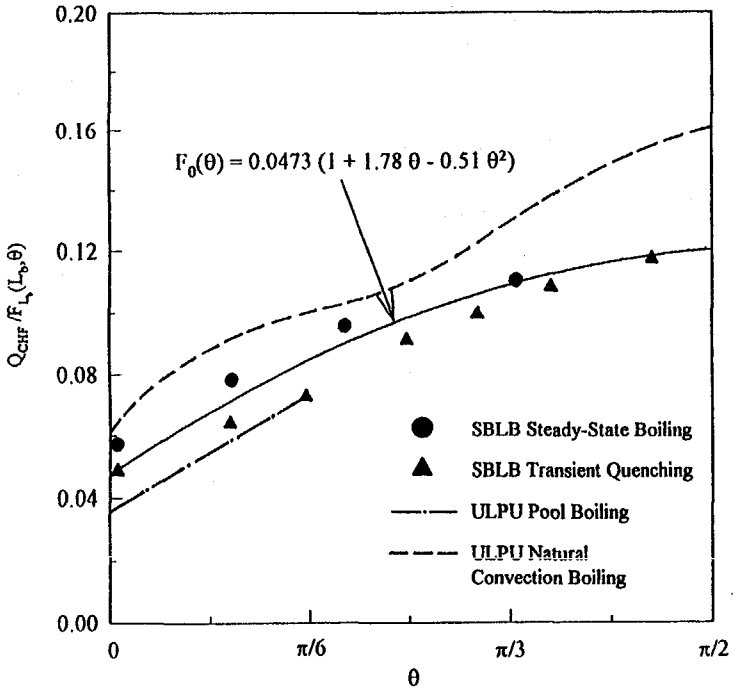

Figure 7. Comparison of the Scaling Law for Saturated Boiling with CHF Data.

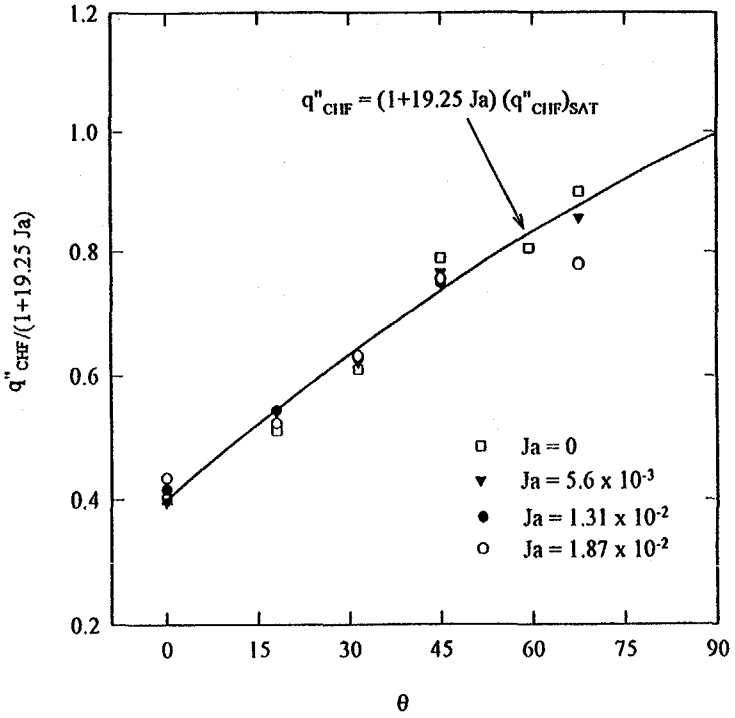

Figure 8. Experimental Data Showing the Effect of Subcooling on the Local Critical Heat Flux.

$$F_{Ja}(Ja) = 1 + 19.25\,Ja \tag{34}$$

The generalized scaling law, which accounts for the effects of the size of the vessel, the level of vessel subcooling, the intrinsic properties of the fluid, and the spatial variation of the local critical heat flux, is applicable to both saturated and subcooled boiling conditions.

Equation (33) is compared with the experimental data of Cheung and Haddad (1994, 1995), Haddad, Liu and Cheung (1995), and Theofanous et al. (1994) in Figure 9. In preparing this figure, the ULPU natural convection data have been corrected for the effect of liquid head by use of the property variation function, F_p, and the correction factor for subcooling, F_{Ja}. By accounting for the liquid head that was present in the experiments performed by Theofanous et al. (1994), the relatively large difference between the ULPU natural convection boiling data and the spatial variation function shown in Figure 7 disappear. The generalized scaling law given by equation (33) tends to merge, within the experimental uncertainties, all the available local CHF data obtained for various vessel sizes under both saturated and subcooled boiling conditions into a single curve.

APPLICATIONS TO COMMERCIAL-SIZE VESSELS

Figure 10 shows schematically a large commercial-size hemispherical vessel submerged in a flooded cavity. The water level, H, is measured from the external bottom center of the vessel. The local liquid head, L, at a given angular position on the hemispherical heating surface is given by

$$L = H - R(1-\cos\theta) \quad \text{or} \quad L = H\left[1 - \frac{R}{H}(1-\cos\theta)\right] \tag{35}$$

where R is the radius of the vessel. It follows that the difference between the local water pressure at θ and the system pressure above the water surface is

$$\Delta P = \rho_f g H\left[1 - \frac{R}{H}(1-\cos\theta)\right] \quad \text{for} \quad 0 \le \theta \le \pi/2 \tag{36}$$

Because of this pressure difference, the water on the hemispherical heating surface is always subcooled. This is true even though the water temperature is at the saturation temperature corresponding to the system pressure at the free surface. In addition to the subcooling, the pressure difference also affect the local fluid properties. Thus the values of F_p and F_{Ja} are dependent on the local liquid level, L, which in turn is a function of the liquid head, H, the length ratio, H/R, and the angular position, θ, as given by equation (35).

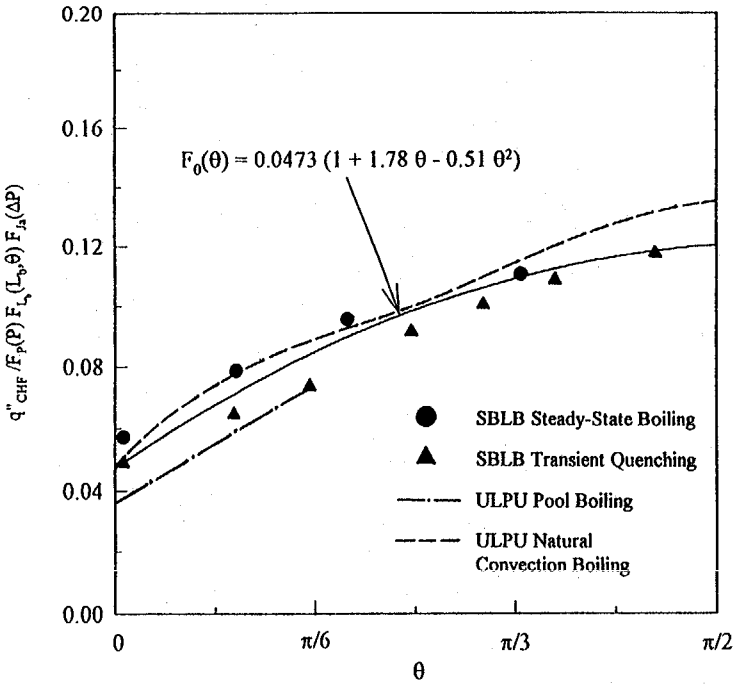

Figure 9. Comparison of the Scaling Law for Subcooled Boiling with CHF Data.

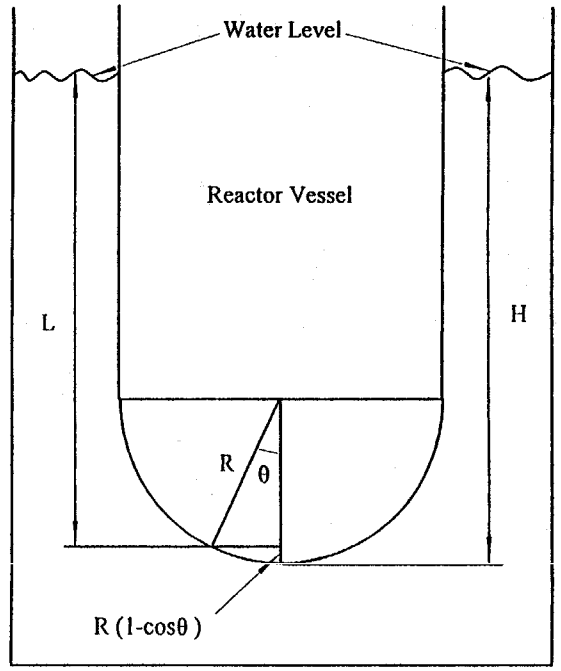

Figure 10. Schematic of a Hemispherical Reactor Vessel in a Flood Cavity.

To provide an example for application of the present scaling law, the water temperature is assumed to be at the saturation temperature corresponding to the system pressure above the water surface. Two saturation temperatures are considered. These are 373K and 393K, corresponding approximately to a system pressure of one and two atmospheres, respectively. At the saturation temperature of T_{sat} = 373K, the degree of subcooling due to the local liquid head can be determined from equation (36) along with the property of saturated water. This is

$$\Delta T_{sub} = 2.54H\left[1-\frac{R}{H}(1-\cos\theta)\right]\left\{1-0.0192H\left[1-\frac{R}{H}(1-\cos\theta)\right]\right\} \tag{37}$$

where H is in meter. From equations (32) and (34), the correction factor for subcooling is given by

$$F_{Ja} = 1+0.0914H\left[1-\frac{R}{H}(1-\cos\theta)\right]\left\{1-0.0192H\left[1-\frac{R}{H}(1-\cos\theta)\right]\right\} \tag{38}$$

Similarly, at the saturation temperature of T_{sat} = 393K, the correction factor for subcooling is given by

$$F_{Ja} = 1+0.056H\left[1-\frac{R}{H}(1-\cos\theta)\right]\left\{1-0.0139H\left[1-\frac{R}{H}(1-\cos\theta)\right]\right\} \tag{39}$$

Calculations of the local critical heat fluxes have been made for vessels having diameters of 3m, 4m, and 6m with water levels varying from $H = R$ to $H = 3R$. Results are shown in Figures 11 to 14. The baseline case under consideration is shown in Figure 11 where R = 2m and T_{sat} = 373K. The dashed line corresponds to the value of q''_{CHF} given by equation (29), which is located below all the solid lines. Evidently, the presence of subcooling due to the liquid head always results in a higher local critical heat flux. The largest increase in q''_{CHF} occurs at the upper edge of the vessel. For a given θ, the local CHF limit increases appreciably as the liquid head is increased.

The calculated critical heat flux variations for the cases of R = 1.5m and R = 3m are shown in Figures 12 and 13 respectively, with T_{sat} being fixed at 373. Again, the dashed lines represent the saturated values given by equation (29), which are always located below the solid lines for subcooled boiling. Comparing to the baseline case (Figure 11), the positions of the three solid lines shown in Figure 12 are relatively lower whereas those in Figure 13 are relatively higher. These differences in the position are due to the subcooling effect associated with the liquid head. Whereas the total liquid head varies from 1.5 to 4.5m in Figure 12, it varies from 3 to 9m in Figure 13. As a result, much higher values of q''_{CHF} are obtained for the case shown in Figure 13.

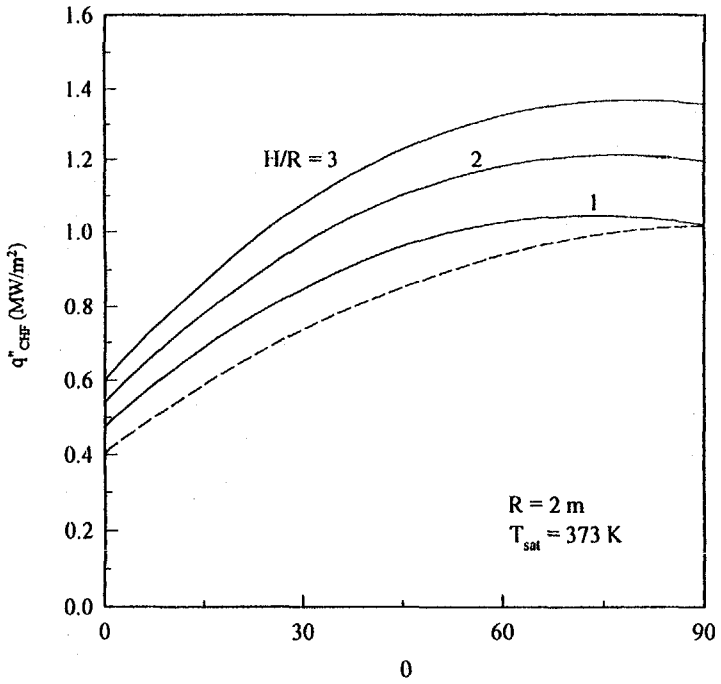

Figure 11. Application of the CHF Scaling Law: Baseline Case (R = 2 m, P ~ 1 atm).

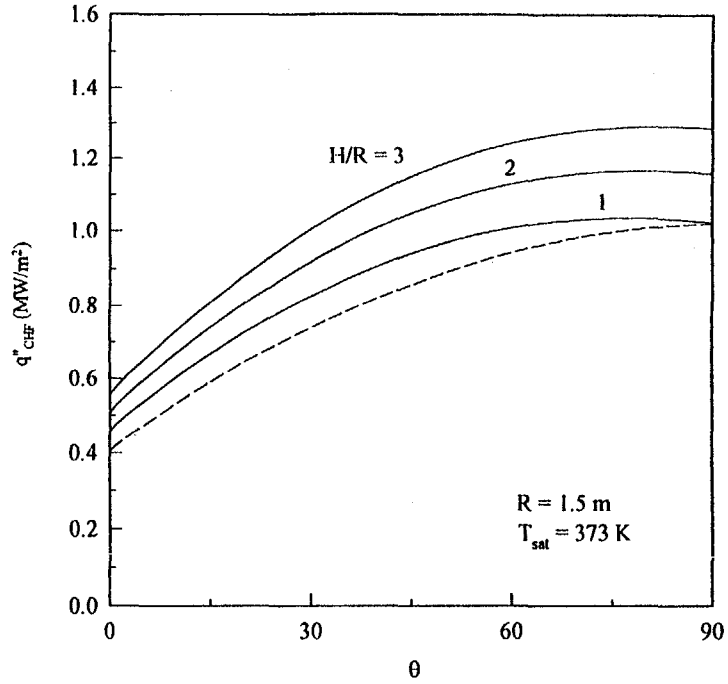

Figure 12. Application of the CHF Scaling Law: Smaller Vessel (R = 1.5 m, P ~ 1 atm).

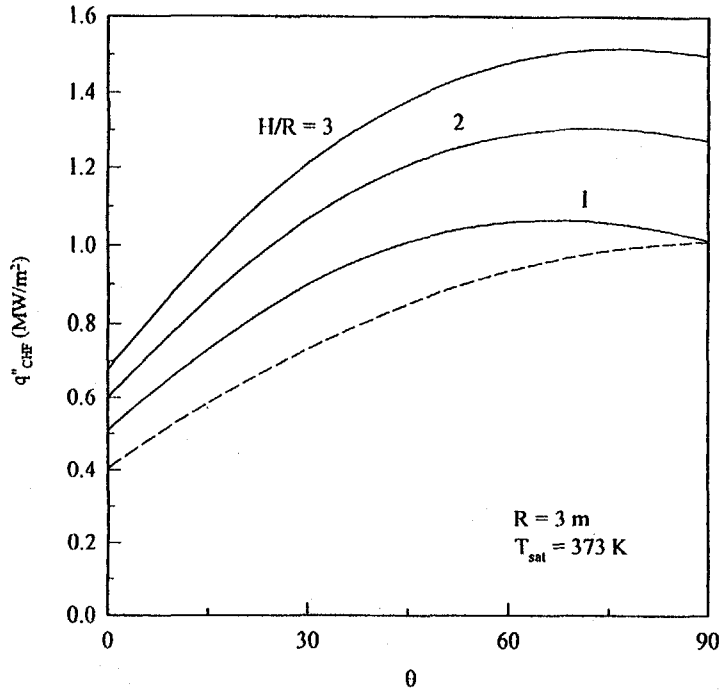

Figure 13. Application of the CHF Scaling Law: Larger Vessel (R = 3 m, P ~ 1 atm).

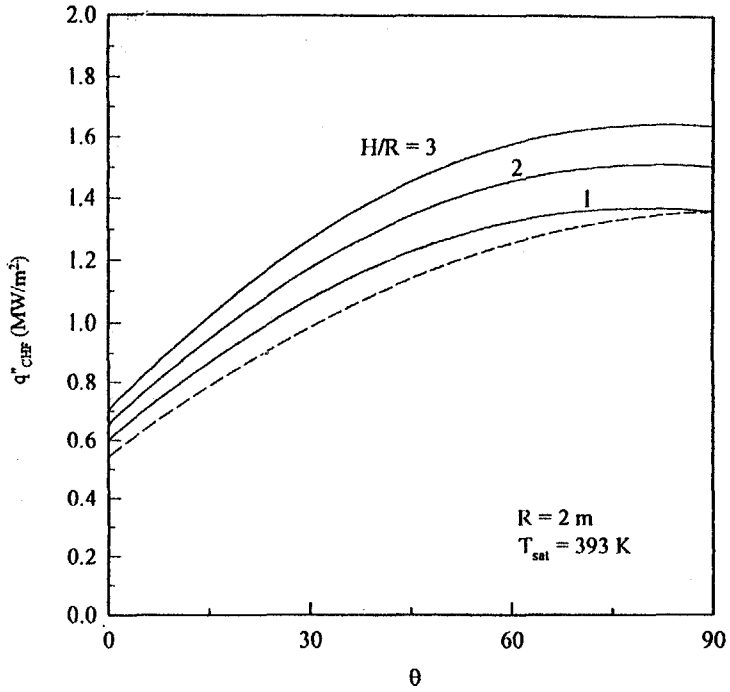

Figure 14. Application of the CHF Scaling Law: Higher Pressure (R = 2 m, P ~ 2 atm).

The effect of system pressure can be seen by comparing the critical heat flux variations shown in Figure 14 with those shown in Figure 11 for the baseline case. In both figures, the vessel size and the water levels are the same. The only difference is the system pressure or, equivalently, the saturation temperature at the free surface of the flooded cavity. For all values of θ and H/R, a high local critical heat flux is obtained as the system pressure is increased, i.e., as the saturation temperature is increased from 373K to 393K. Thus both the system pressure and the local liquid head need to be taken into account in estimating the spatial variation of the CHF limit.

CONCLUSIONS

A CHF scaling law has been developed for saturated and subcooled pool boiling on the outer surface of a heated hemispherical vessel. The scaling law represents the first attempt to estimate theoretically the spatial variation of the critical heat flux and the vessel size effect in pool boiling. Based upon the results of this study, the following conclusions can be made:

1. For hemispherical vessels with diameters considerably larger than the characteristic bubble size (i.e., for small values of L_b), both the local liquid supply rate and the local boundary layer thickness are approximately proportional to the square root of the vessel diameter. Since the critical heat flux depends only on the ratio of the liquid supply rate to the boundary layer thickness, the size effect tends to cancel out altogether. As a result, the critical heat flux for large vessels is almost independent of the physical size of the vessel.

2. For all vessel sizes, there is a significant spatial variation of the CHF from the bottom center to the upper edge of the vessel. However, when the subcooling effect associated with the local liquid head is accounted for separately, the local CHF is almost independent of the vessel size for vessels considerably larger than the characteristic size of the vapor masses.

3. One salient feature of the present problem is the formation of an external buoyancy-driven two-phase liquid/vapor boundary layer flow on the heating surface. Because of the two-phase boundary layer, the local rate of liquid supply increases significantly from the bottom center to the upper edge of the vessel, thus greatly enhancing the local CHF limit. This provides a physical explanation for the large spatial variation of the critical heat flux observed experimentally by Theofanous et al. (1994), Cheung and Haddad (1994, 1995) and Haddad, Liu and Cheung (1995). Evidently, for downward facing surfaces, the critical heat flux cannot be assumed uniform over the entire heating surface.

4. Based upon the scaling law developed in this work, it is possible to merge, within the experimental uncertainties, all the available local CHF data obtained for various vessel sizes under both saturated and subcooled boiling conditions into a single curve.

5. The present scaling law, which accounts for the effects of vessel size, the level of liquid subcooling, the intrinsic properties of the fluid, and the spatial variation of the local critical heat flux, can be used to predict the local CHF limits on large commercial-size vessels.

ACKNOWLEDGMENT

This work was sponsored by the U.S. Nuclear Regulatory Commission under Contract No. NRC-04-93-061.

REFERENCES

Carey, V. P., Liquid-Vapor Phase Change Phenomenon, Hemisphere Publishing Corporation (1992).

Cheung, F. B. and Epstein, M., "Two-phase Gas Bubble-Liquid Boundary Layer Flow Along Vertical and Inclined Surfaces," *Nuclear Engineering and Design,* **99**, 93-100 (1987).

Cheung, F. B. and Haddad, K. H., "Observation of the Dynamic Behavior of the Two-Phase Boundary Layers in the SBLB Experiments," *Proceedings 22nd Water Reactor Safety Meeting,* Washington, D.C., Vol. 2, 87-112 (1994).

Cheung, F. B. and Haddad, K. H., "Steady-State Observations of Critical Heat Flux Phenomenon on a Downward Facing Hemispherical Surface," *Proceedings 23rd Water Reactor Safety Meeting,* Washington, D.C. (1995).

Cheung, F. B. and Haddad, K. H., "A Hydrodynamic Critical Heat Flux Model for Saturated Pool Boiling on a Downward Facing Curved Heating Surface," *Int. J. Heat Mass Transfer,* 1996 (in press).

Chu, T. Y., Bentz, J. H. and Simpson, R. B., "Observation of the Boiling Process from a Large Downward Facing Torispherical Surface," *Proceedings 30th National Heat Transfer Conference* (1995).

El-Genk, M. S. and Glebov, A. G., "Transient Pool Boiling from Downward Facing Curved Surfaces," *Int. J. Heat Mass Transfer,* **38**, 2209-2224 (1995).

Haddad, K. H., Liu, Y. C. and Cheung, F. B., "Spatial Variation of Critical heat Flux on a Downward Facing Hemispherical Surface," *Proceedings 30th National Heat Transfer Conference,* HTD-Vol. 316, 23-32 (1995).

Haramura Y. and Katto, Y., "A New Hydrodynamic Model of Critical Heat Flux, Applicable Widely to Both Pool and Forced Convection Boiling on Submerged Bodies in Saturated Liquids," *Int. J. Heat Mass Transfer,* **26**, 389-399 (1983).

Katto, Y., "Critical Heat Flux," *Advances in Heat Transfer,* **17**, 1-65 (1985).

Kutateladze, S. S., "On the Transition to Film Boiling under Natural Convection," *Kotloturbostroenie,* No. 3, 10-15 (1948).

Lienhard, J. H. and Dhir, V. K., "Hydrodynamic Predictions of Peak Pool-Boiling Heat Fluxes from Finite Bodies," *Trans. Am. Soc. Mech. Engrs.*, Series C., *J. Heat Transfer*, **95** 152-158 (1973).

Lienhard, J. H. and Hasan, M., "On Predicting Boiling Burnout with the Mechanical Energy Stability Criterion," *Trans. Am. Soc. Mech. Engrs.*, Series C., *J. Heat Transfer*, **101** 276-279 (1979).

Morton, B. R., "Modeling Fire Plumes," *Tenth Symp. On Combustion,* The Combustion Institute, Pittsburgh, PA, 973-986 (1965).

Theofanous, T. G., Syri, S., Salmassi, T., Kymalainen, O. and Tuomioto, H., "Critical Heat Flux through Curved Downward Facing, Thick Walls," *Nuclear Engineering and Design,* **151**, 247-258 (1994).

Wallis, G. B., One-Dimensional Two-Phase Flow, McGraw-Hill, New York (1969).

Zuber, N., "Hydrodynamics Aspects of Boiling Heat Transfer," AEC Rep., AECU-4439 (1959).

A Preliminary Assessment of the Effects of Heat Flux Distribution and Penetration on the Creep Rupture of a Reactor Vessel Lower Head

T.Y. Chu, J. Bentz, and R. Simpson
Sandia National Laboratories

R. Witt
University of Wisconsin

Abstract

The objective of the Lower Head Failure (LHF) Experiment Program is to experimentally investigate and characterize the failure of the reactor vessel lower head due to thermal and pressure loads under severe accident conditions. The experiment is performed using 1/5-scale models of a typical PWR pressure vessel. Experiments are performed for various internal pressure and imposed heat flux distributions with and without instrumentation guide tube penetrations. The experimental program is complemented by a modest modeling program based on the application of vessel creep rupture codes developed in the TMI Vessel Investigation Project.

The first three experiments under the LHF program investigated the creep rupture of simulated reactor pressure vessels without penetrations. The heat flux distributions for the three experiments are uniform (LHF-1), center-peaked (LHF-2), and side-peaked (LHF-3), respectively. For all the experiments, appreciable vessel deformation was observed to initiate at vessel wall temperatures above 900K and the vessel typically failed at approximately 1000K. The size of failure was always observed to be smaller than the heated region. For experiments with non-uniform heat flux distributions, failure typically occurs in the region of peak temperature. A brief discussion of the effect of penetration is also presented.

1. INTRODUCTION AND BACKGROUND

In the event of a core meltdown accident, the lower head of the reactor pressure vessel can be subject to significant thermal and pressure loads. As a consequence, the possibility exists that the lower head will fail due to creep rupture. The mode, timing, and size of lower head failure is of prime importance in the assessment of a core meltdown accident because it defines the initial conditions of all ex-vessel events such as coremelt/basemat interaction, fuel/coolant interaction, and direct containment heating. On the other hand, recent studies indicate that the deformation of a reactor vessel lower head due to creep may be a precursor to water ingression between the melt mass and the vessel wall, leading to the possibility of in-vessel core retention without external cooling.

Both processes, creep rupture and water ingression, are prominent in the assessment of the TMI-II accident (Stickler et al., 1993). The TMI-II accident involved the relocation of

molten core material into the lower head of the reactor pressure vessel. The RCS and RPV were largely reflooded with water at the time of melt relocation in the lower plenum. Despite the presence of water, the lower head reached temperatures of ~1300K in a local hot spot at a time when the RCS was at 10 MPa. Although the TMI vessel did not fail, code analyses in support of the OECD/NEA TMI-II Vessel Investigation Project generally predicted creep rupture for these conditions. This fueled speculation that there might be some inherent mechanism, not previously recognized, that could delay or prevent lower head failure. The most widely held belief is that the relocated melt did not adhere to the lower head; consequently, there should be gaps between the inside surface of the vessel and the relocated melt. These gaps, perhaps widened by temperature-induced creep of the lower head, provide a channel for water intrusion and subsequent quenching of the head preventing its creep rupture. OECD/NEA concluded from metallurgical examinations that the 1300K hot spot suddenly quenched at the rate of ~10 - 100 K/s, which seems to support this hypothesis.

Therefore, from both accident assessment and accident mitigation considerations, there is a need to understand the mechanism of lower head creep and rupture, based on the understanding to develop the predictive capability for vessel creep deformation and failure. As a result of questions and possibilities raised by the TMI-II Vessel Integrity Program (VIP), there are currently several international activities investigating the issues of reactor vessel creep (Henry and Hammersley, 1996 and Maruyama, 1996).

2. EXPERIMENTAL APPARATUS

Our scaling analysis (Chu et al., 1995) showed that to achieve similarity between a scaled experiment and a full-scale reactor, it would be necessary to preserve the hoop stress, and the vessel temperature history. Therefore, the experiment should be geometrically scaled against a reactor pressure vessel (RPV) and the heat flux should also be scaled by the same factor to preserve the heating rate.

A schematic of the scaled experiment is shown in Figure 1 and Plate 1. The Apparatus is basically a scaled version of the lower part of a TMI-like reactor pressure vessel (RPV) without the vessel skirt, consisting of a hemispherical head made of SA533B1 steel, and a 30 cm vertical section replicating the lower part of the RPV cylindrical wall. The inner-diameter of the lower head is 0.91 m, corresponding to a geometrical scale factor of 4.85. The wall thickness is typically 30 mm. Due to the forming operation, the wall is slightly thicker at the equator.

The energy transfer to the reactor vessel from the core debris is simulated using a hemispherical heater, see Plate 2. The heater is built in three sections, each with three independently controlled heater segments, for a total of nine segments. For experiments with localized peaks "fences" made of insulation felt are used to isolate (the radiation of) the three heater sections to better achieve localized heating of the vessel bottom, as shown in Plate 2. The inner surface of the bottom head is painted with a Pyromark^{R} black for

efficient radiation absorption. The outer surface of the bottom head and the inner surfaces of the cylindrical section and the top flange are insulated. A cooling band is provided near the bottom of the cylindrical section. The pressure load is provided by a manifold of bottled argon. Typically, the pressure is maintained at a predetermined value and the vessel is heated until failure occurs. Pressure of the vessel is controlled by automatic fill and bleed valves.

Thermocouples are used to measure wall temperature and through-the-wall temperature difference. Linear displacement transducers are used to monitor the deformation of the test vessel. The shape and the local wall thickness of the vessel are measured before and after the experiment, for comparison. A grid system, made visible with punch marks on the vessel surface, is used to map local deformation as well as change in wall thickness. Locations on the hemisphere are described in terms of "longitude" and "latitude." The equator of the bottom head is defined as having 0° latitude and the bottom center of the bottom head is defined as having 90° latitude.

There are two major arrays (A and B) of thermocouples, 90° apart, to measure the interior wall temperature. There is also a matching array of exterior thermocouples for array B. The latitudinal locations of the thermocouples correspond to the center of each heater segment. Depending on the experiment, additional exterior thermocouples at several latitudes and longitudes are deployed for more complete coverage and for symmetry check. The latitude angular range of the heating zones and the corresponding zone-center thermocouple locations are summarized in the table below:

Heat Zone Range and Wall Thermocouple Locations

Heater Zone	Zone center thermocouple Latitude*	Zone Angular Range
1	90° (25mm off center)	75° - 90°
2	68°	60° - 75°
3	55°	49° - 60°
4	45°	41° - 49°
5	37°	33° - 41°
6	30°	26° - 33°
7	23°	20° - 26°
8	15°	10° - 20°
9	6°	0° - 10°

*Latitude 0^0 is equator and 90° is bottom center.

Displacement transducers are typically deployed along a chosen longitude, at typically 3-5 latitude locations. At times, at some key latitudes, transducers are deployed longitudinally, 180° apart, for symmetry check. There are two transducers at each location, one for vertical displacement, and one for horizontal displacement.

3. EXPERIMENTAL RESULTS

We have completed four experiments out of the planned eight-experiment series. The main variables are heat flux distribution, vessel pressure, and whether the vessel bottom has penetration tubes or not. The completed experiments are:

Experiment	Heat Flux Distribution	Penetration Tubes	Vessel Pressure
LHF-1	Uniform	No	10 MPa
LHF-2	Center-Peaked	No	10 MPa
LHF-3	Edge-Peaked	No	10 MPa
LHF-4	Uniform	Yes	10 MPa

The present paper will concentrate on the results of LHF-1 and LHF-2. Only qualitative discussions of the results of LHF-3 and LHF-4 will be presented.

3.1 LHF-1 Experiment - Uniform Heating and No Penetrations

Initially, the test vessel was pressurized to 4.8 MPa (700 psi). The vessel pressure increased as the vessel and gas temperature increased. The test vessel pressure was controlled such that the final test pressure of 10 MPa was reached at or before 800K, a temperature where the vessel material begins to show some decrease in strength. The heating of the lower 70° (latitude 20° to 90°) of the vessel wall was controlled according to a ramp rate corresponding to the desired heat flux. The upper two heater segments were controlled to give a smooth transition of the wall temperature between the heated section of the vessel wall and the cooling band.

Representative temperature histories of the vessel wall are shown in Figure 2, for latitude locations, 30°, 60°, and 90° (bottom center). The initial ramp rate corresponds to approximately 40kW/m^2. Due to increased heat loss at higher temperatures, the ramp rate between 800K and 1000K corresponds to a heat flux of approximately 10 kW/m^2. The vessel pressure history is shown in Figure 3. The test pressure of 10 MPa is reached at 95 minutes into the test.

Creeping of the test vessel, as recorded by displacement transducers, is shown in Figure 3. Significant increase of the creep rate is observed to occur at about 120 minutes into the test; the corresponding wall temperature is at approximately 930K. As the wall temperature increases, the creep rate continued to increase. The vessel failed catastrophically at 145 minutes into the test; the vessel temperature at the time of failure was 1011K. The recorded displacement at vessel bottom center at the time of failure was 0.12 m.

Plates 3A through 3D are posttest photographs of the test vessel; the angle designation corresponds to the longitude angle of the line of sight. For example, Plate 3A has a line of sight of 270°; therefore, it shows the vessel profile in the 180°/0° plane. As shown in Plate 3A, the vessel failed non-symmetrically with respect to the 90°/270° plane. The 180°

longitude (left side) profile shows more deformation than the 0° profile. The deformation is relatively symmetrical with respect to the 0°/180° plane. The shape of the failure, Plates 3C and 3D, is approximately oval, measuring 0.49 m by 0.25 m. The hole opening corresponds to the material bounded approximately by latitude 66° and 80°, and longitude 110° and 240° (based on the original shape of the vessel). Posttest inspection indicates that the initial failure occurs at approximately longitude 150°/latitude 66°.

The overall extension of the vessel is approximately 16 cm, corresponding to an overall strain (based on the vessel outer radius) of 33%. However, the local strain near the failure is significantly larger. The linear strain near the failure location was found to be about 200% (distance between punch grid marks increases by a factor of 3). This corresponds nicely with the thickness reduction of a factor of approximately 9 (3^2), from 29 mm to 3 mm. The wall thickness along the edge of the failure varies from 3 mm to 16.5 mm. Based on these values, the linear strain at failure varies from approximately 34% to 200%.

The pre-test and post thickness maps of the LHF-1 vessel are shown in Figures 5 and 6. Plotted are wall thickness as a function of longitude for different latitudes. Note the pre-test thickness map shows a region of reduced wall thickness between longitude 30° and 240°. This region of reduced wall thickness became exaggerated during vessel creep, see Figure 6, and resulted in the final failure between longitude 110° and 240°.

3.2 LHF-2 Experiment - Center-Peaked Heat Flux and No Penetrations

To have a common reference, the initial heating schedule for LHF-2 followed the same temperature history of LHF-1 up to 700K. Beyond 700K, heater zones 1 and 2 were operated to heat the center region at a similar rate as LHF-1, but zones 3 and 4 were operated to keep the temperature beyond zone 2 at least 100K lower than the wall temperature near the bottom center region. The rest of the heaters were controlled to provide approximately a smooth temperature variation to the cooling ring region.
The experiment was first performed on April 30, 1996. Approximately 180 minutes into the experiment, several of the heaters became inoperable. Because the experiment was well along the way, it was decided to increase the pressure to 12 MPa to effect failure of the vessel. However, with increasing pressure, the vessel was found to have developed leaks, and more heater segments became inoperable; therefore, the experiment was interrupted. The vessel was depressurized in a matter of minutes. Later inspection found that leaks had developed at the weld of two feed-throughs; also several of the SCR's had failed. The leaks and the power supplies were repaired and the experiment was brought to a successful conclusion on May 2, 1996.

Representative temperature histories of the vessel wall are shown in Figure 7; the corresponding pressure history is shown in Figure 8. For convenience, the first section (April 30) of the experiment is designated as LHF-2A and the second section (May 2) is designated as LHF-2B; the starting time of LHF-2B was arbitrarily set as 300 minutes. The initial temperature jump for LHF-2B was due to a malfunction of the heater control

for zones 1 and 2. The vessel failed approximately 210 minutes into the LHF-2B test. The wall temperature distribution, approximately 15 minutes before vessel failure, is plotted in Figure 9; also plotted is the corresponding distribution of ultimate strength. As shown in Figure 9, there is a dramatic contrast between the strength of the center region and the surrounding region. Figure 10 shows the displacement history at latitudes 45°, 60°, 70°, and 90°. As can be seen, the displacement at the center region (70°, and 90°) was larger than the surrounding region. The total displacement at the bottom center (90°) was 16.7 cm, corresponding to a total average strain (based on the radius of the vessel) of 34%, rather close to the 33% observed in LHF-1. Significant displacement occurred at approximately 125 minutes, for LHF-2A and approximately 480 minutes for LHF-2B. The corresponding wall temperature at the initiation of creep in both cases was in the range of 930-950K. The vessel temperature at failure was in the range of 1000-1025K. Both the creep initiation and the failure temperatures are consistent with the observation of LHF-1. Despite the similarity in the temperature for the onset of creep and overall strain; the failure of the LHF-2 experiments is very different from that of LHF-1.

Plates 4A and 4B show two views of the post-test LHF-2 vessel. As shown in the plates, the failure size is quite small for LHF-2. The overall profile of the posttest vessel was shaped like an inverted top half of a pear; there is an inflection point in the 60°-70° region, corresponding to the transition of the ultimate strength distribution, see Figure 9. A close-up view of the failure is shown in Plate 4C. The failure is an oval approximately 4 cm by 7 cm, substantially smaller than the 25 cm by 49 cm of the LHF-1 failure. The minimum wall thickness at failure was approximately 3 mm which is similar to that observed in LHF-1. The failure appeared to have initiated near 77° latitude and 205° longitude. The failure is bounded between 77° to 79° latitude and between 200° and 210° longitude, see Plate 4D.

The pre-test and post-test vessel wall thickness maps are shown in Figures 11 and 12. It is interesting to note, see Figure 11, that the initial wall thickness was slightly thinner in the range of 150° and 250° for latitudes 60° and 70°, although the wall thickness at 80° (near the failure location) was fairly uniform. Again, the region of reduced wall thickness became exaggerated during vessel creep, see Figure 12, and overlapped the final region of failure between 77° to 79° latitude and 200° and 210° longitude.

3.3 LHF-3 Experiment - Edge-Peaked Heat Flux and No Penetration

To have a common reference, the initial heating schedule for LHF-3 was designed to follow essentially the same temperature history of LHF-1 up to an elevated temperature short of any measurable strain (typically 700K-900K). Beyond this temperature, heater zones 5 and 6 were controlled to heat the edge region at a similar rate as LHF-1, but zones 4 and 7 were cut back to achieve edged-peaked heat flux distribution centered around 33° latitude. The remaining heaters were controlled to provide approximately a smooth temperature variation to the cooling ring region. The 33° location is the approximate coremelt level corresponding to 75% of the core of a typical PWR. The edge-peaked heat flux simulates the heat flux distribution due to coremelt convection.

LHF-3 was successfully executed. The range of failure temperature was found to be comparable to LHF-1 and LHF-2. The localization of failure near the region of peak heat flux as found in LHF-2 was also repeated in LHF-3.

3.4 LHF-4 Experiment - Uniform Heating with Penetrations

The purpose of the experiment was to examine the effect of penetrations on vessel failure. The vessel was uniformly heated. The penetration pattern was an exact scaled duplicate of the penetration pattern of a typical PWR in the region of 60° to 90° latitude (bottom center) of the lower head. The range of angular location overlaps the expected region of vessel creep for an uniformly heated lower head, based on the observations of LHF-1. The scaled Inconel penetration tube has a diameter of 8.2 mm. The largest diametrical clearance between a penetration tube and its through-hole is 0.2 mm (0.007 mils). The tube-to-wall weld only penetrates 7.6 mm (0.3 in) into the vessel wall, approximately 1/4 the total wall thickness.

The heating history of the vessel was designed to be comparable to LHF-1. The vessel pressure was 10 MPa. The creep behavior was similar to LHF-1, but the vessel failed prematurely (as compared to LHF-1) due to a failed penetration weld, slightly off bottom center. The diameter of the through-hole for the failed penetration was enlarged by approximately a factor of two. Through-holes of several neighboring penetrations also showed comparable enlargements. Detailed examination of the experiment has yet to be made.

5. MODELING RESULTS

The experimental program is complemented by a modest modeling program based on the application of vessel creep rupture codes developed in the TMI Vessel Investigation Project. The modeling effort is yet to be fully developed. We will present preliminary results for LHF-1 as an example.

The goal of the modeling effort is to specify procedures for using existing material data (Rempe, et al., 1993) to best match the experimental results over a range of experiments. Modifications were made to the TMI-2 version of simulation (Stickler, et al., 1993) in the following areas:

- modify the boundary condition at the equator to accommodate the discontinuity of stress at the transition between the cylindrical section of the test vessel and the hemispherical bottom head;
- modify the code to allow local variation of wall thickness along the meridian;
- modify the code algorithm to start the thermal activation clock for each material point as each point rises above 650K;
- implement a creep strain rate algorithm with explicit terms incorporating temperature and pressure ramp rates; and

- implement logarithmic vs. linear interpolation of TMI-2 VIP material data in temperature space.

The last item has proven to be very important in bring convergence between experiment and simulation. As shown in Figure 13, the logarithmic interpolation results in a large discrepancy between experiment and simulation whereas there is general agreement between the displacements measured in the experiment and the displacement from simulation for the linear interpolation case. The simulation was able to predict the location and timing of failure fairly well, but it underestimated the peak linear strain. We have not yet been able to justify why linear interpolation should be better.

6. CURRENT ASSESSMENTS OF THE LHF EXPERIMENTS

- Localized heating results in localized failure.
- For all experiments, the failure size is substantially smaller than the heated region.
- Temperatures for the initiation of failure and final vessel failure appear to be fairly consistent.
- The wall thickness at the failure appears to be fairly constant.
- The evidence is not very firm/complete. However, it appears that the failure location might be related to some slight variations (such as a slight reduction in wall thickness) in the manufacturing of the vessel.
- Vessel with penetration fails prematurely as a result of weld failure due to the large strain associated with the global deformation of the vessel.

ACKNOWLEDGMENTS

The authors would like to thank the Program Advisory Committee members, Robert E. Henry and Y.R. Rashid, for their insightful comments and suggestions. The authors also express their gratitude to M.M. Pilch and Ali Behbahani for their input and comments.

This work was supported by the U.S. Nuclear Regulatory Commission and was performed at Sandia National Laboratories, which is operated for the U.S. Department of Energy under Contract No. DE-AC04-94AL85000.

REFERENCES

Chu, T.Y., (1995) Letter Report: "Scaling and Design Report for Lower Head Failure Experiments," Sandia National Laboratories, Albuquerque, NM, May 1995.

Henry, R. and R. Hammersley, (1996) "A Scaling and Experimental Approach for Investigating IN-Vessel Cooling," 24th Water Reactor Safety Meeting, Bethesda, MD, Oct. 1996.

Maruyama, Y. et al., (1996) "In-Vessel Debris Coolability Experiments and analyses in ALPHA Program," 24th Water Reactor Safety Meeting, Bethesda, MD, Oct. 1996.

Rempe, J.L., G.L. Tinnes, and S.A. Chavez, (1994) "A Simpler Approach for Predicting LWR Vessel Failure During Severe Accident Conditions," Nuclear Engineering and Design, Vol. 148, pp. 365-383.

Stickler, L.A., J.L. Rempe, S.A. Chavez, G.L. Tinnes, S.D. Snow, R.J. Witt, M.L. Corradini, and J.A. Kos (1993), "Calculations to Estimate the Margin to Failure in the TMI-2 Vessel," OECD-NEA-TMI-2 Vessel Investigation Project, TMI V(93) EG01, Idaho National Engineering Laboratory, Idaho Falls, ID.

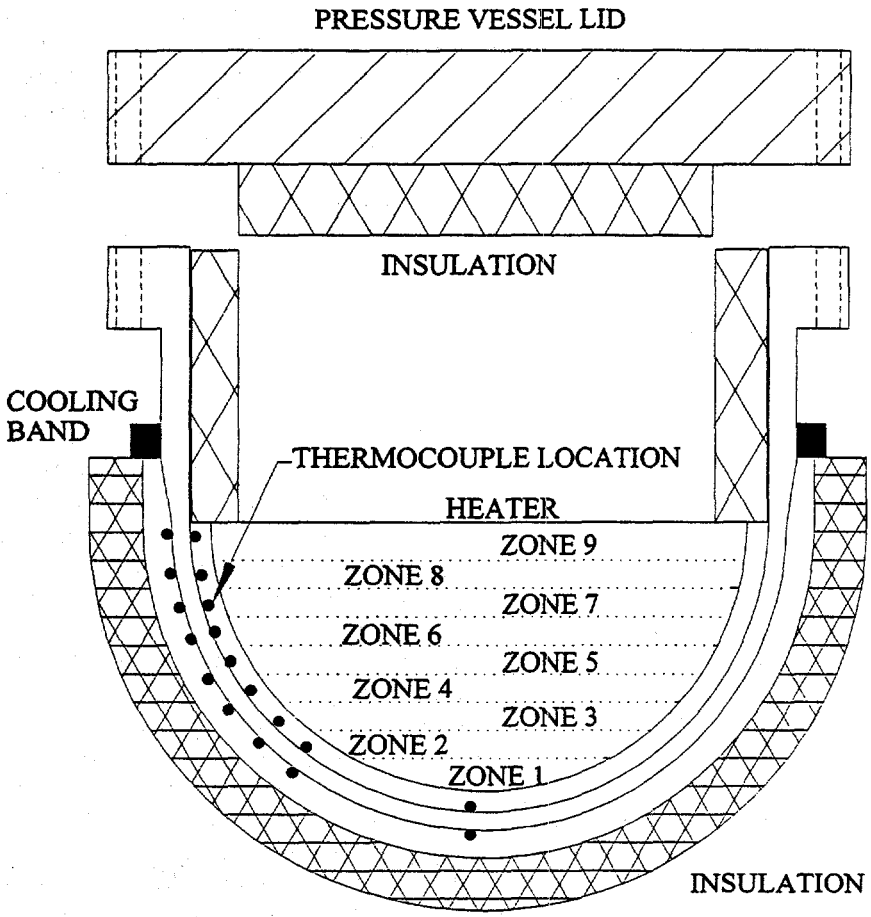

Figure 1 Schematic of LHF Test Apparatus

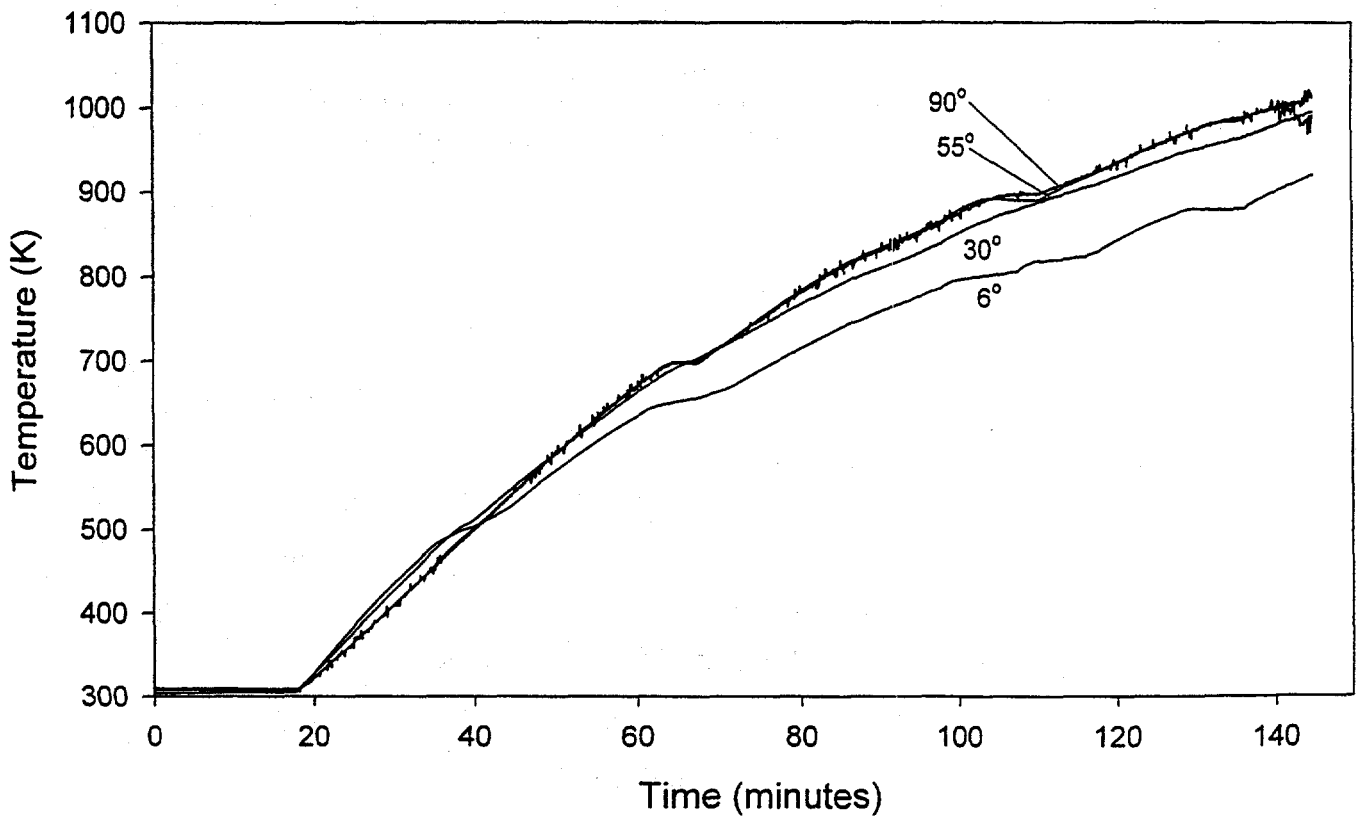

Figure 2. LHF-1 Vessel Wall Temperature

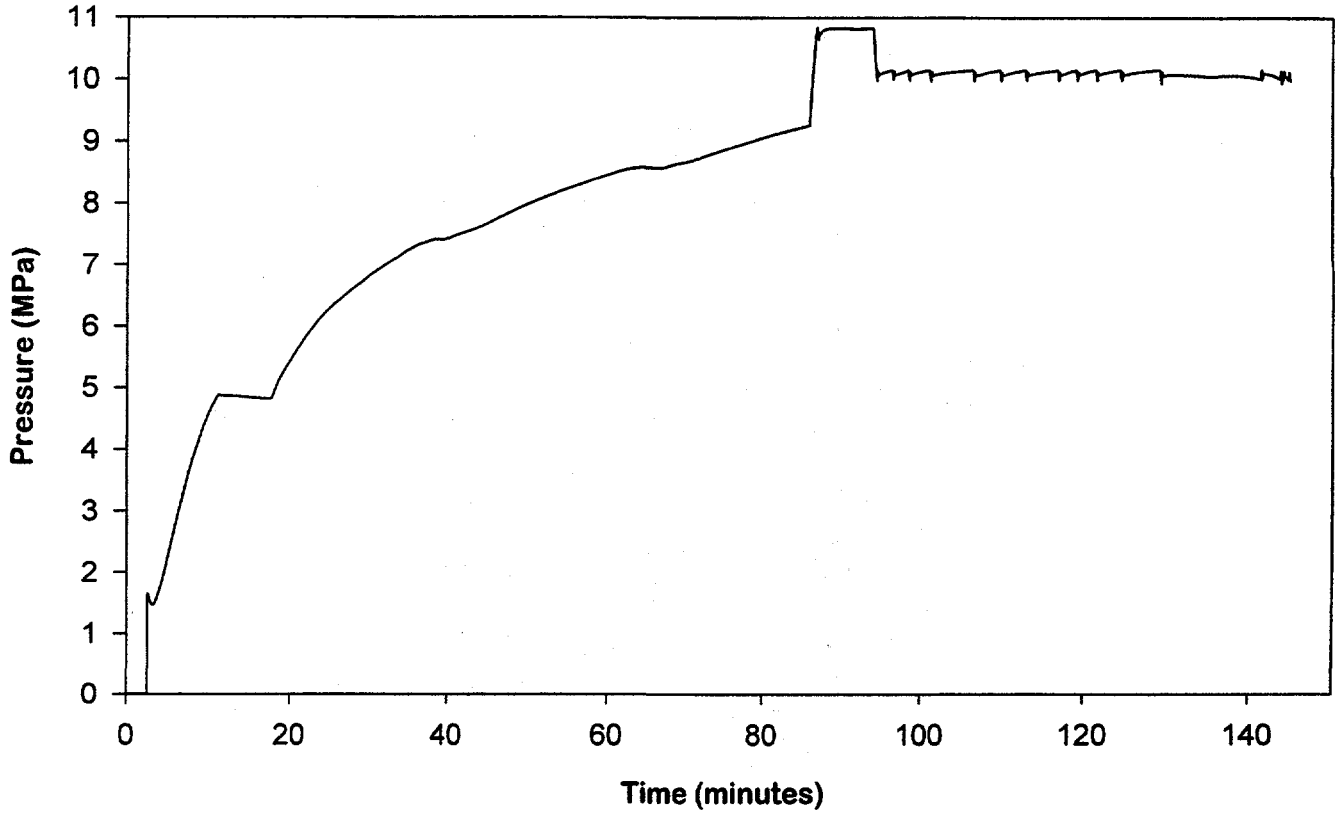

Figure 3. LHF-1 Vessel Pressure History

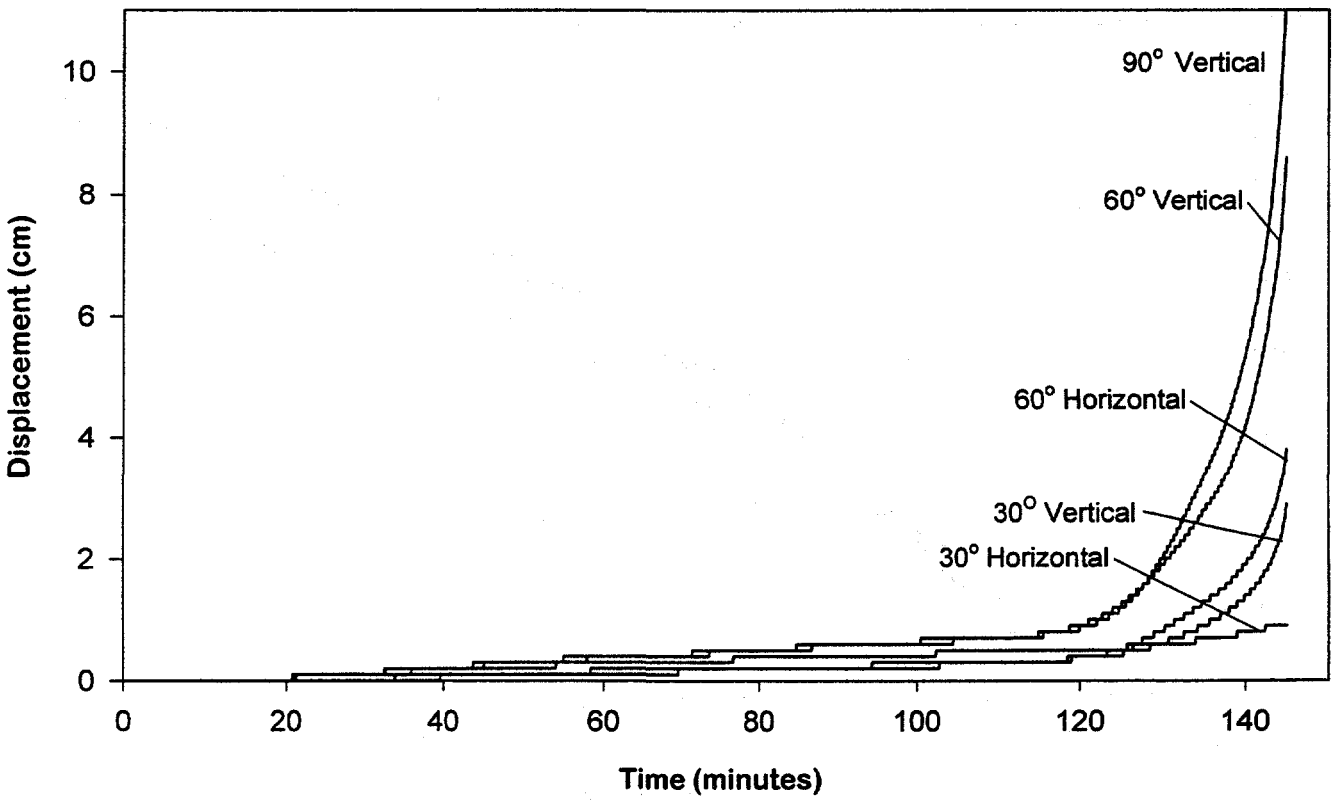

Figure 4. LHF-1 Vessel Head Displacement History

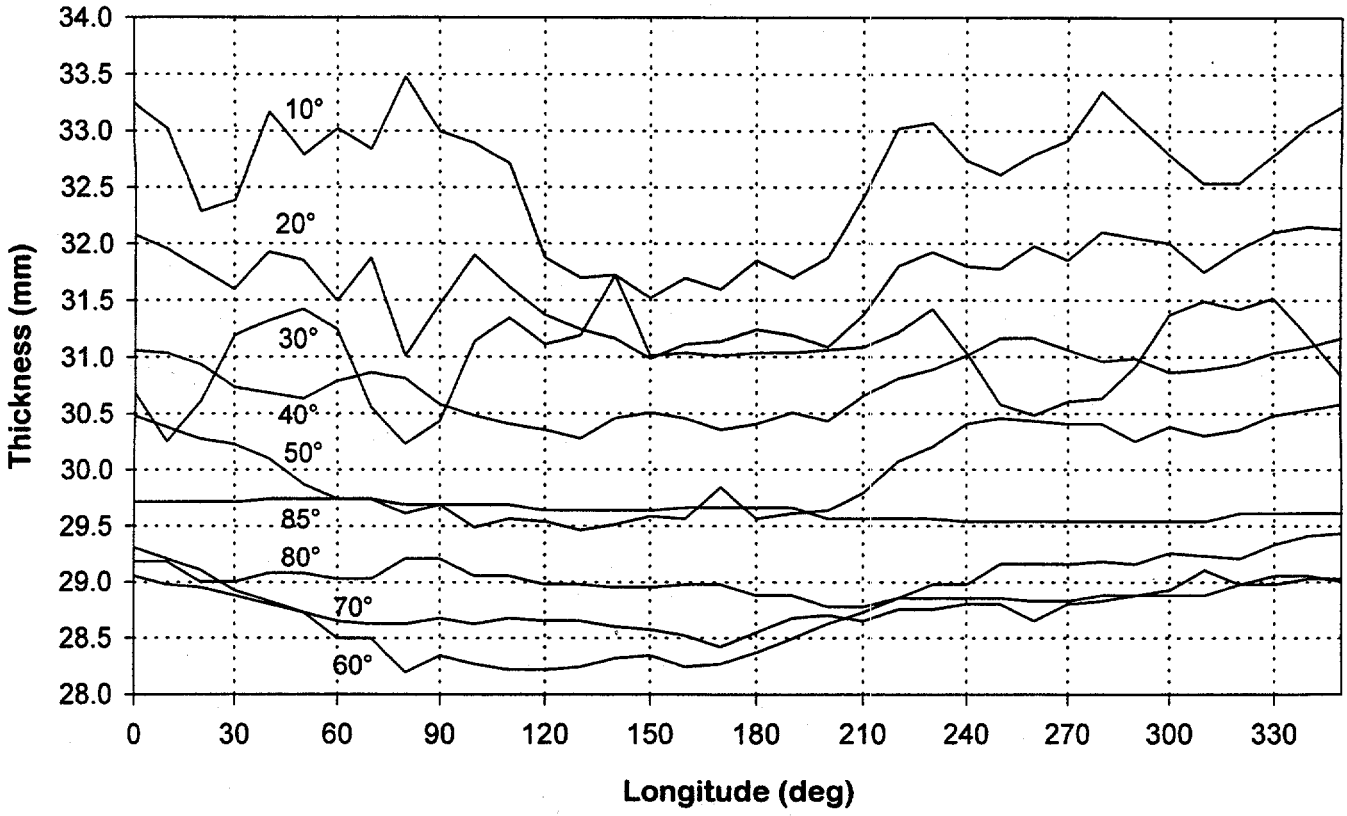

Figure 5. LHF-1 Pre-Test Thickness Map

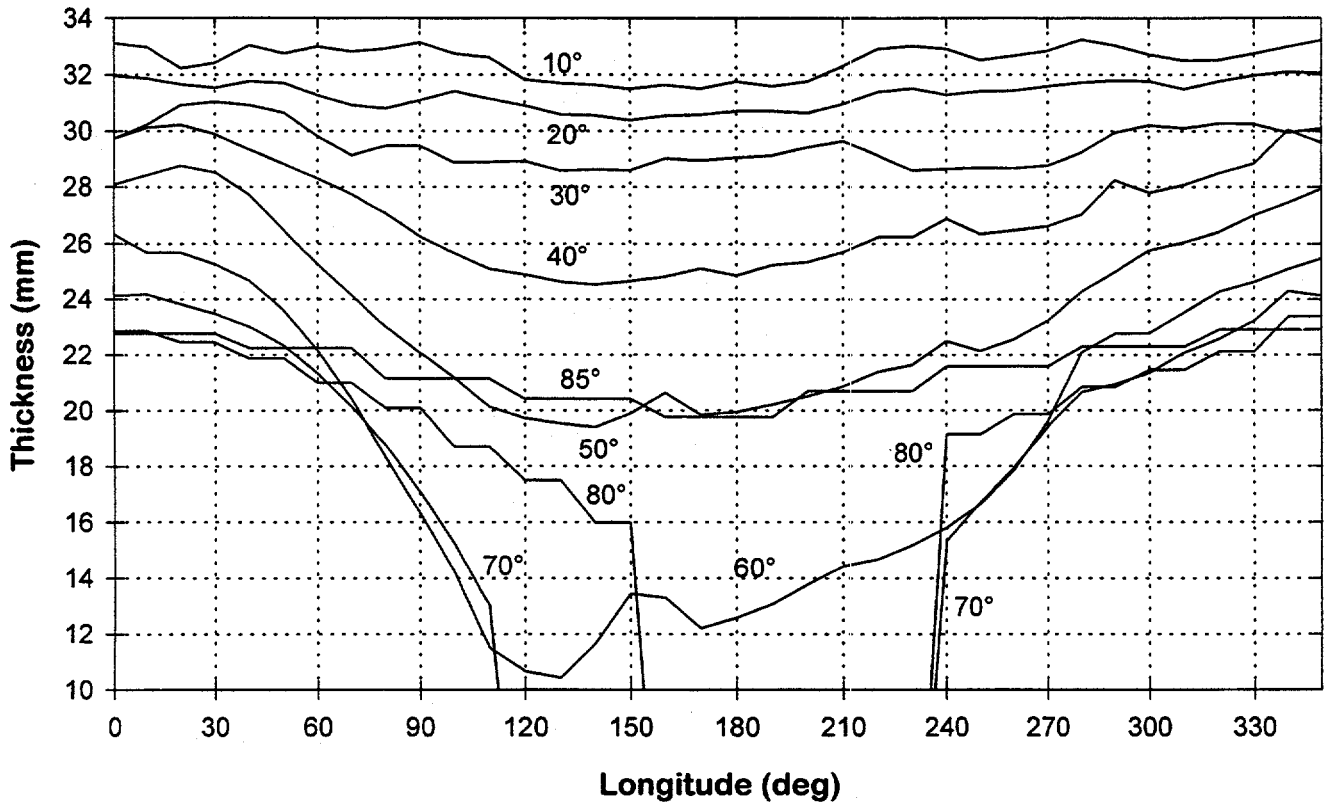

Figure 6. LHF-1 Post-Test Thickness Map

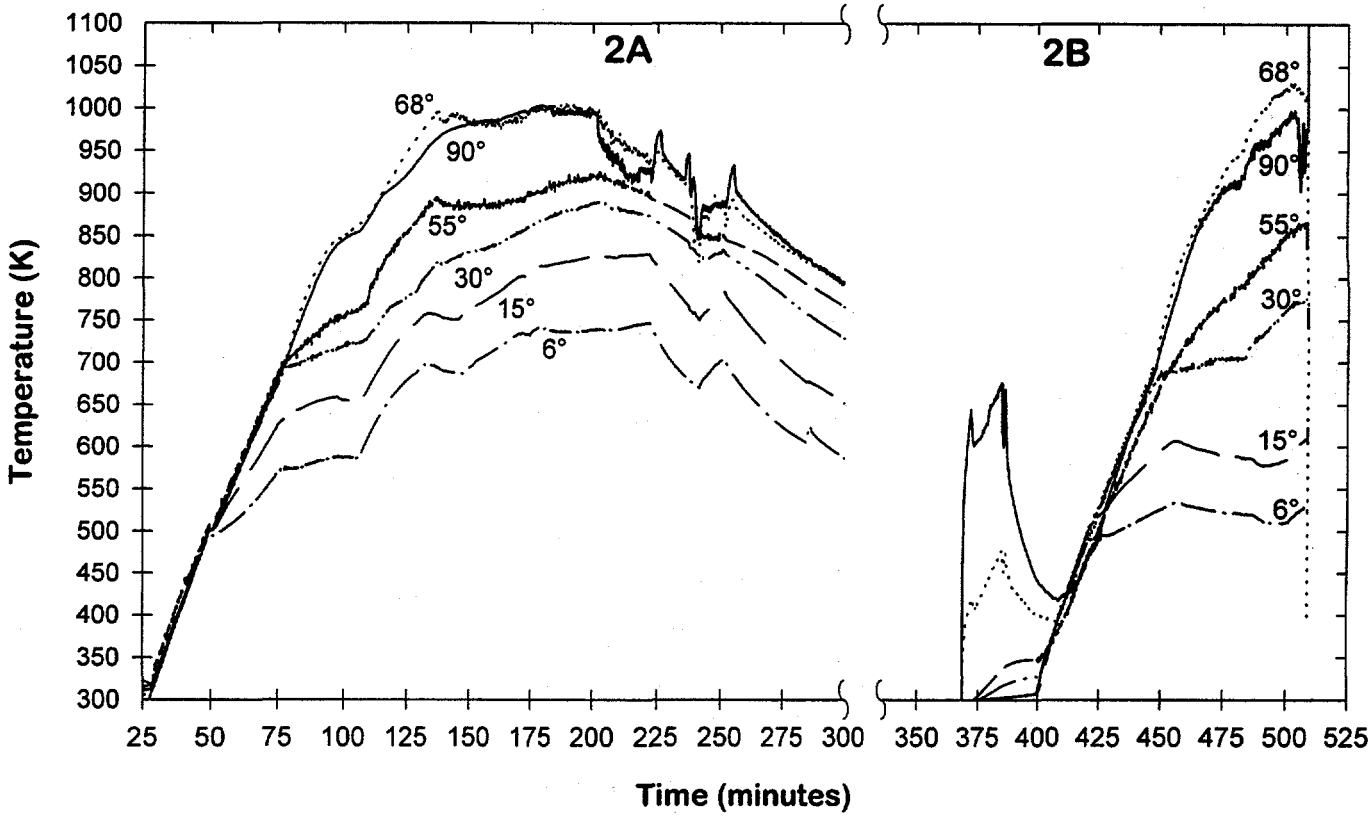

Figure 7. LHF-2 Vessel Temperature History

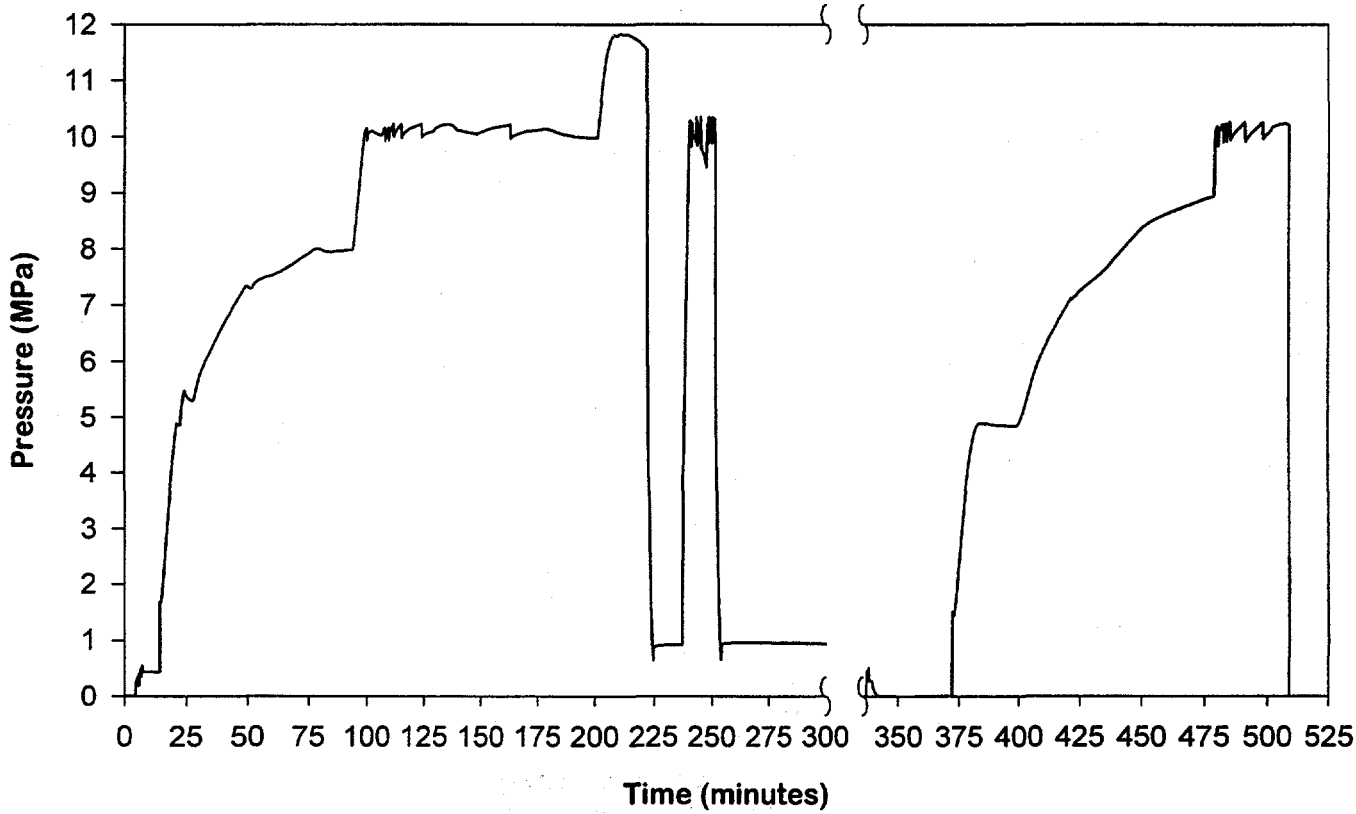

Figure 8. LHF-2 Vessel Pressure History

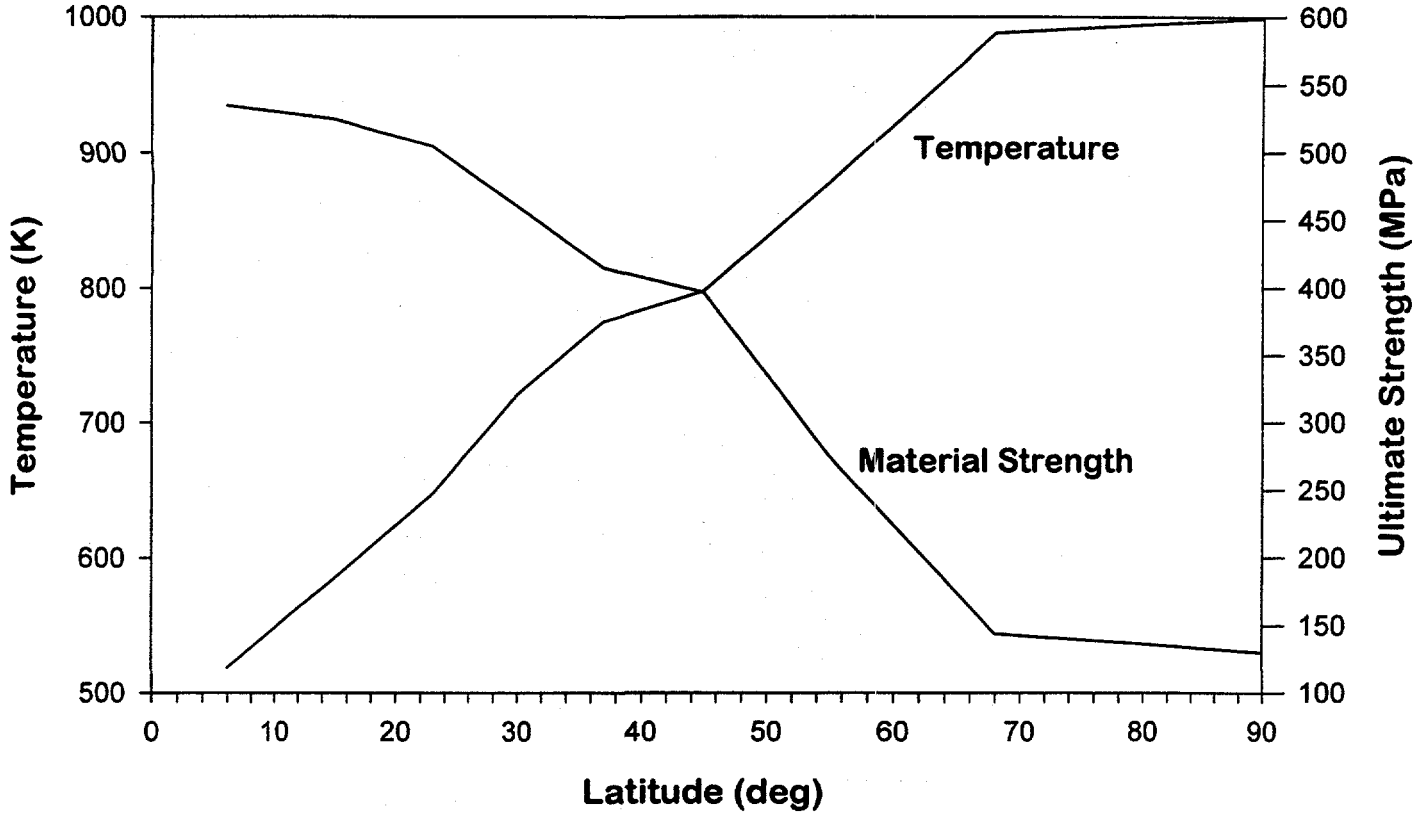

Figure 9. LHF-2 Vessel Temperature and Strength Profile

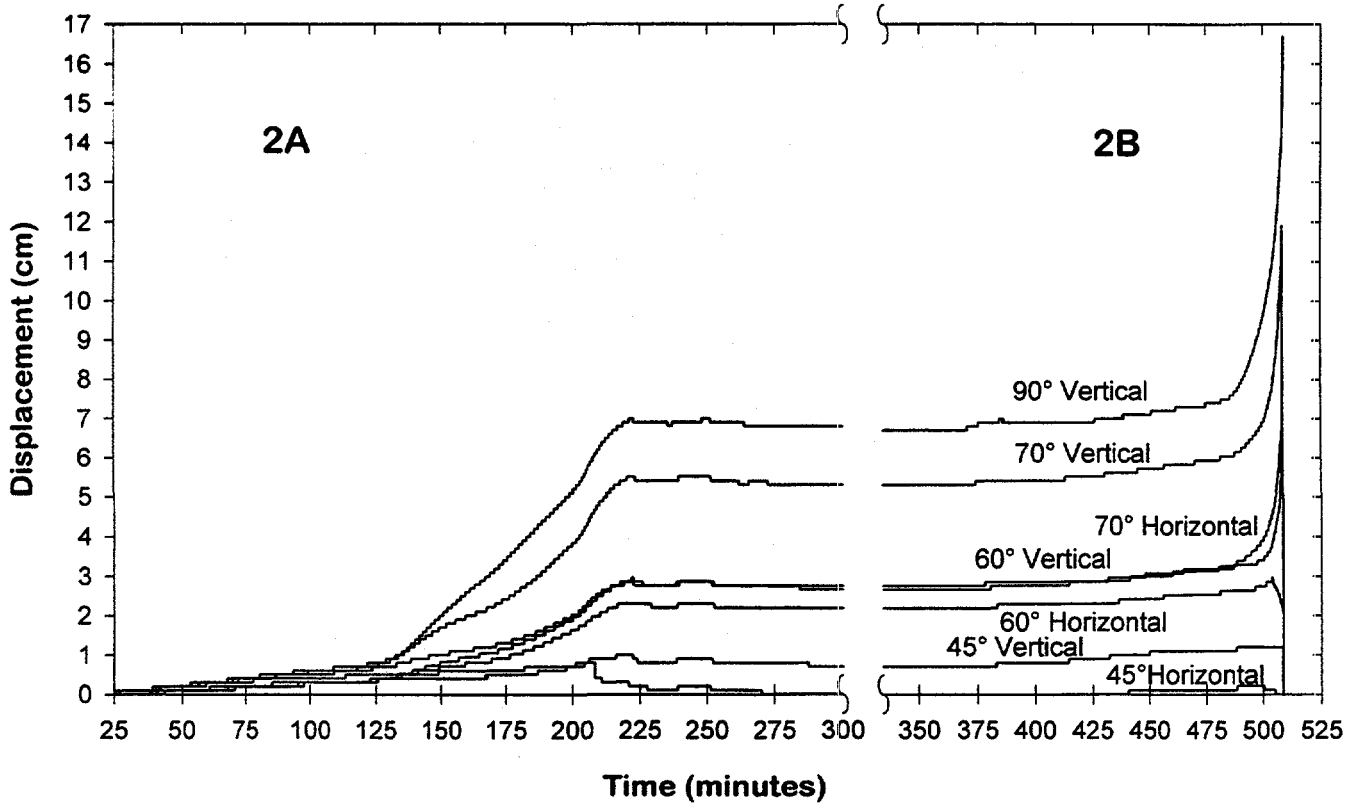

Figure 10. LHF-2 Vessel Displacement History

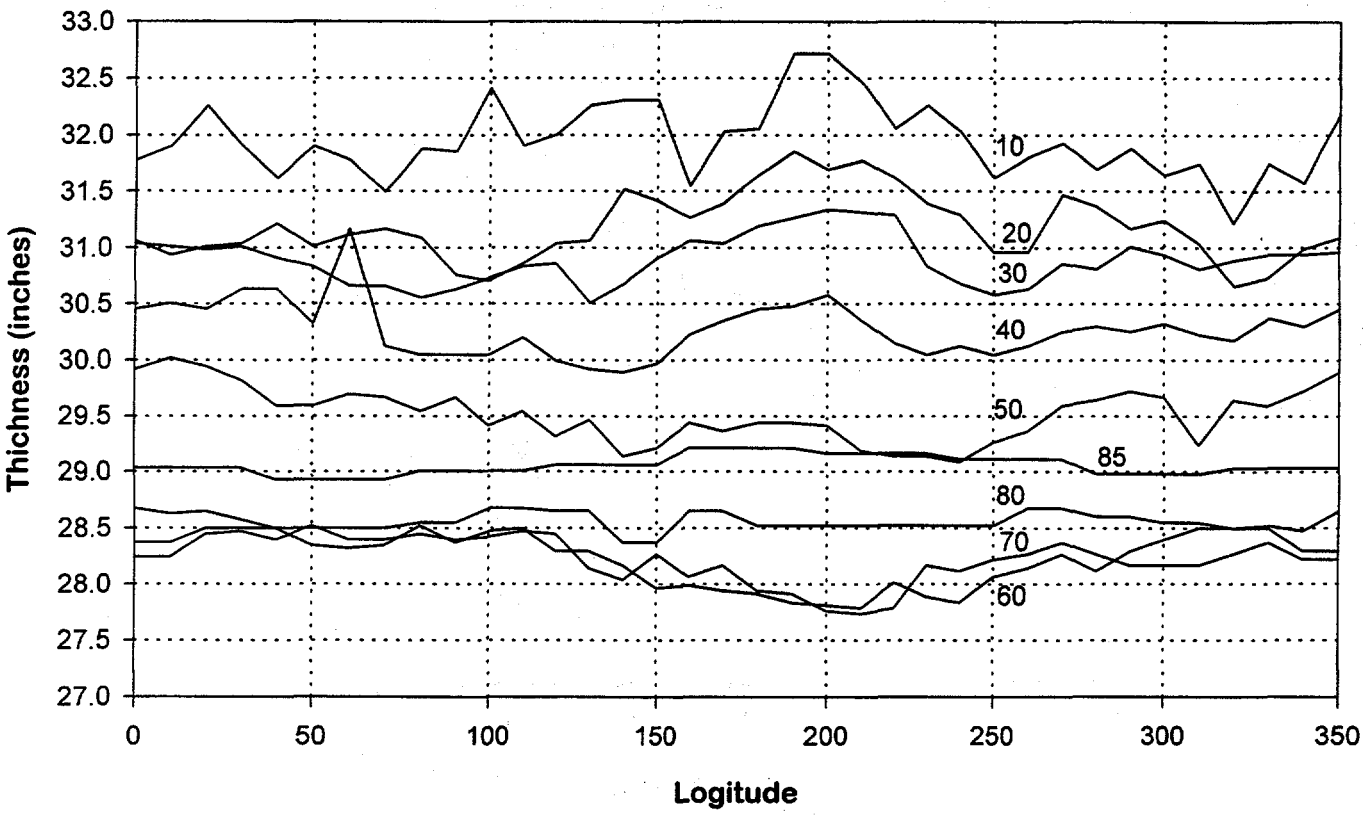

Figure 11. LHF-2 Pre-test Thickness Map

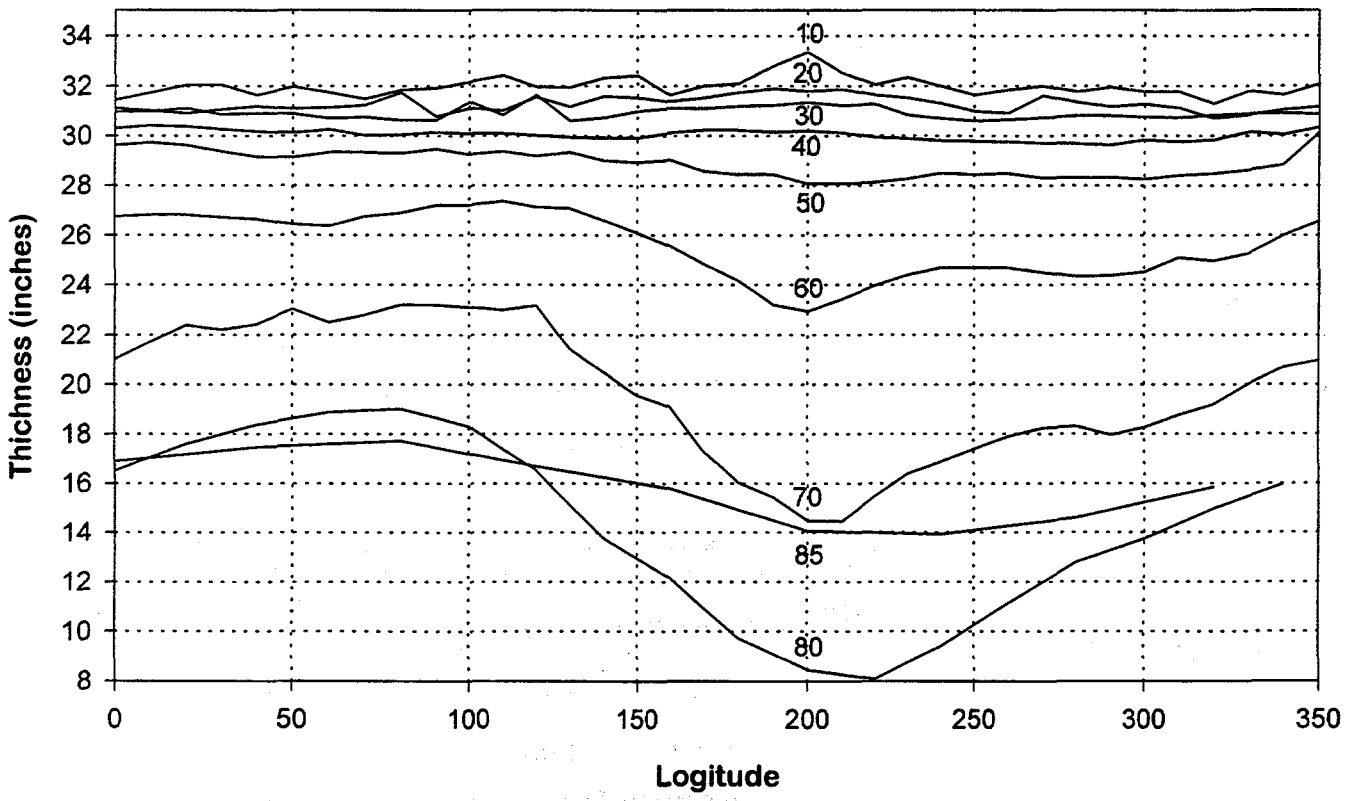

Figure 12. LHF-2 Post-test Thickness Map

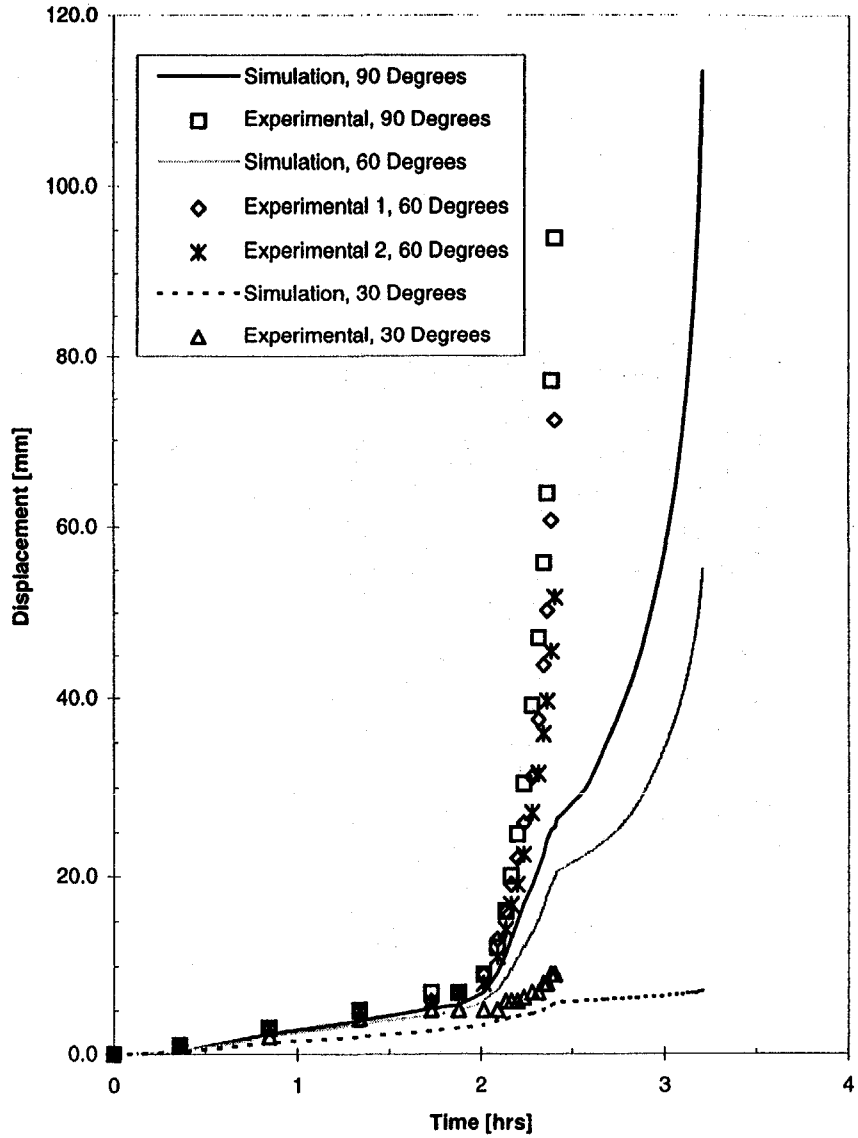

(a) Logarithmic Interpolation

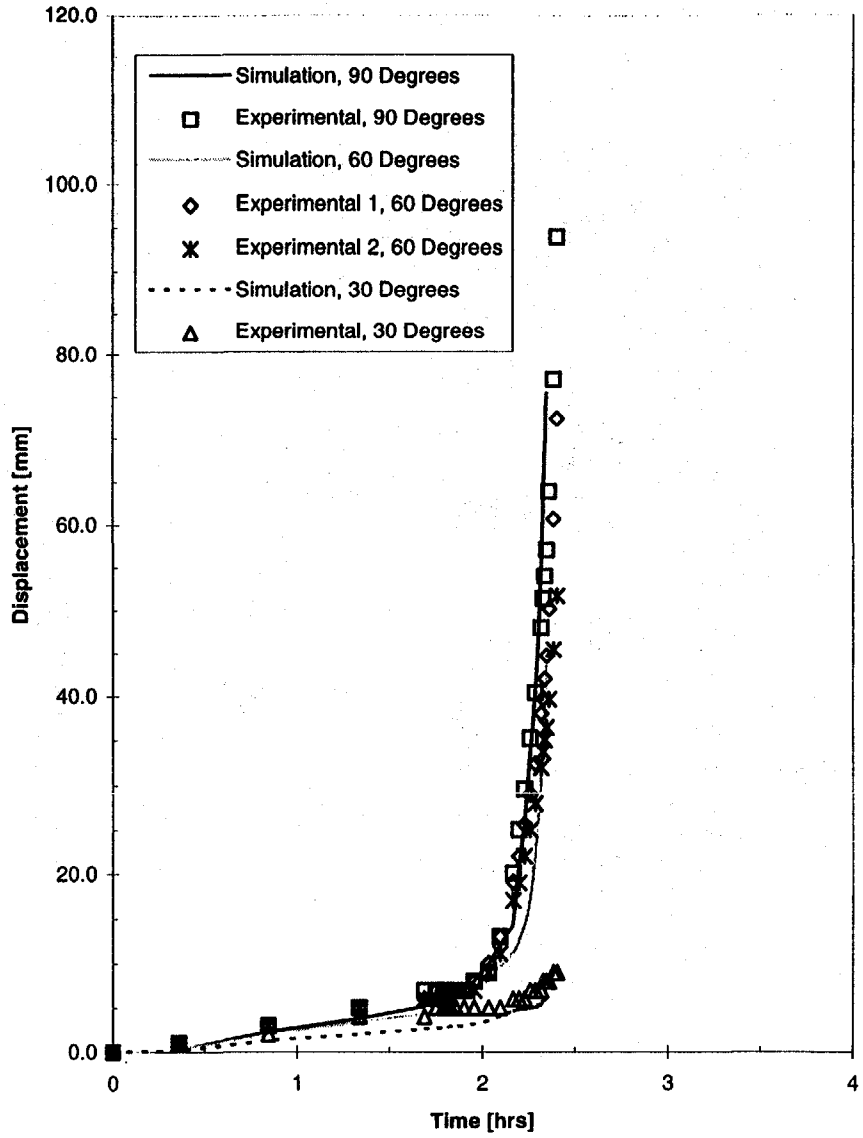

(b) Linear Interpolation

Figure 13. Comparison of LHF1 Simulated Vertical Displacements with Experimental Values

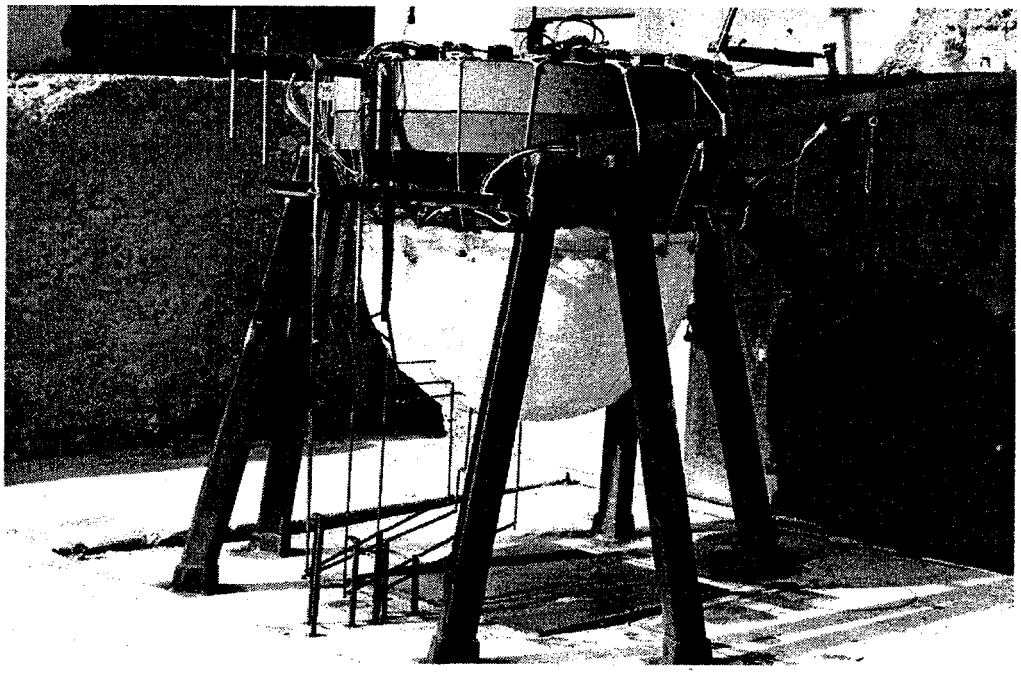

Plate 1. An overall view of the LHF test vessel and support.

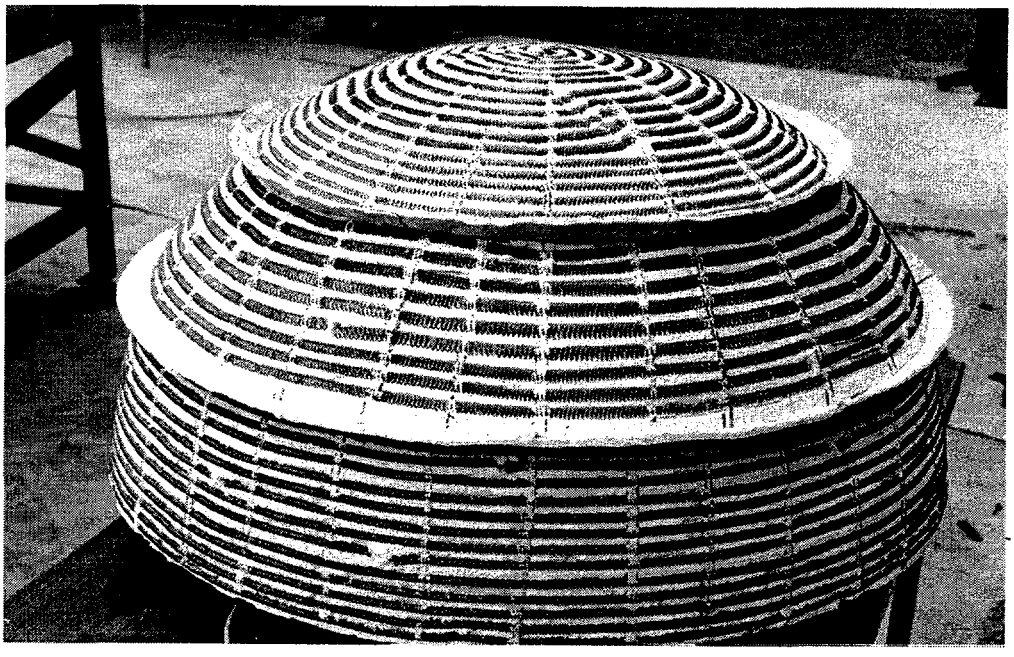

Plate 2. Hemispherical heater with section fences.

Plate 3. LHF-1 Test Results

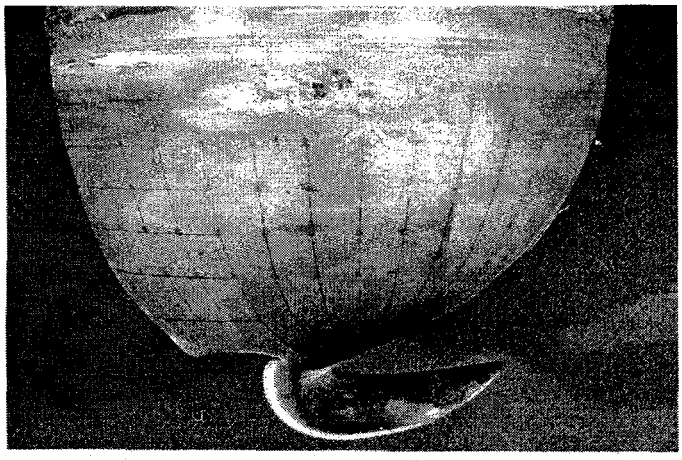

A. Vessel profile 270° view-
180°/0° plane.

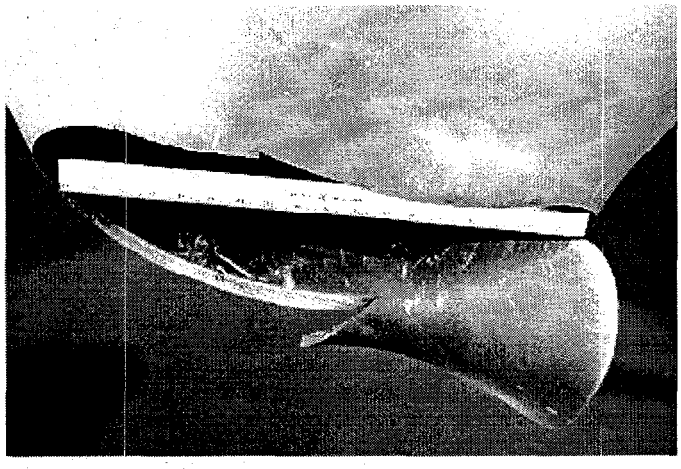

C. Close-up of Failure 180° view.

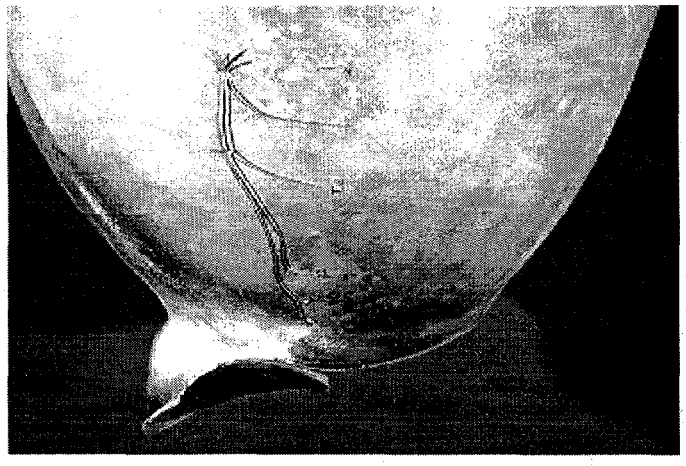

B. Close-up 0° view.

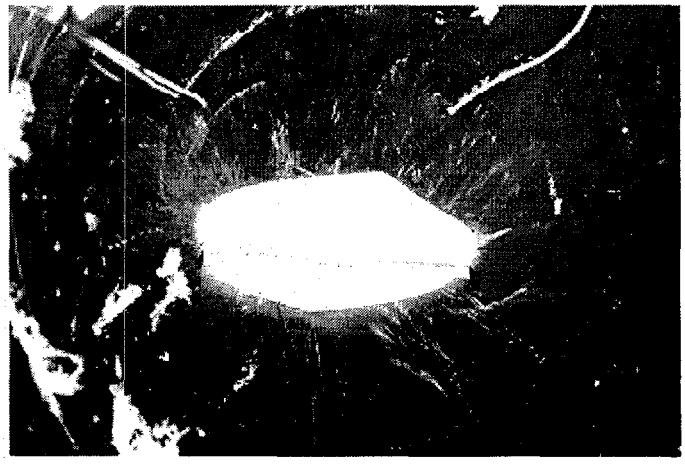

D. View of failure from inside.

Plate 4. LHF-2 Test Results

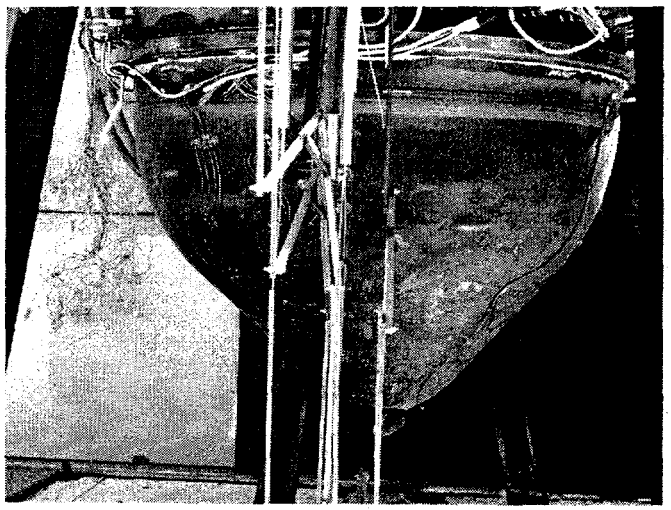

A. Vessel profile, 180° view - 90°/270° plane.

C. Close-up of vessel failure.

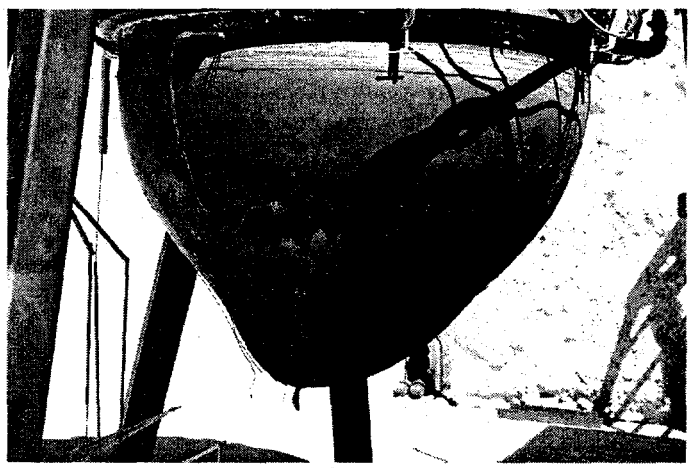

B. Vessel profile, 270° view - 0°/180° plane.

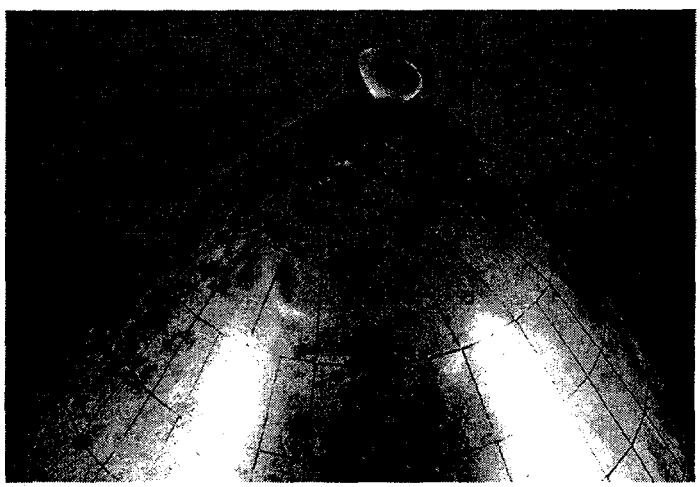

D. Failure location as indicated by (original) latitude/longitude grid.

Overview of Steam Generator Tube Degradation and Integrity Issues*

D. R. Diercks, W. J. Shack, and J. Muscara**
Argonne National Laboratory
Argonne, IL
**Office of Nuclear Regulatory Research, USNRC

Abstract

The degradation of steam generator tubes in pressurized water nuclear reactors, particularly by stress corrosion cracking (SCC) mechanisms, continues to be a serious problem. Primary water SCC is commonly observed at the roll transition zone (RTZ), at U bends, at tube denting locations, and occasionally in plugs and sleeves. Outer-diameter SCC and intergranular attack (IGA) commonly occur near the tube support plate (TSP) crevice, near the tube sheet in crevices, or under sludge piles, and occasionally in the free span. A particularly troubling recent trend has been the increasing occurrence of axial and circumferential cracking at the RTX on both the primary and secondary sides. Outer-diameter stress corrosion cracking in the TSP crevices, commonly made up of segmented axial cracks with interspersed uncracked ligaments, is also becoming more common. Despite recent advances in in-service inspection (ISI) technology, a clear need still exists for quantifying and improving the reliability of ISI methods with respect to the probability of detection of the various types of flaws and their accurate sizing. These improvements are necessary to permit an accurate assessment of the consequences of leaving degraded tubes in service over the next reactor operating cycle.

Degradation modes such as circumferential cracking, intergranular attack, and ODSCC at the tube support plate have affected a large number of tubes. The latter phenomenon in particular has led to the formulation of a new performance-based steam generator rule. This new rule would require the development and implementation of a steam generator management program that monitors tube condition against accepted performance criteria to ensure that the tubes perform the required safety function over the next operating cycle. In formulating the new rule, the NRC is also evaluating the contribution to overall plant risk from severe accidents. Preliminary analyses are being performed for a postulated severe-accident scenario involving station blackout and loss of primary feedwater to determine the probability of failure for degraded tubes.

*Job code: W6487; NRC Program Manager: Dr. J. Muscara

1. Introduction

Reliability problems have plagued steam generators since the very introduction of commercial pressurized water reactor (PWR) technology in the late 1950s. Various forms of steam generator tube degradation have resulted in the plugging of more than 100,000 tubes to date around the world.[1] In 1994, 49% of the 217 operating PWRs included in the annual EPRI report on the worldwide status of steam generator problems were required to plug steam generator tubes. Sixty-one steam generators in 22 PWRs around the world had been replaced by the end of 1994 because of serious tubing degradation, including 35 steam generators at 12 plants in the U.S. The replacement of 85 additional steam generators at 27 plants worldwide was planned; 33 of these steam generators are located at 10 plants in the U.S.[1] The cost associated with such steam generator replacements now typically ranges between $100 million and $200 million per plant, not including power replacement costs.[2]

The causes of steam generator tube plugging have evolved with time, as shown in Fig. 1.[1] Early problems with wastage were found to be associated with the use of a low Na/PO_4 molar ratio phosphate water chemistry, and the problem was essentially eliminated with the introduction of all-volatile secondary-water treatment for pH control. Subsequent problems with tube denting were solved through alternate water chemistry, replacement of copper-bearing alloys in the secondary system, and redesign of the tube support plates (TSPs) to eliminate the use of carbon steel and modify the geometries at the junctions with the tubes. Figure 1 clearly indicates that, in recent years, primary-water stress corrosion cracking (PWSCC) and outer-diameter stress corrosion cracking and intergranular attack (ODSCC/IGA) have become the predominant identifiable causes that lead to plugging of steam generator tubes in the U.S. The remainder of this paper will discuss these forms of tube degradation and their impacts on tube integrity.

2 Corrosion Problems in Steam Generator Tubing

As indicated above, stress corrosion cracking (SCC), both on the primary and secondary sides of steam generator tubes, has become the principal degradation mode leading to tube plugging in the U.S. and worldwide. SCC can occur at any of a number of locations on both sides of steam generator tubes, and it can take on various forms and configurations. These forms and recent trends in observed degradation modes are summarized here.

2.1 Primary-Water Stress Corrosion Cracking

2.1.1 PWSCC in the Roll Transition Zone

PWSCC most commonly occurs in the tube expansion transition region, or roll transition zone (RTZ), where the tube is expanded into the tube sheet. The cracks are usually axial, but circumferential cracking has also been observed and can occur near the end of the expanded region above the tube sheet or farther down in the expanded portion of the tube. This type of cracking is discussed in more detail in Section 2.3 In the latter location, the cracks pose no particular threat to tubing integrity as long as they

are sufficiently contained within the tube sheet to preclude pull-out of a severed tube. However, PWSCC is a serious problem and a leading cause of tube plugging when it occurs near the end of the expanded zone above the tube sheet.

Several processes have been used to expand and seal the tubes against the tube sheets, and the process selected strongly influences the residual stresses present in the RTZ and the tendency toward PWSCC. The mechanical roll expansion process used by Westinghouse and its licensees for many years, in combination with low-temperature mill-annealed (LTMA) tube material, has led to a relatively high incidence of PWSCC in PWR steam generators. The more recent use of hydraulic expansion in Westinghouse steam generators has been demonstrated to produce lower residual stresses and thus less tendency toward cracking. Combustion Engineering plants use an explosive-tube sheet expansion process ("Explansion") in combination with high-temperature mill-annealed (HTMA) tube material, and these units have only recently begun to experience PWSCC in the expansion zone. Babcock & Wilcox (B&W) units utilize mechanically expanded transitions that have been stress relieved and sensitized. Until recently, these units did not experience significant PWSCC, a circumstance that was attributed in large part to the beneficial microstructure and stress relief produced by the heat treatment. However, PWSCC in the tube-sheet region has recently been reported in some B&W units. A two-step roll transition configuration with less severe reductions ("kiss rolling"), used in French[3] and Belgian[4] plants, has experienced early axial cracking at both ends of the step. In any plant design, regardless of fabrication process, fabrication errors such as oversize holes in the tube sheet, incomplete expansion, and overexpansion can increase the susceptibility to PWSCC.[5,6]

2.1.2 PWSCC at U Bends

The forming processes used to produce U bends in steam generator tubes can create residual stresses in the bends, with the greatest stress levels occurring in the inner row tubes with the smallest radius of curvature. These stresses, in combination with a susceptible microstructure, can be sufficient to cause PWSCC problems. Historically, the first such problems were seen in row 1 and 2 U bends of earlier design Westinghouse[7] and Framatome[8] units, where the U bends were not stress relieved and the tubing material was LTMA Alloy 600. The problem was dealt with in a similar manner in both designs. In some cases, the most susceptible tubes were plugged as a preventive measure, but the subsequent development of an in-situ thermal treatment process appears to have solved the problem.[8] Newer designs utilize thermally treated U bends in combination with more resistant material (e.g., Alloy 600 TT or Alloy 690), and the problem has been largely eliminated.

2.1.3 PWSCC at Tube Denting Locations

PWSCC has also been known to initiate at tube dents resulting from TSP corrosion. This phenomenon has probably been most thoroughly documented in the retired Surry Unit 2A steam generator, which was destructively examined at Pacific Northwest National Laboratory (PNNL) in the 1980s.[9] Twenty-seven hot-leg and 11 cold-leg dented tubes were examined for inner diameter (ID) cracking. PWSCC was not observed in any of the tubes with denting strains below 10%, in ≈1/3 of the tubes with strains between 10 and 20%, and in all of the tubes with strains > 20%. Crack depths ranged from 27 to

88% of the wall thickness. The problem of PWSCC at gross denting locations has largely disappeared with the solution to the severe denting problem around 1980 (see Fig. 1), but both axial and circumferential cracking at relatively mild TSP dent locations have been observed in a few plants in recent years, as discussed in Section 2.3.

2.1.4 PWSCC of Plugs and Sleeves

PWSCC can also occur in the plugs that are used to remove steam generator tubes from service. Failures in both Westinghouse and Babcock & Wilcox mechanical plugs have been reported;[10-15] the first reported failure of a Westinghouse plug occurred at North Anna Unit 1 in February 1989, and plug cracking was subsequently detected at several other plants, including Sequoyah 1 and North Anna 2. It was concluded that the thermally treated Alloy 600 plugs were failing by PWSCC and that essentially all of them had come from one of four heats of susceptible material. Another susceptible heat has been more recently identified.[14] In the case of the Babcock & Wilcox plugs, cracking has been detected in several plants prior to gross failure, and a susceptible heat of Alloy 600 material was again implicated.[15] Alloy 690 plugs are used exclusively in current practice, and the NRC has required that all Westinghouse Alloy 600 mechanically expanded plugs be removed from service by the year 2000.

PWSCC of tube regions fitted with repair sleeves is also reported in the literature.[16,17] Cracking typically occurs not in the sleeve itself, but rather in the tube material adjacent to one of the sleeve welds. The problem is associated with residual stresses and the thermal cycle associated with the sleeve welding process. Because the cracked tube material has already proved to be susceptible to PWSCC, the addition of undesirable tensile residual stresses and possible detrimental microstructural changes create an opportune situation for further PWSCC. Pierson and Stubbe[16] report that more than 50% of explosively expanded sleeves used in Belgian reactors produced PWSCC failures in the adjacent tubing within a few months. Guidelines have been developed for sleeve materials, design, joining procedure, and subsequent residual-stress relief.[18]

2.2 Outer-Diameter Stress Corrosion Cracking

2.2.1 ODSCC in the Tube-Support-Plate Crevice

ODSCC/IGA is a leading cause of PWR steam generator tube plugging in the U.S. and worldwide, and the TSP crevice is the predominant location for this process. Corrosion products, mainly from the TSP, and deposited sludge from the secondary-water system eventually fill this crevice with porous material, resulting in a region of restricted secondary-water flow, intermittent dryout, and concentration of corrosive species. The pH of the concentrate in the crevice may be very basic if the cation/anion ratio of the bulk water is high or somewhat acidic if the cation/anion ratio is low.[19] This subject will be described in more detail in a subsequent paper by Millet and Welty titled "A Review of the Current Understanding of PWR SG Crevice Chemistry."

The OD cracking observed in the TSP crevice is generally intergranular and commonly consists of short axial cracks of varying length and depth within the crevice region. Adjacent cracks are often separated by ligaments of sound tubing material, and crack linkage can occur as ligament sections become corroded. Other, more complex,

ODSCC crack configurations have been increasingly observed at the TSP crevice in recent years. For example, intergranular cellular cracking has been seen at this location in a number of reactors, with the extent of cracking ranging from relatively minor in tubes from the Prairie Island[20] and Asco steam generators[21] to more severe in tubes from the Sequoyah[22] and Doel 4[23,24] steam generators. Cracking in all forms tends to occur more commonly in the hot leg of the U tube.

The crevice is essentially inaccessible for the purpose of in-situ analysis of the local water chemistry, but numerous calculations of local chemistry have been performed with computer codes such as MULTEQ and MONA.[25-28] Concentration factors for dissolved salts in the secondary water are predicted to approach 10^8 in the crevices, and, depending upon the nature of the concentrated species, crevice pH can depart greatly from that of the secondary water. Under high cation/anion ratio conditions, NaOH concentrations are calculated to reach several percent, as compared with ppm levels in the bulk secondary coolant. The corresponding crevice pH values at operating temperatures can exceed 10, with the neutral pH at 300°C being 5.7.[26] Under low cation/anion conditions, local concentration of acid sulfates or chlorides may reduce pH values to <2.[28] These pH extremes represent aggressive environments with respect to the cracking of Alloy 600.

ODSCC/IGA at the support plate crevices is most commonly observed in the extended series of Westinghouse steam generator designs with carbon steel support plates and drilled circular holes (Models 44, 51, 51M, D–2, D–3, D–4, and E). These are still the dominant designs in service in the U.S. The susceptibility of these designs to ODSCC/IGA is not surprising, inasmuch as their carbon steel support plates readily corrode in the secondary-water environment and fill the annular crevices with corrosion product, and the LTMA Alloy 600 used for the tubes in these designs is susceptible to IGSCC. Westinghouse has addressed some of the deficiencies in their more recent steam generator designs, using thermally treated (TT) Alloy 600 tubes and broached quatrefoil Type 405 stainless steel support plates in their Model D–5. Alloy 600 TT or Alloy 690 tubes and broached quatrefoil Type 405 stainless steel support plates are used in their Models F and Delta 75 steam generators.

The improved Westinghouse designs appear to have alleviated the severe ODSCC and IGA problems seen in earlier units, although longer service times are needed to verify this. Three reactors (Catawba 2, Byron 2, and Braidwood 2) have used the Model D–5 steam generators for the past seven to nine years, with no ODSCC/IGA reported. Several of the Model F steam generators have been in service for 10 years or more (Turkey Point 3 and 4, H. B. Robinson, Surrey 1 and 2, and Callaway), and again no ODSCC/IGA has been observed.[1] For all but the Callaway plant, these Model F units are replacements for earlier failed steam generators. No Delta 75 steam generators are yet in service, but the replacement units for the cracked Model D–3 steam generators in the V. C. Summer plant are to be of this design.

Combustion Engineering (CE) steam generators have used the more resistant HTMA Alloy 600 tubes from the beginning. Despite this, most of the CE steam generators that have been in service for more than six years have experienced at least some ODSCC/IGA, although less severe than in the Westinghouse steam generators using Alloy 600 LTMA tubes. The replacement units installed at Millstone 2 in 1992, which were built by B&W of Canada, used Alloy 690 TT tube material in response to this concern.

2.2.2 ODSCC in the Tube Sheet Region

ODSCC and IGA also commonly occur in the tube sheet region, either in the built-in crevice that was present between the tube sheet and the tubes in earlier Westinghouse designs or in the sludge pile atop the tube sheet. At either location, the process, similar to that which is operative in the tube support plate crevices, creates highly caustic or acidic conditions in the crevice because of local boiling and concentration effects.

In older Westinghouse steam generator designs (through the early Model 51 units), the roll bond that sealed the tubes to the tube sheets extended only ≈50–75 mm (2–3 in.) above the bottom of the tube sheet, leaving an annular crevice ≈0.2 mm (0.008 in.) in width around the unexpanded portion of the tube for the remaining length of the 530–mm (21–in.) thick tube sheet. This crevice created a favorable environment for the concentration of impurity species, and significant ODSCC/IGA problems at this location were experienced at several units of this design, including Ginna, Point Beach 1 and 2, Robinson 2, Kewaunee, and Cook 1 in the U.S. Doel 2 in Belgium, Beznau 1 and 2 in Switzerland, Ringhals 2 in Sweden, and Takahama 2 in Japan. This problem has been greatly reduced in more modern steam generator designs with the use of full–depth tube expansion. However, even in these newer models, a very shallow crevice typically remains at the top of the tubes to avoid over-expanding the tubes above the tube sheet, and cracking is still possible.

These design improvements have not eliminated deposition of corrosion products and sludge atop the tube sheet, particularly at locations where flow rates are low. The porous sludge deposits effectively create crevice–like regions in the vicinity of the tubes that result in local boiling and impurity concentration.[29] General wastage and pitting of the tubes can result,[30] but the more serious problem is the occurrence of severe ODSCC and IGA.[18,9,31] Residual stresses introduced by the tube expansion process at the RTZ appear to contribute to the cracking process in this region. The resulting RTZ cracking is commonly circumferential, but axial and multidirectional cracks are also commonly observed.[8,32]

ODSCC/IGA can also occur in the sludge pile region at tube locations above the RTZ. These cracks are commonly axial, but more complex multidirectional cracking has been reported in Belgian plants.[32]

2.2.3 ODSCC/IGA in Free-Span Regions

The free span regions of steam generator tubes have generally been thought of as unlikely locations for significant ODSCC because of the apparent absence of crevices or other geometries favorable to the local concentration of impurity species. However, secondary-side ODSCC and IGA in the free-span region have been observed several times over the years, and, in particular, the rupture of a steam generator tube at the Palo Verde 2 plant in March 1993 dramatized the potential for significant free–span ODSCC/IGA.[33]

The free-span cracking incidents observed in recent years may be divided into three categories. The first category includes those incidents in which the tube bundle geometry created a local region favorable for the concentration of impurity species. In some cases, structural occlusions produced local steam pockets (Ft. Calhoun[34] and Maine Yankee[35]),

and, in others, the impurity concentration occurred under corrosion product or sludge deposits on the tube surface (Palo Verde 2[33] and Crystal River 3[36]). The second category also includes those incidents in which aggressive chemical species in the secondary water were responsible for cracking without the need for local concentration. Examples are provided by Doel 4[23,24] and Farley 1,[37] where significant lead (and to a lesser extent copper) contamination was present.

The third category of free span cracking is the most interesting in that ODSCC occurred at a location where neither impurity concentration nor contamination by aggressive species was implicated. Examples are provided by the McGuire 1989[38] and 1992[39] occurrences as well as the Braidwood 1[39] cracking. Most recently, rather extensive free-span cracking has also been reported at Oconee 1.[40] In all these examples, the cracking apparently occurred at preexisting surface flaws, but the chemical species and the concentration mechanism responsible are not obvious.

2.3 Circumferential Cracking at the RTZ and Dented TSPs

A particularly troubling recent trend has been the increasing occurrence of circumferential cracking at the RTZ on both the primary and secondary sides. Such circumferential cracks normally require plugging or sleeving upon detection, because they are difficult to reliably size, the threshold of detection for these cracks may be greater in terms of size than for axial cracks, and their growth rates are difficult to predict.[41] As early as 1992, limited cracking of this type was reported at Arkansas Nuclear One Unit 2,[42] and, at Maine Yankee, 358 tubes were plugged because of this degradation mode prior to 1995.[41,43,44] However, the most dramatic example of this type of failure was provided by Maine Yankee during a later unscheduled shutdown and subsequent refueling outage in early 1995, when an inspection carried out during March and April revealed that more than 60% of the tubes had circumferential crack indications in the RTZ.[44] All of the indications were seen on the hot-leg side of the tubes. This inspection was one of the first that used the advanced Zetec +Point™ eddy current (EC) probe, which was specifically designed to provide improved sensitivity to circumferential cracking. The decision was made to repair all 17,000 tubes in Maine Yankee with Westinghouse laser-welded sleeves, and the plant finally returned to service at 90% power in January of 1996 after an outage of about one year.[45] Even more recently, extensive circumferential RTZ PWSCC at the Salem 1 plant has resulted in a decision to replace the steam generators,[46,47] and significant circumferential PWSCC is being reported at the Braidwood 1 and Byron 1 nuclear plants[48-50] as well as at Sequoyah 1, Diablo Canyon 1, and Callaway 1.[50]

Both axial and circumferential cracking has been observed at dented TSP locations at several of the same plants that have reported circumferential RTZ cracking, including Sequoyah 1, Diablo Canyon 1, and Salem 1.[50] These indications are associated with minor dents that have developed in steam generators with drilled-hole carbon steel support plates despite water chemistry modifications that eliminated the severe denting problem of the late 1970s. The defects were detected with more advanced EC probes such as the Cecco probe or a rotating probe with +Point™ or pancake coils. The examinations suggest that the axial indications initiated at the inner diameter (ID) and the circumferential indications at the OD. However, destructive examination at Diablo Canyon 1 determined that several of the circumferential cracks initiated at the ID.

3 Reliability of Detection and Sizing of Flaws

Conventional EC bobbin coils are currently the principal tool utilized to detect flaws in steam generator tubing. Multiple frequencies are used to acquire data, with the selection of frequencies dependent on the tube material, geometry and inspection objectives. Currently, four frequencies are used to detect and size flaws. In devising an inservice inspection (ISI), it is important to optimize one of the frequencies or find an appropriate frequency mix for detection of small cracks. Bobbin coils allow for fast inspection rates and have been reasonably reliable for the types of flaws generally seen in the past. However, their effectiveness for some of the flaw types observed more recently, such as circumferential intergranular stress corrosion cracking (IGSCC) or cracks in dents, is questionable. Regardless of flaw type, cracks are not generally detectable until they are ≈40-50% throughwall.[51] Supplemental probes of varying design (rotating-pancake-coils, pancake arrays, cross-wound coils, transmit/receive reflection coils, etc.) are employed to help resolve questionable bobbin-coil indications or generally improve inspections.

A clear need exists for quantifying the reliability of ISI methods with respect to the probability of detection (POD) of the various types of flaws and their accurate sizing. This information is necessary to assess the true state of degradation after an ISI so that the consequences of leaving degraded tubes in service over the next reactor operating cycle can be accurately assessed, as discussed below. Improvements in the POD of flaws and sizing accuracy will, in turn, require more sophisticated probes and an increased number of pulled tubes or retired steam generator sections, along with laboratory-generated cracks, against which to qualify procedures and techniques.

A standard convention in the industry is to attempt to relate ODSCC EC voltage amplitude to tube integrity and leakage. This approach is empirical, and the relationship between EC voltage amplitude and crack depth and length is relatively poor. Thus, the use of voltage amplitude for flaw detection and sizing requires a very conservative approach to data analysis and data interpretation, and one concern is the possibility of a small EC voltage arising from a crack with a low burst pressure. It is clear that the robustness of EC voltage parameter and of other flaw characterization parameters and techniques must be evaluated with respect to their range of applicability.

4 Degradation-Specific Management

The U.S. Nuclear Regulatory Commission (NRC) is currently developing a "performance-based" rule and regulatory guidance for steam generator tube integrity. This new rule is being developed because past implementation of regulatory guidance, which was formulated in the 1970s, is becoming outdated with the increasing occurrence of such degradation modes as circumferential cracking, IGA, and discontinuous axial cracking with interspersed intact ligaments. For at least some degradation modes, the past implementation of regulatory guidance, where all flaws were assumed to be infinitely long, can be too conservative. The new rule and regulatory guidance will be discussed in detail in a subsequent presentation by Strosnider entitled "Steam Generator Rule."

To address the problem of ODSCC at the TSP, the industry has developed an alternative voltage-based repair criterion. The new rule will provide flexibility for the implementation of degradation-specific management, which will involve the reliable detection and classification of specific defects. Implementation will also require the calculation of tube burst probabilities and total leak rates under normal operation and design-basis accidents at the end of the cycle for flaws left in service after ISI, as well as for those that develop during the cycle. Therefore, reliable nondestructive evaluation (NDE), integrity models, and corrosion/crack initiation/progression are needed.

Implementation of the new steam generator rule and its provisions for degradation-specific management may result in different acceptance/repair limits for different types of degradation at different locations. For example, flaws that occur in tubes at locations where support structures exist (e.g., axial ODSCC at the TSPs) may be restricted from gross failure and leakage by the presence of those support structures and could possibly require less restrictive acceptance/repair limits than similar cracking in the free span. Another form of degradation that is increasingly observed is cracking made up of numerous small crack segments with interspersed uncracked ligaments. Tubes with this type of cracking exhibit higher failure pressures and lower leak rates than would be predicted for the overall bounding crack. However, as the individual crack segments grow and the ligaments become smaller, the strengthening effect of the ligaments disappears at some stage, and the failure pressure and leak rate predictions for the overall bounding crack then apply. Thus, as long as it can be established that such cracks remain in the "infant" stage, a less demanding acceptance/repair limit might be applied to them.

As the above examples illustrate, the implementation of a performance-based rule and degradation-specific management requires detailed knowledge of the specific nature and severity of the flaws present in a given steam generator. This detailed knowledge, in turn, requires that robust methods be developed for survey inspections, so flaws can be reliably detected and correctly classified and characterized. This will permit appropriate degradation-specific management requirements be applied to them. A subsequent paper in this session by Kupperman and Bakhtiari titled "Modeling of Eddy Current Testing for Steam Generator Tubes" describes, in detail, the results of calculated simulated EC probe responses to typical steam generator OD tube defects. A second paper by the same authors ("Characterization of Flaws in a Tube Bundle Mock-up for Reliability Studies") discusses progress to date on the development of a tube bundle mock-up for the evaluation of current ISI technologies used to detect and characterize tubing degradation. Finally, a paper by Henry and Welty, titled "Steam Generator Tubing NDE Performance," provides a review of current NDE technology for ISI of steam generator tubing.

Some current safety and integrity evaluations are based on calculations of overall projected leak rates over the next operating cycle for degraded tubes that remain in service. Additional information is needed in several areas to implement these evaluations. The first of these areas is, once again, inspection reliability, POD, and sizing accuracy. Detailed information on inspection reliability and POD will permit estimation of the true state of the generator after ISI by including flaws that were missed because of imperfect POD. Similarly, knowledge of sizing accuracy will permit corrections in the flaw sizes obtained from ISI.

Evaluations based on calculated overall projected leak rates also require information on the nature of the specific degradation processes that are active in the steam generator so that the state of degradation at the end of the operating period can be estimated. More specifically, information on crack initiation is needed to estimate the number of cracks that will develop during the operating cycle, and information on crack evolution and morphology will permit estimation of the total growth of cracks present at the beginning of the cycle, as well as of those that initiate during the cycle. In addition, an understanding of the crack evolution and morphology is needed to determine if small cracks and ligaments change during the cycle to produce more planar cracks by the end of the cycle.

Finally, integrity correlations are needed to relate failure pressures, failure modes, and leak rates to crack size, type, and morphology. These correlations can be used to determine if cracks present in the tubes are likely to cause failure under normal or design-basis accident conditions before the end of the operating cycle. If failure is predicted, the models can be used to estimate the resulting leak rates.

The above discussions has been concerned primarily with possible tube failure under normal operating conditions and design-basis accidents. In conjunction with the new rule-making activities, the NRC staff is also evaluating the contribution to overall risk from various postulated severe accident scenarios. A description of the models and methodology being developed to analyze steam generator integrity under severe accident conditions, as well as under accident and normal conditions, is reported in another paper in this session by S. Majumdar, titled "Predictions of Structural Integrity of Steam Generator Tubes under Normal Operating, Accident, and Severe Accident Conditions." A related paper by Gorman et al., entitled "Estimating Probable Flaw Distributions in PWR Steam Generator Tubes," discusses a methodology for estimating the distribution of flaws of various types in steam generator tubes, as required, for example, in calculating the probability of tube failure and primary-to-secondary leakage through steam generator tubes under accident conditions.

5. Summary of Research Needs

This paper has attempted to summarize the principal corrosion-related degradation processes observed in steam generator tubing and to provide the basis for and research needs associated with implementation of degradation-specific management. These research needs may be summarized as follows:

1. Because implementation of degradation-specific management requires a detailed knowledge of the specific nature and severity of the flaws present in a given steam generator, a clear need exists for quantifying the reliability of ISI methods with respect to the POD of the various types of flaws that are observed in steam generator tubes and their accurate sizing. This information is necessary to assess the true state of degradation after an ISI so the consequences of leaving degraded tubes in service over the next reactor operating cycle can be accurately assessed. As a part of this quantification, the robustness of the various NDE parameters and techniques for flaw detection must be evaluated with respect to their range of applicability.

2. The above-cited need for improved POD and flaw sizing requires more sophisticated probes and an increased number of pulled tubes or retired steam generator sections, along with laboratory-generated cracks, to evaluate and validate various procedures and techniques.

3. Evaluations of steam generator tube integrity based on overall projected leak rate and the probability of tube rupture require information on crack initiation to estimate the number of cracks that will develop during an operating cycle. In addition, information on crack evolution and morphology is needed to permit estimation of the total growth of cracks present at the beginning of the cycle, as well as of those that initiate during the cycle. This information is also needed to determine if small cracks and ligaments change during the cycle to produce more planar cracks by the end of the cycle.

4. Integrity correlations are needed to relate failure pressures, failure modes, and leak rates to crack size, type, and morphology. These correlations can be used to determine if cracks present in the tubes are likely to cause failure under normal or accident conditions before the end of an operating cycle, and, if so, to estimate the probability of rupture and resulting leak rate.

Acknowledgments

The authors gratefully acknowledge helpful comments from J. Gorman and R. Clark. This work was supported by the U.S. Nuclear Regulatory Commission, Office of Nuclear Regulatory Research.

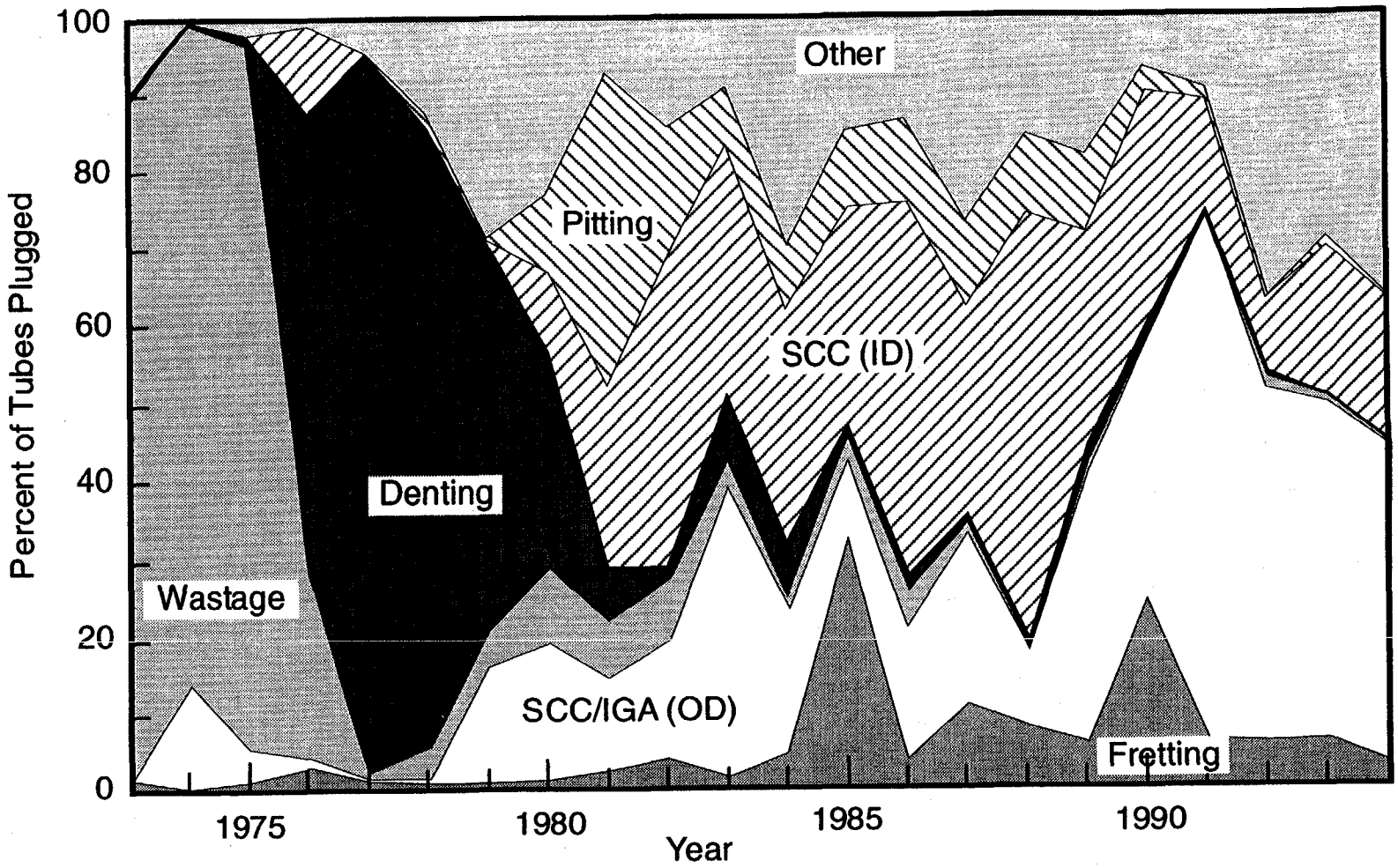

Figure 1. Causes of steam generator tube plugging in U.S. vs. year (from Ref. 1).

References

1. B. L. Dow, Jr., *Steam Generator Progress Report, Revision 11*, EPRI Research Project RP3580-06, Electric Power Research Institute, Palo Alto, CA (Nov. 1995).

2. J. Douglas, *Solutions for Steam Generators*, EPRI Journal (May/June 1995), pp. 28-35.

3. J. C. Fournel, *A Statistical Insight in the Suspected Relations Between PWSCC in R.T.Z. and IGASCC on TSP's*, paper 3 presented at EPRI Workshop on Steam Generator Secondary Side IGA/SCC, Oct. 14-15, 1993 Minneapolis.

4. J. Stubbe, *Alloy 600 Primary Water SCC: a User's (Belgian Electricity Board) Point of View*, presented at Alloy 600 PWSCC Experts Meeting, Arlie, France, April 6-9, 1993.

5. C. S. Welty, Jr. and J. C. Blomgren, *Steam Generator Issues*, pp. 1-27 to 1-36 in Proc. 4th Int. Symp. on Environmental Degradation of Materials in Nuclear Power Systems—Water Reactors, National Assn. of Corrosion Engineers, Houston, TX (1990).

6. C. O. Ruud and M. E. Jacobs, *Residual Stresses in Roller-Expanded Steam Generator Tube Transitions*, EPRI Report TR-102355, Electric Power Research Institute, Palo Alto, CA (May 1993).

7. J. A. Gorman and E. S. Hunt, *Critical Factors Assessment for U-Bend and Transition Cracking*, Paper 5 in Proc. 1985 Workshop on Primary-Side Stress Corrosion Cracking of PWR Steam Generator Tubing, EPRI NP-5158, Electric Power Research Institute, Palo Alto, CA (June 1987).

8. P. Saint Paul and G. Slama, *Steam Generator Materials Degradation*, pp. 39-49 in Proc. 5th Int. Symp. on Environmental Degradation of Materials in Nuclear Power Systems—Water Reactors, American Nuclear Society, La Grange Park, IL (1992).

9. R. J. Kurtz, R. A. Clark, E. R. Bradley. W. M. Bowen, P. G. Doctor, and R. H. Ferris, *Steam Generator Tube Integrity Program/Steam Generator Group Project*, NUREG/CR-5117, U.S. Nuclear Regulatory Commission, Washington, DC (May 1990).

10. *Potential Failure of Westinghouse Steam Generator Tube Mechanical Plugs*, NRC Information Notice 89-33, U.S. Nuclear Regulatory Commission, Washington, DC (March 23, 1989).

11. *Failure of Westinghouse Steam Generator Tube Mechanical Plugs*, NRC Bulletin 89-01, U.S. Nuclear Regulatory Commission, Washington, DC (May 15, 1989).

12. *Failure of Westinghouse Steam Generator Tube Mechanical Plugs*, NRC Bulletin 89-01, Supplement 1, U.S. Nuclear Regulatory Commission, Washington, DC (Nov. 14, 1990).

13. *Failure of Westinghouse Steam Generator Tube Mechanical Plugs*, NRC Bulletin 89-01, Supplement 2, U.S. Nuclear Regulatory Commission, Washington, DC (June 28, 1991).

14. *Unanticipated Crack in a Particular Heat of Alloy 600 Used for Westinghouse Mechanical Plugs for Steam Generator Tubes*, NRC Information Notice 94-87, U.S. Nuclear Regulatory Commission, Washington, DC (Dec. 22, 1994).

15. *Potential for Stress Corrosion Cracking in Steam Generator Tube Plugs Supplied by Babcock and Wilcox*, NRC Information Notice 89-65, U.S. Nuclear Regulatory Commission, Washington, DC (Sept. 8, 1989).

16. E. Pierson and J. Stubbe, *SCC Testing of Steam Generator Tubes Repaired by Welded Sleeves*, pp. 697-705 in Proc. 6th Int. Symp. on Environmental Degradation of Materials in Nuclear Power Systems—Water Reactors, R. E. Gold and E. P. Simonen, Eds., The Minerals, Metals, and Materials Society, Warrendale, PA (1993).

17. *Potential Failure of Steam Generator Tubes with Kinetically Welded Sleeves*, NRC Information Notice 94-05, U.S. Nuclear Regulatory Commission, Washington, DC (Jan. 19, 1994).

18. E. S. Hunt and J. A. Gorman, *Guidelines for PWR Steam Generator Tubing Specifications and Repair. Volume 3: Steam Generator Tube Sleeving: Design, Specification, and Procurement Checklist*, EPRI NP-6743-L, Electric Power Research Institute, Palo Alto, CA (Feb. 1991).

19. J. P. N. Paine, S. A. Hobart, and S. G. Sawochka, *Predicting Steam Generator Crevice Chemistry*, pp. 739-744 in Proc. 5th Int. Symp. on Environmental Degradation of Materials in Nuclear Power Systems—Water Reactors, American Nuclear Society, La Grange Park, IL (1992).

20. R. P. Pearson and S. Lappegaard, *Use of Inhibitors for Secondary Side IGA/SCC at Prairie Island*, presented at EPRI Workshop on Steam Generator Secondary Side IGA/SCC, Minneapolis, Oct. 14-15, 1993.

21. A M. Lancha, D. Gómez-Briceño, and E. López-Toribio, *PWSCC and IGA/SCC in Tubes Pulled out from Operating Steam Generators*, Paper A2 in Proc. IAEA Specialists Meeting on Steam Generator Problems and Replacement, Madrid, Spain, Dec. 13-16, 1993.

22. D. E. Hughes, *Sequoyah Nuclear Plant Tube Pull Results*, presented at EPRI Workshop on Steam Generator Secondary Side IGA/SCC, Minneapolis, Oct. 14-15, 1993.

23. J. Stubbe, C. Laire, and E. Pierson, *Secondary Side Corrosion at Doel 4—Mechanisms and Effects of Phosphate Injection*, presented at EPRI Workshop on Steam Generator Secondary Side IGA/SCC, Minneapolis, Oct. 14-15, 1993.

24. C. Laire, J. Stubbe, and E. Pierson, *Doel 4: Secondary Side Corrosion Mechanisms and Effects of Phosphate Injection*, Paper A3 in Proc. IAEA Specialists Meeting on Steam Generator Problems and Replacement, Madrid, Spain, Dec. 13-16, 1993.

25. J. P. N. Paine, S. A. Hobart, and S. G. Sawochka, *Predicting Steam Generator Crevice Chemistry*, pp. 739-744 in Proc. 5th Int. Symp. on Environmental Degradation of Materials in Nuclear Power Systems—Water Reactors, American Nuclear Society, La Grange Park, IL (1992).

26. C. E. Shoemaker and J. P. N. Paine, *Modeling Nuclear Steam Generator Environments*, pp. 237-242 in Proc. 3rd Int. Symp. on Environmental Degradation of Materials in Nuclear Power systems—Water Reactors, G. J. Theus and J. R. Weeks, Eds., The Metallurgical Society, Warrendale, PA (1988).

27. A. Kishida, H. Takamatsu, H. Kitamura, S. Isobe, K. Onimura, K. Arioka, Y. Hattori, T. Arai, and M. Sato, *The Causes and Remedial Measures of Steam Generator Tube Intergranular Attack in Japanese PWR*, pp. 465-471 in Proc. 3rd Int. Symp. on Environmental Degradation of Materials in Nuclear Power systems—Water Reactors, G. J. Theus and J. R. Weeks, Eds., The Metallurgical Society, Warrendale, PA (1988).

28. A. Stutzmann and F. Nordmann, *Hideout Return in EDF Units*, presented at the EPRI Workshop on Steam Generator Secondary Side IGA/SCC, Minneapolis Oct. 14-15, 1993.

29. P. J. Millet and J. M. Fenton, *A Detailed Model of Localized Concentration Processes in Porous Deposits of SG's*, pp. 745-751 in Proc. 5th Int. Symp. on Environmental Degradation of Materials in Nuclear Power Systems—Water Reactors, American Nuclear Society, La Grange Park, IL (1992).

30. F. Gonzalez and P. Spekkens, *Corrosion of Inconel 600 under Steam Generator Sludge Piles*, pp. 7-108 to 7-120 in Proc. 4th Int. Symp. on Environmental Degradation of Materials in Nuclear Power Systems—Water Reactors, National Assoc. of Corrosion Engineers, Houston, TX (1990).

31. P. LeMaire, *Current Status (1993) of ODSCC at EDF Plants*, presented at the EPRI Workshop on Steam Generator Secondary Side IGA/SCC, Minneapolis, Oct. 14-15, 1993.

32. C. Leblois, *Belgian Steam Generator Experience: The Whole Picture*, Nucl. Eng. Int., Vol. 32 (May 1992), pp. 25-33.

33. K. Sweeney and M. Melton, *Free-Span IGA/SCC at the Palo Verde Nuclear Generating Station*, presented at EPRI Workshop on Steam Generator Secondary Side IGA/SCC, Minneapolis, Oct. 14-15, 1993.

34. K. R. Craig, *Failure Analysis of Tube R20L84, B Steam Generator, Ft. Calhoun*, pp. A6-1 to A6-14 in Proc. 1985 EPRI Workshop on Remedial Actions for Secondary-Side Intergranular Corrosion, EPRI NP-4929, Electric Power Research Institute, Palo Alto, CA (Dec. 1986).

35. *Recent Incidents Involving Rapid Increases in Primary-to-Secondary Leak Rate*, NRC Information Notice 91-43, U.S. Nuclear Regulatory Commission, Washington, DC (July 5, 1991).

36. P. A. Sherburne, K. R. Redmond, and L. P. Sykes, *Laboratory Examinations of OTSG Tubes from Crystal River Unit 3*, pp. 351-362 in Proc. 7th Int. Symp. on Environmental Degradation of Materials in Nuclear Power Systems—Water Reactors, National Assoc. of Corrosion Engineers, Houston, TX (1995).

37. F. D. Hundley, *Examination of Farley Unit-1 Hot Leg Steam Generator Tube*, presented at the EPRI Workshop on Steam Generator Secondary Side IGA/SCC, Minneapolis, Oct. 14-15, 1993.

38. G. A. Murphy, *Selected Safety-Related Events*, Nucl. Safety, Vol. 30, No. 4 (1989), pp. 557-558.

39. *Operational Experience on Steam Generator Tube Leaks and Tube Ruptures*, NRC Information Notice 94-62, U.S. Nuclear Regulatory Commission, Washington, DC (Aug. 30, 1994).

40. *Duke Answers NRC Questions on Axial Cracks in Once-Through SGs*, Inside NRC, Vol. 18, No. 7 (April 1, 1996), p. 1.

41. *Circumferential Cracking of Steam Generator Tubes*, NRC Generic Letter 95-03, U. S. Nuclear Regulatory Commission, Washington, DC (April 28, 1995).

42. *Operation with Steam Generator Tubes Seriously Degraded*, NRC Information Notice 92-80, U.S. Nuclear Regulatory Commission, Washington, DC (Dec. 7, 1992).

43. *Inservice Inspection Deficiencies Result in Severely Degraded Steam Generator Tubes*, NRC Information Notice 94-88, U.S. Nuclear Regulatory Commission, Washington, DC (Dec. 23, 1994).

44. *The big sleeve—Maine Yankee opts not to replace*, Nucl. Eng. Int. Vol. 40 (October 1995), pp. 36-38.

45. *Maine Yankee Back on Line at Reduced Power Level*, Nucleonics Week, Vol. 37, No. 3 (Jan. 18, 1996), p. 7.

46. *Salem-1 Steam Generator Replete with Potential New Crack Type*, Nucleonics Week, Vol. 37, No. 10 (March 7, 1996), p. 1.

47. *Salem-1 Steam Generator Replete with Potential New Crack Type*, Nucleonics Week, Vol. 37, No. 22 (May 30, 1996), p. 5.

48. *ComEd Disputes Braidwood Tube Pull with NRC as More Byron Flaws Found*, Nucleonics Week, Vol. 37, No. 17 (April 25, 1996), p.4.

49. *Braidwood Outage Pending?*, Nucleonics Week, Vol. 37, No. 21 (May 23, 1996), p. 9.

50. *Results of Steam Generator Tube Examinations*, NRC Information Notice 96-38, U.S. Nuclear Regulatory Commission, Washington, DC (June 21, 1996).

51. J. Guerra and R. L. Tapping, *Working Session 2: Tubing Inspection*, Proc. CNRA/CSNI Workshop on Steam Generator Tube Integrity in Nuclear Power Plants, Oct. 30–Nov. 2, 1995, Oak Brook, IL, NUREG/CP-0154, pp. 299-304 (in press).

Steam Generator Tube Integrity - U.S. Nuclear Regulatory Commission Perspective*

Emmett L. Murphy, Edmund J. Sullivan
U.S. Nuclear Regulatory Commission

Abstract

In the U.S., the current regulatory framework was developed in the 1970s when general wall thinning was the dominant degradation mechanism; and, as a result of changes in the forms of degradation being observed and improvements in inspection and tube repair technology, the regulatory framework needs to be updated. Operating experience indicates that the current U.S. requirements should be more stringent in some areas, while in other areas they are overly conservative. To date, this situation has been dealt with on a plant-specific basis in the U.S. However, the NRC staff is now developing a proposed steam generator rule as a generic framework for ensuring that the steam generator tubes are capable of performing their intended safety functions.

This paper discusses the current U.S. regulatory framework for assuring steam generator (SG) tube integrity, the need to update this regulatory framework, the objectives of the new proposed rule, the U.S. Nuclear Regulatory Commission (NRC) regulatory guide (RG) that will accompany the rule, how risk considerations affect the development of the new rule, and some outstanding issues relating to the rule that the NRC is still dealing with.

Background

The importance of assuring SG tube integrity arises from the fact that the tubing constitutes a significant fraction of the reactor coolant pressure boundary. The SG tubing is unique in that a loss of tube integrity translates to a small loss-of-coolant accident bypassing containment. Additional failures of mitigating systems could lead to a direct release of radiological fission products. If a severe accident produces conditions leading to a loss of tube integrity, significant radiological releases would occur.

The current regulatory framework pertaining to SG tube integrity is found in Title 10 of the Code of Federal Regulations (10 CFR), the American Society of Mechanical Engineers (ASME) Boiler and Pressure Vessel Code, and the plant technical specifications (TS). The pertinent portions of 10 CFR include the general design criteria in Appendix A to Part 50 and guideline values for

*Work presented at 24th WRSM by J. Strosnider, NRC.

offsite releases in Part 100. The ASME Code, Section III, gives the requirements for the design and analysis of the steam generators and the SG tubing. The ASME Code, Section XI, gives the requirements for inservice inspection and repairs of SG tubing. Plant TS address inservice inspection of SG tubing and provide (1) a through-wall limit (generally 40%) beyond which degraded tubes must be repaired or plugged, (2) primary-to-secondary leakage limits, and (3) reactor coolant activity limits.

The requirements in the ASME Code, Section XI, and the TS for inspection and repair of SG tubing are highly prescriptive and out of date. These requirements specify only limited inspection sampling of tubes and permit the steam generators to be declared operable after the defective tubes are repaired or removed from service. Although utilities in the U. S. generally far exceed the minimum requirements, present requirements do not focus on the key objective of ensuring adequate tube integrity through the entire cycle of plant operation between inspections during plant outages.

The existing requirements, which were developed when wall thinning and wastage were the dominant modes of degradation, do not reflect current degradation modes or inspection technology. Today, axially and circumferentially oriented stress corrosion cracking (SCC) is the dominant degradation mode being experienced in the U.S. In addition, the TS repair criteria for some forms of degradation, such as SCC, tend to be very conservative. This is because, typically, stress corrosion cracks tend to be short even if they are deep. The 40%-through-wall plugging limit was developed on the premise of uniform thinning of the tube; however, a short crack at a given depth does not have the same structural impact as does a uniformly thin tube.

Reliable stress corrosion crack detection and sizing depend upon non-destructive examination (NDE) technology and practice which are beyond the scope of the plant TS and existing ASME Code requirements. On the basis of the TS plugging criteria, tubes with SCC are repaired or plugged when they are detected because reliable depth sizing techniques for SCC have not been developed and laboratory studies indicate that the threshold of detection for SCC is often 40% through-wall or greater. Therefore, there is no basis for assuming that indications are less than 40% through-wall.

Another difficulty with the current regulatory framework is that, traditionally, this framework does not offer an incentive to apply improved NDE technology as it becomes available. This lack of incentive arises from the depth-based plugging criteria in the TS. If a utility applies a more sensitive NDE technique to inspection for SCC, more indications of possibly lower safety significance are found. The TS also require these indications to be plugged if their depth cannot be reliably determined.

Another shortcoming of the current framework is that there is little guidance on how to deal with leakage issues associated with repair criteria that would accompany through-wall cracks. The TS did not need to deal with leakage issues since they require tubes with through-wall cracks to be repaired or removed from service. It is now recognized that adequate structural and leakage

integrity during postulated accidents can be ensured under certain conditions, even for tubes affected by through-wall SCC.

In the case of outside-diameter stress corrosion cracking (ODSCC) located at drilled hole support plates, it was found that the TS were requiring that a large number of tubes be removed from service although many of these tubes had no defects that were significant from a structural or leakage viewpoint. A lot of attention had to be directed to the inspection technology and practice being applied and to the methodology for assuring acceptably low conditional probability of burst and leakage. Improved NDE techniques and guidelines and a suitable database for developing burst and leakage correlations are now available for this form of degradation and have resulted in revised inspection and repair criteria. We refer to the process for addressing degradation in this manner as "degradation-specific management." This process is being increasingly relied upon as degradation of steam generators in the U.S. increases and is being addressed by the new rule and RG discussed later in this paper.

The shortcomings in our current regulatory framework (discussed above) have made it necessary for NRC staff to oversee SG activities at plants with significant SG tube degradation to assure safe operation of these units.

This oversight has included review of amendments to the repair criteria in plant TS amendment requests; headquarters and onsite review of licensee SG tube inspection scope, data acquisition, data analysis, personnel qualification and training; and preparation of numerous NRC information notices and generic letters relating to problems occurring in the field. These efforts involve extensive plant specific reviews that require substantial NRC and industry resources.

To address the shortcomings in the current regulatory approach, the NRC staff has initiated rulemaking. This rulemaking has several objectives. The new rule, which will be incorporated into 10 CFR, will be performance-based rather than prescriptive, will be adaptable to new degradation mechanisms and new NDE technology, and will be risk-informed. It will provide incentives for advancing the state of the art of NDE technology.

Summary of the Proposed Rule

The proposed rule requires that each holder of an operating license develop and implement a steam generator maintenance program that provides reasonable assurance that the steam generator tubes remain capable of fulfilling their intended safety functions. To ensure that the tubes are capable of performing their safety functions, the proposed rule requires that each licensee's program provide reasonable assurance of adequate SG tube integrity and, to ensure defense in depth, the means to mitigate occurrences involving abnormal leakage or rupture of the tubing. Adequate tube integrity means that the tubes are capable of sustaining the conditions of normal operation, including anticipated operational occurrences, design-basis accidents, external events, and natural phenomena for which the tubing must perform its safety functions, and it means that risk is kept at an acceptably low level.

In keeping with the objective that the rule be performance-based, the proposed rule requires that NRC-accepted performance criteria commensurate with adequate tube integrity be established as part of the program. The proposed rule requires that the program incorporate a balance of preventive, inspection and repair, and leakage monitoring measures, as necessary, to ensure that the performance criteria will be maintained. In addition, the condition of the SG tubes shall be monitored against these performance criteria to confirm that adequate tube integrity is being maintained. Monitoring methods shall enable reliable assessment of tube condition against the performance criteria. The proposed rule requires that failure to meet these performance criteria be reported to the NRC, and that corrective actions be implemented, as appropriate, to ensure adequate tube integrity during future operation.

Summary of the Draft Regulatory Guide

A draft RG has been prepared to provide guidelines for implementing the proposed rule. The RG will provide an acceptable framework for developing an SG program that will satisfy the requirements of the proposed rule.

The flow chart in Figure 1 illustrates the overall program strategy embodied in the draft RG; it shows the major program elements and subelements. The RG is intended to provide broad guidelines concerning the key considerations, parameters, and the constraints that should be addressed during the development of the program elements. Utilities will develop specific implementation details and methodologies for these program elements. The program elements and subelements must ensure that tube integrity performance can be effectively monitored and controlled relative to the tube performance criteria. It is the intent of these guidelines that licensees have the flexibility to adjust the specifics of the program elements within the constraints of these guidelines to reflect, for example, new information, new NDE technology, new degradation mechanisms, and changes in flaw growth rates without NRC approval. To this end, these guidelines are intended to accommodate the development and implementation of degradation-specific management (DSM) strategies to be documented in industry reports. DSM strategies involve an integrated set of program elements, paralleling those in the RG, that address specific-degradation mechanisms. The principal program elements in the overall strategy for ensuring tube integrity are discussed below.

Risk Assessment

Requirements to be addressed in the rule and RG pertaining to risk and risk assessment depend upon the results of risk studies now being performed to support the NRC steam generator rulemaking activities. This assessment is being performed relative to the NRC Safety Goals which provide certain objectives in terms of core damage frequency and the containment performance, that is, the potential for containment bypass and the resultant consequences.

Key elements of this risk assessment involve the frequency of spontaneous tube ruptures and the conditional probability of tube rupture, not just during postulated events, but also as a result of high pressure, high temperature, severe accident sequences.

The findings of this assessment will be considered in the development of the rule, as necessary, and depending on the outcome, could significantly effect some of the program elements discussed below.

Inservice Tube Inspections

As shown in Figure 1, the program strategy begins with a tube inspection following plant shutdown (Program Element 1.0). The inspection provides information concerning the active degradation mechanisms present in the SGs, the identity of tubes containing flaws and the size or relevant NDE response parameter(s) of these flaws for each active degradation mechanism, and the rate of flaw evolution for each active degradation mechanism. This information is used as part of other Program Elements, discussed below, to assess tube integrity performance relative to the tube integrity performance criteria, to determine the appropriate time interval to the next inspection, to determine the appropriate tube repair criteria, to determine which tubes must be repaired or removed from service, and to assess needed improvements in measures being taken to mitigate active degradation mechanisms.

Guidelines concerning the development and implementation of NDE tube inspection programs are categorized into three subelements, as shown in Figure 1. Subelement 1.1 contains guidelines for assessing, before each inservice inspection, degradation mechanisms that may potentially affect the tubing. This is to ensure that appropriate NDE inspection techniques and personnel are used to address each mechanism. Subelement 1.2 contains guidance concerning the development and implementation of NDE data acquisition and analysis procedures to address each potential degradation mechanism. This subelement also contains guidance about the qualification and performance demonstration of NDE techniques and personnel to ensure adequate flaw detection and sizing performance and to quantify this performance to support the tube integrity assessments discussed below. Subelement 1.3 contains guidance pertaining to the frequency of inspection and the size of the tube inspection sample. These guidelines are intended to ensure that the frequency and scope of inspection is defined in such a manner as to ensure that tube integrity performance criteria will be met.

Performance Criteria

The tube inspections are followed by assessments of tube integrity performance relative to NRC performance criteria acceptable to the NRC; these will be given in the RG (Program Element 2.0). These performance criteria address three areas of tube integrity performance; namely, structural integrity, operational leakage integrity, and accident-induced leakage integrity. These performance criteria are expressed in terms of parameters that can be directly measured or that

can be calculated on the basis of direct measurements. The criteria correspond to conditions that are acceptable, without undue risk to public health and safety.

Performance criteria for tube structural integrity are being developed with the objective that tube structural integrity should be maintained consistent with the general design criteria of Appendix A to 10 CFR 50 and consistent with acceptable risk. Two formulations of the structural performance criteria being prepared: deterministic criteria and probabilistic criteria. Either of these sets of criteria may be used for a given application. Deterministic criteria are expressed in terms of minimum factors of safety, which must be maintained for all tubes. The deterministic criteria in the draft RG are consistent with those in the ASME Code, Section III, and NRC Regulatory Guide 1.121, "Bases for Plugging Degraded PWR Steam Generator Tubes." Probabilistic criteria under consideration are a criterion regarding the acceptable frequency of tube ruptures occurring as an initiating event under normal operating conditions and criteria regarding the acceptable conditional probabilities for inducing one or more tube ruptures as a consequence of the most limiting design-basis accident.

Performance criteria for maintaining operational leakage integrity are being developed with the objective that operational leakage shall not exceed the plant TS limit (568 liters per day (LPD)). These performance criteria serve a different purpose from the TS limit. The TS leakage limit is intended to ensure plant shutdown before a leaking tube ruptures. Leakage in excess of this limit would not constitute, in itself, a TS violation as long as the plant is shut down within the specified time interval. However, leakage in excess of this limit may indicate shortcomings in the overall program for ensuring adequate tube integrity. By setting the performance criteria equal to the TS limit, the utility is obliged to assess the root causes of any leakage exceeding 568 LPD and to take corrective actions to prevent a reoccurrence.

Performance criteria for accident-induced leakage are being developed with the objectives that the primary-to-secondary leak rate not exceed the total charging pump capacity of the primary coolant system and that the consequential doses during design-basis accidents should be consistent with applicable guidelines in 10 CFR 100 for offsite dose and GDC-19 for control room dose.

Tube Integrity Assessments

Tube integrity is subject to two different types of assessments, as indicated in Figure 1: a condition monitoring assessment (Program Element 3.0) and an operational assessment (Program Element 4). The condition monitoring assessment is "backward looking" in that its purpose is to confirm that adequate tube integrity has been maintained since the last inspection. Condition monitoring involves an assessment of the "as found" condition of the tubing relative to the tube integrity performance criteria. The condition monitoring assessment may utilize information from the tube inspections or from alternative test/examination methods to assess the condition of the tubing. NRC should be promptly notified (Program Element 11.0) if condition monitoring reveals one or more tubes that fail to meet the performance criteria. Note that this finding may

be indicative of programmatic deficiencies in the licensee's implementation of the proposed rule. In addition, licensees should assess the causal factors associated with this type of finding and implement appropriate corrective actions (Program Element 6.0). The condition monitoring assessment and implementation of necessary corrective actions must be completed before plant restart.

The operational assessment differs from the condition monitoring assessment in that it is "forward looking" rather than "backward looking." Its purpose is to demonstrate reasonable assurance that the tube integrity performance criteria will be met throughout the period leading up to the next scheduled tube inspection. Operational assessment involves projecting, at an appropriate level of confidence, the condition of the tubing at the time of the next scheduled inspection outage relative to the tube integrity performance criteria. This projection is based on the inspection results mentioned above, the tube repair criteria to be implemented for each degradation mechanism in accordance with Program Element 5.1, and the time interval preceding the next scheduled tube inspection. Corrective actions (Program Element 6.0) have to be taken as necessary to ensure that the performance criteria are met. Corrective actions may include inspecting the steam generators at more frequent intervals and reducing the tube repair criteria. The operational assessment and implementation of any necessary corrective actions should be completed within a defined time frame after plant restart. As a practical matter, however, it will be benefit licensees to complete the operational assessment, or to complete a preliminary assessment, before performing tube plugging or other repairs to ensure that the repair criteria being implemented are support the licensee's schedule for performing the next SG tube inspection.

Tube Plugging and/or Repairs

Plugging and repairing defective tubes are based on the results of the tube inspections and operational assessment. Defective tubes are those with indicated flaws exceeding the tube repair limit. Plugging and repairing defective tubes are intended to ensure that tubes remaining in service will meet the tube integrity performance criteria until the next scheduled tube inspection. The appropriate repair limit (Program Element 5.1) for each degradation mechanism is generally determined in parallel with the operational assessment since the outcome of the operational assessment is a function of the tube repair criteria values to be employed. Guidelines are being prepared for developing appropriate plugging and repair methodologies and the associated hardware (e.g., plugs and sleeves).

Preventive Measures

Preventive measures should be developed and implemented (Program Element 7.0). These measures involve mitigating active degradation mechanisms and minimizing the potential for new degradation mechanisms (such as the introduction of loose parts and foreign objects). Guidelines concerning the development of preventive measures are categorized into three subelements, as shown in Figure 1. Subelements 7.1 presents guidelines concerning secondary

water chemistry control. Subelement 7.2 involves guidelines concerning measures to control loose parts and foreign objects within the steam generators. Subelement 7.3 presents guidelines concerning other measures for mitigating active degradation mechanisms. These guidelines are not prescriptive; rather they identify the elements necessary for an effective program. Various preventive measures are implemented continuously during plant operation and shutdown. The need for enhancements to these measures should be reviewed and implemented, as necessary, on the basis of inspection findings and the tube performance assessments.

Accident Mitigation Methods

Program Element 10 presents guidance on maintaining measures to ensure the ability to mitigate occurrences involving abnormal leakage or rupture of the tubing. Program Elements 10.1 and 10.2 address emergency operating procedures and operator training, respectively.

Operational Leakage Monitoring/Limits

Primary-to-secondary leakage monitoring is an important defense-in-depth measure that can assist plant operators in monitoring overall tube integrity during operation. Monitoring also gives operators the information they need to safely respond to a situation in which tube integrity becomes impaired and significant leakage or tube failure occurs.

Although leak before break cannot be totally relied upon for SG tubes, primary-to-secondary leakage monitoring can afford early detection and quick response to rapidly increasing leakage, thereby serving as an effective means for minimizing the incidence of SG tube ruptures. This can be achieved by having approximately real-time leakage information available to control room operators.

The guidelines for operational primary-to-secondary leakage monitoring (Program Element 8) are intended to ensure that leakage is effectively monitored and that appropriate and timely action will be taken before a leaking tube exceeds the tube integrity performance criteria, including tubes leaking at rapidly increasing rates. Guidelines concerning operational primary-to-secondary leakage monitoring are categorized into two subelements, as shown in Figure 1. Subelement 8.1 addresses the development of monitoring programs, such as monitoring strategies, operator response guidelines, and operator training. Subelement 8.1 addresses the development of permissible limits for operational leakage.

Outstanding Issues and Status

A number of issues need to be addressed before the proposed rule can be issued. The first issue, risk, has been addressed above. The next issue involves the rule implementation strategy. For example, under the existing regulatory framework, the NRC explicitly reviews and approves (or denies) licensee repair criteria if the criteria differ from those in the plant TS, and the details of the accompanying inspection methods. This is not the intent under the framework of the

proposed rule. The agency must determine which elements of a licensee's SG program should be subject to NRC approval. This includes such items as performance criteria. It is NRC's current thinking that the performance criteria that are utilized will have to be approved by the NRC. What remains under discussion, however, is whether other aspects of the SG program under the new framework need to be subject to NRC approval. Since, from a regulatory perspective, we will be relying heavily on condition monitoring to provide information on tube integrity performance, a case can be made that the methodology for condition monitoring should be subject to NRC approval.

Another outstanding issue deals with degradation mechanisms for which no NDE technique is qualified and/or for which the detection or sizing performance of the technique is not adequately quantified. Guidance needs to be provided on the alternatives for demonstrating that the structural and leakage performance criteria are being met under these circumstances. The staff is considering alternative methods such as in situ pressure testing and a protocol for determining which tubes are selected for in situ pressure testing.

The schedule for the proposed rule calls for issuing it for public comment in March 1997 and for issuing the final rule in March 1998.

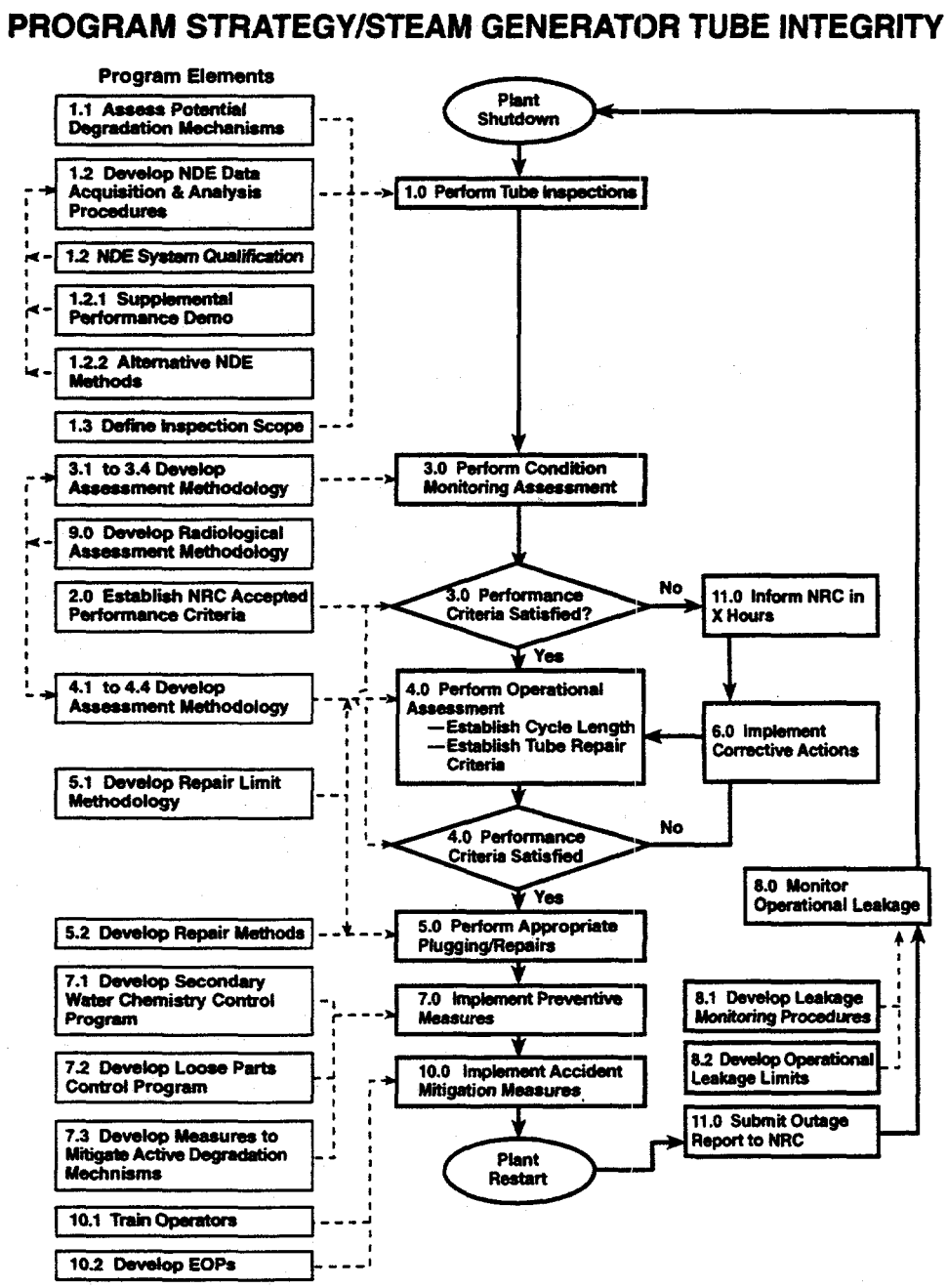

Figure 1. Program strategy/steam generator tube integrity.

Modeling of Eddy Current Probe Response for Steam Generator Tubes

S. Bakhtiari and D. S. Kupperman
Energy Technology Division
Argonne National Laboratory

Abstract - Sample calculations were performed with a three-dimensional (3-D) finite-element model analysis that describe the response of an eddy current (EC) probe to steam generator (SG) tubing artifacts. Such calculations could be very helpful in understanding and interpreting of EC probe response to complex tube/defect geometries associated with the inservice inspection (ISI) of steam generator (SG) tubing. The governing field equations are in terms of coupled magnetic vector and electric scalar potentials in conducting media and of total or reduced scalar potentials in nonconducting regions. To establish the validity of the model, comparisons of the theoretical and experimental responses of an absolute bobbin probe are given for two types of calibration standard defects. Preliminary results are also presented from a recent theoretical study of the effect of ligament size in axial cracks on EC indications with conventional ISI bobbin probes.

INTRODUCTION

Eddy current nondestructive testing (NDT) techniques are currently the primary method for ISI of SG tubing. EC inspection is routinely carried out with bobbin coil probes that are very rapid compared with most other techniques Because of technological advancements in digital electronics, real-time data acquisition and analysis, and probe design, EC inspection techniques provide increased resolution and sensitivity. However, interpretation of these signals is often difficult even for experienced operators. A better understanding of the nature of the interaction of the induction coil field with heterogeneous media can lead to improved analysis and interpretation of EC NDT results. Exact solutions using analytical techniques,[1,2] as well as two-dimensional numerical solutions,[3] are limited to relatively idealized probe/defect geometries. More flexible computational techniques such as the finite-element method (FEM) are required for the analysis of more realistic probe/defect geometries. The results from such calculations can help in development of appropriate characterization schemes and can reduce the need for expensive experimental work. Further, such models may also be used to develop a data base of simulated defect indications that can be used for initial characterization of improved signal processing and real-time data analysis techniques.

Probe responses to typical calibration standard tubing artifacts were calculated with a 3-D FEM-based code ELEKTRA by Vector Fields. The governing electromagnetic (EM) field equations in terms of magnetic vector and electric scalar potentials in conducting media and reduced or total scalar potentials in nonconducting regions are solved using finite-element discretization. Probe impedance is determined through energy and power calculations. The signal trajectory in the impedance plane, due to probe motion, is determined by calculating the response at discrete points along the tube axis. Representative test cases that simulate steady-state solutions using both differential and absolute bobbin coils are presented here. Preliminary results of a recent study of the effect of ligament size in axial cracks on the EC signals from conventional bobbin coil probes are also presented.

EM FORMULATION

The governing field equations used in the 3-D FEM problem space are given next. In the conducting regions, these equations are expressed in terms of the magnetic vector potential $\overline{A}$ and electric scalar potential V. In nonconducting regions, they are expressed in terms of either total (ψ) or reduced (ϕ) scalar potentials. Application of the Coulomb or Lorentz gauge, respectively, would allow simultaneous solution of coupled or decoupled vector and scalar potential equations. In conducting media, where the induced eddy currents flow, the governing equations can be written as[4]

$$\nabla \times \frac{1}{\mu} \nabla \times \overline{A} - \nabla \frac{1}{\mu} \nabla \cdot \overline{A} + \sigma \frac{\partial \overline{A}}{\partial t} + \sigma \nabla V = 0 \tag{1}$$

$$\nabla \cdot \sigma \nabla V + \nabla \cdot \sigma \frac{\partial \overline{A}}{\partial t} = 0 \tag{2}$$

and in nonconducting regions that contain the impressed current sources, the scalar potential equations are defined as

$$\nabla \cdot \mu \nabla \phi - \nabla \cdot \mu \left(\int_{\Omega} \frac{\overline{J} \times \overline{R}}{|\overline{R}|^3} d\Omega \right) = 0 \tag{3}$$

$$\nabla \cdot \mu \nabla \psi = 0, \tag{4}$$

which are then solved using finite-element discretization. The intrinsic electrical properties of each medium are incorporated through permeability μ and conductivity σ. The quantities of interest for EC NDT, namely, the change in the coil resistance and reactance, for impedance probes can be determined through energy and power calculations by using

$$W = \frac{1}{2} \int_{v} \overline{B} \cdot \overline{H} \, dv \tag{5}$$

$$P = \int_{v} \frac{J^2}{\sigma} dv \tag{6}$$

The computer-aided-design-based preprocessor stage of the software allows generation and discretization of the finite-element mesh containing the model geometry. Analysis and display of the solutions are carried out at the postprocessing stage.

NUMERICAL AND EXPERIMENTAL RESULTS

A series of test case simulations were initially carried out to verify the accuracy of the FEM solutions by comparison with detailed experimental measurements. The experimental EC data, supplied by C. V. Dodd,[†] were made on a large aluminum tube containing through-wall holes and axial slits. Measurements were made at three different frequencies with a Hewlett-Packard impedance analyzer and a specially constructed absolute bobbin coil (SN480A). The results presented here compare the experimental data for a through-wall hole and an axial slit with the FEM calculations. The results are expressed in terms of both calculated impedance variations as a function of probe position inside the tube and impedance-plane plots that simulate conventional EC instrument display.

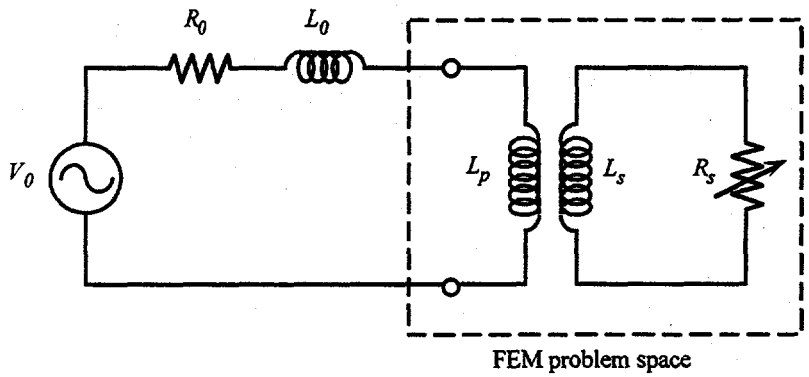

Fig. 1. Lumped element equivalent circuit of EC probe and sample with the region of problem space modeled by FEM shown within the dashed rectangle.

Figure 1 shows the lumped element equivalent circuit for the probe and test sample (tube) interaction modeled as primary and secondary sides of a transformer circuit. Also shown within the dashed rectangle is the part of the circuit modeled by the FEM problem space. In reference to this figure, it should be noted that the final solutions are normalized to eliminate explicit dependence of the parameters on the coil/cable resistance R_0. These normalized parameters are experimentally determined as

$$X_n = \frac{X}{X_0} \tag{7}$$

$$R_n = \frac{R - R_0}{X_0}, \tag{8}$$

[†]Experimental results provided by C. V. Dodd were completed while with Oak Ridge National Laboratory.

where

$$X_0 = \omega L_0 \tag{9}$$

represents the coil reactance in air. By using the normalized variables (equations 7 and 8), R_0 can be ignored. This normalization allows direct comparison of the theoretical and experimental data.

VERIFICATION OF COMPUTATIONAL RESULTS

Figure 2 depicts the aluminum tube standard used in the measurement. It contains three sets of four axially symmetric (repeated every 90° around the tube circumference) artifacts. EC probe readings are the average of nine measurements, each made with a different circumferential orientation. The values of resistance and reactance (in ohms) were determined with a Hewlett-Packard impedance analyzer. In reference to Fig. 3, which shows the cross section of the tube and coil geometry, the tube has inner radius $r_i^t = 38.86$ mm ($\approx$ 1.53 in.) and outer radius $r_o^t = 44.45$ mm ($\approx$ 1.75 in). The through-wall hole artifact has a diameter of $D^h = 11.18$ mm ($\approx$ 0.44 in.), and the slit has a length of $l^g = 36.0$ mm ($\approx$ 1.42 in.) and a width of $w^g = 0.38$ mm ($\approx$ 0.015 in.). The coil has inner radius $r_i^c = 31.75$ mm, outer radius $r_o^c = 38.0$ mm, width $w = r_o^c - r_i^c = 6.25$ mm, and length $l = 6.60$ mm. A measured resistivity value of $\rho = 3.88\,\mu\Omega - cm$ was used to simulate the aluminum tube material. The coil was wound over a Teflon form with #36 gauge wire.

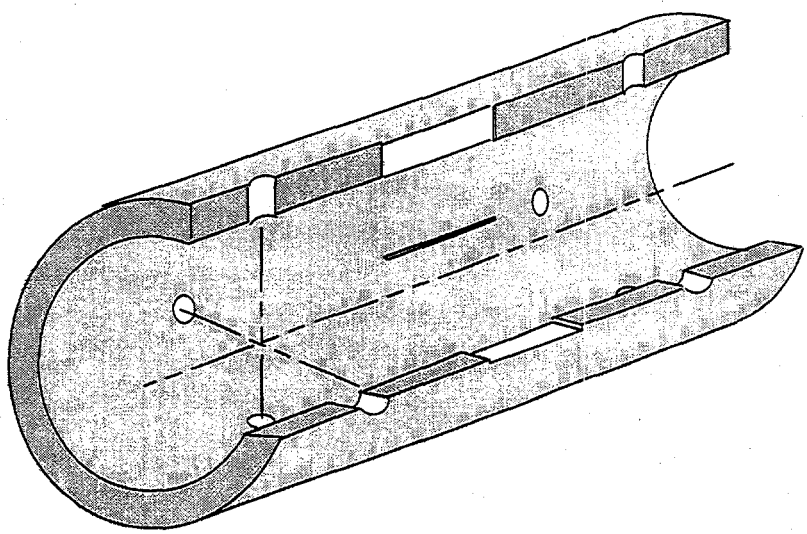

Fig. 2. Geometry of the aluminum tube standard with through-wall hole and axial slit artifacts placed symmetrically (90° apart) around the circumference.

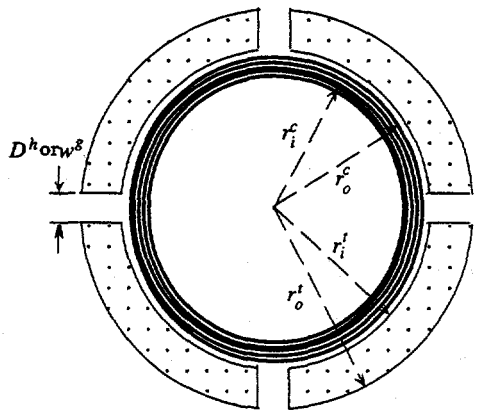

Fig. 3. Cross-sectional geometry of the absolute bobbin coil inside the aluminum tube with one set of through-wall artifacts 90° apart around the circumference.

The computed results are given in terms of both current density distribution over the tube surface and calculated impedance components. In the FEM model, all materials were assumed to be nonmagnetic (i.e., relative permeability $\mu_r = 1$). The coil represents $N = 1836$ turns carrying a unit current density (A/mm^2). Figures 4(a) and (b) depict the tube/coil geometry, along with the distribution of the current density, $|\bar{J}|$, at $f = 0.5$ kHz for the two artifacts modeled here. The coil center in these figures coincides with the defect center in the axial direction. Due to the symmetry of the geometry, only 1/8 of the problem was modeled in both cases. Results are displayed for the case that the probe is positioned at $z = 0$ mm (center of the defect is at $z = 0$ mm). The FEM solution for the distribution of current density on the aluminum tube with a through-wall hole having a diameter of 11.18 mm using an absolute bobbin coil operating at $f = 0.5$ kHz is shown in Fig. 4(a). Current distribution for the slit is shown in Fig. 4(b). The distribution on the tube outer surface at 0.5 kHz shows the distortion along the path of circumferentially induced currents due to presence of through-wall artifacts. It can be observed that the lowest test frequency chosen here allows for detection of outer surface artifacts for the highly conducting aluminum material. On the other hand, attenuation at the highest frequency measured, $f = 7.5$ kHz, would allow detection of only near inner-surface artifacts corresponding to the shallow skin depth.

Figures 5 and 6 show theoretical and experimental results for variation of the coil resistance and reactance as a function of the axial position along the tube and the impedance-plane plot of the same data. The results show close agreement between theory and measurement both for the simulated through-wall hole and axial slit. Agreement for the through-wall hole is not as good at the highest frequency. This could be associated with operating the coil near the coil/cable resonance and the effect of inner winding capacitance at higher frequencies for coils with thick gauge wire. Better consistency between the theory and measurement is generally expected at frequencies away from the resonance where probe sensitivity is minimal to such parameters. The

3-D FEM computations correctly predict the variation of the EC bobbin probe signal in the presence of axisymmetric artifacts.

The above results indicate a substantial difference in the EC signal amplitudes associated with the two artifacts modeled here. Bobbin probe signal amplitude alone can not generally be regarded as an absolute indication of the volumetric extent of defects when comparing different flaw geometries. This can be observed from comparison of the probe impedance responses, which are linearly proportional to the probe output voltage, for the two defect geometries modeled here. Although the through-wall hole has a much greater volume than the axial groove, it results in a smaller perturbation of the coil impedance. Eddy currents always flow through the path of least resistance in a conducting medium. The discontinuity (infinite resistance) introduced by the thin but long axial groove forces the currents to take a contour around the defect which in turn gives rise to a larger impedance mismatch for the probe.

THEORETICAL ANALYSIS OF AXIAL GROOVE WITH LIGAMENT

The preliminary results on the effect of ligaments on bobbin coil signals due to axial grooves are presented below. These test cases pertain to simulation of the probe response to axial grooves, 100% and 75% through-wall, on 22.225-mm (0.875 in.) outer diameter (OD) Inconel 600 tubing with a nominal wall thickness of 1.27 mm (0.05 in.) and conductivity of $\rho = 100.0\ \mu\Omega - cm$. The probes modeled are conventional 18.3 mm (0.72 in.) OD differential and absolute bobbin coils, and the simulations used frequencies of f = 100 kHz and f = 400 kHz, typical frequencies used for multifrequency ISI of SG tubing. Once again, the results are given in terms of both current distribution along the tube and computed resistance and reactance values as a function of probe position. Finally, simulation results are presented to show the expected normalized variation in an absolute bobbin probe signal amplitude at two frequencies as a function of ligament size in axial an groove, 100% and 75% through-wall, respectively.

Figure 7 depicts the cross-sectional geometry of an absolute bobbin coil located symmetrically under an axial slit with a ligament. For all test cases considered here, slit length was arbitrarily chosen to be C = 25.4 mm (1 in.), and unless otherwise specified, the ligament length was taken to be L = 0.127 mm (0.005 in.). The width of the slit was also taken to be 0.127 mm. The ligament was positioned symmetrically in the middle of the slit. Coil length and height were taken to be 1.27 and 1.525 mm, respectively. For the differential bobbin probe, the coil spacing was taken to be 1.525 mm.

Figure 8(a) and (b) show the distribution of current density due to presence of a ligament at f = 100 kHz for a differential and absolute bobbin probe, respectively. To simultaneously display the inner and outer distribution of currents, two 45° top and bottom sections of the tube are shown. In Fig. 8(a), the lagging coil of the differentially wound probe is positioned under the defect at z = 1.5 mm. For the results shown in Fig. 8(b), the absolute coil was positioned in the middle of the axial slit at z = 0. Comparison of the current distributions shown in Fig. 8 with

that shown earlier in Fig. 6(b) for the axial groove without ligament clearly reveals that the small ligament creates a path for the circumferentially induced currents to flow across the slit, which consequently results in a reduction of the probe signal amplitude. Similar results are shown in Fig. 9 for a 75% OD through-wall groove with the same size ligament. Observation of these results also show similar trends except that the presence of a thin layer of normal tubing material under the groove causes currents to flow primarily underneath the artifact and again result in reduction of the signal amplitude relative to the case in which the artifact is 100% through-wall.

Figures 10 and 11 are plots of the computed impedance response of the absolute bobbin probe for the slit, with and without the ligament, at f = 100 kHz and f = 400 kHz, respectively. In both cases, presence of the ligament significantly changes the probe signal variation. Impedance plane plots of the differential coil for the same defect geometry are shown in Fig, 12. Figure 13 shows the computed response for the absolute coil at f = 100 kHz, for the 75% OD slit with and without ligament. As expected, the presence of the ligament results in a significantly smaller change in coil response than for the 100% through-wall slit as a result of the presence of ID tubing material under the defect, which forces the currents to flow primarily underneath the OD artifact. Figure 14 shows impedance variations for the same test case geometry and at the same frequencies except that a differential coil was modeled. For the most part, the results show only small changes in the impedance plane trajectory due to the presence of the ligament, relative to the changes for the 100% through-wall slit.

Finally, to examine the effect of ligament size in a long axial groove on the absolute bobbin coil response, a series of computations were carried out by placing the coil symmetrically under the artifact and then varying the ligament length. The geometry of the model was depicted in Fig. 7. Figure 15(a) shows the result of the analysis at frequencies of 100 and 400 kHz for the 100% through-wall slit. Calculated values are displayed as percent change in probe signal amplitude as a function of ligament length. Similar calculations are shown in Fig. 15(b) for the 75% OD through-wall groove. In both cases, the change in bobbin coil signal amplitude variations quickly drops with the increase in ligament length and approaches the abscissa, which represents no defect.

CONCLUSIONS

Computational electromagnetic results pertaining to modeling of EC NDT of tubing artifacts with absolute and differential bobbin probes were determined with a 3-D FEM analysis code. The validity of solutions for axisymmetric defect geometries was initially demonstrated by comparing theoretical results with laboratory-based measurement data made with an impedance analyzer on an aluminum tube standard. Preliminary simulation results were also presented in an attempt to model the effect of narrow ligaments on bobbin coil indications for a thin slit. These results show the applicability of FEM-based solutions for predicting the response of EC probes to flaws in steam generator tubes, and they also suggest that computational EM models may be helpful for the analysis and interpretation of EC NDT indications.

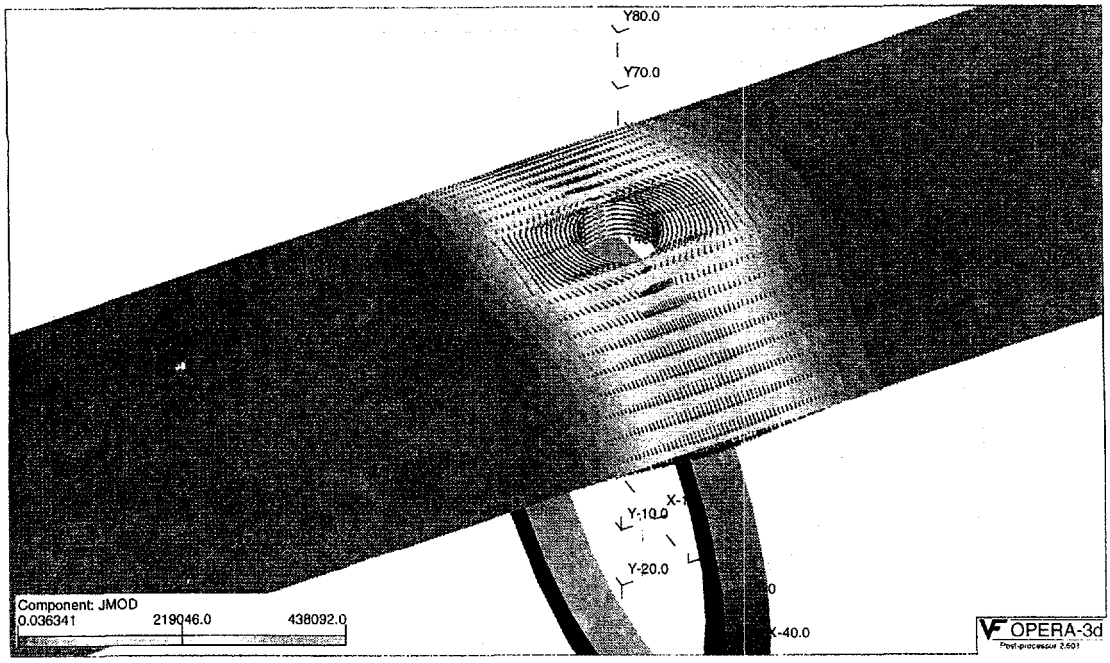

(a)

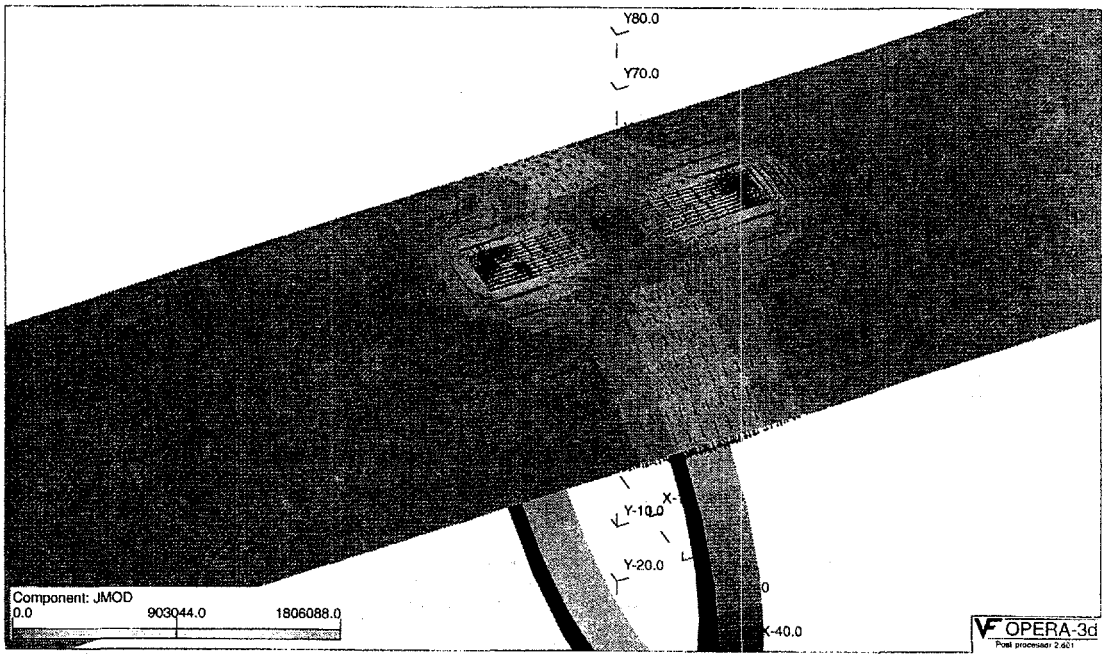

(b)

Fig. 4. FEM solution for the distribution of current density due to an absolute bobbin coil at $f = 0.5$ kHz on the aluminum tube with (a) through-wall hole, and (b) axial slit.

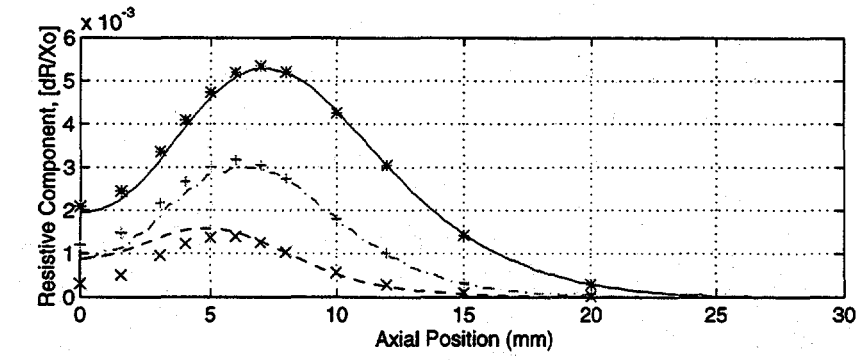

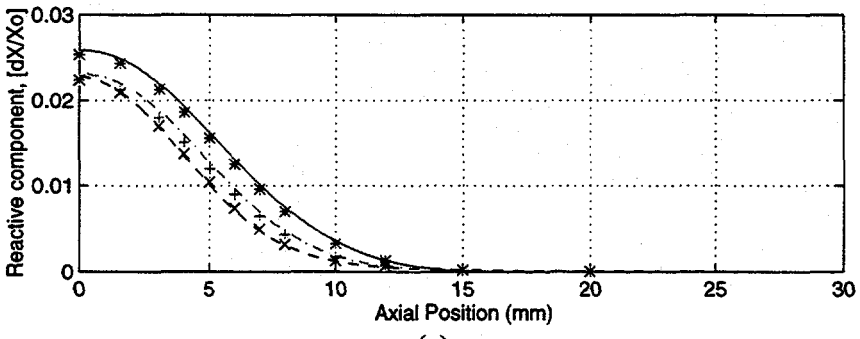

(a)

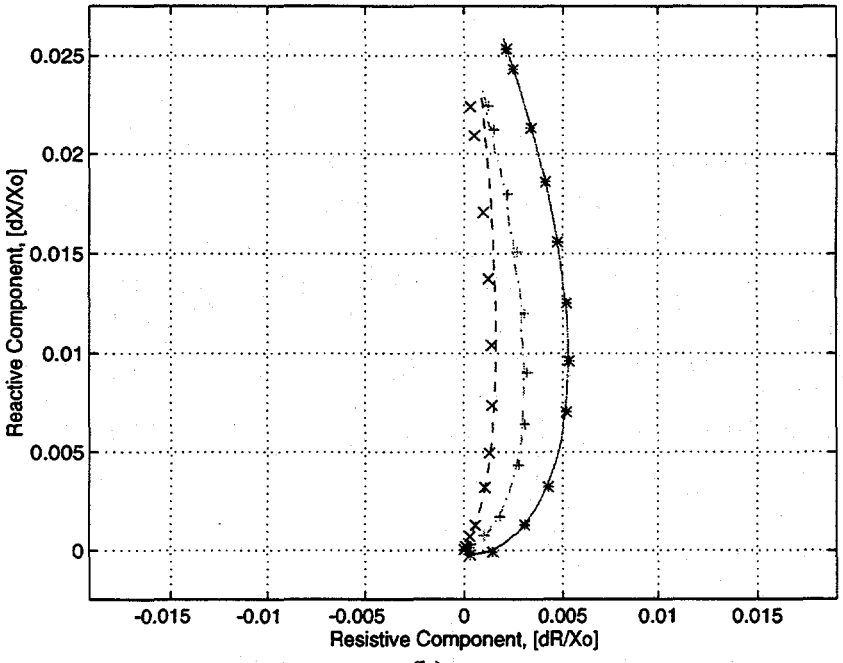

(b)

Fig. 5 Experimental [-, -., --] and numerical [*, +, x] results of (a) resistance and reactance as a function of position of absolute bobbin coil, and (b) impedance-plane signal trajectory, at f = 0.5, 1.2, and 7.5 kHz, respectively. Artifacts are four axially symmetric through-wall holes (90° apart around tube circumference).

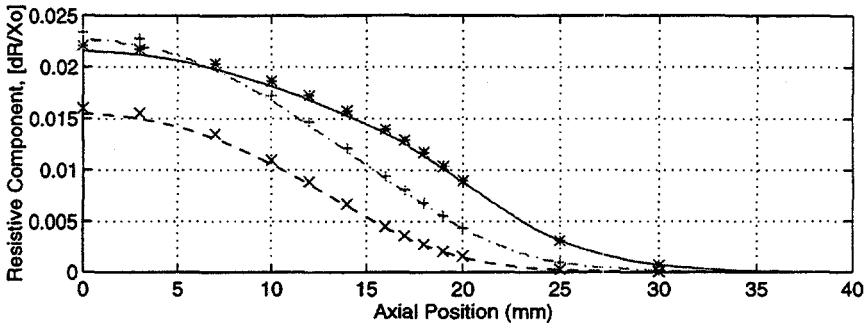

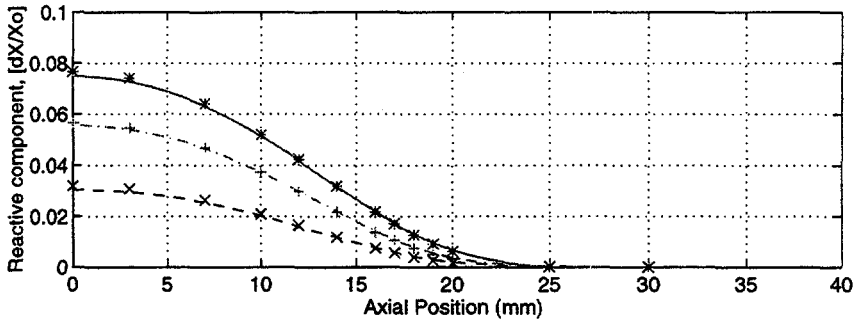

(a)

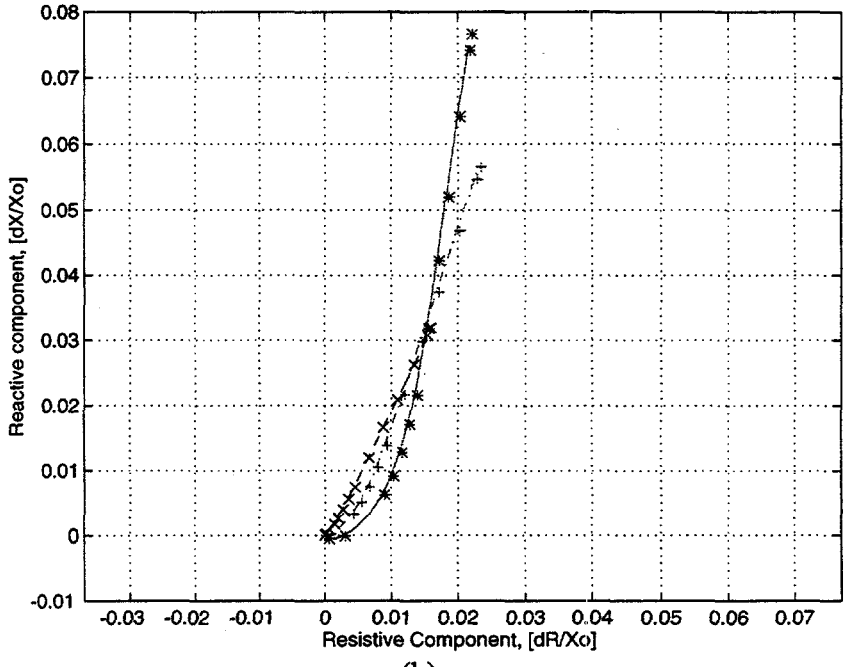

(b)

Fig. 6 Experimental [-, -., --] and numerical [*, +, x] results of (a) resistance and reactance as a function of position of absolute bobbin coil, and (b) impedance-plane signal trajectory, at f = 0.5, 1.2, and 7.5 kHz, respectively. Artifacts are four axially symmetric slits (90° apart around the tube's circumference).

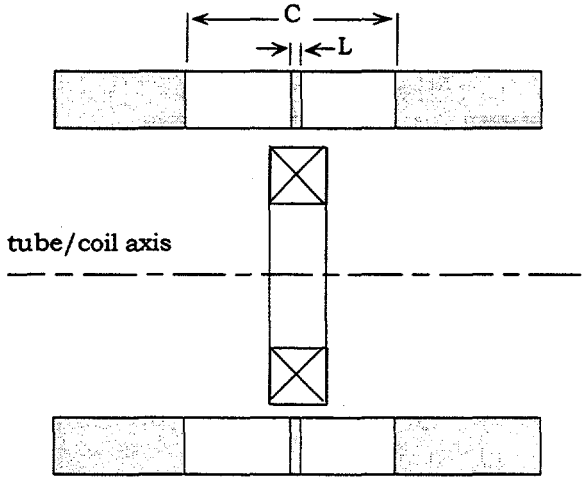

Fig. 7. Cross-sectional geometry of absolute bobbin coil inside a tube with four symmetric axial slits of length C and ligament of length L.

ACKNOWLEDGMENTS

This work was supported by the Office of Nuclear Regulatory Research, U. S. Nuclear Regulatory Commission; Program manager, Dr. Joseph Muscara, Division of Engineering Technology. The authors thank C. V. Dodd for providing the experimental data.

REFERENCES

[1] Pate, J. R., and C. V. Dodd, "Computer Programs for Eddy-Current Defect Studies", Oak Ridge National Laboratory, 1990, NUREG/CR-5553.

[2] C. V. Dodd, "The Use of Computer-Modeling for Eddy-Current Testing," Research Techniques in Nondestructive Testing, ed. R. S. Sharpe, Vol. 3, Ch. 13, pp. 429-479, Academic Press, London, 1977.

[3] Lord, W., and R. Palanisamy, "Development of Theoretical Models for Nondestructive Testing Eddy-Current Phenomena," Eddy-Current Characterization of Materials and Structures, eds. by G. Birnbaum and G. Free, pp 5-21, ASTM, 1981.

[4] Trowbridge, C. W., "An Introduction to Computer Aided Electromagnetic Analysis," Vector Fields Ltd., 1990.

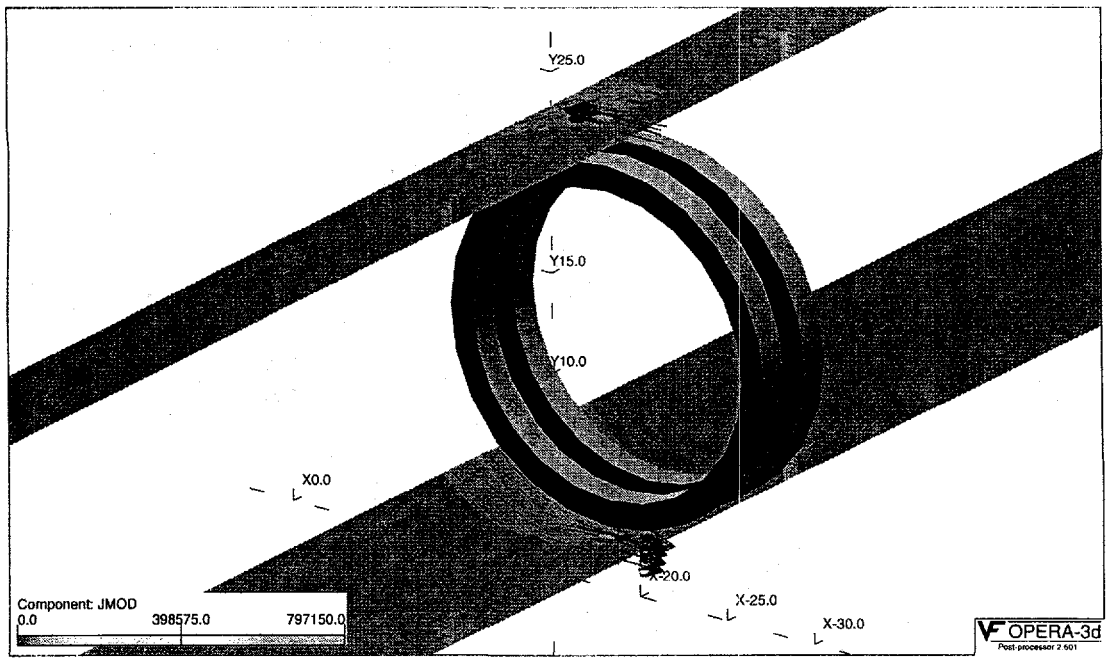

(a)

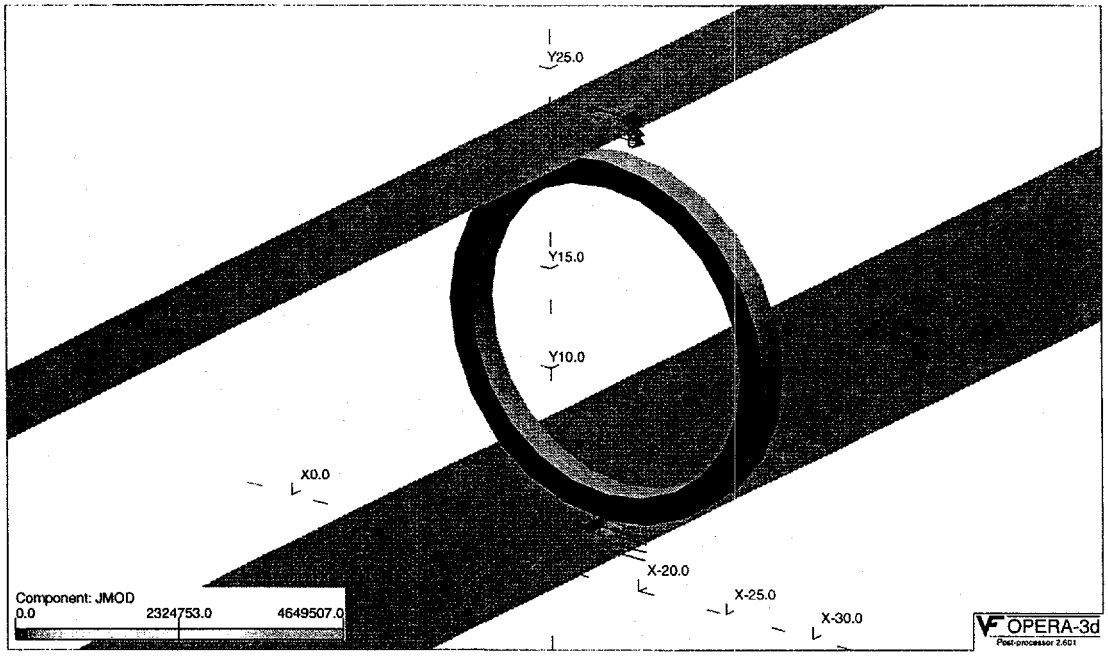

(b)

Fig. 8. FEM solution for distribution of current density due to (a) differential and (b) absolute bobbin coil at f = 100 kHz on Inconel 600 tube with 25.4-mm-long, 0.127-mm-wide axial 100% through-wall slit with 0.127-mm long ligament in center.

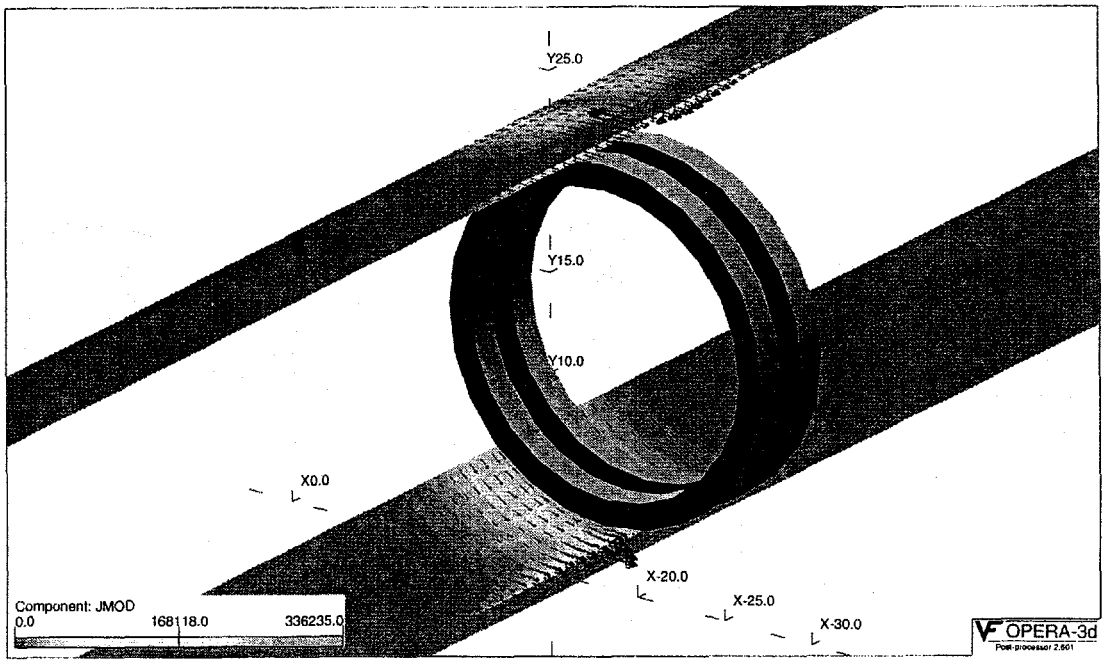

(a)

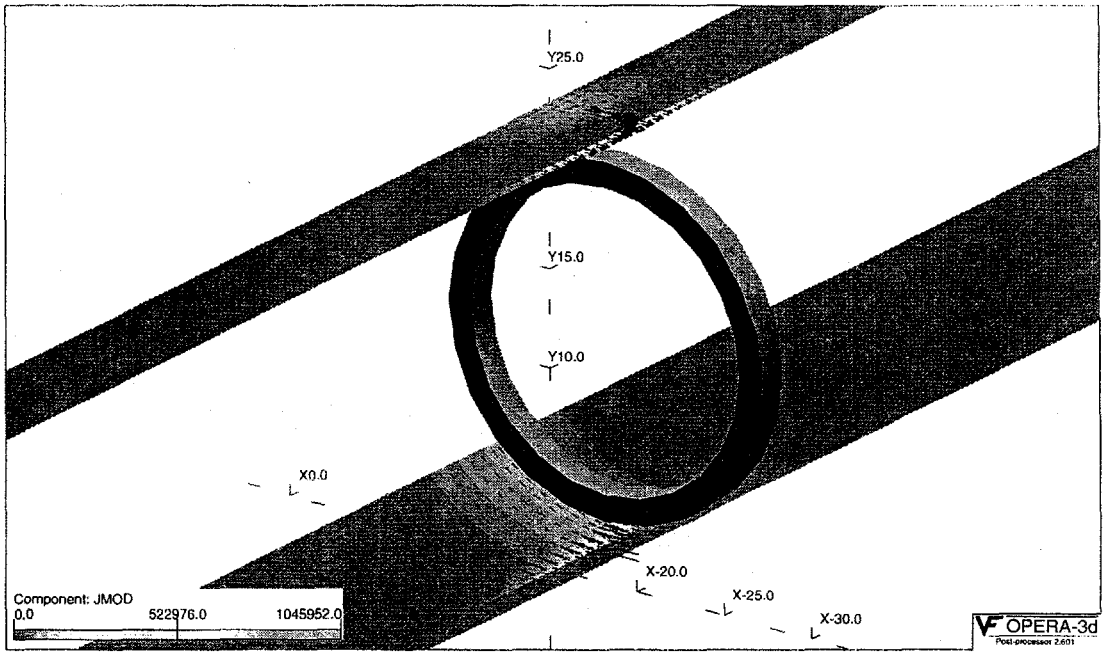

(b)

Fig. 9. FEM solution for distribution of current density due to (a) differential and (b) absolute bobbin coil at f = 100 kHz on Inconel 600 tube with 25.4-mm-long, 0.127-mm-wide 75% OD axial groove with 0.127-mm long ligament in center..

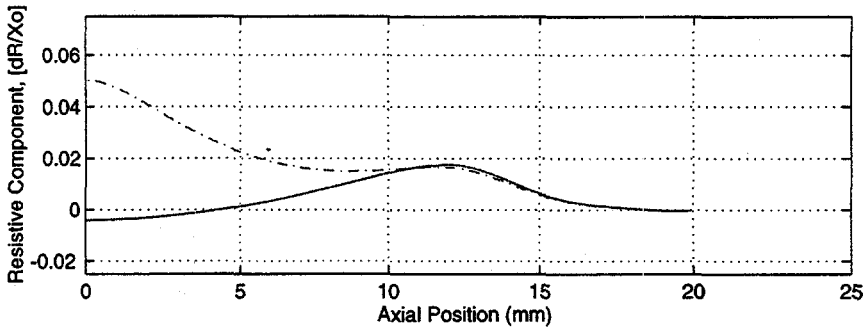

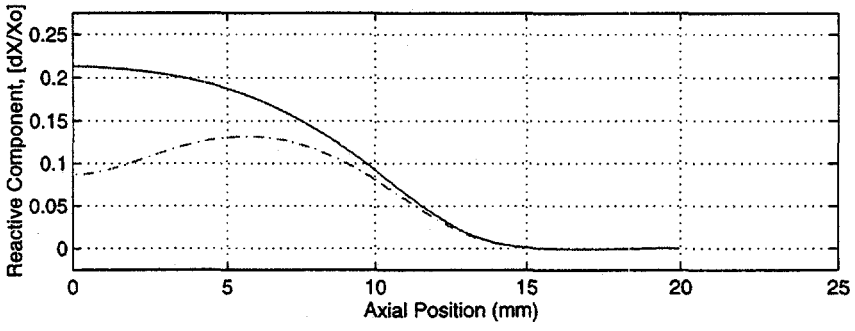

(a)

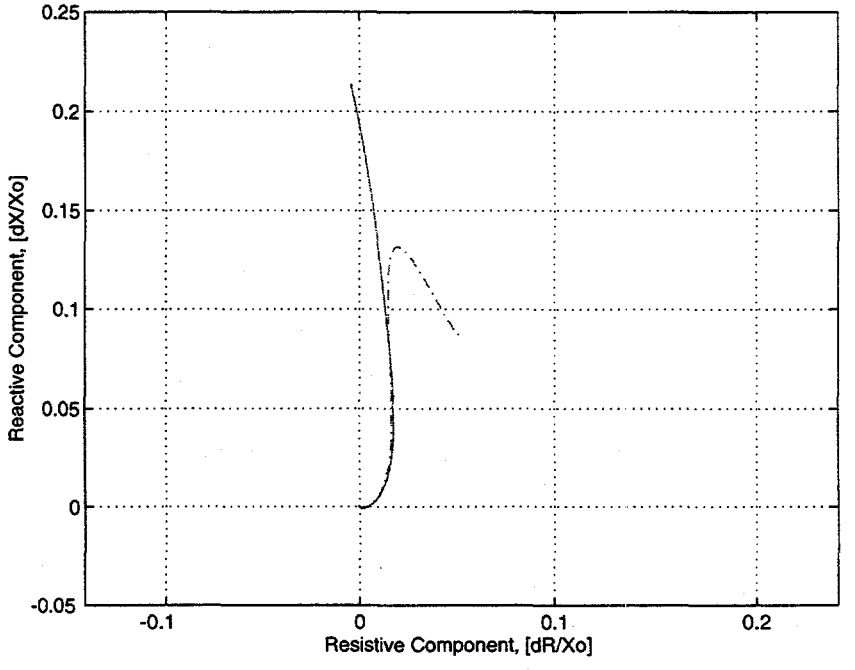

(b)

Fig. 10. Numerical results of (a) resistance and reactance as a function of position, and (b) impedance-plane signal trajectory, at f = 100 kHz. Artifacts are four axially symmetric 100% through-wall slits, without (solid line) and with (dashed line) ligament.

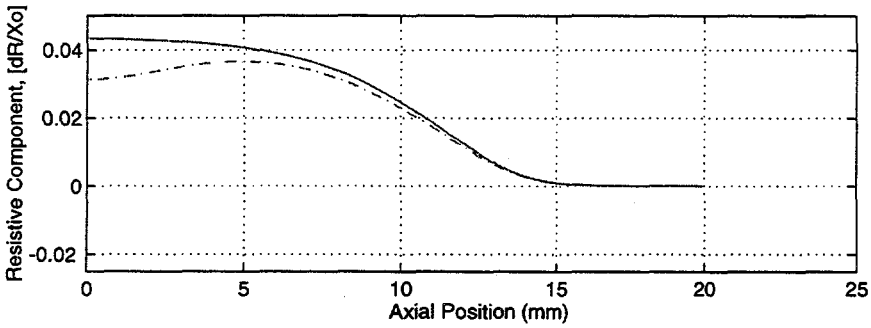

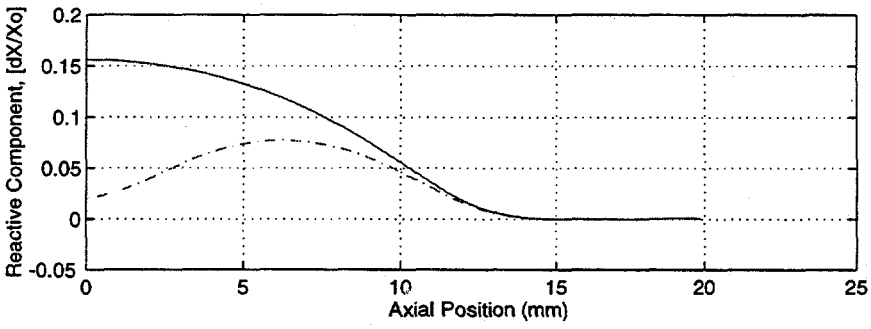

(a)

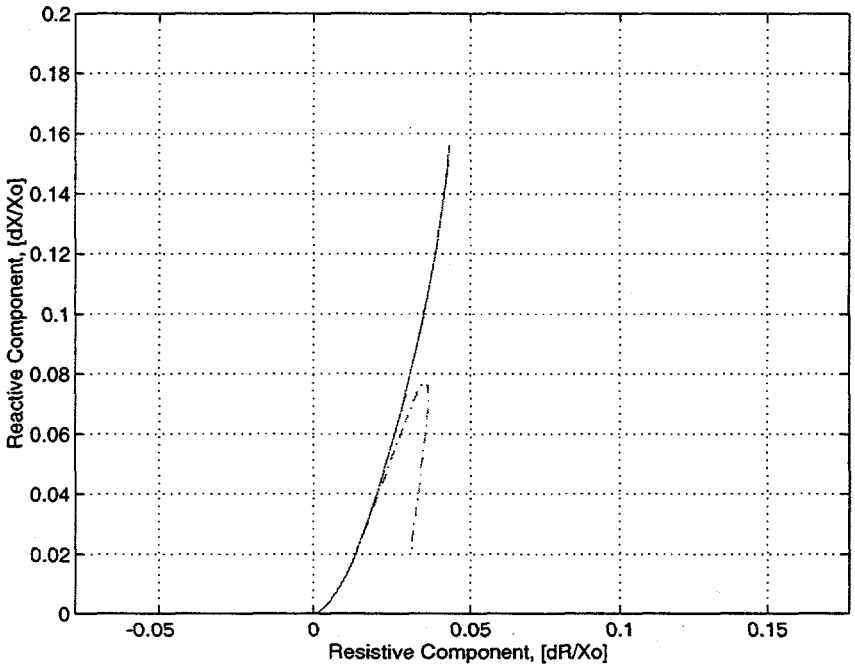

(b)

Fig. 11. Numerical results of (a) resistance and reactance as a function of position, and (b) impedance-plane signal trajectory, at $f = 400$ kHz. Artifacts are four axially symmetric 100% through-wall slits, without (solid line) and with (dashed line) ligament.

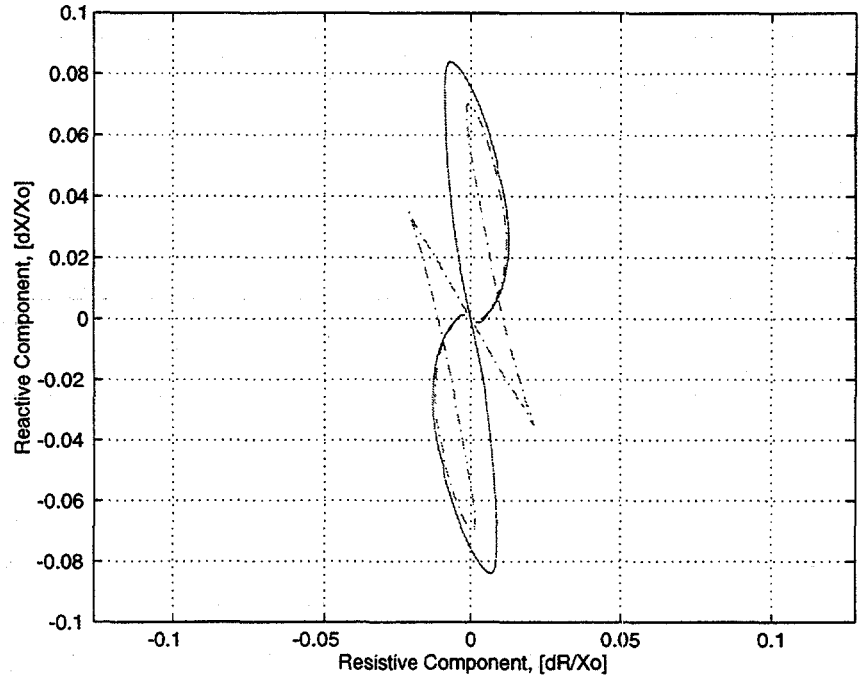

(a)

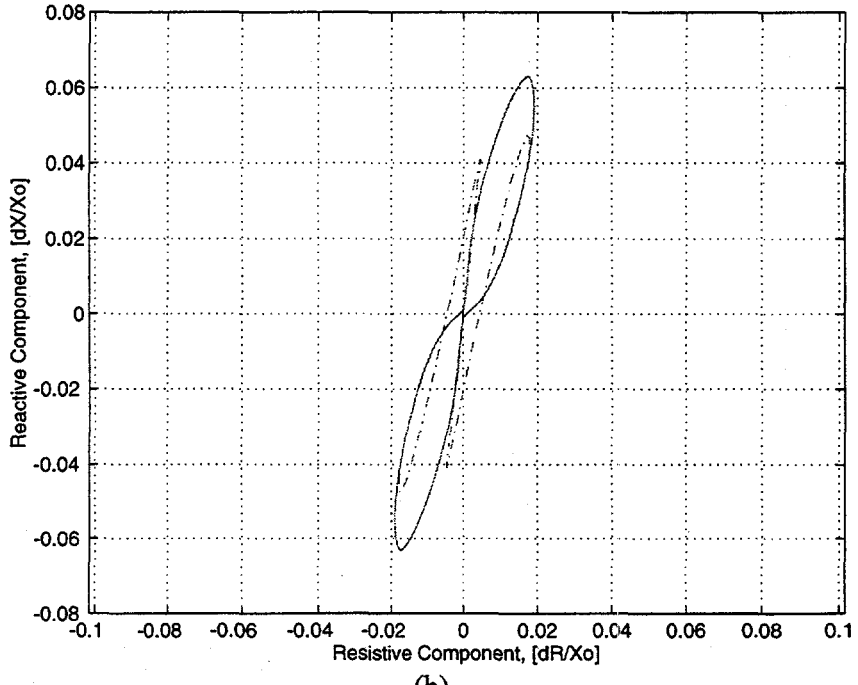

(b)

Fig. 12. Numerical results of impedance-plane signal trajectory, at (a) f = 100 kHz, and (b) f = 400 kHz. Artifacts are four axially symmetric 100% through-wall slits without (solid line) and with (dashed line) ligament.

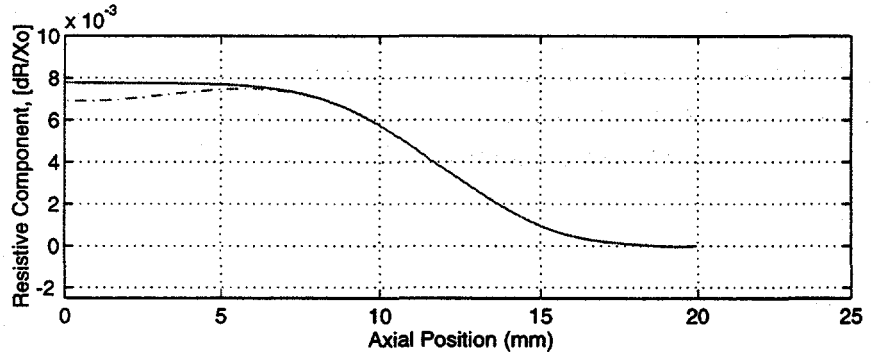

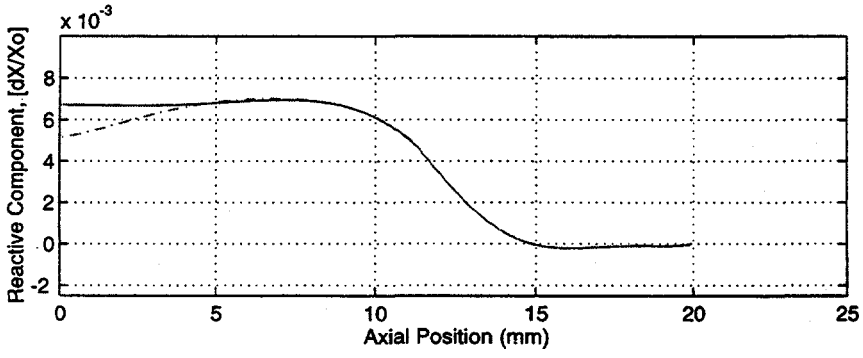

(a)

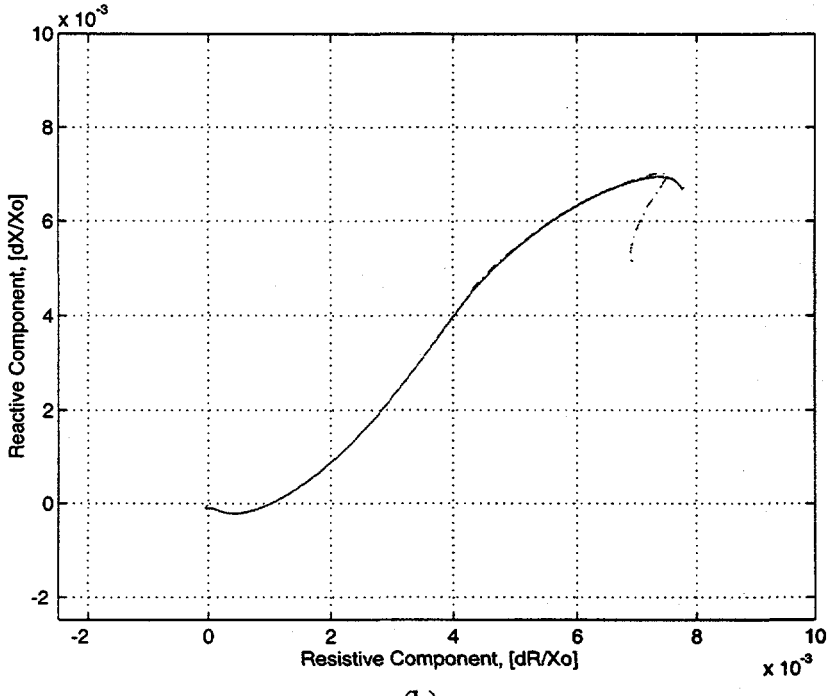

(b)

Fig. 13. Numerical results of impedance-plane signal trajectory for absolute bobbin coil, at (a) f = 100 kHz, and (b) f = 400 kHz. Artifacts are four axially symmetric 75% OD grooves without (solid line) and with (dashed line) ligament.

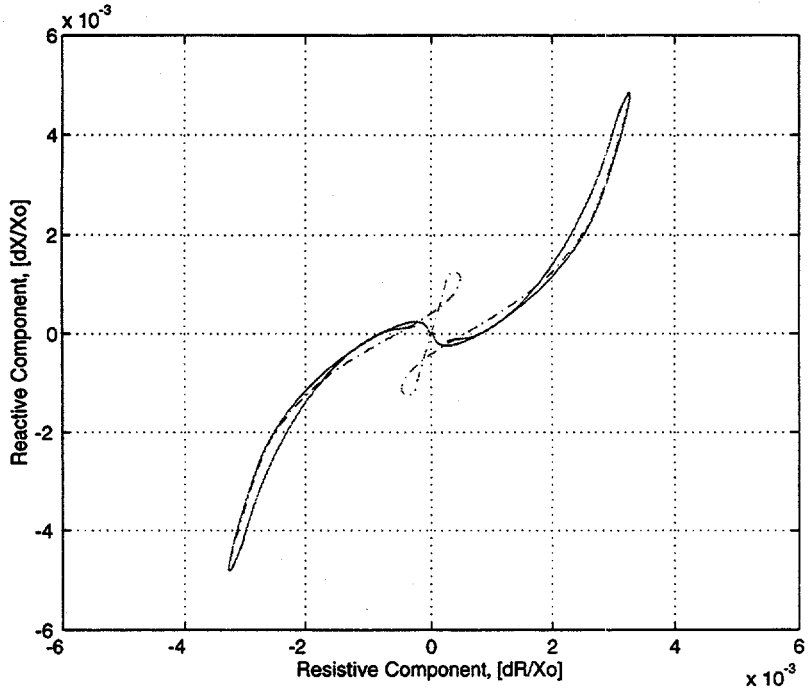

(a)

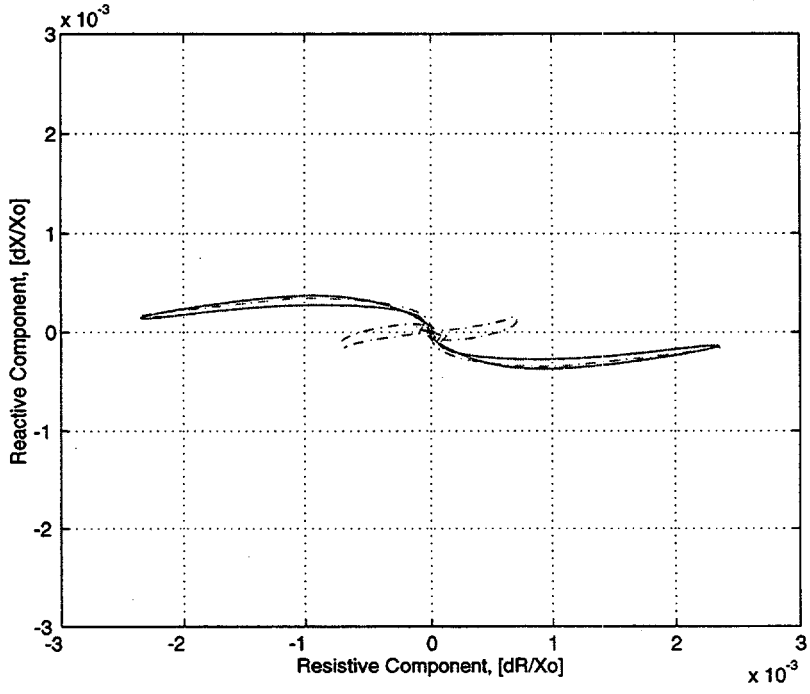

(b)

Fig. 14. Numerical results of impedance-plane signal trajectory for differential bobbin coil, at (a) f = 100 kHz, and (b) f = 400 kHz. Artifacts are four axially symmetric 75% OD grooves without (solid line) and with (dashed line) ligament.

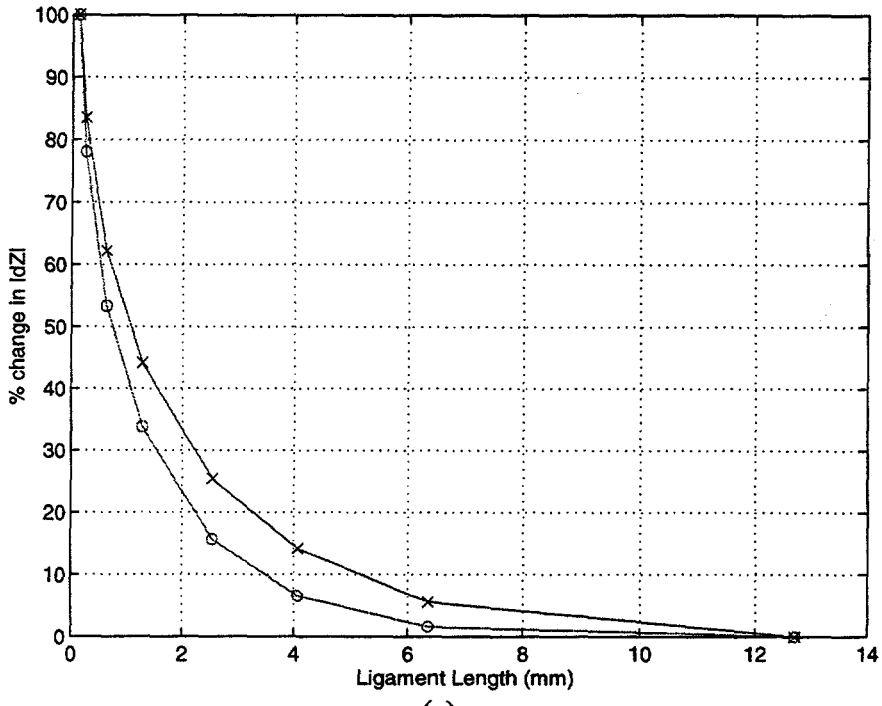

(a)

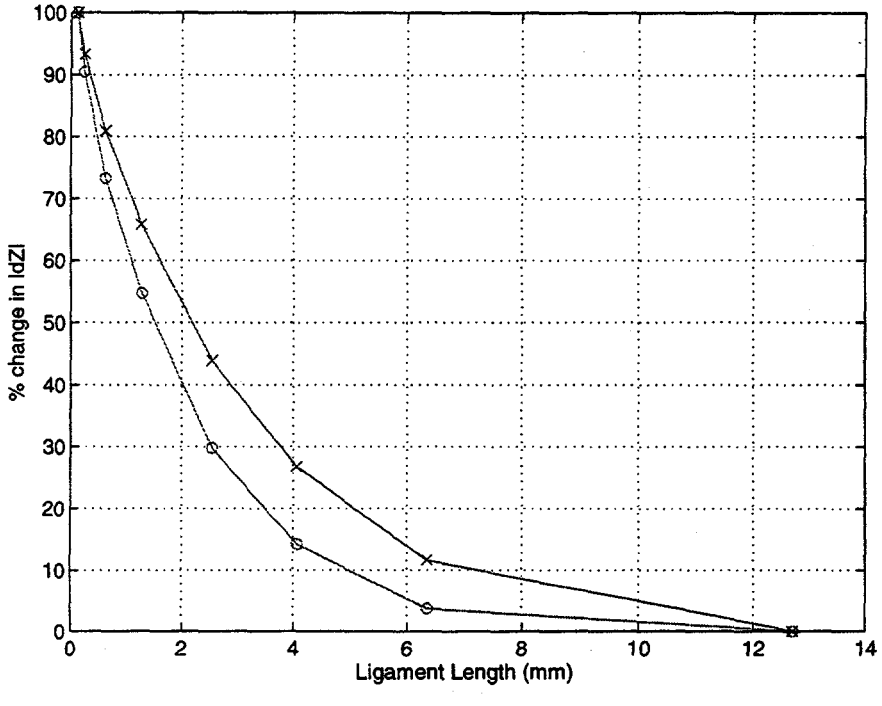

(b)

Fig. (15). Plot of change in absolute probe signal amplitude as a function of ligament length at f = 100 and 400 kHz for (a) 100% through-wall, and (b) 75% OD axial groove.

Characterization of Flaws in a Tube Bundle Mock-Up for Reliability Studies

D. S. Kupperman and S. Bakhtiari

Argonne National Laboratory

Abstract

As part of an assessment of in-service inspection of steam generator tubes, we will assemble a steam generator mock-up for round robin studies and use as a test bed in evaluating emerging technologies. Progress is reported on the characterization of flaws that will be part of the mock-up. Eddy current and ultrasonic techniques are being evaluated as a means to characterize the flaws in the mock-up tubes before final assembly. Twenty Inconel 600 tubes with laboratory-grown cracks, typical of those to be used in the mock-up, were provided by Pacific Northwest National Laboratory for laboratory testing. After the tubes were inspected with eddy current and ultrasonic techniques, they were destructively analyzed to establish the actual depths, lengths, and profiles of the cracks. The analysis of the results will allow the best techniques to be used for characterizing the flaws in the mock-up tubes.

Background

There is a need to provide experimental data and predictive correlations and models to permit the U.S. Nuclear Regulatory Commission (NRC) to independently evaluate the integrity of steam generator (SG) tubes as plants age and degradation proceeds, new forms of degradation appear, and new defect-specific management schemes are implemented. One key area to be addressed to help meet those needs is the assessment of procedures and equipment used for in-service inspection (ISI) of SG tubes. As part of the assessment of in-service inspection of SG tubes, a steam generator mock-up will be used for round robin (RR) studies using currently practiced techniques and as a test bed for evaluating emerging technologies. The mock-up will contain several hundred tube openings and will include a variety of flaws and artifacts.

Eddy current (EC) and ultrasonic techniques (UT) are being evaluated as means to characterize the defects in the mock-up tubes before final assembly. Twenty Inconel 600 tubes with laboratory-grown cracks were provided by Pacific Northwest National Laboratory (PNNL) for laboratory testing. After the tubes were inspected with EC and UT techniques, they were destructively examined to establish the actual depths, lengths, and profiles of the cracks. Analysis of the results will allow the best techniques to be used for characterization of flaws in the mock-up tubes.

The 20 tube specimens were a subset of tubes prepared under laboratory conditions by the Westinghouse Science and Technology Center under a subcontract with PNNL. The specimens exhibit longitudinal inner-surface stress corrosion cracks (LIDSCC), longitudinal outer-surface stress corrosion cracks (LODSCC), circumferential inner-surface stress corrosion cracks (CIDSCC), circumferential outer-surface stress corrosion cracks (CODSCC), and intergranular attack (IGA). Nine of the tubes show a roll transition. The Inconel 600 tubes are ≈0.30 m (12 in.) long, 22.2 mm (0.875 in.) in diameter, and have a wall thickness of 1.27 mm (0.050 in.). The tubes were subjected to ultrasonic depth and length characterization by high-frequency diffraction, Lamb wave, and amplitude drop methods. Eddy current depth and length were estimated by using a rotating pancake coil (RPC), multicoil arrays, a Zetec Plus Point probe, and multiparameter EC data analysis using neural network algorithms.

Tubes were ultrasonically inspected at the Idaho National Engineering Laboratory (INEL) to help determine the optimal method for inspecting tubes before they are integrated into the SG mock-up. High-frequency, longitudinal, and shear waves in a focused, pulse echo mode were used with waves incident at 0 and 45° (for both axial and circumferentially oriented cracks). All of the PNNL/INEL inspections were carried out from the outside of the tube. High-frequency backscatter and frequency analysis was used to characterize IGA. A, B, and C scans were used to characterize all of the cracks and the IGA. Time-of-flight (TOF) data were used to estimate depth when a crack tip echo was detectable, otherwise a 14-dB drop method with signal movement was used to estimate depth. Frequencies of 20-50 MHz were employed in an immersion tank. However, because of the attenuation in Inconel 600, the peak in the frequency spectrum is ≈30 MHz for propagation through the thickness and back (in pulse echo mode). Two calibration tubes were used. The first tube contained two sets of outer-surface saw cuts. The first set included four axial cuts 0.25-1.02 mm (0.010-0.040 in.) deep and 5.08-9.78 mm (0.200-0.385 in.) long. The second set contained five circumferential cuts 0.127-1.016 mm (0.005-0.040 in.) deep and 2.16-6.86 mm (0.085-0.270 in.) long. A second tube contained outer-surface saw cuts (axial and circumferential) and

electro-discharge machining (EDM) notches on the inner and outer surfaces. The saw cuts are 0.25-1.02 mm (0.010-0.040 in.) deep and 3.43-9.53 mm (0.135-0.375 in.) long. The EDM notches are nominally 0.51 mm (0.020 in.) deep and 6.35 mm (0.250 in.) long.

Samples were also inspected at ASEA Brown-Boveri (ABB) AMDATA with an ultrasonic probe that propagated Lamb waves in the tube wall, which are unaffected by a roll transition. These waves propagate in a free tube wall and are capable of detecting inner- or outer-surface circumferential cracks. Although axial cracks are not detectable with this probe unless circumferentially oriented branches are present, in principle, it is possible to make a Lamb wave probe that could detect axial cracks. The probe for the data reported in this paper is used in a scan mode that covers a range of 140 mm (5.5 in.). In general, not enough information is present in the Lamb wave echo signal to determine the depth, but general estimates can be made by measuring the echo amplitude. Defect length is accurately estimated by observing the drop in signal amplitude as the defect is scanned. IGA can be called correctly because the echo signals are generated over a large area of the tube. Calibration was carried out with a tube that contained circumferential EDM notches with through-wall depths of 20, 40, and 60% and arc lengths of 20, 40, and 60°. The signal from the 20% TW, 60 degree arc notch was set to 80% full screen height. The probe was moved axially 1.3 mm (0.05 in.) for every 360° scan. A, B, and C scans were generated. The probe was operated at a frequency of approximately 5 MHz. A PC-based Intraspect ultrasonic system was used to collect the data.

The tubes were also inspected with an EC C5/HD array probe at Atomic Energy of Canada, Ltd. (AECL). The probe consists of three parts, two of which contain differential transmit-receive (TR) pancake coil arrays, while the third contains a bobbin coil that was used simultaneously in differential and absolute modes. Each pancake array consisted of eight independent TR units. The coils in the two arrays are rotated relative to each other to completely cover the entire circumference. Thus, each unit "sees" an arc of 22.5°. The sensitivity to axial and circumferential cracks was comparable. Data could be displayed in Zetec Eddynet C-scan and clip-plot formats. The data from the absolute channels of the bobbin coil were useful in detecting long axial cracks. The amplitude from the bobbin coil was useful in distinguishing axial cracks from IGA. Eddy current (EC) data presented in this report were collected with a Zetec MIZ-30 interfaced with a Hewlett Packard 700 series workstation. Data acquisition and analysis were carried out with Zetec Eddynet software. A standard Zetec 4D probe driver with Zetec PM-1 motor controller was used to pull the probe through the tube at a constant speed of 0.30 m/s (12 in./s). Calibration was carried out with a standard ASME tube, a tube supplied by PNNL that contained axial and circumferential outer-surface notches, and a Westinghouse-supplied calibration tube containing a 20% outer-surface axially symmetric EDM notch, a dent, and 1.6-mm (0.060-in.)-diameter through-wall holes. Lack of calibration tubes with inner-surface notches and limited outer-surface notches somewhat limited the ability to estimate the depth of the cracks. Data were collected as the probe was pulled back through the specimen and then through the calibration tubes. The frequencies used were 45, 90, 180, and 400 kHz. The dent was used to adjust the phase angle while the dent signal was oriented horizontally. The vertical component of the 20% outer-surface notch groove signal was set to 10 V. Frequency dependence of the Lissajous figure orientation and of the vertical component of the signal amplitude were used to distinguish outer-surface from inner-surface flaws and to determine whether the defect was deep or shallow. The expansion transition caused some problems with signal interpretation. If a flaw was detected with the array but not with the bobbin coil, it was called circumferential. If the flaw was detected by both array and bobbin coil, it was identified as axial or IGA.

Using a pancake coil, we conducted a neural-network analysis of the multiparameter (four frequency) EC data collected for the 20 tubes (C. V. Dodd formerly of Oak Ridge National Laboratory)[1,2]. The EC coils were ≈4.6 mm (0.180 in.) in diam. Data were acquired with the standard Zetec MIZ-30 acquire program. Training of the neural net was previously carried out with tube standards and 23 samples with flaws having a somewhat different morphology. These samples also had axial and circumferential outer-surface stress corrosion cracks and IGA that were metallographically sectioned. A complication in this effort was a lack of training data for inner-surface defects and only one training sample with a roll transition. Standards used contained 360° circumferential notches 20, 40, 60, and 80% throughwall. Lift off of 0.1 and 0.2 mm (0.004 and 0.008 in.) was also part of the calibration tube and was used to set the phase shift so the lift-off signal is horizontal. The standard also contained a 100%-deep groove and axial notches.

Results

Figure 1 shows estimated crack depth determined by high-frequency ultrasonic-wave examination and by a neural-network algorithm applied to multiparameter EC data from a pancake coil vs. the maximum crack depth determined by metallographic analysis of the tubes.

The UT technique overestimates the depth of the crack in most cases, especially for the shallow cracks. The main problem for the ultrasonic interrogation was the difficulty in detecting the echo from the crack

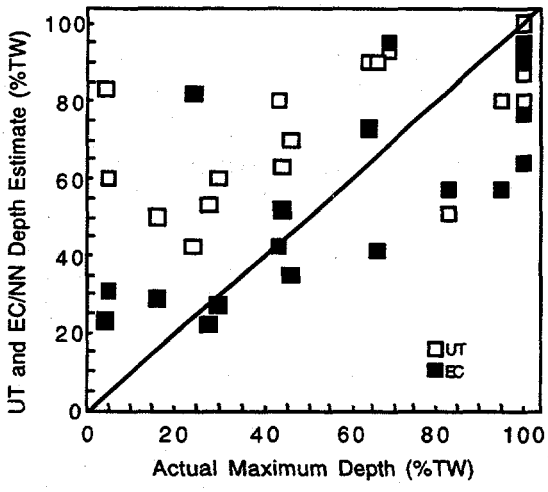

Fig.1. Comparison of estimated depth (PNNL/INEL) using high frequency ultrasonic waves (open squares) and estimated depth from a neural network algorithm applied to EC data (black squares) vs. the maximum depth of crack from metallographic analysis (PNNL) of set of 20 SG tube specimens.

tip that is used to obtain the depth estimate. The results from neural network analysis of EC data are better and are particularly encouraging, because a proper training data set was not available for this analysis. Significant improvements in the correlation are expected when optimized training sets are used with this neural network algorithm. UT and EC neural-network results are compared in Fig. 2. The depth estimated by the UT technique is consistently greater than that predicted by the neural-network algorithm applied to the EC data.

To better understand the problems encountered while estimating depths, data from the 20 tubes have been analyzed in several ways. The data presented in Fig. 3 present the results of depth predictions for tubes with and without a roll transition. No dramatic difference in depth-measuring capability can be observed when using the neural network algorithm and EC data.

Some estimates of flaw depth were also made with an ultrasonic probe from the inner surface of the tube (PNNL/Westinghouse evaluation of tubes). The estimated depth from the inner surface are, on the average, noticeably lower than those from the outer surface. This difference could be the result of differences in probe design but may also be the result of tube curvature effects. Waves incident on the tube inner wall are somewhat focused, whereas waves incident on the outer surface are spread out as they enter the tube wall. Ultrasonic and EC results are presented in Fig. 4.

The results of applying a neural network algorithm to EC data are presented as a function of flaw type in Fig. 5. Preliminary estimates from longitudinal outer- and inner-surface cracks, circumferential outer- and inner-surface cracks, and IGA are separated. No single defect appears significantly easier to characterize than any other, although the correlation coefficient from a linear fit to data restricted to outer surface axial and circumferential cracks is a respectable 0.9 (otherwise it is 0.73 for all data). This result emphasized the success possible with neural network analysis of data if proper training set data are available. However, the result was limited to a small data set and when upper and lower 95% confidence limits are calculated, the need for larger data sets to judge the effectiveness of neural net analysis becomes apparent. The upper and lower confidence limits for the mean and individual (i.e., additional) points can be seen for OD defects in Fig. 6. The range of upper and lower confidence limits is rather large. For example, if a new point were added to the data for an actual maximum depth of 50%, there is a 95% probability that the estimated depth will fall between 15 and 75%, while the mean will still lie between 35 and 55%.

Analysis of EC data from the 20 tube set also includes a phase shift analysis of Plus Point data carried out at Argonne with Zetec Eddynet95 software on data collected at Zetec. Phase analysis was used to estimate the depth of cracks. Calibration was carried out with a series of EDM notches in calibration tubes. The results are reasonable, particularly if restricted to the cracks that are not IGA. Figure 7 shows the results of the analysis of Plus Point data compared to destructive examination. The correlation coefficient is about 0.75 for a linear fit to all the data with especially good results for the ID cracks. Figure 8 shows Plus Point data with 95% confidence limits. Again, the range of the upper and lower confidence limits is very large because of the small size of the data set.

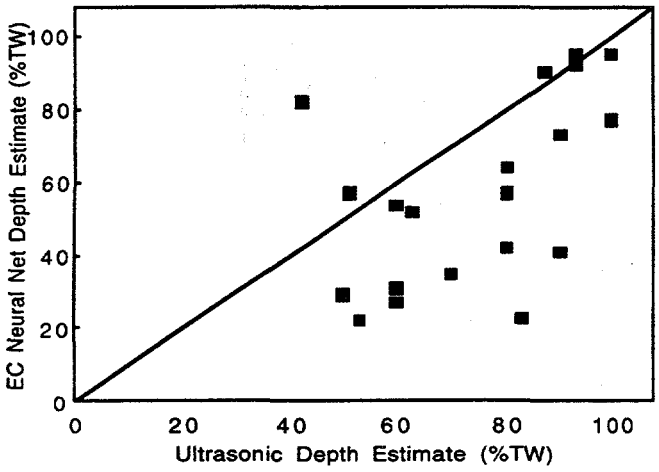

Fig. 2. Comparison of flaw depth estimates from high-frequency ultrasonic wave technique (PNNL/INEL) and neural network algorithm applied to eddy current data.

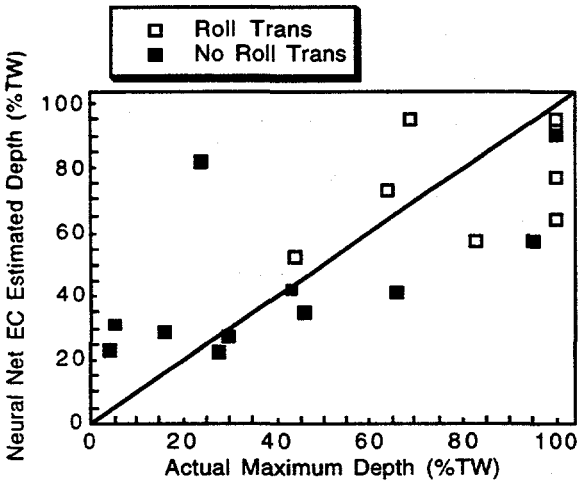

Fig. 3. Comparison of estimated depth applying neural network algorithm to eddy current data for tubes with and without roll transition.

A comprehensive characterization of crack length was also carried out with the Zetec Plus Point probe. Crack lengths estimated from the data are compared with destructive examination (DE) carried out by PNNL. The data were acquired at Zetec and then analyzed at Argonne with Eddynet95 software in the c-scan mode; the results are shown in Fig. 9. For complicated crack structures revealed by DE, the full extent of cracking was compared to the estimated length. If a well-defined deep crack was found among a series of shallow cracks, the length of the deep crack was compared to the EC-determined length. The results for circumferential cracks (0.99 linear fit correlation coefficient [LFCC]) are better than for axial cracks (0.90 LFCC). Defining the ends of the crack is difficult because the EC signal does not end sharply. Subjective judgment is therefore required in estimated circumferential or axial crack lengths. The length of inner wall cracks may be much easier to determine than those of outer wall cracks because the eddy current signal is defined better (0.99 LFCC for ID cracks versus 0.92 LFCC for OD cracks).

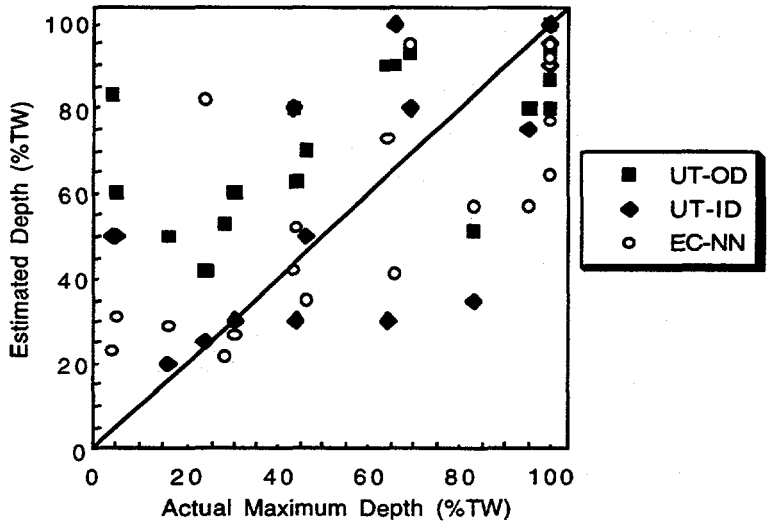

Fig. 4. Estimates of crack depth obtained by ultrasonic wave inspection of inner (Westinghouse/ PNNL) and outer (PNNL/INEL) surfaces of 20 tubes, along with neural network EC results vs. actual maximum depth.

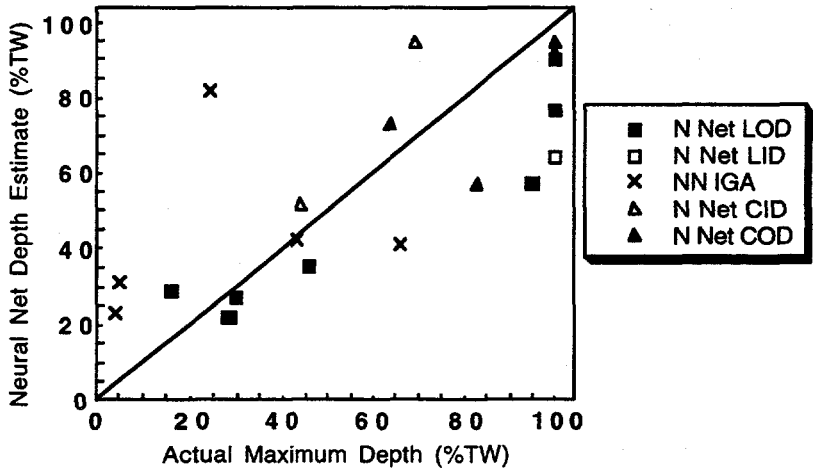

Fig. 5. Results of applying neural network algorithm to eddy current data as a function of longitudinal OD cracks, longitudinal ID cracks, circumferential OD cracks, circumferential ID cracks, and IGA.

An alternative to characterizing crack lengths with eddy currents is the use of ultrasonic techniques. One possibility is to use ultrasonic guided or Lamb waves launched from the inside of the tube and propagating axially in the tube wall. An ultrasonic Lamb wave image (from ABB-AMDATA) of the laboratory-grown CODSCC in one of the Inconel 600 steam generator tubes is shown in Fig. 10. This image suggests six crack segments, five at the same axial location and one offset axially with an arc length of 50°. Total arc length indicated ultrasonically is 130°. The destructive analysis (by PNNL) showed a crack with a total arc length of

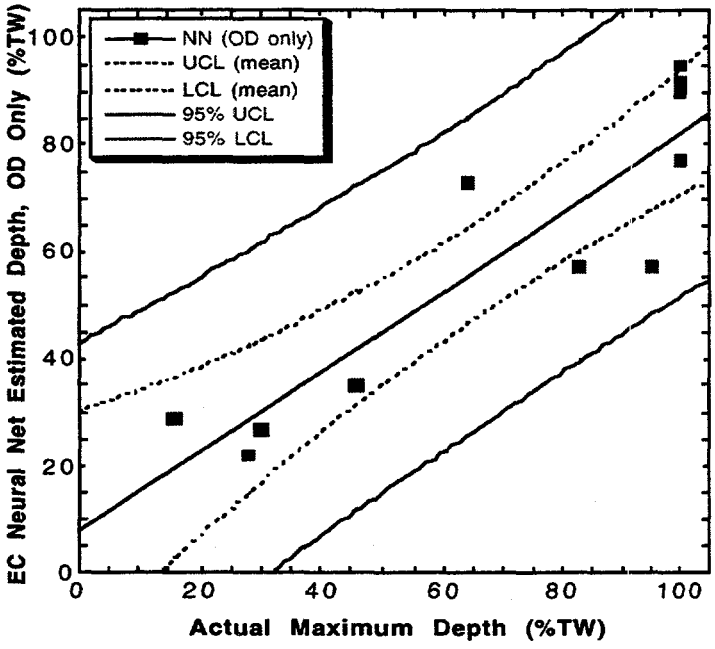

Fig. 6. Upper and lower 95% confidence limits for mean and individual (i.e., additional) points for depth estimates determined by neural network analysis (OD defects only).

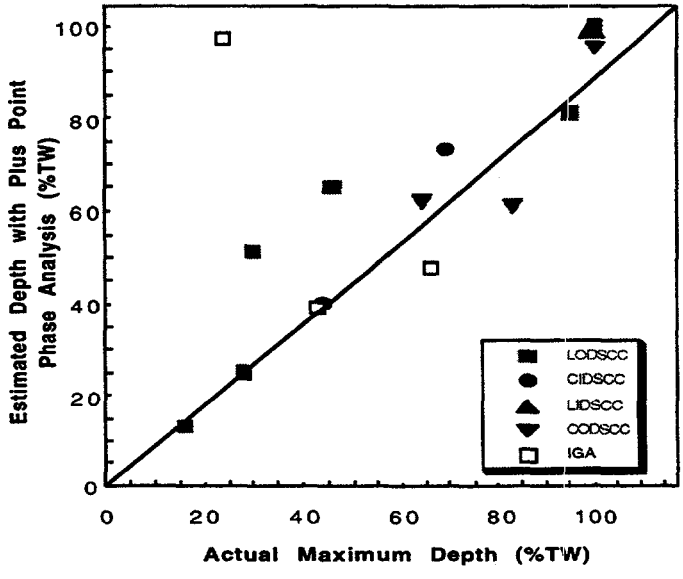

Fig. 7. Crack depth estimates from eddy current data from 20-tube set and phase shift analysis of Plus Point data. Analysis was carried out at Argonne with Eddynet95 software. Calibration used a series of EDM notches in calibration tubes. Correlation coefficient is ≈0.75 for a linear fit to all data.

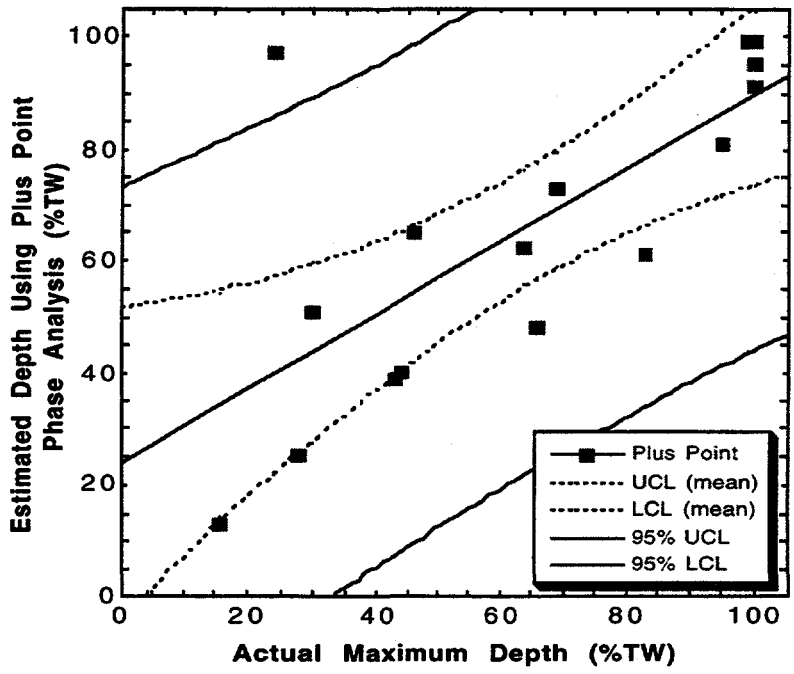

Fig. 8. Depth estimates from Plus Point data with 95% upper and lower confidence limits for mean and additional points. Range of upper and lower confidence limits is very large because of small size of data set.

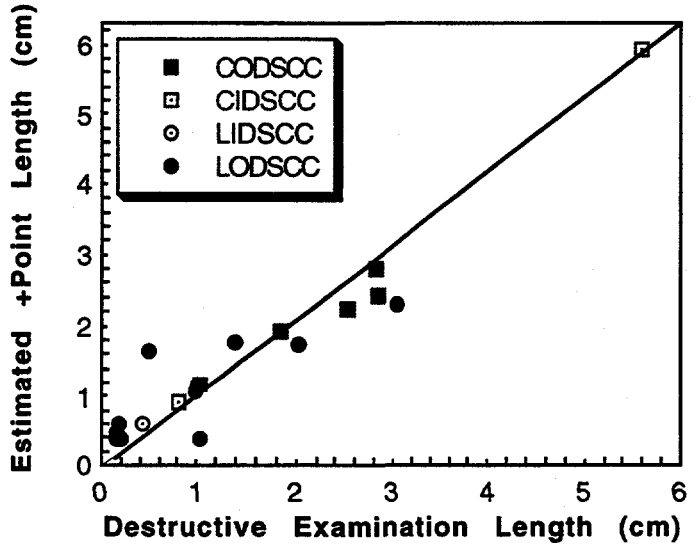

Fig. 9. Estimated crack length vs. destructive examination (DE) from 20-tube set. Estimates were generated from Plus Point eddy current data acquired at Zetec and analyzed at Argonne with Eddynet95 software. For complicated crack structures revealed by DE, full extent of cracking was compared to estimated length. If a well defined deep crack was found among a series of shallow cracks, length of deep crack was compared to eddy-current-determined length.

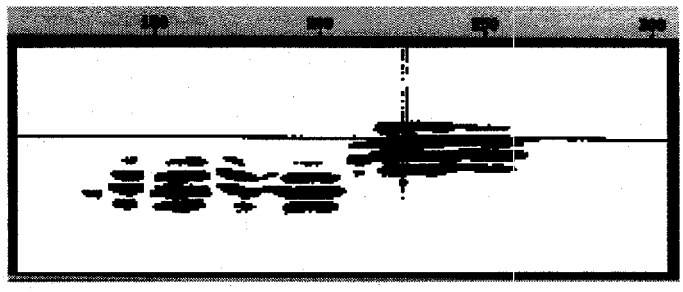

Fig. 10. Ultrasonic Lamb wave image (from ABB-AMDATA) of laboratory grown CODSCC in Inconel 600 SG tube. This image suggests six segments, five at the same axial location and one offset axially with an arc length of 50°. The total arc length indicated ultrasonically is 130°. Destructive analysis showed a crack with total arc length of 160° containing a segment with an arc length of 60° axially offset from the larger segment by about 0.05 in. While destructive examination of lower part of crack shown in this figure does not reveal well-defined segments, the DE does show widely varying depths for this part of crack. Segments indicated ultrasonically are results of low-amplitude signals from shallower parts of continuous crack.

160° and containing a segment with an arc length of 60° axially offset from the larger segment by about 0.05 in. While the destructive examination (DE) of the lower part of the crack shown in this figure does not reveal well-defined segments, the DE does show widely varying depths for this part of the crack. The segments indicated ultrasonically are the result of low-amplitude signals from the shallower parts of the continuous crack.

A second ultrasonic method for characterizing the cracking pattern is the use of high frequency normal-incidence longitudinal waves launched in water. A high-frequency ultrasonic image of an SCC is shown in Fig. 11. The image shows the intersection of a complicated crack with the Inconel 600 tube outer surface. The image shows the roll transition as a horizontal dark line across the center of the image, along with circumferentially and axially oriented crack segments. The axial segments are up to 0.3 in. in extent. A 50-MHz normal-incidence longitudinal focused beam in water was used to create this image (INEL).

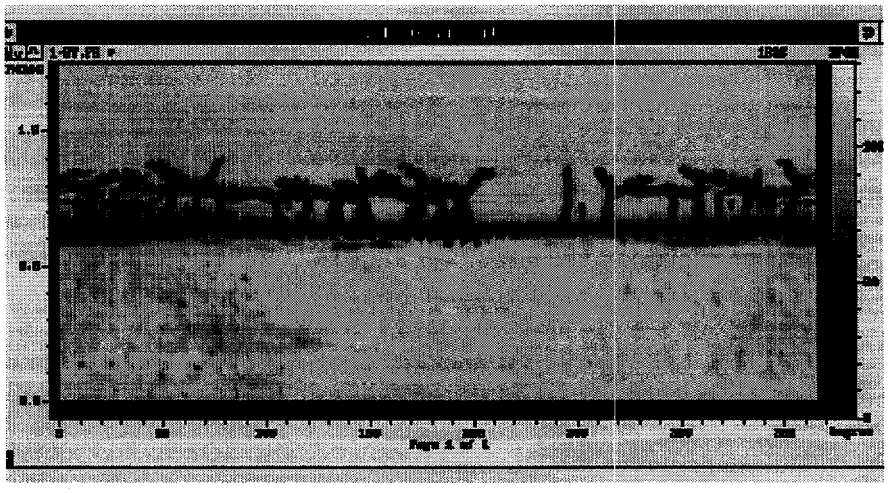

Fig. 11. High-frequency ultrasonic image of an SCC. Image shows intersection of complicated cracks with Inconel 600 tube outer surface. Roll transition appears as a horizontal dark line across center of image, along with circumferentially and axially oriented crack segments. Axial segments are up to 0.3 in. in extent. A 50 MHz normal incidence longitudinal focused beam in water was used to create this image (INEL).

Examples of crack length estimates using UT and EC techniques for selected tubes are shown in Figs. 12-16. The primary emphasis in this set of figures is on circumferential cracks. The data were obtained by both ultrasonic TOF diffraction and amplitude drop (PNNL/INEL) and Lamb waves (ABB AMDATA) for circumferential cracks and EC probes (conventional array analysis/AECL, neural-network algorithm applied to EC data/Dodd and Plus Point/ANL). The results obtained by UT techniques exhibit better resolution, and as a result, cracks that may appear segmented on ultrasonic interrogation may not appear segmented with EC probes. The locations of cracks may vary considerably with the technique used. When symbols are observed between the ends of a line segment in Figs. 12-16 (representing the length of cracks), the segment has "structure" and the location of the symbols indicates the location of signal peaks in the data.

While Lamb waves were not especially useful for measuring crack depth, inspection with Lamb waves appear to be useful for detection of circumferential cracks and length estimates. Lamb waves can also be used to detect axial cracks if they contain circumferential components and exhibit IGA. If they are used in a scanning mode, Lamb waves can be used to provide a good image of a defect.

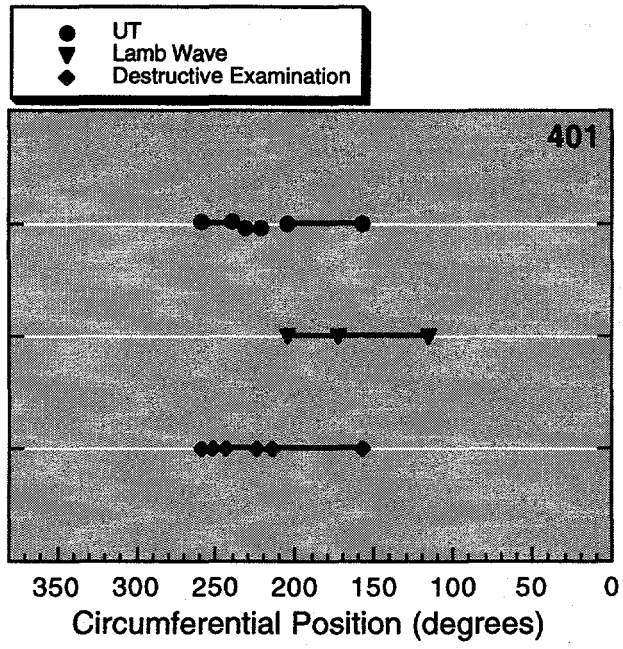

Fig. 12. Comparison of predicted length of circumferential OD crack in 22.2-mm (0.875-in.)-diam. Inconel tube using high-frequency ultrasonic wave (incident to outer surface of tube) (PNNL/INEL) and Lamb wave (ABB). No eddy current array data are available for this tube. Symbol between ends of crack representation indicates segmented structure.

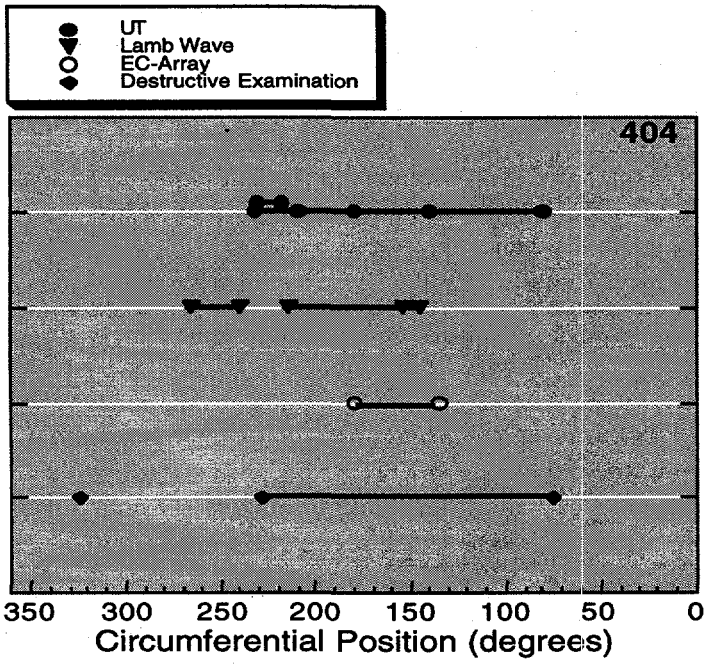

Fig. 13. Predicted length of CIDSCC using high-frequency ultrasonic wave (incident to outer surface of tube) (PNNL/INEL), Lamb wave (ABB), and C5/HD eddy current array (AECL). Symbols between ends of crack representation indicates somewhat segmented structure.

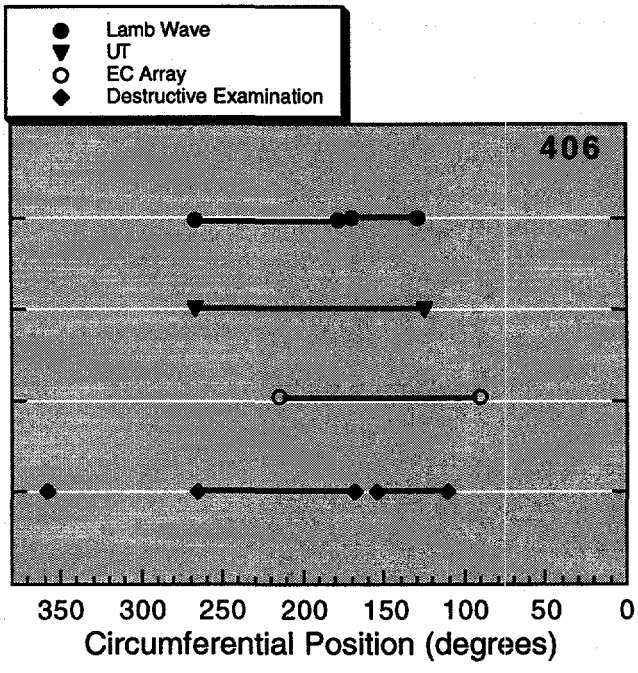

Fig. 14. Predicted length of circumferential ID crack in 22.2-mm (0.875-in.)-diam. Inconel tube using high-frequency ultrasonic wave (incident to outer surface of tube) (PNNL/INEL), Lamb wave (ABB), and C5/HD eddy current array (AECL).

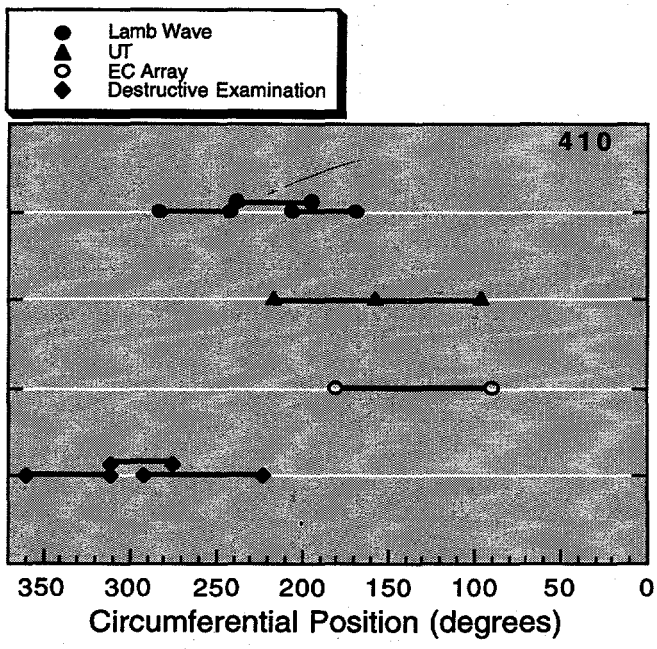

Fig. 15. Comparison of predicted length of circumferential ID crack in 22.2-mm (0.875-in.)-diam. Inconel tube.

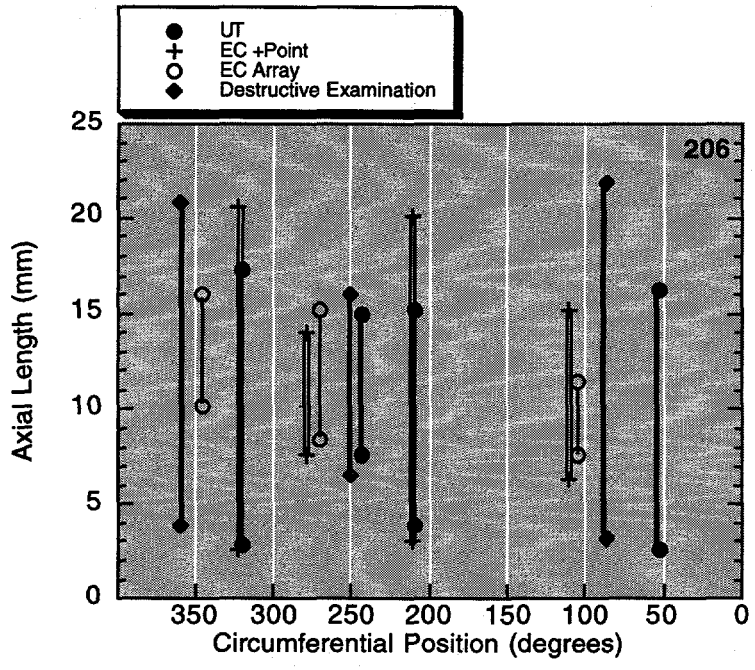

Fig. 16. Predicted length of axial OD crack in 22.2-mm (0.875-in.)-diam. Inconel tube using high-frequency ultrasonic wave (incident to outer surface of tube) (PNNL/INEL), Plus Point probe (ZETEC/ANL), and C5/HD eddy current array (AECL).

Acknowledgments

The authors thank R. Kurtz (PNNL), A. Diaz (PNNL), T. Gomm (INEL), C. Dodd, V. Cecco (Atomic Energy of Canada, Ltd.), M. Brook (ABB AMDATA), and J. Cox (Zetec) for their contributions to the work described in this paper. This work was supported by the Office of Nuclear Regulatory Research, U.S. Nuclear Regulatory Commission.

References

1. C. V. Dodd and J. R. Pate, Advancement in Eddy–Current Test Technology for Steam Generator Tube Inspection, in *Twentieth Water Reactor Safety Information Meeting, NUREG/CP–0126*, Vol. 3, March 1993, pp. 267–276.

2. J. M. Mann, L. W. Schmerr and J. C. Moulder, Neural Network Inversion of Uniform–Field Eddy Current Data, *Mater. Eval.*, Jan. 1991, pp. 34–39.

Steam Generator Tubing NDE Performance

Gary Henry
Electric Power Research Institute
Nondestructive Evaluation Center
Charlotte, NC

C. S. Welty, Jr.
Electric Power Research Institute
Palo Alto, CA

ABSTRACT

Steam generator (SG) non-destructive examination (NDE) is a fundamental element in the broader SG in-service inspection (ISI) process, a cornerstone in the management of PWR steam generators. Based on objective performance measures (tube leak forced outages and SG-related capacity factor loss), ISI performance has shown a continually improving trend over the years. Performance of the NDE element is a function of the fundamental capability of the technique, and the ability of the analysis portion of the process in field implementation of the technique. The technology continues to improve in several areas, e.g. system sensitivity, data collection rates, probe/coil design, and data analysis software. With these improvements comes the attendant requirement for qualification of the technique on the damage form(s) to which it will be applied, and for training and qualification of the data analysis element of the ISI process on the field implementation of the technique. The introduction of data transfer via fiber optic line allows for remote data acquisition and analysis, thus improving the efficiency of analysis for a limited pool of data analysts. This paper provides an overview of the current status of SG NDE, and identifies several important issues to be addressed.

CURRENT PERFORMANCE

Through industry-initiated efforts, SG ISI/NDE has shown steady improvement since the late 1970s when an industry-wide program, the EPRI Steam Generator Owners Group program, was put in place to develop solutions to SG reliability issues. Initially, the incentive for improvement was to reduce the number of tube-leak forced outages and attendant capacity factor loss. Trends of these two measures, published in the annual Steam Generator Progress Report (Ref. 1), indicate that the initial objective is being met. Recently, the incentive for improvement comes from the fact that improved ISI is a fundamental element in the steam generator degradation specific management (SGDSM) approach to implementing damage-specific plugging/repair limits. (This is consistent with the NRC's proposed "performance-based" rule that is being developed to implement SGDSM across the industry.)

In the current regulatory framework, however, improvements are not without drawbacks, some very substantial. Specifically, technology improvements can substantially lower the detection threshold to levels well below the point of structural significance for some damage forms. Since "sizing" capability generally comes after achieving detection capability, this can lead to a situation where detected defects cannot be sized, and where appropriate repair criteria/limits may not exist. This leads to a plug-on-detection scenario, at least until such time as a sizing technique can be developed. However, even at the point that a sizing capability is developed relief may not be available since repair criteria and operating cycle-length determinations require flaw growth rates, which are not available since flaws have been removed based on the initial plug-on-detection scenario/requirement. It is hoped that a "performance-based" approach to this issue can prevent barriers to ISI/NDE improvement.

Guidelines

Developments and improvements in NDE technology have generally been driven by site-specific needs to address newly discovered damage forms, and have been provided by the commercial NDE developers working with impacted utilities. For that reason the industry has focused the generic program on the development of guidance that will provide consistency in approach and application of the available and emerging NDE technology. This focus is provided through the PWR SG Examination Guidelines (Ref. 2) which address, in detail, the six elements of the ISI process:

1. pre-inspection planning based on knowledge of the inspected steam generators—includes determining expected conditions from operating history as well as from other relevant industry experience;

2. data analyst qualification—includes initial training and qualification, periodic retraining and pre-inspection training and performance demonstration;

3. inspection sample—includes sample selection and sample expansion rules;

4. data acquisition—includes equipment and procedure selection as well as appropriate qualification and performance demonstration for expected damage forms;

5. data analysis and review according to site and inspection specific analysis guidelines/rules—includes multi-party data review and discrepancy resolution; and

6. response to inspection results—includes plugging or sleeving tubes that exceed the plugging limit as well as additional inspection and/or tube pulls to resolve discrepancies or to evaluate new or unexpected conditions.

Qualification

NDE performance is a function of the fundamental capability of the technique, and the ability of the analysis portion of the process to properly implement the technique. Each technique consists of two sets of essential variables. The first set deals with the eddy current test (ECT) system and addresses the test instrument and its settings, e.g., frequencies and drive voltages, probe type, probe speed, data acquisition rate, probe fill-factor, frequency response with cabling attached, etc. The second set of variables deals with the tubing conditions, e.g., flaw morphology, flaw location, basic tubing condition such as pilgering, denting, expansion geometry, etc., existence of conductive deposits, and the presence and type of support structure intersection(s). Each technique may address these variables in different ways, and is qualified using the protocol outlined in the Appendix H of the Guidelines. This is a performance-demonstration approach to determine the system capabilities on a set samples without addressing the effects of analyst's performance variability. The sample set used to determine technique performance is based on the availability of specimens and can include any or all of the following: pulled tubes, laboratory cracked tubes, laser cuts, or EDM notches, with the goal being to use the most representative sample set possible. As additional data become available with the proper essential variables the technique qualification data are updated. There are currently some seventy techniques that have been "peer reviewed" and qualified for flaw detection or sizing or both. (Reference 2 contains a listing of these qualified techniques, and the data sheets are available through the EPRI NDE Center.) Where more than one technique exists for a given application, the techniques are not "ranked" relative to one another, and it is the responsibility of the plant owner to determine, from the technique qualification data sheets, the technique(s) that are most appropriate for the particular application. Factors which enter into this decision include, desired detection threshold, need for POD data, proposed run-time until next ISI, etc.

The data analysis portion of the process is addressed separately from the technique qualification. The term "Qualified Data Analyst (QDA)" is defined as an analyst that has demonstrated the capability to follow analysis rules and meets the performance requirements identified in Appendix G of the Guidelines. For this activity, detection and sizing is demonstrated on techniques which have met the requirements of Appendix H. To achieve a sufficiently large sample set for training and testing it has been necessary to supplement the Appendix H data set(s) with field data gathered with Appendix H qualified techniques, with "truth" being determined by "expert" opinion.

for a steam generator inspection at a specific plant, in addition to being a QDA, the analyst(s) must pass a supplemental, site specific performance demonstration prior to analyzing site data. The data used in this activity represents the expected damage mechanisms and ECT equipment which will be used for that site. The data used are typically from the same model steam generator and preferably the same unit which will be examined. However, all mechanisms have not surfaced at all plants. For those plants where potential mechanisms exist, that data is used to acclimate the data analyst.

A centrally managed Performance Demonstration Database (PDD) controls the testing phases for the QDAs. All tests are computer generated and graded. The test data is provided in time-dated reports which are maintained on the database in an encrypted format. Each vendor and utility implementing the PDD has an assigned proctor and is required to protect the contents consistent with their Quality Assurance program. This process results in a software that is centrally maintained, with controlled decentralized implementation.

To aid the utilities with implementation of supplemental, site-specific performance demonstration (SSPD), a software database shell program has been created. This database is similar to the PDD with the exception the user inputs the raw data, determines the truth-answers and establishes the acceptance criteria. The computer selects the tubes and grades the examinations based on the input parameters in the configuration files established by the administrator. This will allow for grading with several options, e.g., by mechanism or inclusive mechanisms, POD, POD at C/L, or point value, sizing is graded by RMS error or with a tolerance. Time dated reports are written to the users accounts with the results of each examination. The results of the supplemental/site specific performance demonstration (SSPD) can be compared with the QDA records to monitor analyst performance over time.

Figures 1 and 2 provide a schematic view of the process described above.

Performance Demonstration

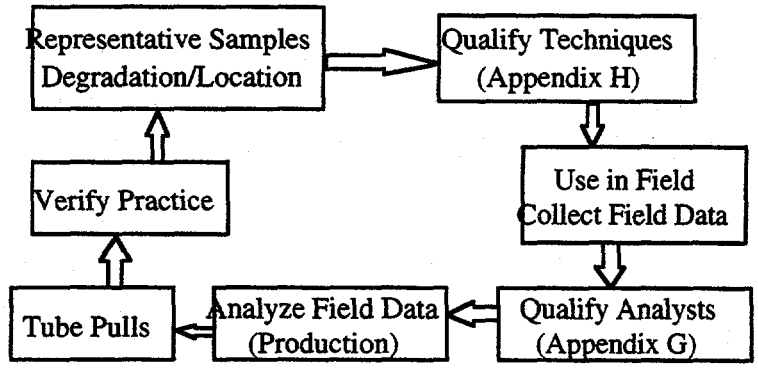

Figure 1

Performance Demonstration Cycle

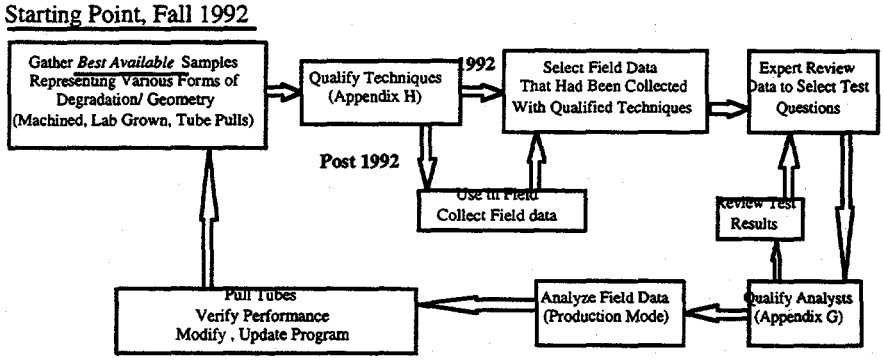

Figure 2

Conformance Assessment

In 1995, at the request of the utilities, the Institute of Nuclear Power Operations (INPO) initiated a program to assess industry and specific utility conformance to the recommendations of the Guidelines. The initial phase of this program consisted of a total of seven plant visits and was completed during the late summer of 1996. The assessment visits are conducted by a review team of approximately four people, two from INPO and two utility "peer reviewers", one a Level III data analyst and one a steam generator "manager". The visits are conducted one to two months prior an outage so that the results (findings and recommendations) can be factored into subsequent outage's ISI

plans. To date, industry support for this activity has been virtually unanimous, both from the standpoint of providing the peer reviewers as well as from supporting the on-site assessment. In as much as the Guidelines are a major element of the industry's steam generator management program, it is hoped that the INPO involvement will result in the same improvement to SG ISI as the analogous involvement in the industry prepared water chemistry guidelines (Refs. 3 and 4) has achieved in the water chemistry program.

Recent Developments/Improvements

In the area of technique development and improvement, recent work has focused on "sizing" cracks in tubes with stress corrosion cracking (SCC)-type flaws, with circumferential cracking being of the most current interest. A number of techniques (probe, coil, equipment, software) have been qualified for SCC detection, and material relative to this work has been previously reported (Ref. 5). For several reasons, current industry supported efforts to develop a length and depth sizing approach for circumferential cracking has focused on the use of the "plus point" rotating coil technology. Developed by Zetec, this coil is designed to minimize the impact of geometric tubing variations (e.g., roll transitions, sleeve joints, etc.) to address both circumferential and axial flaws as the probe is rotated on or near the tube inside surface. The axial and circumferential coil arrangement are connected differentially, such that what is seen by both coils simultaneously results in a null condition. The position of the coils in the coil shoe typically will have the axially orientated (circumferential sensitive) coil closest to the tube inside surface and the circumferentially oriented (axial sensitive) coil directly behind the axially oriented coil. This tends to provide a more sensitive examination for circumferentially oriented ID initiated indications based on the proximity of the coil to the tube wall.

Two techniques for length and depth sizing of axial and circumferential ID initiated cracks in roll transitions using a mid range (frequency) plus point coil have recently been qualified in accordance with Appendix H. By using both amplitude and phase, the sizing error for maximum depth is 10% root mean square (RMS) error. Additionally, percent degraded area (PDA) developed based on this technique has been demonstrated to have 12% RMS error. These techniques have been qualified using a mix of pulled tubes and laboratory crack samples.

Sizing of circumferential cracks is particularly challenging and required the development of software to support the axial lissajous response. Rotating coil data is collected in a rotating helical fashion along the axis of the tube, a process is well suited for axial indications, where the coil translates orthogonal to the indication. The lengths of the flaw, the diameter of the coil and the helical pitch determine the number flaw-indication responses developed. In the case of circumferential flaws, the indication contains very minimal length in the axial direction and the circumferential scan line, which is almost parallel to the flaw plane, provides the information. The solution was development of

software that allows the alignment of the multiple scan lines such that an axial lissajous can be created from the scan line at a point along the circumference that provides the largest signal. This allows phase-angle depth measurements to be made circumferentially around the tube in increments equal to the number of data point around the circumference. From this data a flaw-depth profile can be created. This profile can then be used to determine maximum depth, average depth or PDA as appropriate.

Data Handling

As inspections have become more complex - in scope of tubing examined, in the need to use damage-specific detection techniques for multiple damage forms, in the data required for complex sizing techniques such as those described above - the quantity of data requiring analysis and the need to accomplish this analysis in real-time created a need to make this step in the process much more efficient. One step has been the collection of multiple data simultaneously, e.g., up to eight probes of data in each channel head. While this speeds up the collection process substantially, it also adds additional burden for analysis of the data. With a limited pool of data analysts (approximately 200 QDAs in the US and an additional 100 QDAs outside of the US), a shortage of analysts can exist during the outage seasons. The use of T-1 or T-3 fiber optic lines for data transfer has allowed the ISI service vendors to shift to a centralized team of analysts to perform in multiple functions, thereby easing the requirements for additional analysts. This is accomplished by reduction of travel along with the increased availability of a given analyst.

System Performance Measures

The industry is now working to develop approaches to measure field performance of the NDE system. In one approach, measurement of field performance is accomplished using a tracking system for each data analyst. A table is built by monitoring each hit, miss and overcall as based on the results of the resolution analyst (expert opinion). This adds the ability to monitor individual performance and provide instruction and training on a real-time basis where necessary. This also provides a useful tool to determine, by performance, primary and secondary data reviews. By matching a strong performer with a weaker performer the overall POD performance should increase. This allows for personnel management for peak performance. Monitoring the individual performance will also aid in determining a POD for the mechanisms at each site.

A similar approach was demonstrated and has been reported for ODSCC at tube support plates using resolution results by voltage as the truth and comparing the field primary and secondary analysts results with ten separate analysts in the laboratory on the same data set (Ref. 6).

ISSUES

Use of Defect Depth as ECT Performance Measure

Historically, depth, usually maximum depth, has been considered the property or parameter of most importance in when assessing ECT performance. The assessment is generally based on a comparison of a metallographically determined depth and an ECT-called depth determined by one or more of the ECT signal parameters. While probably appropriate for volumetric flaw-forms (e.g., wear, wastage, pitting), depth is not likely to be the most appropriate comparison measure for crack-like damage, e.g., tube support plate (TSP) ODSCC, top-of-tubesheet (TTS) circumferential cracking, from either a structural or ECT standpoint. Where the cracking is a complex mix of multiple short segments of varying depths (typical of SG tubing SCC) it is difficult to assure that metallography locates the maximum depth. Further, since the physics of ECT results in a volumetric "averaging" which determines the magnitude and form of the resulting ECT response, it is difficult for ECT to determine the maximum depth. The result is a relatively poor correlation between ECT and metallographic depth, which raises questions/concerns regarding the adequacy of the ECT process. From a structural standpoint (i.e., burst and leakage under actual and postulated loads) tubing performance is influenced by other features of the damage - defect/crack length, number of cracks in a given volume of tubing, "bridging" or intact material between cracks, etc. These features tend to impact the ECT response in a manner that relates directly to the impact of the flaw on structural capability, which implies that ECT, though a poor predictor of flaw depth, provides a good measure of structural impact of the flaw (Ref. 7). This has allowed correlations to be developed that directly relate the ECT response to structural performance, providing a better estimate on the ability/accuracy" of ECT to reliably monitor tubing conditions when compared to the accuracy as measured by correlations with metallography. This is the basis of the voltage-based alternate tube repair criteria (ARC) for TSP ODSCC embodied in Generic Letter 95-05 (Ref. 8).

Currently the Appendix H protocol for ECT technique qualification/performance demonstration is based on flaw depth with no consideration of length. This feature can create problems relative to the qualification of techniques for detection of crack-like flaws; e.g., as tube-pull data is acquired to expand the qualification data set, a structurally insignificant flaw at or just below the threshold-of-detection for a particular damage form can be missed. If any portion of the flaw exceeds the Appendix H depth "criteria" failure to detect is counted as a "miss", which can result in the needles disqualification of perfectly adequate ECT techniques. This issue is being addressed as part of the next revision to the SG ISI Guidelines.

Blind Tube-Pulls

In several recent tube-pull campaigns in US PWRs, all of the removed sections have been treated "in-the-blind"; i.e., the entire population was used to assess NDE capability and no specimens were saved to refine NDE capabilities after the initial identification of shortcomings. From a regulatory standpoint this may be appropriate, however, with the scarcity of real specimens for use in NDE technique development, it is desirable that the industry work with the NRC staff to see if a compromise position can be developed as future tube-pull specimens become available.

System Performance Measures

As described above, the Appendices G and H approach to qualifying techniques and analysts separately is a constraint driven by the availability of real, truly representative samples. While the process accounts for the need to update Appendix H technique qualification as more appropriate specimens become available, and these updated techniques are factored into the requalification requirements of Appendix G, the is no current direct measures of the entire process as applied in field inspections. Both the NRC staff and the industry recognize this as a need, which will become increasingly important as performance-based regulation is implemented through the SG Integrity Rule.

CONCLUSIONS

Steam generator ISI/NDE is a major focus of the industry's efforts to improve the reliability of PWR steam generators. Measurable improvements have been made over the years and are continuing to be made at this time. The recent focus of work has been: on developing and qualifying one or more techniques to "size" SCC-type flaws and on improving the quality and quantity of data. There are current issues relative to using depth as a basis for assessing ECT performance, the need to obtain a sufficient quantity of truly representative specimens to both assess and develop/improve NDE capabilities, and the need to develop an agreed upon approach to evaluate the field performance of the NDE component of the ISI process. The industry-prepared "PWR Steam Generator Examination Guidelines" are the cornerstone of the industry effort to improve SG ISI, and a program, through INPO, has recently been put in place to assess industry performance in this area.

REFERENCES

1. "Steam Generator Progress Report", Revision 12, October 1996, Electric Power Research Institute - Steam Generator Strategic Management Project, Palo Alto, California.
2. "PWR Steam Generator Examination Guidelines: Revision 4", EPRI Report TR-106589, Volume 1, Electric Power Research Institute, June 1996
3. "PWR Secondary Water Chemistry Guidelines", Revision 3, EPRI Report TR-1002134, Electric Power Research Institute, May 1993.
4. "PWR Primary Water Chemistry Guidelines: Revision 3", EPRI Report TR-105714, Electric Power Research Institute, November 1995.
5. 15th Annual EPRI Steam Generator NDE Workshop, July 29-31, 1996, Long Beach California.
6. Jackson, P., Sears, M., "Probability of Detection for ODSCC at Tube Support Plates", International conference on Nuclear Engineering 1996, New Orleans, Louisiana, March 1996.
7. "Data Analysis for Steam Generator Tubing Samples", NUREG/CR-6455, ORNL/TM-13206, Oak Ridge National Laboratory, July 1996.
8. USNRC Generic Letter 95-05, "Voltage-Based Repair Criteria for Westinghouse Steam Generator Tubes Affected by Outside Diameter Stress Corrosion Cracking", August 1995.

Estimating Probable Flaw Distributions in PWR Steam Generator Tubes

J. A. Gorman
A. P. L. Turner

Dominion Engineering, Inc., McLean, Virginia

This paper describes methods for estimating the number and size distributions of flaws of various types in PWR steam generator tubes. These estimates are needed when calculating the probable primary to secondary leakage through steam generator tubes under postulated accidents such as severe core accidents and steam line breaks. The paper describes methods for two types of predictions: 1) the numbers of tubes with detectable flaws of various types as a function of time, and 2) the distributions in size of these flaws. Results are provided for hypothetical severely affected, moderately affected and lightly affected units. Discussion is provided regarding uncertainties and assumptions in the data and analyses.

I. Introduction

The objective of this paper is to describe methods for estimating the number and size distributions of flaws of various types in PWR steam generator tubes, and to provide some results for typical hypothetical units. Such estimates are needed, for example, when calculating the probable primary to secondary leakage through steam generator tubes under postulated accidents.

A basic assumption of the approach used in this paper is that estimating the expected distribution of flaw sizes in steam generator tubes can be broken into two steps: (1) estimating the number of tubes with detectable flaws as a function of time using a "defect occurrence distribution," in which the number of detectable flaws varies with time, and (2) distributing the sizes of these defects using a second "flaw size distribution" that is either independent of time or varies with time or number of flaws in some known way. In accordance with this basic assumption, this paper discusses (1) how to predict the number of tubes with detectable flaws for several flaw types and classes of steam generators, based on industry experience and engineering analysis, (2) the methods typically used to characterize the size distribution of these flaws, and (3) how the above two steps are combined to provide an integrated prediction.

The types of flaws considered in this paper include:

a. Circumferential cracks at the top of the tube sheet (TTS) of steam generators with full depth expanded mill annealed alloy 600 (600MA) tubes.

b. Axial primary water stress corrosion cracks (PWSCC) at roll transitions of steam generators with hard roll expanded low temperature mill annealed (LTMA) alloy 600 tubes.

c. Freespan cracks in units with 600MA tubes.

d. Axial OD cracks (ODSCC) at tube support plates (TSPs) of units with drilled hole tube support plates and LTMA 600 tubes.

e. Circumferential OD cracks at TSP dents of tubes of units with drilled hole TSPs and LTMA 600 tubes.

f. Axial cracks associated with IGA/SCC in sludge pile areas of tubes with LTMA tubing.

g. Flaws due to damage from loose parts.

The above flaw types were selected primarily on the basis that they are the flaws causing most of the tube degradation currently being detected in US plants. An exception is flaws due to loose parts. These flaws are not a major cause of tube plugging, but are important because they have caused two tube ruptures and about 20 to 30 primary to secondary leaks throughout the industry. An additional factor is that they can affect units that are resistant to corrosion damage, and which may not be inspected with the same frequency and extent as units that are experiencing detected corrosion damage.

There are several degradation mechanisms in addition to the mechanisms listed above that may be worth evaluating, not because they result in large numbers of tube repairs, but because they could entail risks of large flaws being present as a result of infrequent inspections or low probability of detection when employing normal inspection practices. These could include, for example, wear due to antivibration bars (AVBs), PWSCC in small radius U-bends, and cold leg thinning or wastage. In cases where a complete evaluation is desired, such additional flaw mechanisms may need to be quantified.

II. Hypothetical Plants

In order to illustrate the methodology described in this paper, examples are given using hypothetical moderately affected, severely affected, and lightly affected plants. The characteristics of the steam generators at the hypothetical plants were selected to be as follows:

Steam Generator Model: Model 51
No. of Steam Generators: 3
No. of Tubes: 3*3388 = 10,164
Tube Material: LTMA 600
Expansion Method: Explosive expansion for full tube sheet depth (Wextex)
Hot Leg Temperature: 605°F
Calendar Age: 20 years
Effective Full Power Years (EFPY): 14.0
EFPY per cycle: 1.2
Detected Degradation Modes:

- Axial ODSCC at TSPs (non dented)
- Circumferential SCC at TTS (mostly PWSCC)
- Sludge pile IGA/SCC
- Circumferential ODSCC at Dents at TSPs (associated with minor denting at TSPs)
- Free Span ODSCC

The number of tubes expected to have detectable flaws at the end of the next full operating cycle, i.e., at 15.2 EFPY, were estimated for each of the above degradation methods. For each

mode, numerical values were calculated for the moderately affected, severely affected and lightly affected cases. This was done using Monte Carlo sampling methods to sample statistical distributions for the degradation process, as described in the next section. Median (50th percentile) results were used as the moderate case, 84th percentile results for the severe case, and 16th percentile results for the lightly affected case.

Tube degradation due to loose part wear was also evaluated, using the same average industry data for all three cases.

III. Prediction of the Number of Tubes with Detectable Flaws

For plants with already detected flaws of the type being considered, standard statistical distributions, such as Weibull or log-normal, are used to predict the number of detectable flaws in the future as a function of operating time. This methodology is described in several industry reports.[1,2,3] A brief summary is given below:

a. Plants with Reliable Data from Two or More Inspections. For cases where two or more reliable data points are available for the defect mode under consideration , the process used for developing predictions of the number of flaws likely to be present in the future is as given below. "Reliable data points" as used here are data points based on inspections that involved all or a large sample of the susceptible tubes, and that used inspection methods of known and constant sensitivity to the flaw type involved.

- The fraction of the susceptible tube population with detected flaws is calculated for each inspection outage. The inspection sensitivity must be constant at all of the inspections, or adjustments must be made to account for differences in sensitivity.

- A two-parameter Weibull or log-normal distribution (or other selected statistical distribution function) is fit to the inspection data. The two-parameter Weibull distribution is given by the following:

$$F = 1 - e^{-\left(\frac{t}{\theta}\right)^b} \qquad (1)$$

where

F	=	fraction of susceptible population that has experienced degradation
t	=	operating time, normally in terms of effective full power years EFPY)
b	=	Weibull slope, a fitted parameter determined by analysis of failure data that describes the shape of the distribution
θ	=	Weibull characteristic time, a fitted parameter determined by analysis of failure data. It corresponds to the time when 63.2% of the susceptible tubes have experienced degradation.

- The fitted distribution is used to estimate the fraction of susceptible tubes with detectable flaws expected in the future.

- If plant conditions that affect the rate of degradation in a known way are changed, such as a hot leg temperature reduction, the predictions are adjusted to account for the changes.

b. Plants with Data from One Inspection. For cases where there is only one reliable data point for the defect mode under consideration (usually the latest inspection), the process used for developing predictions of the number of flaws likely to be present in the future is as follows:

- A projection (rather than a fit) is initiated from the one available data point.
- The slope for the rate of increase is estimated from industry data for the set of plants with similar designs and water chemistry type.
- The prediction for fraction of susceptible of tubes with detectable flaws in the future is then made using equation (1), by using the slope b selected from the previous step and requiring F to equal the measured fraction at the time of the last inspection (this allows parameter θ to be determined). The resulting b and θ values define the projected distribution.

c. Susceptible Plants with No Detected Flaws. For cases where it is known from experience with similar units that the unit in question is susceptible to a mode of degradation, but the mode has not been detected thus far at the plant, the process used for developing predictions of the number of flaws likely to be present in the future is as follows:

- The times at which the mode of degradation was detected at a specific cumulative level, e.g., 0.1% of the total tube population, are determined for all plants of the same type (same design features and general water chemistry type). These times are then adjusted to the selected plant's hot leg temperature using the Arrhenius equation and an appropriate activation energy, e.g., 50 kcal/mole for PWSCC and 54 kcal/mole for secondary side IGA/SCC.[4] Those plants which have not reached the selected level are considered to be suspended tests. A median rank with suspended items analysis is performed to determine the median time at which the mode can be expected to occur for this type of plant; this median time is typically used as the intercept or starting point for the tube failure projection. A suggested method for performing this median rank with suspended items analysis is given in the references.[5] Figure 1 shows the results of applying this methodology to the time to 1% of tubes with detectable ODSCC at drilled hole TSPs of feedring steam generators.
- To account for the period of time during which the mode of degradation was not detected at the subject plant, a process called truncation is used.[6] In essence, this process renormalizes the distribution so that the cumulative fraction "failed" after the time of truncation equals 1.0. This process is explained in the reference and is illustrated in Figures 2 and 3.
- The slope used for the projection is the same as described earlier, i.e., the median slope exhibited by similar plants is typically used.

d. Plants with Improved Designs. Lower rates of degradation are expected to occur in steam generators with improved design features, such as thermally treated alloy 600 (600TT) tubing in lieu of 600MA tubing, broached hole stainless steel TSPs in lieu of drilled hole carbon

Figure 1. Industry Time to 1% Tubes Repaired Due to Hot Leg TSP IGA/SCC
Median Rank Analysis
Westinghouse Feedring Plants with Drilled Hole TSPs, no Prior Phosphate Water Chemistry, and LTMA Tubing

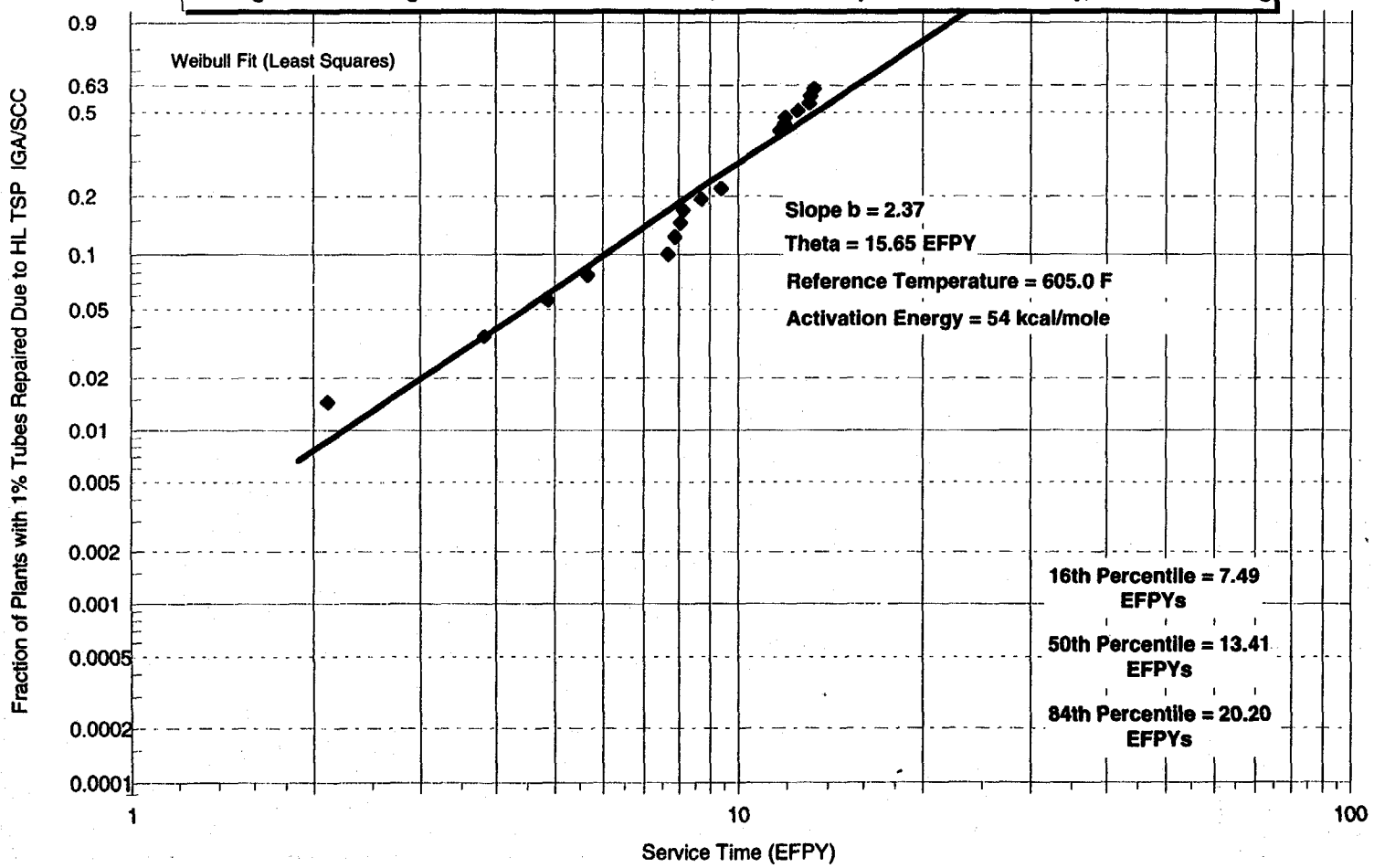

Figure 2. Truncated Distribution - Density Function

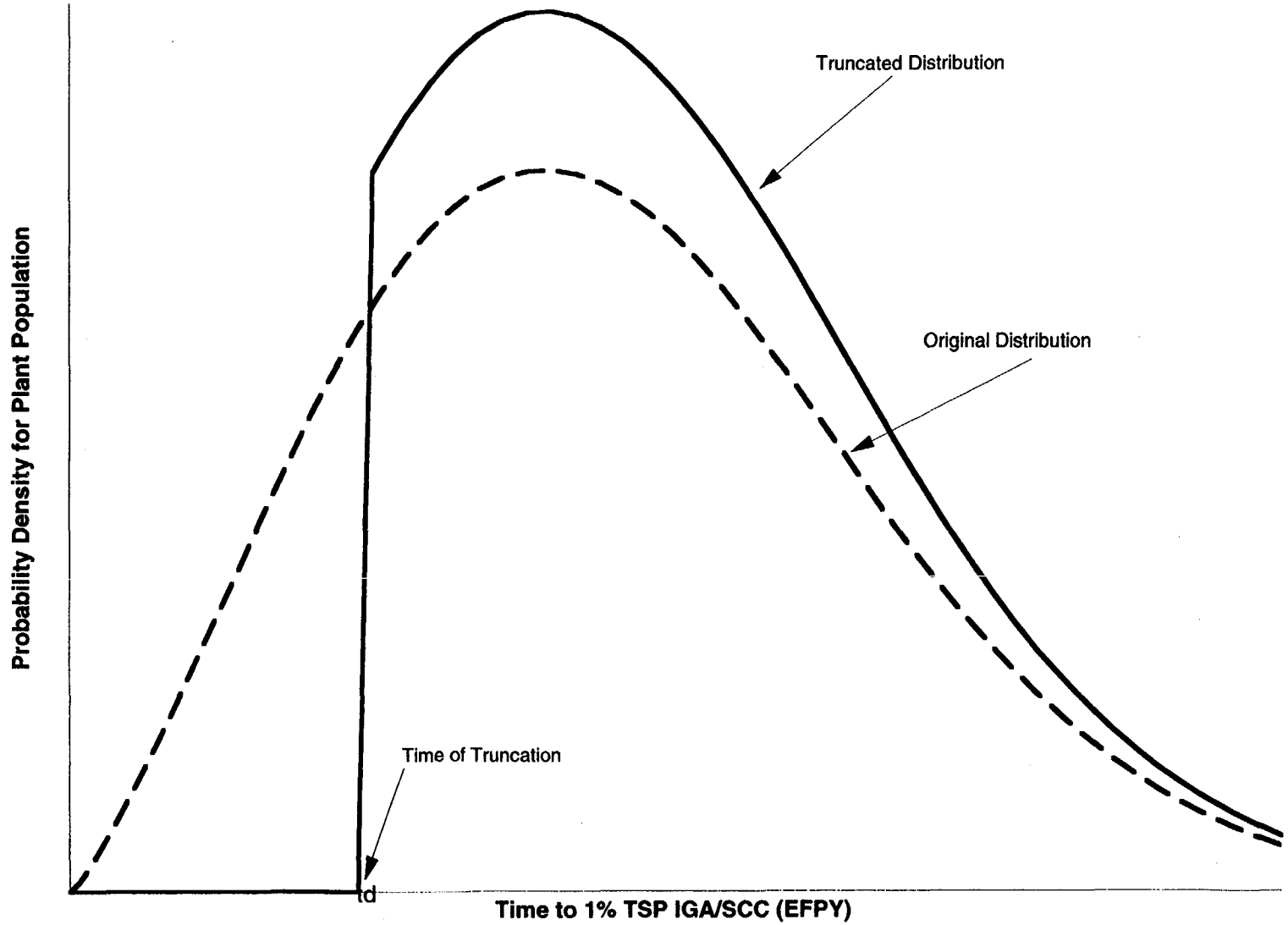

Figure 3. Truncated Distribution - Cumulative

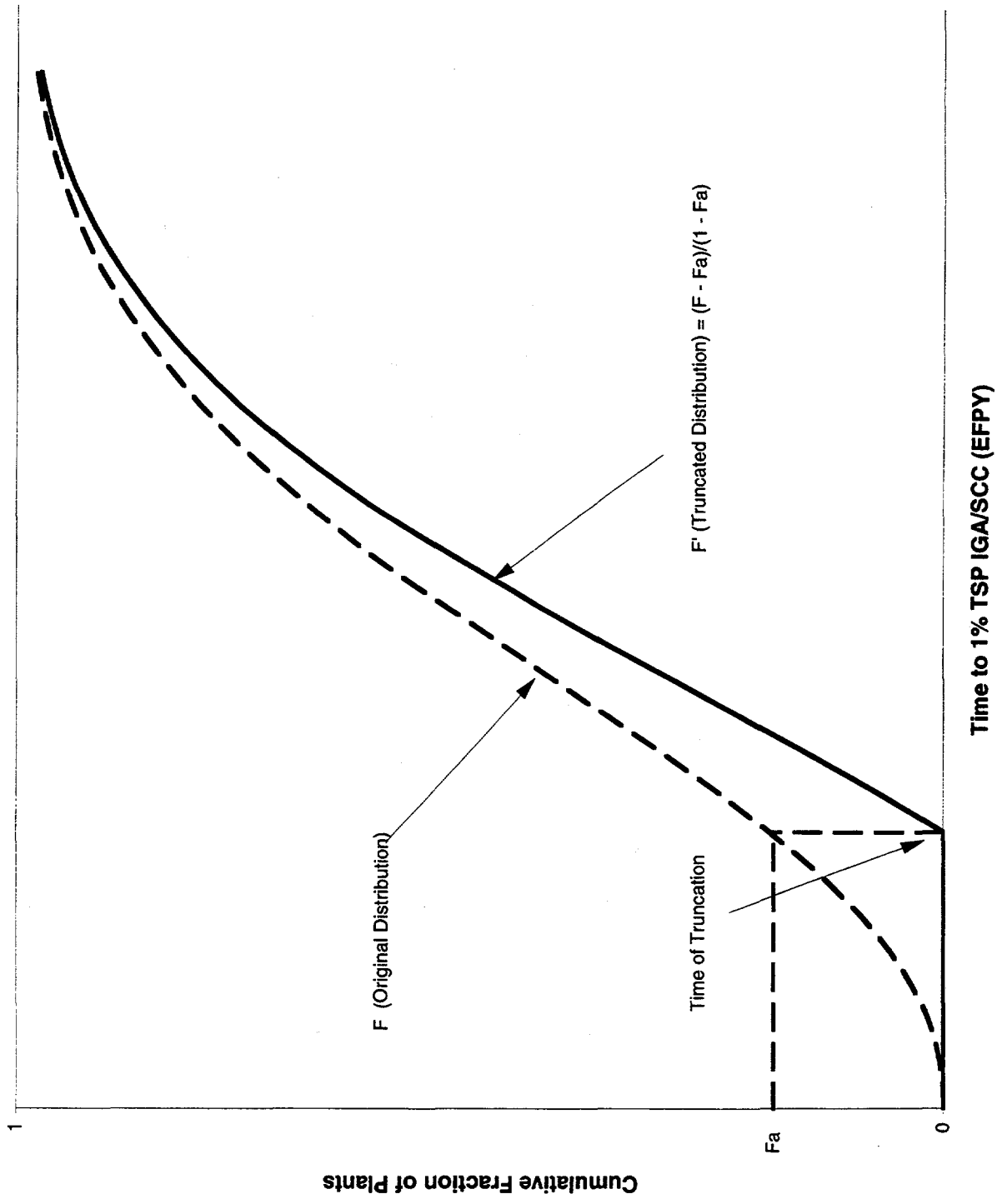

steel TSPs, and hydraulic tube expansions in lieu of full depth hard rolling. The suggested approach for modeling the number of degraded tubes in these improved steam generators is identical to that described above for as yet unaffected steam generators of older susceptible designs, except that improvement factors on time to cracking should be used to account for material and design improvements. As documented in a draft EPRI report for Model D5 and F steam generators, efforts have been made to quantify appropriate improvement factors for the new designs relative to the old designs, considering laboratory test results and field experience.* Some of the more important improvement factors include:

- Improvement factor for rate of experiencing PWSCC attack, 600TT vs. 600MA, assuming the same fabrication and tube installation methods (i.e., similar residual stresses and cold work): 2.5.

- Improvement factor for rate of experiencing IGA/SCC attack, 600TT vs. 600MA, assuming the same design and operating features, e.g., in sludge piles: 2.0.

- Improvement factor on time for IGA/SCC attack at TSPs, for 600TT tubes in broached hole TSPs vs. 600MA tubes in drilled hole TSPs, considering both material and design improvements: 3.0.

e. Numbers of Tubes with Detectable Flaws in Typical Hypothetical Moderately, Severely, and Lightly Affected Plants

For accident analyses it is sometimes desired to have defect distributions for typical hypothetical plants rather than for specific plants. For this case, the suggested method to predict the number of tubes with detectable defects of any specific mode is as follows:

- The design characteristics, temperature, beginning of cycle (BOC) EFPY, and end of cycle (EOC) EFPY of the typical plant are selected.

- All plants that have similar design characteristics are identified.

- The intercept times (e.g., times to 1%) for the mode of degradation being considered are determined for each plant with the same design characteristics. These times are adjusted to the reference plant's temperature using the method discussed earlier.

- A median ranks with suspended items analysis is performed of the adjusted intercept times. This provides a set of intercept time versus fraction of plants affected data. A statistical distribution (e.g., a Weibull., log normal, normal or gamma) is fitted to these data.

- The Weibull slopes for the set of similar plants are determined. A statistical distribution (e.g., a Weibull., log normal, normal or gamma) is fitted to these data, or to some suitable portion of the data.

- If the fraction of the tubes that is susceptible to the degradation mode is variable, this variability is modeled using some suitable distribution.

---

* J. E. Harris, A. P. L. Turner, and J. A. Gorman, Predicted Tube Degradation for Westinghouse Model D5 and F Steam Generators, draft report dated February 1996 for publication by EPRI.

- The fraction of tubes that develop detectable flaws as a function of time are evaluated using a Monte Carlo sampling approach. For each trial, an intercept time, a Weibull slope, and a susceptibility fraction are randomly selected from the distributions developed as described above. The fractions of the total tube population with detectable flaws at the beginning and end of the cycle are determined using the selected intercept time, slope, and susceptibility fraction, and the difference determined. The difference represents the number of newly detectable flaws that developed during the cycle for that trial. A large number of trials is performed, such as 1000 to 10,000. The median value from this set of trials is taken as representing a moderately affected unit, the 16th percentile as representing a lightly affected unit, and the 84th percentile as representing a severely affected unit.

f. Supporting Data for Predicting Numbers of Tubes with Detectable Flaws, and Example Application

To make use of the methods described above, data for intercept times and slopes are required. Data for several degradation modes have been obtained from the literature.* An example application for the hypothetical plants of Section 2 is given below for one degradation mode, circumferential cracking at the TTS.

Circumferential cracking at the TTS has been detected at all Wextex units. The results of a median ranks analysis for the set of Wextex units is given in Figure 4. Note that all of the data have been adjusted to the hypothetical plants' hot leg temperature of 605°F. The distribution shown on Figure 4 provides a distribution of intercept times to a failure fraction of 0.026%. The rates of increase of this mode of degradation are shown on Figures 5A and 5B, which show a list of Weibull slopes and a Weibull distribution fit to this list. The intercept times and Weibull slopes shown on these figures were used in a Monte Carlo analysis of the type described above to predict the numbers of tubes with detectable flaws of this type as a function of time for the moderately affected, severely affected, and lightly affected hypothetical plants. A distribution for fraction of susceptible tubes was not required for this mode of degradation since all tubes appear to be susceptible. It was assumed that all flaws detected at the start of the operating cycle (14.0 EFPY) were plugged. Thus, the number of flaws detected at the end of the cycle (15.2 EFPY) was calculated by determining the cumulative number of flaws at the beginning and end of the cycle (14.0 and 15.2 EFPY respectively) and taking the difference. Results of this analysis are included in Table 1.

Table 1 also shows results of analyses for the other degradation modes considered. Some points to note about the analyses for other flaw types include:

- With regard to circumferential ODSCC at TSP dents, it was assumed that the median fraction of tubes with dents was 10%, that the fraction of tubes dented could be described by a log normal distribution, and that a factor of ten change occurs in the affected population per standard deviation.

- With regard to numbers tubes with axial ODSCC at non dented TSP intersections, the analysis for numbers of tubes with flaws was performed for flaws that were repairable by

* J. A. Gorman, et al., Estimating Probable Flaw Distributions in PWR Steam Generator Tubes, in course of publication by ANL.

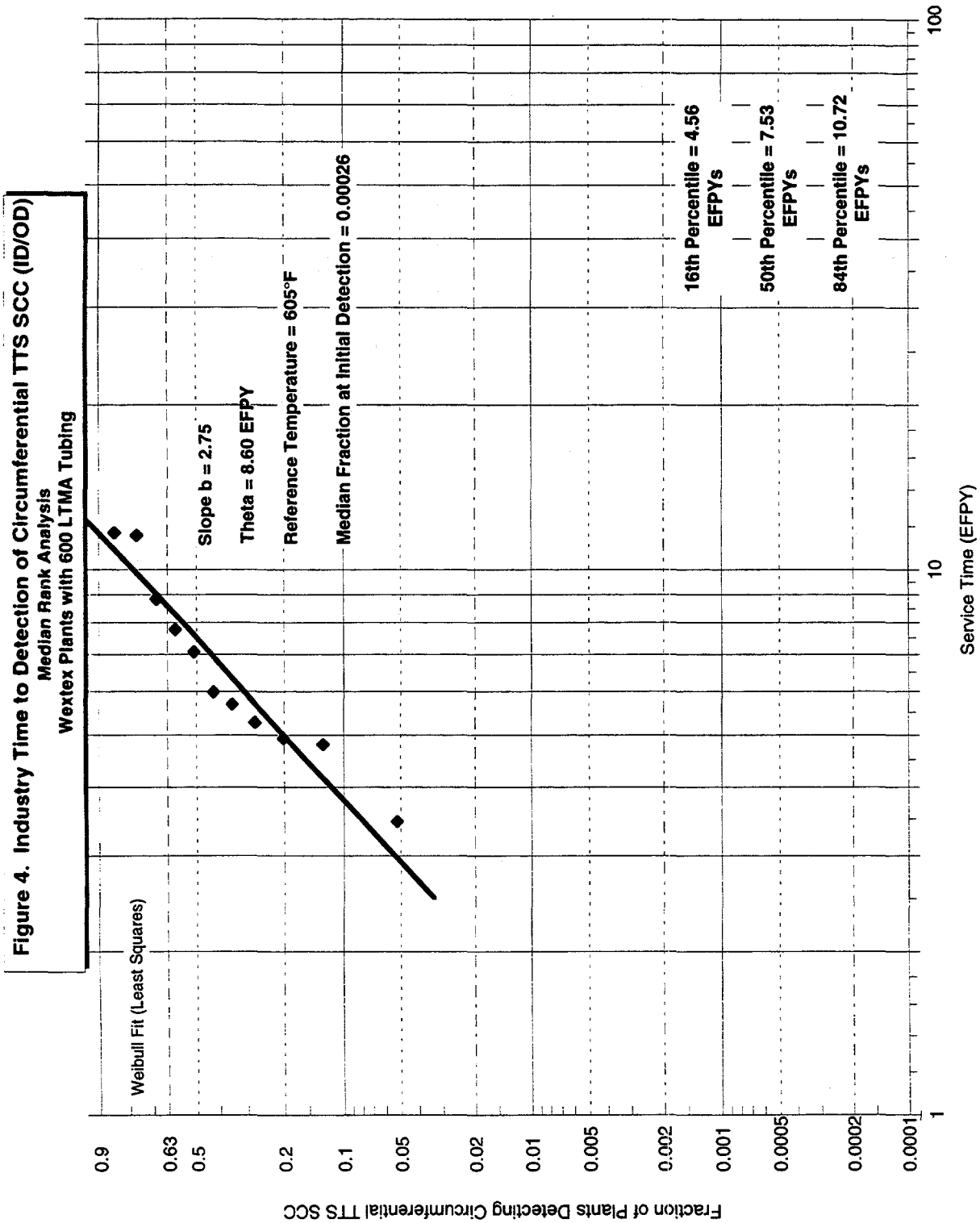
Figure 4. Industry Time to Detection of Circumferential TTS SCC (ID/OD)
Median Rank Analysis
Wextex Plants with 600 LTMA Tubing
Weibull Fit (Least Squares)
Slope b = 2.75
Theta = 8.60 EFPY
Reference Temperature = 605°F
Median Fraction at Initial Detection = 0.00026
16th Percentile = 4.56 EFPYs
50th Percentile = 7.53 EFPYs
84th Percentile = 10.72 EFPYs
Fraction of Plants Detecting Circumferential TTS SCC
0.9
0.63
0.5
0.2
0.1
0.05
0.02
0.01
0.005
0.002
0.001
0.0005
0.0002
0.0001
1
10
100
Service Time (EFPY)

Figure 5A. Weibull Slopes for Wextex Plants with Circumferential TTS SCC (before peening)

				Median Slope =	**2.82**
				16% Slope =	**2.13**
				84% Slope =	**4.16**
No.	**Plant**	**Slope**	**% Error**	**Points**	**Median Rank**
1	A	2.00	9.4	4	0.130
2	B	2.78	32.6	6	0.315
3	C	2.82	6.6	3	0.500
4	D	3.35	8.2	3	0.685
5	E	4.32	21.2	5	0.870

5 < Number of Plants

Updated: Jul-96

Figure 5B. Weibull Fit to Wextex Plant TTS Circumferential SCC Slopes

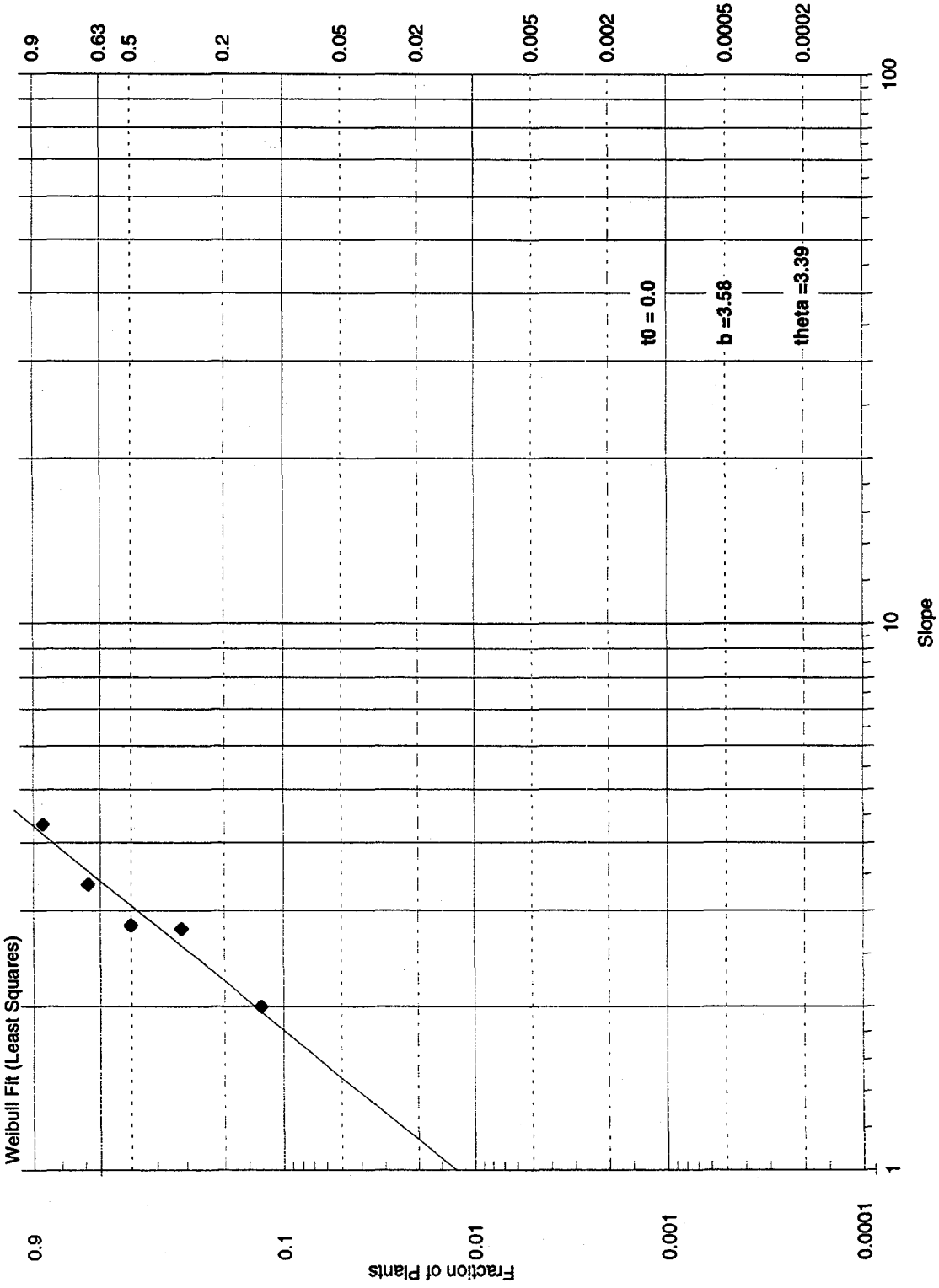

Table 1. Flaw Distributions for Hypothetical Example Cases

Plant Characteristics				
No. of Steam Generators:	3			
No. of Tubes = 3*3388 =	10164			
Tube Material	LTMA 600			
Expansion Method:	Wextex			
Hot Leg Temperature, °F:	605			
BOC EFPY:	14			
EOC EFPY:	15.2			

		Moderately Affected Plant	Severely Affected Plant	Lightly Affected Plant
1. Circumferential SCC at TTS (Mostly PWSCC)				
Number of tubes with Circ. SCC at TTS at 15.2 EFPY (Note 1) =		7.0	46.3	1.4
Gamma distribution parameters for crack arc length;				
arc length in degrees (Note 2):*	α =	2.84	2.84	2.84
	β =	28.6	28.6	28.6
Detection efficiency, >20° arc length:		71.2%	71.2%	71.2%
*For macrocracks. Macrocracks consist of series of 0.3 * thru-wall cracks separated by 0.05" long ligaments.				
2. Circumferential ODSCC at Dents at TSPs				
Number of tubes with cracks at15.2 EFPY Note 1) =		4.2	40.1	0.32
Gamma distribution parameters for crack arc length;				
arc length in degrees (Note 2):*	α =	34.4	34.4	34.4
	β =	3.23	3.23	3.23
Detection efficiency, >20° arc length:		94.8%	94.8%	94.8%
*For individual macrocracks. There are typically two near thru-wall diametrically opposed macrocracks per cracked location. See Figures C-6 and 7 for distribution of combined crack lengths.				
3. Free Span ODSCC				
Number of tubes with cracks at 15.2 EFPY (Note 1) =		5.2	60.2	1.7
Gamma distribution parameters for length, in. (Note 2):*	α =	0.17	0.17	0.17
	β =	0.88	0.88	0.88
Detection Efficiency, >0.1 inches:		66.0%	66.0%	66.0%
Gamma distribution parameters for depth, % wall (Note 2):*	α =	17.0	17.0	17.0
	β =	3.80	3.80	3.80
Detection Efficiency, >20% of wall:		88.4%	88.4%	88.4%
* Crack length and depth distributions are assumed to be independent.				
4. IGA/SCC in Hot Leg Sludge Pile				
Number of tubes with cracks at 15.2 EFPY (Note 1) =		39.6	60.2	18.9
Gamma distribution parameters for length, in. (Note 2):*	α =	0.17	0.17	0.17
	β =	0.88	0.88	0.88
Detection Efficiency, >0.1 inches:		66.0%	66.0%	66.0%
Gamma distribution parameters for depth, % wall (Note 2):*	α =	17.0	17.0	17.0
	β =	3.80	3.80	3.80
Detection Efficiency, >20% of wall:		88.4%	88.4%	88.4%
* Crack length and depth distributions are assumed to be independent.				
5. Axial ODSCC at TSPs				
Number of tubes with ODSCC (0.85 volt level) at 15.2 EFPY (note 1) =		569.7	6024.6	131.1
Gamma distribution parameters for depth of 0.75" long cracks;				
depth in % of wall:	α =	0.770	0.770	0.770
	β =	4.480	4.480	4.480
Detection efficiency, >10% of wall:		24.4%	24.4%	24.4%
6. Flaws Due to Loose Parts				
Number of tubes with flaws at 15.2 EFPY =		0.7	0.7	0.7
Gamma distribution parameters for length, in.:*	α =	1.900	1.900	1.900
	β =	0.458	0.458	0.458
Detection efficiency (assumed):		100%	100%	100%
Gamma distribution parameters for depth, % wall:*	α =	2.275	2.275	2.275
	β =	17.235	17.235	17.235
Detection efficiency (assumed):		100%	100%	100%
* Flaw length and depth distributions are assumed to be independent.				

Notes

1. Numbers of tubes are totals that reflect adjustment for detection efficiencies.
2. Gamma distributions are for "actual" flaws, i.e., after adjustment for measurement error and POD.

older "40% of wall" plugging criteria. It was assumed that only those flaws that would have required plugging by 14.0 EFPY per a 2 volt alternate repair criteria would have been plugged. Thus, most tubes with this type of flaw were assumed to have remained in service.

- Estimating the number of tubes with loose part damage was performed by evaluating overall industry statistics for occurrence of ruptures and leaks due to loose parts, and not by the type of Weibull analysis described in this paper.

IV. Flaw Size Distributions

Experience over a period of several years at Arkansas Nuclear One Unit 2 (ANO 2) and Millstone 2 with regard to flaw size distributions for circumferential cracks at the TTS is described in an Entergy report.[7] As discussed in that report, the gamma distribution was found to provide the best fit to the crack size distribution, and its fitted parameters to remain reasonably constant from inspection to inspection. Based on that experience, the model used to evaluate inspection intervals for Millstone 2 and ANO 2 has been based on use of the gamma distribution for evaluating the probability of crack sizes exceeding allowed limits.

Detailed evaluations of the changes in flaw size distributions over a period of years have been performed in Belgium for axial PWSCC cracks at the TTS.[8] These evaluations indicate that the gamma distribution fits the data well, but that the parameters need to be adjusted in a systematic way from cycle to cycle to account for the growth of cracks. This is most likely the result of the use of alternate repair criteria which allow cracks below defined length limits to remain in service, such that the average length of the whole set of cracks grows with time.

Detailed evaluations of the changes in flaw size distributions over a period of years appear to be available for only the two types of flaws mentioned above, i.e., average depths of circumferential cracks at the TTS and lengths of axial PWSCC at the TTS of full depth hard rolled units. The stability or rate of change of size distributions for other types of flaws do not appear to have been discussed in the open literature.

As noted above, extensive use has been made of the gamma distribution for describing the size distribution of flaws, and it is used for this purpose in this paper. The gamma distribution is described by the following:[9]

$$f(x) = \frac{\beta^{-\alpha} x^{\alpha-1} e^{-x/\beta}}{\Gamma(\alpha)} \text{ if } x > 0 \qquad (2)$$

$f(x) = 0$ otherwise

where:

$\Gamma(\alpha)$ = the standard gamma function

α and β = fitted parameters (α is shape parameter, β is scale parameter)

x = size parameter such as depth or arc length

Use of the gamma distribution requires that the parameters α and β be determined for the flaw type being evaluated. These parameters are determined by first performing statistical fits to measured flaw size data to select best estimate values of the α and β parameters. Then, adjustments

to the parameters are made as described later to account for probability of detection (POD) and measurement error, to develop estimates of the "actual" flaw size distributions.

In some cases, alternate distributions fit the size distribution of flaws better than the gamma distribution and have been used, at least on a trial basis. For example, in some cases the beta distribution has been found to provide a better fit to TTS circumferential crack average depth data than the gamma fit. Another example is that the sizes of axial PWSCC cracks at the top of the tube sheet that are allowed to remain in service due to use of alternate repair criteria have been found, in some cases, to be better fit by a Weibull.[10]

Two adjustments are typically required to measured flaw size data. One adjustment is to account for the variation in probability of detection (POD) of flaws as flaw size changes. The general approach is to divide the number of observed flaws by the POD, thus increasing the estimated number of flaws in each size category. The POD curve has to be determined for each specific defect type - inspection method combination. Typically, smaller flaws have lower PODs than larger flaws, with the POD approaching zero as the flaw size decreases. Instrument capabilities are such that, for larger flaws, the POD could theoretically approach 1.0. However, because of human error, it is considered that a POD over 0.95 is generally not realistic. Adjustment for the POD may not be useful for very small defects, where the uncertainty in the adjusted values can be so large as to make them misleading. For this reason, in some cases data for very small defects are excluded from the flaw distributions.

The second adjustment is to correct for measurement error. This involves adjusting the data to account for mean or systematic error in the measured flaw size versus the actual flaw size, and to account for the scatter or uncertainty in the measurement. The fact that the measurements have some uncertainty leads to measured flaw sizes having a greater spread and higher peak values than the actual flaw sizes. Corrections for this effect can be made using convolution type analyses[11] or Monte Carlo methods.

For the examples presented in Table 1, the adjustments for POD and measurement error were performed using the method described by Heasler.[12] This method consists of selecting a distribution function for the actual flaw size distribution, using a convolution integral to combine that distribution with the POD and measurement error, and selecting the parameters of the actual flaw size distribution to maximize likelihood for the observed flaw size distribution.

A typical example of the development of a size distribution is for the arc length of circumferential cracks at the TTS of Wextex units. Figures 6A and 6B show the measured length distribution in density and cumulative form. Figures 6C and 6D show the "actual" crack arc length after adjustment for POD and measurement error. The instrument error was estimated by comparing pulled tube results with the length measured by eddy current test (mean error of 6.0° (overcall of the length), with a standard deviation of 5.7°).[13] Based on data in the same report, together with engineering judgment, the POD for these defects was approximated as being zero at 25°, 0.95 at 75° and higher angles, with a straight line variation between these two values. The flaw distribution parameters are shown on the figures and also on Table 1. Table 1 also lists the flaw size distribution parameters for the other flaw types considered in the hypothetical examples.

In addition to the flaw size distribution, a "detection efficiency" parameter and minimum flaw size are listed for each flaw type. The detection efficiency indicates the fraction of the "actual" flaws that were detected, based on the assumed POD curve. The minimum flaw size indicates the minimum flaw size that was considered when determining the detection efficiency (i.e., flaws

Figure 6A. Wextex TTS Circumferential Crack Arc Lengths (North Anna 1 1991)

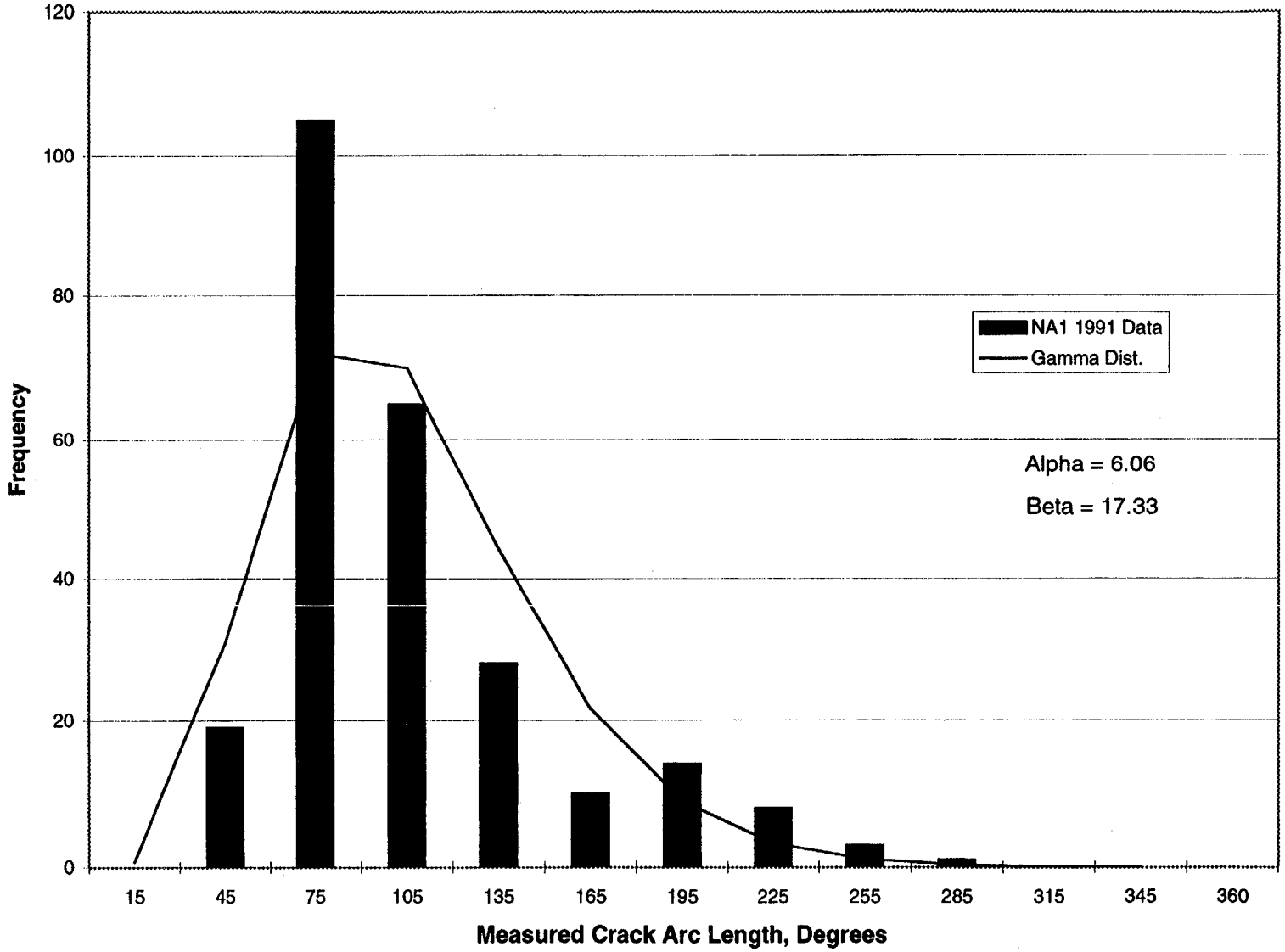

Figure 6B. Wextex TTS Circumferential Crack Arc Lengths (North Anna 1 1991)

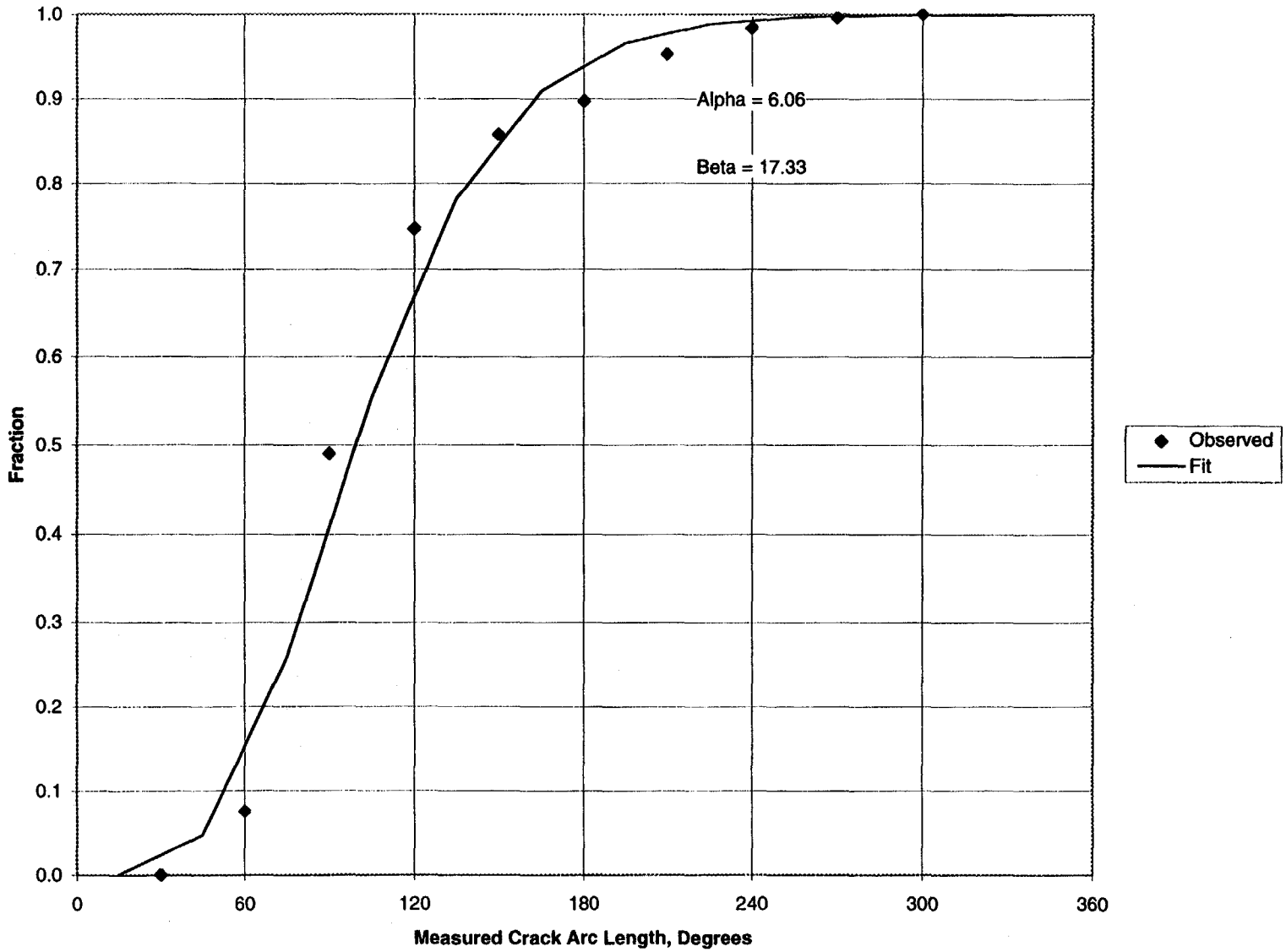

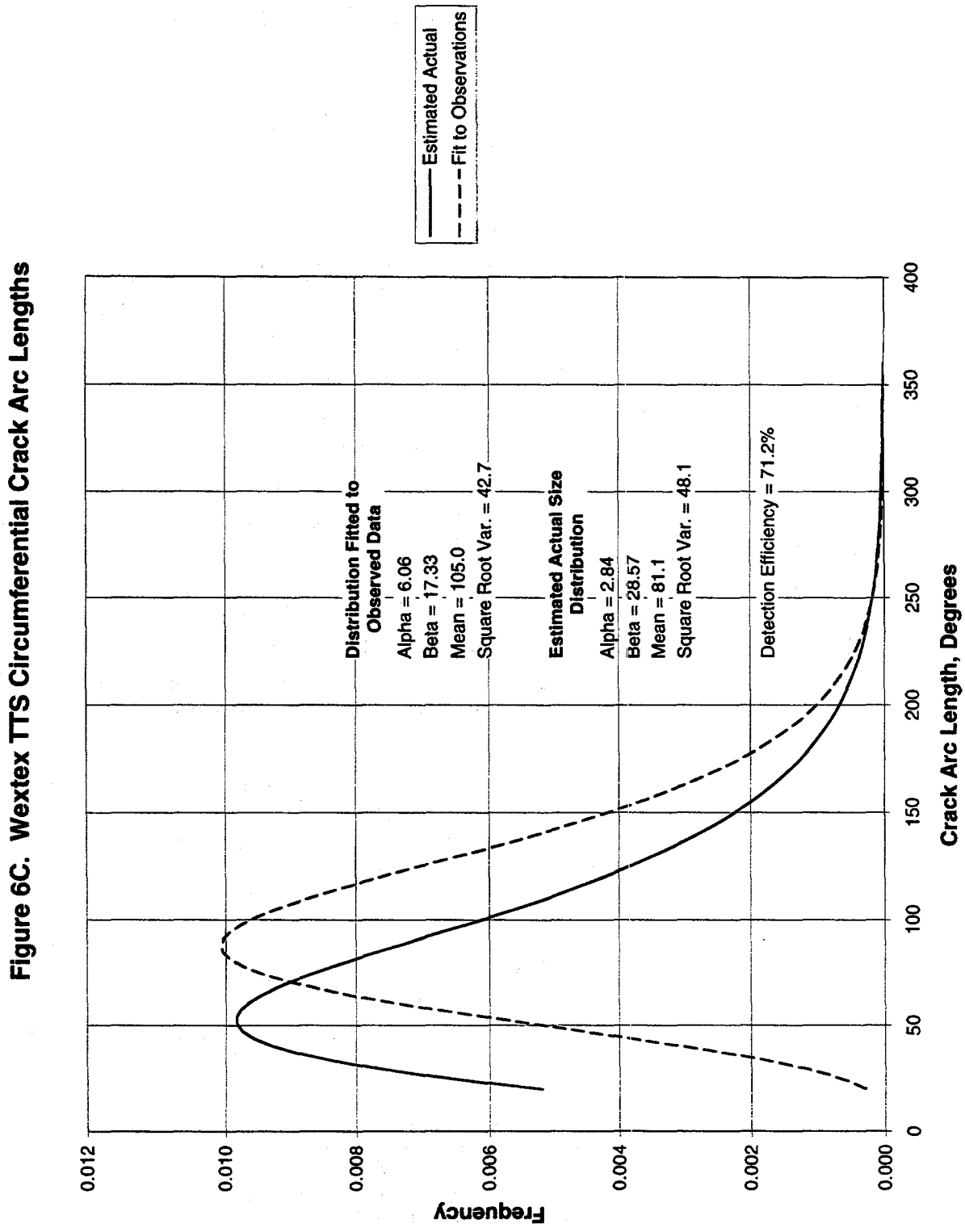

Figure 6C. Wextex TTS Circumferential Crack Arc Lengths

Figure 6D. Wextex TTS Circumferential Crack Arc Lengths

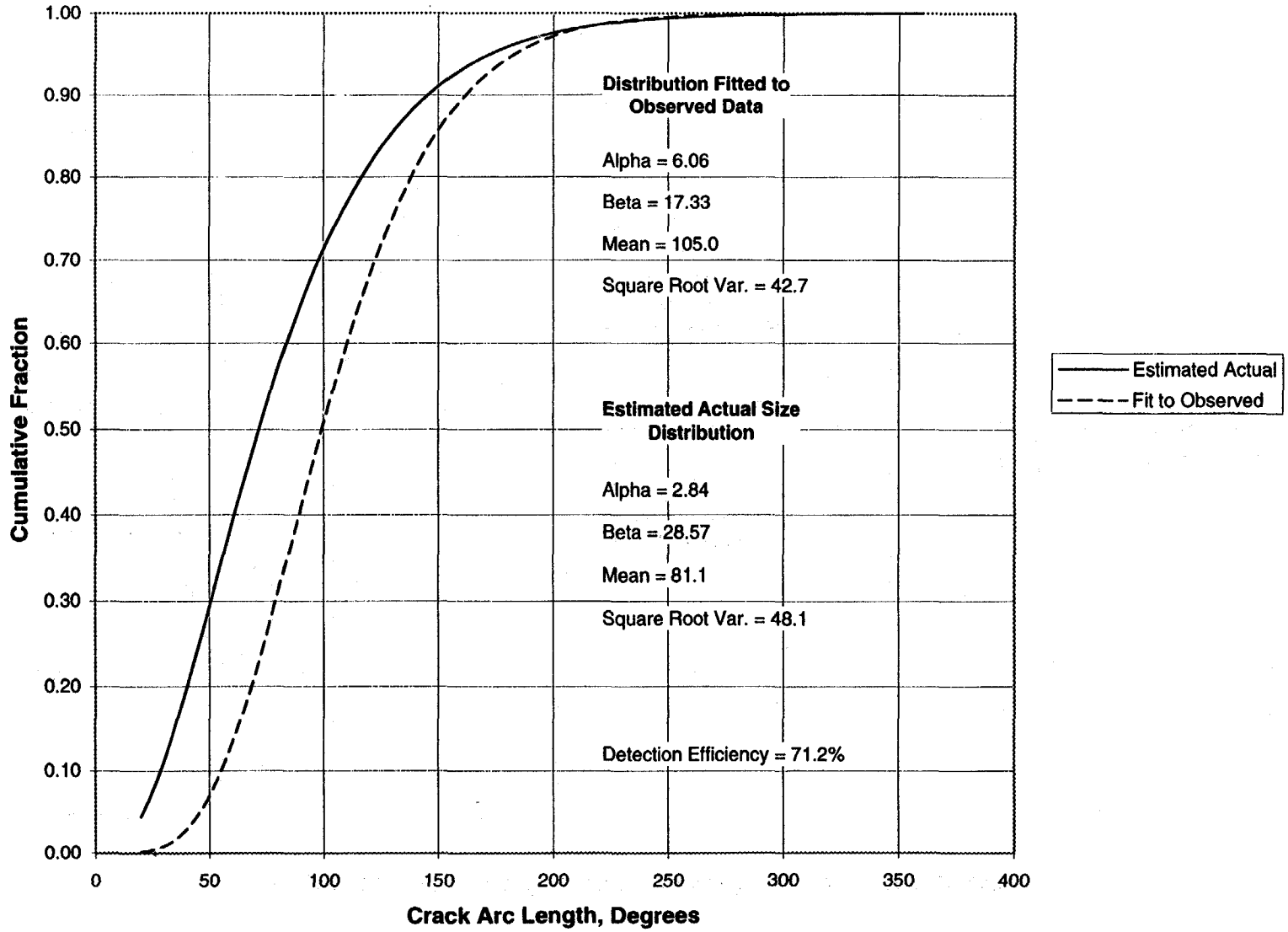

below the limit were excluded). When using the flaw size distribution, if it is applied to measured data for numbers of flaws, the number of detected tubes over the size limit should be divided by the detection efficiency to determine the expected number of actual flaws over the size limit.

Some points to note about the flaw size distributions listed in Table 1:

- The larger circumferential cracks at the TTS of Wextex units were found by examination of removed tubes to be 90 to 100% through wall, but to contain 0.05 inch long ligaments about every 0.3 inches.[14] A tube integrity evaluation in 1992 for the plant from which the tubes were removed indicated that some of the new cracks detected in the next operating cycle were expected to be through wall, but that Regulatory Guide 1.121 burst capability requirements would nevertheless be satisfied.[15]

- The arc length distribution for circumferential cracks at dented TSP intersections are for equivalent through wall arc lengths. Examination of removed tubes showed that dented TSP intersections with larger circumferential cracks typically have two cracks per location (e.g., top edge of TSP).[16] Thus, since the crack distribution parameters listed on Table 1 for this type of crack are for individual cracks, it is necessary to assume that many intersections will have a second diametrically opposed crack at the same elevation. On the assumption that the lengths of these two cracks are independent, a distribution for the total length of the two cracks was developed by Monte Carlo sampling and is shown on Figure 7. Examination of removed tubes indicated that the ligaments in the cracks had largely been corroded away.

- The length distribution for freespan flaws is based on data from Palo Verde 2.[17] However, the depth distribution, while originally based on Palo Verde data, was adjusted to result in larger depths, such that about 2% of free span flaws would reach through wall (though typically with short lengths, such that little leakage would result), and about 0.1% of such flaws would cause a burst, where burst is considered as occurring if the flaw has both a length over 1.8 inches and a depth over 90% of wall (for 3/4" diameter tubes). This adjustment was made based on engineering judgment to reflect expected behavior for units that are subject to routine inspections for freespan defects, e.g., routine screening using bobbin coil eddy current test methods, as opposed to intensive screening for this type of defect such as performed at Palo Verde.

- The defect size distributions for IGA/SCC in sludge piles were assumed to be the same as for freespan defects discussed above. This selection was based on discussions at a meeting among NRC, ANL, and industry experts on August 26, 1996 in Rockville. This is considered reasonable since the Palo Verde freespan attack is associated in many cases with corrosion under heavy deposits, and thus is similar to corrosion under sludge piles.

- The flaw size distribution given for axial ODSCC at TSPs is for an assumed crack length of 0.75 inches, which is typically the maximum observed length of this type of flaw. It was based on correlations between the bobbin coil eddy current test (ECT) voltage and burst pressure, and between burst pressure and flaw size. The many small crack depths indicated by the distribution is an artifact of the assumption of all flaws having a length of 0.75 inches. In actual fact, many small flaws are shorter but deeper. However, this is not considered important from a structural standpoint.

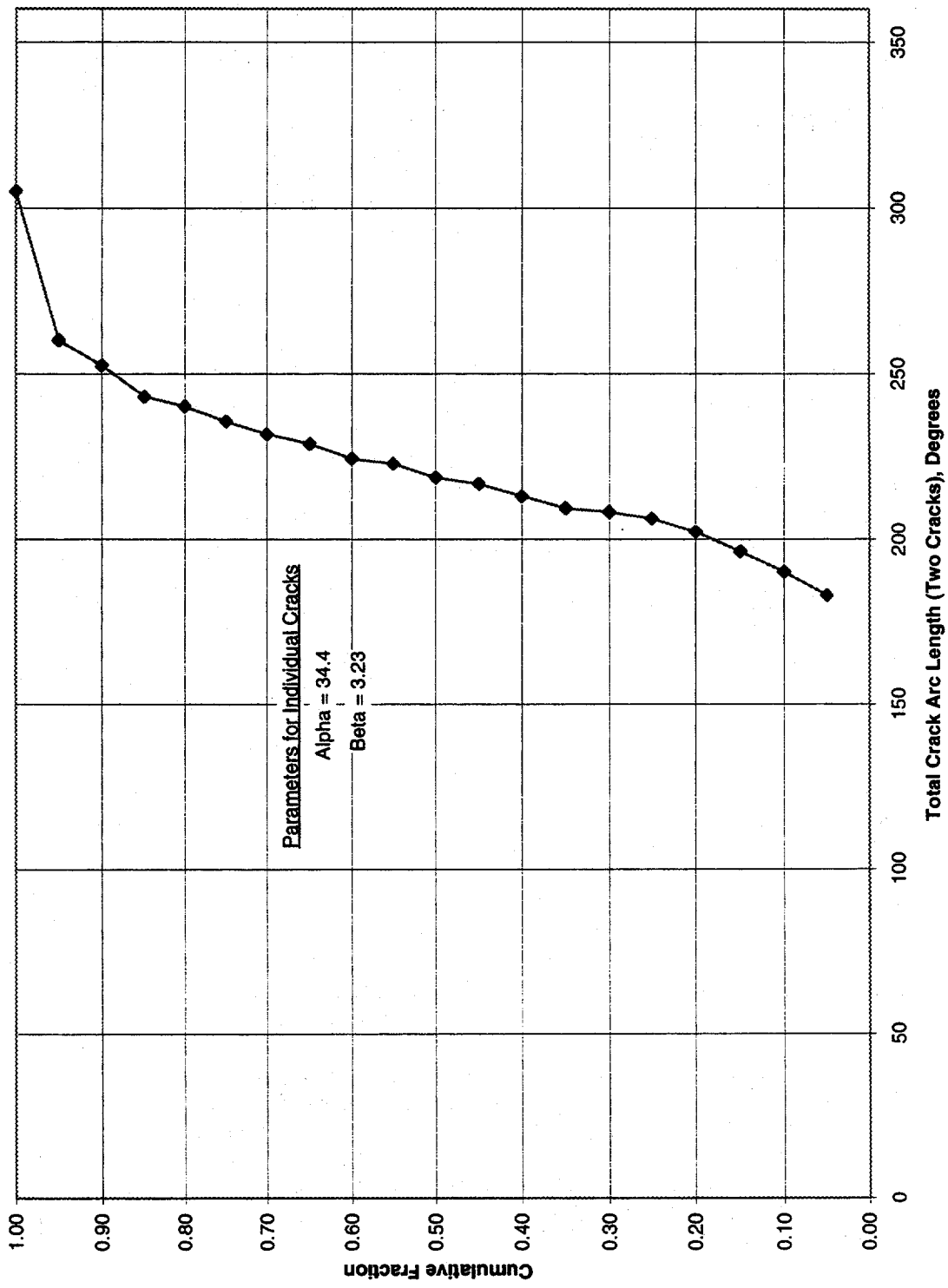

Figure 7. Total Arc Length of Two Cracks at TSP Dent

- The depth distribution for loose part flaws is based on proprietary measured data. It indicates that 3% of the LP flaws will be 100% of wall in depth, which is consistent with industry leakage history (about 30 leakage events for nearly 1000 tubes plugged for loose part flaws). The length distribution was selected by trial and error using Monte Carlo methods to result in an average of two bursts per 1000 flaws, consistent with industry experience. Burst was defined as occurring when the flaw length exceeded 2.15 inches and the flaw depth exceeded 90% of wall in the same trial (for 7/8" diameter tubes).

V. Combined Prediction

The methods of Section III and Section IV taken together provide a complete method for predicting the distribution of the flaws: the analyses of Section III determine the numbers of tubes with detectable flaws of various types as a function of time, and the analyses of Section IV determine the distributions of the sizes of these flaws, again for each flaw type. The results of this type of combined prediction are illustrated in Table 1, as previously described in Sections III and IV.

References

1 J. A. Gorman, et al., Statistical Analysis of Steam Generator Tube Degradation, EPRI NP-7493, September 1991.

2 A. P. L. Turner, et al., Statistical Analysis of Steam Generator Tube Degradation: Additional Topics, EPRI TR-103566, July 1994.

3 J. A. Gorman, et al., PWSCC Prediction Guidelines, EPRI TR-104030, July 1994.

4 J. A. Gorman, "Correlation of Hot Leg Temperature with Rate of Steam Generator Tube Corrosion," draft report for EPRI, February 1993.

5 Pages 3-22 through 3-25, J. A. Gorman, et al., Statistical Analysis of Steam Generator Tube Degradation, EPRI NP-7493, September 1991.

6 Pages 4-8 through 4-10, A. P. L. Turner, et al., Statistical Analysis of Steam Generator Tube Degradation: Additional Topics, EPRI TR-103566, July 1994.

7 Arkansas Nuclear One Unit Two Steam Generator Circumferential Cracking Evaluation, Entergy, February 1995, in NRC PDR, 9502230211 950217, Docket No. 50-368.

8 P. Hernalsteen, "Prediction Model for the PWSCC Degradation Process in Tube Roll Transitions," presented at CSNI/UNIPEDE Specialist Meeting, 16-20 September, 1991, Brussels, Belgium.

9 A. M. Law and W. D. Kelton, Simulation Modeling and Analysis, McGraw-Hill, New York, 1991.

10 L. Cizelj, B. Mavko and P. Vencelj, "Reliability of Steam Generator Tubes with Axial Cracks," PVP-Vol. 288, Service Experience and Reliability Improvement: Nuclear, Fossil, and Petrochemical Plants, ASME, 1994.

11 P. G. Heasler, et al., Analysis Before Test: Estimation of Fabrication Defect Rates in Reactor Pressure Vessels, Draft PNL report for NRC, Nov. 1994.

12 Ibid.

13 North Anna Unit 1 Steam Generator Operating Cycle Evaluation, Westinghouse WCAP-13035, August 1991, forwarded by Virginia Electric and Power Company letter dated August 30, 1991, in NRC PDR, 9109100132 910880, Docket No. 50-338.

14 Ibid.

15 Attachment to NRC Meeting Summary of March 2, 1992, "Westinghouse Tube Integrity Evaluation," in NRC PDR, 9204090355 920402, Docket No. 50-338.

16 North Anna Unit 1 Steam Generator Operating Cycle Evaluation, Westinghouse WCAP-13035, August 1991, forwarded by Virginia Electric and Power Company letter dated August 30, 1991, in NRC PDR, 9109100132 910880, Docket No. 50-338.

17 J. Begley, "Structural Integrity Analysis," Attachment to NRC meeting report "Summary of Meeting Held on September 20, 1995, to Discuss Steam Generator Issues," March 5, 1996, in NRC PDR, 9603140103 960305, Docket No. 50-528.

Predictions of Structural Integrity of Steam Generator Tubes under Normal Operating, Accident, and Severe Accident Conditions

Saurin Majumdar
Argonne National Laboratory
Argonne, Illinois 60439

Abstract

Available models for predicting failure of flawed and unflawed steam generator tubes under normal operating, accident, and severe accident conditions are reviewed. Tests conducted in the past, though limited, tended to show that the earlier flow-stress model for part-through-wall axial cracks overestimated the damaging influence of deep cracks. This observation was confirmed by further tests at high temperatures, as well as by finite-element analysis. A modified correlation for deep cracks can correct this shortcoming of the model. Recent tests have shown that lateral restraint can significantly increase the failure pressure of tubes with unsymmetrical circumferential cracks. This observation was confirmed by finite-element analysis. The rate-independent flow stress models that are successful at low temperatures cannot predict the rate-sensitive failure behavior of steam generator tubes at high temperatures. Therefore, a creep rupture model for predicting failure was developed and validated by tests under various temperature and pressure loadings that can occur during postulated severe accidents.

Introduction

Operating experience with PWR steam generators in both the U.S. and abroad has shown that cracks of various morphologies can and do occur in steam generator tubes, starting early in life. These may be single cracks that are axial or circumferential, ID or OD initiated, part-through-wall or through-wall, or they may be multiple cracks that are parallel or form a network. Tests have shown that, depending on the location and morphology of these cracks, the steam generator tubes can be weakened to various extents.

Under normal operating conditions, the pressure across a PWR steam generator tube wall, Δp_{no}, is ≈ 9 MPa (1300 psi); under a main steamline break (MSLB) in which the secondary side has dropped to atmospheric pressure, the pressure across the tube wall, Δp_{MSLB}, is ≈18 MPa (2560 psi). Degraded tubes must actually be capable of withstanding $3 \cdot \Delta p_{no}$ ≈27 MPa (3900 psi) and $1.4 \cdot \Delta p_{MSLB}$ ≈25 MPa (3660 psi) to meet requirements for continued operation. For typical unflawed steam generator tubes made of Alloy 600, the burst pressure, p_b, is ≈ 65 MPa (9400 psi).

Severe accidents involving significant core damage are unlikely events in nuclear reactors. Even in the unlikely event that such an accident should occur, in most cases any potential risk to the public is mitigated by the presence of a robust containment. The behavior of steam generator tubing during such severe accidents is of particular interest, since failure of the steam generator tubes could lead to bypass of the containment. As part of its effort to develop a new steam generator rule, the NRC and its contractors and EPRI have been investigating the potential for failure of steam generator tubes during severe

accidents. The accident sequences that appear to produce the greatest risk of steam generator tube failure are those in which the reactor pressure vessel fails to depressurize, but depressurization does occur on the secondary side. Even in these cases, preliminary investigations[a, b] suggest that failures are likely to occur in the hot–leg nozzle or the inlet surge–line nozzle leading to depressurization of the reactor system which prevents steam generator tube failure. However, such calculations are subject to large uncertainties and the NRC is pursuing additional studies to better understand the progression of such sequences, the temperature of the steam generator tubes during such accidents, and the behavior of steam generator tubes at the high temperatures associated with such accidents. An objective of the present work at Argonne is the development and validation of models to describe the failure of flawed steam generator tubes at high temperatures. The tests and analyses do not attempt to accurately simulate any particular severe accident scenario, rather they are intended to provide tools that can be used to determine failure under a broad range of pressure and temperature histories.

There is substantial literature[1-6] on the development and validation of analytical models to describe the behavior of flawed tubes at normal reactor operating temperatures (288–320°C). These models and data can be used to analyze the potential for failure during design basis accidents, during which the temperature of the steam generator tubing is less than 350°C. In this temperature range, creep effects are negligible in Alloy 600. However, in postulated severe accidents,[a, b] much higher temperatures are possible. At these higher temperatures, plastic deformation is likely to be much more extensive than at normal reactor operating temperatures, and creep effects can no longer be neglected. Until recently there were no test data or validated models to predict the failure of flawed tubes at temperatures associated with postulated severe accidents. Therefore, the NRC has initiated a program at ANL to generate failure data on flawed and unflawed steam generator tubes at high temperatures. The purpose of these tests was to help develop predictive models for failure of steam generator tubes under given severe accident conditions. The tests were therefore carried out to failure under various pressure and temperature histories (not necessarily simulating any particular severe accident scenario) to provide a broad data base for developing such models. A creep rupture model for failure of the remaining ligament of a part-through crack has been developed and validated by tests on tubes containing axial flaws.

All of the analytical models discussed in this paper are applicable to steam generator tubes containing a single dominant crack. Although there has been some limited analytical and experimental studies of failure of tubes containing multiple cracks, the current practice generally applies the existing models to a single enveloping crack.

Low-Temperature Failure of Tubes

Axial cracks

The critical pressures and crack sizes for the unstable failure (rupture) of a thin-wall internally pressurized cylindrical shell with a single through-wall axial crack can be estimated with an equation originally proposed by Hahn et al.[1] and later modified by Erdogan: [2]

$$p_{cr} = \frac{\bar{\sigma}h}{mR_m} = \frac{p_b}{m}, \qquad (1a)$$

where:

$$\bar{\sigma} = \text{flow stress} = k(\sigma_y + \sigma_u) \quad (\text{with } k = 0.5 - 0.6), \qquad (1b)$$

[a] P. G. Ellison, L. W. Ward, C. Dobbe. S. A. Chavez, C. L. Atwood, C. L. Smith, L. M. Wolfram, J. L. Jones, L. N. Haney, and W. J. Reece, The Risk Significance of Induced Steam Generator Tube Rupture, INEL-95/0641, Rev. 1 (Draft), Lockheed Martin Idaho Technologies, Inc., Idaho National Engineering Laboratory, December 15, 1995.

[b] E. L. Fuller, M. A. Kenton, M. Epstein, R. E. Henry, and N. G. Cofie, Risks from Severe Accidents Involving Steam Generator Tube Leaks or Ruptures, EPRI TR-106194, Electric Power Research Institute, Palo Alto, CA (to be published).

σ_y and σ_u are the yield and ultimate tensile strengths, respectively, (1c)

$$m = 0.614 + 0.481\lambda + 0.386\exp(-1.25\lambda), \quad (1d)$$

$$\lambda = \left[12(1-\nu^2)\right]^{\frac{1}{4}} \frac{c}{\sqrt{R_m h}} = \frac{1.82c}{\sqrt{R_m h}}, \quad (1e)$$

$$p_b = \frac{\bar{\sigma} h}{R_m} = \text{burst pressure of an unflawed virgin tubing}, \quad (1f)$$

R_m and h = mean radius and wall thickness of tube, respectively, and (1g)

2c = axial crack length. (1h)

For a single part-through axial crack, the pressure required to fail the remaining ligament can be calculated with an empirical equation (referred to as the BCL equation) reported by Kiefner et al.[4]

$$p_{sc} = \frac{\bar{\sigma} h}{m_p R_m} = \frac{p_b}{m_p}, \quad (2a)$$

where:

$$m_p = \frac{1 - \frac{a}{mh}}{1 - \frac{a}{h}}, \text{ and} \quad (2b)$$

a = axial crack depth.

Under the auspices of an NRC-sponsored steam generator tube integrity program, the Pacific Northwest National Laboratory (PNNL) conducted a series of tests on tubes containing part–through axial notches. Based on these tests, PNNL[6] developed an empirical formula for the failure pressure of a tube containing a part–through axial crack. This formula, which was later validated by testing on specimens with stress corrosion cracks, is of the same form as Eq. 2a but where Eq. 2b is replaced by:

$$m_p = \left[1 - \frac{a}{h} + \frac{a}{h}\exp(-0.41\lambda)\right]^{-1}. \quad (3a)$$

Chavez et al.[7] reanalyzed the PNNL tube test data and proposed that the value of k in Eq. 1b should be taken as 0.5973 and that Eq. 3a should be modified (referred to as the INEL equation) to:

$$m_p = \left[1 - \frac{a}{h} + \frac{a}{h}\exp(-0.51\lambda)\right]^{-1}. \quad (3b)$$

As the crack depth approaches 100% of the wal thickness (i.e., a/h = 1), Eqs. 2a-2b predict that p_{sc} approaches 0, while Eqs. 3a and 3b do not predict that p_{sc} approaches 0, i.e., they predict higher pressure for ligament failure than do Eqs. 2a-2b for short, deep cracks. Eventually, Eqs. 3a-3b would become unconservative for very deep cracks. On the other hand, Eq. 2a tends to be overly conservative for short and deep cracks. Therefore Shack[a] has re-analyzed the PNNL tube test data and proposed that Eq. 2b be modified as follows (referred to as the ANL equation):

[a] W.J. Shack, Argonne National Laboratory, personal communication, 1996.

$$m_p = \frac{1-\alpha\frac{a}{mh}}{1-\frac{a}{h}}, \tag{2c}$$

where:

$$\alpha = 1+0.9\left(\frac{a}{h}\right)^2\left(1-\frac{1}{m}\right).$$

Except for short, deep cracks, Eq. 2c predicts similar failure pressures as in Eq. 2b.

Based on burst tests on tubes, Flesch and Cochet[5] recommended the use of Eqs. 2a-b for flaw depths greater than 85% of the wall thickness. However, in order to reduce the degree of conservativetism that was apparent from comparison with experimental results, they used σ_u instead of $\overline{\sigma}$. For predicting failure of the remaining ligament by plastic instability of tubes with flaw depths between 20% and 85% of wall thickness, they recommended replacing Eq. 2b by the following empirical equation (referred to as the EDF equation):

$$m_p = \left(1-\frac{\frac{c}{h}\frac{a}{h}}{1+\frac{c}{h}}\right)^{-1} \quad \text{for } 0.2 < a/h < 0.85, \tag{4a}$$

and

$$m_p = \frac{1-\frac{a}{mh}}{1-\frac{a}{h}}\frac{\overline{\sigma}}{\sigma_u} \quad \text{for } a/h > 0.85. \tag{4b}$$

It should be emphasized that Eq. 2a gives only the pressure required to fail the remaining ligament. The stability of the resulting through-wall crack can be analyzed using Eq. 1a. If $p_{cr} > p_{sc}$, the through-wall crack is stable. Although the crack will leak, it will not increase in length without a further increase in pressure. If $p_{cr} < p_{sc}$, the resulting crack will be unstable and will rapidly increase in length without any additional increase in pressure.

A comparison of the values of stress magnification factor m_p as computed by the various equations is shown in Figs. 1a-b. Note that although the values of m_p as computed by the various equations are within 20-30% of each other for a shallow crack (a/h = 0.5), they can differ by as much as a factor of 2 for deep (a/h = 0.9) and short cracks (≈ 0.25 in.). Failure tests on tubes containing deep cracks (to be discussed later) have shown that the m_p values are more in accordance with the ANL equation (Eq. 2c) than the BCL equation (Eq. 2b). To verify this analytically, detailed elastoplastic finite-element analyses were conducted for a 22-mm (7/8 in.)-diameter tube with a 25-mm (1 in.) long and 50% deep axial crack and a 6-mm (0.25 in.)-long and 90% deep axial crack subjected to rapidly increasing internal pressure at 300°C and 750°C. The stress-strain curves at these temperatures are shown in Fig. 2a. The results presented in Fig. 2b show that the maximum hoop stress magnification in the ligament for the shallower crack is independent of the stress-strain curve of the material. Further, the hoop stress magnification factor (defined as the ratio of the average hoop stress in the ligament and the average hoop stress in an unflawed tube) changes very little with internal pressure and its variation with crack depth is more in agreement with the ANL equation than with the BCL equation.

Circumferential cracks

Failure loads for tubing with circumferential cracks can also be calculated by plastic limit load analyses described by Ranganath and Mehta,[8] which were based on earlier work by Kanninen et al.[9] For an unconstrained tube with a through-wall crack of angular length 2θ and no applied primary bending stress, the critical burst pressure is

$$p_{cr} = \frac{2\bar{\sigma}h}{R_m}\left(1 - \frac{\theta}{\pi} - \frac{2\beta}{\pi}\right), \tag{5a}$$

where

$$\beta = \sin^{-1}\left(\frac{\sin\theta}{2}\right) \tag{5b}$$

Limit load analyses have also been proposed for part–through cracks.[10-11]

Equation 5a is applicable to one extreme case where the tube is completely free to bend. In the opposite extreme case of total constraint against bending, a criterion based on maximum shear stress in the net section as proposed by Cochet et al.[12] can be used to calculate the instability limit pressure:

$$p_{cr} = \frac{2(\gamma^2 - 1)(\pi - \theta)\bar{\sigma}}{2\pi + (\pi - \theta)(\gamma^2 - 1)}, \tag{6a}$$

where:

$$\gamma = \frac{R_o}{R_i}. \tag{6b}$$

The following thin-shell, uniaxial approximation to Eq. 6a is often used for predicting failure of steam generator tubes that are fully constrained against bending:

$$p_{cr} = \frac{2\bar{\sigma}h}{R_m}\left(1 - \frac{\theta}{\pi}\right). \tag{6c}$$

In reality, the tube support plates offer a significant but not total restraint against bending, which tends to increase the failure pressure to somewhere between those predicted by Eqs. 5a and 6a (or 6c).

Hernalsteen[13] has developed a semiempirical approach to account for the stiffening effects of the tube support plate on the burst pressure of a steam generator tube containing a circumferential crack at the top of the tube sheet. By conducting a number of pressure tests of circumferentially flawed steam generator tube/tube sheet/tube support plate assembly and measuring the failure pressures p_{burst}, as well as the restraining loads (thus the bending moments M_{burst} at the tubesheet) at the tube support plate at burst, he developed an empirical correlation between the stress index K and the elastic rotational stiffness of the tube S, where

$$K = \frac{\left(\frac{M_{burst}}{\pi R_m^2 h} + \frac{p_{burst} R_m}{2h}\right)}{\bar{\sigma}} \tag{7a}$$

and

$$S = \frac{M}{EIy'}, \tag{7b}$$

where:

EI is the flexural stiffness of the tube, and

M and y' are the bending moment, and rotation at the tube sheet, respectively.

Based on this correlation, Hernalsteen determined the value of K from the value of S that corresponds to the steam generator tube configuration under consideration and computed the burst pressure from Eq. 7a. Typical values of K ranged from 0.6 for 2-3 m span to 0.9 for 3-4 cm span between the tube sheet and the tube support plate.

A series of elastoplastic finite-element analyses are being conducted at ANL to determine the effects of a lateral constraint on the burst pressure of a tube with a single through-wall circumferential crack. Initially, two tubes with 180° and 240° through-wall circumferential cracks were analyzed. A typical finite-element model and displacements for the free-bending case are shown in Figs. 3 a-b. Note that the beam bends almost like a rigid body about a hinge at the cracked section. Figure 4a shows the variations of the free-end displacements and the maximum rotation with the normalized burst pressure for a 180° and a 240° circumferential through-wall cracks. The displacement and rotation curves coincide, confirming that the displacement is of the rigid-body-rotation type. Both cracked tubes reach maximum pressures at a rotation of $\approx 10°$. This is in agreement with the experimental observation by Hernalsteen[13] that tubes appear to fail at a fixed rotation of the cracked section. Figure 4b shows a comparison between available burst pressure data reported by Cochet and Flesch[14] and predictions by the simple beam free-bending model (Eq. 5a) and finite-element analysis. The simple model underpredicts both the test burst pressures and the finite-element results slightly. Preliminary analysis of a transversely supported tube (to simulate the tube support plate) with a 240° crack showed that the maximum pressure capability is increased significantly over that of a free-bending tube (Fig. 5a). The critical pressure for a span of 0.67 m (26 in.) appears to be much closer to the fully constrained case than the free-bending case (Fig. 5b).

High-Temperature Failure of Tubes

The behavior of flawed steam generator tubing during severe accidents has recently been considered in a report by INEL[a] and in an EPRI report.[b] In both reports, the failure of unflawed tubing and other components such as the surge line nozzle was described in terms of creep damage failure. In contrast, both analyses assumed that failure of flawed (axial crack) steam generator tubing in severe accidents can be described in terms of the models described by Eqs. 1–3 by taking the flow stress to be a function of temperature. With this assumption, the failure pressure of a flawed tube depended only on the flaw geometry and temperature and was independent of the detailed time/temperature/pressure history.

Intuitively, failure would be expected to be controlled by flow stress if the temperature ramps are sufficiently rapid so that there is insufficient time for creep to influence the deformation or damage of the tube. At the other extreme, if the temperature ramps are sufficiently slow (in the limit, a constant temperature hold), failure should be controlled by creep processes. In loading histories at intermediate rates, the damage processes are more complex and difficult to analyze.

To better understand the behavior of steam generator tubing during severe accidents, the NRC has sponsored a series of tests at ANL to help develop and validate a model for predicting failure of both flawed and unflawed steam generator tubes under such accidents. Recent tests conducted at ANL have shown that pressure and temperature ramp rates have significant influences on the failure pressure (Fig. 6a) and failure temperature (Fig. 6b), respectively. Therefore, a creep rupture model

[a] P. G. Ellison, L. W. Ward, C. Dobbe. S. A. Chavez, C. L. Atwood, C. L. Smith, L. M. Wolfram, J. L. Jones, L. N. Haney, and W. J. Reece, The Risk Significance of Induced Steam Generator Tube Rupture, INEL-95/0641, Rev. 1 (Draft), Lockheed Martin Idaho Technologies, Inc., Idaho National Engineering Laboratory, December 15, 1995.

[b] E. L. Fuller, M. A. Kenton, M. Epstein, R. E. Henry, and N. G. Cofie, Risks from Severe Accidents Involving Steam Generator Tube Leaks or Ruptures, EPRI TR-106194, Electric Power Research Institute, Palo Alto, CA (to be published).

for predicting failure of flawed and unflawed tubes is developed in the present paper. Predictions based on this model for high-temperature tests conducted at ANL under a variety of loading histories are much more in agreement with test results than those based on the flow stress models. However, for completeness, the flow stress models are also discussed in this paper.

Consider a tube with a flaw subjected to a temperature history T(t) and nominal hoop stress history $\sigma(t)$. To analyze the behavior of a tube under such a general loading history, both the flow stress and the creep rupture models make the following assumptions:

(1) The failure time and temperature of a flawed tube are the same as those of an unflawed tube subjected to a nominal hoop stress history $m_p\sigma(t)$ and the same temperature history T(t).

(2) The values of the magnification factor m_p determined from burst tests of flawed tubes at low temperatures are also applicable at high temperatures.

These assumptions may be valid for certain classes of creep and plasticity problems.[15] They are not strictly valid for the problem considered here, but the test program at ANL has shown that they can provide a reasonable approximation.

Flow stress models

In flow stress models, it is assumed that, for any arbitrary history of hoop stress $\sigma(t)$ and temperature T(t), failure of the remaining ligament occurs at a temperature T and nominal hoop stress σ whenever the following failure equation is satisfied, independent of stress-temperature history:

$$\sigma = \frac{\overline{\sigma(T)}}{m_p}, \tag{8}$$

where:

$\overline{\sigma(T)}$ is the flow stress at temperature T, and

m_p is a model-dependent hoop stress magnification factor that accounts for the crack (see Eqs. 2-4).

Flow stresses (computed with k = 0.5) for Alloy 600 from various sources[6, 7, 17,18] are plotted in Fig. 7a. Most of these tests were conducted under stroke-control at a nominal strain rate of 34%/min. Note that although there may be a wide variation in flow stress at low temperatures, the product form variations in the flow stress diminish rapidly with increasing temperature. Therefore, the INEL flow stress curve, which covers the widest range of temperature, is used for failure predictions. In Fig 7b, results from isothermal pressure ramp tests at two ramp rates are used to define "effective" flow stresses which are compared with the flow stress curve based on the INEL tensile tests. The rate-dependence of the flow stress is evident, and as expected, higher ramp rate leads to higher flow stress. Conceptually, it is possible to include rate effects within the framework of a flow stress model by generalizing the constitutive equation so that the flow stress is a function of both strain rate and temperature. In fact, several such constitutive relations based on the so-called equation of state theory are currently available (for example, see Ref. 16). However, in addition to being quite complex, they are not easily amenable to the problem of predicting failure of steam generator tubes, particularly those that contain flaws and are subjected to typical temperature and pressure histories expected during a severe accident. In this paper, the term flow stress models is used exclusively to denote simple rate-independent flow stress models. Because of their success at low temperatures, they were used initially to determine if they would provide reasonable failure predictions for the high-temperature tests of interest.

Creep rupture model

Creep failure of a uniaxially loaded specimen under a varying stress and temperature history can be predicted by a relatively straightforward analysis[15] and is often based on a linear time-fraction damage rule (e.g., Code Case N 47 of the ASME Code, Section III), as follows:

$$\int_0^{t_f} \frac{dt}{t_R(T,\sigma)} = 1 \tag{9}$$

where:

t_R is the time to creep rupture for a uniaxial specimen under a stress σ and temperature T, both of which may be functions of time, and

t_f is the time to failure.

A rigorous analysis of flawed tubes under a similar loading would be very complex. Therefore, the creep failure model was extended to flawed tubing using the assumptions referred to earlier, i.e., it was assumed that failure can be predicted by

$$\int_0^{t_f} \frac{dt}{t_R(T,m_p\sigma)} = 1 \tag{10}$$

To apply the creep rupture model for predicting failure under postulated severe accident conditions, creep rupture properties (particularly at short lives) of Alloy 600 tubes in the hoop direction are needed. Available creep rupture data (uniaxial tests) from the literature were collected and the following Larson-Miller representation for the data was established[a]:

$$t_R = 10^{\frac{P_{lm}}{T} - 15} \tag{11a}$$

where:

T is in K and

the Larson-Miller parameter P_{lm} is defined in terms of the stress σ (in ksi) as follows:

$$P_{lm} = \begin{cases} 23.14 - 2.4\log_e(\sigma) \text{ for } \sigma \geq 5.7\,\text{ksi} \\ 24.18 - 3.0\log_e(\sigma) \text{ for } \sigma < 5.7\,\text{ksi} \end{cases} \tag{11b}$$

To establish the applicability of Eqs. 11a-b to our tubing material, constant-pressure creep-rupture tests were conducted on unflawed 22-mm (7/8-in.)-dia. tubes using both isothermal and constant temperature ramp loading. The experimental results are plotted in Fig. 8 against predicted times to failure, using Eqs. 11a-b. In all cases, the predicted times to failure are well within a factor of 2 (which is typical of the scatter in the uniaxial creep rupture data) of the experimental failure times, thus indicating that the above Larson-Miller representation of the data is adequate for our material.

Validation tests for the creep rupture model

To validate the creep rupture model, several types of tests were conducted on both flawed and unflawed steam generator tubes. The tests were conducted in a single zone furnace using programmable temperature and high pressure nitrogen gas to apply internal pressures on the tubes. A temperature profile measured transiently as well as steady state showed a maximum of 5°C axial variation within a central 50 mm (2 in) section with the center being the hottest. The maximum through thickness temperature gradient was less than 1°C. Tests were conducted on both unflawed and flawed tubing. The flaws were created

[a] W.J. Shack, Argonne National Laboratory, personal communication, 1996.

in the specimens using electro–discharge machining (EDM). Such notches are not as sharp as real cracks, but previous tests at lower temperatures have shown that there is very little effect of crack tip geometry on the failure loads.[6] At higher temperature the effect of the crack tip geometry would be expected to be of even less significance.

Isothermal failure tests

First, tests were conducted on flawed tubing by subjecting them to isothermal constant pressure loading. A summary of all the tests conducted to date together with the failure times predicted by the creep rupture model are given in Table 1. The predicted failure times using four different values of m_p are plotted against the experimental failure times in Fig. 9a for tubes containing $a \approx 60\%$ deep, 25-mm (1 in.)-long crack. In addition to the diagonal perfect prediction line, Fig. 9a also shows differences of factor of 2 (which is typical of the scatter in the uniaxial creep rupture data) between the predicted and the observed times to failure by means of two additional lines. Except for a test at 667°C, the predicted failure times by the ANL m_p (Eq. 2c) are within a factor of 2 of the experimental failure times of the specimens. The predicted lives using m_p values as determined by the BCL (Eq. 2b) and EDF (Eq. 4a) equations are also reasonable, but those by the INEL equation (Eq.3b) underpredict the lives by more than a factor of 2 in most cases. It should be noted that the flow stress model is incapable of predicting time to failure for tests of this type and, in fact, would predict that none of the tubes should have failed.

Failure tests of specimens with deep cracks

There is some experimental evidence[5] that the numerical values of m_p computed by the BCL equation for short and deep cracks are too high for tests conducted at low temperatures where a flow stress model is valid. Results from tests, summarized in Table 2 and shown in Fig. 9b, confirm that this is also true at high temperatures. All the test specimens referred in this figure had ≥90% deep cracks. Note that the BCL equation grossly overestimates the damaging influence (i.e., underestimates the time to failure) of these cracks. The INEL and ANL equations do account for the less damaging influence of the deeper cracks than of the shallower cracks. Predictions by the EDF equation are not shown in Fig. 9b because at high temperatures, they are essentially the same as those by the BCL equation. At low temperatures the EDF model[5] predicts a smaller m_p for cracks that are more than 85% deep than the BCL model because the flow stress in the BCL equation is replaced by the ultimate tensile strength in the EDF equation (see Eq. 4b). However, there is little difference between the flow stress and the ultimate tensile strength at high temperatures because strain hardening is greatly reduced. Consequently, the EDF equation fails to account for the less damaging influence of deep cracks at high temperatures. Overall, the ANL correlation for m_p (Eq. 2c) gives the best predictions for failure times of specimens with shallow as well as deep cracks and is used for predicting failure of the rest of the high-temperature tests.

Pressure and temperature ramp tests

To evaluate the importance of loading rates on the failure conditions and compare the predictive capabilities of the creep rupture model and the flow stress model, two additional types of tests were conducted. In the first type, the specimens were heated to a temperature and then pressurized isothermally at a constant pressure ramp until failure. In the second type, the specimens were first pressurized at low temperature and then, with the pressure held constant, they were subjected to a constant temperature ramp until failure. A summary of all the tests of these types conducted to date together with the failure pressures and temperatures predicted by the creep rupture model are given in Tables 3-4. Results from both types of tests, plotted in Figs 6a and 6b, show that the loading rate (pressure or temperature), which is ignored in a simple flow stress model, has a significant influence even on the failure conditions of unflawed tubes. Note that the experimental results are closer to predictions of the creep rupture model than those of the flow stress model in all cases. For the tests at higher pressure ramp rate, the creep rupture model overestimates the failure pressures by a maximum of 25% whereas the flow stress model underestimates the failure pressures by as much as 50%. The failure temperatures for the temperature ramp tests are predicted almost exactly by the creep rupture model whereas the flow stress model can either underestimate or overstimate

the failure temperatures by 70°C. Fig 7b shows results from pressure ramp tests on flawed and unflawed tubes, clearly indicating that although the flow stress model would predict the failure pressures reasonably well for the lower ramp rate tests, it would underestimate the failure pressures at ≥ 800°C by almost a factor of 2 for the higher ramp rate tests if the INEL flow stress curve were used. The failure pressures are much closer to those predicted by the creep rupture model, see Fig. 10a. The pressures in the temperature ramp tests on flawed specimens were selected such that the product of m_p and the nominal hoop stresses were approximately equal for two crack geometries. Thus, the predicted failure temperatures for both geometries fall approximately on a single line for either the creep rupture or flow stress models, as shown in Fig. 10b. The experimental results are in much better agreement with the predictions of the creep rupture model and confirm that the effect of flaws on failure can be characterized by the m_p approach.

Failure tests for evaluating postulated severe accident time-temperature histories

Tests were performed at ANL to determine the behavior of flawed tubes under time/temperature histories that could be used to evaluate the failure of steam generator tubes under postulated severe accident conditions. An additional purpose of the tests was to provide further validation of the appropriate model to support its use to determine the time to failure of flawed tubes under time/temperature histories that could reach temperatures as high as 850°C.

In all the tests under this category, the internal pressure was held constant at 16 MPa (2.35 ksi). Tests were conducted on both 19 mm (3/4 in) and 22 mm (7/8 in) outer diameter tubes with wall thicknesses 1 mm (0.043 in) and 1.3 mm (0.050 in), respectively. Four different nominal flaw geometries with axial lengths 6 mm (0.25 in) , 25 mm (1 in.), and 50 mm (2 in) and depths varying from 20% to 65% of thickness were tested. The actual flaw depths were determined by fractography after the tests. In many cases, they were also measured prior to the tests by a replica technique. The differences between the two measurements, when available, were not large. Duplicate tests were run for all the 22 mm (7/8 in) diameter tube tests.

For the tests to date, two time/temperature histories have been considered. Both are based on preliminary analyses of an accident sequence involving total station blackout with a stuck-open steam generator secondary-side atmospheric dump valve, resulting in loss of feedwater and secondary-side depressurization. One, which is referred to as the "INEL ramp", is based on a preliminary analyses by INEL[a] and the other, referred to as the "EPRI ramp", is based on a preliminary analysis reported by EPRI[b]. The time-temperature scenarios calculated by INEL[a] and EPRI[b] for some postulated severe accident sequences are shown in Figs. 11a and 11b, respectively, which also show the time-temperature histories used in the ANL tests. In both series of tests the specimens were first heated rapidly to 300°C, equilibrated at 300°C, and then subjected to the test ramps. Both analyses also predict depressurization of the system due to the failure of the surge line. Because the primary purpose of our tests was to help develop a failure model, the tests have ignored the predicted depressurization. The EPRI analysis also predicts a reduction in temperature following a short 5 min. hold at 667°C. To increase the contribution of creep damage in the tests, the "EPRI" temperature history was arbitrarily modified to include a 2 h holdtime at 667°C and ignored the predicted reduction of temperature after the hold. If the specimen did not fail in 2 hours of constant temperature hold, it was subjected to a temperature ramp of 2°C/min. until failure. Neither ramp chosen for the tests was intended to be an accurate representation of a particular sequence, but together they can represent a range of histories for which a failure model would be needed. Thus, although the INEL and EPRI analyses predict that failure of the surge line nozzle and consequent depressurization of the system will occur prior to the failure of the steam generator tubes, the tests at ANL were continued with full pressure until failure occurred.

A summary of all the tests conducted to date together with the failure temperatures predicted by the creep rupture model are given in Tables 5 and 6. The experimental temperatures and times (above 300°C) to failure are compared with predicted

[a] P. G. Ellison, L. W. Ward, C. Dobbe. S. A. Chavez, C. L. Atwood, C. L. Smith, L. M. Wolfram, J. L. Jones, L. N. Haney, and W. J. Reece, The Risk Significance of Induced Steam Generator Tube Rupture, INEL-95/0641, Rev. 1 (Draft), Lockheed Martin Idaho Technologies, Inc., Idaho National Engineering Laboratory, December 15, 1995.

[b] E. L. Fuller, M. A. Kenton, M. Epstein, R. E. Henry, and N. G. Cofie, Risks from Severe Accidents Involving Steam Generator Tube Leaks or Ruptures, EPRI TR-106194, Electric Power Research Institute, Palo Alto, CA (to be published).

failure temperatures and times in Figs. 12a and 12b, respectively. The predicted values were calculated with the creep rupture model by using the Larson-Miller parameter, Eq. 11a-b, and the stress magnification factor (Eq. 2c). In most cases, predicted times (above 300°C) and temperatures are quite close to the experimentally observed values.

Similar comparisons for the flow stress model predictions are shown in Figs. 13 a-b. The predicted values were calculated with the INEL flow stress curve (Fig. 7a) and the stress magnification factor (Eq. 2c). Note that the failure temperatures and times (above 300°C) for the tests using the INEL ramp were underpredicted significantly. The accurate prediction of the EPRI ramp tests was probably a fortuitous consequence of the average strain rates in the ligament being close to the strain rate used in the tensile tests from which the flow stress curve was derived.

It is evident that the creep rupture model not only provides more accurate predictions of the failure loadings than the flow stress models but also accounts for loading rate effects. Therefore, the creep rupture model can be expected to predict failure under varying temperature and pressure histories during postulated severe accidents more reliably than a simple rate-independent flow stress model.

Conclusions

Available flow stress models for predicting failure of flawed steam generator tubing under normal operating conditions and design basis accidents have been reviewed. All the models predict similar failure pressure for shallow axial cracks, but give significantly different failure pressures when the cracks are deep. A new correlation developed under this study using the PNNL data from earlier studies appears to correlate data for all flaw depths better than the existing ones. The new correlation is supported by detailed finite-element analysis.

The failure pressure for tubes containing unsymmetrical circumferential cracks has recently been observed experimentally to increase in the presence of lateral constraint. Detailed finite-element analyses show that such behavior is to be expected and that a tube support plate spacing of 0.65 m (26 in.) or less should increase the failure pressure to almost that of a fully constrained tube.

Tests conducted on unflawed and flawed specimens at the high temperatures postulated for severe accidents show that the failure pressure at a constant temperature is dependent on the pressure ramp rate and that the failure temperature at a constant pressure is dependent on the temperature ramp rate. While rate-independent flow stress model cannot predict such a behavior, the creep rupture model developed under this study can do so.

The creep rupture model has been validated with failure tests on flawed specimens under a variety of loading histories. While the flow stress model is incapable of predicting the time to failure of flawed specimen under isothermal, constant pressure loading, the creep rupture model can do so. Finally, the creep rupture model can predict failure times and temperatures of both flawed and unflawed tubes subjected to varying temperature and pressure histories more accurately than the flow stress models.

Acknowledgment

The author would like to acknowledge helpful discussions with Drs. W. J. Shack and D. R. Diercks of Argonne National Laboratory and Dr. J. Muscara of the U. S. Nuclear Regulatory Commission. Thanks are also due to Messrs. J. Franklin and L. Knoblich for conducting the high-temperature failure tests and to Mr. K. Mruk for providing the measured crack parameters. This work was supported by the Office of Nuclear Regulatory Research, U.S.Nuclear Regulatory Commission.

References

1. G. T. Hahn, M. Sarrate, and A. R. Rosenfield, "Criteria for crack extension in cylindrical pressure vessels," *Int. J. Fracture Mech.*, Vol. **5**, No. 3, 1969.

2. F. Erdogan, "Ductile failure theories for pressurized pipes and containers," *Int. J. of Pres. Ves. & Piping*, Vol. **4**, 1976.

3. R. J. Eiber, W. A. Maxey, A. R. Duffy, and T. J. Atterbury, "Investigation of the Initiation and Extent of Ductile Pipe Rupture," BMI–1908, Battelle Memorial Institute, June 1971.

4. J. F. Kiefner, W. A. Maxey, R. J. Eiber, and A. R. Duffy, "Failure stress levels of flaws in pressurized cylinders," in *Progress in Flaw Growth and Fracture Toughness Testing*, Kaufman, J. G., Natil. Symp. on Fracture Mechanics (6th : 1972 : Philadelphia), American Society for Testing and Materials, Committee E–24 on Fracture Testing of Metals, American Society for Testing and Materials, ASTM Special Technical Publication 536, Philadelphia, 1973.

5. B. Flesch and B. Cochet, "Crack stability criteria in steam generator tubes," *Int. Cong. on Pressure Vessel Technology*, Beijing, Sept. 1988.

6. R. J. Kurtz, R. A. Clark, L. R. Bradley, W. M. Bowen, P. G. Doctor, R. H. Ferris, and F. A. Simonen, *Steam Generator Tube Integrity Program/Steam Generator Group Project, Final Project Summary Report,* NUREG/CR–5117, PNNL, Richland, WA, May 1990.

7. S. A. Chavez, C. L. Atwood, P. G. Ellison, and J. L. Jones, "Estimating structural failure frequency of degraded steam generator tubes," Submitted to ASME.

8. S. Ranganath and H. S. Mehta, "Engineering Methods for the Assessment of Ductile Fracture Margin in Nuclear Power Plant Piping," Elastic Plastic Fracture 2nd Symp., Vol. 2, Fracture Resistance Curves and Engineering Applications, American Society for Testing and Materials, ASTM Special Technical Publication 803, Philadelphia, 1983.

9. M. F., Kanninen, A. Zahoor, G. M. Wilkowski, I. Abou–Sayed, C. Marschall, D. Broek, S. Sampath, C. Rhee, and J. Ahmad, "Instability Predictions for Circumferentially Cracked Type 304 Stainless Steel Pipes under Dynamic Loading," EPRI NP–2347 (Vol.1: Summary; Vol. 2: Appendices), Electric Power Research Institute, Palo Alto, CA, April 1982.

10. K. Hasegawa, T. Shimizu, and S. Shida, Consideration of Allowable Flaw Size for Pressurized Pipes, *Nucl. Eng. and Design*, Vol. 87, 1985.

11. R. Kurihara, S. Ueda, and D. Sturm, Estimation of the Ductile Unstable Fracture of Pipe with a Circumferential Surface Crack Subjected to Bending, *Nucl. Eng. and Design*, Vol. 106, 1988.

12. B. Cochet, J. Engstrom, and B. Flesch, "PWR steam generator tube and tube support plate plugging criteria," Paper 4.1, *Steam generator tubes mechanical, LBRB, and probabilistic studies*, EDF, France, 1990.

13. P. Hernalsteen, "Structural and Leakage Integrity of Tubes Affected by Circumferential Cracking," presented at NEA/CNRA/CSNI Int. Workshop on Steam Generator Integrity in Nuclear Power Plants, Oak Brook, IL, Oct. 30-Nov. 2, 1995.

14. B. Cochet and B. Flesch, "Application of the leak before break concept to steam generator tubes," SMIRT–9, Vol. D, Lausanne, Switzerland, 1987.

15. I. Finnie and W. R. Heller, *Creep of Engineering Materials,* New York, McGraw-Hill, 1959.

16. E. W. Hart, "A phenomenological theory for plastic deformation of polycrystalline metals," Acta Met., Vol. 18, 1970.

17. J. L. Rempe, S. A. Chavez, G. L. Thinnes, C. M. Allison, G. E. Korth, R. J. Witt, J. J. Sienicki, S. K. Wang, L.A. Stickler, C. H. Heath, and S. D. Snow, *"Light Water Reactor Lower Head Failure Analysis,"* NUREG/CR-5642, EGG-2618, I.N.E.L, Idaho Falls, ID, Oct., 1993.

18. International Nickel Co., "Engineering Properties of Inconel Alloy 600," Tech. Bull. T-7, 1964.

Table 1 *Constant-pressure rupture tests at various temperatures on specimens with and without flaws to validate m_p approach. Also shown are the predicted failure times by the ANL creep rupture model.*

Test	Crack Geometry			Loading History		Failure Conditions			
No.	2c (in.)	a/h	m_p	T	p	T_f	p_f	t_f	Pred. t_f
T-37	1	0.59	1.96	Ramp to 667°C and hold	Constant 2350 psi	667°C	2350 psi	336 min.	128 min.
T-56[a]	1	0.65	2.21	Ramp to 667°C and hold	Constant 2350 psi	667°C	2350 psi	74 min.	62 min.
T-38	1	0.62	2.07	Ramp to 700°C and hold	Constant 1915 psi	700°C	1915 psi	28 min.	88 min.
T-41	Unflawed		1	Ramp to 700°C and hold	Constant 4500 psi	700°C	4500 psi[b]	38 min.	42 min.
T-61[c]	Unflawed		1	Ramp to 700°C and hold	Constant 4450 psi	700°C	4450 psi	49 min.	45 min.
T-47	1	0.55	1.82	Ramp to 750°C and hold	Constant 1400 psi	750°C	1400 psi	186 min.	176 min.
T-60	Unflawed		1	Ramp to 750°C and hold	Constant 3290 psi	750°C	3290 psi	29 min.	43 min.
T-48	1	0.55	1.82	Ramp to 800°C and hold	Constant 1400 psi	800°C	1400 psi	26 min.	32 min.
T-42	Unflawed		1	Ramp to 800°C and hold	Constant 2350 psi	800°C	2350 psi	33 min.	50 min.

[a] Duplicate of test listed immediately above.

[b] Pressure decreased gradually from 4750 psi to 4250 psi during hold.

[c] Duplicate of test listed immediately above, but with pressure held constant at 4450 psi during hold.

Table 2 *Constant-pressure failure tests with deep cracks to validate the new m_p correlation proposed by ANL. Also shown are the predicted failure times by the ANL creep rupture model.*

Test	Crack Geometry			Loading History		Failure Conditions			
No.	2c (in.)	a/h	m_p	T	p	T_f	p_f	t_f	Pred. t_f
T-55	0.25	0.91	2.45	Ramp in 1h to 800°C, then pressurize and hold	Constant 750 psi	800°C	750 psi	420 min.	180 min.
T-78[a]	0.25	0.92	2.61	Ramp to 800°C and hold	Constant 750 psi	800°C	750 psi	246 min.	130 min.
T-83	Unflawed		1	Ramp to 800°C and hold	Constant 1800 psi	800°C	1800	228 min.	202 min.
T-72	1	0.92	7.62	Ramp to 800°C and hold	Constant 356 psi	800°C	356 psi	19 min.	23 min.
T-84	1	0.91	6.85	Ramp to 800°C and hold	Constant 450 psi	800°C	450 psi	2 min	18 min.
T-87	Unflawed		1	Ramp to 800°C and hold	Constant 2910 psi	800°C	2910 psi	12 min.	15 min.
T-66	2	0.90	7.83	Ramp to 800°C and hold	Constant 300 psi	800°C	300 psi	23 min.	15 min.
T-85	Unflawed		1	Ramp to 800°C and hold	Constant 3000 psi	800°C	3000 psi	10 min.	13 min.

[a] Duplicate of test listed immediately above.

Table 3 *Constant-pressure temperature ramp tests to validate creep rupture model. Also shown are the predicted failure temperatures by the ANL creep rupture model.*

Test	Crack Geometry			Loading History		Failure Conditions	
No.	2c (in.)	a/h	m_p	T	p	T_f	Pred. T_f
T-62	Unflawed		1	Ramp to 600°C in 1 h, then 20°C/min	Constant 2350 psi	913°C	916°C
T-63	Unflawed		1	Ramp at 2°C/min	Constant 2350 psi	843°C	838°C
T-71	Unflawed		1	Ramp at 0.2°C/min	Constant 2350 psi	779°C	770°C
T-67	1	0.65	2.21	Ramp at 20°C/min	Constant 1065 psi	892°C	916°C
T-68	1	0.65	2.21	Ramp at 0.2°C/min	Constant 1065 psi	770°C	778°C
T-74	1	0.93	8.60	Ramp at 0.2°C/min	Constant 270 psi	860°C	918°C
T-73	1	0.93	8.60	Ramp at 0.2°C/min	Constant 1065 psi	612°C	604°C
T-76	0.25	0.89	2.22	Ramp at 20°C/min	Constant 1090 psi	915°C	911°C
T-77	0.25	0.9	2.32	Ramp at 0.2°C/min	Constant 1040 psi	778°C	766°C
T-59	2	0.79	3.93	Ramp at 2°C/min	Constant 750 psi	810°C	801°C
T-79	2	0.92	9.68	Ramp at 0.2°C/min	Constant 245 psi	815°C	914°C
T-80[a]	2	0.92	9.68	Ramp at 0.2°C/min	Constant 245 psi	859°C	914°C
T-81	2	0.93	10.99	Ramp at 0.2°C/min	Constant 217 psi	678°C	768°C

[a] Duplicate of test listed immediately above.

Table 4 *Isothermal pressure ramp tests to establish the maximum flow stress curve. Also shown are the predicted failure pressures and times by the ANL creep rupture model.*

Test	Crack Geometry			Loading History		Failure Conditions			
No.	2c (in.)	a/h	m_p	T	p	p_f	t_f	Pred. p_f	Pred. t_f
T-35	Unflawed		1	840°C (isothermal)	Ramped at 2300 psi/min. to 3000 psi and hold	3000 psi	3.3 min.	3000 psi	5.8 min.
T-36	Unflawed		1	840°C (isothermal)	Ramped at 2300 psi/min. to 4000 psi and hold	4000 psi	1.8 min.	4000 psi	2.8 min.
T-46	Unflawed		1	840°C (isothermal)	Ramped at 2300 psi/min	4190 psi	1.8 min.	4987 psi	2.2 min.
T-45	Unflawed		1	840°C (isothermal)	Ramped at 230 psi/min	3090 psi	13 min.	3390 psi	15 min.
T-86	Unflawed		1	800°C (isothermal)	Ramped at 230 psi/min	3730 psi	16 min.	4115 psi	18 min.
T-82	Unflawed		1	800°C (isothermal)	Ramped at 2300 psi/min to 4800 psi and hold	4800 psi	2.2 min.	4800 psi	3.4 min.
T-57	0.25	0.75	1.58	800°C (isothermal)	Ramped at 2300 psi/min	3520 psi	1.5 min.	3520 psi	1.8 min.
T-58	1	0.79	3.32	800°C (isothermal)	Ramped at 2300 psi/min	1590 psi	0.7 min.	2194 psi	0.9 min.
T-70	1	0.65	2.21	840°C (isothermal)	Ramped at 2300 psi/min	2250 psi	1.0 min.	2570 psi	1.1 min.
T-69	1	0.65	2.21	800°C (isothermal)	Ramped at 2300 psi/min	2740 psi	1.2 min.	3020 psi	1.3 min.
T-75	1	0.65	2.21	700°C (isothermal)	Ramped at 2300 psi/min	3370 psi	1.5 min.	4860 psi	2.1 min.

Table 5 *Flaw sizes and temperatures at failure for INEL ramp tests. Also shown are the predicted failure temperatures by the ANL creep rupture model.*

	3/4 in. diameter tube				7/8 in. diameter tube			
2c (in.)	Test No.	a/h	T_f	Pred. T_f	Test No.	a/h	T_f	Pred. T_f
Unflawed	T-2	Unflawed	823°C	837°C	T-10	Unflawed	835°C	844°C
Unflawed	T-13	Unflawed	826°C	837°C	T-30	Unflawed	843°C	844°C
0.25	T-12	0.59	798°C	806°C	T-7	0.65	803°C	806°C
0.25	-	-	-	-	T-34	0.62	802°C	809°C
1	T-11	0.61	758°C	752°C	T-9	0.54	768°C	784°C
1	-	-	-	-	T-33	0.54	778°C	792°C
2	T-3	0.45	774°C	788°C	T-6	0.36	808°C	805°C
2	T-14	0.35	805°C	803°C	T-32	0.41	800°C	803°C
2	T-4	0.2	808°C	816°C	T-5	0.16	825°C	824°C
2	-	-	-	-	T-31	0.22	817°C	818°C

Table 6 *Flaw sizes and temperatures at failure for EPRI ramp tests. Also shown are the predicted failure temperatures by the ANL creep rupture model.*

	3/4 in. diameter tube				7/8 in. diameter tube			
2c (in.)	Test No.	a/h	T_f	Pred. T_f	Test No.	a/h	T_f	Pred. T_f
Unflawed	T-22	Unflawed	828°C	833°C	T-19	Unflawed	839°C	842°C
Unflawed	-	-	-	-	T-28	Unflawed	843°C	842°C
0.25	T-23	0.57	767°C	772°C	T-18	0.66	779°C	786°C
0.25		-	-	-	T-24	0.66	781°C	782°C
1	T-29	0.54	726°C	702°C	T-16	0.57	724°C	692°C
1	-	-	-	-	T-27	0.55	724°C	727°C
2	T-21	0.40	760°C	745°C	T-15	0.30	794°C	786°C
2	-	-	-	-	T-26	0.41	770°C	762°C
2	T-20	0.12	814°C	814°C	T-17	0.20	816°C	802°C
2	-	-	-	-	T-25	0.21	817°C	811°C

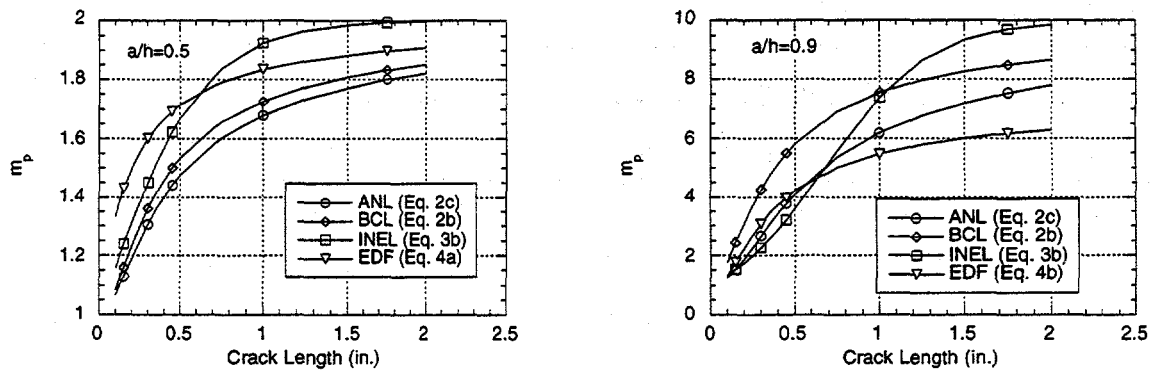

(a) (b)

Fig. 1 *Magnification factor m_p as computed by BCL (Kiefner et al.) equation (Eq. 2b), ANL (Shack) equation (Eq. 2c), INEL (Chavez et al.) equation (Eq. 3b), and the EDF (Flesch and Cochet) equation (Eqs. 4a-b) as a function of crack length for crack depth-to-thickness ratios (a) a/h=0.5 and (b) a/h=0.9.*

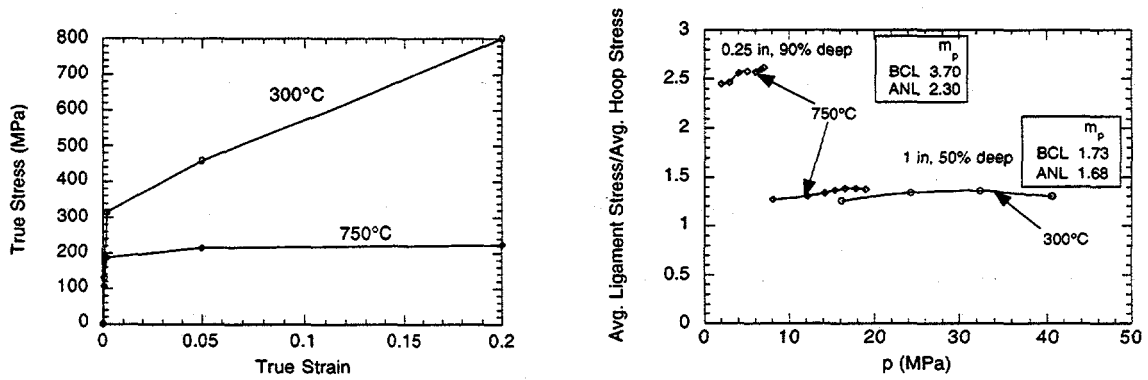

(a) (b)

Fig. 2 *(a) True stress-strain curve used in finite-element analysis and (b) variation of calculated hoop stress enhancement factor in the ligament with pressure for a 22 mm (7/8 in.) dia. tube with two axial part-through crack geometries at 300 and 750°C.*

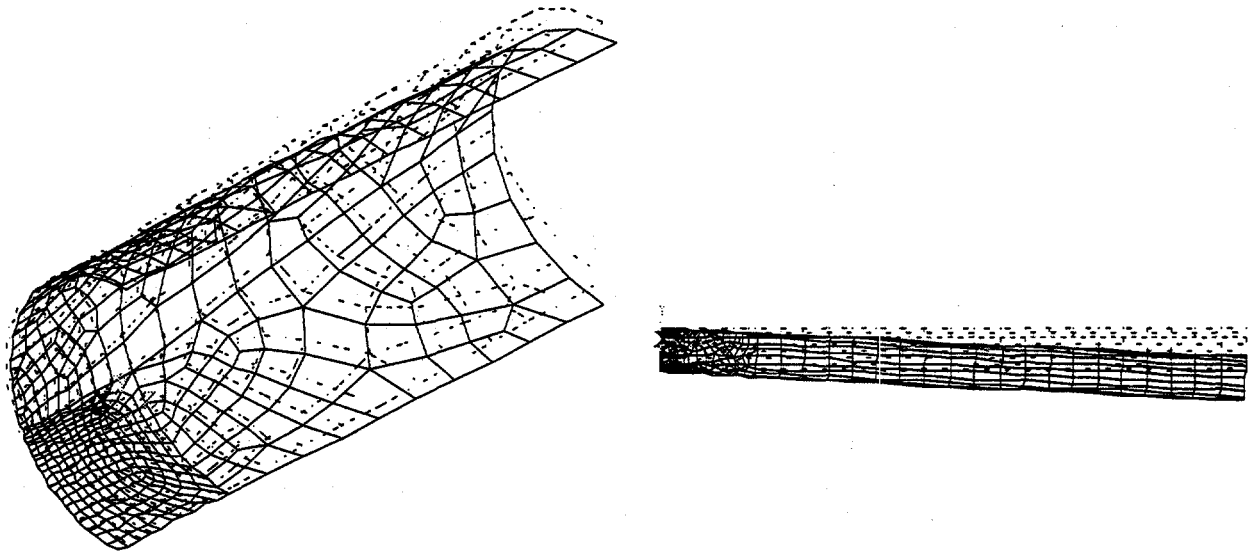

(a) (b)

Fig. 3 *(a) Typical near-tip finite-element model for tube with a through wall circumferential crack; (b) typical displaced shape of tube for free-bending case.*

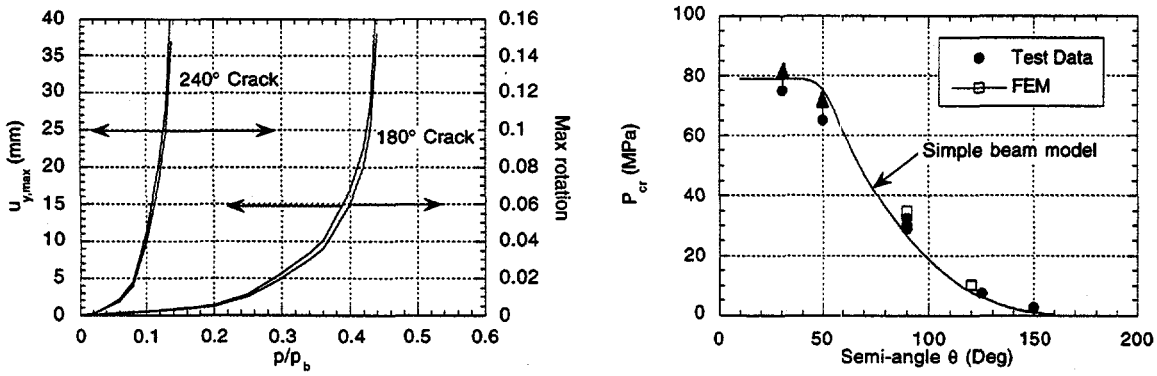

(a) (b)

Fig. 4 *(a) Variations of free end displacements and maximum rotations with normalized burst pressure for tubes with 240° and 180° through-wall circumferential cracks. (b) Comparison of experimental burst pressure data with predicted burst pressures using a simplified beam model and finite-element method.*

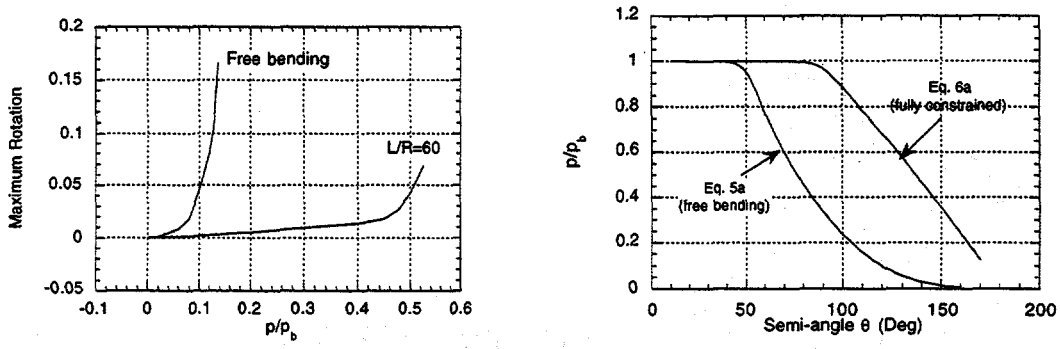

Fig. 5 *(a) Maximum rotation of section of 22 mm (7/8 in.) dia. tube containing a 240° circumferential crack when free to bend and when supported laterally at a span of 0.67 m (26 in.) and (b) variation of critical burst pressure with semi-angle of crack for free-bending and fully constrained cases.*

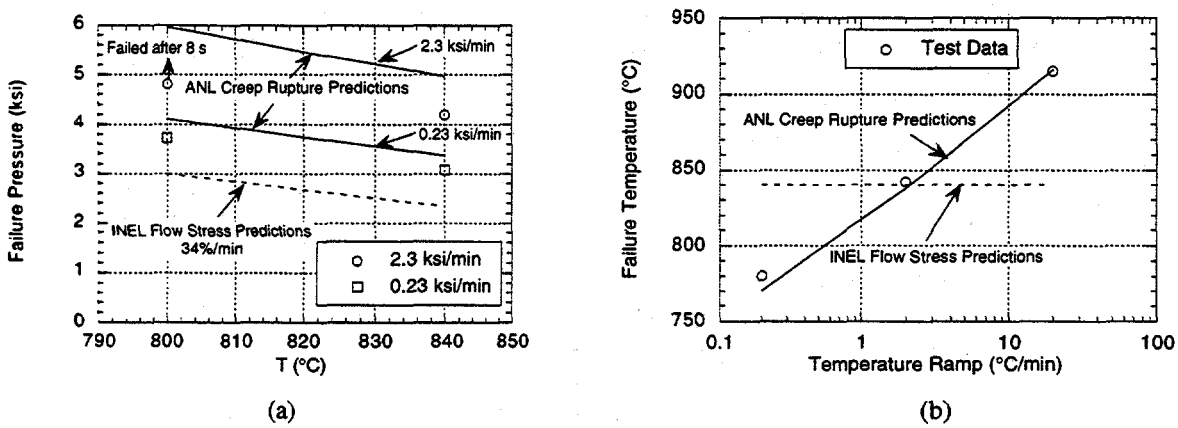

Fig.6 *Effects of (a) loading rate on failure pressure in isothermal burst test and (b) temperature ramp on failure temperature in burst test at a constant pressure of 16 MPa (2.35 ksi) of unflawed 22 mm (7/8 in.) dia. Inco 600 tube. Also shown are predicted failure pressures and temperatures by flow stress model (dashed lines) using INELflow stress curve and by ANL creep rupture model (solid lines).*

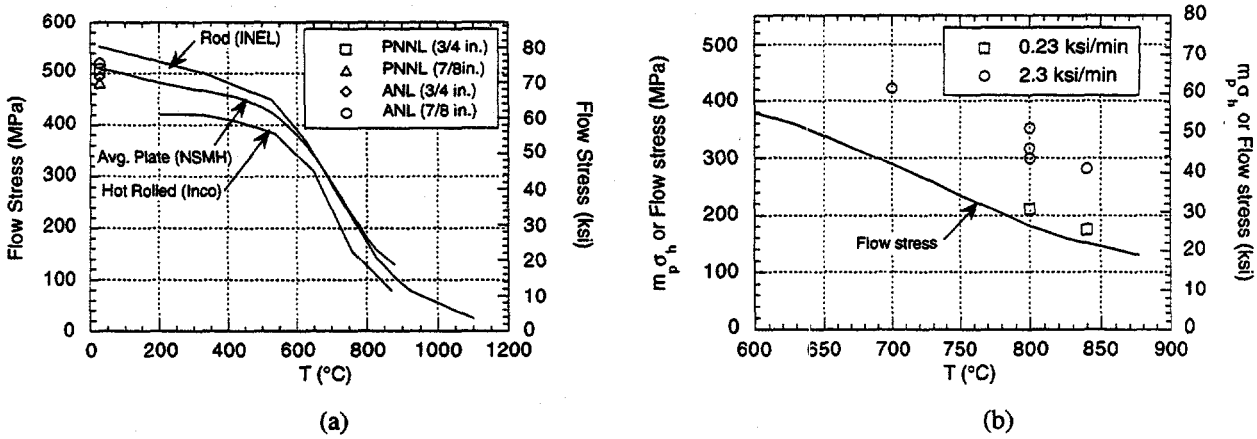

Fig. 7 *(a) Flow stress for various product forms of Inco 600 as a function of temperature. (b) Comparison of flow stress curve with those obtained experimentally by pressure ramp tests on flawed and unflawed tubes.*

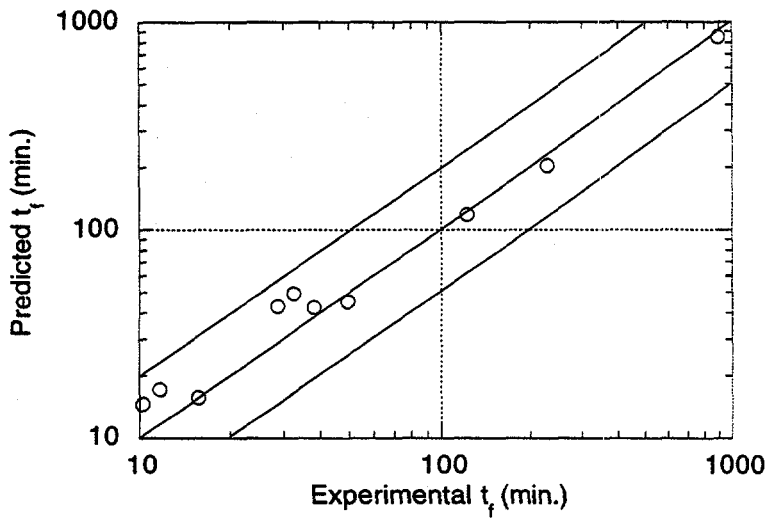

Fig. 8 *Comparison of experimental and predicted times to failure of unflawed Inco 600 tubing under constant internal pressure. Tests were conducted isothermally and under constant temperature ramps of 0.2°C/min., 2°C/min., and 20°C/min.*

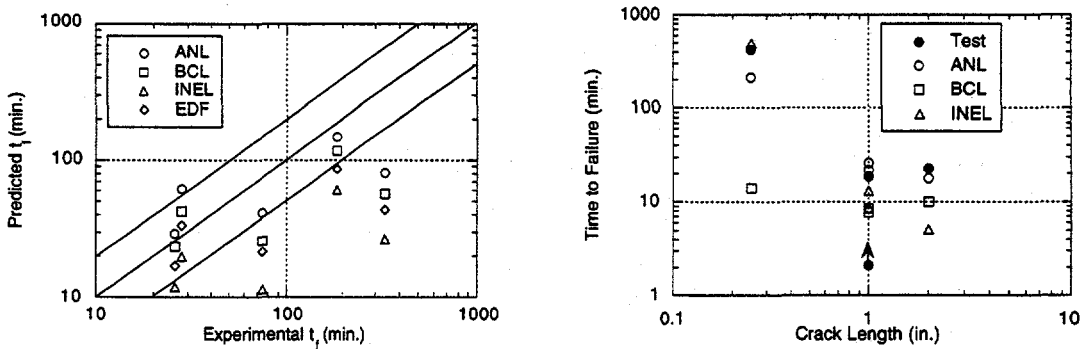

Fig. 9 *Comparison of experimental and predicted times to failure of flawed Inco 600 tubing tested isothermally under constant internal pressure, for (a) shallow flaws of length of 25 mm (1 in.) and depths ranging from 56% to 65% and at temperatures between 667°C and 800°C and (b) deep flaws with depths between 90% and 92% at a temperature of 800°C. Arrow indicates pin hole failure in which pressure was undiminished after failure, but the test was interrupted.*

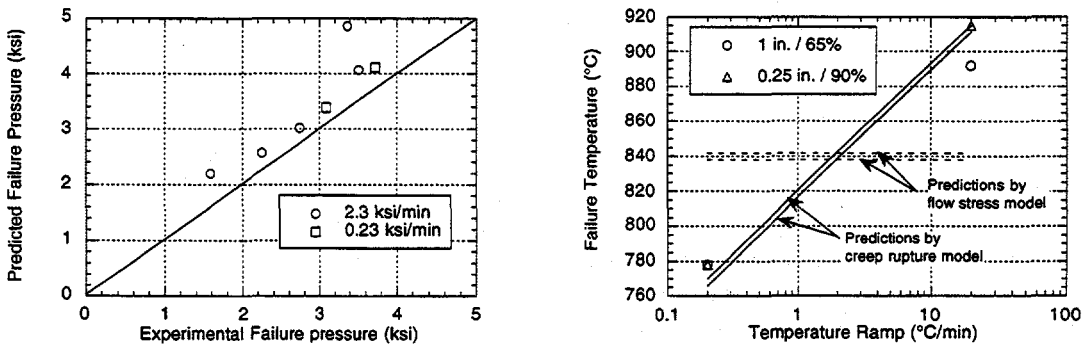

Fig. 10 *Comparison of experimental and predicted (a) failure pressures of flawed and unflawed tubes subjected to two pressure ramps isothermally at 700 - 840°C and (b) failure temperatures of flawed tubes subjected to two temperature ramps with constant internal pressures chosen such that the product of m_p and nominal hoop stress were kept approximately constant.*

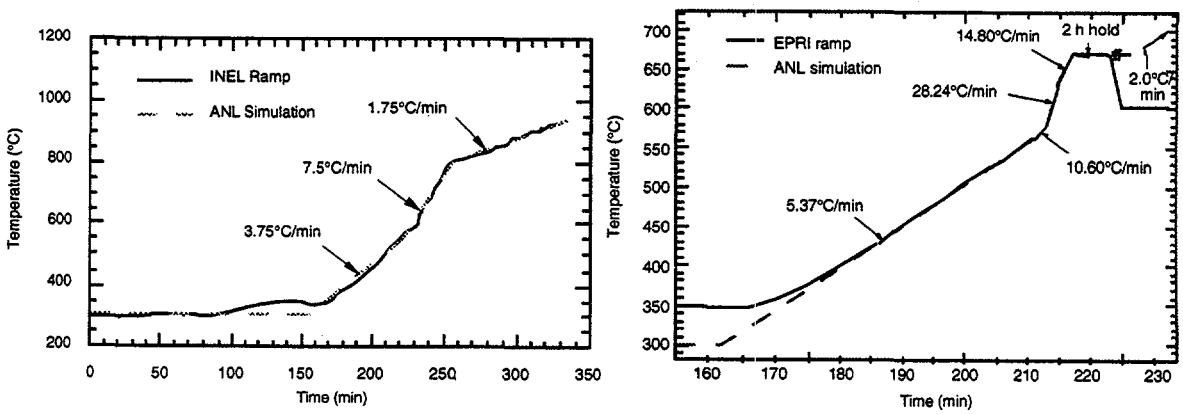

Fig. 11 Calculated and ANL simulation of (a) INEL ramp and (b) EPRI ramp for high-temperature tests.

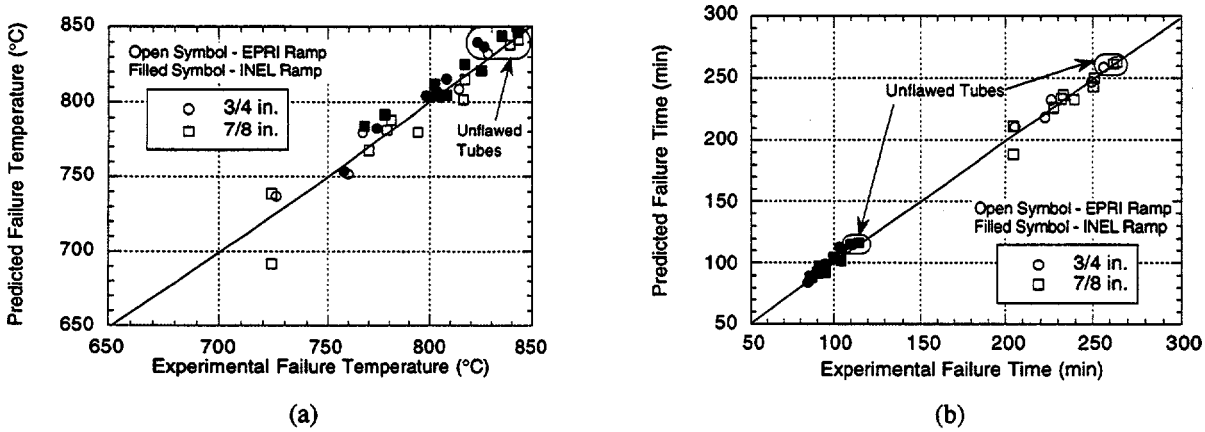

Fig. 12 Comparison of predicted (by creep rupture model) versus observed (a) failure temperatures and (b) times (above 300°C) to failure for high-temperature failure tests conducted with the INEL and EPRI temperature ramps.

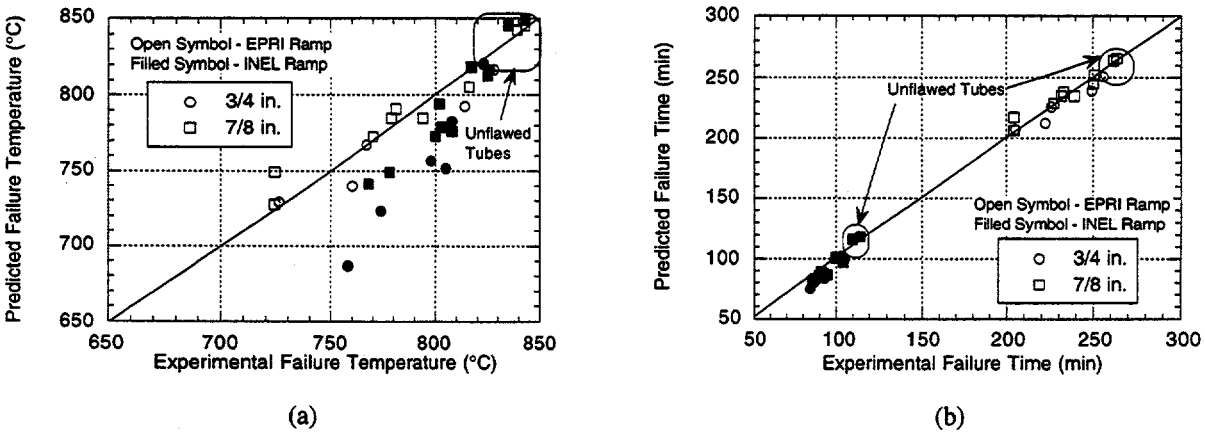

Fig. 13 Comparison of predicted (by flow stress model) versus observed (a) failure temperatures and (b) times (above 300°C) to failure for high-temperature failure tests conducted with the INEL and EPRI temperature ramps.

Modeling Local Chemistry in PWR Steam Generator Crevices

P. J. Millett

EPRI
PO Box 10412
Palo Alto, CA 94303 USA

ABSTRACT

Over the past two decades steam generator corrosion damage has been a major cost impact to PWR owners. Crevices and occluded regions create thermal-hydraulic conditions where aggressive impurities can become highly concentrated, promoting localized corrosion of the tubing and support structure materials. The type of corrosion varies depending on the local conditions, with stress corrosion cracking being the phenomenon of most current concern. A major goal of the EPRI research in this area has been to develop models of the concentration process and resulting crevice chemistry conditions. These models may then be used to predict crevice chemistry based on knowledge of bulk chemistry, thereby allowing the operator to control corrosion damage. Rigorous deterministic models have not yet been developed; however, empirical approaches have shown promise and are reflected in current versions of the industry-developed secondary water chemistry guidelines.

INTRODUCTION

Over the past two decades, steam generator (SG) corrosion has been one of the major problems associated with operating Pressurized Water type Nuclear Reactors (PWR). These costs include replacement of SG's after only 10-15 years of a 40 year design lifetime. The maintenance of existing SG's results in extended refueling outages and forced shutdowns. These outages can cost up to one million dollars per day for replacement power.

Localized corrosion of the SG tubes and other SG components is due to the presence of an aggressive environment in local crevices and occluded regions. In crevices and on vertical and horizontal tube surfaces, corrosion products and particulate matter can accumulate in the form of porous deposits. The SG water contains impurities at extremely low levels (ppb). Low levels of non-volatile impurities, however, can be efficiently concentrated in crevices and sludge piles by a thermal hydraulic mechanism. The temperature gradient across the SG tube, coupled with local flow starvation, produces local boiling in the sludge and crevices. Since mass transfer processes are inhibited in these geometries, the residual liquid becomes enriched in many of the species present in the SG water. The resulting concentrated solutions have been shown to be aggressive and can corrode the SG materials. This corrosion may occur under various conditions which result in different types of attack such as pitting, stress corrosion cracking, wastage and denting. A major goal of EPRI's research program has been the development of models of the concentration process and the resulting crevice chemistry. An improved understanding should eventually allow utilities to reduce or eliminate the corrosion by the appropriate manipulation of the steam generator water chemistry and/or crevice conditions.

EXPERIMENTAL STUDIES AND CONCENTRATION MODELS

Packed Crevices

A number of investigators have developed mathematical models which attempt to predict the rate of increase in concentration and the maximum concentration of impurities and additives which can be achieved in packed crevices and porous deposits under heat transfer conditions. Because it is diffcult to describe the fluid flow, heat, and mass transfer processes associated with the local concentration process, much effort has been associated with developing semi-empirical models based on the operation of model boilers and heated crevices in the laboratory.

A number of experimental studies have been carried out on tube support plate type geometries. These crevices are double ended and can be packed with corrosion product deposits. EPRI has sponsored several experimental programs focusing on concentration processes in crevices packed with corrosion products, carbon fibers and powdered magnetite as simulants of the natural corrosion product which deposits in crevices in the field. This includes the work of Mann (1), Campan (2), Baum (3), and Balakrishnan (4). All of these studies have shown that packed crevices can achieve significant concentration factors in relatively short times. Additionally, the maximum concentration factor in the crevice is a strong function of the available superheat and is only weakly dependent on the absolute bulk water concentration. On the other hand, the rate of accumulation is directly proportional to the bulk water concentration.

Although accelerated corrosion has occurred under the sludge pile region of many steam generators, only one systematic study of hideout processes within sludge has been performed. Gonzalez and Spekkens (5) performed a study of sludge pile concentration processes using a simulated sludge. Brunet and Campan (6) also studied sludge pile concentration processes,

although the main thrust of this work was tube sheet crevices. Studies performed for tubesheet crevice conditions were performed by Finnegan (7).

More recently, Takamatsu and co-workers (8) have investigated concentration processes in a single ended crevice. Their crevice was left unpacked and they measured the rate and extent of accumulation of impurities in the crevice in both the laboratory and in the field. The field measurements at Ohi were qualitatively in agreement with the results of both their own and other laboratory programs with respect to key aspects of the concentration process. This work has increased the confidence level in extrapolating results from other laboratory programs to field conditions.

Lumsden (9) has also been conducting tests in a highly instrumented heated crevice. The first measurements were made in a crevice similar to that of Takamatsu and the results were similar. Later tests have been performed in a diamond packed tube support type crevice. Diamond packing is being used because it is inert and will not interfere with electrochemical and reman spectroscopy measurments planned for the crevice. Early results from Lumsden have shown that sodium hydroxide concentrates to excessive levels in the crevice, resulting in a lower crevice electrochemical potential than the bulk water as expected. The maximum concentration appears to be a function of the available superheat. After thorough laboratory testing, Lumsden's device will be installed at the Ohi plant in Japan. It is planned to perform in-situ electrochemical and reman spectroscopy measurements at Ohi. Direct sampling of the crevice solution will also be possible as in the laboratory device. It is hoped that the evolution of the concentration process and electrochemistry in the crevice can be followed on a near real-time basis.

The experimental studies mentioned above have stimulated the development of a number of mathematical models which describe how impurities accumulate in local regions of the SG (4-5,10-12). Most of the models can generally be characterized as macroscopic, where the liquid solution in the crevice or sludge is considered well-mixed so that an average concentration can be used to describe the liquid solution. A mass balance is performed on the control volume (crevice or sludge pile pore solution). The mass balance considers a mass flowrate of impurities into the control volume. The impurities are removed from the control volume by volatilization, mechanical carryover, and diffusion. One or more of these processes have been neglected by different authors. The model for the sludge pile is quite similar to the support plate models, owing to the similarity in the transport processes. Some of the models do a reasonable job of predicting the rate at which impurities accumulate in the crevice, which has been shown to be directly related to the rate of heat transfer in the occluded region and the concentration in the bulk water. The heat transfer rate is dependent on a number of factors including whether the crevice or sludge is partially steam blanketed. When removal from the occluded region by volatility considerations, diffusion and or mechanical carryover are small compared to the rate at which the specie accumulates by boiling, the accumulation rate is directly proportional to the bulk water concentration. This has led to the recognition that the concentration in the crevice could be correlated to the bulk water concentration multiplied by the exposure time (ppm x hrs). This simple concept has been shown to be adequate for describ

The accumulation rate in the crevice must eventually go to zero and an equilibrium concentration in the crevice must be reached. If the specie being concentrated is sufficiently soluble and is relatively non-volatile, the equilibrium concentration has been shown experimentally to be dictated by the available superheat and the boiling point elevation characteristics of the specie under consideration. This experimental fact is in direct contradiction with predictions of the well-mixed model discussed above when mass transfer is considered. Using any reasonable diffusion or mass

transfer coefficient, one would conclude that the equilibrium concentration would be limited by mass transfer considerations under most conditions.

As equilibrium is approached, the experimental data show a somewhat rapid transition from a linear accumulation rate to equilibrium. Mann and others noted that these obsevations likely result from a mechanism where the non-boiling solution fills the crevice from the middle first and then grows towards the mouth of the crevice. The average diffusion length will be proportional to the distance between the mouth of the crevice and the non-boiling solution. The diffusion flux will rapidly increase as the diffusion length decreases and bring about equilibrium. These observations led to the development of more sophisticated mathematical models of concentration processes in sludge and crevices which recognize that concentration profiles must exist in the liquid, and therefore the solution cannot be assumed to be well-mixed.

This more fundamental approach to modeling transport processes in occluded regions considers the crevice or sludge to consist of a number of differential elements which must be integrated with appropriate boundary conditions. Such detailed models of local concentration processes in porous deposits of PWR steam generators have been developed by Millett and Fenton (13) and Pan and co-workers (14). The model described in ref. 12 is based on the application of the first principles of heat, mass and momentum transfer. The model shows that fully packed crevices and sludge piles will achieve concentration factors which are limited by the available superheat under high heat flux conditions. Reducing the heat flux or the length of the deposit or crevice can cause the concentration factor to be limited by mass transfer considerations. The model shows that species with vapor-liquid distribution coefficients slightly less than one will concentrate to some degree locally. The 1-D model indicates that there is little back mixing in packed crevices and sludge. Impurities will reach the thermodynamic limit deep within the crevice first and then fill towards the mouth. Therefore, it can be concluded that much simpler well-mixed models of the crevice appear to be inadequate for describing fully packed crevices and sludge piles.

MacDonald and co-workers have taken the model of Millett and Fenton and expanded it to describe the electrochemistry of the crevice (15) under EPRI sponsorship. The ultimate goal is to produce a mixed potential model of the crevice. Early results suggest that the crevice may be polarized by several hundred millivolts under some conditions. The plan is to compare the model predictions to measurements taken in Lumsden's experimental program both in the laboratory and at the Ohi plant.

Open Crevices

In open or partially fouled crevices, impurities may concentrate at or near the contact point of the tube with the support. This can occur in broached support plates and in eggcrate type supports. Much less experimental data is available for these types of crevices. Limited data is available for eccentric drilled hole crevices where the tube is touching the support plate but the crevice is otherwise empty (4, 16). In these studies, a linear accumulation rate is observed initially. The equilibrium mass of a given specie is significantly lower than in the fouled crevice. It is speculated that the concentration takes place only at or very close to the contact point and therefore the volume of the concentrated liquid is much smaller. Away from the contact point, mass transfer processes are suff~cient to prevent the buildup of impurities.

Little attention has been given to modeling these types of crevices. It is likely that the mixing in this crevice is better than in the completely packed crevice. An alternative to the well-mixed or the differential element model would be to describe the crevice as several small well mixed control volumes in series. This approach describes the mixing as somewhat intermediate

between the other two approaches. The well-mixed model assumes that the entire crevice can be described by one control volume and the differential approach assumes an infinite number of control volumes in series. In all likelihood, both packed crevices and sludge piles may also be more appropriately modeled using this approach. The number of control volumes would be fitted to detailed experimental data. This approach can be taken using EPRI's MULTEQ code as described by Millett and Paine (17).

CREVICE CHEMISTRY

All of the concentration models discussed so far describe the thermal-hydraulic and mass transfer processes for a single specie concentrating in the crevice. These models can in theory be extended to more complex crevice solutions, however, this would make the models nearly intractable. First, it must be recognized that many of the parameters used in the concentration models will be a function of the detailed solution composition. The solution composition is a function of thermodynamic and kinetic processes associated with dissociation, volatilization and precipitation. These processes in turn are influenced by the thermal-hydraulics. A complete rigorous mathematical model of the crevice will require close coupling of both the thermal-hydraulics and solution thermodynamic equations.

As a first approach, EPRI has addressed this issue in the MULTEQ code by providing several simplified models of the concentration process. These models assume that the system is in thermodynamic equilibrium at all times. Rate processes such as the reaction kinetics of the solid metal surface interacting with the local environment are not included in the present models. The thermodynamic model does account for complex ion formation, solute precipitation, and distribution of the volatile neutral species into the steam phase. Redox reactions are considered in one version of the code, so that the redox potential can be calculated. These thermodynamic processes are important and are believed to dictate the solution composition.

Several different options are available in MULTEQ to describe the conservation of mass as evaporation of water takes place in a water/steam/solid system. These different options or models can be used to simulate the local concentration process which occurs within SG's. The models are flexible so that the degree of mixing in the crevice as described previously can be simulated by the user. The main difficulty in modeling crevice chemistry with MULTEQ is the uncertainty in the concentration of impurities in the bulk water which is a required input. Impurity levels in the SG blowdown of a well operated PWR are on the order of a ppb or less. Simple parametric studies performed by varying the input concentrations of various bulk water species show that sign)ficant variations are predicted in the final solution composition. Several innovative approaches are currently being evaluated to predict crevice chemistry using hideout return data. These approaches will be discussed in the remainder of this paper.

Real- or Near Real-Time Crevice Chemistry Predictions

Several approaches can be taken to predict the crevice chemistry. One approach is to measure the bulk water impurities on a real time basis and through modeling or empirical measurements, assess the rate at which the bulk water impurities are concentrating in the crevices. This rate is then integrated over time to yield the crevice inventory. The crevice pH is calculated directly from the inventory. This approach offers the advantage that the crevice pH is calculated on a real time basis. Instantaneous changes in the bulk water chemistry are reflected in the calculated pH. In practice, this approach fails for a number of reasons. First, as previously indicated, the bulk water impurities are often at or near their detection limits. Secondly, although tremendous insights have been developed from modeling the thermal-hydraulic phenomena responsible for the

concentration of species in crevices, a single tractable 'a priori' model has not yet been developed. Alternatively, an empirical approach has been pursued. Here the average "hideout" or concentration rate is measured for the entire steam generator (18). Measurements in operating plants have shown that the average hideout rate is proportional to the bulk water concentration for most impurities, in agreement with analytical models of crevice concentration processes that have been developed. This approach has been incorporated into an algorithm known as CREV-SIM (19) designed to track the crevice chemistry on a real time basis. So far, this approach has not been entirely successful. As the analytical models suggest, it is likely that the hideout rate is both a function of the crevice chemistry (e.g. pH, potential, etc.) and the physical condition of the steam generator crevices (e.g. porosity, permeability, etc.). Many of these variables change quickly enough that frequent measurement of the "hideout" effficiency may be required to improve this technique as a method of predicting crevice chemistry.

Another approach is based on an evaluation of the hideout return chemistry in the steam generator when the plant is shut down. When the heat flux is reduced, the concentrated solution can diffuse out of the crevice and into the bulk water. In practice, this is observed and is detected as an increase in concentration of impurities in the bulk water. Assuming that the rate of "hideout" return is much greater than the rate of input of impurities into the steam generator through the feedwater, the increase in concentration in the steam generator during a shutdown can be assumed to have come from the crevices. This approach to assessing the crevice chemistry has two limitations. First, only an average crevice chemistry across the thousands of crevices can be inferred, and secondly, the hideout return can only be measured perhaps once per year or less frequently when the plant shuts down. Nonetheless, evaluation of hideout return data is believed to yield the most useful insight into the crevice chemistry at this time.

Establishing a Target based on Hideout Return Data

Even though hideout return of several species may offer the best chance at assessing the crevice chemistry, the data is still too uncertain to allow one to confidently assess such important parameters as the crevice pH(t). This is due to an array of uncertainties, including an incomplete knowledge of how compounds precipitate in the crevice, and the inability to distinguish species hideout return from their respective steam generator hideout locations. However, a logical approach has been developed which is believed to provide a high probability that the crevice pH(t) is in the range which will minimize IGSCC.

The approach is based on the theory that the crevice pH(t) will be within the target range if the ratio of the highly soluble cation and anion impurities in the crevice is near one, and if sufficient quantities of less soluble impurities are present to buffer the solution pH in the target range. This approach is probabilistic in the statistical sense, since being within the target range is a function of both more certain parameters (e.g. the ratio of highly soluble cation and anion impurities) and uncertain parameters (e.g. the insoluble compounds). Previous deterministic approaches to predicting crevice chemistry using MULTEQ incorporate all of the cations and anions observed in the hideout return (e.g. both highly soluble and less soluble species) as a basis for calculating the crevice pH(t). It is recognized that impurities having limited solubility in the crevice such as calcium, magnesium and silica can impact the pH(t) by a large amount. However, the quantity of these species that actually exists in equilibrium with the highly soluble impurities (e.g. sodium and chloride) in the crevice is extremely uncertain. In the new approach, a Molar Ratio Index (MRI) is defined as follows:

$$MRI=(Na+K)/(Cl+\text{ excess } SO_4)$$

where the quantities in the MRI are obtained directly from hideout return data. The MRI is based on the relative ratio of impurities that are believed to be returning from the crevice solution during hideout return. The excess sulfate term takes into account the fact that sulfate in excess of that required to produce a precipitate of calcium sulfate may exist in the crevice. If sulfate is not found to be in excess of calcium, sulfate is excluded from the MRI. The MRI is based on the physical chemistry of high temperature solutions as predicted by MULTEQ. The interested reader is referred to reference 20 for a more detailed description of this approach.

If it is accepted that the MRI using hideout return data is a useful indicator for the target crevice chemistry, one must then address what hideout return data should be used for establishing the MRI. There are numerous factors involved in the hideout process (e.g., operating history, design and fouling conditions of the steam generators, etc.). Hideout return evaluations must consider these factors, since the locations from which the species returned must be known to predict the environment. To date, crevice chemistry estimates generally have been based on what has been referred to as "prompt" hideout return. This is the cumulative mass of impurity return occurring on shutdown prior to initiation of cooldown of the plant. To increase confidence in crevice chemistry predictions developed from HOR data, development of a HOR model that distinguishes between impurity return from crevices, sludge piles, and tubing surfaces as well as that due to desorption (particularly sulfate) is the ultimate goal. Such an approach is being evaluated at several US utilities (21).

SUMMARY

Although the ultimate goal of the industry is to develop rigorous deterministic models to predict crevice chemistry from the measured bulk water, it is recognized that more empirical approaches must be taken in the interim. In particular, probabilistic type models offer potential for insuring the crevice chemistry is in a pre-defined target range. Based on the principles outlined above, it is believed that attempts to modify the crevice solution to produce a MRI as close as possible to one gives a higher probability of achieving a crevice pH within the target range. Although this approach is believed to be more conservative than the conventional technique using tools like MULTEQ, it is still useful to employ MULTEQ to develop insight into the composition of the crevice chemistry. In addition, thermal-hydraulic models of the crevice provide great insight into the behavior of impurities and additives and can be used in conjunction with other tools to establish the chemistry control program.

REFERENCES

1. MANN G.M.W. and CASTLE R. "Hideout and Return of Chloride Salts in Heated Crevices Prototypic of Support Plates in Steam Generators," EPRI Report NP-5015, 1987.

2. CAMPAN J.L. and SHOEMAKER C.E. "Sodium Hideout Studies in Steam Generator Crevices," Proceedings of Environmental Degradation of Materials in Nuclear Power Systems, Water Reactors, Traverse City, 1988.

3. BAUM A.J., SMITH-MAGOWEN D. and LEE A.Y. "Crevice Hideout Return Testing," EPRI Report NP-4678, 1986.

4. BALAKRISHNAN P.V. "Hideout and Return of Complex Mixtures in Crevices," EPRI Report NP-7494, 1991.

5. GONZALEZ F. and SPEKKENS P. "Concentration Processes under Tubesheet Sludge Piles in Nuclear Steam Generators," Nuclear Journal of Canada, vol 1:2, 129-240.

6. CAMPAN J.L. and BRUNET J.P. "Hideout of Sodium Salts in Tubesheet Crevices," EPRI Report NP-5265, 1987.

7. FINNEGAN D.J. and FORREST J.E. "Chemical Concentration and Corrosion in PWR Steam Generator Tubesheet Crevices," Proceedings of Water Chemistry of Nuclear Reactor Systems 5, BNES, London, 1989.

8. TAKAMATSU H., MATSUEDA K., KADOKAMI E., ARIOKA K., TSURUATA T., OKAMATO S., and UENO T. "Evaluation of SG Crevice Environment By Directly Sampled Method Using an On-Site Autoclave Facility," Proceedings of Environmental Degradation of Materials in Nuclear Power Systems-Water Reactors, Monterey, 1991.

9. LUMSDEN J., STOCKER P., and MILLETT P.J. "Effects of Feedwater Chemistry on Hideout in a Prototypic SG Tube/Tube Support Plate Crevice," to be published in Proceedings of Water Chemistry of Nuclear Reactor Systems 7, BNES, London, 1996.

10. BAUM A.J. Restricted Geometries and Deposits The ASME Handbook on Water Technology For Thermal Power Svstems, P. Cohen, editor, ASME, Chapter 6.

11. CLEARY J.G., VONNIEDA G.E. and LINDSAY W.T. "Diffusion and Hideout in Crevices," EPRI Report NP-2979, 1983.

12. MILLETT P.J. and FENTON J.M. "Transport Processes in PWR Support Structure Crevices," Proceedings of Environmental Degradation of Materials in Nuclear Power Systems-Water Reactors, Jekyll Island, 1989.

13. MILLETT P.J. and FENTON J.M. "A Detailed Model of Localized Concentration Processes in Porous Deposits of SG's," Proceedings of Environmental Degradation of Materials in Nuclear Power Systems-Water Reactors, Monterey, 1991.

14. PAN C. "On the Concentration Limits in Steam Generator Tube-Support-Plate Crevices," Nuclear Engineering and Design, 1991, vol. 127, 69-84.

15. ENGELHARDT G., URQUIDI-MACDONALD M., SEHGAL A., MACDONALD D., and MILLETT P. "Modeling Corrosion in Steam Generator Crevices under Heat Transfer Conditions," Proceedings of Control of Corrosion on the Secondary Side of Steam Generators, NACE, Airlie, 1995.

16. MILLETT P.J., ALEXANDER J.H. and OSCARSON J. "MULTEQ: Equilibrium of an Electrolytic Solution with Vapor-Liquid Partitioning and Precipitation, Volume 3, Theory Manual," EPRI Report NP-5561-CCML, August 1992.

17. MILLETT P.J. and PAINE, J.P.N. "Modeling Local Chemistry in PWR Steam Generator Crevices," Proceedings of Water Chemistry of Nuclear Reactor Systems 6., BNES, London, 1992.

18. SAWOCHKA S.G., and CHOI S.S., "Prairie Island-2 Steam Generator Hideout," EPRI NP-7236, April 1991.

19. SAWOCHKA S.G., CHOI S.S., and MILLETT P.J., "Prediction of Crevice Chemistry in PWR Steam Generators," Proceedings of International Conference on Chemistry in Water Reactors: Operating Experience and New Developments, Nice, France, SFEN, April 1994.

20. MILLETT P.J., "Developing a Crevice Chemistry Control Target from Uncertain Data," Proceedings of Control of Corrosion on the Secondary Side of Steam Generators, NACE, Airlie, 1995.

21. BROBST G.E., and RIDDLE J.M., "POOR Molar Ratio Control Guidelines Volume 3: Hideout Return Evaluation Guidelines," EPRI TR-104811, Volume 3, October 1995.

NRC FORM 335 (89) NRCM 1102, 3201, 3202

U.S. NUCLEAR REGULATORY COMMISSION

BIBLIOGRAPHIC DATA SHEET

(See instructions on the reverse)

1. REPORT NUMBER (Assigned by NRC, Add Vol., Supp., Rev., and Addendum Numbers, if any.)

NUREG/CP-0157
Vol. 2

2. TITLE AND SUBTITLE

Proceedings of the Twenty-Fourth Water Reactor Safety Information Meeting

- Reactor Pressure Vessel Embrittlement and Thermal Annealing
- Reactor Vessel Lower Head Integrity
- Evaluation and Projection of Steam Generator Tube Condition and Integrity

3. DATE REPORT PUBLISHED

MONTH	YEAR
February	1997

4. FIN OR GRANT NUMBER

A3988

5. AUTHOR(S)

Compiled by Susan Monteleone, BNL

6. TYPE OF REPORT

Conference Proceedings

7. PERIOD COVERED *(Inclusive Dates)*

October 21-23, 1996

8. PERFORMING ORGANIZATION - NAME AND ADDRESS *(If NRC, provide Division, Office or Region, U.S. Nuclear Regulatory Commission, and mailing address; if contractor, provide name and mailing address.)*

Office of Nuclear Regulatory Research
U.S. Nuclear Regulatory Commission
Washington, DC 20555-0001

9. SPONSORING ORGANIZATION - NAME AND ADDRESS *(If NRC, type "Same as above"; if contractor, provide NRC Division, Office or Region, U.S. Nuclear Regulatory Commission, and mailing address.)*

Same as Item 8 above.

10. SUPPLEMENTARY NOTES

C. Bonsby, NRC Project Manager. Proceedings prepared by Brookhaven National Laboratory

11. ABSTRACT *(200 words or less)*

This three-volume report contains papers presented at the Twenty-Fourth Water Reactor Safety Information Meeting held at the Bethesda Marriott Hotel, Bethesda, Maryland, October 21-23, 1996. The papers are printed in the order of their presentation in each session and describe progress and results of programs in nuclear safety research conducted in this country and abroad. Foreign participation in the meeting included papers presented by researchers from Finland, France, Japan, Norway, Russia and the United Kingdom. The titles of the papers and the names of the authors have been updated and may differ from those that appeared in the final program of the meeting.

12. KEY WORDS/DESCRIPTORS *(List words or phrases that will assist researchers in locating the report.)*

BWR Type Reactors - Reactor Safety, Nuclear Power Plants - Reactor Safety, PWR Type Reactors - Reactor Safety, Reactor Safety - Meetings, Annealing, Embrittlement, Fracture Mechanics, Fracture Properties, Pressure Vessels, Reactor Components, Steam Generators

13. AVAILABILITY STATEMENT

Unlimited

14. SECURITY CLASSIFICATION

(This Page) Unclassified

(This Report) Unclassified

15. NUMBER OF PAGES

16. PRICE

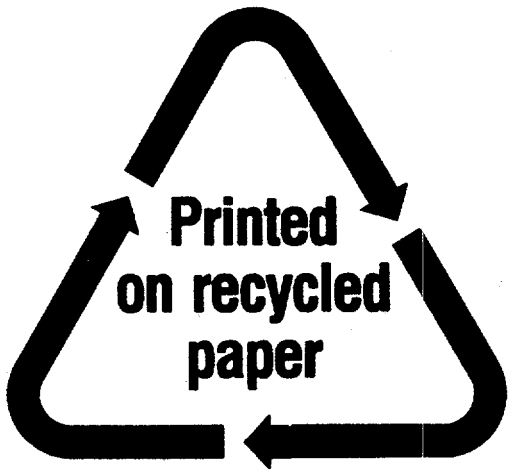

Federal Recycling Program